AN UNSTEADY AERODYNAMICS REDUCED-ORDER MODELING METHOD FOR MANEUVERING, FLEXIBLE FLIGHT VEHICLES

A Dissertation
Presented to
The Academic Faculty

by

Brett R. Hiller

In Partial Fulfillment
of the Requirements for the Degree
Doctor of Philosophy in the
School of Aerospace Engineering

Georgia Institute of Technology
August 2019

AN UNSTEADY AERODYNAMICS REDUCED-ORDER MODELING METHOD FOR MANEUVERING, FLEXIBLE FLIGHT VEHICLES

Approved by:

Professor Dimitri Mavris, Advisor
School of Aerospace Engineering
Georgia Institute of Technology

Professor Marilyn Smith
School of Aerospace Engineering
Georgia Institute of Technology

Dr. Bradford Robertson
School of Aerospace Engineering
Georgia Institute of Technology

Dr. Neal Frink
Configuration Aerodynamics Branch
NASA Langley Research Center

Dr. Walter Silva
Aeroelasticity Branch
NASA Langley Research Center

Date Approved: June 13th 2019

To my younger brothers and sisters,

May this work serve as a reminder that you are capable of achieving any goals you set forth.

ACKNOWLEDGEMENTS

This dissertation marks the end of my long, yet fulfilling journey as a graduate student at Georgia Tech. Over the past six years, I have had the privilege of gaining several mentors and friends, whom I now consider family. Without their contributions, advice, and support, this achievement would not have been possible. I would like to gratefully acknowledge those who made a difference along the way.

First and foremost, I would like to express my sincere gratitude for the members of my dissertation committee and technical reviewers of my work. I would like to thank my Ph.D. advisor, instructor, and mentor Professor Dimitri Mavris for welcoming me into the Aerospace Systems Design Laboratory, instilling in me sound fundamentals in aircraft design/analysis/optimization, providing me with continuous advice and support throughout each phase of the Ph.D. process, and ultimately, setting me up with the opportunity to begin my career at NASA Langley Research Center. I would like to thank Professor Marilyn Smith for taking the time out of her schedule to review my work and provide valuable technical feedback. I would like to express my great appreciation for Dr. Bradford Robertson for meeting with me on a weekly, and often daily, basis in the proposal phase of this dissertation. His guidance and criticisms were instrumental in the formulation of a deliberate and well-scoped research plan. I would like to thank Sally Viken and Steve Bauer from NASA Langley Research Center for their thorough and vital content revisions. Last but not least, I would like to acknowledge Dr. Neal Frink and Dr. Walter Silva for their unwavering mentorship and encouragement throughout this dissertation. Their technical expertise and feedback regarding the topics of computational fluid dynamics, reduced-order modeling, and aeroelasticity were invaluable to any resulting success I may have achieved.

My graduate school experience would not have been as enjoyable or productive without the support and advice of many fellow graduate students and friends. Therefore, I would like to thank all of my friends from ASDL that I've had the pleasure of knowing. Marcus Bakke, François Bolduc-Teasdale, and Yann Charront, among several others, for the friendship and memories created during first year. Tejas Puranik and Etienne Demers-Bouchard for providing an outsider's perspective on the ideas and explanations in my work. A special mention goes to my roommate, training partner, and lifetime friend, Michael Bozeman for the countless hours spent solving white board problems together in preparation for qualifying exams, the feedback provided throughout each phase of this dissertation, the support in diagnosing/solving technical problems on a daily basis, and the friendship beyond work and school. Finally, thanks to my lifelong friend Wesley Barrows, for his relentless support and encouragement since high school.

I would like to thank my parents and siblings for the continuous support, guidance, and encouragement that they have provided throughout my life. While neither of my parents completed high school, they have always inspired me to incessantly pursue my goals, no matter how formidable and no matter our current circumstances. Despite his lack of formal education, my father remains one of the most logical and proficient problem solvers that I have ever met. He will always inspire me to understand all attributes of a problem and seek solutions, however simple or atypical at first glance.

Finally, I would like to thank to my best friend and the most important person in my life, my wife, Sarah. Over the past 10 years, she has been unfaltering in listening and providing advice on my most stressful days, supporting our life responsibilities on my busiest days, and providing encouragement on my many days of self-doubt. She is a constant source of happiness, humor, and love. This dissertation is as equally yours as is mine. You da real MVP.

TABLE OF CONTENTS

LIST OF TABLES

LIST OF FIGURES

SUMMARY

Accurate aerodynamic predictions remain a cornerstone of the aircraft design process due to their significance in determining the performance and stability and control characteristics of aircraft. Traditional flight dynamics modeling has historically relied on the use of quasisteady stability derivatives, often calculated using simplified linear aerodynamic methods. These models are inherently incapable of predicting the nonlinear, unsteady aerodynamics encountered by modern flexible aircraft. Inaccurate predictions of such phenomena can lead to suboptimal vehicle performance and/or inaccurate control law design, potentially leading to loss of control of the vehicle.

Recent advances in digital computing have motivated interest toward virtual flight simulation, for which multidisciplinary numerical simulations are used to evaluate an aircraft's performance and stability and control characteristics at full-scale flight Reynolds and Mach numbers. Despite their demonstrated feasibility, these simulations often require thousands of computational hours, limiting their adoption and widespread application for aircraft design and analysis.

Reduced-order modeling is viewed as a key enabler for the viable application of virtual flight simulation methods. Reduced-order models are mathematical models aimed at accurately predicting the fundamental dynamics of a system at a computational cost much less than what is required in solving the original governing equations. These methods approximate the full-order numerical simulations of a system by extracting and reconstructing pertinent dynamic data solutions, without making any limiting physical modeling assumptions.

Significant progress in reduced-order modeling has been made over the past two decades with the development of a variety of reduced-order models for efficient unsteady aerodynamic predictions. However, most unsteady aerodynamic reduced-order models have been primarily used for either predicting the aerodynamic response of rigid maneuvering vehicles or identifying aeroelastic instabilities, such as a flutter. Multidisciplinary reduced-order models for virtual flight simulations remain a desirable, yet relatively unexplored area of research.

The objective of this dissertation is to develop a reduced-order model capable of providing quantitatively accurate, yet computationally efficient predictions of the nonlinear, unsteady aerodynamics encountered by maneuvering, flexible flight vehicles. Indicial response theory is a nonintrusive reduced-order modeling approach, which characterizes a system's dynamics through identification of the system response due to unit step changes in a system's inputs. A CFD-based dynamic modal aeroelastic analysis is proposed for identification of indicial responses with respect to the vehicle motion parameters. Linear and nonlinear indicial response reduced-order models, based on the mathematical principle of convolution, are extended to predict the unsteady aerodynamic response of flexible flight vehicles subject to arbitrary vehicle maneuvers.

The proposed reduced-order model is evaluated through comparisons to full-order numerical simulations of the NASA X-56A Multi-Utility Technology Testbed Aircraft undergoing a series of prescribed forced oscillation motions and a generalized six-degree-of-freedom trajectory. Quantified assessments of the trade-off in computational cost and accuracy of the proposed reduced-order model demonstrate performance improvements relative to high-fidelity aeroelastic simulations and traditional stability derivative models for increasingly unsteady vehicle maneuvers, where computational benefits increase with the number of maneuvers needed to characterize operation within a vehicle's planned flight envelope.

CHAPTER I

MOTIVATION AND BACKGROUND

This chapter provides a brief overview of the historical challenges in accurately predicting the performance and stability and control characteristics of maneuvering aircraft, motivating interest toward the use of numerical simulation tools for improved assessments. A summary of notable research efforts and practical limitations of computational fluid dynamics-based aircraft flight dynamics modeling is presented. Reduced-order modeling is then introduced as a key enabler for the viable incorporation of high-fidelity multidisciplinary simulations in the aircraft design process.

1.1 Aerodynamic Prediction Challenges for Maneuvering Aircraft

Accurate aerodynamic predictions remain a cornerstone of the aircraft design process due to their significance in determining performance and Stability and Control (S&C) characteristics. This is exemplified by the widespread coupling of aerodynamics to other aircraft disciplines for design applications including aerodynamic shape optimization, structural sizing, static and dynamic stability analysis, control law development, and flight performance evaluations.

The aerodynamic information required in aircraft design can range from scalar quantities, such as cruise drag, maximum lift at low speed, or S&C metrics to vector-valued field variables, such as pressure distributions along an aircraft's surface. Pertinent data are typically provided throughout the design process using a variety of aerodynamic data sources, which are generally categorized as either historical regression, linear aerodynamic modeling, numerical simulation, wind tunnel testing, or flight testing. The aerodynamic data needed and the data source utilized are often a

consequence of the design objectives of the design phase under consideration.

The aircraft design process is commonly partitioned into three principle phases: conceptual, preliminary, and detailed design. Beginning with conceptual design, the primary objective is to rapidly explore and assess candidate vehicle configurations for their potential to meet specified mission and flight performance requirements. Design tools are employed to perform trade-off analyses between weight, drag, fuel consumption, payload/range, thrust, and other system-level performance metrics to arrive at a down-selected design configuration. The nature of the conceptual design phase necessitates quantified performance metrics accurate enough to make confident design decisions, yet generated in an efficient enough manner to enable exploration of the most configurations possible. In the context of flight dynamics, these requirements have traditionally encouraged the use of historical regressions or simplified aerodynamic models.

Several aerodynamic models exist for use in aircraft design and primarily differ based on their respective physical modeling assumptions to the full-order Navier-Stokes equations. Figure 1 illustrates the trade-off in required computational resources versus modeling applicability, i.e., fidelity, for each of the aerodynamic modeling methods. These simplifications provide greater computational efficiency at the cost of reducing their general applicability.

The linear aerodynamic models commonly used in conceptual design are often based on the potential flow equations. The potential flow equations simplify the Navier-Stokes equations by assuming zero viscosity, zero vorticity, and small perturbations about an idealized flow condition. Such physical modeling simplifications allow for accurate aerodynamic predictions of the important steady-state flight conditions considered in conceptual design, such as cruise, with a significant cost savings over higher fidelity models.

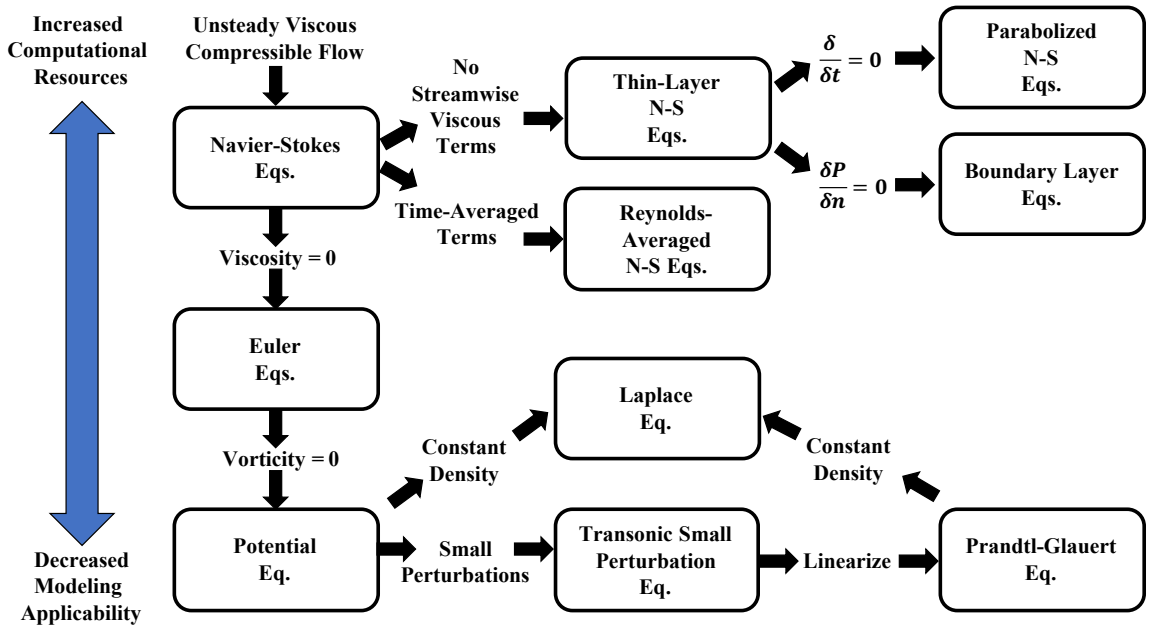

Figure 1: Physical modeling assumptions of NS equations (adapted from Jameson et al. [51]).

While the historical use of simplified aerodynamic models early in the aircraft design process allows for efficient design space exploration, downselected configurations are often characterized by significant design uncertainty, only reduced through incorporation of higher fidelity aerodynamic data sources, such as numerical simulations, wind tunnel tests, or flight tests. The impact on design knowledge, design freedom, and cost committed as a program transitions from conceptual to detailed design is illustrated in Fig. 2.

The trends depict a design process characterized by a slow increase in design knowledge, a rapid decrease in design freedom, and a rapid increase in cost committed. By reserving higher fidelity information sources for later in design, issues with the aircraft may not be discovered until a time when the opportunity to make major design changes is limited. This is evidenced by the vast number of commercial and military aircraft programs discovering undesirable performance and S&C problems

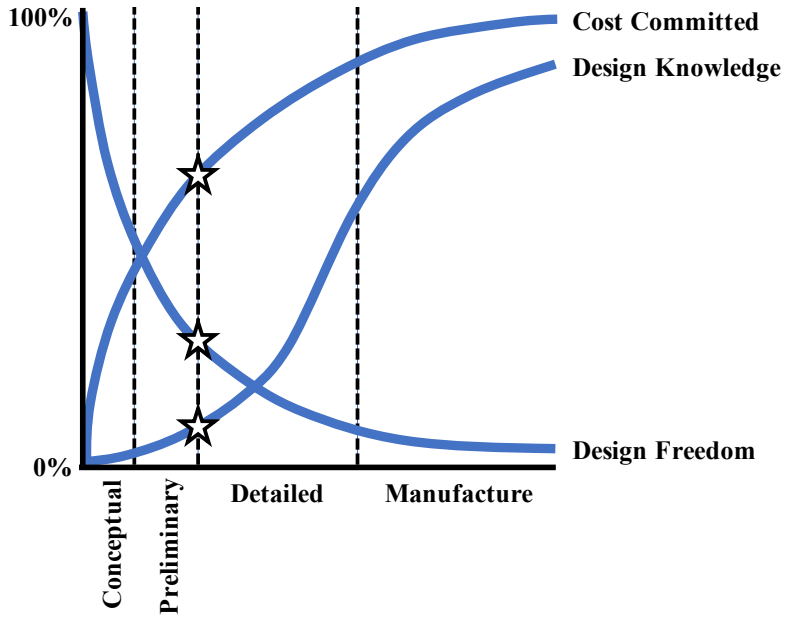

Figure 2: Aircraft design cycle (adapted from Mavris et al. [73]).

during flight testing. Notable examples include: the F-84, F-104, Harrier, F-16, F/A-18E/F, F/A-22, V-22, Space Shuttle Orbiter, B-737NG, and the B-777 [14, 95].

A consequence of this traditional design process is an industry-adopted 'fly-and-fix' approach, whereby configuration changes must be made late in the design process, resulting in significant aircraft development costs and program delays [107]. Furthermore, these designs may be prone to mission limitations, nonoptimum performance, and even fatal accidents. It is apparent that the reliance on historical regression and linear aerodynamic modeling methods has led to a suboptimal design process. These lower fidelity models often fail to provide realistic estimates of the nonlinear, unsteady aerodynamic phenomena prevalent in maneuvering aircraft flight.

Nonlinear, unsteady aerodynamic flows are frequently encountered by modern aircraft operating within and near the extremes of their flight envelopes. Unsteady flight conditions can result from sudden control deflections, maneuvering flight at high angles of attack and/or fast motion rates, wind gusts, or fluid-structure interactions. Nonlinear variations in aerodynamic loads are often attributed to shock wave motions

and separated flow effects. The present challenges in predicting such phenomena are expected to become even greater as aircraft manufacturers pursue unconventional vehicle configurations, expanded operational envelopes, and composite structures. Thus, the inclusion of higher fidelity data sources earlier in the design process may allow for more accurate and cost-effective evaluations of future aircraft configurations.

Recent advances in digital computing have led to increased interest in the utilization of Computational Fluid Dynamics (CFD) numerical simulations for advancing the state of the art in aircraft S&C predictions and incorporating these tools earlier in the design process [19, 20, 50]. CFD simulations offer the capability to better predict nonlinear, unsteady aerodynamic phenomena encountered by modern aircraft at full-scale flight Reynolds numbers across various Mach number regimes. By leveraging CFD data for aircraft flight dynamics modeling, a virtual flight simulation capability may be developed to provide more realistic assessments of an aircraft's performance and S&C characteristics prior to physical testing.

1.2 The Pursuit of Virtual Flight Simulation

Virtual Flight Simulation (VFS), also referred to as digital flight [107], has been described as "the ability to simulate in a computer a flight maneuver satisfying the governing flow equations, the aircraft aeroelastic characteristics, the six degree-of-freedom (6DOF) equations, the flight control system, and the propulsion system." The development of such a capability would provide high-fidelity, quantitative descriptions of the complex, multidisciplinary interactions experienced by maneuvering flight vehicles, reducing the need for extensive flight testing programs.

Simulation of an aircraft's maiden flight via computer experiments would allow for the identification of inadequate performance or S&C characteristics earlier in the aircraft design cycle when the opportunity for design changes is greatest. Foreseeable benefits include reductions in developmental risks and design cycle times, in addition

to drastic cuts in mid- to long-term program costs afforded by stepwise certification [59]. Initial VFS research efforts have focused on coupling the aircraft equations of motion with CFD to predict maneuvering aircraft flight through two approaches, referred to as *Flying Through The Database* and *Flying By the Equations*.

Each of these virtual flight simulation capabilities rely on a keen understanding of aircraft flight dynamics, the science of predicting and controlling aircraft motion. Aircraft flight dynamics predictions are provided by solving the aircraft 6DOF equations of motion, which relate the position and orientation of an aircraft at any given time to the forces and moments experienced during flight. The derivation of these equations using Newton's Second Law are well-documented in any flight dynamics textbook and summarized below for introduction purposes. The conservation of linear momentum yields the three equations given by Eq. 1, and the conservation of angular momentum yields the three equations given by Eq. 2.

$$\begin{aligned} F_x &= m(\dot{u} + qw - rv) \\ F_y &= m(\dot{v} + ru - pw) \\ F_z &= m(\dot{w} + pv - qu) \end{aligned} \tag{1}$$

$$\begin{aligned} L &= m[I_{xx}\dot{p} - I_{xy}\dot{q} - I_{xz}\dot{r} + q(-I_{xz}p - I_{yz}q - I_{zz}r) - r(-I_{xz}p + I_{yy}q - I_{yz}r)] \\ M &= m[-I_{xy}\dot{p} + I_{yy}\dot{q} - I_{yz}\dot{r} - p(-I_{xz}p - I_{yz}q - I_{zz}r) + r(I_{xx}p - I_{xy}q - I_{xz}r)] \\ N &= m[-I_{xz}\dot{p} - I_{yz}\dot{q} + I_{zz}\dot{r} + p(-I_{xy}p + I_{yy}q - I_{yz}r) - q(-I_{xx}p - I_{xy}q - I_{xz}r)] \end{aligned} \tag{2}$$

The coupled nonlinear 6DOF equations of motion relate the external forces (F_x, F_y, F_z) and moments (L, M, N) acting on the aircraft to the vehicle dynamics, as described by the translational (u, v, w) and angular velocities (p, q, r). In practice, the external forces and moments may be the result of contributions from aerodynamic loads, propulsive thrust, ground effects, and/or weight. The two VFS capabilities,

Flying Through The Database and *Flying By the Equations*, primarily focus on CFD-calculated aerodynamic loads, but couple to separate forms of the 6DOF equations of motion for flight dynamics predictions.

1.2.1 Flying Through the Database

The 6DOF equations of motion require a model of the aerodynamic forces and moments experienced in flight. The choice of aerodynamic model is not limited, as the underlying mathematical structure may vary based on the assumed functional dependencies and degree of linearity. In general, the aerodynamic properties of an aircraft can vary considerably over a flight envelope with the aerodynamic loads depending nonlinearly on past and present values of several vehicle-state parameters, e.g., angle of attack, Mach number, etc. The first of the two VFS capabilities, *Flying Through The Database*, seeks to improve aircraft flight dynamics predictions by incorporating CFD simulation data into what is commonly known as the stability derivative flight dynamics model.

The most historic approach to modeling aerodynamic loads for the equations of motion is the stability derivative model, introduced by Bryan and Williams in 1904 [12, 13]. Bryan used the theory of small-perturbations to linearize the equations of motion (Eqs. 1 and 2) about steady-state flight, separating them into longitudinal and lateral modes, and introduced the mathematical concept of stability derivatives for aerodynamic load modeling. In this approach, the aerodynamic forces and moments are approximated as functions of an aircraft's instantaneous translational velocity, rotational velocity, and control surface deflection(s) values, specifically their perturbations, from a trimmed flight condition. Equation 3 expresses the aerodynamic loads as a converging Taylor-Series expansion with respect to the vehicle- and control-state parameters.

$$
\begin{aligned}
C_i = C_{i_0} &+ \frac{\partial C_i}{\partial \alpha}\Delta\alpha + \frac{1}{2}\frac{\partial^2 C_i}{\partial \alpha^2}\Delta\alpha^2 + ... \\
&+ \frac{\partial C_i}{\partial \beta}\Delta\beta + \frac{1}{2}\frac{\partial^2 C_i}{\partial \beta^2}\Delta\beta^2 + \frac{\partial C_i}{\delta\alpha}\frac{\partial C_i}{\partial \beta}\Delta\alpha\Delta\beta + ... \\
&+ \frac{\partial C_i}{\partial \delta}\Delta\delta + \frac{1}{2}\frac{\partial^2 C_i}{\partial \delta^2}\Delta\delta^2 + \frac{\partial C_i}{\partial \alpha}\frac{\partial C_i}{\partial \delta}\Delta\alpha\Delta\delta + \frac{\partial C_i}{\partial \beta}\frac{\partial C_i}{\partial \delta}\Delta\beta\Delta\delta + ...
\end{aligned} \tag{3}
$$

As means of further simplifying flight dynamics predictions, the aerodynamic functions are linearized to the more amenable form shown in Eq. 4.

$$
\begin{aligned}
C_i &= C_{i_0} + \frac{\partial C_i}{\partial \alpha}\Delta\alpha + \frac{\partial C_i}{\partial \beta}\Delta\beta + \frac{\partial C_i}{\partial \delta}\Delta\delta + ... \\
&= C_{i_0} + C_{i_\alpha}\Delta\alpha + C_{i_\beta}\Delta\beta + C_{i_\delta}\Delta\delta + ...
\end{aligned} \tag{4}
$$

In this model, resultant aerodynamic coefficients are linearly dependent functions of the steady-state aerodynamic coefficient at trim, C_{i_0}, perturbations in the vehicle-state and command variables, $\Delta\alpha$, $\Delta\beta$, and $\Delta\delta$, and the S&C derivatives, C_{i_α}, C_{i_β}, and C_{i_δ}. As the name suggests, S&C derivatives reflect a change in force or moment coefficients based on changes in vehicle state and control surface deflection, respectively. Because the flow is assumed to reach a steady-state instantaneously, the model is quasisteady. *This assumption inherently ignores any influence of previous motion states.* Regardless, Bryan's approach has found widespread success in modeling the aerodynamics of conventional aircraft configurations maneuvering at slow motion rates within benign flight regimes.

By 1920, the limitations of Bryan's stability derivative model had been recognized, and additional terms were introduced to improve agreement between predicted and observed aircraft motion [47]. The inability to account for changes in the wing-induced downwash at the tail, due to convective time delays, led to the addition of dynamic or acceleration derivatives to the pitching moment predictions [49]. In doing so, time lag of the aerodynamic response could be modeled by including the dependence on the

rate of change in pitching moment with respect to rate of change in angle of attack, $C_{m_{\dot{\alpha}}}$.

First introduced for longitudinal motions, the model has since been extended for generalized longitudinal and lateral aircraft motion predictions by including dynamic derivatives associated with the angular velocities and rate of change in angle of attack. The benefit in adding dynamic derivatives to the stability derivative model was the ability to better capture vehicle motion history effects, while retaining the practical advantage of describing the aircraft flight dynamics with a set of first-order linear differential equations.

Equations 5 and 6 represent the modern form of the stability derivative model for longitudinal and lateral aerodynamic loads, respectively. Longitudinal aerodynamic forces and moments are represented by C_j, where $j = L$, D, or m. Lateral aerodynamic forces and moments are represented by C_k, where $k = Y$, l, or n. As done in the original formulation, the assumption of aircraft symmetry motivates the decoupling of longitudinal and lateral motion modes, where the dependence of longitudinal aerodynamic loads is assumed independent of lateral state-variables, and vice versa.

$$C_j = C_{j_0} + C_{j_\alpha}\Delta\alpha + \overline{C}_{j_q}\Delta q\frac{c}{2U_\infty} + C_{j_\delta}\Delta\delta \tag{5}$$

$$C_k = C_{k_0} + C_{k_\beta}\Delta\beta + C_{k_p}\Delta p\frac{b}{2U_\infty} + C_{k_r}\Delta r\frac{b}{2U_\infty} + C_{k_\delta}\Delta\delta \tag{6}$$

The longitudinal aerodynamic forces and moments are functions of angle of attack, control surface settings, and an equivalent dynamic derivative term, $\overline{C}_{j_q}$. Incorporation of both the angular velocity and the first-order derivative for angle of attack presents an identification problem in isolating the independent effects of $\dot{\alpha}$ and q [22]. Because these terms are inherently coupled for longitudinal motions, the contributions are approximated with the equivalent term, $\overline{C}_{j_q} = C_{j_{\dot{\alpha}}} + C_{j_q}$. For lateral quasisteady

motions, dependencies on $\dot{\beta}$ are typically assumed to be negligible. The lateral aerodynamic forces and moments are then functions of sideslip angle, roll rate, yaw rate, and control surface settings.

The static and dynamic derivatives of Eqs. 5 and 6 have been historically identified via wind tunnel testing through steady-state and forced-oscillation tests [48], respectively. For identifying dynamic derivatives, test rigs are used to force longitudinal or lateral sinusoidal oscillations about an aircraft's center of gravity to observe the dynamic aerodynamic response, often as a function of oscillation frequency and amplitude. Once initial transients decay, the derivatives may be determined by measuring the in-phase and out-of-phase aerodynamic response to the forced motion [58]. Numerical techniques, such as frequency domain or regression analyses, are then used to post-process experimental data to form estimates of the dynamic derivative values.

Because the flight envelope of maneuvering aircraft are generally nonlinear, the values for the S&C derivatives are dependent on the vehicle state and flight conditions. A series of wind-tunnel tests may be used to capture S&C derivative variability throughout the envelope. The resulting derivatives are then stored in extensive tabular aerodynamic databases. Using the stability derivative approach to flight dynamics modeling, the databases are then interpolated based on a given vehicle state and flight condition to model the aerodynamic response and subsequently, estimate the trim conditions required to satisfy a target trajectory.

Developing accurate S&C derivative predictions using CFD flow solvers relies on solving two separate challenges: (1) improving the physical modeling capability of the solvers to adequately resolve the unsteady, viscous flow effects present throughout a maneuvering vehicle flight envelope and (2) developing computational techniques to efficiently extract stability and control information from CFD solutions. The *Flying through the Database* VFS approach focuses on research toward solving the latter challenge. Mader [70] provides a thorough background on two main approaches for

computing stability derivatives with CFD, which will be summarized as follows.

The first approach uses conventional derivative computation methods applied to steady CFD flow solutions to calculate static stability derivatives. The most common formulations are based on finite-differencing [15], automatic differentiation [94], or adjoint sensitivities [46]. These approaches were later extended to compute dynamic derivatives by modifying the CFD formulations to include motion based on dynamic parameters [3, 66, 93]. As an example of one of the latest approaches, Mader and Martins [69] combined the computational efficiency of analytical sensitivity methods with simple implementation of automatic differentiation to form an automatic differentiation adjoint (ADjoint) approach to compute stability derivatives. The authors demonstrate the capability of computing a complete set of static and dynamic stability derivatives using a three-dimensional CFD solver with a cost comparable to seven steady flow solutions. The primary benefit of the approaches based on standard derivative computations is that only steady CFD solutions were required, reducing the complexity of implementation.

The second CFD-based approach for evaluating dynamic derivatives leverages the harmonic forced oscillation approach prevalent in wind tunnel experimental methodologies. As done in experimental testing, forced oscillation data is collected, and the resulting unsteady solution is post-processed using numerical analysis techniques to estimate the dynamic derivatives. Many commercial CFD solvers are now capable of specifying forced motion, allowing for the simulation of sinusoidal oscillations about a chosen body axis at a fixed oscillation frequency and amplitude. In this approach, multiple flow solutions must be provided for each axis of rotation to compute the full set of derivatives.

Several studies have been coordinated to evaluate the prediction capabilities and computational costs associated with the second approach. Some of the most notable efforts have recently been led by the Applied Vehicle Technology (AVT) Task Group

under the Research Technology Organization (RTO) within the North Atlantic Treaty Organization (NATO) [19]. The NATO AVT group aimed to assess the state of the art of CFD for static and dynamic stability predictions with an emphasis on military vehicles in the air and sea domains. To that end, a number of studies explored the use of forced oscillation techniques with a variety of CFD solvers, including Reynolds-averaged Navier-Stokes (RANS) [22, 31, 62, 81, 82, 129], direct eddy simulation (DES) [17, 132], and harmonic balance (HB) [23, 25] solvers. The studies demonstrate the ability of CFD to generally capture the dynamic effects of sinusoidal oscillation in comparisons to wind tunnel data, as well as a general dependency on frequency of oscillation, for both military and commercial aircraft. A summary of their efforts can be found in [19, 20].

Following the development of methods for predicting S&C derivatives using CFD, a number of industry and academic research efforts have focused on exploring the modeling capabilities and limitations of the *Flying through the Database* flight dynamics approach. In 2004, Greenwell [49] provided one of the most preeminent reviews of the mathematical correctness of the stability derivative model using dynamic derivatives, as well as their frequency dependency. The author notes the 'ad-hoc' treatment of extending the stability derivative model, in simply treating the dynamic derivatives as additional terms in the Taylor series expansion of the aerodynamic response. Such an approach is mathematically incorrect, as the acceleration perturbation variables are not mutually independent. Furthermore, the review noted severe limits on the motion rates and motion forms for which such a model is applicable.

More recent studies [34, 45, 76, 77] provide a general consensus that the modeling applicability of the stability derivative method does indeed depend on the aircraft and maneuver considered. Complex flows dominated by significant nonlinear, unsteady flow phenomena, either due to vehicle geometry or maneuver characteristics, are incapable of being predicted without unsteady aerodynamic modeling. Given

the inherent quasisteady assumption of the stability derivative modeling approach, a higher fidelity flight dynamics approach is desired, which can more accurately incorporate time history effects. With continuous advances in numerical simulation methods, an alternative approach to VFS, known as *Flying by the Equations*, investigates the potential for using coupled numerical simulations to predict the flight dynamics of maneuvering aircraft without any time-limiting modeling assumptions.

1.2.2 Flying By the Equations

The *Flying by the Equations* approach represents the highest fidelity form of VFS, in which the governing fluid dynamics equations are coupled with the nonlinear 6DOF equations (Eqs. 1 and 2) to predict time-accurate aircraft motions subject to responses from control surface deflections, engine power, and aeroelastic deformations. During the VFS, the fluid-structure interactions are converged in pseudotime using coupled disciplinary solvers; the resulting vehicle state is then coupled to the flight dynamics equations at each timestep to predict the aircraft motion, which in turn would allow for an update of the vehicle's power and/or control surface settings to satisfy a goal trajectory. By coupling the Navier-Stokes equations to the nonlinear 6DOF equations, the *Flying by the Equations* approach provides an opportunity to model the nonlinear, unsteady aerodynamic phenomena for an aircraft maneuvering throughout its flight envelope.

Some of the most prominent studies in pursuit of this capability have been demonstrated by the Department of Defense (DoD) Computational Research and Engineering Acquisition Tools and Environments (CREATE) Program [2] and the German DLR Digital-X Project [59]. These initiatives seek to develop flexible, efficient frameworks for the multidisciplinary analysis and optimization of fixed wing and rotary wing vehicles using high-fidelity simulations.

In 2008, the DoD CREATE program began with the development of three computational engineering tool sets to be used in the design of aircraft, ships, and radio-frequency antennas. Of particular interest is the air vehicle suite, CREATE-AV [80], which is comprised of three software products: Kestrel [88], a high-fidelity fixed wing vehicle simulation tool, Helios [109], a high-fidelity rotary wing vehicle simulation tool, and DaVinci [106], an end-to-end aircraft design tool. Since its development the CREATE-AV tool suite has grown significantly, demonstrating complex virtual flight simulations that were previously infeasible.

In their initial publication, DoD researchers outlined Kestrel's modular approach for coupling traditional monolithic solvers for VFS [88]. As illustrated in Fig. 3, Kestrel uses an Infrastructure and Executive (KIE) central module to coordinate each disciplinary analysis through a component-unaware, publish-and-subscribe event model. The first version of Kestrel [86] coupled the aerodynamics, structural dynamics, kinematics, and kinetics disciplines for three main capabilities: single static grid simulation, single grid rigid body motion simulation, and a deforming single grid aeroelastic simulation.

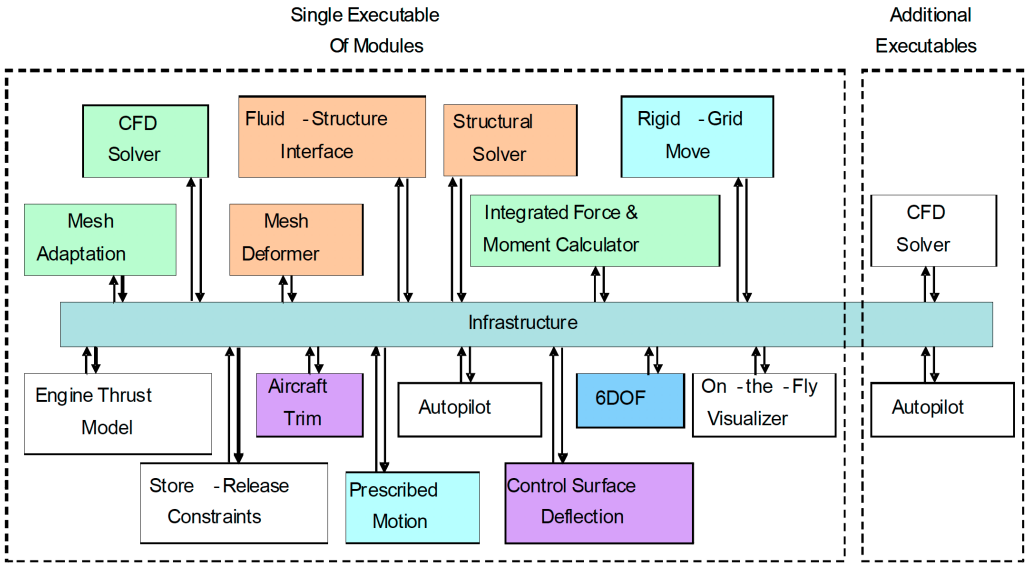

Figure 3: Kestrel architectural layout [88].

Over the past decade, subsequent versions of Kestrel have introduced components for simulating control surface movement, single mesh 6DOF predictive motions, multi-body relative motions, and modal/finite-element aeroelastic solvers [27, 30, 78, 79, 83–85, 87]. Future releases aim to introduce improved propulsion integration for turbo-machinery simulations and the addition of an automatic flight control module. The autopilot module will allow for the motion of bodies or control surfaces in response to the aerodynamic loads encountered during flight. It is evident that the inception and development of the CREATE-AV Kestrel software had advanced the state-of-the-art in virtual flight simulation.

In addition to the innovations by the DoD, the German DLR Digital-X project has made recent developments toward the deployment of their own high-fidelity flight dynamics platform for aircraft and helicopters [59]. In their platform, CFD models are coupled to computational structural mechanics (CSM), flight mechanics (FM) and flight control modules for the simulation of of free-flying elastic aircraft. In support of a CFD-based load analysis initiative with Airbus, the Digital-X team showcased their framework in the simulation of gust interactions for a generic transport aircraft model, the XRF-1, as shown in Fig. 4.

With a high-fidelity numerical simulation approach, the researchers were able to evaluate the complex nonlinear, unsteady aerodynamics encountered in transonic flight and examine the variability in the predictive effect of gust loads in consideration of different degrees of multidisciplinary interactions. Results showed a 63% difference in loads calculated using CFD alone versus the full scope of multidisciplinarity as represented by the coupled CFD-CSM-FM approach.

The recent developments by the CREATE and Digital-X programs demonstrate the feasibility of VFS. The coupling of high-fidelity numerical simulations for aircraft flight dynamics will allow for better evaluations of flight performance for operational

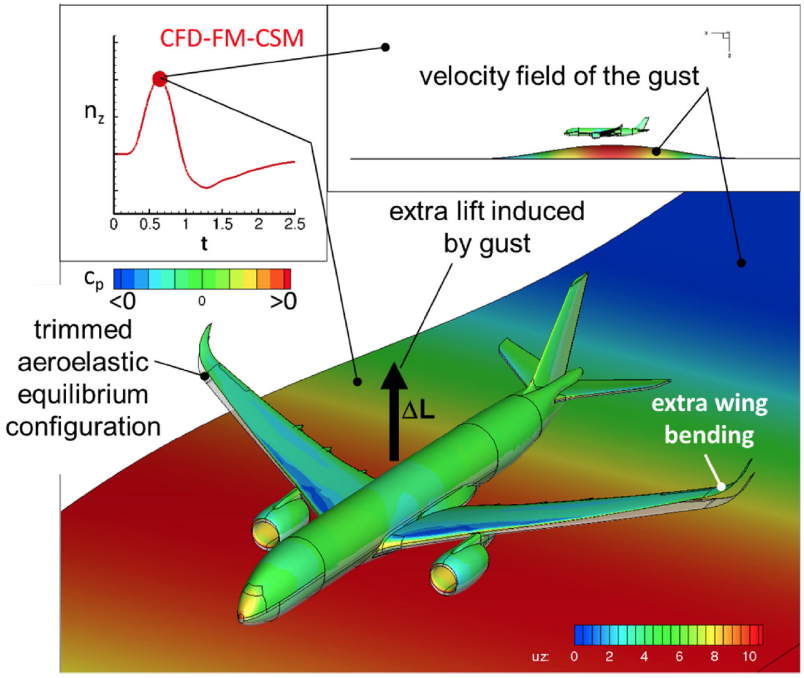

Figure 4: Digital-X: virtual flight simulation of transonic gust response [59].

envelopes dominated by nonlinear, unsteady aerodynamic loads. Despite these technical advances, these simulations often require thousands of computer hours, limiting their practical application in the earlier stages of design. Given the significant computational costs associated with numerical simulation and the limited modeling applicability of quasisteady aerodynamic models, a balanced solution is sought through unsteady aerodynamic reduced-order modeling.

1.3 The Need for Reduced-Order Modeling

Reduced-Order Modeling (ROM) is a field centered on the development of mathematical models capable of accurately predicting the fundamental dynamics of a system at a computational cost much less than what is required in solving the original governing equations [68]. ROM methods approximate the full-order numerical simulations of a system by extracting and reconstructing pertinent data solutions, without any physical modeling assumptions. The data of interest may be either static or dynamic

depending on the system and corresponding feature of interest. Reduced-order modeling methods originated in the field of signal and image processing, but have now expanded into other areas of research, including aerospace engineering. Reduced-order models for aircraft flight dynamics predictions could enable viable VFS in the early stages of the aircraft design process.

In aerospace engineering, significant progress has been made in the past two decades toward the development of reduced-order models for steady and unsteady aerodynamics based on approximations of computational fluid dynamics (CFD) simulations. For steady-state applications, reduced-order models based on Proper Orthogonal Decomposition (POD) have seen extensive use in the prediction of aerodynamic distributions for load evaluations [105]. These reduced-order models sample the pressure distributions at predefined flight conditions and are then used to efficiently predict aerodynamic loads at new flight conditions of interest. Unsteady aerodynamic ROMs have been widely studied for maneuvering vehicle predictions and include the following methods: indicial response, Volterra theory, surrogate-based recurrence frameworks, etc. [42]. Additionally, unsteady ROMs for coupled simulations have been studied in the field of aeroelasticity [68, 120]. In these analyses, aerodynamic and structural reduced-order models are independently identified and successively combined to create coupled reduced-order models to rapidly predict the dynamic response of wings or aircraft in an attempt to identify aeroelastic instabilities, such as flutter.

Despite the notable progress in reduced-order modeling of aerodynamic systems, significant gaps persist in the development of ROMs for virtual flight simulation applications. The use of multidisciplinary reduced-order models for aeroelasticity have been largely confined to the study of aeroelastic phenomena and remain relatively unexplored for the aeroelastic prediction of maneuvering vehicles. Additionally, the generation of multidisciplinary ROMs capable of describing the interaction between

aerodynamics and flight control systems remains confined to ROMs developed for simplified physical systems [21]. In order to advance the field of reduced-order modeling and enable virtual flight simulation applications, it is imperative to not only create reduced-order models for aerodynamic analyses, but also develop reduced-order models that can be used to capture the multidisciplinary interactions present in modern flexible aircraft.

The present work seeks to advance the state of the art in reduced-order modeling for viable virtual flight simulations. First, the advantages and limitations of existing unsteady aerodynamic ROM formulations are investigated through a formal literature review. Following these observations, an unsteady aerodynamic reduced-order modeling method is selected for extension to maneuvering, flexible flight vehicle predictions.

1.4 Thesis Objectives and Outline

Driven by the pursuit of unconventional vehicle configurations, expanded operational envelopes, and composite-structured vehicles, there is an apparent need for modeling the nonlinear, unsteady aerodynamic flow phenomena dominant in these flight applications. The aircraft design process has traditionally emphasized the use of quasisteady stability derivative flight dynamics models capable of providing rapid performance estimates for efficient design exploration.

Despite their widespread use, these methods often make physical modeling assumptions that generally limit their application to steady, linear flight regimes. This inability to predict nonlinear, unsteady flow phenomena has led to the discovery of stability and control problems late in the design process for a number of military and commercial flight programs. Given the recent advances in digital computing, there has been increased interest in leveraging numerical simulations within the earlier stages of design to identify flight performance problems at a point when the opportunity for

making design changes is greatest.

VFS offers the capability to improve aircraft flight predictions through the coupling of high-fidelity numerical simulations. Advances in physical modeling, grid motion and adaptation, and the integration of CFD nonlinear, aeroelastic predictions and control systems have enabled virtual flight simulation capabilities for generating aerodynamic predictions for vehicle-specific models at full-scale Reynolds numbers for Mach numbers representative of the planned flight envelope, and for any generalized 6DOF maneuver. While virtual flight simulation offers a substantial increase in prediction capability over physical modeling alone, significant computational costs restrict its application to the later stages of design where a single design is evaluated as a means of reducing flight performance uncertainty.

Reduced-order modeling presents an opportunity to provide quantitatively accurate descriptions of a system's dynamics at a cost much lower than the governing equations describing the system of interest. Such reduced-order modeling techniques have recently been pursued for aerodynamic predictions, but have been largely confined to aerodynamic predictions of rigid vehicles flying prescribed trajectories.

Given the physical modeling challenges listed in Section 1.1, it is important to consider the development of ROMs for modern aircraft subject to complex aerostructural interactions in flight. Furthermore, it is clear that reduced-order modeling presents an opportunity to enable the widespread use of virtual flight simulation in aircraft design. These models will allow for aircraft flight dynamic predictions with comparable accuracy as full-order models, but at a cost appropriate for the earlier stages of design. Research challenges associated with this endeavor include the evaluation of candidate reduced-order modeling techniques for extension to aeroelastic vehicle predictions and consideration for changes in the identification and parameterization of ROMs for this class of methods. Based on these observations, the following overarching research objective serves as the focus of this dissertation.

Research Objective:

Develop a reduced-order modeling approach capable of predicting the nonlinear, unsteady aerodynamics encountered by maneuvering, flexible flight vehicles.

The remainder of this dissertation is organized as follows:

- Chapter 2 reviews previous developments in reduced-order modeling methods as applied to the field of aircraft flight dynamics and outlines the methods beneficial for extension to flexible vehicles.
- Chapter 3 presents the research questions, hypotheses, and proposed experiments supporting the overarching research objective.
- Chapters 4, 5, and 6 provide details of the technical approach, including: the full-order simulation framework, the reduced-order modeling methodology, and the aircraft test configuration.
- Chapter 7 summarizes the procedure, simulation guidelines, and modeling sensitivities for aeroelastic ROM identification.
- Chapter 8 provides comparisons between aeroelastic ROM predictions and full-order simulation solutions for a series of forced oscillations and a generalized flight test maneuver.
- Chapter 9 quantifies the performance benefits of the aeroelastic ROM in comparison to full-order simulations and the traditional stability derivative modeling approach.
- Chapter 10 contains the conclusions, contributions, and impact of the work undertaken in this dissertation.

CHAPTER II

LITERATURE REVIEW

The following chapter begins with a brief overview of important classification terms frequently used in describing unsteady aerodynamic reduced-order modeling methods. A summary of notable research efforts in unsteady aerodynamic reduced-order modeling is then presented, followed by observations that influenced the research objectives and technical approach implemented in this dissertation.

2.1 Reduced-Order Modeling Classifications

Intrusive vs. Nonintrusive: Intrusivity pertains to the ROM identification process. Intrusive methods involve manipulation of a system's governing equations in identifying its dynamics, whereas nonintrusive methods rely on system identification techniques to replace the original computational model with a smaller size system.

Parametric vs. Nonparametric: A parametric method assumes an explicit functional form for the model of a system's behavior and proceeds to define the coefficients of that particular model. A nonparametric method uses input-output mappings to develop the best functional representation of a system.

Linear vs. Nonlinear: Linear methods assume that a system's response is linearly dependent on the system's inputs. Nonlinear methods assume a nonlinear dependency on the inputs with the potential for cross-coupling of terms. The distinction between linear and nonlinear models exists for both parametric and nonparametric methods.

Time-Domain vs. Frequency-Domain: The classification of either time-domain or frequency-domain refers to a system's dynamic behavior, typically as a result of time-varying or frequency-varying inputs. The nature of these inputs are largely dependent on the application of interest.

2.2 Historical Methods

In the earliest developments of unsteady aerodynamic models, analytical methods were derived from first principles to describe the longitudinal aerodynamic response for idealized flat plate airfoils undergoing 2D motions. The models of Wagner and Theodorsen are among the most widely known historical methods, as their analytical solutions provide a valuable benchmark for the linear models that followed them.

Quasisteady Model

Thin-airfoil theory linearly relates the steady-state lift coefficient for an airfoil in an inviscid fluid to angle of attack, α, via Eq. 7. For modeling airfoil motion, a natural approach is to begin with a quasisteady model, which assumes the motion varies "gradually", allowing the flow field to reach a local equilibrium over time.

$$C_L = 2\pi\alpha \tag{7}$$

The steady model can be extended to a quasisteady model for 2D pitching and plunging motions by introducing an effective angle of attack, α_e. Pitching motions, denoted by $\dot{\alpha}$, result in local vertical velocities along the airfoil, which may be viewed as a distribution of local angle of attack. This distribution may be modeled as an effective camber that contributes to a change in angle of attack equal to $\Delta\alpha = c\dot{\alpha}(1-2a)/4U_\infty$, where U_∞ is the freestream velocity and a is the pitch axis location with respect to midchord, where the leading edge corresponds to $a = -1$ and the trailing edge corresponds to $a = 1$. For plunging motions, denoted by $\dot{h}$, downward vertical velocities result in local changes in angle of attack equal to $\Delta\alpha = \tan^{-1}(\dot{h}/U_\infty) \approx \dot{h}/U_\infty$. The effective angle of attack terms for each of the longitudinal motions can then be added to the original steady model to form the quasisteady lift model given in Eq. 8. In this form, the lengths are nondimensionalized by $2b$ and time is nondimensionalized by $2b/U_\infty$, where b is the half-chord length.

$$C_L = 2\pi \left[\alpha + \dot{h} + \frac{1}{2}\dot{\alpha}\left(\frac{1}{2} - a\right)\right] \tag{8}$$

Wagner's Model

In 1925, Wagner [134] introduced one of the first unsteady aerodynamic models by solving for the lift distribution around an idealized airfoil undergoing motion of an arbitrary time history. The time-domain model was developed by analytically computing the effect of idealized planar wake vorticity on the circulation around an airfoil in response to a step in angle of attack. This system response, circulatory lift, due a step-change in system input, angle of attack, is also known as an *indicial response*. Using an efficient and powerful mathematical technique known as convolution, or Duhamel's superposition, these fundamental responses may be scaled, shifted, and superpositioned to reconstruct the system response to any arbitrary time-accurate system input.

In a similar form as the quasisteady model, Wagner's indicial response model for circulatory lift C_L^c is given in the time-domain by Eq. 9:

$$C_L^c(t) = 2\pi \left(\alpha(0)\phi(t) + \int_0^t \phi(t-\tau)\dot{\alpha}(\tau)d\tau \right) = 2\pi\alpha_e(t) \tag{9}$$

In this equation, 2π is the inviscid lift slope, ϕ is Wagner's indicial response function, $\dot{\alpha}$ is the time rate of change in angle of attack for the arbitrary input motion, and α_e is the effective angle of attack due to the induced circulation from the wake history. Exact solutions to Wagner's indicial response function are given in terms of Bessel functions. The resulting model can then be used to predict the circulatory lift in response to any infinitesimal, longitudinal motion, e.g., plunging, pitching, etc., as a function of time-varying angle of attack.

Theodorsen's Model

In contrast to Wagner's time-domain model, Theodorsen [128] developed a frequency-domain model to describe the aerodynamic response of an idealized airfoil due to *sinusoidal* pitching and plunging motions. Initially developed to study flutter instability, Theodorsen's model consists of apparent-mass terms that account for the reaction force due to the mass of fluid directly accelerated by the airfoil, in addition to circulatory terms that account for lift due to the induced vorticity on the airfoil resulting from wake effects.

Theodorsen's model is given by Eq. 10:

$$C_L = \frac{\pi}{2}\left[\ddot{h} + \dot{\alpha} - \frac{a}{2}\ddot{\alpha}\right] + 2\pi\left[\alpha + \dot{h} + \frac{1}{2}\dot{\alpha}\left(\frac{1}{2} - a\right)\right]C(k) \tag{10}$$

The first set of terms represent the apparent-mass, or noncirculatory, contribution. The second set of terms represent the circulatory lift, which multiples the circulatory lift from quasisteady thin airfoil theory (Eq. 8) by Theodorsen's transfer function, $C(k)$, to account for lift reduction by wake vorticity. Because the theory was developed for sinusoidal motions, the transfer function accounts for the change in magnitude and phase of circulatory lift with changes in reduced frequency, k.

Equation 11 expresses Theodorsen's function as a complex valued function, consisting of both real and imaginary parts, in terms of Hankel functions, H_0 and H_1. Hankel functions are complex functions, $H_v^{(2)} = J_\nu - iY_\nu$, where J_ν and Y_ν are Bessel functions of the first and second kind, respectively. Analytical solutions for Theodorsen's function may be determined for airfoils maneuvering in inviscid, incompressible flows.

$$C(k) = \frac{H_1^{(2)}(k)}{H_1^{(2)}(k) + iH_0^{(2)}(k)} = F(k) - iG(k) \tag{11}$$

Figure 5 shows the variation in real and imaginary parts of the Theodorsen function for reduced frequencies up to a value of two, within the empirical limits of quasisteady models. For the steady case, the reduced frequency equals zero and Theodorsen's function simplifies to a real value of one, consistent with the circulatory lift of quasisteady theory. For moving airfoils, Theodorsen's function will have a real and imaginary part due to the phase lag present between the motion variables and unsteady loads.

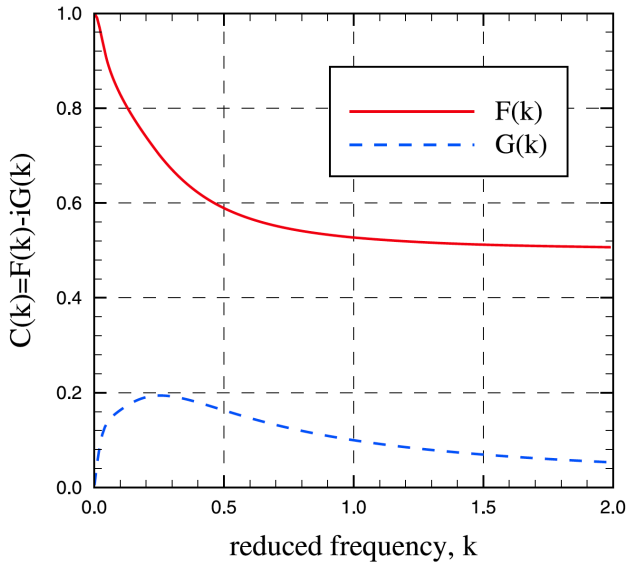

Figure 5: Theodorsen's function [42].

Concluding Remarks

Wagner and Theodorsen's methods were the first of many analytical approaches for modeling the unsteady aerodynamic response of idealized airfoils. Other notable approaches include those of Küssner [61] and Sears [110] who extended the methods of Wagner and Theodorsen, respectively, to model the aerodynamic response to moving gusts. Among others, these models pioneered the field of unsteady aerodynamics between 1920-1950, allowing for efficient characterization of the aerodynamic responses to longitudinal airfoil motions.

By the 1950s, the thin-airfoil assumptions, which made historical methods computationally tractable, became inadequate as the geometric complexity of military and commercial vehicles increased. Additionally, these methods assume motion within inviscid, incompressible flows. For modern aircraft maneuvering through flight regimes characterized by the aerodynamic phenomena listed in Section 1.1, nonlinear, unsteady aerodynamic models are required. The following sections review the modern CFD-based unsteady aerodynamic ROMs attempting to fulfill this need.

2.3 Indicial Response Modeling

Driven by the success of analytically-calculated indicial response functions (Wagner's Method), researchers began to explore the development of indicial response models for predicting the unsteady aerodynamics for three-dimensional wings and aircraft. Linear indicial response models based on convolution were the first to be developed, as first-order responses could be identified relatively easily using experimental or numerical methods.

Theory

An indicial response is defined as a system's output response due to a unit step change in a system's control input. A linear indicial response model assumes that the flow can be linearized with respect to a system's forcing function. Under this assumption, convolution is used to reconstruct the system response to any arbitrary time-varying input via the superposition of scaled and time-shifted indicial responses.

In the context of unsteady aerodynamics, consider the relationship between the lift coefficient, C_L, and angle of attack α. Linear flight regimes are characterized by a linear variation of the lift coefficient with angle of attack up to a stall angle of attack, α_{stall}, after which the flow responds nonlinearly due to separated flow effects. In this example, linear indicial response models can be used to resolve any time-varying motion within the linear flight regime. Equation 12 represents a linearization of the

time-varying lift coefficient about some angle of attack, i.e., system input, α_0. The term $\partial C_L/\partial\alpha$ is a step response, dependent only on the time t after the step. Because the flow is assumed to vary linearly with angle of attack, the response does not depend on the value of α.

Written as a Taylor series expansion, the higher-order terms of Eq. 12 may be truncated to form the linearized model shown in Eq. 13. The term $\tilde{C}_L(t)$ is the indicial response or output in response to a step input, $\dot{\alpha} = \delta(t)$, where $\delta(t)$ is the Dirac delta function. The Dirac delta function, or unit impulse function, represents an instantaneous unit perturbation in the system's input.

$$C_L(t) = C_L(\alpha_0, t_0) + \left.\frac{\partial C_L}{\partial \alpha}\right|_{\alpha_0} \Delta\alpha + O(\Delta\alpha^2) \tag{12}$$

$$C_L(t) = C_L(t_0) + \frac{\partial C_L}{\partial \alpha}(t)\Delta\alpha = C_L(t_0) + \tilde{C}_L(t)\Delta\alpha \tag{13}$$

A linear indicial response model uses the convolution principle to reconstruct a system response, in this case $C_L(t)$, to an arbitrary input, $\alpha(t)$, by linear superposition of scaled and time-shifted copies of the indicial response function. Equation 14 defines this mathematically, where α is the forcing function, and $\alpha(0)$ is the angle of attack at time zero. The indicial response is $\tilde{C}_L(t)$, but is often decomposed as $\tilde{C}_L(t) = dC_L/d\alpha \cdot \phi(t)$, where $dC_L/d\alpha$ is the lift-curve slope and $\phi(t)$ is the normalized indicial response with $\lim_{t\to\infty} \phi(t) = 1$.

$$C_L(t) = \tilde{C}_L(t)\alpha(0^-) + \int_0^t \tilde{C}_L(t-\tau)\dot{\alpha}(\tau)d\tau \tag{14}$$

An illustration of convolution is given in Fig. 6. In this example, the input function is a linear ramping of angle of attack, where its first-order time-derivative is represented by a step function. At each point in time, the system response to the linear ramping of angle of attack is calculated via convolution. Simply put, convolution is the summation of indicial response functions, first initialized at each point in time and then scaled by the local value of the input derivative. This process effectively models the influence of previous system input states on the system output at any later time, i.e., an unsteady response to any arbitrary time-varying input.

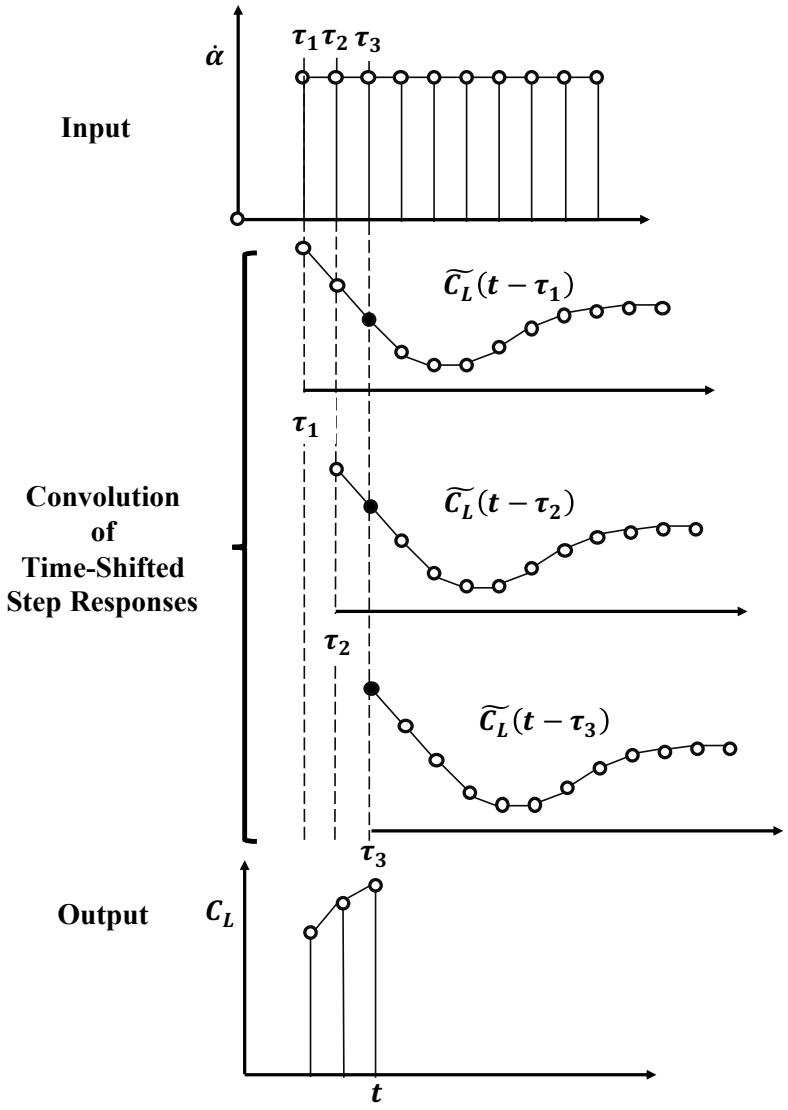

Figure 6: Illustration of indicial response theory.

Flight Dynamics Modeling

Initial efforts in applying indicial response theory for unsteady aerodynamics modeling for maneuvering flight vehicles are detailed by Tobak et al. [130,131] and Reisenthal et al. [102,104]. Using the same assumed dependent vehicle-state parameters as the stability derivative approach, the unsteady aerodynamic response to longitudinal motions could be modeled within linear flight regimes using indicial theory by accounting for contributions due to previous states of angle of attack and pitch rate. Equation 15 expresses the lift and pitching moment, $C_j = [C_L, C_M]$ as a function of the convolution integrals with respect to angle of attack, α, and pitch rate, q.

$$C_j(t) = C_{j_0} + \alpha_0 C_{j_\alpha}(t) + \int_0^t C_{j_\alpha} \dot{\alpha}(\tau) d\tau + \int_0^t C_{j_q} \dot{q}(\tau) d\tau \tag{15}$$

In Eq. 15, C_{j_0} denotes the zero-angle-of-attack lift or pitching moment coefficients, which may be identified by steady-state data. The term α_0 is the angle of attack at the initial time of motion. As will be discussed later, application of the convolution integrals requires the initial motion to be steady-state to satisfy mathematical feasibility. For this reason, the initial pitch rate term, $q(0)$, is zero and therefore not required within the expression. The differential theorem of the convolution integral is a mathematical transformation often applied to Eq. 15 to get the alternative form shown in Eq. 16 or Eq. 17. By factoring out the time derivative, vehicle motions defined by angle of attack and pitch rate may be readily integrated to calculate the unsteady aerodynamic response via convolution.

$$C_j(t) = C_{j_0} + \frac{d}{dt}\left[\int_0^t C_{j_\alpha}(t-\tau)\alpha(\tau)d\tau\right] + \frac{d}{dt}\left[\int_0^t C_{j_q}(t-\tau)q(\tau)d\tau\right] \tag{16}$$

$$\begin{aligned} C_k(t) = \frac{d}{dt}\left[\int_0^t C_{k_\beta}(t-\tau)\beta(\tau)d\tau\right] + \frac{d}{dt}\left[\int_0^t C_{k_p}(t-\tau)p(\tau)d\tau\right] \\ + \frac{d}{dt}\left[\int_0^t C_{k_r}(t-\tau)r(\tau)d\tau\right] \end{aligned} \tag{17}$$

The model given by Eq. 16 may be applied to flows that respond linearly to changes in forcing functions. For nonlinear flows, the linear indicial response theory may be extended as a nonlinear indicial response theory by use of parameterized indicial response functions.

As shown in Eq. 18, nonlinearity may be captured by sampling a system's indicial response as a function of the forcing function values. Similar to the application of aerodynamic databases for stability derivative aircraft flight dynamic predictions, the degree of nonlinearity resolved scales with the number of indicial responses identified. In the case of longitudinal aerodynamics, the indicial response with respect to angle of attack is assumed to vary with angle of attack and Mach number, whereas for pitch rate, the indicial response is assumed to vary only with Mach number with negligible variations in angle of attack at low to moderate angles of attack. These parameterizations are consistent with those typical of aerodynamic databases, resulting in an unsteady extension enabled by reduced-order modeling.

$$C_j(t) = C_{j_0}(M) + \frac{d}{dt}\left[\int_0^t C_{j_\alpha}(t-\tau,\alpha,M)\alpha(\tau)d\tau\right] + \frac{d}{dt}\left[\int_0^t C_{j_q}(t-\tau,M)q(\tau)d\tau\right] \tag{18}$$

Ghoreyshi and Cummings [38] later extended this formulation for the prediction of unsteady aerodynamic responses to lateral motions, in an attempt to predict the aerodynamics for 6DOF maneuvering aircraft. Consistent with traditional aircraft flight dynamics assumptions, the lateral loads are assumed to only depend on side-slip angle (β), normalized roll rate (p), and normalized yaw rate (r). The unsteady lateral aerodynamics, namely side force (Y), rolling moment (l), and yawing moment (n) may then be calculated using Eq. 19. The parameterization of the indicial responses are also consistent with those used in the longitudinal formulation.

$$C_k(t) = \frac{d}{dt}\left[\int_0^t C_{k_\beta}(t-\tau,\alpha,M)\beta(\tau)d\tau\right] + \frac{d}{dt}\left[\int_0^t C_{k_p}(t-\tau,M)p(\tau)d\tau\right] + \frac{d}{dt}\left[\int_0^t C_{k_r}(t-\tau,M)r(\tau)d\tau\right] \tag{19}$$

Model Identification

Initial research toward indicial response identification began with the work of Wagner in his analytical derivation of indicial lift responses for airfoil motions in incompressible flows. These responses were known exactly in terms of Bessel functions, but regarded as impractical for the majority of analyses due to the repetitive function evaluations required. In an effort to reduce solution costs, researchers began investigating the use of exponential functions to numerically approximate the Wagner function. One of the most widely known approximations is the exponential approximation with four coefficients, developed by Jones [52]. While these approximations proved to be beneficial in the analysis of airfoils in incompressible flows, these theories were inadequate for three-dimensional configurations and/or compressible flows.

Indicial responses in subsonic compressible flow cannot be exactly known through analytical derivation. Additionally, the direct identification of indicial responses via experimental testing is largely impractical as test rigs are kinematically incapable of simulating true impulse or step motions. Garrick [33] observed early on that Wagner's "indicial lift" function and the "alternating lift" function of Theodorsen were fundamentally related by a Fourier integral or Laplace Transform pair. Recognizing the advantage of this relationship, researchers began to explore the indirect identification of indicial response functions using Laplace transforms of harmonic (oscillatory) motions. Examples of this identification method include the works of Mazelsky et al. [74, 75] and Dowell [28], who obtained indicial response function approximations from subsonic and transonic oscillatory data, respectively. The general consensus regarding this approach is that the indicial response results using harmonic motions largely depends on the amplitude and frequency of motion. Moreover, the practical

difficulties of obtaining high reduced frequency data at high subsonic Mach numbers limit the use of the approach for all relevant flight conditions.

Recently, CFD simulations have been explored as an alternative approach to approximating indicial response functions via intrusive and nonintrusive approaches. Some of the earliest computational investigations began in the 1970s and include the works of Ballhaus et al. [6] and Magnus [71] in the approximate identification of indicial responses using finite-difference flowfield computations in the study of airfoils. In 1997, Singh and Baeder [122] modified an unsteady Euler solver to calculate the indicial response of a rectangular wing with respect to angle of attack. In their approach, a field velocity approach was used, such that an impulsive change in angle of attack was modeled as an equivalent change in the velocity field using grid time metrics. The benefit of this approach was an efficient means of determining the indicial response with respect to a pure step change in angle of attack, eliminating indirect contributions from pitch rate, which are often confounded with harmonic oscillations. The primary drawback of these identification methods is their intuitive nature, requiring modification to the source code to perform the analysis.

More recently, Ghoreyshi et al. [40] leveraged the grid motion capabilities of modern CFD solvers to extend the idea of direct indicial response identification for maneuvering aircraft. The procedure assumes that the CFD solver allows specification of all translational and rotational degrees of freedom. These degrees of freedom are defined with respect to a reference point on the aircraft at each time step of the simulation. For successive points in time, the aircraft's reference point velocity in the inertial reference frame is calculated and specified to achieve the angle of attack, sideslip angle, and forward speed defining a prescribed maneuver. The translational degrees of freedom are defined by the relative velocity vector of the aircraft's reference point. Rotation of the aircraft about the reference point is then defined using the yaw, pitch, and roll rotation angles. The ability to simulate such 6DOF maneuvers using

CFD simulation allows for both full-order and reduced-order models to be created.

Using this grid motion technique, CFD-calculated approximations for the indicial response with respect to angle of attack and pitch rate may be obtained, as illustrated in Fig. 7. In their approach, a step change in angle of attack is achieved by specifying a grid motion, beginning at $t = 0$, to the right and downward. A constant velocity vector is specified to have a consistent translation. With this grid motion, changes in the aerodynamic loads are isolated to changes in angle of attack, as rotation eliminates any contribution from pitch rate. For a unit step change in pitch rate, the grid rotates at a constant, unit pitch rate. Because angle of attack changes with rotation, an additional grid motion is specified to the right and upward in an effort to eliminate angle-of-attack contributions. This grid motion technique can also be implemented for the approximation of responses with respect to lateral motion parameters.

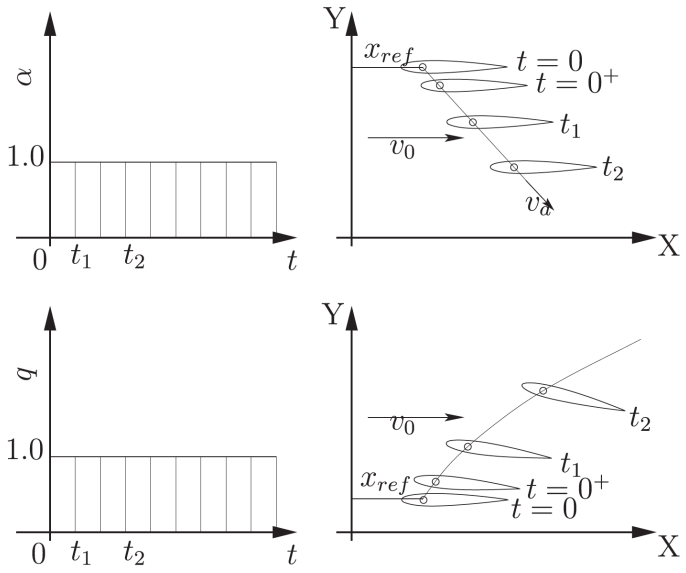

Figure 7: Grid motion simulation of indicial responses [42].

The benefit of this approach is that indicial responses for 2D or 3D configurations can be calculated at any flight condition, overcoming the identification problems experienced by analytical and experimental methods. Researchers within the NATO AVT group have recognized the utility of this method and have explored its use in

creating linear and nonlinear unsteady aerodynamic ROMs for maneuvering vehicles.

Notable Studies

DaRonch et al. [24] assessed the validity of linear indicial response models, among other ROM techniques, for flight dynamic-related studies. Euler and Navier-Stokes flow solvers were used to simulate an NACA 0012 airfoil undergoing harmonic pitching oscillation motions at transonic flight conditions. In comparison to unsteady time-domain solutions, the results confirmed the ability of linear indicial response models to accurately predict the aerodynamics due to pitch oscillations at low mean angles of attack with small pitching amplitudes, e.g., one degree. However, the linear formulation failed to predict the nonlinear aerodynamic coefficients of large amplitude pitch oscillations.

In 2012, Ghoreyshi et al. [40] introduced the indicial response identification approach via grid motion to create both linear and nonlinear longitudinal indicial response models using the Cobalt flow solver. The models were used to generate unsteady aerodynamic predictions for both an NACA 0012 airfoil and an unmanned combat air vehicle configuration undergoing a variety of ramping, pitch oscillation, and frequency-sweep motions. Collectively, the results reinforced the inherent capability of the indicial response to capture all frequency content of the systems dynamics, allowing for the accurate prediction of unsteady maneuvers at any rate of motion. Furthermore, nonlinear ROM predictions were shown to agree well with full-order simulation values for large amplitude longitudinal motions. As for costs, the identification of the linear and nonlinear models required about 0.6 and 6.0 hours of CPU time, respectively, while making online maneuver predictions on the order of seconds. In contrast, CFD simulations required about 1.8 and 0.8 CPU hours per cycle for the low and high frequency pitch oscillations, respectively. The cost comparisons illustrate an immediate computational savings for linear ROM predictions and computational savings for nonlinear ROM predictions for multiple maneuver evaluations.

In a subsequent study, Ghoreyshi et al. [35] extended the indicial function modeling approach for predictions of lateral force and moments with respect to sideslip angle, roll rate, and yaw rate. This development enabled the capability to evaluate the unsteady aerodynamics of any prescribed 6DOF trajectory. Comparisons between time-accurate CFD simulations and ROM predictions for the Half Lazy-8 and Immelmann turn maneuvers showed good agreement in the lift force, pitching moment, and side force. However, disagreement was found in rolling and yawing moment results. The authors attribute the lateral moment discrepancies due to the dependency on angle of attack and Mach number, for which the linear model could not predict.

By 2014, Ghoreyshi et al. [38] had recognized the need for nonlinear forms of the indicial response model in predicting longitudinal and lateral loads of complex maneuvers. Such models require a large number of indicial responses to capture nonlinear variations over a wide flight envelope. In order to facilitate more efficient predictions, a time-accurate surrogate modeling approach was developed to interpolate indicial response functions as a function of the vehicle-state space. In their approach, Design of Experiment (DoE) methods were used to sample the input space. CFD was then used to simulate the sampled indicial responses, resulting in an unsteady aerodynamic database. Kriging surrogate modeling was then used to interpolate the database and approximate indicial responses for the flight conditions corresponding to each step in the trajectory. Their results showed the consistency of aerodynamic predictions for all longitudinal and lateral force and moment coefficients for maneuvers involving angles of attack below 15°. For high angles of attack, difficulties were encountered in obtaining converged indicial response functions, which have been noted in more recent studies [36]. Additionally, the model results suggest that the inclusion of angle of attack as a dependent parameter for the angular rate indicial responses may improve predictions for the configuration and maneuvers tested.

Concluding Remarks

Indicial response ROMs characterize a system's dynamics using the observed system response (output) to unit step changes in a system's inputs. For virtual flight simulation applications, linear and nonlinear indicial response ROMs have been demonstrated to provide accurate and efficient unsteady aerodynamic predictions of rigid aircraft maneuvering along prescribed trajectories. CFD grid movement is used to numerically simulate indicial responses with respect to step changes in the vehicle-state parameters defining a trajectory.

The primary benefits of indicial response ROMs is the ease of implementation given its nonintrusive nature, and the ability to simulate arbitrary trajectories at any desired motion rate. This is primarily due to the nonparametric characteristics of indicial responses and their ability to capture the entire frequency spectrum of a system's dynamic response. The primary drawback of this method is the requirement for sufficient flight space resolution in sampling indicial responses for nonlinear ROM evaluations. However, surrogate modeling has been demonstrated as a key enabler toward efficient generation and application of indicial response models.

2.4 Volterra Theory

Volterra theory [133] was developed in 1930 as an approach for modeling nonlinear dynamic systems in the time and frequency domains. Initially studied in the fields of electrical and biological systems engineering, Volterra theory has since expanded to a wide range of disciplines including aerospace engineering for the study of nonlinear fluid and structural dynamics systems.

Theory

Volterra theory can be used to model any dynamic system that may be classified as nonlinear and time-invariant. A time-invariant system is one whose fundamental properties do not change with time. This classification describes the system itself

and makes no inference to the inputs or outputs of the system. Practically speaking, the governing equations of a time-invariant system are not explicit functions of time, whereas inputs and outputs may be time-accurate.

Classical Volterra theory is based on functional Taylor series expansions, where functionals are defined as functions of other functions. Volterra series and Taylor series share the same fundamental basis in that a nonlinear system may be linearized about an operating point by an expanded series of linear and nonlinear terms. With a sufficient number of nonlinear terms, the expansion may provide an excellent approximation of nonlinear system behavior. Volterra series model the response of a continuous-time system about an initial state due to an arbitrary input $u(t)$ for $t \geq 0$ using a multidimensional convolution, as given by Eq. 20.

$$\begin{aligned} y(t) = h_0 + \int_0^t h_1(t-\tau)u(\tau)d\tau + \int_0^t \int_0^t h_2(t-\tau_1, t-\tau_2)u(\tau_1)u(\tau_2)d\tau_1 d\tau_2 \\ + \sum_{n=3}^{N} \int_0^t \cdots \int_0^t h_n(t-\tau_1, \ldots, t-\tau_n)u(\tau_1)\ldots u(\tau_n)d\tau_1 \ldots d\tau_n \end{aligned} \tag{20}$$

The Volterra series in Eq. 20 consists of three terms. The first term, h_0, is a constant, steady-state term representing the initial system state. The second term, $\int_0^t h_1(t-\tau)u(\tau)d\tau$, is the first response term, where h_1 is the first-order Volterra kernel. This term is the convolution of the first-order kernel with a time-arbitrary system input, $u(t)$, over a time interval, 0 to t. The final terms are higher-order terms representing the convolution of the input with the N-th order Volterra kernel.

In applying Volterra theory to a linear system, as represented by Eq. 21, the first-order Volterra kernel $h_1(t)$ represents the system's response to a unit impulse response, $u(t_1) = \delta_0(t_1)$, where δ_0 is the Dirac-Delta function. The Dirac-Delta function is a continuous time unit impulse function defined with an amplitude reaching infinity while its width approaches zero with an integral equal to one. When applied to a continuous-time, linear time-invariant system, the system's impulse response is

observed as illustrated in Fig. 8.

$$y(t) = h_0 + \int_0^t h_1(t-\tau)u(\tau)d\tau \tag{21}$$

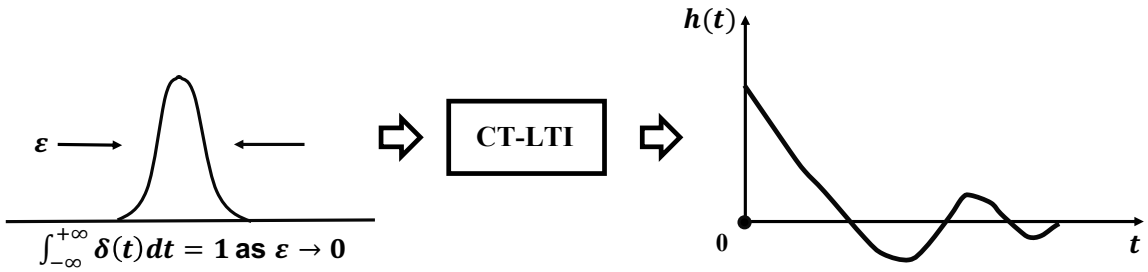

Figure 8: Impulse response to unit impulse function in continuous time [121].

For nonlinear systems, higher-order kernels represent the response of the system to multiple unit impulses, where the number of applied impulse functions is equal to the order of the kernel of interest. For example, a second-order kernel, h_2, would be the response of the nonlinear system to two separate unit impulses applied at two distinct points in time, t_1 and t_2. As a result, the second-order kernel is a two-dimensional function of time.

Notable Studies

First observed by Silva [121], the discretized Navier-Stokes equations can be characterized as a discrete-time, nonlinear, time-invariant system of equations. As opposed to applying continuous-time impulse functions, Silva [113, 114, 121] recognized the necessity to develop and apply discrete-time unit impulses for computational aerodynamic problems.

In discrete-time, the Volterra series may be used to model a system response $y[n]$ to an arbitrary system input $u[n]$ using a multidimensional convolution via Eq. 22. In this expression, time is indexed by the time step, n, where $t = n\Delta t$. The convolution integral is taken from the initial time, $t = 0$, to the final time, $t = N$, and k_n represents impulses at time step n.

$$y[n] = h_0 + \sum_{k=0}^{N} h_1[n-k]u[k] + \sum_{k_1=0}^{N}\sum_{k_2=0}^{N} h_2[n-k_1, n-k_2]u[k_1]u[k_2] + \sum_{k_1=0}^{N}\cdots\sum_{k_n=0}^{N} h_n[n-k_1,\ldots,n-k_n]u[k_1]\ldots u[k_n] \tag{22}$$

Discrete-time unit impulse functions are defined to have a value of unity at a single point in time and a value of zero for all other times. This discrete-time formulation can then be easily implemented by numerical simulations of unsteady aerodynamic and aeroelasticity problems, which operate in discrete-time. An illustration of such system applications is given in Fig. 9.

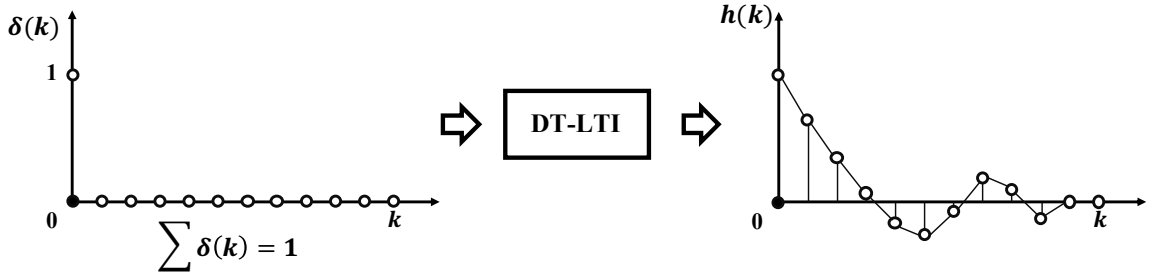

Figure 9: Impulse response to unit impulse function in discrete time [121].

The convergence of the Volterra series (Eq. 22) is dependent on the magnitude of the system's input and the degree of system nonlinearity about the operating point of linearization. In many practical applications of Volterra theory for computational aerodynamic ROMs, it is assumed that the aerodynamic system of interest may be considered weakly nonlinear and accurately modeled using a truncated second-order Volterra series (Eq. 23) [99, 121].

$$y[n] = h_0 + \sum_{k=0}^{N} h_1[n-k]u[k] + \sum_{k_1=0}^{N}\sum_{k_2=0}^{N} h_2[n-k_1, n-k_2]u[k_1]u[k_2] \tag{23}$$

A comparison between the Volterra and indicial response theories illustrates a similarity in that both methods estimate a system's dynamic behavior using the

convolution principle. Linear indicial response models are equivalent to the first-order Volterra theory with the primary difference being that indicial response modeling recasts the integral in terms of the step response and input-derivative, wheras Volterra theory uses the impulse response (step-derivative) and input itself. Thus, Volterra models theoretically offer improved prediction capabilities over linear indicial response theory based on the addition of higher-order terms.

In his dissertation, Silva [121] derived the first- and second-order kernels, Eqs. 24 and 25, for the truncated second-order Volterra series in continuous-time.

$$h_1(t) = 2y_1(t_1) - \frac{1}{2}y_2(t_1) \tag{24}$$

$$h_2(t_1, t_2) = \frac{1}{2}\left(y_1(t_1, t_2) - y_1(t_1) - y_1(t_2)\right) \tag{25}$$

In these equations, $y_1(t_1)$ represents the time response of the system to a unit impulse at time 0, $y_2(t_1)$ is the time response of the system to an impulse of twice unit magnitude at time 0. For a linear system, superposition holds and $y_2 = 2y_1$ and thus, $h_1 = y_1$, recovering the linear impulse response discussed earlier. For nonlinear systems, the first-order kernel captures the system's dependence on amplitude of the input. In Eq. 25, the increased complexity in identifying the second-order kernel is apparent as it depends on two time parameters, associated with impulse functions applied at separate times. Here, $y_1(t_2)$ is the response of the system to an impulse applied at time t_2 and $y_1(t_1, t_2)$ is the response to an impulse at t_1 and later at t_2. For linear systems, the second-order kernel would be zero, as expected. For nonlinear systems, the second-order kernel represents the nonlinearity of the system not predicted by the linear first-order kernel.

Using the discrete-time, second-order Volterra series along with the direct kernel identification expressions, Silva demonstrated the Volterra modeling of aerodynamic systems by analyses of both a three-dimensional aeroelastic wing in transonic flow

using the Computational Aeroelasticity Program Transonic Small Disturbance (CAP-TSD) code [115] and a supercritical RAE airfoil undergoing large plunge motions in transonic flow using the CFL3D Navier-Stokes flow solver [116]. Despite their widespread application, implementation of the direct impulse identification method is not without challenge.

Raveh [97] investigated the performance of first- and second-order, impulse-type Volterra ROMs and step-type indicial ROMs for the evaluation of generalized aerodynamic forces (GAFs) in response to forced-harmonic motions for the aeroelastic AGARD 445.6 wing. Difficulty was observed in correctly identifying the system's kernels using impulse response functions, as impulse responses showed significant sensitivity to the choice of input amplitude and time step. Inaccurate impulse responses and subsequent ROM predictions were observed for impulse response functions numerically simulated using relatively large amplitudes and small time steps. In contrast, step responses were shown to be less sensitive to step amplitude and time step, where step-type ROMs showed favorable predictions for forced-harmonic responses in the linear regime.

In a parallel study, Raveh et al. [100] further investigated the application of step-type, first-order ROMs for the efficient evaluation of an aeroelastic wing's generalized aerodynamic forces for use in a transonic flutter analysis. CFD-based step responses with respect to the wing's structural modes served as the ROM's kernels. The identified ROM was then used to evaluate the resulting GAFs for sinusoidal oscillations at various reduced frequencies. The flutter speed index and flutter frequency ratio were computed using the ROM-based GAFs and shown to be in excellent agreement with wind tunnel tests. The study further illustrated the computational benefits of step-type ROMs for generating frequency-domain GAFs in comparison to full-order CFD solutions. However, while step responses were shown to be more robust than impulse responses, step responses incur a greater computational cost as a new state

is reached and thus, requires additional time steps for convergence.

As an alternative to direct Volterra kernel identification, indirect kernel identification methods have also been explored. These methods assume that the Volterra kernels may be represented by an expansion of some basis function set as shown in Eq. 26. The term ξ_j represents the j^{th} time-accurate basis function, e.g., decaying exponentials, and x_{jn} represents the j^{th} component of N_b total basic function coefficients for the n^{th} order Volterra kernel.

$$h_n(t) = \sum_{j=1}^{N_b} x_{jn}\xi_j(t) \tag{26}$$

Indirect kernel identification methods recast the Volterra series (Eq. 20) into a linear system of equations, as shown in Eq. 27.

$$\mathbf{y}=\mathbf{A}\mathbf{b} \tag{27}$$

The left-side term, $\mathbf{y} = (y(0), y(1), \ldots, y(n))^T$, represents the system response or time-varying aerodynamic loads calculated from CFD simulation. The term $\mathbf{A}$ contains the permutations of the system input parameters used to excite the system's response, and the vector b contains the unknown Volterra kernel coefficients. Multiple input-output measurements, $u(t_i), y(t_i)$, of the system's behavior are collected and serve as training data, i.e., constraints, for which the unknown basis function coefficient may be solved. The resulting set of linear equations form an overdetermined system, typically solved by least squares numerical methods. Once the Volterra kernel coefficients, $\mathbf{b}$, are identified, new maneuvers/motions are used to compute the motion matrix, $\mathbf{A}$, and the resulting unsteady aerodynamic loads, $\mathbf{y}$, may be solved using the ROM.

Indirect kernel identification has been demonstrated in several aerodynamic studies. Reisenthel et al. [103] created first- and second-order Volterra ROMs using decaying exponential basis functions for modeling the unsteady aerodynamics of a rectangular wing undergoing pitch oscillations. Kurdila et al. [60] and Prazenica et

al. [96] used wavelet approximations of Volterra kernels to analyze an aeroelastic system undergoing large amplitude, limit cycle oscillations. Balajewicz et al. [4] used a polynomial-weighted moving average representation of the discrete-time Volterra series to efficiently model the unsteady aerodynamic loads induced by limit-cycle oscillations of an NACA 0012 benchmark model. One additional contribution was the recognition of the large computational cost associated with standard Volterra ROMs, in that identification costs scale exponentially with modeling order. A sparse Volterra ROM methodology has since been proposed, which sets all off-diagonal terms of the Volterra kernel to zero, allowing for training maneuver cost to scale linearly with order of representation.

The majority of Volterra modeling research has been used to represent single-input-single-output systems. As noted by Silva [112], there have been few applications of Volterra theory to multidegree-of-freedom systems. The primary issue lies in the need to simultaneously excite multiple degrees of freedom to identify any cross-coupling relationships between the degrees of freedom. Previous attempts in modeling multidegree-of-freedom systems have been confined to the study of nonlinear aerodynamics resulting from individual perturbations of structural modes. To determine the aerodynamic loads resulting from simultaneous motions, superposition of the individual nonlinear responses to the forcing functions is required. However, the superposition principle does not hold for nonlinear responses and alternative methods are required.

Balajewicz et al. [5] proposed a multi-input Volterra series as means of modeling nonlinear multidegree-of-freedom aerodynamic systems through the inclusion of Volterra cross kernels. The cross kernels capture any coupling dynamic nature between the nonlinear system's degrees of freedom. The model was demonstrated by modeling the transonic, unsteady flows of an airfoil undergoing a defined heave-pitch motion. Improved results were found using the multi-input formulation in comparison

to the standard single-input formulation.

Ghoreyshi et al. [44] presented a multi-input Volterra series for modeling the transonic aerodynamic loads for an X-31 aircraft undergoing pitching motions. For modeling pitching oscillations, the system's input functions were specified as angle of attack, pitch rate, and pitch acceleration, while the output functions were time-varying lift, drag, and pitching moment. Overall, the authors noted accurate results provided by the Volterra ROMs, but also considered a nonlinear model based on indicial functions, which yielded more accurate results.

Concluding Remarks

Volterra theory is a classical system dynamics concept that models the response of a system using a multidimensional convolution of a system's inputs. Similar to indicial response theory, Volterra theory is a nonparametric, nonintrusive ROM method, but characterizes a system using fundamental unit impulse functions. These two methods are intrinsically related in that the impulse is merely the derivative of the step function. The primary advantage of the Volterra series is its ability to form nonlinear approximations of the system of interest using higher-order kernels. Moreover, the identification costs for impulse functions are lower in comparison to indicial functions, which require a greater number of iterations to converge to the new system state.

Discrete-time Volterra series ROMs have been successfully demonstrated for unsteady aerodynamic predictions of maneuvering vehicles and in the field of aeroelasticity for the identification of vehicle instabilities, such as flutter. The primary challenges of this method is the difficulty associated with identification of higher-order terms and the numerical simulation of impulse functions, as they are typically less robust in comparison to step functions with respect to impulse amplitude and time step of the simulation.

2.5 State Space Modeling

The indicial response and Volterra reduced-order modeling techniques presented in the previous sections require identification of characteristic step or impulse responses, respectively, which are then convolved with arbitrary time-domain maneuver or modal motion inputs to predict an unsteady aerodynamic response. While beneficial for prescribed motions, the mathematical form of the convolution integral is not suitable for use in multidisciplinary, preliminary design environments. Even for aeroelastic modeling applications, the fundamental impulse or step response functions are often simulated at specific Mach numbers and dynamic pressures, inherently limiting their utility to the modal frequency input space.

Modern virtual flight simulation capabilities require an accurate description of the interactions between structure, aerodynamics, and controls, such that control laws may be designed for flutter suppression, load alleviation, or vehicle maneuverability. Modern controller techniques predominantly use formulations based on state-space modeling. Noting the previous challenges, recent efforts have investigated the transformation of impulse responses into state-space form using system identification tools, including Eigensystem Realization Algorithm (ERA) [54] and Observer/Kalman Filter Identification (OKID) [55]. These numerical methods are combined into a toolbox called SOCIT (System/Observer/Controller Identification Toolbox) [53], developed at the NASA Langley Research center. The resulting aerodynamic state-space models can be coupled with other disciplinary state-space models to form multidisciplinary CFD-based ROMs.

Theory

A finite-dimensional, discrete-time, linear, time-invariant dynamic system may be modeled in state-space form as shown in Eqs. 28 and 29, where $\mathbf{x}$ is the n-dimensional state vector, $\mathbf{u}$ is the m-dimensional control input vector, $\mathbf{y}$ is the p-dimensional

measurement output vector, and k is the discrete time index.

$$x(k+1) = Ax(k) + Bu(k) \tag{28}$$

$$y(k) = Cx(k) + Du(k) \tag{29}$$

The components of the control input vector $\mathbf{u}$ are associated with the vehicle or structural motion parameters. For maneuvering vehicles, these components may be the wind incidence angles and body rotation rates, whereas for aeroelasticity applications these components may be the structural mode perturbation amplitudes. The components of the measurements output vector $\mathbf{y}$ consist of the aerodynamic response. For maneuvering vehicles, these components may be the vehicle-level 6DOF force and moment coefficients, whereas for aeroelasticity applications these components may be the generalized aerodynamic forces for each structural mode.

The order of the dynamic system often refers to the dimension, n, of the state vector $\mathbf{x}$. In the simulation of fluid dynamics systems, the state vector consists of the flowfield properties (P, ρ, T, etc.) at each grid point of the spatially-discretized model. Even for coarsely resolved systems, the order of the system may be in the millions. The goal of state-space modeling is to use known input-output data to calculate the constant matrices A, B, C, and D, governing the system's dynamics without explicit definition of the state vector. Once identified, the state-space model may be used to predict the system response to an arbitrary set of system inputs.

Solving Eq. 28 with zero initial conditions yields Eq. 30, which may then be substituted into Eq. 29 to produce Eq. 31.

$$x(k) = \sum_{i=1}^{k} A^{i-1} B u(k-i) \tag{30}$$

$$y(k) = \sum_{i=1}^{k} C A^{i-1} B u(k-i) + Du(k) \tag{31}$$

In analogy to Volterra theory representation (Eq. 22), the system response y to a

control input u may be compactly written as the convolution shown in Eq. 32

$$y(k) = \sum_{i=0}^{k} Y(i)u(k-i) \tag{32}$$

where Y is a $p \times m$ matrix known as the Markov parameters.

$$Y(k) = \begin{cases} D, & \text{for } k = 0 \\ CA^{k-1}B, & \text{for } k \geq 1. \end{cases} \tag{33}$$

The ERA algorithm is a method of model reduction that begins with defining the generalized Hankel matrix based on discrete-time impulse responses, collected either via experiment or numerical simulation, for all input/output combinations of interest. The algorithm uses the singular value decomposition (SVD) to compute the A, B, and C matrices characterizing the state-space model.

The OKID algorithm was initially developed to complement the ERA method in applications involving experimental systems with noisy input-output measurements, but has evolved to help solve a number of numerical complications encountered for dynamic systems. For systems characterized by zero control initial value or poor control frequency content, the control matrix **u** can become uninvertible or ill-conditioned. Additionally, the control matrix for lightly damped systems may be large, making inversion a computationally expensive process. Lastly, experimental noise cannot be optimally filtered using simple inversion of **u** for the Markov parameters. The OKID method allows for more robust numerical solutions and the identification of systems with nonzero initial conditions by artificially increasing the system damping. The computational steps of this method may be reviewed in the work of Juang et al. [55]. In summary, the SOCIT toolbox applies the ERA/OKID methods to impulse responses, transforming them into unsteady aerodynamic state-space models.

Notable Studies

Silva and Bartels [119] used the state-space modeling approach for the development of linearized, unsteady aerodynamic ROMs for the prediction of flutter and

aeroelastic responses of an AGARD 445.6 wing using the CFL3D flow solver. A mode-by-mode excitation was used to generate modal impulse responses, which served as the inputs and outputs, respectively, for system identification. The resulting unsteady aerodynamic state-space ROM was coupled with a structural state-space model in a MATLAB/SIMULINK environment to create an aeroelastic ROM. The aeroelastic capability was exercised for the rapid computation of aeroelastic transients including flutter. Comparisons to full-order CFL3D simulations were shown to be in excellent agreement but with significantly lower computational costs.

Additionally, several numerical considerations with respect to time/frequency resolution and amplitude-dependent convergence were presented in regard to generating impulse responses. It was noted that the use of a larger nondimensional time step allows for both larger input amplitudes and a smaller frequency resolution, whereas increased subiterations allow for the minimization of numerical error that may be introduced with larger time steps or modal amplitudes. A smaller frequency resolution allows for more accurate predictions of frequency-domain phenomena, while a larger input amplitude allows for an improved chance of exciting nonlinear terms.

The work by Silva and Bartels successfully demonstrated the feasibility of creating CFD-based aerodynamic state-space models using a mode-by-mode excitation for system identification. For the AGARD wing studied, only four structural modes were considered and their computational solutions were reasonable. For more complex models, the number of modes can be an order of magnitude large for which the mode-by-mode excitation method becomes impractical. As a solution, several authors have explored methods for simultaneously exciting all relevant structural modes in a single CFD run, enabling the practical generation of ROMs for complex models.

Raveh [98] used filtered white Gaussian noise to simultaneously excite structural modes. Kim et al. [56, 57] introduced a method based on staggered step inputs, using one step per mode. Silva [118] compared four different types of excitations

used to simultaneously excite each of the structural modes for a supersonic semispan model, while enabling the identification of the individual responses using the SOCIT toolbox. These methods consist of the lagged step input, block pulse input, and the Walsh function input. Generalized aerodynamic force predictions generated by the unsteady aerodynamic state-space model using the simultaneous excitation methods were found to compare well to those using the mode-by-mode excitation method.

Each of the previously mentioned state-space ROM applications in aeroelasticity consider the CFD simulation of system excitation functions at converged static aeroelastic conditions. As a result, the applicability of the ROM is limited to dynamic pressures close to that of the static aeroelastic condition about which the model is linearized. Silva [117] introduced an enhanced ROM approach capable of computing combined static and dynamic aeroelastic responses, as well as matched-point solutions, i.e., various combinations of dynamic pressure and velocity, using a single multidisciplinary ROM. This was accomplished by resampling the existing unsteady aerodynamic and structural ROMs using a newly defined time step based on the input velocity. Reasonable correlation was found compared to CFL3D responses.

All of the previous studies develop unsteady aerodynamic ROMs for identifying aeroelastic instabilities. However, the approach is also beneficial in the characterization of aerodynamic performance for maneuvering vehicles. Shelton et al. [111] implemented the state-space modeling approach for computing the aerodynamic damping coefficients of an Army-Navy Finner Projectile subject to rigid body longitudinal motions. The Walsh functions demonstrated in [118] were leveraged as computational training maneuvers to efficiently excite the impulse response to vehicle-state motion inputs. The SOCIT tool generates state space aerodynamic models using the simulated inputs/outputs. Once the individual impulse responses are identified, the system dynamics concept of convolution can be used to predict the aerodynamic response to arbitrary time-accurate motions.

Concluding Remarks

State-space models are equivalent representations of Volterra series reduced-order models in a form compatible with modern controller frameworks. Recent studies have demonstrated initial attempts at the formation of multidisciplinary ROMs for identifying aeroelastic characteristics of flexible vehicle models. The SOCIT toolbox developed for generating state-space models enables efficient identification of impulse response functions when paired with specialized composite training maneuvers. In order to take advantage of state-space models for virtual flight simulation predictions, advances in the automated CFD simulation of articulating control surfaces are needed.

2.6 Surrogate-Based Recurrence Frameworks

Theory

Surrogate-Based Recurrence Frameworks (SBRF) share the same fundamental mathematical description of dynamic systems as state-space ROMs. A discrete-time dynamic system may be described by Eqs. 34 and 35, where k is the discrete-time index. The vector $\mathbf{u}$ is the vector of system input variables, $\mathbf{x}$ is the vector of state variables, and $\mathbf{y}$ is the vector of system output variables.

$$x_{k+1} = f(x_k, u_k) \tag{34}$$

$$y_k = h(x_k) \tag{35}$$

The principle differences between SBRF and state-space ROMs is the method of approximating the system and the process for system identification. SBRF ROMs approximate the nonlinear Navier-Stokes equations as a multi-input/multi-output dynamic system as given by Eq. 36. In discrete-time, Eq. 36 writes the output vector at any instant in time, k, as a function of the past n values of the inputs and the past m values of the outputs, where ϕ is a vector-valued nonlinear function that

maps the inputs to the outputs of the system.

$$y(k) = \phi\left(y_k, y_{k-1}, \ldots, y_{k-m+1}, x_k, x_{k-1}, \ldots, x_{k-n+1}\right) \tag{36}$$

The mapping function, ϕ, is often represented using neural networks or general surrogate-based models without any specifically required functional form. Whereas Volterra kernels are used to provide a direct means of physical interpretation of the system dynamics, SBRFs essentially provide a curve fit based on observed system dynamics [121]. In this manner, the input-output mapping, ϕ, can be learned using known time histories of input and output variables as generated by training maneuvers. Mindful selection of the training maneuvers is necessary to ensure the model identifies the system dynamics of interest, e.g., motion frequency, amplitude, etc. These frameworks are noted as recurrent since the network output becomes part of the next input vector [29].

Notable Studies

Ghoreyshi et al. [44] created ROMs based on both Radial Basis Functions (RBFs) and a Kriging-based surrogate model for predicting the unsteady aerodynamic loads of an X-31 aircraft undergoing pitching motions in the transonic speed regime. For the RBF ROM, three training maneuvers were considered for system identification: the linear chirp, spiral, and Schroeder, each defined in terms of angle of attack, amplitude, and angular velocity. For the Kriging model, a Design of Experiment (DOE) method was used to sample the Mach number and pitching amplitude space for which pitching simulations were run and interpolated for predictions at new pitching conditions. Each of the ROMs produced accurate results when compared to full-order CFD simulations. The noted ROMs were also compared to ROMs based on the Volterra theory and linear/nonlinear indicial response theory. The authors note that the nonlinear indicial response theory performed the best of all the models.

Ghoreyshi et al. [36] later investigated the use of the same RBF ROMs, in comparison to indicial response ROMs, for predicting the unsteady lift of an NACA 0012

airfoil oscillating and translating in nonlinear flight regimes. A chirp motion starting from zero degrees angle of attack was simulated for two seconds of time up to an amplitude of 10°. The training maneuver was used to create the RBF ROM and subsequently used for predicting an airfoil plunging motion for a reduced frequency of $k = 1$. The model results were shown to be in excellent agreement with the full-order CFD simulation results for the plunging oscillation. In contrast, the indicial response models encountered difficulties at high angles of attack due to numerical stability problems in identifying step responses.

Ghoreyshi et al. [41] extended the SBRF model in Eq. 36 to allow for both primary, y, and secondary, $\tilde{y}$, output measurements as shown in Eq. 37.

$$y(k) = \phi\left(y_k, y_{k-1}, \ldots, y_{k-m+1}, x_k, x_{k-1}, \ldots, x_{k-n+1}, \tilde{y}_k, \tilde{y}_{k-1}, \ldots, \tilde{y}_{k-m+1}\right) \tag{37}$$

Such a model is useful when multifidelity information sources are available. For example, higher fidelity information sources, e.g., Navier-Stokes, may be used to characterize nonlinear regions of a flight parameter space. The interior or linear regions of the flight envelope may then be sampled using cheaper, lower-fidelity information sources, e.g., Euler, as a means of reducing computational cost.

The multifidelity SBRF model was demonstrated using an RBF neural network identification approach. The linear chirp, spiral, and Schroeder maneuvers used in previous studies were used for system identification. The model was then demonstrated for an NACA 0012 airfoil undergoing pitching and plunging motions. The results were shown to closely represent the actual aerodynamic response, when compared to full-order CFD solutions, at over half the computational cost.

Concluding Remarks

Surrogate-based recurrence frameworks are nonintrusive, parametric ROMs, which rely on identification of a vehicle's dynamic behavior using specialized training maneuvers parameterized in terms of flight conditions and motion rates of interest. Once

generated, these models may be used to predict the unsteady aerodynamics for maneuvers within the range of observed responses. The primary drawback of such methods, in comparison to the nonparametric indicial response and Volterra series ROMs, is that they are generally more expensive to identify and do not capture the dynamics of the system using fundamental responses. In essence, these methods essentially act as a time-accurate curve fit with no direct physical interpretation of a system's response characteristics and rely on reasonable training maneuvers, which capture the dynamics of interest.

2.7 Modal Projection Methods

Theory

Modal projection methods are based on the manipulation of a system's governing equations and consist of a systematic procedure for identifying the dynamics of a system using both linear and nonlinear ROMs, regardless of the mathematical formulation used to describe the system [127]. These methods accomplish this by performing an eigenvalue stability analysis on the system in the neighborhood of an equilibrium point.

Consider the governing equations of a system with manipulatable inputs, $\tilde{u}$, about an equilibrium point, $\tilde{x}$, as described by Eq. 38.

$$\mathbf{F}(\tilde{\mathbf{x}}, \tilde{\mathbf{u}}) = 0 \tag{38}$$

The stability analysis then begins with the definition of a small increment with respect to the initial equilibrium point, $\mathbf{w} = \mathbf{x} - \tilde{\mathbf{x}}$. The linearized homogeneous system about the equilibrium point, $\tilde{\mathbf{x}}$ is then described by the expression shown in Eq. 39, where $\mathbf{A}$ is the system's Jacobian matrix.

$$\dot{\mathbf{w}} = \mathbf{A}\mathbf{w} \tag{39}$$

As is commonly done in eigenvalue analyses, consider a solution to Eq. 39 in the

exponential form shown in Eq. 40, where λ is a constant scalar and ϕ is a constant n-dimensional vector.

$$\mathbf{w} = \phi e^{\lambda t} \tag{40}$$

Substitution of the eigenvalue solution of Eq. 40 into the linearized system equation of Eq. 39 yields the right and left eigenvalue problems given by Eq. 41, where $i = 1, 2, ..., n$. Details toward solving the left and right eigenvalue problems for large computational models are summarized by DaRonch et al. [21].

$$\begin{aligned} \text{right: } & \lambda_i \phi_i = \mathbf{A}\phi_i \\ \text{left: } & \lambda_i \psi_i = \mathbf{A}^{\mathbf{T}}\psi_i \end{aligned} \tag{41}$$

In analogy to the modal analysis common to structural dynamics, a transformation of coordinates is used to define the system perturbations in terms of a linear combination of modal vectors, as given by Eq. 42. In effect, the full order model is projected onto a small basis of m representative eigenvectors representing the coupled system dynamics.

$$\mathbf{w} \approxeq \sum_{i=1}^{m} (\phi_i z_i + \overline{\phi_i}\,\overline{z_i}) \tag{42}$$

Substitution of the transformation of coordinates into the original system of governing equations (Eq. 39) yields a reduced-order nonlinear residual expanded as a Taylor series around the equilibrium point. The resulting equations consist of m uncoupled ordinary differential equations. Linear and nonlinear formulations may be developed based on the order of terms retained in the Taylor series expansion. The eigenvectors and eigenvalues of the reduced-order system, as applied to virtual flight simulations, describe the dynamic interactions between the fluid, structure, and flight mechanics fields.

Notable Studies

DaRonch et al. [21] demonstrated the modal projection approach for the model reduction of a large dimension fluid-structure-flight model for studying the dynamics

of a flexible wing. A two-dimensional problem was modeled with aerodynamics predicted using CFD and a structural wing model using geometrically-exact nonlinear beam equations. The coupled system was subject to small and large deformations around different static aeroelastic deflection states, with reduced-order models found to achieve good agreement.

In a later study, DaRonch et al. [26] used the modal projection approach to perform efficient time domain gust response analysis for an airfoil modeled using a combination of linear and nonlinear structural and aerodynamic models. The results demonstrated the ability of the method to enable efficient worst case gust searches.

In a recent study, Pagliuca et al. [90] investigated use of the model reduction technique for coupled simulations involving computational fluid dynamics and flight dynamics. The reduced-order models were developed for an NACA 0012 airfoil and a large civil transport aircraft and were shown to retain the quantitative accuracy of the full order system in predicting the flight dynamics responses and loads resulting from external gust disturbances with reductions in computational cost by two orders of magnitude.

Concluding Remarks

Modal projection ROMs are intrusive methods based on manipulation of a system's governing equations to determine the dynamics of interest. An eigenvalue stability analysis is used to reduce the system to a subset of system modes, which describe the dynamic interactions of a coupled system. In the context of VFS, these modes describe the interactions between the fluid, structure, and flight mechanics disciplines. The benefits of this method is a significant reduction in model size with the capability of extracting the original state-space vector using coordinate transformations. Given that the identification process relies on identification of a system's Jacobian matrix with respect to the system's inputs, the approach is fairly difficult to implement, expensive, and has been mostly limited to simplified physical models.

2.8 Summary of Observations and Characteristics of the Present Approach

Based on the results and conclusions of the most notable studies previously reviewed, the following pertinent observations may be made:

1. **Need for Reduced-Order Modeling in VFS**

   Reduced-order models offer an opportunity to enable viable integration of virtual flight simulations earlier in the design process. Significant progress has been made in the development of ROM methods for unsteady aerodynamic predictions of rigid maneuvering vehicles and aeroelastic instability predictions, but the development of multidisciplinary ROMs for VFS is relatively limited.

2. **Intrusive vs. Nonintrusive ROMs**

   The majority of established unsteady aerodynamic reduced-order modeling methods are categorized as nonintrusive, allowing for their general application across any available CFD solver. Intrusive methods require significant implementation costs as these methods involve manipulation of the governing equations for identification of system modes. As such, most intrusive ROMs have been limited to applications involving lower fidelity physical models.

3. **Parametric vs. Nonparametric ROMs**

   Parametric methods, such as surrogate-based recurrence frameworks, require special training maneuvers to excite the system dynamics of interest and are generally more costly to develop compared to nonparametric approaches. Nonparametric methods based on fundamental responses, such as indicial response and Volterra series models, capture the entire frequency spectrum of a system's dynamic response and can therefore, resolve any motion rate with a single response.

4. **State Space Modeling**

   Existing flight simulation frameworks predominantly use formulations based on state space modeling. As a result, several state space ROM methods have been recently developed, differing primarily based on their modes of model identification. Such methods include those based on: fundamental responses, training maneuvers, and modal decomposition. Thus, it is apparent that equivalent state space model may be generated for any desired ROM identification method.

5. **Indicial Response vs. Volterra Series ROMs**

   Each of these methods formulate dynamic system predictions through convolution of a system's input(s) with fundamental responses. Indicial response models utilize the step response, whereas Volterra series models use the impulse response. These methods are intrinsically related in that the impulse function is merely the derivative of the step function. While the impulse response is more efficient to identify, it is typically less robust to identify with respect to amplitude and time step of the simulation. Additionally, nonlinear Volterra models require the identification of higher-order kernels, which are inherently more complex. Nonlinear indicial response models make use of responses parameterized by flight condition, resulting in an unsteady aerodynamic database that may be queried in a process familiar to traditional stability derivative predictions.

6. **Extending Current ROM Capabilities for VFS**

   Existing indicial response methodologies have been developed for unsteady aerodynamic predictions of maneuvering vehicles and aeroelastic stability predictions of flexible vehicles. An opportunity exists for extending current methodologies for unsteady aerodynamic predictions of maneuvering flexible vehicles

provided aeroelastic indicial responses may be identified in response to trajectory-based motion inputs.

A multidisciplinary ROM for unsteady aerodynamic predictions of flexible vehicles is sought as means of *efficiently* evaluating candidate flight configurations prior to physical flight testing. Based on the presented observations, a nonintrusive model is preferred as these ROMs present a more *generalized* approach that is applicable to any aeroelastic numerical simulation tool without modifications to the underlying source code for model identification. Furthermore, nonparametric approaches based on fundamental system responses are of interest as these methods are capable of capturing the entire frequency response spectrum and require no specialized training maneuvers. Additionally, these fundamental responses are *insightful* in that they provide means by which system dynamics can be readily interpreted. Both indicial and impulse response ROMs fall under these two classifications, presenting equally intriguing approaches. Given the more robust identification traits of the step response and the rich history of use in rigid maneuvering vehicle predictions, the indicial response method is chosen for extension to aeroelastic maneuvering vehicle evaluations.

CHAPTER III

PROBLEM FORMULATION

3.1 Research Objective

Given the need for virtual flight simulation and the challenges and opportunities presented by reduced-order modeling, the overarching research objective of this dissertation is stated as follows:

Research Objective:
Develop a reduced-order modeling approach capable of predicting the nonlinear, unsteady aerodynamics encountered by maneuvering, flexible flight vehicles.

From the main objective and supported by the literature review, the following secondary objectives are derived:

- Develop a technical approach for extending the indicial response reduced-order modeling method to flexible maneuvering flight vehicles.
- Identify an efficient numerical solution strategy for dynamic aeroelastic simulations of maneuvering vehicles.
- Improve the understanding of the aerodynamic response of flight vehicles subject to fluid-structure interactions for maneuvers in linear and nonlinear flight regimes.
- Quantify the performance benefits of multidisciplinary ROMs in comparison to full-order simulations, as well as traditional stability derivative models.

Additionally, there are certain assumptions or constraints under which the technical approach presented in this dissertation are applicable. These assumptions serve to scope the proposed work in consideration of the analysis capabilities required to satisfy the overarching research objective.

1. The first assumption is that the proposed reduced-order model will be used to evaluate the unsteady aerodynamics of a flexible vehicle maneuvering through *prescribed trajectories*. The use of predefined maneuvers eliminates the need to consider the complete coupling between the aerodynamic, structural, and flight mechanics disciplines. By doing so, the increased complexity and computational costs associated with the automated CFD simulation of articulating control surfaces may be avoided, while still supporting progress toward the development of multidisciplinary ROMs for VFS.

2. The second assumption is related to the degree of linearity associated with the flight vehicle system. In this dissertation, the ROM is applicable to flexible flight vehicles performing maneuvers in both linear and nonlinear aerodynamic flight regimes, where the structural system is assumed to be linear. By assuming a linearly varying structural system, i.e., small to moderate structural deflections in flight, a modal structural representation may be leveraged. This assumption circumvents the need for nonlinear Finite Element Models (FEM), which require costly external coupling to CFD solvers.

3. The final assumption is the consideration of a fixed vehicle configuration for maneuver analyses. The benefits of the proposed ROM are demonstrated in evaluating the macroscopic aerodynamic coefficients for maneuvering trajectories, where utility of the ROM increases for repeated use. The proposed ROM lays the foundation for rapid vehicle loads analysis and structural optimization, when combined with spatial ROMs used for resolving pressure distributions.

3.2 Research Questions

The overarching research objective identified may be realized by addressing the major research questions identified in the following sections.

3.2.1 Model Identification

Indicial response ROMs developed for maneuvering *rigid* flight vehicle predictions use rigid body motions within CFD solvers to perform specialized maneuvers, which isolate the aerodynamic response due to independent step changes in vehicle-state parameters, e.g., angle of attack, pitch rate, etc. [38]. The same model identification procedure can be readily extended for *flexible* flight vehicle predictions provided an underlying aeroelastic simulation is leveraged. Coupled CFD-structural mode simulations for maneuvering vehicles have been recently demonstrated by several commercial numerical simulation software packages [86,101]. During such simulations, rigid-body motion files are used to specify prescribed trajectories during which time-varying aerodynamic loads are encountered. The fluid-structure interactions (FSI) resulting from these aerodynamic loads are captured at the subiteration level through internal coupling to a structural solver. Mesh deformation capabilities allow for the grid volume mesh to adapt due to deformation of the vehicle's structure.

The dynamic aeroelastic simulation used in the present work is governed by coupling the Euler equations with a linear structural modal solver. Each set of equations represents a discrete-time, time-invariant system, which fulfills the requirements for application of indicial response theory, provided the equations are well-converged in time [121]. There are two requirements for simulating aeroelastic indicial responses: (1) a small enough time step be chosen to adequately resolve the highest frequency structural mode used to model the vehicle structure, and (2) a sufficient number of time steps are prescribed to attain a converged solution. In theory, the identified aeroelastic indicial responses are then capable of capturing the complete frequency

spectrum of fluid-structure interactions present in a flexible vehicle's response to changes in the time-varying vehicle-state parameters. These discussions motivate the first major research question:

Research Question 1:
How does accounting for vehicle flexibility impact the indicial response ROM identification process?

For linear flow regimes, these aeroelastic indicial responses are used in Eqs. 16 and 17 to predict the unsteady aeroelastic response to trajectories defined in terms of $\alpha(t)$, $\beta(t)$, $p(t)$, $q(t)$ and $r(t)$. Since the model assumes a linear relationship between the aerodynamic response and the system inputs, e.g., angle of attack, the linear aeroelastic ROM is generally applicable to linear portions of the flight envelope or limited to small-amplitude motions (locally linear) in nonlinear flight regimes, such as prestall flight. Identification of a single aeroelastic indicial response with respect to each vehicle-state parameter at the initial flight condition is required for ROM generation.

$$C_j(t) = C_{j_0}(M) + \frac{d}{dt}\left[\int_0^t C_{j_\alpha}(t-\tau,\alpha,M)\alpha(\tau)d\tau\right] + \frac{d}{dt}\left[\int_0^t C_{j_q}(t-\tau,M)q(\tau)d\tau\right] \tag{16}$$

$$\begin{aligned} C_k(t) = \frac{d}{dt}\left[\int_0^t C_{k_\beta}(t-\tau,\alpha,M)\beta(\tau)d\tau\right] + \frac{d}{dt}\left[\int_0^t C_{k_p}(t-\tau,M)p(\tau)d\tau\right] \\ + \frac{d}{dt}\left[\int_0^t C_{k_r}(t-\tau,M)r(\tau)d\tau\right] \end{aligned} \tag{17}$$

As discussed earlier in the motivation (Chapter 1), nonlinear, unsteady aerodynamic predictions are particularly important for maneuvering, flexible vehicles for which fluid-structure interactions can lead to more complex aerodynamic responses

relative to rigid vehicles. Differences between rigid and aeroelastic aerodynamic responses are typically present in both static and dynamic solutions. An improper solution strategy may fail to capture the impact of vehicle flexibility in ROM predictions. Furthermore, an efficient strategy is desired to reduce the computational cost associated with ROM identification, increasing the utility of the ROM for flight maneuver predictions. Therefore, the following secondary question need to be addressed:

Research Question 1.1:

What is an appropriate solution strategy for aeroelastic indicial response identification?

The identification of rigid indicial response solutions is composed of two steps: (1) a static time-accurate initialization solution at a sampled flight condition, and (2) a time-accurate dynamic trajectory simulation of the indicial response function, i.e., a step change with respect to α, q, β, p, or r [38]. The standard solution strategy for rigid maneuvering vehicle predictions is to perform time-accurate simulations for the static and dynamic solutions, where a characteristic time step of $\Delta t^* = \Delta t U_\infty / L_{ref} = 0.01$ is generally advised based on guidelines established for predicting time-accurate flows [18,31]. Indicial response simulations are restarted from the static solutions and advanced in time until a converged solution is obtained at the new vehicle-state.

In contrast, the traditional dynamic simulation process for aeroelastic studies consists of three steps: (1) a steady, rigid initialization solution at a sampled flight condition, (2) a static time-accurate aeroelastic solution, initialized from the steady, rigid solution, and (3) a dynamic simulation of a harmonic excitation in displacement, initialized from the static aeroelastic solution [16]. The characteristic time step chosen for dynamic simulations is often based on resolving a vehicle's expected flutter frequency by a sampling rate, N, with general guidelines of $N = 200$. For the static time-accurate aeroelastic solution, the modal damping to the system is artificially set

to a value $\approxeq 1$ in order to attenuate dynamic transients and quickly resolve the static aeroelastic deflections due to the flow [117].

In simulating aeroelastic indicial responses, aspects of both previous approaches are necessary to correctly simulate indicial response functions and resolve all potential frequencies of fluid-structure interactions encountered during planned flight envelope maneuvers. While evaluating aeroelastic instabilities is not the focus of these predictions, it is still prudent to consider selection of a time step based on the structural mode frequencies. In creating the most robust ROM, a time step should be selected based on a sampling of the highest frequency structural mode included in the analysis. The number of required time steps for the dynamic aeroelastic simulation would then be based on a damping of fluid-structure transients until a converged static aeroelastic state is reached. The time step requirements for the aeroelastic simulations are likely to exceed those required for rigid ROMs that do not model multidisciplinary couplings.

In terms of initialization strategy, it is important to evaluate the merits of using a steady, rigid restart solution followed by a time-accurate static aeroelastic solution versus a time-accurate static aeroelastic solution in isolation. Any improvement in the efficiency of generating static initialization solutions would reduce the overall cost for ROM generation. Successive levels of convergence in the rigid, restart solution may translate to a reduction in the required number of time steps for the static time-accurate aeroelastic simulations. For highly flexible vehicles, such as the X-56A, it is expected that the flow solution when accounting for structural deformation presents a significant difference relative to rigid vehicles, such that use of a steady, rigid flow solution would serve only to increase computational costs without accelerating aeroelastic simulation convergence. Additionally, a larger time step for the static time-accurate aeroelastic solutions may expedite convergence, provided numerical stability issues are not encountered.

Under the previous considerations, the following hypothesis for research question 1.1 is formulated:

Hypothesis 1.1: *The most appropriate aeroelastic indicial response solution strategy consists of (1) a static time-accurate aeroelastic simulation with an artificially high modal damping value, followed by (2) a dynamic aeroelastic simulation of an indicial function, using a time step based on resolving the highest frequency structural mode, where an increased number of steps are required for converging to the deformed state.*

For nonlinear flows, linear aerodynamic ROMs can be extended by use of parameterized indicial response functions [35, 37]. Analagous to aerodynamic databases, flow nonlinearity may be captured by sampling a system's indicial response as a function of the flight space parameter values, where the degree of nonlinearity resolved scales with the sampling of indicial responses. The generalized nonlinear indicial response model for longitudinal and lateral coefficients are given by Eqs. 18 and 19, respectively.

$$C_j(t) = C_{j_0}(M) + \frac{d}{dt}\left[\int_0^t C_{j_\alpha}(t-\tau,\alpha,M)\alpha(\tau)d\tau\right] + \frac{d}{dt}\left[\int_0^t C_{j_q}(t-\tau,M)q(\tau)d\tau\right] \tag{18}$$

$$\begin{aligned} C_k(t) = \frac{d}{dt}\left[\int_0^t C_{k_\beta}(t-\tau,\alpha,M)\beta(\tau)d\tau\right] + \frac{d}{dt}\left[\int_0^t C_{k_p}(t-\tau,M)p(\tau)d\tau\right] \\ + \frac{d}{dt}\left[\int_0^t C_{k_r}(t-\tau,M)r(\tau)d\tau\right] \end{aligned} \tag{19}$$

Previous studies [32, 38, 39] implementing nonlinear indicial response ROMs for rigid vehicles typically assume a nonlinear dependency on angle of attack and Mach number for the indicial responses with respect to angle of attack (C_{j_α}) and sideslip angle (C_{k_β}), while the indicial responses with respect to rotations rates ($C_{j_q}, C_{k_p}, C_{k_r}$)

are assumed to vary only with Mach number. Extension of the indicial response ROM method to flexible vehicle evaluations requires consideration of how the sensitivities of these responses may change for aeroelastic simulations. Therefore, the following secondary question is proposed:

Research Question 1.2:

How do flight envelope sensitivities differ between rigid and aeroelastic indicial responses?

For flexible flight vehicles, the strength of fluid-structure interactions is proportional to the aerodynamic loads encountered at a given flight condition. The lift force acting upward against the wing leads to a bending that causes tension stress on the bottom of the wings and compression stress on the top of the wings. These stresses induce strain in the vehicle structure, which act to return the vehicle to its former state. This process repeats, resulting in either a stable or oscillatory aerodynamic response. For aeroelastic indicial responses, it is generally expected that dynamic transients are to be encountered due to the onset of grid motion, followed by a dynamic fluid-structure response that will dampen toward a converged static aeroelastic solution at the final vehicle state. Because fluid-structure interactions are a function of the lift produced at a given flight condition, it is expected that the differences between rigid and aeroelastic responses will become more pronounced as either angle of attack or Mach number are increased. The indicial responses with respect to step changes in the lateral vehicle-state parameters are likely to be less sensitive to these flight space variables relative to longitudinal steps, due to less pronounced changes in lift and sideforce. Based on these discussion points, the following hypothesis for research question 1.2 is formulated:

Hypothesis 1.2: *Aeroelastic indicial responses due to step changes in angle of attack*

or pitch rate will require a richer sampling of the flight envelope space relative to rigid indicial responses as a result of fluid-structure interactions.

Experiment 1.1 is used to determine the optimal solution strategy for indicial response initialization. Experiment 1.2 is designed to assess flight envelope sensitivities of aeroelastic indicial responses with respect to step changes in longitudinal and lateral vehicle-state parameters. The experiments are summarized here and detailed in Chapter 7.

Experiment 1.1: Identification of Aeroelastic Indicial Response Solutions
NASA's FUN3D - a production flow analysis and design tool - possesses the aeroelastic simulation requirements and will serve as the high-fidelity aeroelastic truth model for maneuvering vehicles predictions [10]. FUN3D's multiple-motion-driver capability will be exercised for coupling an Euler, rigid-body motion simulation with a linear modal structural solver. Beginning from a static aeroelastic solution, indicial response function trajectories, isolating unit step changes in the vehicle-state parameters are specified as a function of time using rigid body transformation matrices. In pseudo-time, vehicle structural deformations resulting from the unsteady aerodynamic loads are converged using a set number of FSI subiterations. The grid volume mesh is deformed to match vehicle surface deformations at each FSI subiteration.

The X-56A Multi-Utility Technology Testbed aircraft with four primary structural modes will serve as the test configuration. A static characterization study will first be performed to identify the nonlinear and unsteady flight envelope regimes for the rigid and flexible vehicle configurations. This will allow for a more judicious choice of test maneuvers when evaluating the linear and nonlinear variants of the aeroelastic indicial response ROM, as well as provide insight into sampling requirements. The computational costs will be assessed for converging static time-accurate aeroelastic

solutions restarted from different static time-accurate rigid initialization solutions, each with successive increases in flow convergence. The maximum allowable time step for the static time-accurate aeroelastic simulations will then be assessed based on successive decreases in sampling resolution of the highest frequency structural mode. Finally, the impact of time step on fluid-structure interaction resolution will be assessed for dynamic aeroelastic indicial responses.

Experiment 1.2: Sensitivity of Aeroelastic Indicial Response Solutions

Using the aeroelastic indicial response solution strategy established in the previous experiment, Expt. 1.2 seeks to assess the sensitivity of rigid and aeroelastic indicial responses with respect to step changes in angle of attack, pitch rate, sideslip angle, roll rate, and yaw rate as a function of the flight space variables, angle of attack, Mach number, and sideslip angle. Exploring these sensitivities will allow for the validity of the traditional nonlinear indicial response ROM's assumptions to be assessed for application to flexible vehicles, and provide further insight into response sampling requirements. The indicial response solutions will be advanced in time until static aeroelastic convergence is achieved in order to understand how the ROM identification requirements change, if at all, when modeling fluid-structure interactions.

3.2.2 Model Evaluation

As noted in the literature review (Section 2.3), previous studies by the NATO-AVT group have demonstrated the application of convolution-based ROMs for the unsteady aerodynamic predictions of maneuvering *rigid* flight vehicles. Linear and nonlinear indicial response ROMs were demonstrated to accurately predict the unsteady longitudinal and lateral aerodynamic coefficients for generalized 6DOF maneuvers at various motion rates and angles of incidence. Using the numerically simulated indicial response functions for flexible flight vehicles (Expt 1.1), the ROM formulations

are to be evaluated for predicting the unsteady aerodynamics of flexible flight vehicles undergoing arbitrary time-accurate trajectories. It is necessary to explore whether the approach may be used to capture the fluid-structure interactions present in full-order trajectory simulations of flexible flight vehicles. These discussions motivate the next research question:

Research Question 2:

What are the aerodynamic prediction capabilities of indicial response ROMs applied to maneuvering, flexible flight vehicles?

In order to answer this research question there are two important directions in which research needs to be directed - motion rates and flight space nonlinearity. As discussed earlier in the motivation (Section 1), nonlinear, unsteady aerodynamic predictions are important for vehicles operating at fast motion rates and high angles of incidence. Limitations of the aeroelastic indicial response ROM should be explored with respect to both trajectory characteristics. Therefore, the following secondary question needs to be addressed:

Research Question 2.1:

What are the unsteady aerodynamic ROM prediction capabilities for flexible flight vehicles maneuvering at various rates of motion?

The convolution integral is a general mathematical principle for reconstructing a system's response by performing a linear superposition of scaled and shifted step or impulse responses with respect to a system's inputs. The principle only requires that the specific dynamic system under consideration be a linear, time-invariant system. For the coupled aeroelastic simulations, the system is governed by the time-invariant Euler and linear structural dynamics equations. Thus, the convolution formulation

used in previous flight dynamics studies may be readily applied to predict the unsteady aerodynamics of flexible maneuvering vehicles given properly converged aeroelastic indicial response functions. The fundamental capability of indicial response functions to capture the entire frequency spectrum of a vehicle's dynamic response allows for resolution of any vehicle motion rate. Under these considerations the following hypothesis for research question 2.1 is formulated:

Hypothesis 2.1: *With proper numerical convergence, an aeroelastic indicial response ROM captures the fluid-structure interactions present in full-order trajectory simulations for any feasible rate of motion.*

Research Question 2.2:
What are the unsteady aerodynamic ROM prediction capabilities for flexible flight vehicles maneuvering in nonlinear flight regimes?

Nonlinear indicial response ROMs have been successively demonstrated for the unsteady aerodynamic predictions of rigid vehicles performing generalized maneuvers in 'weakly nonlinear' flow regimes, where time-accurate surrogate models are used to interpolate between indicial responses sampled at flight conditions through the maneuver space. The limits of the nonlinear indicial response ROM were investigated by Ghoreyshi [36, 43] for 2D and 3D models performing forced oscillation and generalized 6DOF trajectories at high angles of incidences. Numerical convergence issues were reported for indicial responses sampled at or beyond the stall angle of attack. The responses were characterized by either small persistent oscillations or excessive lengths of simulation time without reaching a steady-state value. The use of these indicial responses in the ROM demonstrated the practical limitations of such models at high angles of incidence. It is expected that similar limitations are encountered for

aeroelastic ROMs with the added limitation of avoiding simulation failure due to negative volumes encountered during mesh deformation for large structural displacements.

Hypothesis 2.2: *With sufficient sampling of the flight space, a nonlinear aeroelastic indicial response ROM can resolve flow nonlinearities encountered up to stall angles of attack, where feasible response identification limits may be encountered.*

Experiment 2.1 is designed to evaluate the ability of linear indicial response ROMs to predict the unsteady aerodynamics of flexible flight vehicles subject to FSI for longitudinal motions at various maneuver motion rates. Experiment 2.2 is designed to evaluate the ability of nonlinear indicial response ROMs to predict the unsteady aerodynamics of flexible flight vehicles subject to FSI for longitudinal motions at various maneuver angles of incidence. Experiment 2.3 is a generalized demonstration of the aeroelastic indicial response ROM's capability to evaluate flexible flight vehicles undergoing generalized 6DOF trajectories. The experiments are detailed in Chapter 8 and summarized as follows:

Experiment 2.1: Linear ROM Evaluation using Longitudinal Motions
Numerically simulated indicial responses for the X-56A aircraft will be used for evaluating the applicability of a linear ROM for predicting longitudinal and lateral motions. The linear indicial response ROM is coded in MATLAB with a formulation for longitudinal aerodynamic predictions based on the convolution of indicial responses, due to step changes in angle of attack and pitch rate, with prescribed trajectories parameterized by the same vehicle-state parameters. For lateral aerodynamic predictions, convolution is performed with respect to step changes in sideslip angle, roll rate, and yaw rate. A series of forced rolling, yawing, and pitching oscillations with varied motion frequency rates are evaluated using the linear aeroelastic indicial response ROM.

These frequencies range from quasisteady to unsteady. Comparisons are made between ROM predictions and full-order CFD simulation results for the unsteady force and moment coefficients time histories for both the rigid and flexible vehicle.

Experiment 2.2: Nonlinear ROM Evaluated using Longitudinal Motions

A nonlinear indicial response ROM is coded in MATLAB with a formulation based on the convolution of indicial responses due to step changes in angle of attack and pitch rate with prescribed motions parameterized by the same vehicle-state parameters. The indicial response functions are sampled at 1 degree increments in angle of attack and interpolated based on the given motion state to create time-accurate indicial response models for each trajectory state. A series of forced pitching oscillations, ranging from quasisteady to unsteady reduced frequencies, at a mean angle of attack of five degrees and a pitching amplitude of 4 degrees are predicted using the nonlinear aeroelastic indicial response ROM. Model results in the form of unsteady lift and pitching moment coefficients are compared with full-order simulations to quantify the formulation's prediction accuracy.

Experiment 2.3: Generalized ROM Capability using a 6DOF Maneuver

In order to test the generalization of ROMs based on aeroelastic indicial responses, a prescribed right turn maneuver, supplied by the NASA Armstrong Flight Research Center, will be evaluated using an extension of the formulation evaluated in Expt. 1.2. Additional indicial response functions are simulated with respect to sideslip angle, roll rate, and pitch rate for lateral aerodynamic coefficient predictions. Also, because 6DOF maneuvers often extend into nonlinear flight regimes, the formulation requires parameterization of indicial responses based on the vehicle flight envelope (angle of attack and Mach number). A uniform sampling of the flight space, as defined by the evaluated trajectories, is used to specify the response functions to be numerically

identified/simulated. A time-accurate surrogate modeling MATLAB toolbox is used to interpolate between the observed database of indicial responses as a function of the current trajectory vehicle state. The flight test maneuver will be simulated via FUN3D's high-fidelity dynamic aeroelastic simulation analysis capability, and subsequently predicted using the generalized ROM formulation, where flight dynamics assumptions are reevaluated for flexible vehicles.

3.2.3 Model Performance

The experiments related to research questions 1 and 2 seek to verify a technical approach for creating quantitatively accurate ROMs for flexible flight vehicles performing generalized trajectories in both linear and nonlinear flight regimes at various rates of motion. Referring to the overarching research objective, it is equally necessary to establish the computational efficiency of the developed ROM to enable viable VFS studies. This motivates the final research question:

Research Question 3:

What are the performance benefits of the aeroelastic indicial response ROM?

The research question was divided into two components that dealt with two difference performance considerations of the proposed ROM. The first component pertains to the trade-off in computational costs versus accuracy in comparison to high-fidelity simulations. This is summarized by research question 3.1 and hypothesis 3.1 presented as follows:

Research Question 3.1:

What are the performance benefits relative to full-order aeroelastic simulations?

Indicial response models developed for maneuvering flight vehicle predictions require a large upfront cost associated with simulating indicial responses. Generalized

6DOF maneuvers incur additional costs associated with the identification of responses with respect to lateral vehicle-state motion parameters. For prescribed motions extending into nonlinear flight regimes, nonlinear indicial response ROMs require the interpolation of a database of sampled indicial responses. The number of time steps required for resolving fluid-structure interactions could increase the ROM generation computational costs significantly. Once the model is identified, it may be reused to sample any generalized trajectory (within the sampled flight envelope) at any motion rate. The computational benefits of the ROM grow with repeated use.

Hypothesis 3.1: *The linear ROM provides a performance benefit relative to full-order simulations for single maneuver evaluations, whereas the nonlinear ROM becomes beneficial only for multiple maneuver evaluations.*

Research Question 3.2:
What are the performance benefits relative to traditional stability derivative models?

In comparison to traditional stability derivative flight dynamics models, the underlying aeroelastic simulation capability may also be leveraged to predict nonlinear flow effects throughout a given flight envelope. The primary difference is that the aeroelastic indicial responses are capable of resolving the frequency spectrum of the flexible vehicle's dynamic response, whereas stability derivatives are inherently quasisteady. While the ROM is computationally more expensive due to the required dynamic simulations, the modeling predictions will be more accurate for maneuvers of increasing motion rates.

Hypothesis 3.2: *Aeroelastic indicial response ROMs provide more accurate unsteady aerodynamic predictions compared to stability derivative models for maneuvers at high*

motion rates. For slowly-varying maneuvers, the stability derivative method remains the most efficient aerodynamic model.

Experiment 3.1: Comparison to Full-Order Simulation

The objective is to quantify the computational costs versus accuracy between high-fidelity aeroelastic simulation results and linear and nonlinear aeroelastic indicial response ROM predictions. Modeling error will be quantified in terms of the mean and standard deviation of the local error relative to CFD simulations for each point in the trajectory. Computational costs will be measured in terms of CPU hours. The performance of linear and nonlinear ROM variants will be assessed based on generating the maneuver predictions of Experiments 2.1-2.3. Prediction performance will be explored based on modeling assumptions and the number of time steps used for converging aeroelastic indicial responses. The utility of the ROM will be established based on determining the break even point in computational cost relative to full-order simulations - in terms of maneuver length.

Experiment 3.2: Comparison to Stability Derivative Method

Quasisteady stability derivatives may be extracted from the previously identified aeroelastic indicial responses and evaluated using the traditional linear flight dynamics modeling approach for prediction comparisons. The error metrics used in Experiment 3.1 will be used to compare the performance between the aeroelastic reduced-order model and stability derivative method using the test maneuvers from Experiments 2.1-2.3.

CHAPTER IV

MANEUVERING AIRCRAFT AEROELASTIC SIMULATIONS

4.1 Computational Fluid Dynamics Solver

FUN3D (Fully Unstructured Navier-Stokes 3D) is a production flow analysis and design tool developed by NASA Langley Research Center [1, 11]. FUN3D includes a node-based unstructured CFD solver capable of solving the Reynolds-Averaged Navier-Stokes (RANS) or Euler equations for steady or time-accurate flows. Additionally, it can be used to solve fully compressible or incompressible flows. FUN3D employs a second-order accurate spatial discretization and has temporal discretization options ranging from first- to fourth-order with temporal error controllers. A wide variety of flux splitting schemes and turbulence models are available depending on the flow regime of interest.

In addition to its baseline solver capabilities, FUN3D has been extended to handle general mesh movement involving rigid and deforming meshes. Rigid mesh movement is useful for the analysis of rigid bodies in rotation and/or translation, for which all points in the mesh must move simultaneously. Deforming meshes are useful in aeroelastic simulations, such as flutter analyses, for which the volume mesh must deform to accommodate model surface deflections.

Given the need to simulate flexible flight vehicles undergoing time-accurate trajectories, FUN3D was chosen based on its capability to provide flow solutions for bodies undergoing a combination of elastic and rigid motions. FUN3D performs mesh deformation for elastic bodies using a robust formulation based on the linear elasticity structural governing equations [8]. FUN3D's methods for specifying rigid

body motions and for performing aeroelastic analyses are detailed in Sections 4.2-4.3. FUN3D's formulation for solving the governing fluid dynamics equations with respect to moving control volumes is detailed by Biedron et al. [8] and summarized here as follows.

FUN3D uses the Arbitrary Lagrangian-Eulerian (ALE) formulation to provide flow solutions for either stationary or moving control volumes. At the highest fidelity, the unsteady Navier-Stokes equations may be written in integral form using the ALE formulation as shown in Eq. 43.

$$\frac{\partial}{\partial t}\int_V \mathbf{q}dV + \oint_{\partial V}\left(\overline{\mathbf{F}}^* - \overline{\mathbf{F}}_\mathbf{V}\right)\cdot\hat{\mathbf{n}}dS = 0 \tag{43}$$

Here, the conservation laws are expressed as seen by an observer in an inertial reference frame, where V is the control volume, bounded by control surface ∂V, with local control volume face velocity $\mathbf{W}$. The tensors $\overline{\mathbf{F}}^*$ and $\overline{\mathbf{F}}_\mathbf{V}$ represent the convective and diffusive fluxes of the conserved variables, $\mathbf{q}$, respectively. The convective fluxes account for relative changes in flux through the control surface due to the local control surface speed. The convective flux through the moving control volume is expressed as $\overline{\mathbf{F}}^* = \overline{\mathbf{F}} - \mathbf{q}\mathbf{W}^T$, where $\overline{\mathbf{F}}$ is the standard flux tensor for stationary control volumes. The detailed components of the inviscid and viscous flux vectors can be found in Refs. [8]. The detailed components for the stress tensor, heat flux vector, and auxiliary closure equations are listed in Ref. [9]. Details of the spatial discretization and time-advancement schemes may be found in Ref. [1] and [9], respectively.

FUN3D's ALE formulation for the governing fluid dynamics equations may be used to predict the unsteady aerodynamics of maneuvering flight vehicles provided that the vehicle motion is specified at each point in time with respect to the inertial reference frame. At time $t = 0$, the inertial reference frame and flight vehicle (body) reference frame are equivalent. For successive points in time, the body may undergo translations and rotations with respect to the inertial reference frame. FUN3D accounts for this rigid body motion via reference frame transformation matrices.

4.2 Trajectory Simulation via Rigid Body Motion

4.2.1 Reference Frames

Figure 10 illustrates a notional unmanned combat air vehicle configuration within the two primary axes systems: 1) the traditional flight mechanics reference frame (blue), and 2) the CFD reference frame (red) common to the FUN3D flow solver. The CFD reference frame differs from the traditional flight mechanics reference frame by a 180 degree rotation about the y axis.

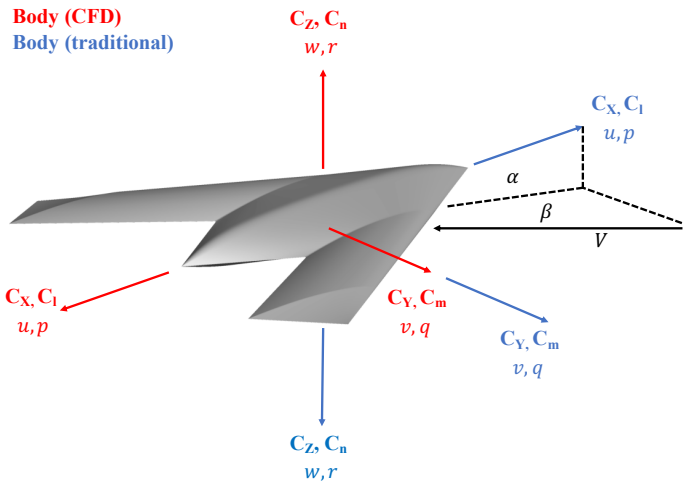

Figure 10: Trajectory axes systems.

In the traditional flight reference frame, the aerodynamic force coefficients are:

- Axial force, $C_X > 0$ along x-nose,
- Side force, $C_Y > 0$ along y-right, and
- Normal force, $C_Z > 0$ along z-down,

while in the CFD reference frame, the aerodynamic force coefficients are:

- Axial force, $C_X > 0$ along x-tail,
- Side force, $C_Y > 0$ along y-right, and
- Normal force, $C_Z > 0$ along z-up.

The aerodynamic moment coefficients are defined to be positive according to the right-hand rule for the respective coordinate systems. In the traditional flight reference frame, the aerodynamic moments coefficients are:

- Rolling moment, $C_l > 0$ with right-wing-down,
- Pitching moment, $C_m > 0$ with nose-up, and
- Yawing moment, $C_n > 0$ with nose-right,

while in the CFD reference frame, the aerodynamic moment coefficients are:

- Rolling moment, $C_l > 0$ with right-wing-up,
- Pitching moment, $C_m > 0$ with nose-up, and
- Yawing moment, $C_n > 0$ with nose-left.

4.2.2 Trajectory Transformation

Vehicle flight trajectories are defined by a wind velocity (α, β, M) and orientation (ϕ, θ, ψ) at each point in time. The initial assumption for the trajectory transformation is that the grid orientation at $t = 0$ aligns with the inertial or horizontal axis, i.e., $\phi_0 = \theta_0 = \psi_0 = 0$. Furthermore, the initial trajectory values for the velocity in the wind axis (V_0), angle of attack (α_0), and sideslip angle (β_0) are specified in the CFD case input file to define the freestream wind. For successive points in time, the trajectory is specified relative to the initialized freestream conditions.

The initial flow conditions at $t = 0$ are used to establish a reference velocity for the grid motion. Assuming $\phi = \theta = \psi = 0$, the components of the reference velocity are defined by Eq. 44.

$$\begin{Bmatrix} u_{ref} \\ v_{ref} \\ w_{ref} \end{Bmatrix} = V_0 \begin{Bmatrix} cos(\alpha_0)cos(\beta_0) \\ sin(\beta_0) \\ sin(\alpha_0)cos(\beta_0) \end{Bmatrix} \tag{44}$$

Next, transform the prescribed time-accurate $\alpha(t)$, $\beta(t)$, and $V(t)$ from the wind axis to body axis, using Eq. 45.

$$\begin{Bmatrix} u_b(t) \\ v_b(t) \\ w_b(t) \end{Bmatrix} = V(t) \begin{Bmatrix} cos(\alpha(t))cos(\beta(t)) \\ sin(\beta(t)) \\ sin(\alpha(t))cos(\beta(t)) \end{Bmatrix} \tag{45}$$

Then, transform through the Euler angles (roll, pitch, and yaw) from the body axis to the horizontal axis aligned with the inertial axes at time $t = 0$ using Eqs. 46, 47, and 48.

$$R(t) = R_z(\psi(t))R_y(\theta(t))R_x(\phi(t)) \tag{46}$$

$$R_z(\psi) = \begin{Bmatrix} cos\psi & -sin\psi & 0 \\ sin\psi & cos\psi & 0 \\ 0 & 0 & 1 \end{Bmatrix}, R_y(\theta) = \begin{Bmatrix} cos\theta & 0 & sin\theta \\ 0 & 1 & 0 \\ -sin\theta & 0 & cos\theta \end{Bmatrix}, R_x(\phi) = \begin{Bmatrix} 1 & 0 & 0 \\ 0 & cos\phi & -sin\phi \\ 0 & sin\phi & cos\phi \end{Bmatrix} \tag{47}$$

$$\begin{Bmatrix} u_h(t) \\ v_h(t) \\ w_h(t) \end{Bmatrix} = R(t) \begin{Bmatrix} u_b(t) \\ v_b(t) \\ w_b(t) \end{Bmatrix} \tag{48}$$

The final grid velocity is computed by subtracting the reference velocity, Eq. 44, from the horizontal axis velocity components, Eq. 48, as noted by Eq. 49. It is important to note the x- and z-velocity component sign changes, which correct for the 180 degree rotation about the y-axis between the flight and CFD reference systems.

$$\begin{Bmatrix} U_h(t) \\ V_h(t) \\ W_h(t) \end{Bmatrix} = \begin{Bmatrix} -u_h(t) \\ v_h(t) \\ -w_h(t) \end{Bmatrix} - \begin{Bmatrix} -u_{ref} \\ v_{ref} \\ -w_{ref} \end{Bmatrix} \tag{49}$$

Finally, the change in translation at each time step in the CFD coordinate system is calculated as the change in position due to the average translation velocity between two successive time steps, as given by Eq. 50. Once the translation is calculated, the position is calculated as the sum of the initial CG position and the translation vector, given by Eq. 51.

$$\begin{Bmatrix} T_x(t_{i+1}) \\ T_y(t_{i+1}) \\ T_z(t_{i+1}) \end{Bmatrix} = \begin{Bmatrix} T_x(t_i) \\ T_y(t_i) \\ T_z(t_i) \end{Bmatrix} + \Delta t \begin{Bmatrix} \frac{U_h(t_{i+1})+U_h(t_i)}{2a_0} \\ \frac{V_h(t_{i+1})+V_h(t_i)}{2a_0} \\ \frac{W_h(t_{i+1})+W_h(t_i)}{2a_0} \end{Bmatrix} \tag{50}$$

$$\begin{Bmatrix} CG_x(t) \\ CG_y(t) \\ CG_z(t) \end{Bmatrix} = \begin{Bmatrix} CG_x(t_0) \\ CG_y(t_0) \\ CG_z(t_0) \end{Bmatrix} + \begin{Bmatrix} T_x(t) \\ T_y(t) \\ T_z(t) \end{Bmatrix} \tag{51}$$

4.2.3 Motion File Definition

FUN3D defines all rigid motions via application of 4 x 4 matrices to described affine transformations [10]. The 4 x 4 transformation matrix contains both translation and orthonormal rotation components, as shown in Eq. 52, and maps a vehicle's initial position at time $t = 0$, when aligned with the inertial reference frame, to its translated position at successive points in time, $t = t_i$.

$$\begin{Bmatrix} x \\ y \\ z \\ 1 \end{Bmatrix} = \begin{Bmatrix} R_{11} & R_{12} & R_{13} & T_x \\ R_{21} & R_{22} & R_{23} & T_y \\ R_{31} & R_{32} & R_{33} & T_z \\ 0 & 0 & 0 & 1 \end{Bmatrix} \begin{Bmatrix} x_0 \\ y_0 \\ z_0 \\ 1 \end{Bmatrix} \tag{52}$$

For maneuvering vehicle simulations, FUN3D maps from the fixed reference frame to the moving body coordinate frame through the sequence of "Origin to CG - Rotate about CG - CG to Origin - Translate" as shown by Eq. 53.

$$[T(t)] = [T_{CG}][R_{CFD}(t)][T_{CG}]^{-1} + [T_{grid}(t)] \tag{53}$$

The pure translation to the vehicle's CG location consists of a transform matrix defined by a 3 x 3 rotation submatrix consisting of an identity matrix with the final column accounting for the pure translation to the CG position coordinates from the inertial frame axes origin, as shown in Eq. 54. The rotation matrix consists of a composite rotation matrix calculated via chained rotation matrices from the flight trajectory Euler angles, as shown in Eq. 55. Note that the roll and yaw angles are defined to be negative to account for the change between the traditional reference frame and CFD reference frame. The translation matrix accounting for translation back to the origin is simply the inverse transform of the original translation matrix, as shown in Eq. 56. The second transform component is the pure grid translation component, which is calculated based on the time-accurate body velocity transformed into the inertial axes frame via Eq. 50.

$$[T_{cg}] = \begin{Bmatrix} 1 & 0 & 0 & CG_x(t_0) \\ 0 & 1 & 0 & CG_y(t_0) \\ 0 & 0 & 1 & CG_z(t_0) \\ 0 & 0 & 0 & 1 \end{Bmatrix} \tag{54}$$

$$[R(t)] = [R_z(-\phi(t))][R_y(\theta(t))][R_x(-\psi(t))] \tag{55}$$

$$[T_{grid}(t)] = \begin{Bmatrix} 0 & 0 & 0 & T_x(t) \\ 0 & 0 & 0 & T_y(t) \\ 0 & 0 & 0 & T_z(t) \\ 0 & 0 & 0 & 1 \end{Bmatrix} \tag{56}$$

The FUN3D motion files defining the rigid body motion via transform matrices are formatted as outlined by Table 1. Starting from a static initialization, the vehicle CG location is defined relative to the origin with an identity matrix defining the coincident inertial and body reference frames. For successive iterations, the first line consists of a single entry defining the nondimensional time, the second line consists of the updated CG location resulting from the transform matrix, which is then defined for the given iteration. The motion file should include the initial, intermediate, and final motion states for the trajectory.

Table 1: Example format of FUN3D rigid body motion file.

t_0			
$CG_X(t_0)$	$CG_Y(t_0)$	$CG_Z(t_0)$	
1	0	0	0
0	1	0	0
0	0	1	0
0	0	0	1
$t_0 + \Delta t$			
$CG_X(t_1)$	$CG_Y(t_1)$	$CG_Z(t_1)$	
$R_{11}(t_1)$	$R_{12}(t_1)$	$R_{13}(t_1)$	$T_x(t_1)$
$R_{21(t_1)}$	$R_{22}(t_1)$	$R_{23}(t_1)$	$T_y(t_1)$
$R_{31}(t_1)$	$R_{32}(t_1)$	$R_{33}(t_1)$	$T_z(t_1)$
0	0	0	1
$\vdots$	$\vdots$	$\vdots$	$\vdots$
t_n			
$CG_X(t_n)$	$CG_Y(t_n)$	$CG_Z(t_n)$	
$R_{11}(t_n)$	$R_{12}(t_n)$	$R_{13}(t_n)$	$T_x(t_n)$
$R_{21(t_n)}$	$R_{22}(t_n)$	$R_{23}(t_n)$	$T_y(t_n)$
$R_{31}(t_n)$	$R_{32}(t_n)$	$R_{33}(t_n)$	$T_z(t_n)$
0	0	0	1

4.3 Modal Structural Dynamics Modeling

FUN3D's aeroelastic module provides the capability for performing static and dynamic aeroelastic analyses via time integration of the linear structural dynamics equations. The static aeroelastic analysis is useful for problems in which the coupling between the aerodynamics and structures disciplines is relatively weak and may

be done infrequently, e.g., cruise conditions. Whereas, the dynamic analysis is useful for problems involving a strong, unsteady coupling between the two disciplines, as found in maneuvering aircraft flight.

As opposed to externally coupling FUN3D's CFD solver with a nonlinear Finite Element Method (FEM) model, FUN3D uses a self-contained, mode-based linear structural model. The modal aeroelastic analysis formulation is capable of predicting the fluid-structure interactions for models subject to small or moderate surface deflections, and its use has become routine for flutter predictions. Details of the modal aeroelastic analysis and time integration scheme may be found in Ref. [8] and is summarized here.

The coupled linear structural dynamics equations are expressed in Eq. 57. The term $[\mathbf{M}]$ is the mass matrix, $[\mathbf{D}]$ is the damping matrix, $[\mathbf{K}]$ is the stiffness matrix, $\delta(\mathbf{x}, t)$ is the displacement, and $\mathbf{F}_a$ is the aerodynamic loading.

$$[\mathbf{M}]\,\ddot{\delta} + [\mathbf{D}]\,\dot{\delta} + [\mathbf{K}]\,\delta = \mathbf{F}_a \tag{57}$$

As opposed to solving for the displacement at each point in the structural model, it is more computationally efficient to recast the displacements as a linear superposition of natural mode shapes. These structural modes may be obtained by performing an eigenvalue analysis of the FEM vehicle model. The results of the analysis yields a series of natural vibration mode shapes with corresponding natural frequencies, as illustrated for an AGARD 445.6 flexible wing in Figure 11.

The original displacements of the structural model, $\delta(\mathbf{x}, t)$, may be rewritten as a linear superposition of natural mode shapes, $\phi_i(\mathbf{x})$, as shown in Eq. 58. The term, $\mathbf{q}_i(t)$, is referred to as a generalized coordinate and represents the scaling constant for each mode shape at a given point in time.

$$\delta = \sum_{i=1}^{N_{modes}} \mathbf{q}_i(t)\phi_i(\mathbf{x}) \tag{58}$$

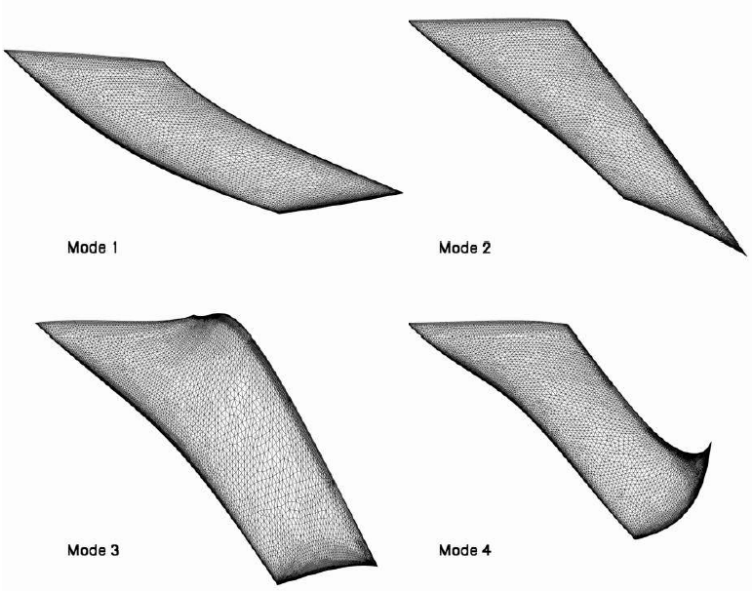

Figure 11: First four flexible structural mode shapes for the AGARD 445.6 wing.

Substitution of the series representation of (Eq. 58) into the coupled linear structural dynamics equations (Eq. 57) and multiplying by ϕ^T yields the reduced-order linear structural dynamics equations of Eq. 59.

$$\ddot{\mathbf{q}} + [\zeta]\,\dot{\mathbf{q}} + [\omega]\,\mathbf{q} = \phi^T \mathbf{F}_a = \hat{\mathbf{F}}_a \tag{59}$$

The resulting equations are now decoupled and can be written as a sequence of scalar second-order equations in terms of the generalized coordinates. The terms $[\zeta] = \phi^T[\mathbf{D}]\phi$ and $[\omega] = \phi^T[\mathbf{K}]\phi$ represent diagonal matrices. For the i^{th} mode, the element of the damping matrix $[\zeta]$ is $2\omega_i\zeta_i$ and the element of the stiffness matrix $[\omega]$ is ω^2. The terms ζ_i and ω_i represent the structural damping ratio and natural frequency of the i^{th} structural mode.

4.4 Summary

The numerical simulation requirements for predicting the unsteady aerodynamics of a flexible flight vehicle were summarized. CFD flow solvers require an Arbitrary Lagrangian-Eulerian (ALE) formulation in order to solve the governing fluid dynamics equations for moving control volumes. Additionally, the chosen CFD solver should

be capable of performing rigid mesh movement in order to simulate time-accurate trajectories. Because the flow equations are specified in the inertial reference frame, there is a need to specify transformation matrices that map the vehicle's trajectory in the body reference frame to the inertial reference frame for each simulation time step.

For flexible flight vehicles, there is an added requirement for resolving fluid-structure interactions resulting from the unsteady aerodynamic loads encountered over the course of the maneuvers. A modal aeroelastic analysis provide a simplified, efficient structural dynamics model for predicting small to moderate vehicle surface deflections in flight. Coupling of the CFD flow solver to the modal aeroelastic analysis at the subiteration level allows for convergence of the flexible vehicle-state at each point along the maneuver. Finally, the chosen CFD solver should be capable of performing elastic mesh movements at the subiteration level for the changing vehicle state.

CHAPTER V

INDICIAL RESPONSE REDUCED-ORDER MODELING

5.1 Flight Dynamics Assumptions

In conventional flight dynamics modeling, the longitudinal aerodynamics forces and moments are assumed to depend primarily on angle of attack (α) and pitch rate (q), whereas the lateral aerodynamic forces and moments are assumed to depend primarily on sideslip angle (β), roll rate (p), and yaw rate (r). Unsteady aerodynamic models for maneuvering vehicles seek to predict the time-accurate variations in aerodynamic forces and moments as a function of these vehicle-state parameters, as expressed in Eq. 60, where $j = L$ (lift), D (drag), or m (pitching moment) and $k = Y$ (side force), l (rolling moment), or n (yawing moment).

$$\begin{aligned} \Delta C_j(t) &= f(\alpha(t), q(t)) \\ \Delta C_k(t) &= f(\beta(t), p(t), r(t)) \end{aligned} \tag{60}$$

Then, assume that the independent contributions of each of these vehicle-state parameters with respect to the aerodynamic response may be isolated, resulting in the general modeling form of Eq. 61.

$$\begin{aligned} \Delta C_j(t) &= f(\alpha(t)) + f(q(t)) \\ \Delta C_k(t) &= f(\beta(t)) + f(p(t)) + f(r(t)) \end{aligned} \tag{61}$$

Reduced-order models seek to accurately and efficiently model the system dynamics, $\Delta C_j(t)$ and $\Delta C_k(t)$, due to arbitrary values of each of these parameters, defining a maneuver of interest. Indicial response models accomplish this by first identifying the system's response due to unit step changes in each of these parameters, then using the mathematical principle of convolution to predict the system's response for any motion of interest.

5.2 Indicial Response Theory

5.2.1 Linear Formulation

As discussed in the literature review, the convolution principle can be used to predict the dynamics of systems that may be mathematically classified as time-invariant. For time-invariant systems, a shift in the input to a later time yields an identical response, only shifted in time. First recognized by Silva [121], the discrete-time Navier-Stokes equations, linear structural dynamics equations, and many other governing equations of interest in engineering do not explicitly depend on time, and thus are time-invariant (provided steady-state convergence).

In this dissertation, the system of interest is a maneuvering flexible flight vehicle with system dynamics described via a CFD-based modal dynamic aeroelastic analysis, as outlined in Chapter 4. Because the fluid dynamics and structural dynamics equations are coupled at the subiteration level, numerical simulations of such aeroelastic systems are also time-invariant. This is evidenced by the successful application of convolution-based ROMs for efficiently identifying flutter characteristics of flexible vehicles.

The primary difference between these two applications is a matter of relevant system inputs and outputs. For flutter studies, the goal is to identify the stability of the generalized aerodynamic forces in each structural mode in response to amplitude/velocity perturbations in each of the structural modes. For maneuvering vehicle studies, the goal is to identify the vehicle-level aerodynamic response due to changes in the vehicle-state parameters, which define a time-accurate maneuver, where fluid-structure-interactions effects are captured implicitly in the analysis.

In order to address Expt. 2.1, a linear indicial response ROM is proposed for efficiently capturing the effects of fluid-structure interactions on the unsteady aerodynamic response of flexible vehicles maneuvering within linear flight regimes. At

higher angles of attack, the locally linear variations in the aerodynamic response reside in a much smaller range of angle of attack in comparison to low angle-of-attack maneuvers. Either the Euler or RANS equations may be used to capture the unsteady aerodynamics, while the modal structural dynamics equations may be used to capture small to moderate vehicle deformations in flight.

Convolution-based ROMs use step or impulse functions to capture a system's fundamental dynamic behavior. For the proposed linear time-invariant aeroelastic system, either a single unit step or a unit impulse function with respect to each vehicle-state parameter, u, may be numerically simulated in discrete time to capture each motion parameter's contribution to the overall flexible vehicle dynamics, $y = C_j$ or C_k, as shown in Fig. 12. The system response due to a unit step function is referred to as the unit step or indicial response, s, while the system response due to a unit impulse function is referred to as the unit impulse response, h.

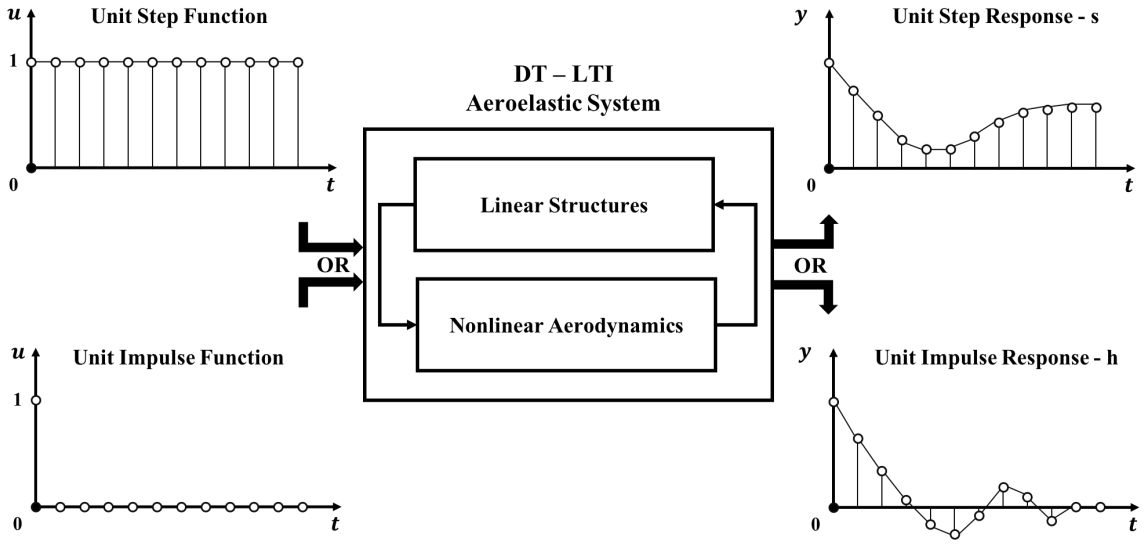

Figure 12: Discrete-time, linear time-invariant aeroelastic system.

The unit step and unit impulse functions fundamentally represent the memory of the system. These functions are related in that the impulse function is merely the

derivative of the step function. For linear time-invariant systems, the response to these functions may be scaled, shifted in time, and superpositioned to predict the system dynamics to arbitrary vehicle maneuvers using convolution.

Motivated by its decreased sensitivity to amplitude and time step size, the step response was chosen for the present study [97]. The convolution of each indicial response function with any arbitrary vehicle-state motion input gives the time-accurate vehicle response in terms of longitudinal and lateral aerodynamic coefficients, as given by Eqs. 16 and 17, respectively. The terms, C_{j0} and $C_{\kappa 0}$, represent the aerodynamic coefficient values at the initial static aeroelastic condition from which the maneuver begins.

$$C_j(t) = C_{j_0}(M) + \frac{d}{dt}\left[\int_0^t C_{j_\alpha}(t-\tau,\alpha,M)\alpha(\tau)d\tau\right] + \frac{d}{dt}\left[\int_0^t C_{j_q}(t-\tau,M)q(\tau)d\tau\right] \tag{16}$$

$$\begin{aligned} C_k(t) = \frac{d}{dt}\left[\int_0^t C_{k_\beta}(t-\tau,\alpha,M)\beta(\tau)d\tau\right] + \frac{d}{dt}\left[\int_0^t C_{k_p}(t-\tau,M)p(\tau)d\tau\right] \\ + \frac{d}{dt}\left[\int_0^t C_{k_r}(t-\tau,M)r(\tau)d\tau\right] \end{aligned} \tag{17}$$

5.2.2 Nonlinear Formulation

In the linear indicial response ROM formulation, the vehicle-state parameters defined a constant-speed maneuver assumed to lie within a locally linear portion of the flight regime. The formulation assumption is that the indicial responses could be scaled linearly, i.e., $C_{j\alpha}|_{\alpha=0^\circ}^{\alpha=1^\circ} = C_{j\alpha}|_{\alpha=1^\circ}^{\alpha=2^\circ}$. However, when considering high performance flight vehicles, the maneuvers of interest are often characterized by varying vehicle speed with angles of incidence potentially extending to near-stall regions. Previous research by the NATO AVT-161 task group has shown the importance of considering variability in the step response with increasing angles of attack and Mach number [35, 38, 42].

Their investigations illustrate the inability of indicial response calculated at low angles of attack to accurately represent the system dynamics at high angles of attack, i.e., $C_{j\alpha}|_{\alpha=0^\circ}^{\alpha=1^\circ} \neq C_{j\alpha}|_{\alpha=10^\circ}^{\alpha=11^\circ}$.

Figure 13 provides a notional example summarizing how indicial responses have historically varied for rigid vehicles across the flight maneuver space, as parameterized by angle of attack and Mach number. Each point within the maneuver space represents a separate indicial response resulting from a 1° change in angle of attack at a given Mach number. The variation in the unsteady aerodynamic lift response due to only changes in angle of attack and only changes in Mach number are shown in the bottom figures on the left and right, respectively.

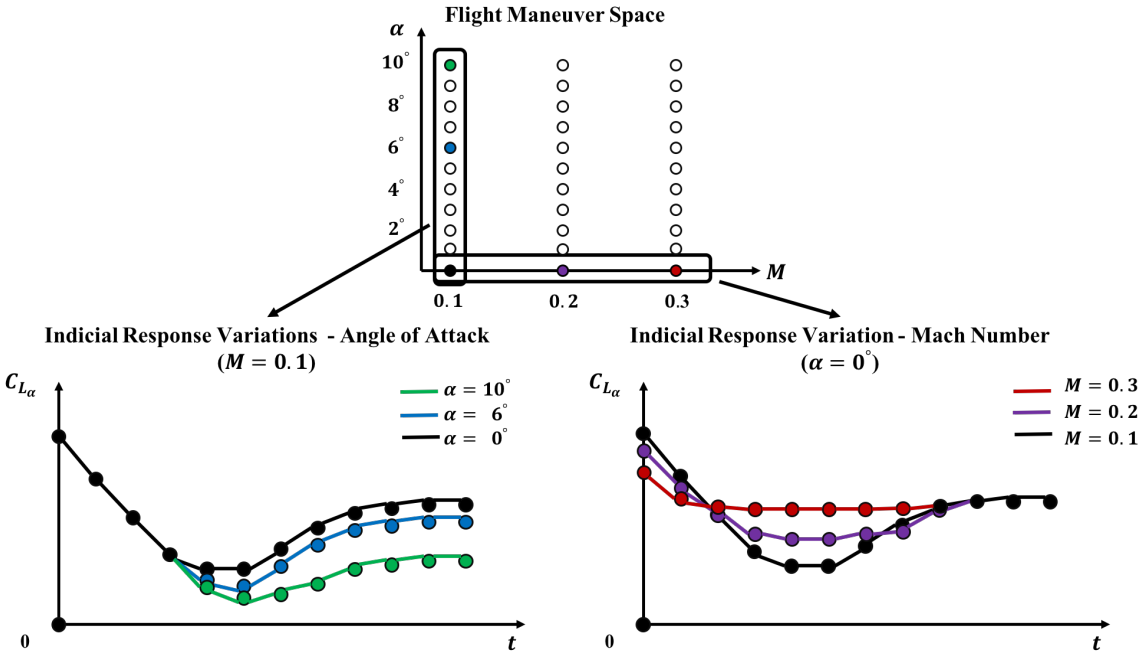

Figure 13: Indicial response sensitivity to flight maneuver space.

The lift response common to both figures ($\alpha = 0^\circ$, $M = 0.1$) represents the baseline response that might typically be used in isolation for the linear indicial response ROM for a constant-speed maneuver at $M = 0.1$. Beginning at the steady-state initial condition, the grid is immediately moved to simulate a step change in angle of attack to 1° while maintaining the initial flight speed. The lift response experiences

a sharp peak resulting from the rapid formation of compression and expansion waves forming on the lower and upper surfaces of the vehicle, respectively [40]. As the simulation progresses, the noncirculatory lift diminishes, while the circulatory lift, due to vorticity, grows asymptotically until reaching a final steady-state value.

The variation in the lift response due to step changes in angle of attack, as sampled at higher angles of attack, within the flight maneuver space is depicted in the left figure. It is generally observed that while the initial peak values of the response are invariant with angle of attack, the transient trend and steady-state values change. The variation in the lift response due to step changes in angle of attack at zero angle-of-attack for different Mach numbers is shown on the right. For the case of increasing Mach number, the initial peak in the response typically decreases with increased compressibility effects. Leishman [63] attributes this to the propagation of pressure disturbances at the speed of sound for compressible flows, whereas for incompressible flows the disturbances are assumed to propagate at infinite speed. Similar variations have been found for indicial responses with respect to step changes in pitch rate, but are generally assumed to vary linearly for low to moderate angles of attack [35].

$$C_j(t) = C_{j_0}(M) + \frac{d}{dt}\left[\int_0^t C_{j_\alpha}(t-\tau,\alpha,M)\alpha(\tau)d\tau\right] + \frac{d}{dt}\left[\int_0^t C_{j_q}(t-\tau,M)q(\tau)d\tau\right] \tag{18}$$

$$\begin{aligned} C_k(t) = \frac{d}{dt}\left[\int_0^t C_{k_\beta}(t-\tau,\alpha,M)\beta(\tau)d\tau\right] + \frac{d}{dt}\left[\int_0^t C_{k_p}(t-\tau,M)p(\tau)d\tau\right] \\ + \frac{d}{dt}\left[\int_0^t C_{k_r}(t-\tau,M)r(\tau)d\tau\right] \end{aligned} \tag{19}$$

Based on these observed variations, Ghoreyshi et al. [38] extended the linear indicial response ROM in Section 5.2.1 to the nonlinear IR ROM shown in Eqs. 18 and 19 for maneuvering rigid flight vehicles. Here the indicial responses with respect to angles of incidence (α, β) are assumed to vary with angle of attack and Mach number, whereas the indicial responses with respect to rotation rates (p, q, r) are assumed to vary with Mach number. The nonlinear assumptions with respect to the vehicle-state parameters are to be investigated for flexible vehicles via Experiments 2.2-2.3.

5.3 Aeroelastic Indicial Response Identification

Ghoreyshi et al. [40] introduced an approach for the CFD simulation of indicial functions with respect to the angles of incidence and rotation rates for rigid maneuvering vehicles using specialized grid motions. The same approach may be used to accurately identify indicial response functions for flexible flight vehicles provided an aeroelastic simulation is used to resolve the fluid-structure interactions at the subiteration level. Aeroelastic indicial responses are identified through convergence at a static aeroelastic condition, followed by a coupled aerostructural simulation of a prescribed trajectory consistent with a step change in a desired vehicle-input parameter.

The static aeroelastic simulation process, shown in Fig. 14, is a two-step process beginning with reading in the CFD grid and boundary condition files to the CFD flow solver and performing a static rigid simulation at the initial flight conditions. Then, the structural mode shape and mode frequency files must be specified as inputs to the static aeroelastic simulation. Note that the mode shapes should be mapped from the FEM surface grid to the CFD surface grid in preprocessing using a mapping tool such as the Discrete Data Transfer Between Dissimilar Meshes (DDTBDM) tool [108].

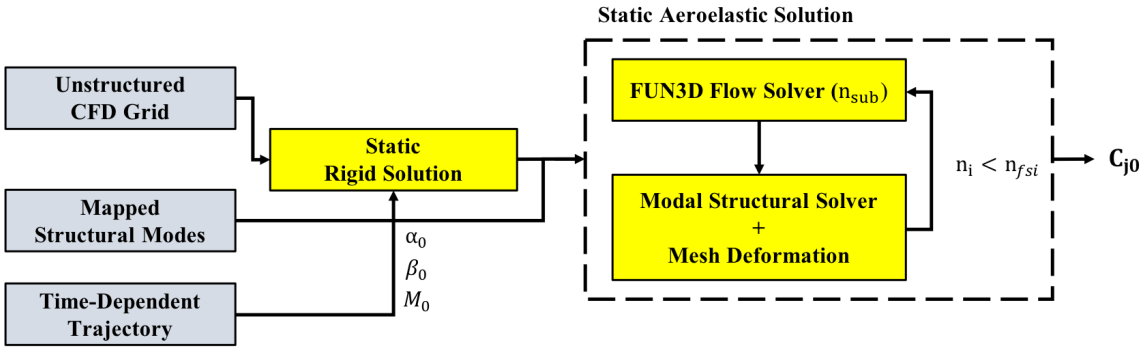

Figure 14: Static aeroelastic simulation process.

Using the results of the static rigid solution as the restart flow condition, a static aeroelastic simulation can then be executed, where the fluid-structure interactions are converged over n_f steady-state time steps. An artificially high structural critical damping ratio (≈ 1) is typically used to accelerate the convergence of the static aeroelastic solution. The result of the numerical simulation process is a deformed vehicle configuration due to the steady-state flight condition. The output static aerodynamic force and moment coefficients represent the constant terms in the indicial response ROM of Eqs. 16-18.

Once the initial static aeroelastic condition has been identified, the next step is to numerically simulate the indicial response functions representing unit step changes in the vehicle-state parameters defining the motion of interest. For longitudinal motions, these parameters are angle of attack and pitch rate, whereas for lateral motions, these parameters are sideslip angle, roll rate, and yaw rate.

Assuming use of a flow solver capable of accounting for rigid mesh movement, as outlined in Section 4.2, then all translational and rotational degrees of freedom may be specified at each point in discrete time in relation to a reference point on the aircraft, e.g., center-of-gravity (CG). Additionally, rotation of the flight vehicle about this reference point is defined using the Euler rotation angles of yaw, pitch, and roll in the body reference frame.

The initial vehicle velocity, v_0, representing the inertial reference frame velocity is defined by the initial Mach number, angle of attack, and sideslip angle. For each subsequent time step, the aircraft reference velocity, v_a, is specified such that the prescribed angles of attack, sideslip, and forward speed can be met. The relative velocity, $v_a - v_0$, for each point in simulation time is implicitly defined using the rigid body transformation matrices that define the location/orientation of the body with respect to the inertial reference frame at $t = 0$.

A summary of the CFD simulation process for identifying indicial responses with respect to a unit step change in angle of attack is illustrated in Fig. 15. The goal of the dynamic simulation is to specify a trajectory such that the angle of attack is incremented instantly, while the pitch rate is held constant. Isolation of a step change in angle of attack is accomplished by translating the grid to the right and downward, beginning at $t = 0$, with a constant velocity vector. The dynamic aeroelastic simulation is executed for n time steps to identify the transients representing the fundamental system dynamics until a converged deformed vehicle state, $C_{j_\alpha}(\infty)$, is reached. The result is a discrete-time indicial response with respect to angle of attack, $C_{j_\alpha}(t)$ in Eq. 16. A similar process is implemented in the lateral plane for identification of indicial responses with respect to sideslip angle.

A summary of the CFD simulation process for identifying indicial responses with respect to a unit step change in pitch rate is illustrated in Fig. 16. The goal of the dynamic simulation is to specify a trajectory such that the pitch rate is incremented instantly, while angle of attack is held constant. Isolation of a step change in pitch rate is accomplished by defining a unit pitch rate at $t = 0$, with a constant translational velocity vector to the right and upward in order to maintain a constant effective angle of attack. For example, this may be a unit change in pitch rate from 0 rad/s to 1 rad/s. The dynamic aeroelastic simulation is executed for n time steps to identify the transients representing the fundamental system dynamics until a converged deformed

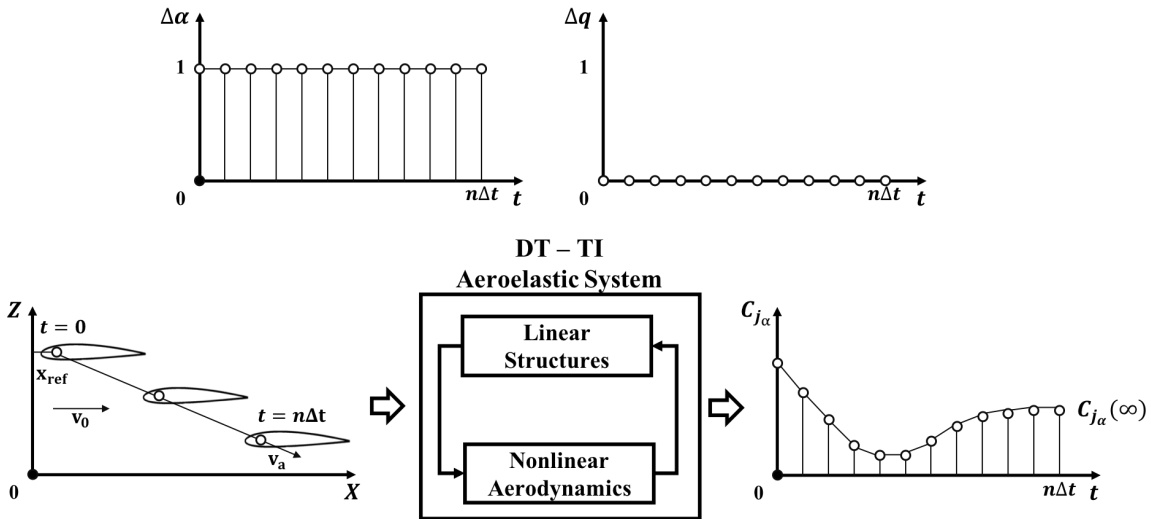

Figure 15: Simulation of step response due to a unit step in angle of attack.

vehicle state, $C_{j_q}(\infty)$, is reached for a constant pitch rate of 1 deg/s. The result is a discrete-time indicial response with respect to pitch rate, $C_{j_q}(t)$ in Eq. 16. Note that the number of iterations required to converge the indicial response for pitch rate may differ relative to those for angle of attack. A similar process is implemented in the lateral planes for identification of indicial responses with respect to roll and yaw rate.

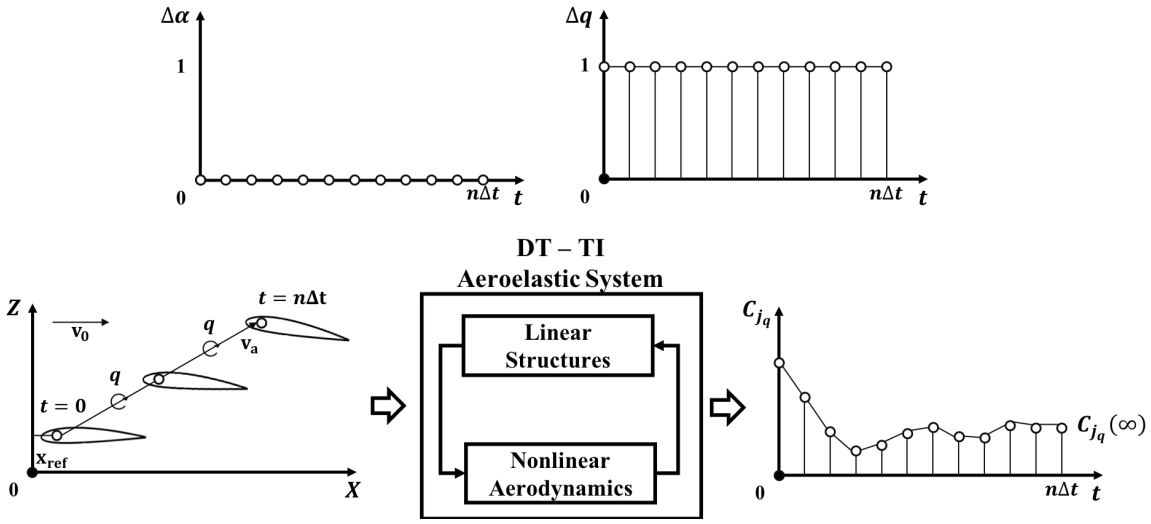

Figure 16: Simulation of step response due to a unit step in pitch rate.

The process for simulating the dynamic behavior of the discrete-time, linear time-invariant aeroelastic system in Figs. 15 and 16 is summarized in Fig. 17. For a given trajectory, a well-converged, static time-accurate aeroelastic solution is first generated at the initial flight condition (α_0, β_0, M_0). The vehicle velocity components $(\alpha(t), \beta(t), M(t))$ and Euler angles $(\phi(t), \theta(t), \psi(t))$ are mapped to translations $(X(t), Y(t), Z(t))$ relative to the inertial reference frame at each point in the trajectory. The calculated vehicle translations and rotations are then used to create a FUN3D motion history file, defined by a series of 4 x 4 transformation matrices for each trajectory time step, as shown in Section 4.2.3. A time-accurate dynamic aeroelastic simulation is then initialized from the static aeroelastic solution and advanced in time using a specified time step size until the maneuver is complete at a final time (t_f). For each step in time, a set number of subiterations (n_{sub}) are used to converge the fluid dynamic state due to the change in vehicle-state at each time instance along the trajectory. These converged aerodynamic loads serve as inputs to FUN3D's mode-based linear structural model, which then solves for the resulting vehicle deformation. Finally, the CFD mesh is deformed by solving the linear elasticity equations for mesh deformation. The coupling between the flow solver and structural solver may be repeated up to a prescribed number of iteratations (n_{fsi}).

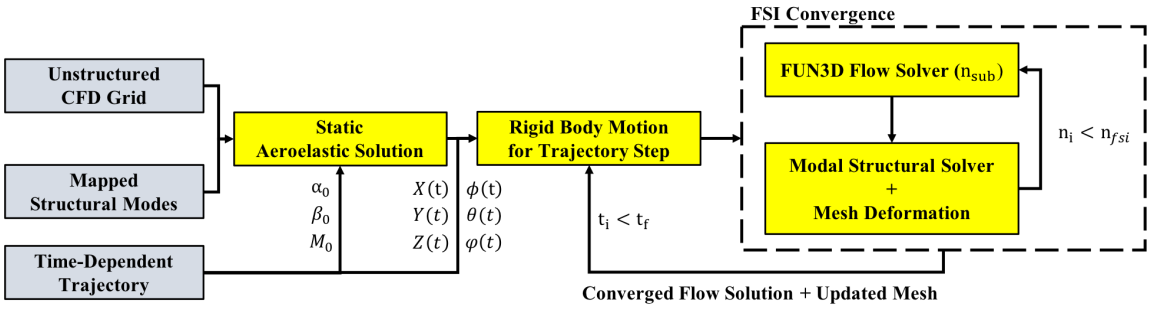

Figure 17: Dynamic aeroelastic simulation process.

5.4 Surrogate Modeling

Surrogate modeling based on kriging interpolation has found widespread use in flight dynamics and aeroelastic studies as a means of reducing the computational costs associated with model identification [38, 123]. Kriging modeling is implemented in the present work using the MATLAB Design and Analysis of Computer Experiments (DACE) toolbox [67].

Following the formulation implemented in Refs. [32,38], the indicial responses are viewed as a set of time-correlated spatial processes, where the output is a simulated or 'observed' transient response. Universal-type kriging surrogate models may be used to estimate indicial responses at a previously unsampled flight condition without the need for direct simulation of the response. Thus, indicial responses for each vehicle-state parameter are predicted for each point along the maneuver, corresponding to a unique combination of (α, M), using a surrogate model developed from a database of time-accurate, CFD-simulated indicial responses.

The modeling process begins with the definition of an input matrix, $\mathbf{X}(m \times d)$, and a corresponding output matrix of observed responses, $\mathbf{Y}(m \times n)$, in Eq. 62. The columns of the input matrix represent the number, d, of independent flight space variables, x, whereas the rows of the input matrix represent the number of samples, m, or unique combinations of values for the input variables. In modeling indicial responses with respect to angle of attack using the current sampling strategy, there are $d = 2$ independent variables, α and M, corresponding to indicial responses sampled at m unique locations in the flight maneuver space. The rows of the output matrix also correspond to the number of samples, however, the columns of the output matrix now correspond to the n time steps of the numerically simulated indicial responses.

$$\mathbf{X} = \begin{bmatrix} x_{11} & x_{12} & \dots & x_{1d} \\ x_{21} & x_{22} & \dots & x_{2d} \\ \vdots & \vdots & \vdots & \vdots \\ x_{m1} & x_{m2} & \dots & x_{md} \end{bmatrix} \text{ and } \mathbf{Y} = \begin{bmatrix} y_{11} & y_{12} & \dots & y_{1n} \\ y_{21} & y_{22} & \dots & y_{2n} \\ \vdots & \vdots & \vdots & \vdots \\ y_{m1} & y_{m2} & \dots & y_{mn} \end{bmatrix} \tag{62}$$

Universal kriging models the prediction at a given point in time, $\hat{y}_i$, at a new combination of values in the input variable space, $\mathbf{x}^*$, as the sum of a deterministic mean response value, μ_i, and a zero-mean autocorrelated error, ϵ_i, as given by Eq. 63.

$$\hat{y}_i(\mathbf{x}^*) = \mu_i(\mathbf{x}^*) + \epsilon_i \tag{63}$$

The objective of kriging modeling is to minimize the mean squared error, ϕ in Eq. 64, of the modeling prediction $\hat{y}$ over the parameter space, where $E[...]$ is the covariance of the quantity of interest [67]. For a linear regression of the parameter space, the resulting mathematical expressions for the mean response and autocorrelated error are given by Eqs. 65 and 66.

$$\phi(\mathbf{x}^*) = E[(\hat{y}(\mathbf{x}^*) - y(\mathbf{x}^*))^2] \tag{64}$$

The mean response is written as a linear combination of regression functions, f_j, and their corresponding regression coefficients, β_{ij}, for the j-th regression function at time step i, for $i = 1, \dots, n$. In the present work, the regressions are defined as follows: $f_0(\mathbf{x}^*) = 1$, $f_1(\mathbf{x}^*) = \alpha^*$, and $f_2(\mathbf{x}^*) = M^*$.

$$\mu_i(\mathbf{x}^*) = \sum_{j=0}^{n} \beta_{ij} f_j(\mathbf{x}^*) \tag{65}$$

The autocorrelated error is written in terms of $\mathbf{r}(\mathbf{x}^*)$, the correlation matrix between the sampled points and the new evaluation point, $\mathbf{R}$, the correlation function matrix for sampled points, $\mathbf{F}$, the regression functions at the sampling points, $\mathbf{Y}$, and

β. Substituting the expressions for the mean response and autocorrelated error into Eq. 63 results in the final prediction expression given by Eq. 67.

$$\epsilon_i(x^*) = \mathbf{r}^T\mathbf{R}^{-1}(\mathbf{Y} - \mathbf{F}\beta) \tag{66}$$

$$\hat{y}_i(\mathbf{x}^*) = \sum_{j=0}^{n} \beta_{ij} f_j(\mathbf{x}^*) + \mathbf{r}^T\mathbf{R}^{-1}(\mathbf{Y}_i - \mathbf{F}\beta) \tag{67}$$

An illustration of the kriging surrogate modeling process for the prediction of a single indicial response (with respect to angle of attack) for a notional point in a maneuver, where $\alpha = 4.5°$ and $M = 0.25$, is shown in Fig. 18. In this modeling procedure, n surrogate models are generated, one for each point in discrete time. In consideration of the convolution process, an interpolated indicial response is needed at each point in time along the maneuver based on the current value of the flight space parameters. This process is utilized for the nonlinear indicial responses with respect to angle of attack and sideslip angle. A linear interpolation is used for the indicial responses with respect to the angular rates.

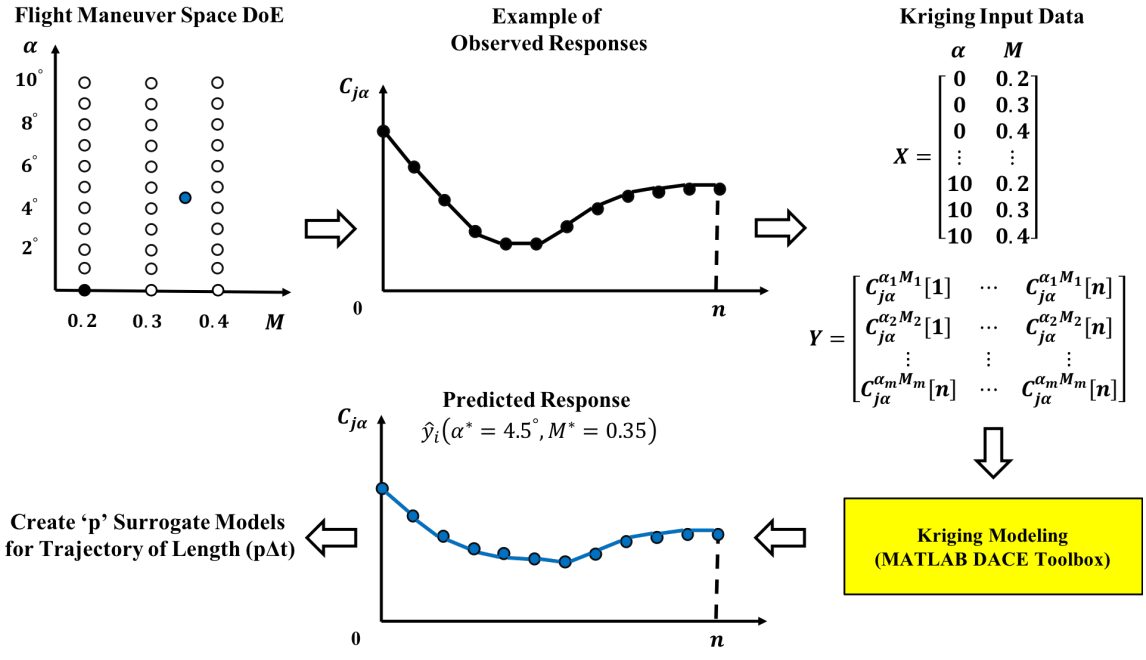

Figure 18: Kriging modeling of indicial responses.

5.5 Summary

A top-level overview of the aeroelastic indicial response model is illustrated in Fig. 19. This dissertation aims to retain the components of the methodology, as developed for rigid vehicles, with emphasis placed on establishing the feasibility of application to coupled dynamic aeroelastic simulations of flight vehicles maneuvering through prescribed trajectories.

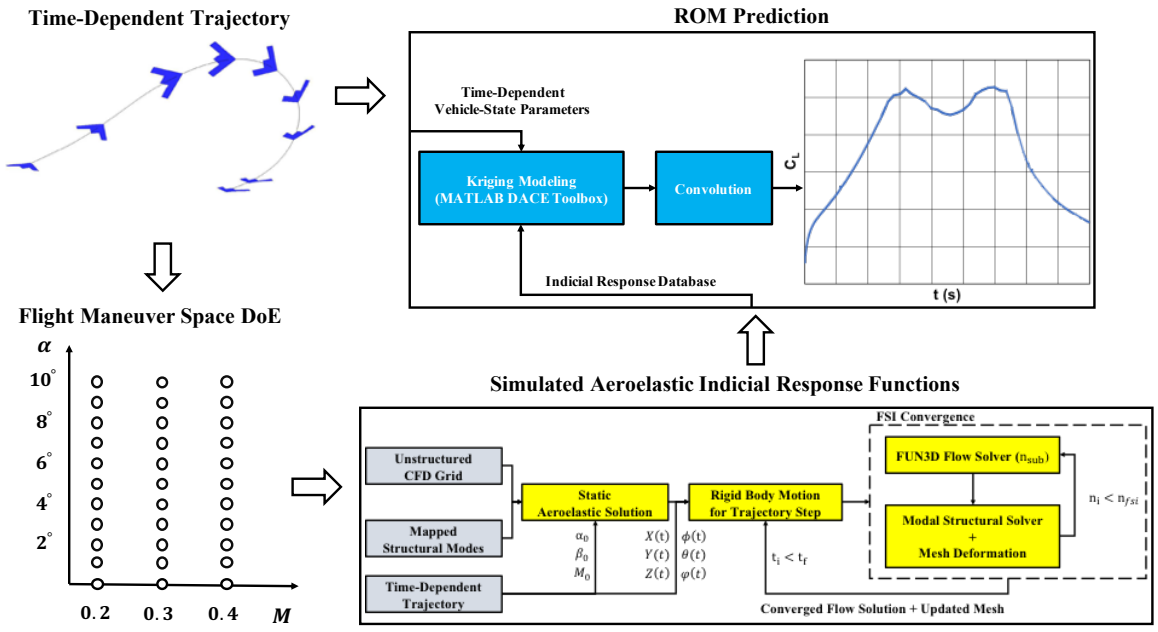

Figure 19: A top level overview of the information flow in the aeroelastic indicial response reduced-order model.

The experiments in Chapters 7-9 seek to identify best-practices for efficient and robust identification of aeroelastic indicial responses, to evaluate the accuracy of ROM predictions for maneuvers at various motion rates across linear and nonlinear flight regimes, and quantify the performance benefits of the aeroelastic ROM in comparison to the purely aerodynamic ROM, as well as the traditional stability derivative method. In the process, typical flight dynamics assumptions for vehicle-state parameter depencies are challenged for flexible flight vehicles, depending on the configuration and flight envelope of interest.

CHAPTER VI

TEST CONFIGURATION

6.1 X-56A Multi-Utility Technology Testbed Aircraft

The X-56A configuration is a lightweight, flexible aircraft developed by the U.S. Air Force Research Laboratory (AFRL) to serve as a Multi-Utility Technology Testbed (MUTT). An illustration of the X-56A is given in Fig. 20. The primary goals of the X-56A efforts were to investigate active flutter suppression technology and active shape control. To date, several topics of research have been published for the configuration and include: the stability of closed-loop flutter wing models [125, 126]; stabilizing and controlling wing shape [124]; fly-by-feel sensing and control [72]; airframe structural optimization [64, 65]; and most recently, CFD-based dynamic aeroelastic analysis for flutter prediction [101]. All of these research topics, including the present work, rely on a structural model of the aircraft that has been verified and validated with ground vibration test (GVT) results [91].

Figure 20: X-56A multi-utility technology testbed (Courtesy: Lockheed Martin).

Table 2: Dimensions and mass properties of the X-56A configuration.

Description	Symbol	Value	Units
Chord Length	c	24.0	in
Wingspan	b	336.0	in
Wing Area	A	8064.0	in^2
Moment Center	$\mathbf{x}_M$	$\{165.0, 0.0, 101.3\}$	in
Moment Lengths	$\mathbf{L_M}$	$\{336.0, 24.0, 336.0\}$	in
Center of Gravity	$\mathbf{x}_{CG}$	$\{163.3, 0.2311, 101.3\}$	in
Weight	W	495.6	lb

The aircraft consists of a rigid center body and flexible detachable wings, allowing for different structural properties and sensor packages to be tested. Additional details for the design and development of the X-56A can be found in the work by Beranek et al. [7] and Nicolai et al. [89]. The size, geometric quantities, and weight of the X-56A are summarized in Table 2 [7]. The specified reference lengths and area were used in nondimensionalizing the resulting aerodynamic forces and moments from full-order aeroelastic simulations, while the center of gravity served as the reference point for prescribing rigid-body flight trajectories.

6.2 Structural Model

The structural model used in this work was originally developed at Lockheed Martin Skunkworks and further validated and calibrated to match ground vibration test results from NASA Armstrong [91,92]. It is a finite element model (FEM) constructed in NASTRAN using 8,249 nodes. To take advantage of the modal structural dynamics solver within FUN3D, a linear modal solution is used in the present work instead of relying on an externally coupled simulation to the high-fidelity FEM model. The full modal solution contains 6 rigid-body modes and 34 elastic modes with a range from 3-60 Hz where numerous modes contain control surface deflections. Pak & Truong [91] found the first four elastic modes to be the most critical to predicting the three flutter modes of the X-56A.

The present work will incorporate the four primary modes for high-fidelity maneuvering vehicle aeroelastic simulations as means of simplifying the experiments. In practice, the ROM methodology may use either a nonlinear FEM model or linear modal structural solver, where the costs are invariable with the number of structural modes included. It is important to note that the engine mounts, control surfaces, and landing gear are present in the structural mode shapes, but are not modeled in the CFD grids to further simplify simulations. The four elastic modes correspond to symmetric wing first bending (SW1B), antisymmetric wing first bending (AW1B), symmetric wing first torsion (SW1T), and antisymmetric wing first torsion (AW1T), as shown in Fig. 21.

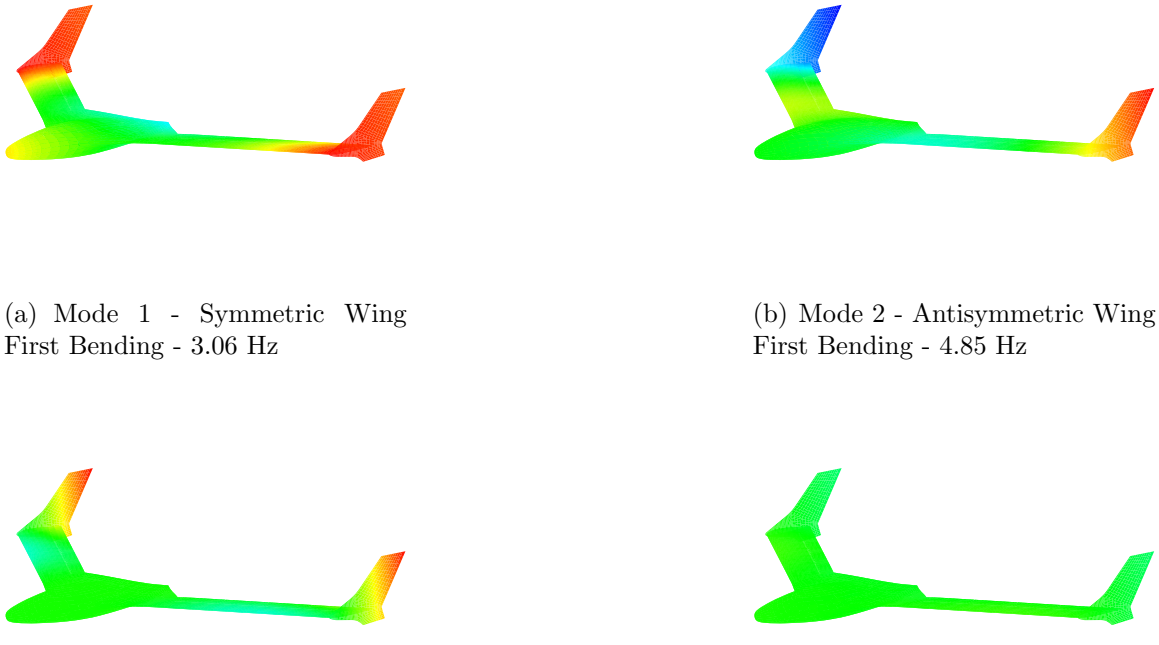

(a) Mode 1 - Symmetric Wing First Bending - 3.06 Hz

(b) Mode 2 - Antisymmetric Wing First Bending - 4.85 Hz

(c) Mode 3 - Symmetric Wing First Torsion - 11.09 Hz

(d) Mode 4 - Antisymmetric Wing First Torsion - 11.95 Hz

Figure 21: Four primary flexible modes of the X-56A.

6.3 Computational Grid

The grid used for the present work was generated with Pointwise V18.0 using IGS formatted computer-aided-design (CAD) geometry, provided by Christopher Acuff of NASA Armstrong Flight Research Center, exported from SolidWorks 2014. The X-56A model consists solely of the center body and flexible wings with the landing gear, control surfaces, and engines removed as a means of reducing computational costs and mesh deformation complexity.

A single mixed-element, coarse grid was generated for the dynamic coupled Euler-aeroelastic analyses and consists of 579,506 total nodes, of which 74,914 were surface nodes. The resulting surface resolution is shown in a top semispan view in Fig. 22(a). Both the leading and trailing edges of the configuration were resolved using Pointwise's T-Rex cells, which consisted of layers of anisotropic quadrilateral cells emanating from the boundary curves. Figure 22(b) illustrates the resulting layers in a closeup view of the center body and leading edge on the left wing. The initial spacing and growth rate for each of the layers was specified as 0.1 in. and 20%, respectively, where the initial spacing is approximately 20% of the trailing edge thickness.

The computational domain was generated using a 'sphere primitive' centered at the model moment center with a radius of 100 chord-lengths (2400 inches). Figure 23 illustrates the growth of the grid domains at the y=0 plane, where Fig. 23(a) focuses on the domain growth near the center body profile, and Fig. 23(b) shows the resolution extending to the spherical farfield domain. In its development, the grid was first generated as a hemisphere volume with an x-z symmetry plane, and subsequently, copied and mirrored about the symmetry plane to yield a symmetric volume grid. While not completely essential for a CFD-to-ROM comparison, this is a desirable practice when simulating complex 6DOF trajectories. For the CFD boundary conditions, the vehicle surface was set as the zero normal velocity tangency condition (3000), and the farfield was set as the external freestream condition (5050).

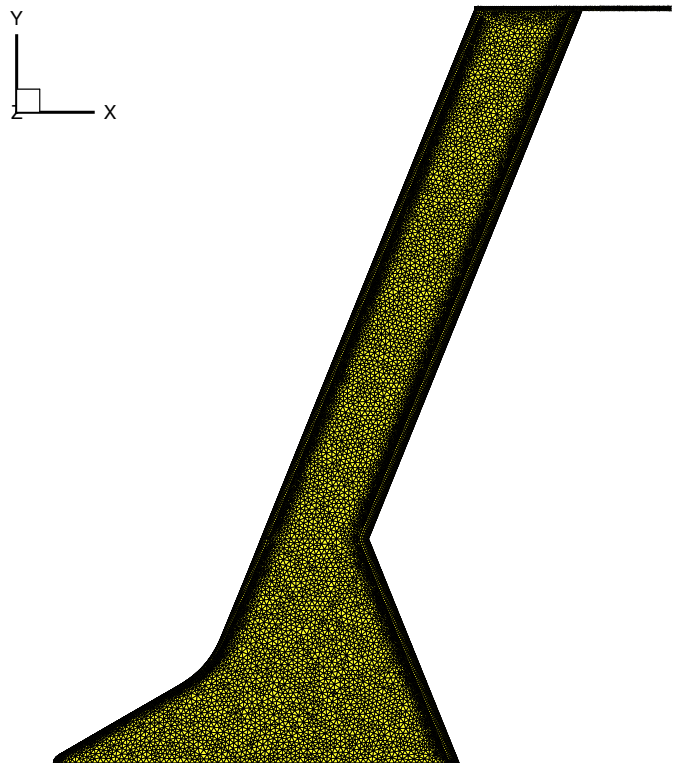

(a) top view of semispan

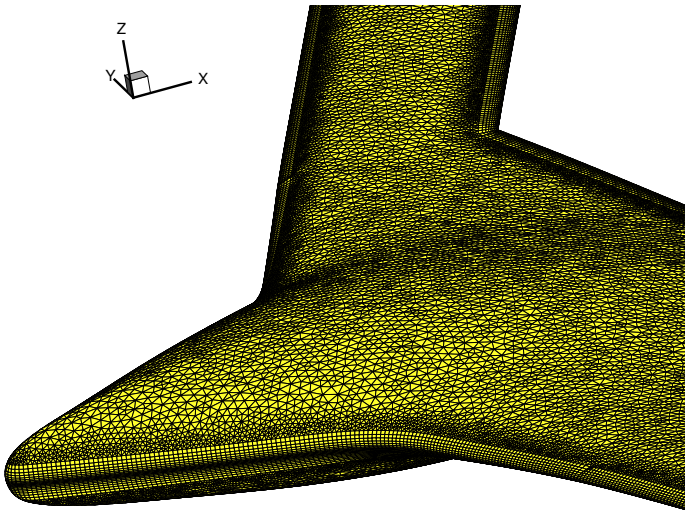

(b) closeup of center body and leading edge

Figure 22: X-56A grid surface resolution.

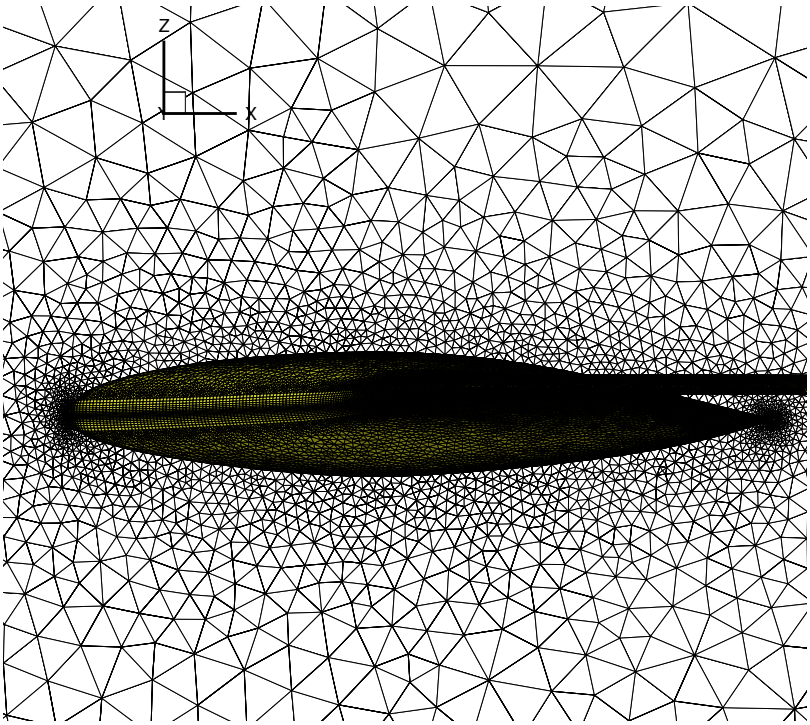

(a) near body

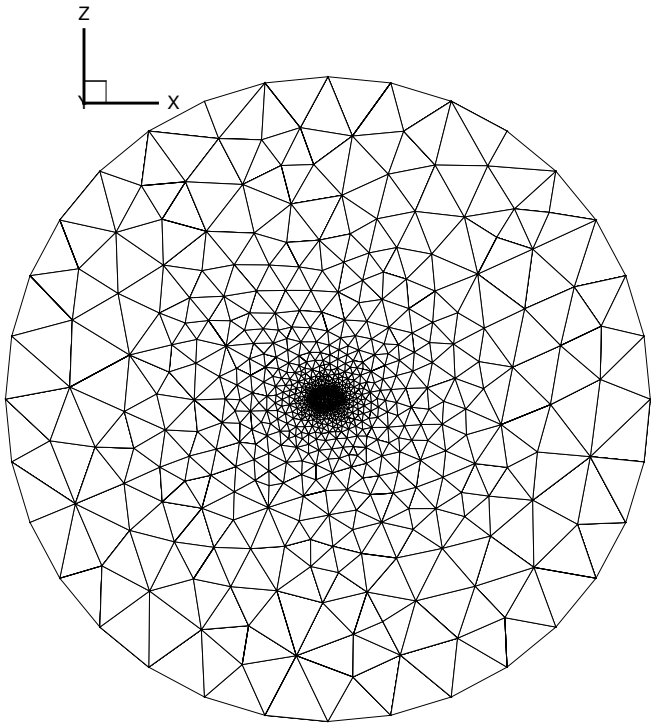

(b) spherical farfield

Figure 23: X-56A grid domain growth.

6.4 Baseline Flight Condition

The X-56A is a flying wing configuration used to test and mature aeroservoelastic technologies, designed to be highly flexible, and thus, more susceptible to aeroelastic phenomena such as flutter, divergence, etc. As a result, the structure is expected to have less of a dampening effect relative to more maneuverable military aircraft. Pak et al. [91] notes a maximum Mach number of 0.284.

Table 3 defines the X-56A's baseline flight condition parameters, corresponding to an assumed flight altitude of 2,500 ft. for the present work. These properties define the initialized freestream conditions for the maneuvers used in evaluating the linear and nonlinear ROM formulations, as discussed in the following sections. For variable speed maneuvers, the resulting body-frame aerodynamic coefficients are scaled by the local body-frame velocity to give representative aerodynamic forces and moments.

Table 3: X-56A baseline flight condition.

Description	**Value**	**Units**
Altitude	2,500	ft
Temperature	509.5	$^{\circ}R$
Density	2.2E-03	sl/ft^3
Viscosity	3.7E-07	lbf-s/ft2
Mach Number	0.13	–
Reynolds Number	1.7E+06	–

CHAPTER VII

MODEL IDENTIFICATION (RESEARCH QUESTION 1)

The purpose of this chapter is to describe Experiments 1.1 and 1.2, which are aimed at identifying how accounting for vehicle flexibility impacts the indicial response identification and ROM generation processes. A static alpha sweep study of the X-56A is described in Section 7.1 to establish the aerodynamic differences between the rigid and flexible vehicle configuration. The identification of a solution strategy for aeroelastic indicial response identification (Experiment 1.1) is outlined in Section 7.2. The assessment of indicial response sensitivity to flight conditions (Experiment 1.2) is presented in Sections 7.3-7.5. Additionally, the symmetry of indicial responses due to positive and negative step changes in angle of attack are evaluated at positive and negative angles of attack in Section 7.6.

7.1 Static Characterization

Prior to simulating dynamic maneuvers and developing reduced-order models, it is necessary to characterize the nonlinear and unsteady aerodynamic regimes of the X-56A. By identifying the unsteady aerodynamic regimes, test maneuvers may be defined to avoid near-stall flight conditions. Identification of flight envelope nonlinearity allows for the linear and nonlinear ROMs to be evaluated within their corresponding limits of application. It is important to reemphasize that 'nonlinearity' in the present work refers to the relationship between aerodynamic coefficients and vehicle-state parameters. Additionally, rigid and aeroelastic simulations are compared to observe how these regimes may vary when accounting for vehicle flexibility.

Toward this purpose, a series of static and static aeroelastic time-accurate Euler flow solutions were generated at the baseline flight conditions across a range of $\alpha =$

[$-5°$ to $20°$]. Using Eq. 68, a characteristic time step of $\Delta t = 0.0004$ s was chosen, where f_{AW1T} is the highest frequency structural mode, i.e., asymmetric wing first torsion, and $N \approxeq 200$.

$$\Delta t = \frac{1}{f_{AW1T} N} \tag{68}$$

Defining the time step in terms of the highest frequency structural mode ensures that any potential aeroelastic instabilities across the frequency spectrum may be identified. A total of 10,000 time steps were simulated at each angle of attack to guarantee convergence at lower angles of attack and to resolve unsteady aerodynamic phenomena at higher angles of attack. Aeroelastic simulations were restarted from the converged rigid solutions to aid in numerical stability at higher angles of attack.

Figure 24 illustrates the static lift and pitching moment coefficient results for both the rigid (blue) and flexible (red) vehicle. Each data point represents the average aerodynamic coefficient value over the last 1,000 time steps of the time-accurate simulations. Additionally, the minimum and maximum coefficient values over the last 1,000 time steps are represented at each angle of attack by error bars, which serve as a measure of flow unsteadiness. The choice of 1,000 time steps was adequate for capturing several cycles of solution periodicity at the higher angles of attack.

The aerodynamics of the rigid vehicle is characterized by a nonlinear stall pitch-up behavior at higher angles of attack with unsteady effects beginning near $\alpha = 16°$ as a result of periodic vortex shedding. For $\alpha < 12°$, the aerodynamic response follows a generally linear trend with no significant measure of flow unsteadiness. A gradual pitching moment break is observed near $\alpha = 12°$. In comparison, the flexible vehicle exhibits greater nonlinearity and unsteadiness across the entire range of angle of attack.

At $\alpha = 0°$, the aerodynamic coefficient results for the rigid and flexible vehicle are fairly similar. For angles of attack up to $\alpha = 13°$, the flexible vehicle experiences a significant increase in lift coefficient relative to the rigid vehicle with the largest

difference occuring at $\alpha = 10°$, where the lift coefficient is approximately 45% greater. Additionally, the presence of unsteady flow phenomena is observed beginning at $\alpha = 11°$, much earlier than the rigid vehicle at $\alpha = 16°$. For $\alpha > 12°$, the lift coefficient begins to decrease more gradually before reaching a value comparable to that of the rigid vehicle. The pitching moment remains comparable up to $\alpha = 8°$ before increasing at a greater rate relative to the rigid vehicle, which is indicative of earlier flow separation on the wing.. Mesh boundary animations were generated at the converged flight conditions to provide further insight into how the structure deforms subjects to fluid-structure interactions.

Figure 25 shows the static deformation of the flexible vehicle compared to the rigid vehicle for $\alpha = 10°$ at the baseline flight condition. The front and side views depict a noticeable wingtip deflection, in addition to a pitch-up deformation of the vehicle's center-body, which provides rationale for the observed increase in lift coefficient. A three-view illustrated in Fig. 25(c) also shows a small reverse twist of the winglet and a slight decrease in wing sweep. The increased deflection and higher incidence angle at the wing tip would explain the observation of an earlier onset stall accompanied by stronger unsteady aerodynamic phenomena. The results further demonstrate the pronounced flexibility of the X-56A aeroservoelasticity technology testbed aircraft.

Overall, the static aerodynamic characterization illustrates a significant difference in the extent of linear and nonlinear angle-of-attack ranges between the rigid and flexible X-56A aircraft. The aerodynamic response of the rigid vehicle remains fairly linear for $\alpha = [-5° \text{ to } 10°]$ with a stall region beginning at $\alpha = 16°$, as commonly observed for subsonic vehicles. In contrast, the flexible vehicle shows a generally nonlinear aerodynamic response even at lower angles of attack with locally linear variations confined to amplitudes of $\Delta\alpha = [1° \text{ to } 3°]$, and an unsteady aerodynamic region beginning at $\alpha = 11°$. The impact of a deforming center-body and wing results in an overall higher lift coefficient and a more limited flight envelope when avoiding the

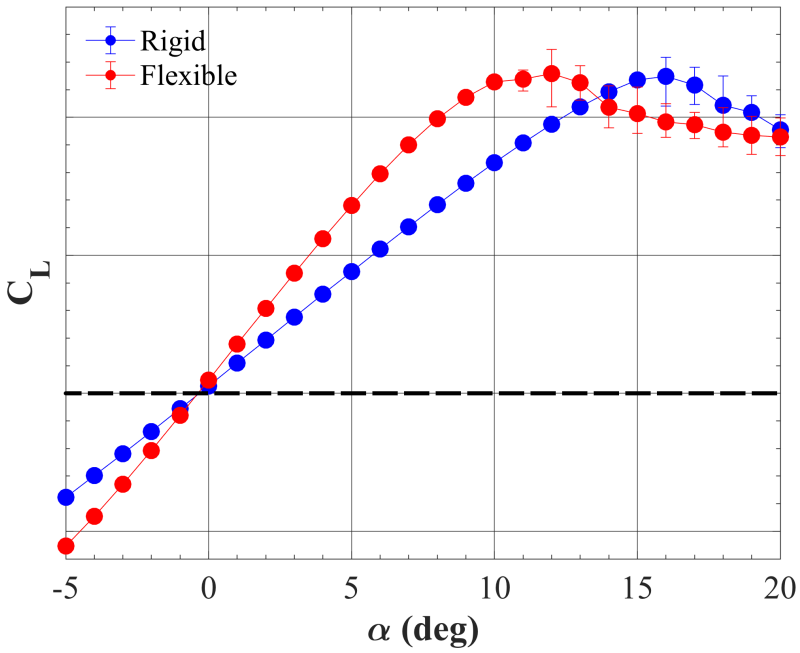

(a) Lift coefficient

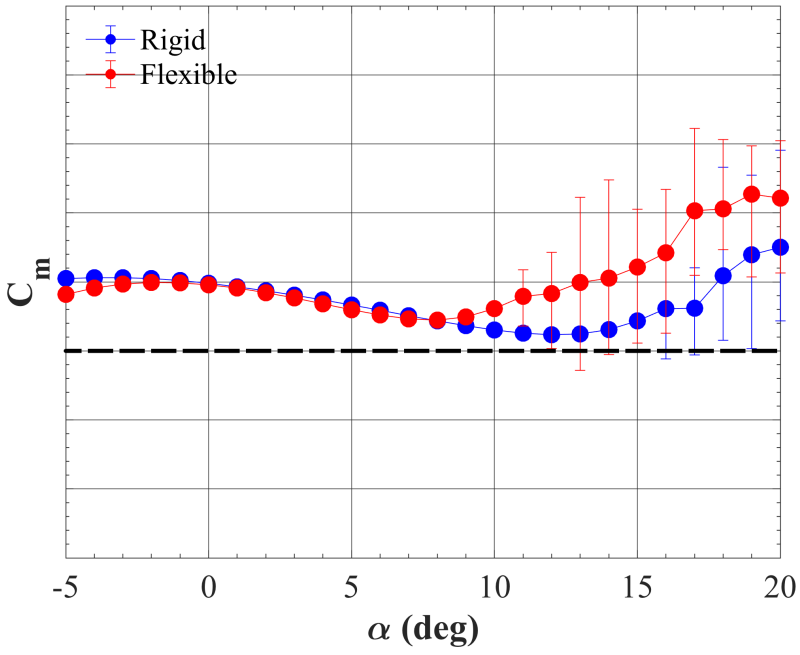

(b) Pitching moment coefficient

Figure 24: X-56A static lift and pitching moment coefficient for rigid (blue) and flexible (red) vehicle structures, $M = 0.13$.

presence of unsteady aerodynamic phenomena. By characterizing the flight envelope, a more judicious selection of flight maneuvers may be made in evaluating the linear and nonlinear variants of the aeroelastic ROM.

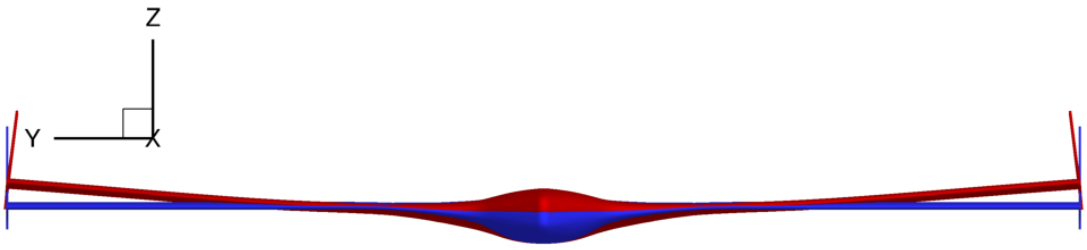

(a) Front view

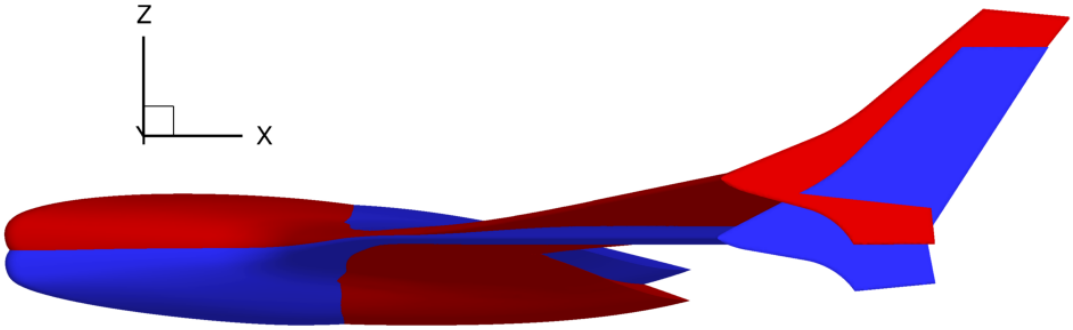

(b) Side view

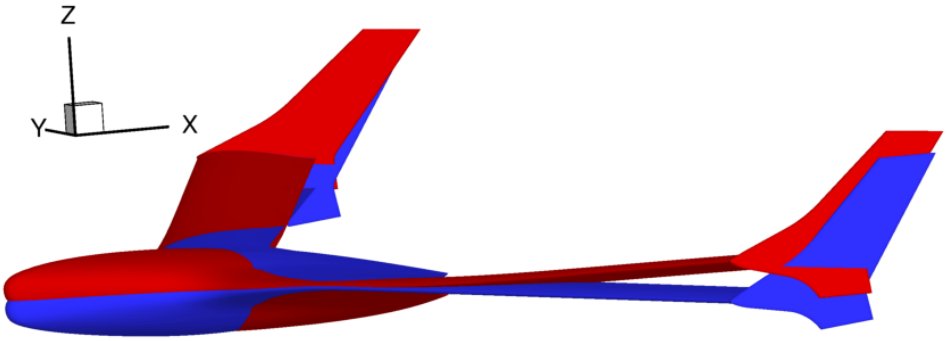

(c) Three-view

Figure 25: Static deformation of the flexible vehicle (red) compared to the rigid vehicle (blue) at $\alpha = 10°$, $M = 0.13$.

7.2 Aeroelastic Indicial Response Solution Strategy

In the previous section, an aerodynamic characterization study was conducted utilizing a significant number of time steps to establish a set of "well-converged" static aerodynamic solutions at various angles of attack. Aeroelastic simulations were restarted from the converged rigid flow solutions, and fluid-structure interactions were converged using the same number of time steps to predict the deformed vehicle state.

Figure 26 shows the convergence history for the log of the root-mean-square (RMS) residual reduction (left) and lift coefficient (right) for the "well-converged" static (a) and static aeroelastic (b) solutions at $\alpha = 10°$. The RMS residuals were calculated using the values at each step in physical time, where the reduction was calculated relative to the initial iteration residuals. Only the first 5,000 of the 10,000 total time steps are shown, as the solution is strongly converged with negligible changes in residual or aerodynamic coefficients for the remaining time steps.

For the static (rigid) simulation, the RMS residual converges near 10-orders of magnitude ($log(R/R_0) < -10$) and the change in lift coefficient for successive iterations reaches 1/100th of a drag count ($\pm 1E-06$) in approximately 1,675 iterations. The computational cost for the static simulation was approximately 453 CPU hours. Restarting from the rigid solution, the static aeroelastic (flexible) simulation's RMS residual encounters an initial transient behavior due to significant fluid-structure interactions as the deformed vehicle structure is converged upon. In this case, the RMS residual converges near 5-orders of magnitude, and the lift coefficient converges to similar resolution as the rigid simulation in approximately 1,475 iterations. It is important to note that the static aeroelastic simulation's peak residual reduction is expected to be less compared to the static simulation given that it is restarting from a converged fluid state, where the residuals are already of low magnitude. The cost of the static aeroelastic simulation alone was 606 CPU hours for a total of 1,059 CPU hours when accounting for the cost of the rigid restart solution.

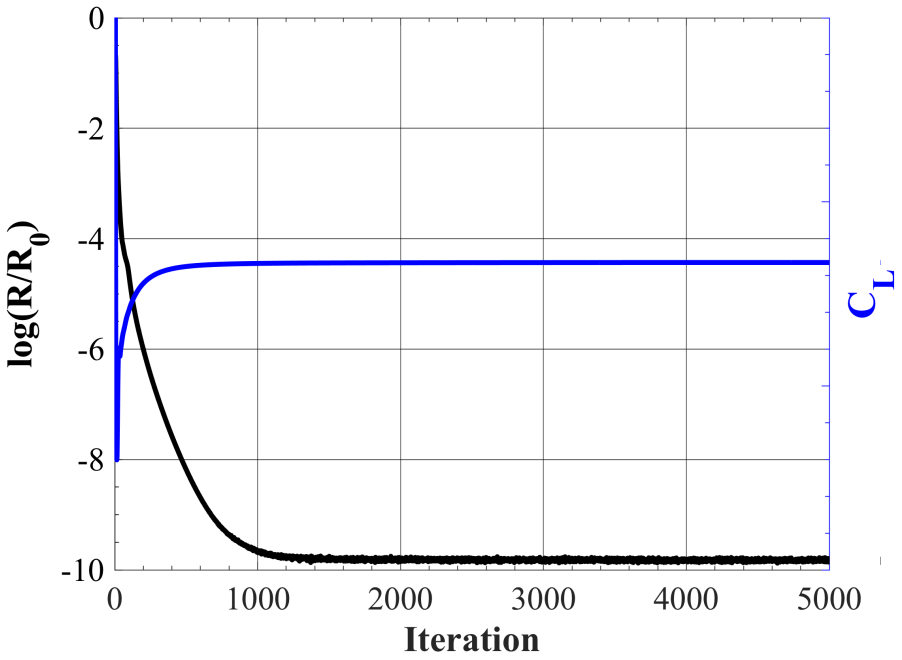

(a) Static rigid simulation

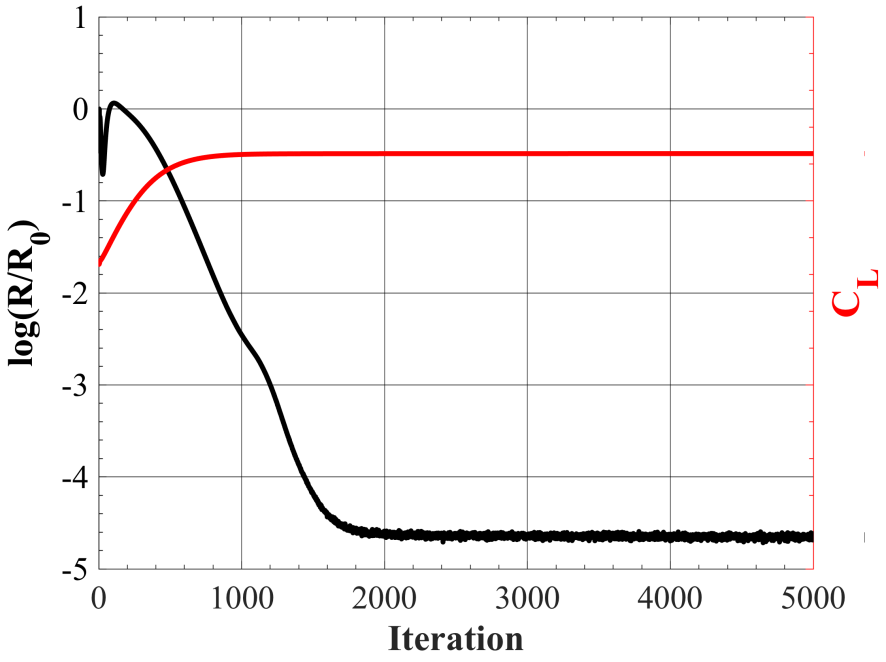

(b) Static aeroelastic simulation

Figure 26: Static and static aeroelastic simulation RMS residual reduction and lift coefficient advancement for "well-converged" solution at $\alpha = 10°$, $M_\infty = 0.13$.

The previous plots illustrated convergence at $\alpha = 10°$, the upper limit of the flexible vehicle flight envelope without unsteady aerodynamic phenomena. Figure 26 shows the convergence history for the log of the RMS residual reduction (left) and lift coefficient (right) for the "well-converged" static (a) and static aeroelastic (b) solutions at $\alpha = 16°$. In agreement with the lift curve in Fig. 24(a), these plots confirm the presence of unsteady aerodynamics for both the rigid and flexible vehicle. Oscillatory variations in the residual reduction and lift coefficient begin near iteration 1000 with periodic variations continuing for the entire simulation length. Given the dynamic fluid state, the residuals for the rigid vehicle do not reach more than 5-orders of magnitude. In the flexible vehicle case, the solution restarts from the rigid case at its peak residual reduction. As such, the residuals increase while resolving the fluid-structure state before converging nearly 3-orders of magnitude greater than the rigid solution. Similar computational costs were incurred for the simulations at $\alpha = 16°$.

The static aerodynamic characterization solution strategy is shown to be appropriate for generating "well-converged" solutions in the exploration of an unknown flight envelope. This strategy relied on the use of a time step adequate for resolving dynamic aeroelastic effects and prescription of a sufficiently large number of iterations to produce overconverged solutions at lower angles of attack and to resolve several cycles of periodic aerodynamics at higher angles of attack. Additionally, the aeroelastic solution was restarted from a converged static solution without computational efficiency considerations.

Given that the ROM's computational cost is primarily attributed to model identification, an efficient static initialization solution strategy is sought to minimize the cost in simulating aeroelastic indicial responses. There are two considerations when developing a solution strategy: (1) what is the most efficient initialization approach for a static aeroelastic simulation, and (2) what is the maximum time step that can be used to quickly converge the fluid-structure interactions?

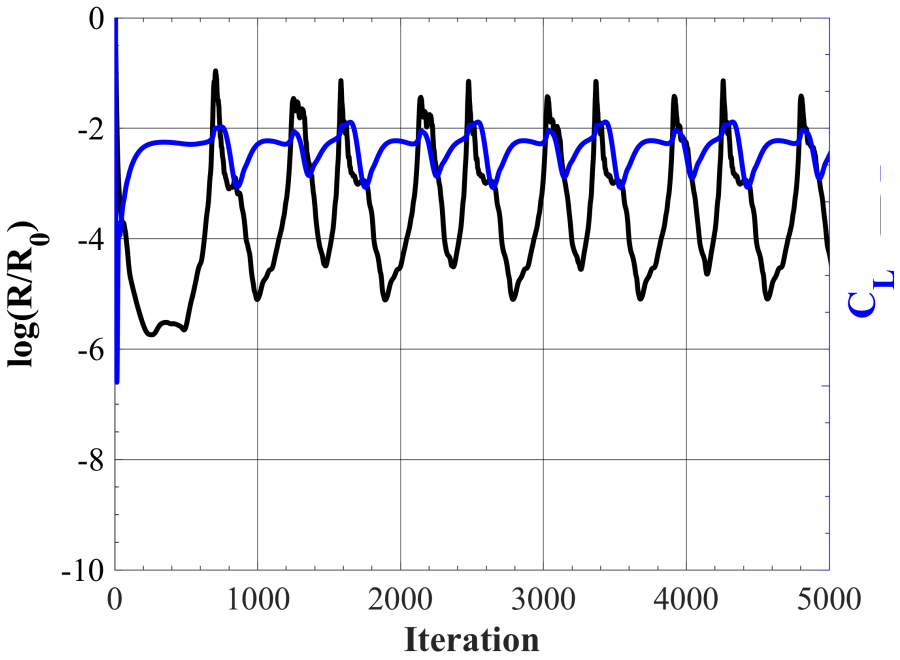

(a) Static rigid simulation

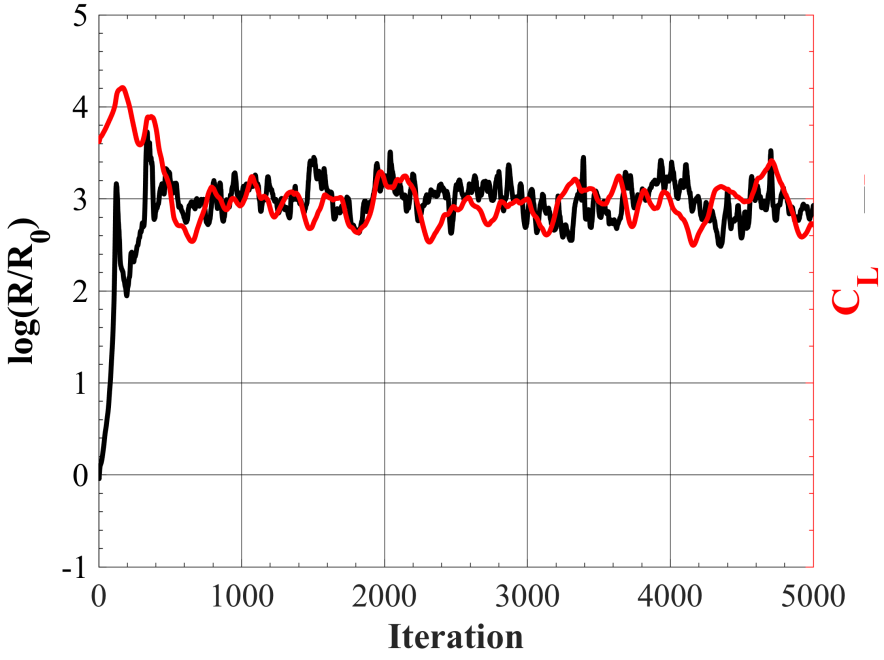

(b) Static aeroelastic simulation

Figure 27: Static and static aeroelastic simulation RMS residual reduction and lift coefficient advancement for "well-converged" solution at $\alpha = 16°$, $M_\infty = 0.13$.

In terms of initialization approaches, there are two potential alternatives. The first approach mimics the solution strategy used in the static aerodynamic characterization study, where the static aeroelastic simulation is restarted from a static flow solution. Within this approach, the fluid state is first converged assuming a rigid structure, and then the fluid-structure interactions due to vehicle deformation are converged. The second alternative is a "cold start" approach, where the static aeroelastic simulation relies on no rigid solution initialization, and the bulk fluid-structure interactions are converged simultaneously. For the restart approach, the computational cost would be a sum of the rigid and aeroelastic simulation costs, whereas the cold start approach cost would depend on the aeroelastic simulation cost alone. The primary objective is to determine how the total static aeroelastic simulation costs vary in the restart approach for successive levels of rigid solution convergence, and in turn, compare those costs relative to a cold start approach.

Initialization Approach

In determining an efficient initialization approach, it is desirable to identify a robust strategy, applicable to all planned flight conditions. In developing efficient solution strategies for rigid, maneuvering aircraft simulations, it is generally advised to create a convergence strategy based on a single "worst case" condition in the complex nonlinear portions of the angle-of-attack range of interest [31]. The same considerations are taken for the present work, where the X-56A undergoes various maneuvers throughout a flight envelope of $\alpha = [0 \text{ to } 10°]$. Thus, each initialization approach is evaluted with respect to $\alpha = 10°$ at the baseline flight conditions.

In consideration of the restart approach for static aeroelastic initialization, the results previously shown in Fig. 26 represent the overconverged case, where the rigid flow solution is converged until the RMS residual reduction reaches 10-orders of magnitude, while the lift coefficient varies within $\pm 1E-08$ between successive iterations. Restarting from the rigid solution, the static aeroelastic simulation is

converged to a similar resolution. For the present work, the convergence criteria set for a "well-converged" solution is a lift coefficient variation within $\pm 1E-06$. Based on this criteria, the last 8,000 of the 10,000 total iterations in each simulation fail to further converge the solution, increasing computational costs with no added benefit.

In general, aeroelastic simulations incur greater computational costs relative to the aerodynamic simulations due to coupling with a modal structural solver. The present study investigates the impact of rigid solution convergence on the number of static aeroelastic iterations required for convergence, and consequently, the total computational cost. Toward this objective, a series of rigid, restart cases with varying levels of solution convergence were simulated and used as initialization solutions for static aeroelastic simulations, which were then converged to the stated lift convergence criteria. Computational costs for the static and static aeroelastic simulations are calculated in each case and compared to the cold start aeroelastic simulation cost.

Table 4 lists the number of time steps and corresponding convergence criteria for each of the initialization cases, simulated at $\alpha = 10°$. The cold start (CS) case requires no static solution initialization and converges the fluid-structure interactions beginning with the first iteration. The restart cases (RS 1-4) converge the static solution lift coefficient ranging from $1E-03$ to $1E-06$ in an attempt to limit the number of aeroelastic simulation iterations.

Table 4: Convergence metrics for static initialization cases at $\alpha = 10°$.

Case	Static Time Steps	Residual Reduction	C_L Convergence
CS	0	-	-
RS-1	125	-5.1	±1E-03
RS-2	375	-7.4	±1E-04
RS-3	825	-9.4	±1E-05
RS-4	1,675	-9.8	±1E-06

Table 5 lists the static, static aeroelastic, and total computational costs for each initialization case. The cold start case requires no static simulation, resulting in a total

cost of 106 CPU hours due to the static aeroelastic simulation. For each restart case, the static simulation cost increases with successive level of flow solution convergence. The subsequent static aeroelastic simulation costs do decrease for increased levels of static simulation convergence, however, the total cost increases as well. Due to the X-56A's highly flexible structure, it is apparent that the fluid-structure interactions are great enough such that none of the restart solutions provide a performance benefit over the CS strategy. The RS-1 case represents an equally efficient strategy compared to the CS case. For a less flexible vehicle and/or for more rigorous flight conditions, the restart approach may provide computational benefits or numerical stability over the cold start approach. Given the negligible difference between the CS and RS-1 cases, the CS strategy is chosen for indicial response static initialization to simplify the simulation steps.

Table 5: Computational costs for static initialization cases.

	Computational Cost (CPU Hours)		
Case	Static	Static Aeroelastic	Total
CS	0	106	106
RS-1	5	101	106
RS-2	20	94	114
RS-3	40	87	127
RS-4	80	80	160

Figure 28 provides an illustration of the lift convergence using the CS, RS-2, and RS-4 cases. The CS case begins converging the fluid-structure interactions from the initial iteration until the aeroelastic lift coefficient is converged within $\pm 1E-06$. The restart cases are characterized by a set of transients/plateaus with the first representing static solution convergence followed by the static aeroelastic solution convergence. Each of the restart case solutions are plotted using the minimum number of static aeroelastic iterations needed to reach the converged cold start lift coefficient. The plot reaffirms the efficiency of the CS strategy for initializing indicial responses.

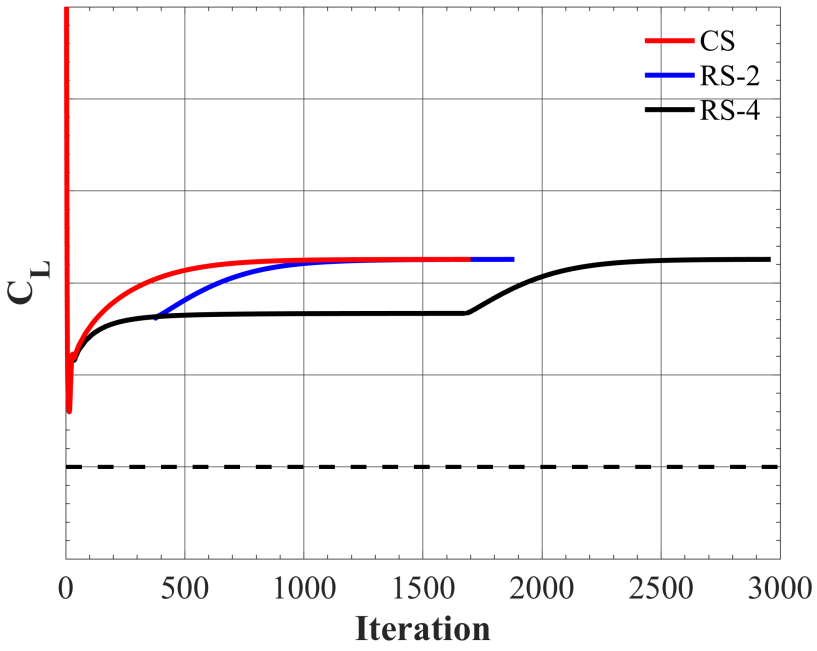

Figure 28: Lift coefficient convergence history for static initialization cases.

Time Step Evaluation

The second consideration in developing an efficient initialization approach is determining the maximum allowable time step in order to converge the static aeroelastic solution using the minimum number of iterations. In the static characterization study, the time step was chosen based on resolving the highest frequency structural mode, according to Eq. 68, using a sampling of $N = 200$. This time step is typical for dynamic maneuvering vehicle simulations, but represents a conservative and unneccesarily small time step for static initializations. The present study seeks to identify the maximum time step or minimum sampling factor, N_{min}, that can be used to advance the static aeroelastic solution without numerical stability issues.

Table 6 lists a series of static aeroelastic cases simulated with time steps of increasing magnitude relative to the baseline simulation ($N = 200$) from the initialization strategy investigation. Iteration values are listed corresponding to the number of static aeroelastic iterations needed to reach a lift convergence of $\pm 1E-06$, and the

computational cost in terms of CPU hours is given for each case. In each of the cases, the simulation was able to converge without encountering numerical stability issues. A decrease in the number of required iterations was observed for an increase in time step value. A nonlinear variation is initially observed up to $N = 10$, followed by an asymptote for greater time steps.

Table 6: Computational costs for static timestep cases.

N	Δt (s)	Time Steps	Cost (CPU Hours)
200	4.0E-4	1,700	106
50	1.6E-3	778	49
20	4.0E-3	387	24
10	8.0E-3	76	5
5	1.6E-2	56	3
1	8.0E-2	41	3

Figure 29 shows the lift coefficient convergence history for the $N = 200$, $N = 20$, and $N = 1$ cases. In each case, only the number of iterations required to meet the lift convergence criteria were plotted. As noted in Table 6, the $N = 1$ simulation proved to be the most efficient of all the cases as it was able to quickly overcome the initial transients and converge to the aeroelastic lift coefficient for a total cost of 3 CPU hours. For efficient static initialization of the indicial responses, the cold start initialization approach using a time step corresponding to $N = 1$ will be used.

The dynamic solution strategy for the indicial response simulations consists of using the same time-accurate aeroelastic simulation as the static initialization, but with a time step corresponding to $N = 200$. Using such a time step will allow for a fine resolution of the highest frequency structural mode, while capturing the dynamics required for resolving any feasible maneuver rate. As an initial guideline, the indicial responses will be simulated using a total number of time steps corresponding to resolving at least 5 periods of the lowest frequency structural mode, allowing for the identification of any potential short-period aeroelastic instabilities.

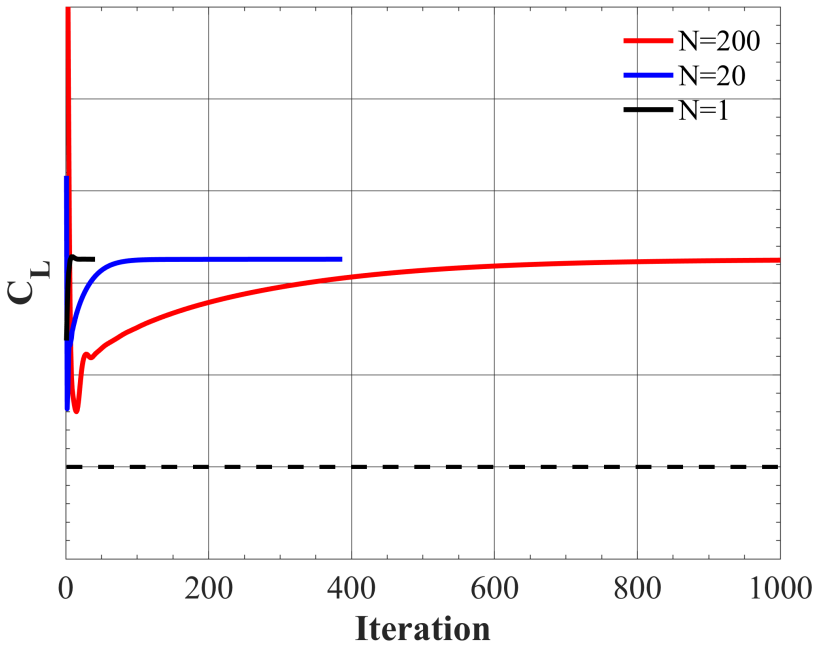

Figure 29: Lift coefficient convergence history for static time step cases.

7.3 Sensitivity to Angle of Attack

Rigid and aeroelastic indicial responses with respect to a step change in angle of attack were simulated at $\alpha_i = 0°$, $5°$, and $9°$ at $M = 0.13$. In these simulations, the solution is initialized using time-accurate static and static aeroelastic simulations for the rigid and aeroelastic responses, respectively. Then, a trajectory is prescribed such that $\alpha = \alpha_i + 1°$ is held constant for all $t > 0$ with all other vehicle-state parameters held zero. Each dynamic simulation was simulated using a characteristic time step corresponding to an $N = 200$ sampling of the highest frequency structural mode. A total of 4,000 time steps were simulated based on capturing at least five periods of the lowest frequency structural mode. Such an approach allows for resolution of all aeroelastic frequency content, while providing enough time for fluid-structure transients to decay.

The lift and pitching moment coefficient responses for the rigid (blue) and aeroelastic (red) simulations are shown in Fig. 30. The response values are plotted versus

a nondimensional time, s, which represents the distance traveled by a fluid particle in terms of integer semichord lengths. Each of the lift coefficient responses for the rigid vehicle exhibit initial transients as the flow adjusts to the impulsive unit change in angle of attack before converging at the $\alpha = \alpha_i + 1^\circ$ state near $s = 20$. The responses initialized from $\alpha = 0^\circ$ and 5° are nearly identical, confirming the linearity of the flight envelope within the given angle-of-attack range, as previously shown in Fig. 24. The response at $\alpha = 9^\circ$ exhibits convergence to a lower response value than the lower angles of attack. This result confirms the lower value of the lift curve slope and the need to consider a nonlinear model for the rigid X-56A aircraft maneuvering beyond $\alpha > 8^\circ$. Pitching moment coefficient response results illustrate a less significant variation with an increase in angle of attack, and in fact, no discernable trend as the response at $\alpha = 5^\circ$ has the most negative value. This observation is in agreement with the static characterization shown in Fig. 24, where the pitching moment varies linearly up to $\alpha = 10^\circ$ with slight variations in slope within each two degree interval.

In comparison, the aeroelastic responses illustrate a greater nonlinearity with significant differences evident even between the lower angle-of-attack responses at $\alpha = 0^\circ$ and 5°. The response at $\alpha = 9^\circ$ converges to a smaller mean value, resulting in a strong nonlinearity as previously shown in Fig. 24. The large variability in the mean response values suggests that an increased sampling of aeroelastic indicial responses with respect to angle of attack will be required for resolving maneuvers within a fixed amplitude range, relative to the rigid response sampling. Additionally, the responses exhibit a periodic, yet stable unsteadiness as a result of fluid-structure interactions. These interactions appear to be of smaller magnitude and higher frequency with an increase in angles of attack.

In contrast to the rigid responses, the pitching moment coefficients for the aeroelastic responses present a nonlinear variation within the sampled angle-of-attack range. Moreover, the response at $\alpha = 9^\circ$ has a positive mean value, whereas the lower

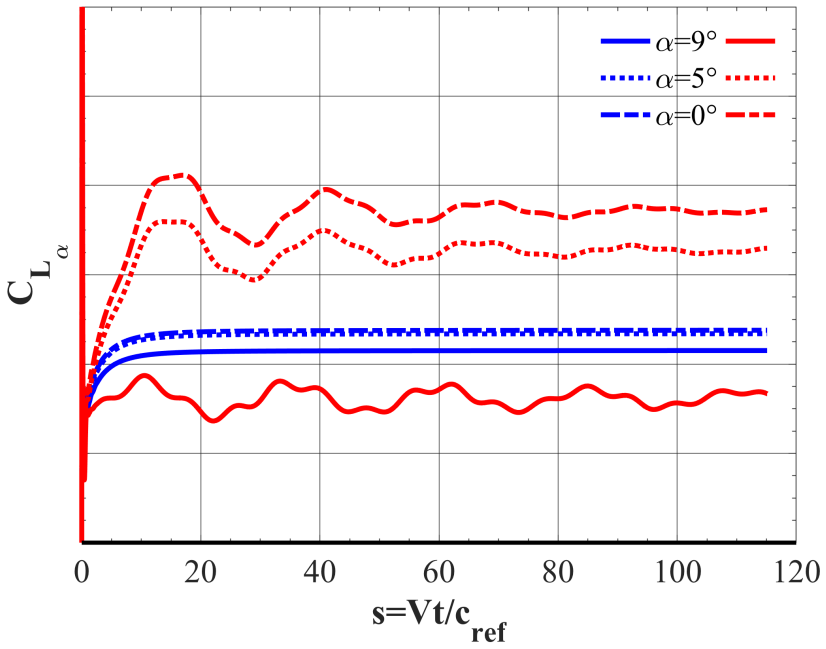

(a) Lift coefficient

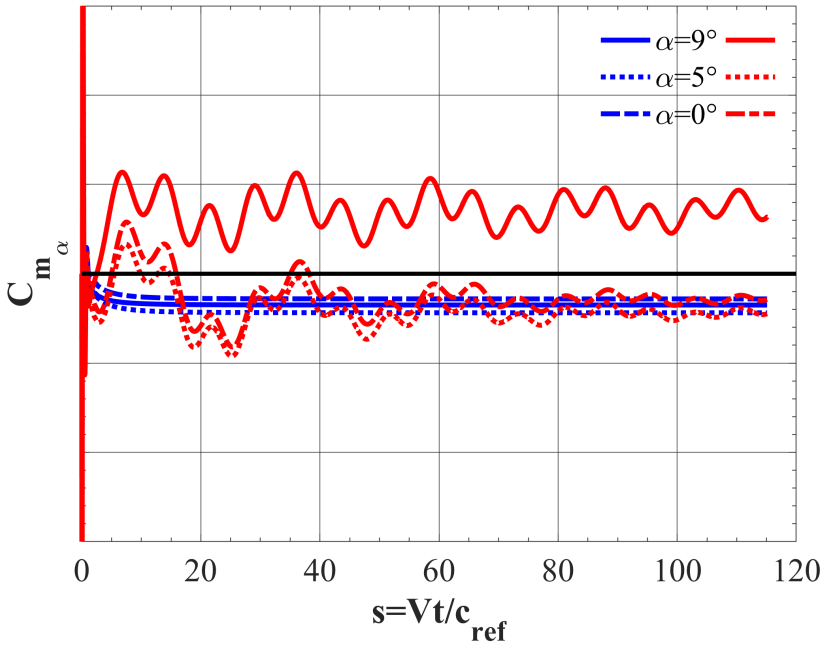

(b) Pitching moment coefficient

Figure 30: Angle-of-attack indicial responses for the flexible (red) and rigid (blue) vehicle at $\alpha = 0°$, $5°$, and $9°$, $M = 0.13$.

angle-of-attack responses have a negative mean value. This result confirms the observations made from the static characterization plots of Fig. 24, where a pitching moment break occurs earlier for the flexible vehicle at $\alpha = 8°$ compared to the rigid vehicle at $\alpha = 13°$. A periodic oscillation is also observed for the pitching moment coefficient, though similar in frequency and magnitude with change in angle of attack.

Overall, the angle-of-attack indicial responses sensitivity to angle of attack directly correlate with the nonlinearity of the static and static aeroelastic characterization curves. Thus, a nonlinear dependence on angle of attack should be considered when predicting longitudinal coefficients for maneuvers outside the ranges of $\alpha = [0°$ to $5°]$ for the rigid vehicle and maneuvers for which $\Delta\alpha >= 1°$ anywhere in the flight envelope for the flexible vehicle. Additionally, these initial aeroelastic step responses appear to capture complex fluid-structure interactions, which periodically oscillate at a given flight condition. This result suggests that hysteresis effects will be of greater importance for flexible vehicles, and the aeroelastic ROM may provide increased performance benefits compared to a traditional quasisteady stability derivative model.

Figure 31 shows the rigid and aeroelastic indicial responses with respect to pitch rate that were simulated at $\alpha_i = 0°$, $5°$, and $9°$ at $M = 0.13$. The solution is initialized using the same time-accurate static and static aeroelastic solutions as the angle-of-attack step responses. In this case, a trajectory is prescribed such that $q = 1$ rad/s is held constant for all $t > 0$ with all other vehicle-state parameters held zero. The dynamic simulations were conducted using the same solution strategy as the angle-of-attack responses and were continued to be used for all subsequent dynamic simulations.

The indicial response ROM methodology implemented for rigid vehicles assumes no sensitivity to angle of attack for the pitch rate indicial responses. The lift and pitching moment results for the rigid vehicle responses shown in Fig. 31 confirm the appropriateness of this assumption with negligible differences for $\alpha = [0°$ to $9°]$.

Each responses' transients dampen out by $s = 10$ before converging to approximately the same fixed value beyond $s = 20$. In contrast, the aeroelastic indicial responses with respect to pitch rate depict a significant sensitivity to angle of attack. The lift coefficient responses initialized from $\alpha = 0°$, $5°$, and $9°$ all encounter initial transients followed by a periodic oscillation about noticeably different mean response values. While less significant at lower angles of attack, a sensitivity to angle of attack is evident throughout the entire flight space of the flexible vehicle. The pitching moment coefficient shows a weaker sensitivity, as the responses at $\alpha = 0°$ and $5°$ having negligible variation throughout the response's time history. The response at $\alpha = 9°$ has an amplitude of periodic oscillation similar to that of the responses at lower angles of attack, but oscillations about a less negative mean pitching moment response value. These observations lead to the recommendation that a nonlinear dependence on angle of attack for pitch rate responses should be assumed for aeroelastic ROM predictions.

Figure 32 illustrates the side force and rolling moment coefficient results for the rigid and aeroelastic indicial responses with respect to a step change in sideslip angle at $\alpha_i = 0°$, $5°$, and $9°$ at $M = 0.13$. The yawing moment coefficient is typically considered for changes in the lateral vehicle-state parameters, but is not shown here for brevity as the presented coefficients provide enough data to justify angle-of-attack sensitivity. In observing both the side force and rolling moment coefficient results, the rigid responses show a discernable variability in converged derivative value. The side force coefficient response decreases with an increase in angle of attack, whereas the rolling moment coefficient response increases. For each response, the initial transients decay rapidly, and a converged value is reached by $s = 5$. Similar results are found for the aeroelastic responses with an apparent sensitivity to angle of attack for both the side force and rolling moment coefficients. The indicial response ROM methodology implemented for rigid vehicles assumes sensitivity to angle of attack for the sideslip angle indicial responses. The results shown for the X-56A confirm the suitability of

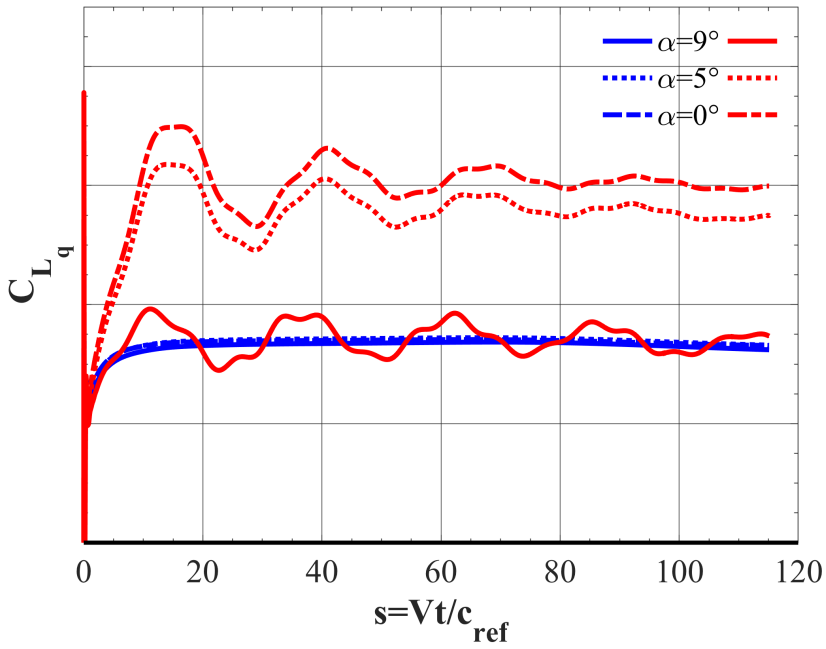

(a) Lift coefficient

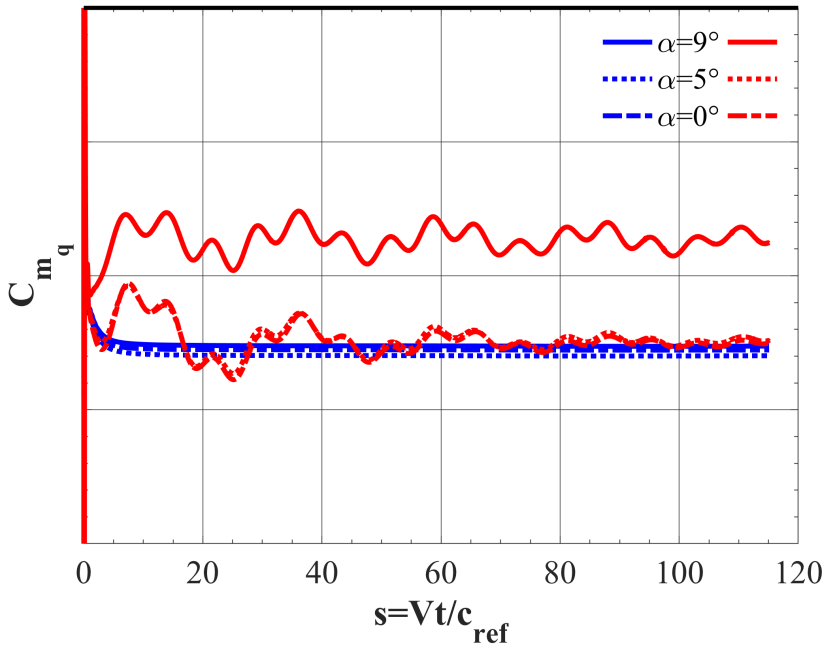

(b) Pitching moment coefficient

Figure 31: Pitch rate indicial responses for the flexible (red) and rigid (blue) vehicle at $\alpha = 0°$, $5°$, and $9°$, $M = 0.13$.

this assumption for both the rigid and aeroelastic vehicle.

Figure 33 shows the side force and rolling moment coefficient results for the rigid and aeroelastic indicial responses with respect to a 1 rad/s step change in roll rate at $\alpha_i = 0°$, 5°, and 9° at $M = 0.13$. For the rigid vehicle, the side force coefficient responses show an incremental change in converged derivative values between each angle of attack with positive values for $\alpha \leq 5°$. The rolling moment coefficient responses show negligible sensitivity for the lower angle-of-attack range, but a noticeable difference in converged values between the $\alpha = 5°$ and 9°. For the flexible vehicle, the side force coefficient responses show an incremental change in converged value between the lower angles of attack with a very small magnitude periodic oscillation of period $\Delta s = 10$. At $\alpha = 9°$, the response undergoes significant initial fluid-structure transients up to $s = 25$ before settling into a large magnitude periodic oscillation with a period approximately twice as long relative to the lower angles of attack. The rolling moment coefficient shows greater variation with each increase in angle of attack and a periodic nature similar to that of the side force coefficient. The indicial response ROM methodology typically assumes no sensitivity to angle of attack for roll rate indicial responses. The results shown here indiciate that angle-of-attack sensitivity may increase modeling accuracy of ROM predictions for both the rigid and flexible X-56A vehicle, particularly at higher angles of attack for the flexible vehicle.

Figure 34 shows the side force and yawing moment coefficient results for the rigid and aeroelastic indicial responses with respect to a 1 rad/s step change in yaw rate at $\alpha_i = 0°$, 5°, and 9°, $\beta = 0°$, at $M = 0.13$. For the rigid vehicle, each of the coefficient responses see an initial transient for $s < 10$ before converging to a steady value. The side force coefficient shows an incremental and increasing change in converged value with an increase in angle of attack. The rolling moment coefficient responses show a similar sensitivity to angle of attack. For the aeroelastic vehicle, each of the coefficient responses sees an initial transient for $s < 10$ as well and converges to a steady value

at lower angles of attack. At $\alpha = 9°$, the response exhibits a low magnitude periodic oscillation of period $\Delta s = 15$. Overall, both the side force and yawing moment coefficient time histories depict a sensitivity to angle of attack throughout the flight envelope. The indicial response ROM methodology typically assumes no sensitivity to angle of attack for yaw rate indicial responses.

The results of the present study indiciate that the assumptions traditionally invoked in application of indicial response ROMs for rigid vehicles may require modification for accurate modeling predictions of flexible vehicles. Previous works [38, 42] typically only assume a sensitivity to angle of attack for the indicial responses with respect to step changes in angle of attack and sideslip angle.

The angle-of-attack indicial responses were shown to be sensitive to angle of attack for both the rigid and flexible X-56A with a greater sensitivity demonstrated for the flexible vehicle. The aeroelastic indicial responses were characterized by significant fluid-structure interactions, where converged derivative values correlated with the nonlinearity of the static lift and pitching moment curves shown in Section 7.1. For the pitch rate indicial responses, negligible differences were observed for the rigid responses at each angle of attack, whereas the aeroelastic responses illustrated a strong sensitivity to angle of attack. This result suggests accurate ROM predictions for the unsteady longitudinal aerodynamic predictions for the flexible vehicle may require inclusion of a dependency on angle of attack for the pitch rate indicial responses.

The sideslip angle indicial responses were shown to be sensitive to angle of attack for both the rigid and flexible X-56A, confirming the validity of the original ROM assumptions, where the flexible responses showed a greater sensitivity. In contrast, the roll rate and yaw rate indicial responses showed a dependency on angle of attack for both the rigid and flexible vehicles. Addition of this dependency to lateral rotation rates may be necessary due to the X-56A configuration itself.

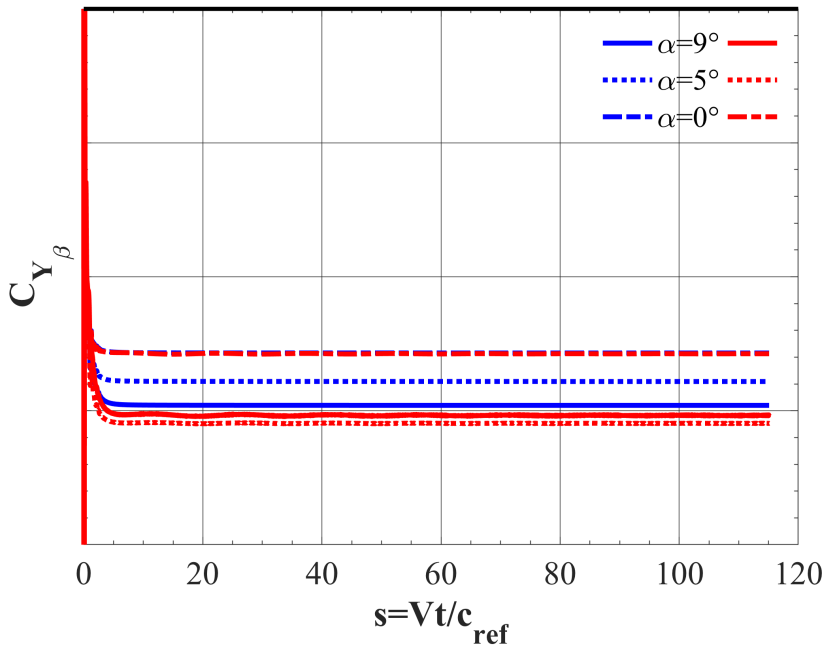

(a) Side force coefficient

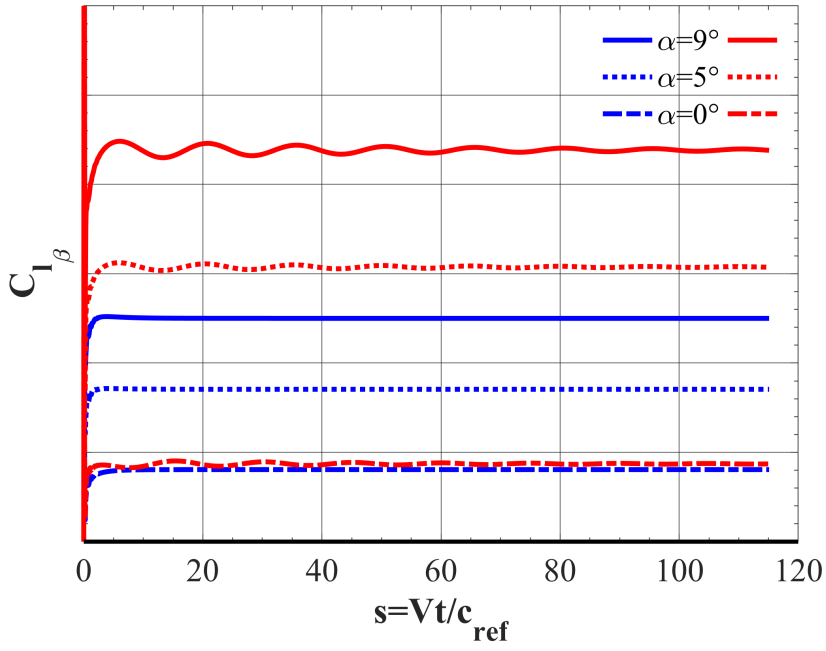

(b) Rolling moment coefficient

Figure 32: Sideslip angle indicial responses for the flexible (red) and rigid (blue) vehicle at $\alpha = 0°$, $5°$, and $9°$, $M = 0.13$.

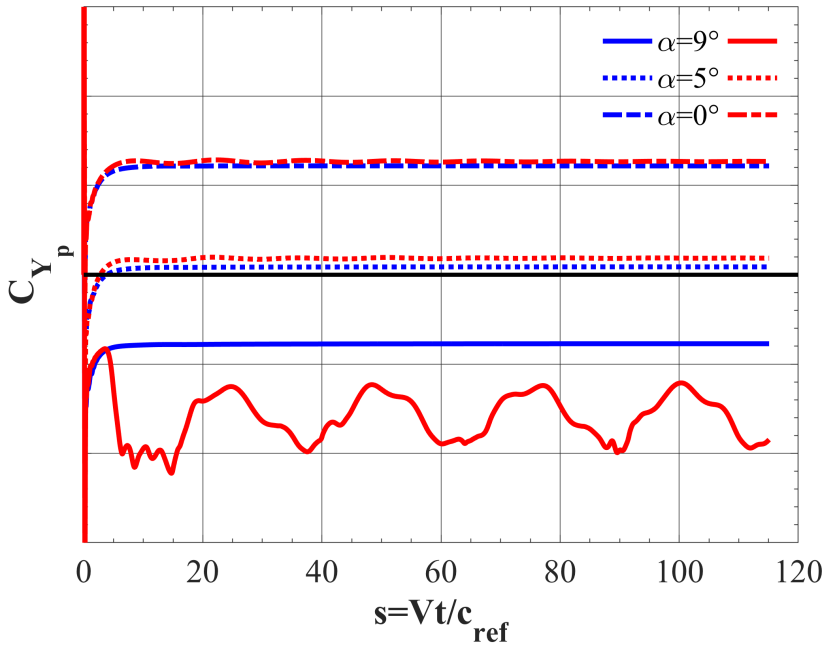

(a) Side force coefficient

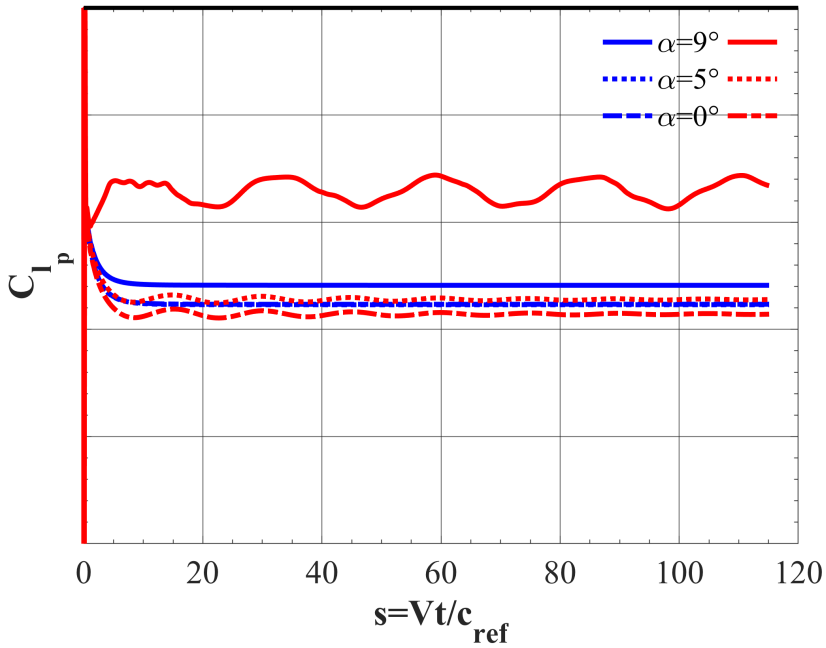

(b) Rolling moment coefficient

Figure 33: Roll rate indicial responses for the flexible (red) and rigid (blue) vehicle at $\alpha = 0°$, $5°$, and $9°$, $M = 0.13$.

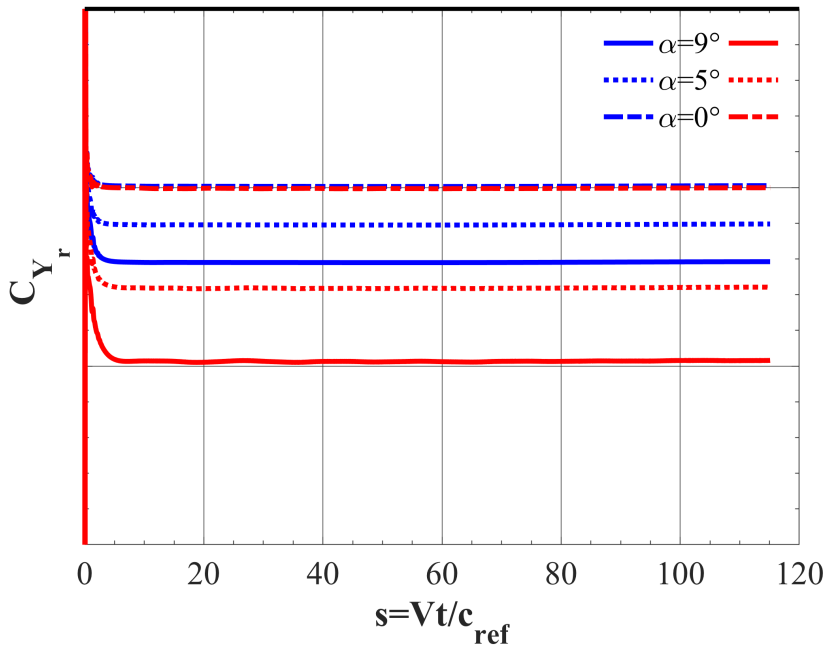

(a) Side force coefficient

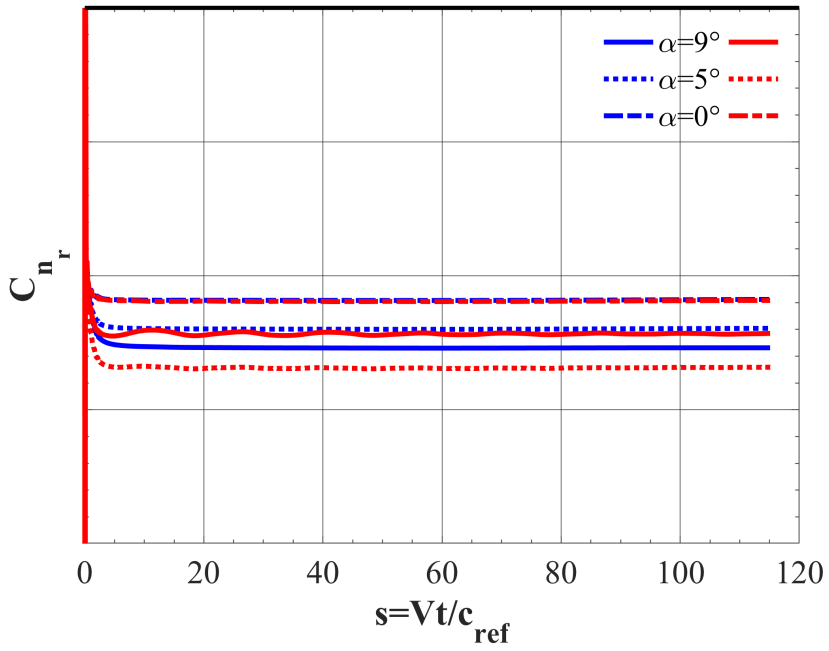

(b) Yawing moment coefficient

Figure 34: Yaw rate indicial responses for the flexible (red) and rigid (blue) vehicle at $\alpha = 0°$, $5°$, and $9°$, $M = 0.13$.

7.4 Sensitivity to Mach Number

Indicial response ROMs developed for rigid vehicles typically assume that all longitudinal and lateral vehicle-state parameters are dependent on Mach number. The present section seeks to verify the suitability of this assumption for the rigid and flexible X-56A aircraft, and if observed, note the strength of sensitivity to establish sampling requirements for maneuver predictions. Toward this effort, rigid and aeroelastic indicial responses were simulated for each vehicle-state parameter at $M = 0.10$, 0.15, and 0.20. Each dynamic simulation was simulated using a characteristic time step corresponding to an $N = 200$ sampling of the highest frequency structural mode for a total of 4,000 time steps. As a result, the nondimensional time duration is longer for larger Mach numbers for which the flow travels a greater distance in a given amount of physical time.

Figures 35 and 36 show the rigid (blue) and aeroelastic (red) lift and pitching moment responses due to step changes in angle of attack and pitch rate, respectively. As expected, the angle-of-attack and pitch rate indicial responses for the rigid vehicle are nearly identical, showing little sensitivity over the sampled Mach number range. In each case, the response encounters a brief initial transient and converges to a steady derivative value by $s = 15$. In contrast, the aeroelastic lift and pitching moment responses show a significant sensitivity to Mach number, even with a limited sampling interval of $\Delta M = 0.1$. The responses show an initial peak, positive for lift and negative for pitching moment, as the steady flow around the vehicle is disturbed by compression and expansion waves forming on the lower and upper surface of the vehicle due a step change in grid motion. As the simulation time progresses, the waves begin to move away from the vehicle and the fluid-structure interactions begin to settle at the final vehicle state. For the lift coefficient responses, the fluid-structure interactions exhibit a periodic unsteadiness, which decreases in frequency at higher Mach numbers. At $M = 0.20$, the time required for converged aeroelastic responses is

nearly 10 times greater than the rigid responses. This demonstrates that motion history effects are much greater for the flexible vehicle. The pitching moment coefficient shows an even stronger sensitivity to Mach number, due to the rapidly fluctuating surface pressures, with nonperiodic transients persisting up to $s = 100$.

Figure 37 illustrates the rigid (blue) and aeroelastic (red) side force and rolling moment responses due to a step change in sideslip angle. For the rigid vehicle, both coefficients experience a short duration transient before converging to steady derivative values with negligible sensitivity to Mach number. The aeroelastic side force coefficient responses compare favorably with the rigid responses between $M = [0.10$ to $0.15]$, but converge to a more negative derivative value at $M = 0.20$. More pronounced differences are observed for the rolling moment coefficient responses, which exhibit a small amplitude periodic oscillation up to $s = 100$ and have noticeable differences in mean derivative value at each sampled Mach number.

The rigid (blue) and aeroelastic (red) side force and rolling moment responses due to a step change in roll rate are shown in Fig. 38. In contrast to the sideslip angle indicial responses, slight differences are observed in the converged rigid response values for side force coefficient. These differences become even more pronounced for the aeroelastic responses, which exhibit small-amplitude periodic oscillations that dampen more rapidly with a decrease in Mach number. Between the rigid and aeroelastic simulations, the rolling moment coefficient results share a similar qualitative behavior. Though, the aeroelastic responses show a stronger sensitivity to Mach number relative to the rigid responses.

Finally, Fig. 39 depicts the rigid and aeroelastic side force and yawing moment responses with respect to a step change in yaw rate. Each of the coefficient responses for both the rigid and aeroelastic vehicle exhibit a relatively steady response time-history with initial transients decaying and a converged derivative value attained by $s = 10$ at each Mach number. At $M = 0.10$ and 0.15, the rigid and aeroelastic

response values agree for both aerodynamic coefficients. At $M = 0.20$, there is a pronounced difference in the converged rigid and aeroelastic response values for both coefficients. Within the sampled Mach number range, a general sensitivity is present that strengthens for greater Mach numbers. At the lower Mach number range, fluid-structure interactions are minimal with identical results achieved between the rigid and aeroelastic simulations.

Overall, the rigid and aeroelastic responses with respect to the longitudinal and lateral vehicle-state parameters demonstrate various degrees of sensitivity to Mach number. For $s \leq 10$, the initial transients between the rigid and aeroelastic responses match fairly well with a decrease in peak response magnitude with an increase in Mach number. As the flow adjusts to the step change in grid motion, the rigid responses converge to a steady flow state, whereas the aeroelastic responses experience an unsteady response due to the fluid-structure dynamics being resolved. The observed unsteadiness was more significant for the longitudinal vehicle-state parameters relative to the lateral vehicle-state parameters. As Mach number increases, a pronounced difference between the rigid and aeroelastic responses is generally observed. These results verify the need to include a dependency on Mach number for ROM predictions, and suggest the need for a finer sampling of the Mach number envelope for aeroelastic predictions or a more constrained flight envelope. Additionally, the long duration transients for the aeroelastic responses pose the requirement of simulating more time steps for response identification relative to the rigid responses.

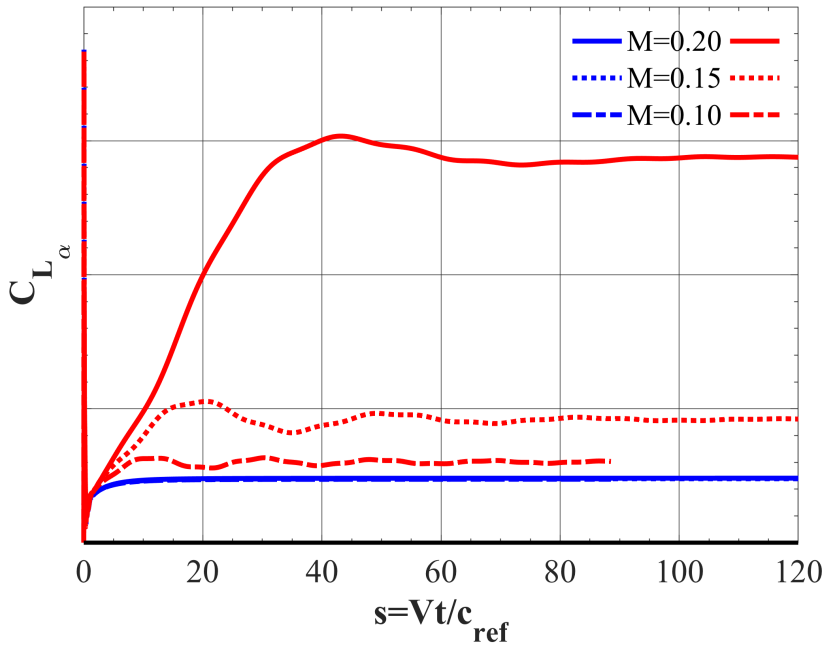

(a) Lift coefficient

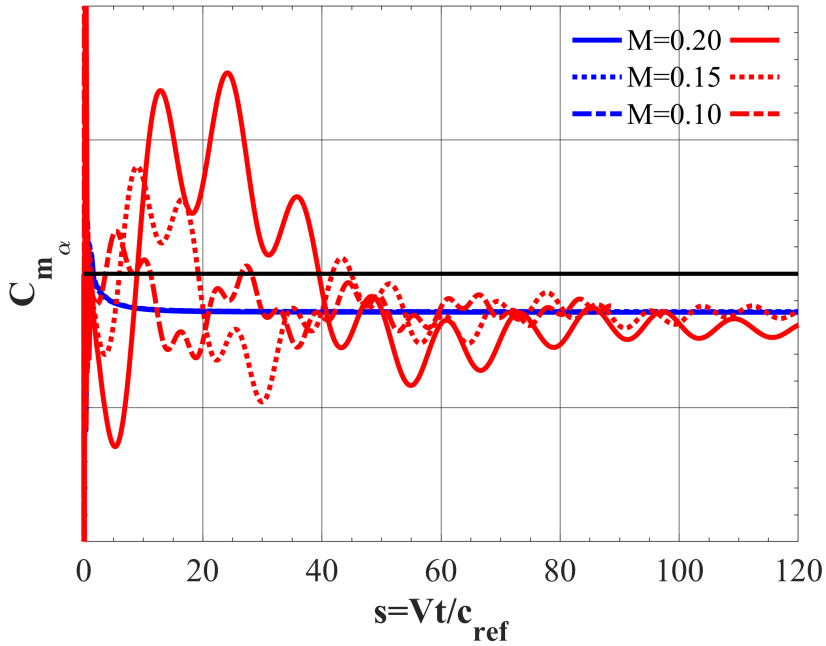

(b) Pitching moment coefficient

Figure 35: Angle-of-attack indicial responses for the flexible (red) and rigid (blue) vehicle at $M = 0.10$, 0.15, and 0.20, $\alpha = 0°$.

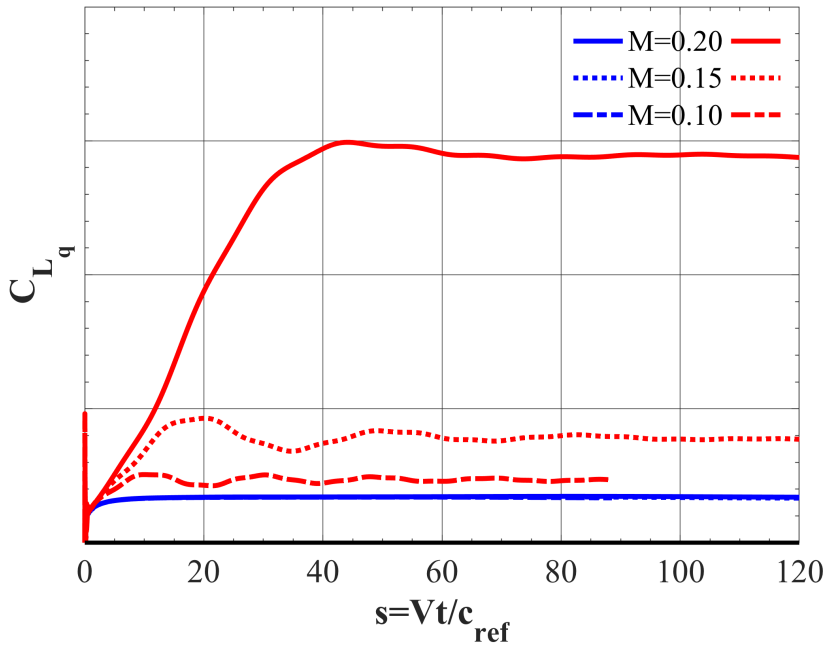

(a) Lift coefficient

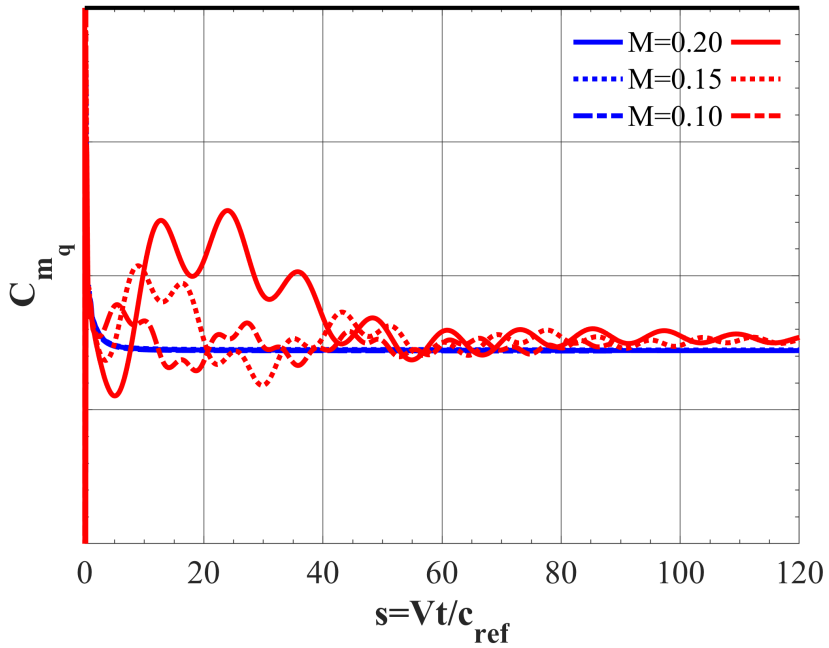

(b) Pitching moment coefficient

Figure 36: Pitch rate indicial responses for the flexible (red) and rigid (blue) vehicle at $M = 0.10$, 0.15, and 0.20, $\alpha = 0°$.

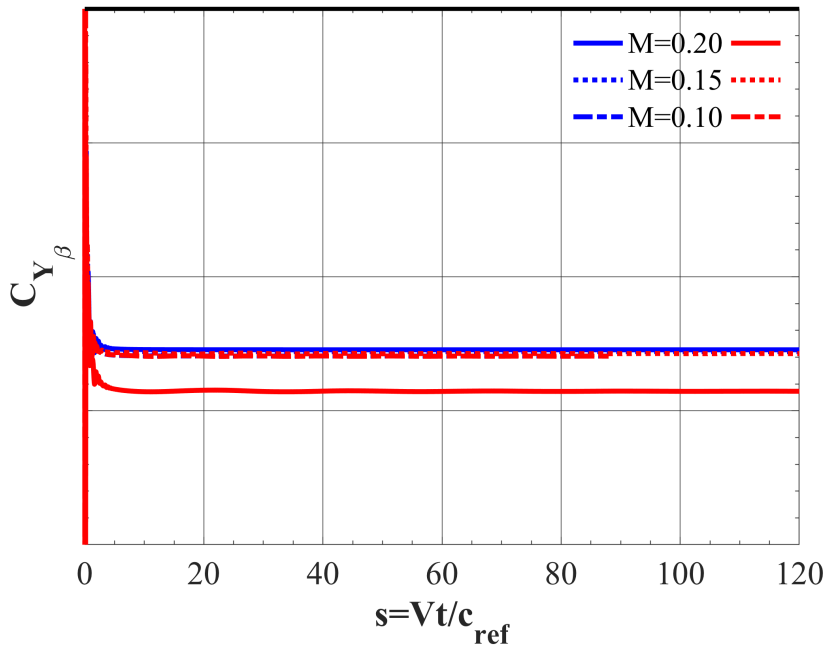

(a) Side force coefficient

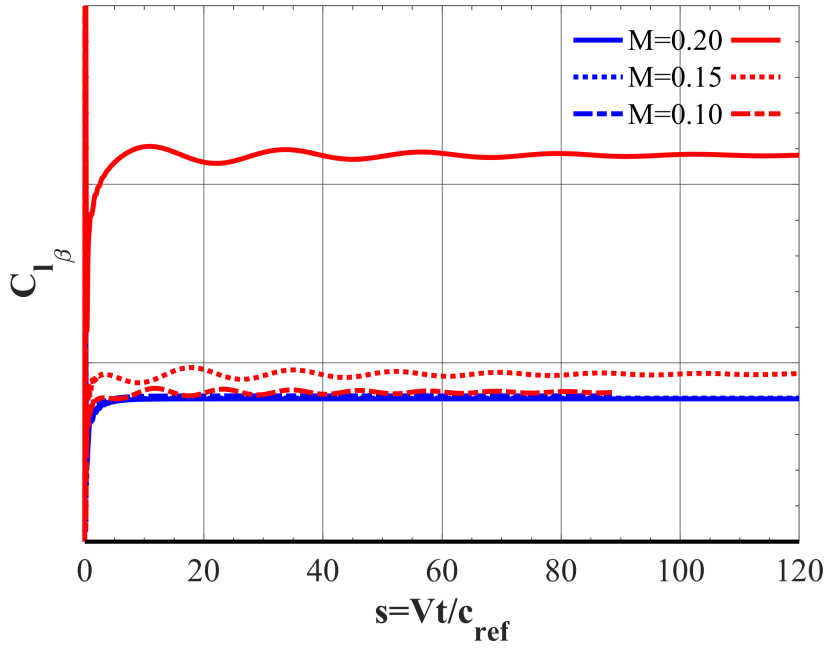

(b) Rolling moment coefficient

Figure 37: Sideslip angle indicial responses for the flexible (red) and rigid (blue) vehicle at $M = 0.10$, 0.15, and 0.20, $\alpha = 0°$.

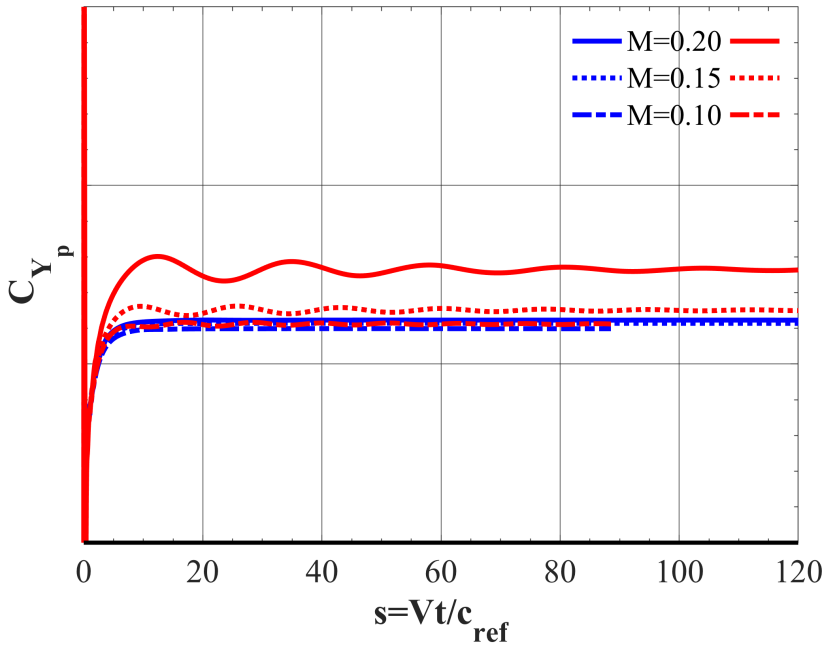

(a) Side force coefficient

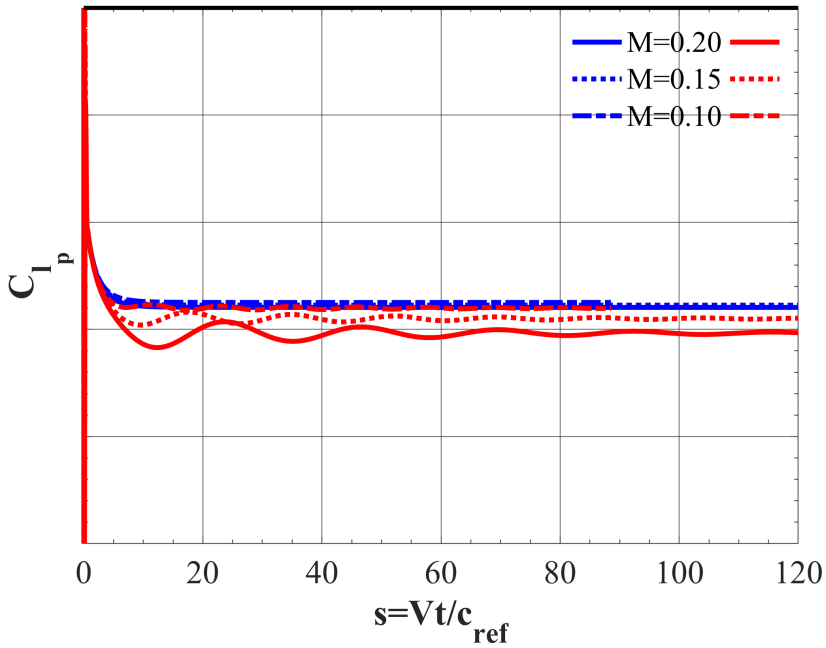

(b) Rolling moment coefficient

Figure 38: Roll rate indicial responses for the flexible (red) and rigid (blue) vehicle at $M = 0.10$, 0.15, and 0.20, $\alpha = 0°$.

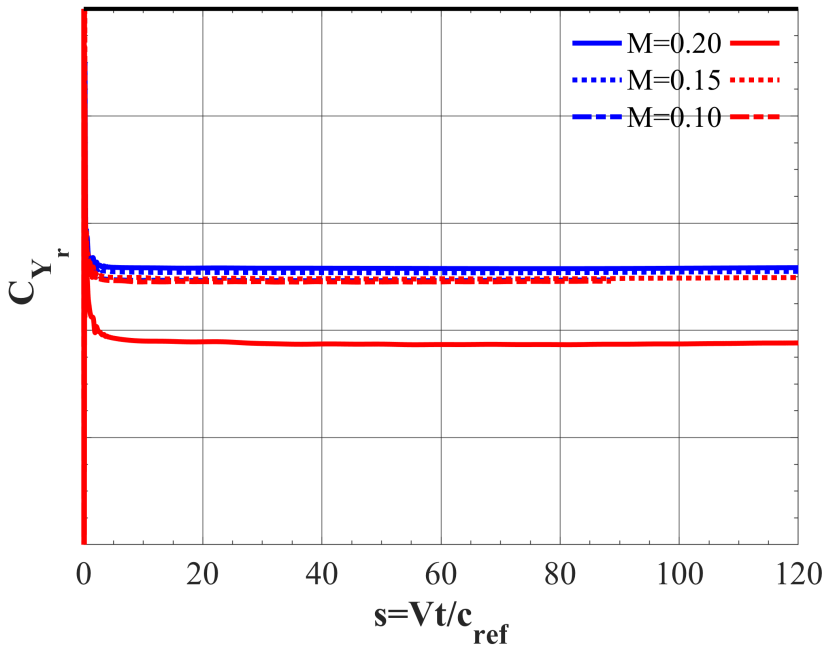

(a) Side force coefficient

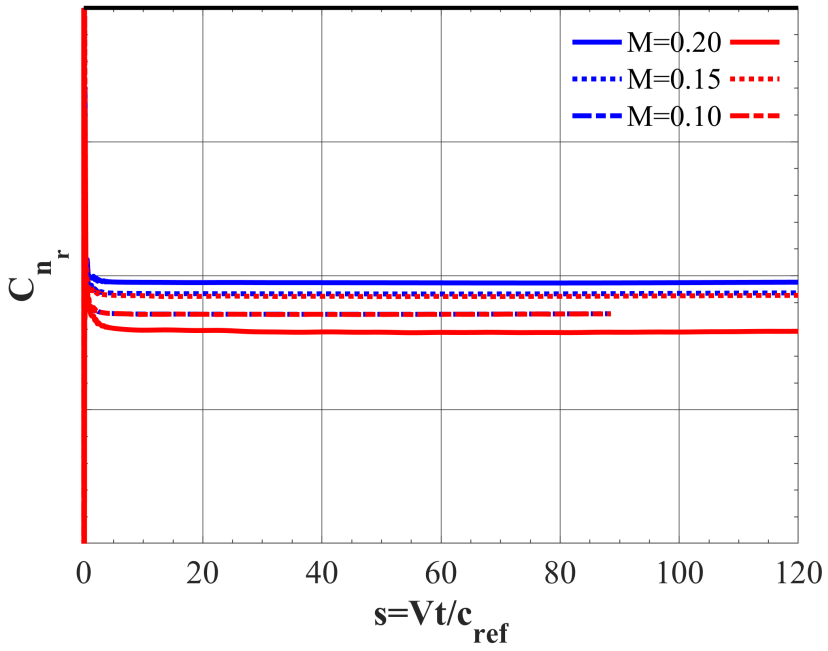

(b) Yawing moment coefficient

Figure 39: Yaw rate indicial responses for the flexible (red) and rigid (blue) vehicle at $M = 0.10$, 0.15, and 0.20, $\alpha = 0°$.

7.5 Sensitivity to Sideslip Angle

Rigid and aeroelastic indicial responses with respect to each vehicle-state parameter were simulated at $\beta_i = 0°$, 5°, and 10° at $M = 0.13$ to assess the response sensitivity to sideslip angle. In these simulations, the solution is initialized using time-accurate static and static aeroelastic simulations for the rigid and aeroelastic responses, respectively. Then, a trajectory is prescribed such that a step change in the desired vehicle-state parameter is simulated while β is held constant for all $t > 0$, with the exception of the sideslip angle step response, and all other vehicle-state parameters are held zero. Each dynamic simulation was simulated using a characteristic time step corresponding to an $N = 200$ sampling of the highest frequency structural mode for a total of 4,000 time-accurate time steps, in order to capture at least five periods of the lowest frequency structural mode.

The lift and pitching moment coefficient responses for the rigid (blue) and aeroelastic (red) simulations due to a step change in angle of attack at various sideslip angles are shown in Fig. 40. Each of the responses for the rigid vehicle exhibit an initial transient, before converging to a steady derivative value by $s = 20$. The angle-of-attack indicial responses for the rigid vehicle are nearly identical, showing no sensivity to sideslip angle for $\beta = [0°$ to $10°]$. In contrast to the steady, well-converged values found for the rigid vehicle, the aeroelastic responses are characterized by prolonged fluid-structure interactions, which continue up to $s = 75$. For both the lift and pitching moment coefficients, the responses show negligible sensitivity to changes in sideslip angle. Similar results are found for the rigid and aeroelastic indicial responses with respect to pitch rate in Fig. 41. The rigid and flexible responses show little variability with changes in sideslip angle, and the aeroelastic responses are characterized by periodic oscillations for the simulation duration. Overall, the results are in agreement with the traditional assumptions for indicial response ROMs in that there is no dependency on sideslip angle for the longitudinal vehicle-state parameters.

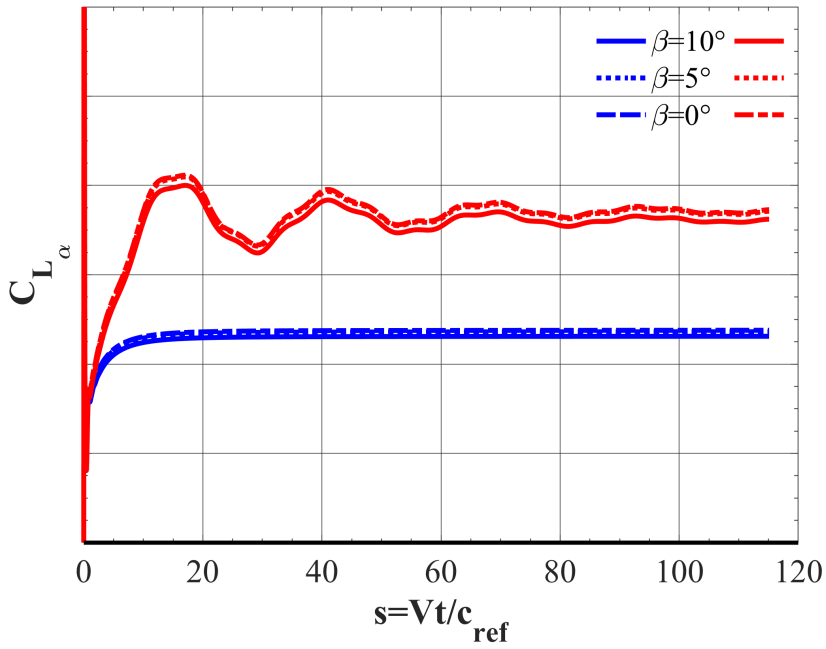

(a) Lift coefficient

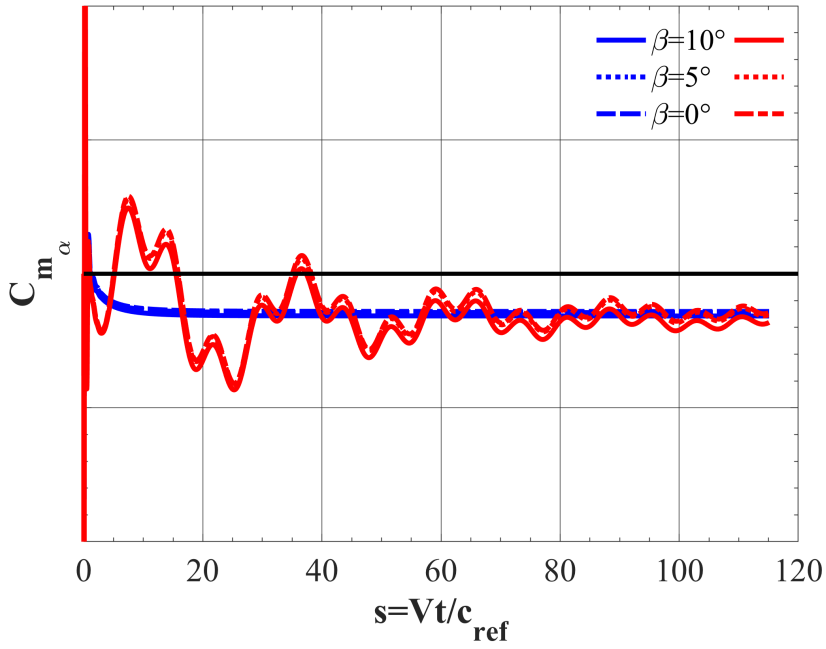

(b) Pitching moment coefficient

Figure 40: Angle-of-attack indicial responses for the flexible (red) and rigid (blue) vehicle at $\beta = 0°$, $5°$, and $10°$, $M = 0.13$.

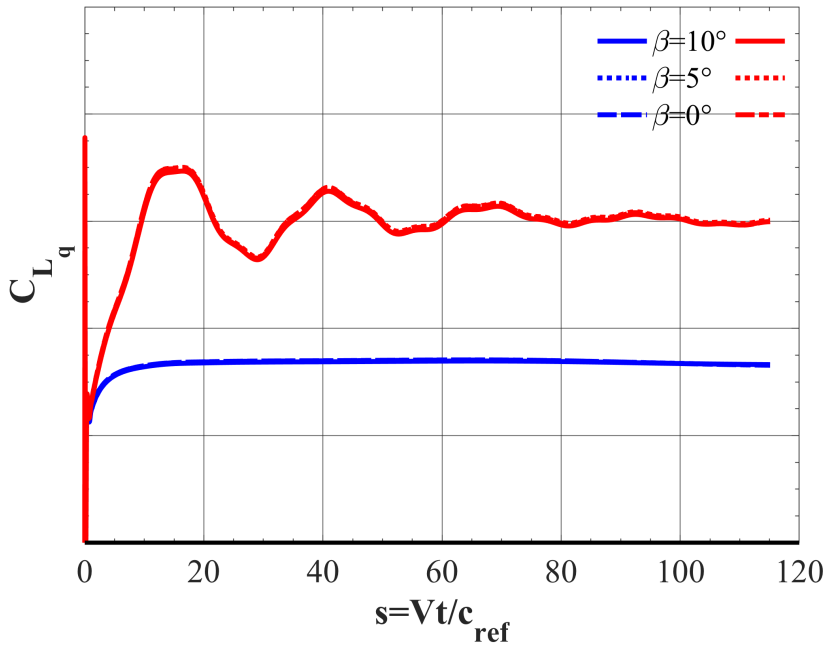

(a) Lift coefficient

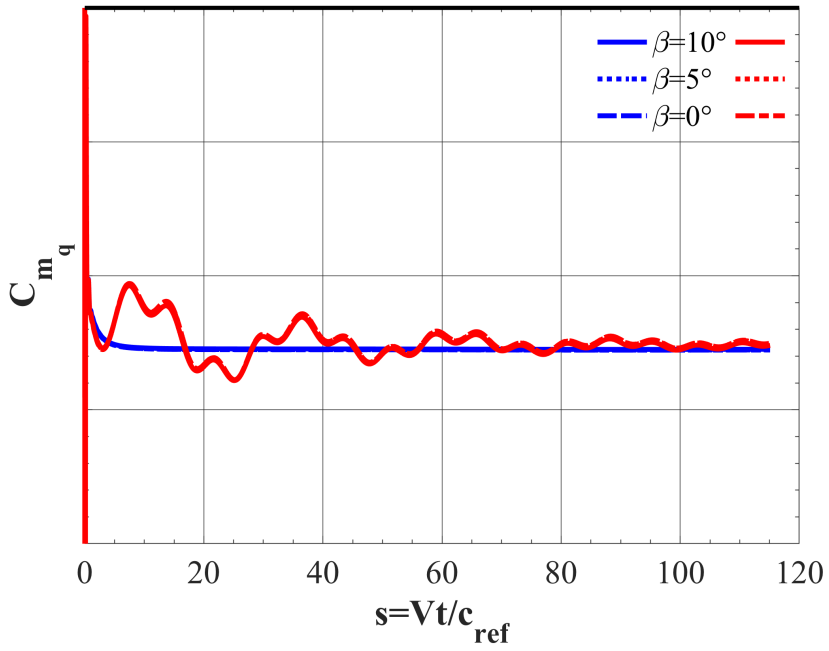

(b) Pitching moment coefficient

Figure 41: Pitch rate indicial responses for the flexible (red) and rigid (blue) vehicle at $\beta = 0°$, $5°$, and $10°$, $M = 0.13$.

The side force and rolling moment coefficient responses for the rigid (blue) and aeroelastic (red) simulations of a step change in sideslip angle at various sideslip angles are shown in Fig. 42. Each of the rigid vehicle's coefficient responses exhibit a brief initial transient, before converging to a steady derivative value by $s = 15$. These responses show a noticeable sensivity to sideslip angle between $\beta = 0°$ and 5°. The differences in converged response values are less pronounced between $\beta = 5°$ and 10°. In comparison, the aeroelastic side force coefficient responses are nearly identical to those of the rigid vehicle, whereas the rolling moment coefficient responses are characterized by periodic fluid-structure interactions for the duration of the simulation with mean values slightly greater than those for the rigid vehicle. The aeroelastic simulations do, however, also show a sensitivity to sideslip angle at lower angles of attack.

Figure 43 illustrates the side force and rolling moment coefficient results at various sideslip angles for the rigid (blue) and aeroelastic (red) roll rate indicial responses. Each of the rigid vehicle's responses exhibit a brief initial transient, before converging to a steady derivative value by $s = 15$ for both the side force and rolling moment coefficients. The side force coefficient results show a nonlinear sensitivity with the response at $\beta = 0°$ in slight disagreement with the responses at $\beta = 5°$ and 10°. The rolling moment coefficient appears to be insensitive to sideslip angle. For the flexible vehicle, the side force and rolling moment coefficient responses show a stronger initial transient before transitioning to a small amplitude oscillation that decays by simulation end. Similar to the rigid vehicle, the flexible vehicle shows a slight nonlinear sensitivity to sideslip angle, but negligible variability for the rolling moment coefficient responses. Overall, the rigid and aeroelastic indicial responses due to a step change is roll rate show a negligible sensitivity to sideslip angle.

Finally, the rigid and aeroelastic side force and yawing moment indicial responses due to a step change in yaw rate are shown in Fig. 44. In this case, the rigid and

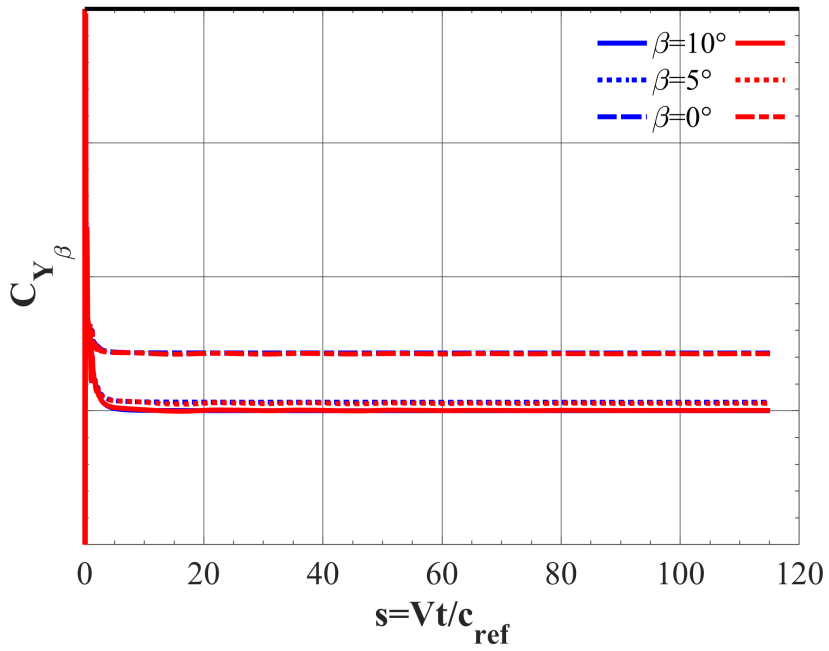

(a) Side force coefficient

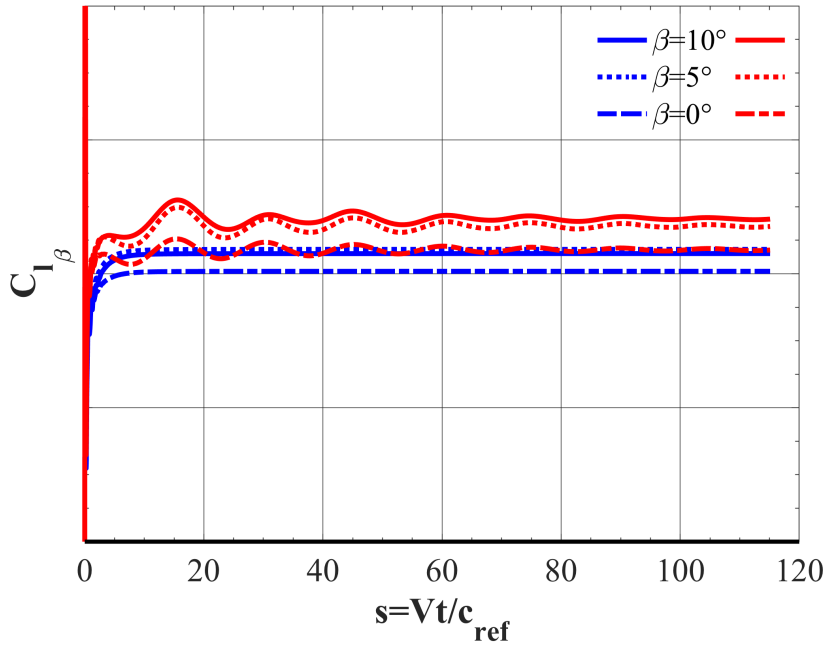

(b) Rolling moment coefficient

Figure 42: Sideslip angle indicial responses for the flexible (red) and rigid (blue) vehicle at $\beta = 0°$, $5°$, and $10°$, $M = 0.13$.

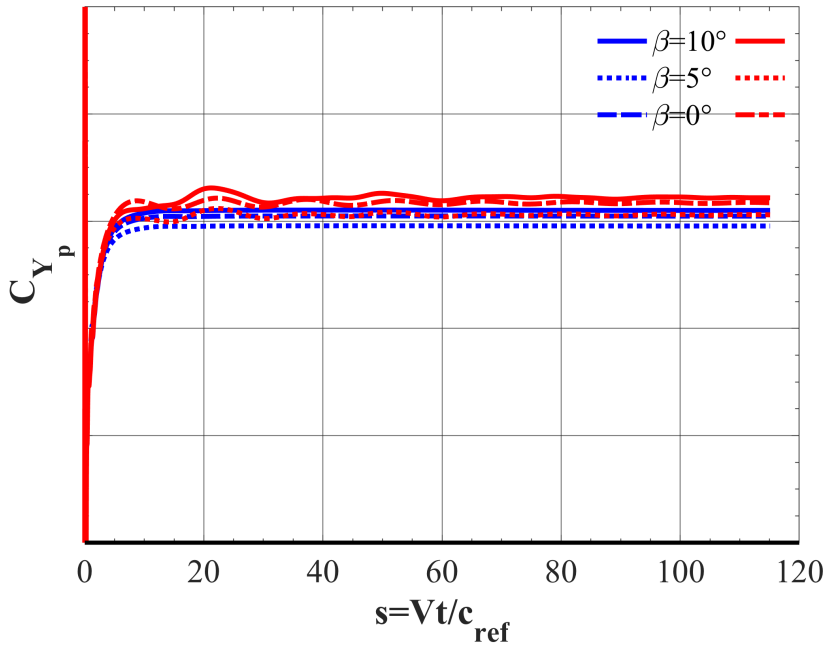

(a) Side force coefficient

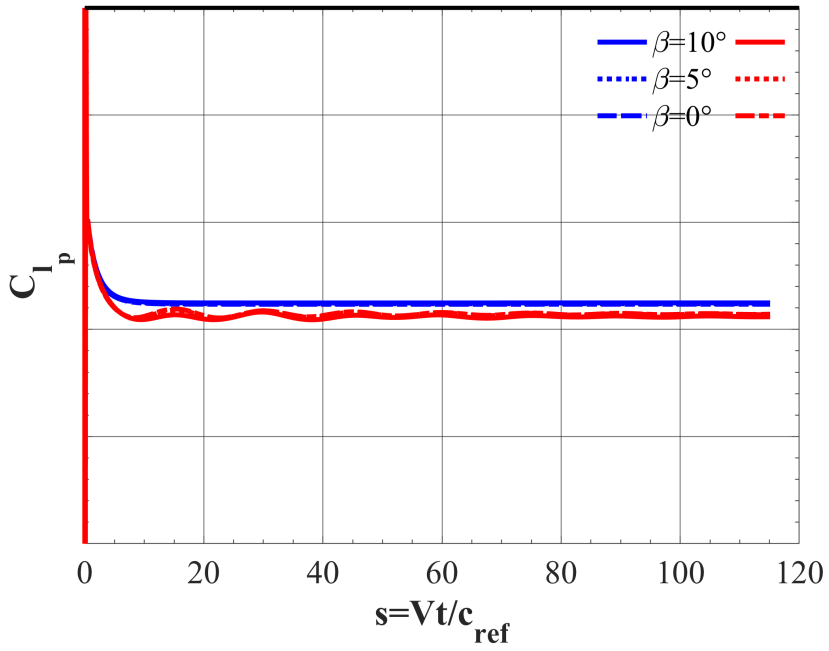

(b) Rolling moment coefficient

Figure 43: Roll rate indicial responses for the flexible (red) and rigid (blue) vehicle at $\beta = 0°$, $5°$, and $10°$, $M = 0.13$.

aeroelastic responses are in general agreement for both coefficients. Each response encounters an initial transient that dampens out by $s = 10$ and converges to a steady derivative value with observed solution oscillations only at $\beta = 10°$. The sensitivity to sideslip angle is apparent in both the rigid and flexible simulations with noticeable differences in converged values for the steps initialized at $\beta = 0°$, $5°$, and $10°$. This sensitivity becomes weaker as the sideslip angle is increased.

Previous works typically assume no dependency on sideslip angle for both the longitudinal and lateral vehicle-state parameter indicial responses. The longitudinal vehicle-state parameters, angle of attack, pitch rate, and roll rate, were shown to be independent of sideslip angle for both the rigid and flexible vehicle. This finding is in agreement with typical methodology assumptions. However, the sideslip angle and yaw rate indicial responses were shown to have a slight nonlinear sensitivity to sideslip angle. While including a sideslip angle sensitivity for these indicial responses may increase modeling accuracy, it is recommended that traditional ROM modeling assumptions be implemented as the rigid and aeroelastic responses compare favorably. Further increases in modeling prediction accuracy may not be warranted due to the computational costs associated with increased indicial response sampling requirements.

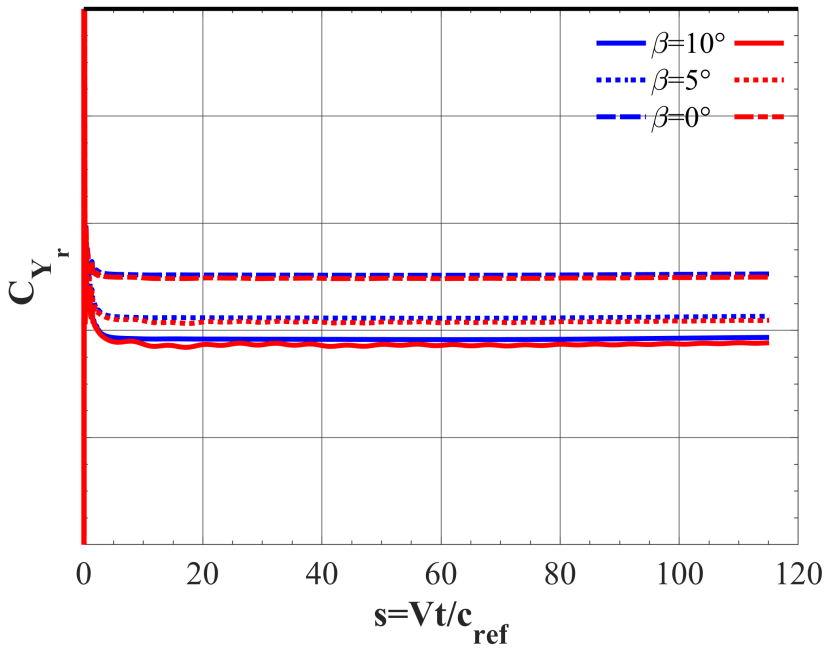

(a) Side force coefficient

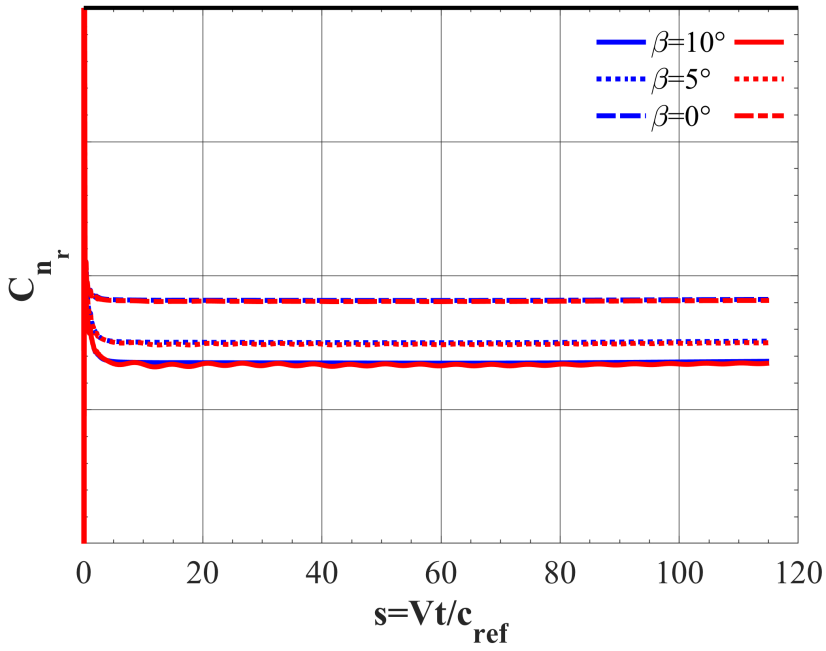

(b) Yawing moment coefficient

Figure 44: Yaw rate indicial responses for the flexible (red) and rigid (blue) vehicle at $\beta = 0°$, $5°$, and $10°$, $M = 0.13$.

7.6 Symmetry of Step Responses

Previous applications of indicial response ROMs for predicting the unsteady aerodynamic responses of maneuvering vehicles typically assume a symmetric flow response with respect to both direction of step change and angle of attack. In regard to step change, indicial responses with respect to angle of attack are usually initialized at a given angle of attack, α_0, and then a trajectory is prescribed such that a positive step change is taken to reach $\alpha = \alpha_0 + 1$. These positive responses are then used in ROM predictions through convolution with a prescribed trajectory's angle-of-attack time history. In doing so, this assumes that the aerodynamic response is identical for positive and negative step changes in angle of attack. To elaborate, this would imply that the time-dependent response due to a step change from $\alpha_0 = 0°$ to $\alpha = 1°$ would be the same in magnitude but opposite in sign as the response from $\alpha_0 = 0°$ to $\alpha = -1°$, i.e., $-C_{j_\alpha}(t)|_0^1 = C_{j_\alpha}(t)|_0^{-1}$ or $-C_{j_\alpha}(t)|_5^6 = C_{j_\alpha}(t)|_{-5}^{-6}$. Assuming identical converged stability derivative values would imply a symmetry of the static response, e.g., lift curve, about α_0 for a given vehicle. This modeling assumption would likely be invalid for both rigid and flexible vehicles due to generally asymmetric outer mold lines and/or aerodynamic nonlinearities, and potentially for flexible vehicles that may have asymmetric structural responses for opposite loading directions. The validity of this assumption is investigated for the rigid and flexible X-56A aircraft in the present section.

Figure 45 illustrates the lift and pitching moment coefficient time histories for rigid vehicle responses due to a positive ('+' marker) step change in angle of attack at $\alpha = 5°$, a negative (dash marker) step change in angle of attack at $\alpha = -5°$, and positive and negative step changes in angle of attack at $\alpha = 0°$. The lift coefficient responses due to positive and negative steps at $\alpha = 0°$ are shown to be in general agreement for both the transient response, as well as the converged derivative value. Further away from the initial angle of attack, it is observed that the positive step

at $\alpha = 5^\circ$ and negative step (mirrored) at $\alpha = -5^\circ$ share a qualititatively similar transient response, but converge to different stability derivative values. Furthermore, the pitching moment responses at $\alpha = 0^\circ$ show a slight discrepancy in converged stability derivative value. The differences between the responses at $\alpha = -5^\circ$ and $\alpha = 5^\circ$ are more pronounced with a more rapid transient decay and a stability derivative value that is opposite in sign for the negative step (mirrored) at $\alpha = -5^\circ$. The results observed for the lift and pitching moment results are supported by the static characterization study, previously shown in Fig. 24 of Section 7.1, as evidenced by the local changes in slope of the lift and pitching moment curves.

Figure 46 illustrates the lift and pitching moment coefficient time histories for rigid vehicle responses due to a positive ('+' marker) step change in angle of attack at $\alpha = 5^\circ$, a negative (dash marker) step change in angle of attack at $\alpha = -5^\circ$, and positive and negative step changes in angle of attack at $\alpha = 0^\circ$. Overall, similar trends are found with respect to the lift and pitching moment responses. The lift coefficient response for positive and negative steps at $\alpha = 0^\circ$ are in general agreement, whereas different converged stability derivative values are obtained between the positive step at $\alpha = 5^\circ$ and the negative step (mirror) at $\alpha = -5^\circ$. Additionally, the pitching moment response for positive and negative step changes at $\alpha = 0^\circ$ compare favorably during the initial transients until $s = 10$ before converging to slightly offset stability derivative values. The pitching moment responses at $\alpha = -5^\circ$ and $\alpha = 5^\circ$ show qualitatively similar transient behaviors, but converge to stability derivative values opposite in sign. Again, these results are confirmed by the differences in slope of the lift and pitching moment curves for the flexible vehicle.

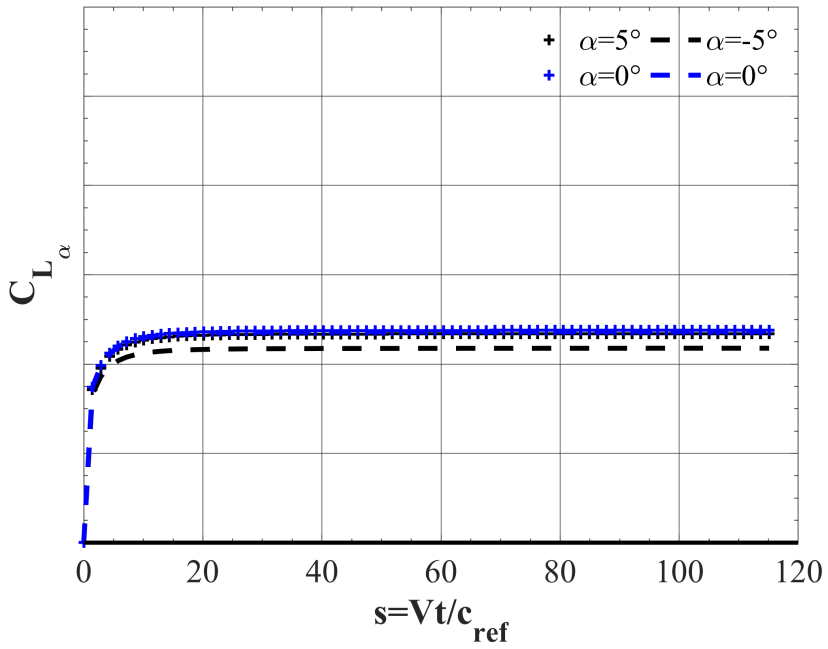

(a) Lift coefficient

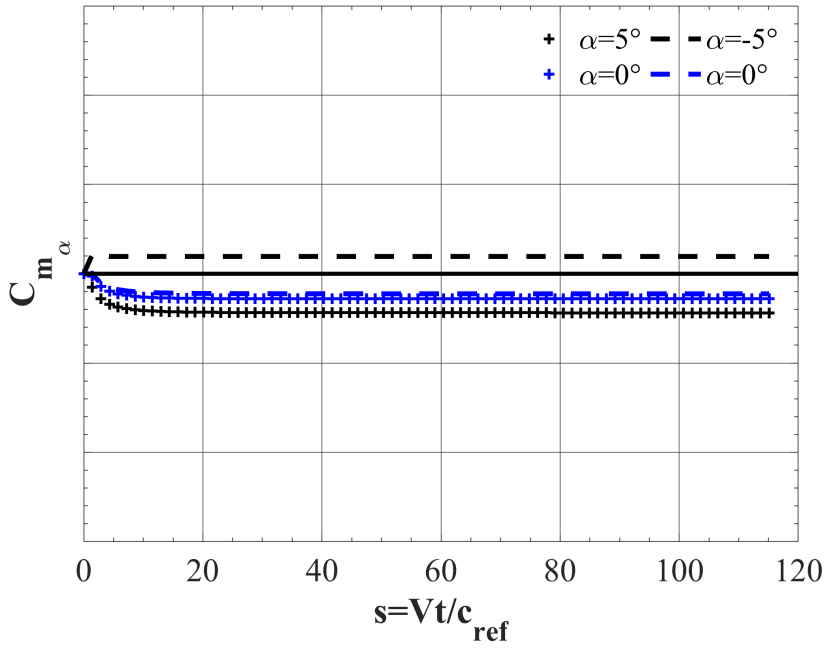

(b) Pitching moment coefficient

Figure 45: Angle-of-attack indicial responses due to positive (plus marker) and negative (dashed line) steps for the rigid vehicle at $\alpha = 0°$, $5°$, and $-5°$, $M = 0.13$.

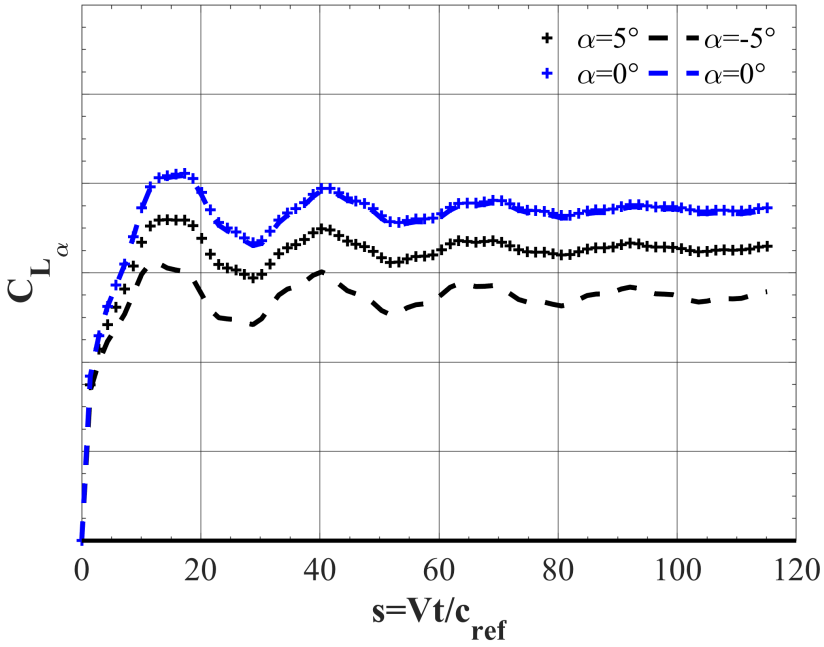

(a) Lift coefficient

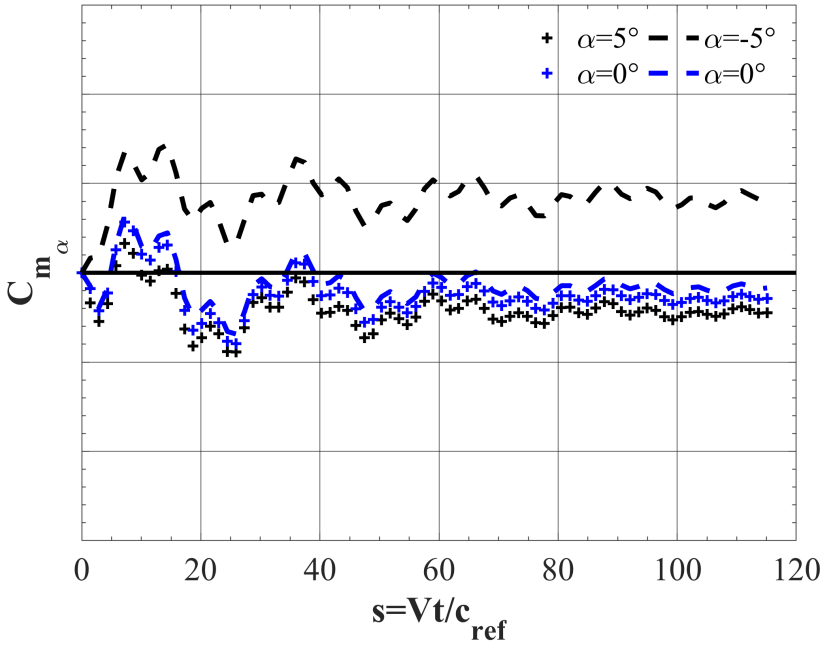

(b) Pitching moment coefficient

Figure 46: Angle-of-attack indicial responses due to positive (plus marker) and negative (dashed line) steps for the flexible vehicle at $\alpha = 0°$, $5°$, and $-5°$, $M = 0.13$.

7.7 Summary

The results presented in Sections 7.1-7.6 can be used to review the research questions initially presented in Section 3.2.1. The first overarching research question posed was:

Research Question 1:
How does accounting for vehicle flexibility impact the indicial response ROM identification process?

In order to answer this question, it was decomposed into two areas of research: (1) identification of an aeroelastic indicial response solution strategy and (2) assessment of indicial response sensitivity to flight space variables. Toward the first area of research, the subresearch question and its corresponding hypothesis was:

Research Question 1.1:
What is an appropriate solution strategy for aeroelastic indicial response identification?

Hypothesis 1.1: *The most appropriate aeroelastic indicial response solution strategy consists of (1) a static time-accurate aeroelastic simulation with an artificially high modal damping value, followed by (2) a dynamic aeroelastic simulation of an indicial function, using a time step based on resolving the highest frequency structural mode, where an increased number of steps are required for converging to the deformed state.*

Section 7.1 established a set of 'well-converged', time-accurate static rigid and static aeroelastic solutions to characterized the aerodynamics of the X-56A over an angle-of-attack range of $\alpha = [-5^\circ \text{ to } 20^\circ]$. These solutions were advanced in time using a time step corresponding to a fine sampling resolution, $N = 200$, of the highest frequency structural mode for a total of 10,000 time steps, where the static aeroelastic

solution was restarted from the static rigid solution. While beneficial for characterizing the nonlinear and unsteady aerodynamic regions of the flight envelope, this solution strategy is an inefficient means of initializing rigid and aeroelastic indicial responses. Section 7.2 sought to evaluate the total required computational costs of providing converged static aeroelastic solutions using static rigid solutions characterized by varying levels of convergence. The primary idea being that the rigid solutions are cheaper to provide and computational benefits might be gained by first converging toward the fluid-structure state using rigid initialization solutions.

The results showed that the 'cold-start' approach, where the static aeroelastic simulation leverages no static rigid restart solution, provides the most simplified and computationally efficient means of identifying the converged static aeroelastic state. For highly flexible vehicles, the structural deformation is significant enough to drastically change the solutions between the rigid and flexible state, such that the rigid solution provides no benefits in accelerating aeroelastic solution convergence. For less flexible vehicles, the use of rigid initialization solutions may provide improved computational benefits. For more stringent flight conditions, these rigid initialization solutions may also aid in numerical stability. In the 'cold-start' approach, use of a coarse time step based on the period ($N = 1$) of the highest frequency structural mode was shown to accelerate convergence of the static aeroelastic state without numerical stability issues while reaching the same solution as an $N = 200$ sampling factor. An artificially high modal damping factor $\approxeq 1$, per previously recommended guidelines, was used to accelerate the static intialization process. Overall, these results confirm the hypothesis in that no rigid restart solution is necessary for aeroelastic indicial response initialization. The time step used in advancing dynamic solutions should correspond to a baseline recommendation of an $N = 200$ sampling of the highest frequency structural mode to inherently capture a wide frequency spectrum of fluid-structure interactions for ROM predictions.

The second subresearch question and its corresponding hypothesis was:

Research Question 1.2:

How do flight envelope sensitivities differ between rigid and aeroelastic indicial responses?

Hypothesis 1.2: *Aeroelastic indicial responses due to step changes in angle of attack or pitch rate will require a richer sampling of the flight envelope space relative to rigid indicial responses as a result of fluid-structure interactions.*

Using the dynamic solution strategy established in Experiment 1.1, indicial responses due to step changes in angle of attack, pitch rate, sideslip angle, roll rate, and yaw rate were simulated at various angles of attack (Section 7.3), Mach numbers (Section 7.4), and sideslip angles (Section 7.5) to evaluate the merits of traditional ROM assumptions, as applied to rigid vehicles. It is generally assumed that only the angle-of-attack and sideslip angle indicial responses are dependent on angle of attack. While valid for the rigid X-56A, the flexible X-56A showed that the pitch rate indicial response was also dependent on angle of attack. Additionally, both the rigid and flexible X-56A vehicle showed a dependency on angle of attack for the roll and yaw rate indicial responses. The need of incorporating these lateral rate indicial response sensitivities into nonlinear ROM predictions is investigated in Experiment 2.3. Furthermore, the angle-of-attack sensitivity was shown to be stronger for the flexible vehicle, and thus, would require a finer sampling of the angle-of-attack flight space relative to the rigid vehicle for comparable prediction quality.

The indicial response sensitivity to Mach number is generally assumed for every longitudinal and lateral vehicle-state parameter. The results of Experiment 1.2 confirm the validity and need of this assumption for both the rigid and flexible X-56A aircraft. In particular, the flexible vehicle encounters drastic changes in lift and

pitching moment coefficient responses for a given change in Mach number relative to the rigid vehicle. Long duration, complex fluid-structure interactions are observed, which require a significant increase in the number of time steps for indicial response convergence.

Finally, sideslip angle sensitivities are not usually included for longitudinal or lateral unsteady aerodynamic predictions. The results of Experiment 1.2 showed negligible sensitivity to sideslip angle for angle-of-attack and pitch rate indicial responses, for both the rigid and flexible X-56A aircraft. Additionally, the roll rate indicial responses were shown to have an observable, yet weak sensitivity to sideslip angle for both the rigid and flexible vehicle. The sideslip and yaw rate indicial responses were in general agreement between rigid and aeroelastic simulations, demonstrating a sensitivity to sideslip angle that was stronger near $\beta = 0°$.

In the following chapter, the aeroelastic indicial response reduced-order model is evaluated using a series of forced pitching, rolling, and yawing oscillations at various reduced frequencies, corresponding to different levels of flow unsteadiness, followed by a generalized 6DOF right turn maneuver. In these evaluations, the prediction limits of the linear and nonlinear aeroelastic ROM variants are to be determined by enforcing a dense sampling of the flight variable space for indicial response identification. In doing so, prediction error can be primarily attributed to the reduced-order model assumptions, as opposed to insufficient sampling. The final chapter investigates the trade-off in computational cost vs. prediction accuracy of ROM predictions, using various assumptions of linearity, compared to high-fidelity simulations and stability derivative predictions.

CHAPTER VIII

MODEL EVALUATION (RESEARCH QUESTION 2)

Having demonstrated an ability to capture the effects of vehicle flexibility within indicial responses using a modal dynamic aeroelastic analysis, as well as the sensitivity of these aeroelastic indicial responses with respect to the vehicle-state parameters, the next part of this research focuses on generating unsteady aerodynamic ROM predictions for the X-56A performing a variety of flight maneuvers. This is aimed at answering Research Question 2, which is restated below:

Research Question 2:
What are the aerodynamic prediction capabilities of indicial response ROMs applied to maneuvering, flexible flight vehicles?

In order to address this research question, it is divided into two important components: the ability of aeroelastic indicial response ROMs to resolve (1) a wide range of motion frequencies and (2) flight envelope nonlinearities. The evaluation of the linear indicial response ROM formulation using small-amplitude forced rolling, yawing, and pitching oscillations at various motion frequencies is presented in Section 8.1. A nonlinear indicial response ROM formulation accounting for sensitivity to angle of attack is evaluated using large-amplitude pitching oscillations in Section 8.2. Finally, a generalized nonlinear indicial response ROM formulation is evaluated using a right turn maneuver, representative of a flight test conducted by the NASA Armstrong Flight Research Center, in Section 8.3.

8.1 Experiment 2.1 - Linear ROM Evaluation

Experiment 2.1 addresses Research Question 2.1 and tests Hypothesis 2.1, both of which are restated below:

Research Question 2.1:
What are the unsteady aerodynamic ROM prediction capabilities for flexible flight vehicles maneuvering at various rates of motion?

Hypothesis 2.1: *With proper numerical convergence, an aeroelastic indicial response ROM captures the fluid-structure interactions present in full-order trajectory simulations for any feasible rate of motion.*

The results from Chapter 7 illustrate a distinct difference between the indicial responses for the rigid and flexible X-56A aircraft. The indicial responses for the rigid vehicle were characterized by an initial transient as the flow adjusted to an immediate step change in the given vehicle-state parameter, followed by a smooth convergence to a static response value at the final vehicle-state. The indicial responses for the flexible vehicle were shown to be in general agreement with the rigid responses during the initial transients, as the aerodynamic response is dominated by the rapid motion change. Following the initial aerodynamic transients, differences between the rigid and aeroelastic simulations become apparent as fluid-structure interactions are modeled. These interactions are characterized by initial fluid-structure transients followed by low-frequency periodic oscillations before converging to the static aeroelastic response at the final vehicle-state.

Indicial response ROMs use a convolution-integral scheme to reconstruct a system's response to an arbitrary system input by performing a linear superposition of scaled and shifted indicial responses with respect to a system's inputs. As previously noted by Silva [121], this mathematical principle has been used in many fields,

e.g., signal processing, aerodynamics, and is applicable to any system described by a time-invariant system of equations. The aeroelastic system in the present work represents one such system, as the simulations are governed by the time-invariant Euler equations coupled to a time-invariant linear modal structural solver. The aeroelastic indicial responses identified in the previous chapter were simulated with a time step small enough to adequately resolve the highest frequency structural mode and with enough time steps to resolve the longest period structural mode. Since the time step required for resolving the structural response is smaller than those required for feasible motion rates and because the indicial response resolves the entire frequency spectrum of the aerodynamic response, the aeroelastic indicial response ROM is hypothesized to accurately predict the unsteady aerodynamic response of longitudinal and lateral motions of any desired motion rate.

8.1.1 Purpose of Experiment

The following are identified as the main objectives of this numerical experiment:

1. Explore the differences in the unsteady aerodynamic responses between the rigid and flexible X-56A aircraft for forced oscillations at increasing motion rates

2. Demonstrate the ability of aeroelastic linear indicial response ROMs to accurately predict the unsteady aerodynamic response to longitudinal and lateral motions at any desired motion frequency

8.1.2 Experiment Setup

Typical S&C databases may require forced oscillations at multiple flight conditions, amplitudes, and frequencies. The computational efficiency of the ROM provides an opportunity to estimate high-fidelity simulation data at a fraction of the cost as would be require for full-order solutions, but with comparable modeling accuracy. Chapter 8 seeks to first evaluate the ability of the proposed aeroelastic ROM's linear modeling variant to capture motion frequency effects using both longitudinal and lateral forced oscillation (FO) maneuvers.

For a one-degree-of-freedom longitudinal oscillatory test, the vehicle-state parameters of interest are angle of attack and pitch rate. During the motion, the angle of attack undergoes a sinusoidal time history with $q = \dot{\alpha}$, as defined by Eq. 69. In regard to the CFD simulation, the angle-of-attack history is defined via a time-varying pitch angle, which is calculated as $\theta = \alpha(t) - \alpha_0$ and gives the body's rotation relative to the inertial reference frame. Pitch rate is implicitly defined via the time-varying Euler pitch angle.

$$\begin{aligned} \alpha(t) &= \alpha_0 + \alpha_A \sin(\omega t) \\ q(t) &= \dot{\alpha}(t) = \alpha_A \omega cos(\omega t) \end{aligned} \tag{69}$$

Additionally, it is necessary to evaluate the linear aeroelastic ROM's ability to capture the frequency spectrum of lateral responses due to both yaw and roll FO. Equations 70 and 71 define the pertinent vehicle-state parameters for yaw and roll FO, respectively. During the motions, the yaw (ψ) and roll (ϕ) angles undergo a sinusoidal time history, while the yaw (r) and roll (p) rates correspond to their first-order time-derivatives. In the CFD simulation of the lateral oscillations, only the Euler angle time histories are required for trajectory specification while the baseline flight condition (α_0, β_0, M_0) remains constant.

$$\begin{aligned} \psi(t) &= \psi_A \sin(\omega t) \\ r(t) &= \dot{\psi}(t) = \psi_A \omega cos(\omega t) \end{aligned} \tag{70}$$

$$\begin{aligned} \phi(t) &= \phi_A \sin(\omega t) \\ p(t) &= \dot{\phi}(t) = \phi_A \omega cos(\omega t) \end{aligned} \tag{71}$$

The salient scaling parameter for the FO simulations is reduced frequency (k), given in terms of motion frequency or angular frequency by Eq. 72. In this expression, reduced frequency is defined in terms of the motion frequency (f), a reference length (L_{ref}), and the freestream velocity (U_∞). The reference length is equal to the semichord length ($c_{ref}/2$) for pitch oscillations and the semispan length ($b_{ref}/2$) for roll and yaw oscillations.

$$k = \frac{2\pi f L_{ref}}{U_\infty} = \frac{\omega L_{ref}}{U_\infty} \tag{72}$$

Simulated reduced frequencies correspond to varying levels of aerodynamic unsteadiness and are generally classified by the following [110]:

- Quasisteady - $0 \leq k \leq 0.05$
- Quasiunsteady - $0.05 \leq k \leq 0.2$
- Unsteady - $k > 0.2$

Table 7 lists nine forced oscillation tests, three each for yaw, roll and pitch, to be used in evaluating the linear aeroelastic ROM's ability to capture the frequency spectrum of longitudinal and lateral unsteady aerodynamic responses. The reduced frequencies range from quasisteady ($k = 0.05$) to unsteady ($k = 0.20$) values, which will allow for performance comparisons relative to the traditional stability derivative method. An oscillation amplitude of 1 deg. was chosen to limit the aerodynamic

Table 7: Linear Model: Forced Oscillation Tests.

Oscillation Type	α_0 (deg)	Amplitude (deg)	(k)
Roll/Yaw/Pitch	0	1	0.05
Roll/Yaw/Pitch	0	1	0.10
Roll/Yaw/Pitch	0	1	0.20

response to the linear regime, consistent with the linear aeroelastic ROM modeling applicability.

The simulation framework outlined in Chapter 4 was used to generate full-order rigid and aeroelastic CFD solutions for the low-amplitude forced rolling (Section 8.1.4), yawing (Section 8.1.5), and pitching oscillations (Section 8.1.6). Rigid and aeroelastic indicial responses were simulated with respect to the longitudinal and lateral vehicle-state parameters at the initial motion state using the best practices established in the previous chapter. Motion files were generated for the forced oscillation and indicial response trajectories using a trajectory post-processing MATLAB code. Linear ROM predictions for the unsteady aerodynamic response to each forced oscillation motion type at various reduced frequencies were generated using the *CFD2ROM* MATLAB code.

8.1.3 Linear ROM Generation

Experiment 2.1 seeks to evaluate the predictive capability of the aeroelastic indicial response ROM at various motion rates/frequencies for single-plane longitudinal and lateral motions. Nonlinear sensitivities to flight conditions are not considered in the present experiment as the purpose is to determine whether aeroelastic indicial responses capture the complete frequency spectrum. For each forced oscillation type, amplitudes were limited to ensure a locally linear flight envelope.

Equations 16 and 17 represent the generalized linear reduced-order modeling formulation for longitudinal (C_j) and lateral (C_k) unsteady aerodynamic predictions,

respectively. Equation 16 predicts the lift (C_L) and pitching moment (C_m) coefficients due to the steady-state contribution at the initial flight condition (C_{j_0}) and unsteady contributions, calculated using convolution integrals, due to changes in angle of attack (α) and pitch rate (q). Equation 17 predicts the side force (C_Y), rolling moment (C_l) and yawing moment (C_n) coefficients due to unsteady contributions due to changes in side-slip angle (β), roll rate (p), and yaw rate (r).

$$C_j(t) = C_{j_0} + \frac{d}{dt}\left[\int_0^t C_{j_\alpha}(t-\tau)\alpha(\tau)d\tau\right] + \frac{d}{dt}\left[\int_0^t C_{j_q}(t-\tau)q(\tau)d\tau\right] \tag{16}$$

$$\begin{aligned} C_k(t) = \frac{d}{dt}\left[\int_0^t C_{k_\beta}(t-\tau)\beta(\tau)d\tau\right] + \frac{d}{dt}\left[\int_0^t C_{k_p}(t-\tau)p(\tau)d\tau\right] \\ + \frac{d}{dt}\left[\int_0^t C_{k_r}(t-\tau)r(\tau)d\tau\right] \end{aligned} \tag{17}$$

For forced pitching oscillations, time histories are defined for $\alpha(t)$ and $q(t)$, such that Eq. 16 may be directly used for linear ROM predictions. However, for forced rolling oscillations, the motion is isolated to a single axis of rotation and only the roll rate has a defined time history, $p(t)$, whereas $\beta(t) = r(t) = 0$. As a result, the lateral force and moment coefficients are only dependent on unsteady contributions due to roll rate, as defined by Eq. 73. In the case of forced yawing oscillations, only the sideslip angle and yaw rate have a defined time history, $\beta(t)$ and $r(t)$, whereas $p(t) = 0$. As a result, the lateral force and moment coefficients are only dependent on unsteady contributions due to sideslip angle and yaw rate, as defined by Eq. 74.

$$C_k(t) = \frac{d}{dt}\left[\int_0^t C_{k_p}(t-\tau)p(\tau)d\tau\right] \tag{73}$$

$$C_k(t) = \frac{d}{dt}\left[\int_0^t C_{k_\beta}(t-\tau)\beta(\tau)d\tau\right] + \frac{d}{dt}\left[\int_0^t C_{k_r}(t-\tau)r(\tau)d\tau\right] \tag{74}$$

Table 8 defines the motion file input parameters used in creating the CFD motion input file. For each step type, the initial condition is set to $\alpha = \beta = \phi = \theta = \psi = 0°$. For the β-step, the simulation imposes a pure translation to the right and slightly aft to maintain $\Delta r = 0$ rad/s. For the r-step, there is a constant-rate yaw rotation (1 rad/s) of the grid coupled with a sideways and aft translation, such that $\alpha = \beta = 0°$ is maintained during the motion. For the p-step, an incremental step of $\Delta p = 1$ rad/s $= 180/\pi$ deg/s is enforced for $t > 0$. This indicial trajectory results in an impulsive roll of the grid about the body axis.

Table 8: Motion file inputs for creating indicial trajectories ($t > 0$).

Indicial	α (deg)	β (deg)	ϕ (deg)	θ (deg)	ψ (deg)	M_0
α-step	1	0	0	0	0	0.13
β-step	0	1	0	0	0	0.13
p-step	0	0	$\Delta p \cdot t$	0	0	0.13
q-step	0	0	0	$\Delta q \cdot t$	0	0.13
r-step	0	0	0	0	$\Delta r \cdot t$	0.13

Rigid and aeroelastic indicial step responses were computed with FUN3D using the temporal parameters presented in Table 9. Using the solution strategy developed in Experiment 1.1, the lateral responses were advanced using a time step of $\Delta t = 4E{-}04$ or $\Delta s = 0.029$ for a total of $4,000$ time steps, where asymptotic convergence to steady state was achieved for both the rigid and aeroelastic simulations. For the longitudinal responses, 4,000 time steps were used to attain converged solutions for the rigid vehicle. Due to the long duration fluid-structure interactions observed for the aeroelastic indicial responses, the length of the simulation was set to 6,550 time steps to coincide with the length of three cycles of forced pitch oscillation at the lowest reduced frequency. This ensures all motion history effects are accounted for to establish validity of the ROM predictions.

Table 9: Temporal parameters for indicial responses simulations (rigid and flexible).

Indicial	Mach	Δt (s)	Δt^*	N_{sub}	Total Time Steps	Total Iterations	Structure
α-step	0.13	4.0E-4	0.029	20	4,000	80,000	Rigid
α-step	0.13	4.0E-4	0.029	20	6,550	131,000	Flexible
q-step	0.13	4.0E-4	0.029	20	4,000	80,000	Rigid
q-step	0.13	4.0E-4	0.029	20	6,550	131,000	Flexible
β-step	0.13	4.0E-4	0.029	20	4,000	80,000	Rigid/Flexible
p-step	0.13	4.0E-4	0.029	20	4,000	80,000	Rigid/Flexible
r-step	0.13	4.0E-4	0.029	20	4,000	80,000	Rigid/Flexible

8.1.4 Forced Rolling Oscillations

8.1.4.1 CFD Simulations

Figure 47 depicts the motion history for the forced rolling oscillations at reduced frequencies of $k = 0.05, 0.10$, and 0.20. An increase in reduced frequency translates to a decrease in maneuver time, which serves to illicit a more unsteady aerodynamic response where the influences of previous motion states are more prominent. As observed in Fig. 47, the 'quasisteady' ($k = 0.05$) case is characterized by a slow-varying oscillation with an approximate period of 12 seconds. This period of motion is halved in each of the successive 'quasiunsteady' ($k = 0.10$) and 'unsteady' ($k = 0.20$) cases. Three cycles were simulated for both the rigid and flexible vehicle cases to allow for the initial transient response to decay and to explore potential differences in the convergence of the hysteresis loops when accounting for structural flexibility.

Each forced oscillation case was initialized from a well-converged, static time-accurate simulation. For the aeroelastic simulations, a static aeroelastic time-accurate simulation was conducted without using a static time-accurate restart solution, as detailed in Section 7.2. Both the rigid and aeroelastic simulations were advanced in time using a characteristic time step of $\Delta t^* \approxeq 0.5$ for 75 time steps, where 20 subiterations were used to converge the solution in pseudotime. The static initialization time step is approximately the same as the period of the highest frequency structural mode and

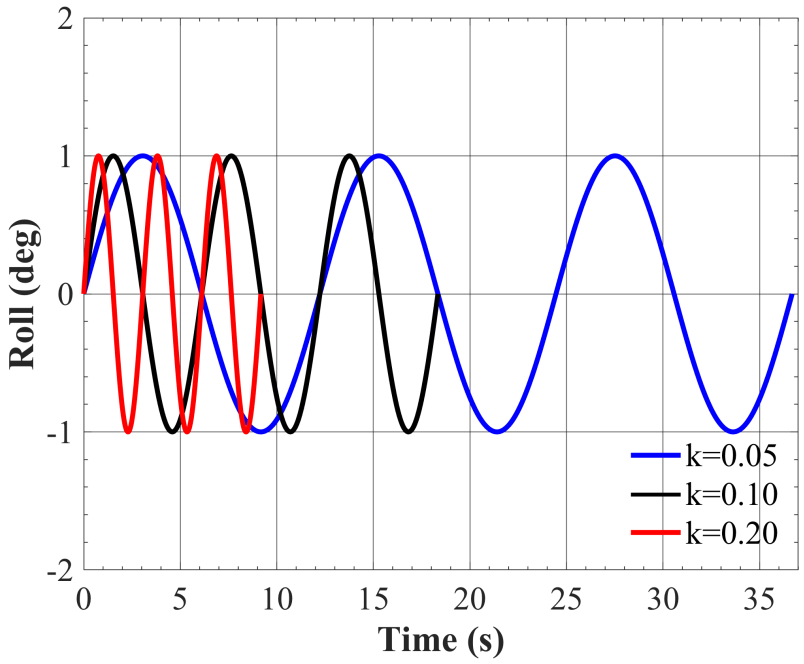

Figure 47: Motion history for forced rolling oscillations with one degree amplitude for $k = 0.05, 0.10$, and 0.20 at $\alpha = 0°$, $\beta = 0°$, $M = 0.13$.

provides an efficients means of producing a converged static aeroelastic response for the forced oscillation initial condition.

The dynamic solution strategy implemented was consistent for the rigid and aeroelastic forced oscillation cases and was chosen to satisfy the more strict temporal resolution requirements for the flexible vehicle. To elaborate, the most dynamic motion case ($k = 0.20$) corresponds to an oscillation frequency of 0.32 Hz, whereas the highest structural mode frequency is much greater at 11.95 Hz. Thus, a time step selected based on resolution of the much greater structural mode frequency will be more than sufficient in simulating dynamic motions of any feasible frequency of interest. A sampling factor of $N = 200$ was selected to resolve the highest frequency structural mode, resulting in a characteristic time step of $s \cong 0.002$ for all dynamic simulations, consistent with the indicial response simulations.

Table 10 summarizes the temporal parameters used in the forced rolling oscillation simulations. The total number of time steps was set based on resolving the three cycles

of motion. The trajectory time history, defined by the aerodynamic angles (α and β), Mach number (M), and the Euler angles (ϕ, θ, and ψ), was converted to a motion input file using the trajectory post-processing MATLAB code.

Table 10: Temporal parameters for forced rolling oscillation simulations.

k	M	Δt (s)	s	N_{sub}	Total Time Steps
0.05	0.13	4.0E-4	0.002	20	91,705
0.10	0.13	4.0E-4	0.002	20	45,852
0.20	0.13	4.0E-4	0.002	20	22,926

The solution strategy proved to be robust in producing stable, well-converged dynamic simulations for both the rigid and flexible vehicle at every prescribed motion frequency. Examples of subiterative convergence for the $k = 0.20$ case are shown in Figures 48(a) and 48(b) for the rigid (top) and flexible (bottom) vehicle cases, respectively. The plots illustrate the order-of-magnitude convergence in the FUN3D time-accurate solution residual drop ($log(R/R_0)$) and the rolling moment coefficient (C_l) convergence versus fractional iterations. Iteration 1,911 is shown, which coincides with the positive peak roll amplitude during the first oscillation cycle, where each point signifies the convergence achieved at each of the 20 subiterations. The rigid simulation presents approximately 7-orders of convergence in residual drop with sufficient convergence in the rolling moment coefficient, based on a 0.0002% difference between the final two subiterations. Similar levels of convergence were achieved in the aeroelastic simulation. While not illustrated, the same convergence behavior was observed for the $k = 0.10$ and $k = 0.05$ motion cases with even greater orders of convergence in residual drop due to the increased number of time steps per oscillation cycle.

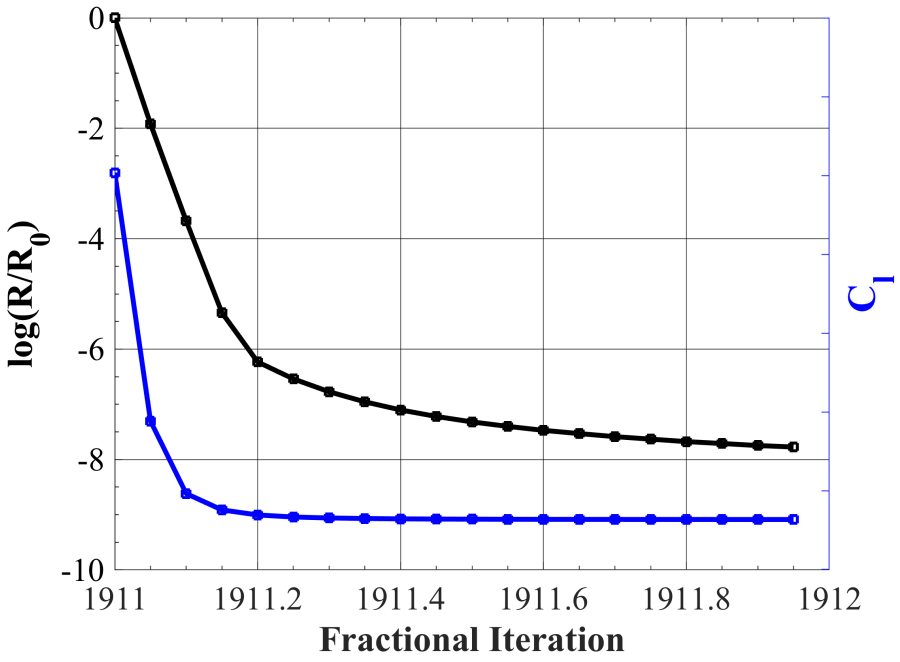

(a) Rigid

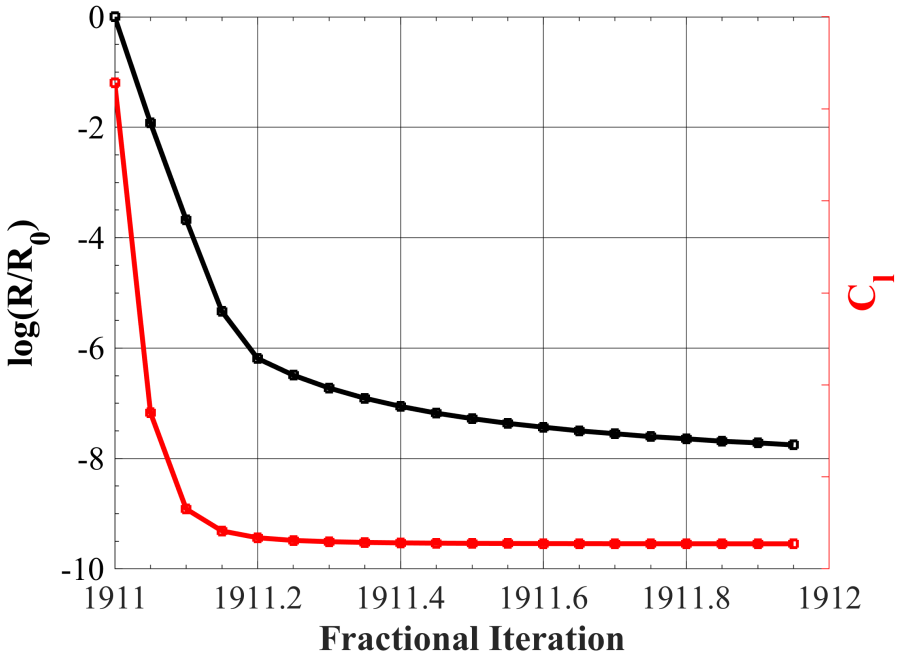

(b) Flexible

Figure 48: X-56A: FUN3D subiterative convergence for forced rolling oscillation with three degree amplitude and $k = 0.20$ at $\alpha = 0°$, $M = 0.13$ for the rigid (blue) and flexible (red) cases. Iteration 1,911 - peak roll amplitude within first oscillation cycle.

Figure 49 illustrates the FUN3D simulation results for the rigid vehicle undergoing forced rolling oscillations with one degree amplitude for $k = 0.05, 0.10$, and 0.20 at $\alpha = 0°$, $\beta = 0°$, $M = 0.13$. For brevity, only the side force coefficient (C_Y) and rolling moment coefficient (C_l) results are shown. The side force coefficient solution is characterized by an initial, positive peak due to the onset of grid motion followed by a transient decay in the first 0.5 degree change in rolling amplitude leading to a clockwise hysteresis loop. In contrast, the rolling moment coefficient is characterized by an initial, negative peak followed by a quicker transient decay within the first 0.25 degree change in rolling amplitude leading to a counterclockwise hysteresis loop. The impact of increasing the reduced frequency is an aerodynamic damping effect, observed by a widening of the hysteresis loops for both coefficients. For each successive increase in reduced frequency, a proportional widening of the loops is observed. The minimum and maximum side force and rolling moment values are not affected by reduced frequency.

Figure 50 illustrates the FUN3D simulation results for the flexible vehicle undergoing forced rolling oscillations with one degree amplitude for $k = 0.05, 0.10$, and 0.20 at $\alpha = 0°$, $\beta = 0°$, $M = 0.13$. Overall, nearly identical results are observed between the rigid and flexible simulations. While difficult to see, the primary difference observed is a slightly longer duration transient decay, where the transients for each coefficient demonstrate a small-magnitude periodic oscillation before converging to the hysteresis loop just before reaching peak positive amplitude within the first cycle. Such a result was to be expected based on the subtle differences between the rigid and aeroelastic indicial responses with respect to step changes in roll rate (see Fig. 43), as first identified in Chapter 7. Minor differences in the initial static coefficient are observed along with a slight difference in magnitude of the side force coefficient's initial peak transient. Physically, it is expected that the impact of vehicle flexibility is less pronounced for lateral motions, for which vehicle deformation is minimal.

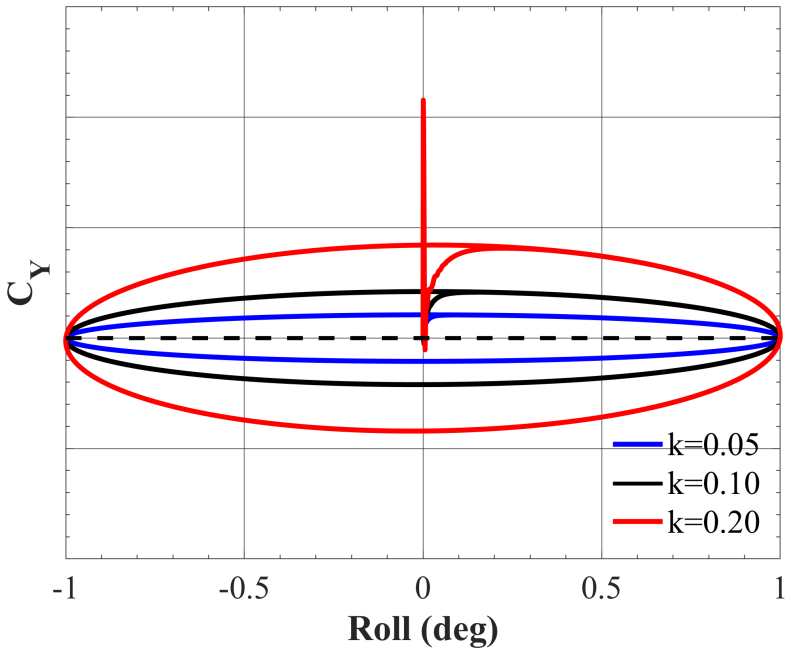

(a) Side force coefficient

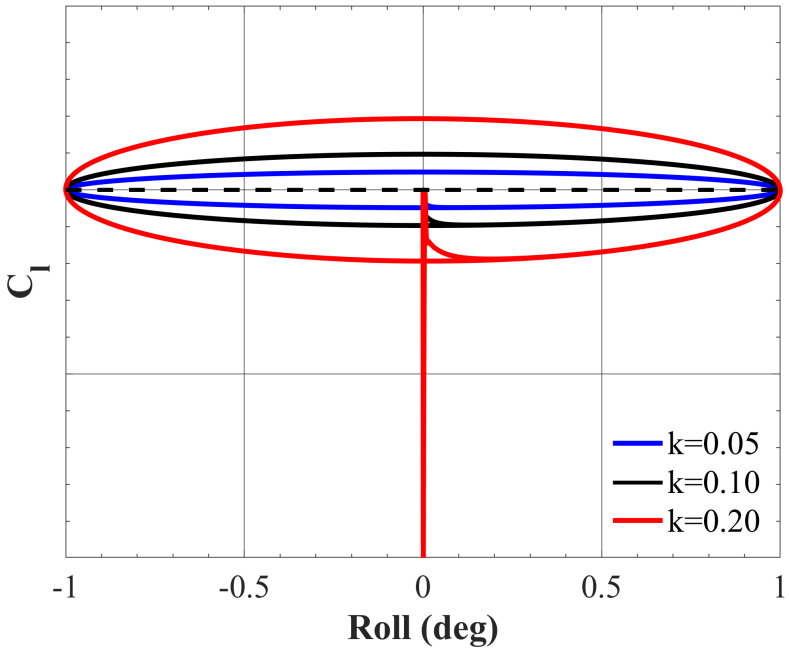

(b) Rolling moment coefficient

Figure 49: Rigid X-56A: FUN3D simulation results for forced rolling oscillations with one degree amplitude for $k = 0.05, 0.10$, and 0.20 at $\alpha = 0°$, $M = 0.13$.

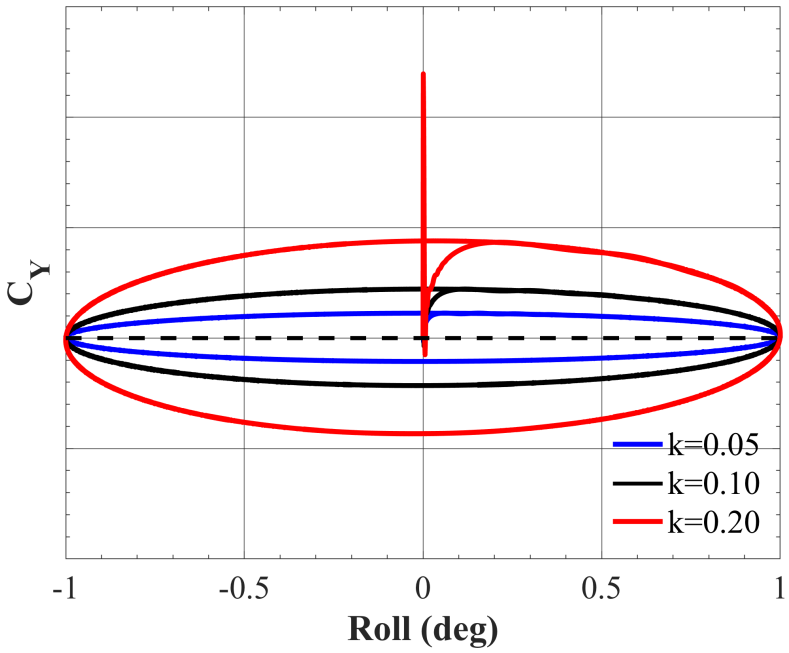

(a) Side force coefficient

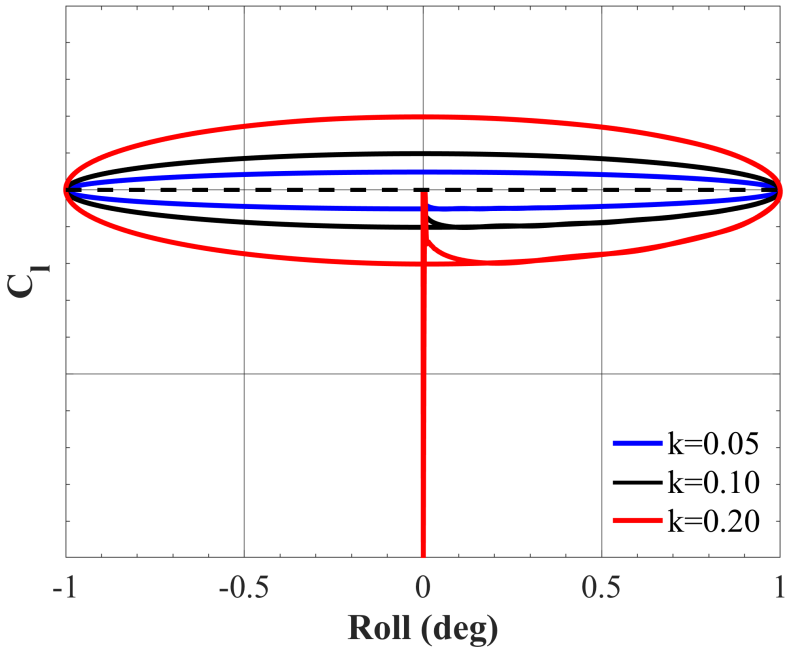

(b) Rolling moment coefficient

Figure 50: Flexible X-56A: FUN3D simulation results for forced rolling oscillations with one degree amplitude for $k = 0.05, 0.10$, and 0.20 at $\alpha = 0°$, $M = 0.13$.

8.1.4.2 ROM Predictions

For each aerodynamic coefficient of interest, CFD simulation results are compared to linear ROM predictions, calculated via Eq. 73, as a function of roll angle. To quantify the ROM prediction accuracy, a global percent error (ϵ) is calculated using Eq. 75, where $C_{j/k}^{ROM}$ and $C_{j/k}^{CFD}$ represent the coefficient value, longitudinal (j) or lateral (k), with respect to the ROM and CFD, respectively. Prediction error is plotted versus roll angle to better understand how modeling accuracy varies over the course of the maneuver. Positive error represents an overprediction of the aerodynamic coefficient by the ROM relative to CFD simulation results, whereas negative error represents an underprediction. The error metric is normalized by the range of the CFD coefficient time history to give a more global perspective of the modeling accuracy, such that local coefficient value discrepancies near zero do not bias the error. The mean ($\bar{\epsilon}$) and standard deviation (σ) of the prediction error is provided for each test case.

$$\epsilon(t_i) = \frac{C_{j/k}^{ROM}(t_i) - C_{j/k}^{CFD}(t_i)}{|max(C_{j/k}^{CFD}(t)) - min(C_{j/k}^{CFD}(t))|} \times 100 \tag{75}$$

Figure 51 illustrates a comparison between CFD and ROM results (left) and the ROM prediction error (right) for each of the forced rolling oscillation cases (top to bottom) with respect to side force coefficient for the rigid vehicle. Overall, the ROM predictions show great qualitative agreement with CFD simulation results, correctly resolving the initial transient response and the hysteresis loop widening with successive increases in reduced frequency. The ROM error is most pronounced near the initial roll angle with a slight underprediction during the negative rotation and overprediction during the positive rotation. From a quantitative perspective, the trends in ROM error are consistent between each case with no mean error and a standard deviation $< 1\%$.

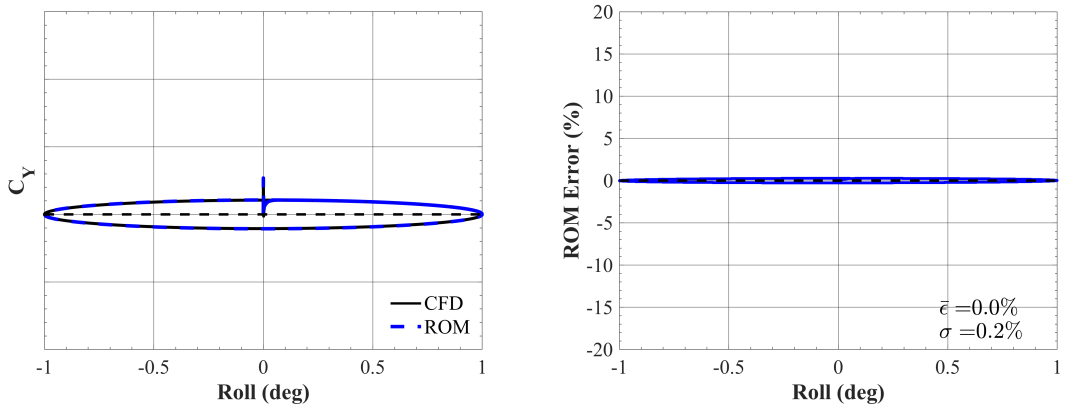

(a) Side force coefficient ($k = 0.05$)

(b) ROM error ($k = 0.05$)

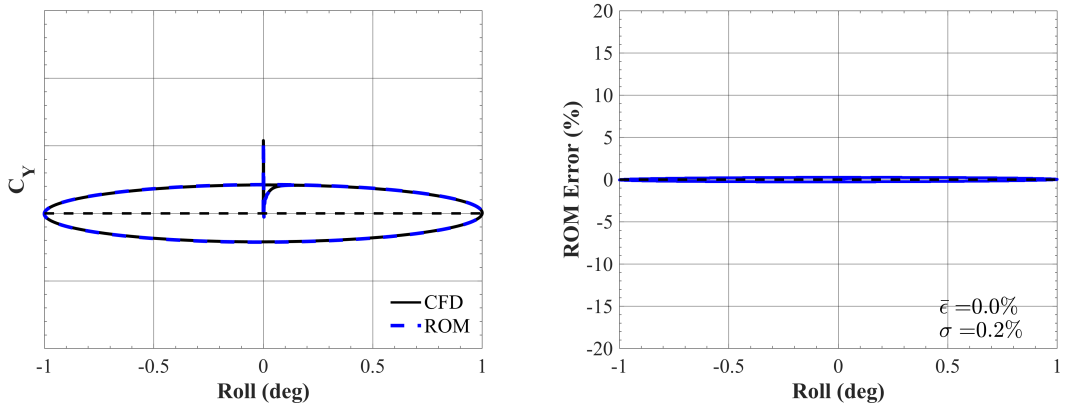

(c) Side force coefficient ($k = 0.10$)

(d) ROM error ($k = 0.10$)

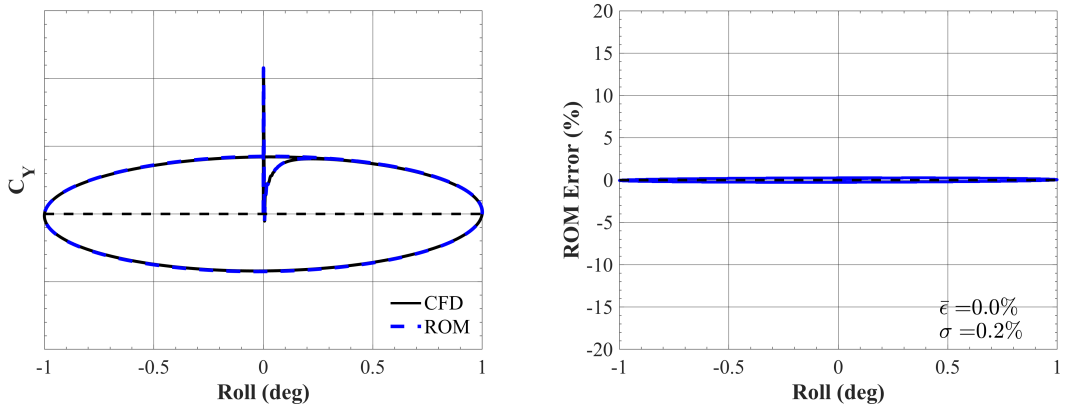

(e) Side force coefficient ($k = 0.20$)

(f) ROM error ($k = 0.20$)

Figure 51: Rigid X-56A: ROM vs. CFD side force coefficient results (left) and ROM error (right) for forced rolling oscillation with one degree amplitude for $k = 0.05$ (top), 0.10 (middle), and 0.20 (bottom) at $\alpha = 0°$, $\beta = 0°$, $M = 0.13$.

Figure 52 presents the CFD and ROM comparisons (left) and the ROM prediction error (right) for each of the forced rolling oscillation cases (top to bottom) with respect to rolling moment coefficient for the rigid vehicle case. Similar to the previous force coefficient predictions, the ROM predictions are in great qualitative agreement with CFD simulation results, correctly resolving the initial transient response and the hysteresis loop widening with successive increases in reduced frequency. Additionally, the predictions are in great quantitative agreement with both a zero mean and standard deviation ROM error for each frequency case. In general, the ROM accurately models the unsteady side force and rolling moment coefficient of the rigid X-56A performing forced rolling oscillations at various frequencies.

Figure 53 illustrates the CFD and ROM comparisons (left) and the ROM prediction error (right) for each of the forced rolling oscillation cases (top to bottom) with respect to side force coefficient for the flexible vehicle case. The ROM predictions are observed to be in great qualitative agreement with CFD simulation results, correctly resolving the transient response and hysteresis loop widening with increases in motion frequency. Similar to the rigid cases, the ROM error is greatest near the initial roll angle due to under- and overpredictions during the negative and positive rolling motions, respectively. Additionally, a faint buzzing of the ROM error is attributed to the complex fluid-structure interactions observed during indicial response identification. Regardless, the mean ROM error is zero, and the standard deviation is $< 1\%$ for each frequency case. Figure 54 presents the same plots with respect to rolling moment coefficient for the flexible vehicle. The moment results also show a great qualitative agreement with full-order simulations with both a zero mean error and standard deviation. In each case, the linear indicial response ROM shows an ability to accurately predict lateral unsteady aerodynamic coefficients for forced rolling oscillations under a wide range of reduced frequencies for both rigid and flexible simulations.

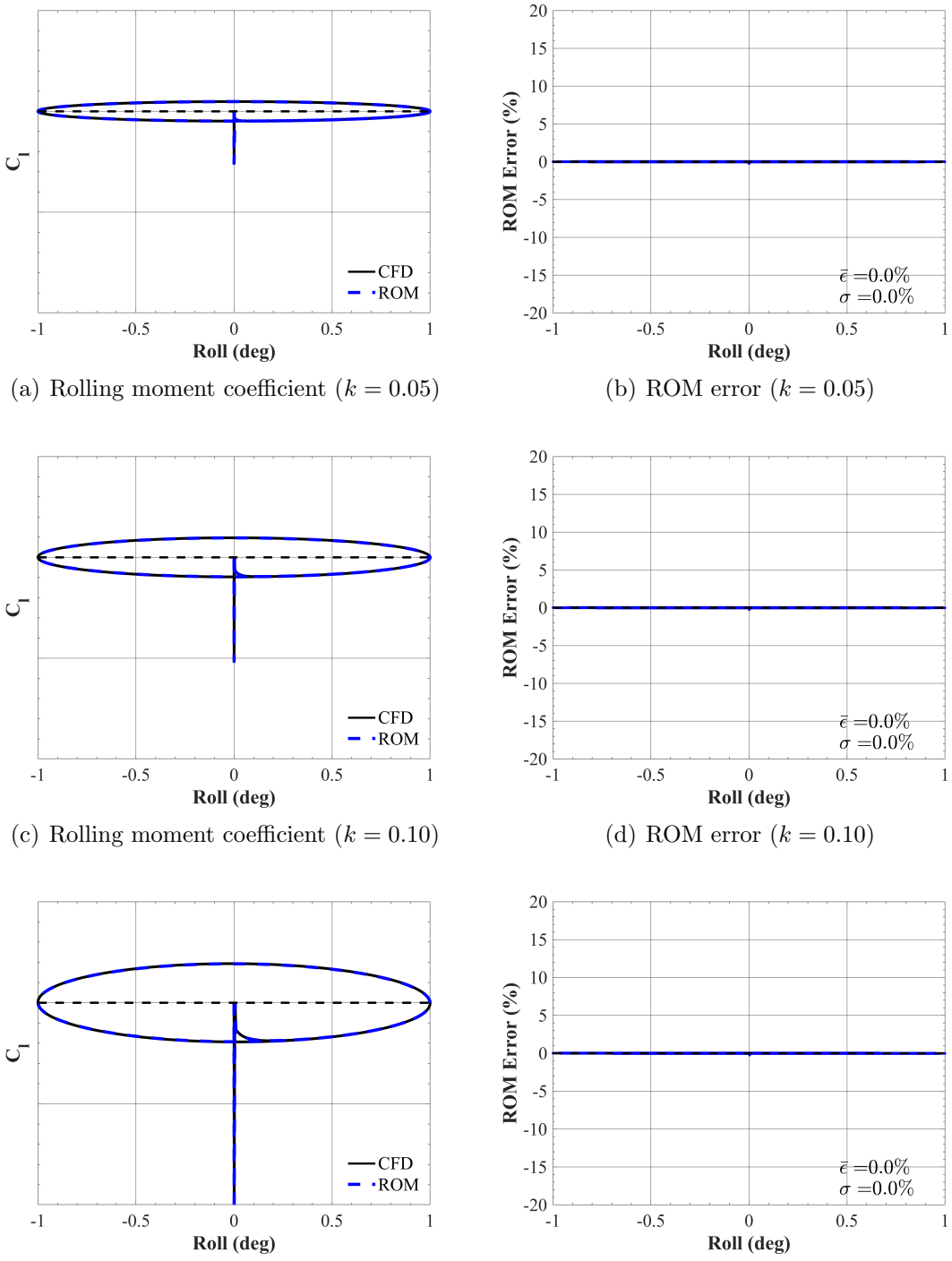

(a) Rolling moment coefficient ($k = 0.05$)

(b) ROM error ($k = 0.05$)

(c) Rolling moment coefficient ($k = 0.10$)

(d) ROM error ($k = 0.10$)

(e) Rolling moment coefficient ($k = 0.20$)

(f) ROM error ($k = 0.20$)

Figure 52: Rigid X-56A: ROM vs. CFD rolling moment coefficient results (left) and ROM error (right) for forced rolling oscillation with one degree amplitude for $k = 0.05$ (top), 0.10 (middle), and 0.20 (bottom) at $\alpha = 0°$, $\beta = 0°$, $M = 0.13$.

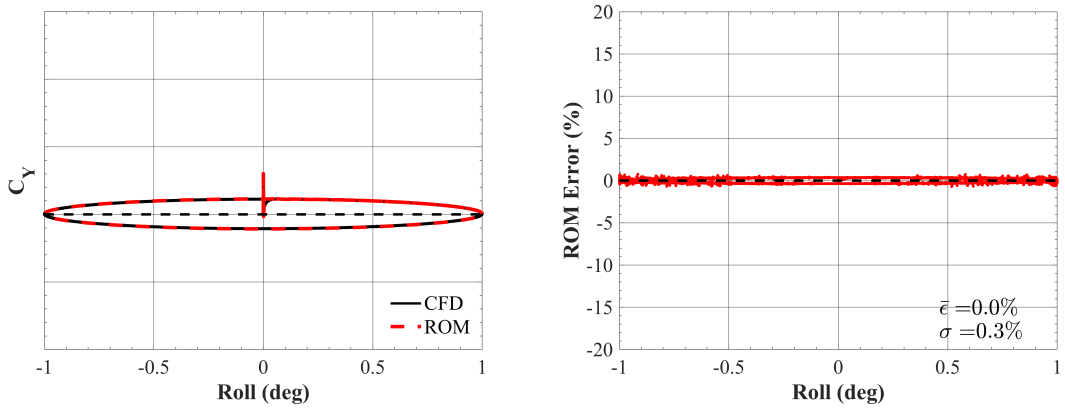

(a) Side force coefficient ($k = 0.05$)

(b) ROM error ($k = 0.05$)

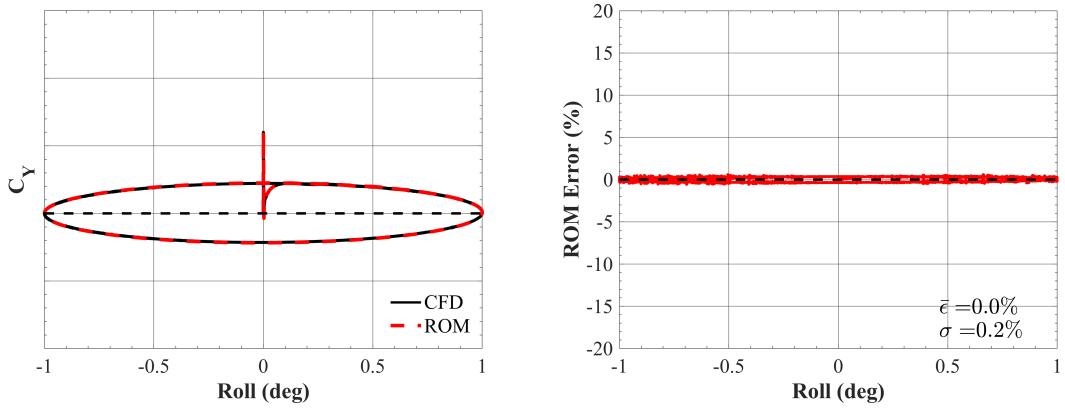

(c) Side force coefficient ($k = 0.10$)

(d) ROM error ($k = 0.10$)

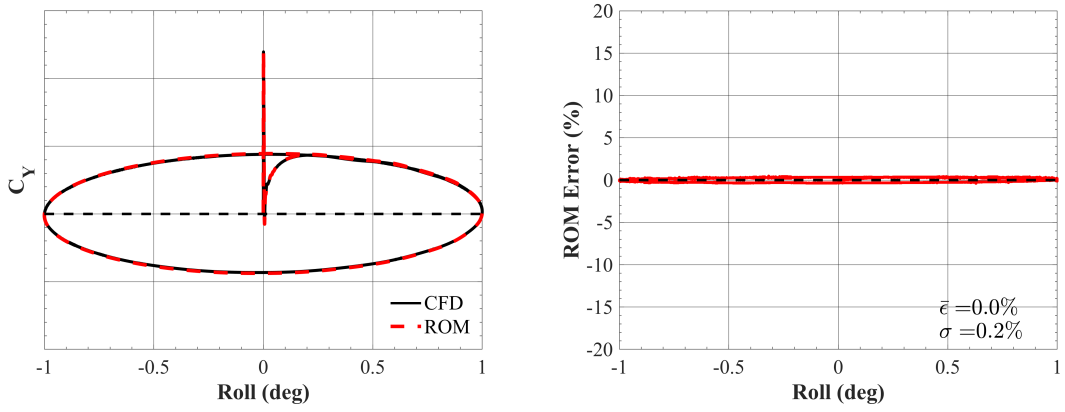

(e) Side force coefficient ($k = 0.20$)

(f) ROM error ($k = 0.20$)

Figure 53: Flexible X-56A: ROM vs. CFD side force coefficient results (left) and ROM error (right) for forced rolling oscillation with one degree amplitude for $k = 0.05$ (top), 0.10 (middle), and 0.20 (bottom) at $\alpha = 0°$, $\beta = 0°$, $M = 0.13$.

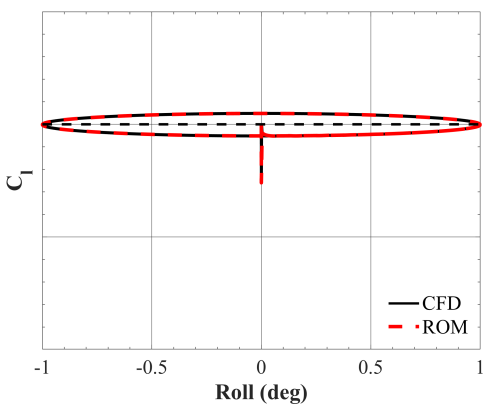

(a) Rolling moment coefficient ($k = 0.05$)

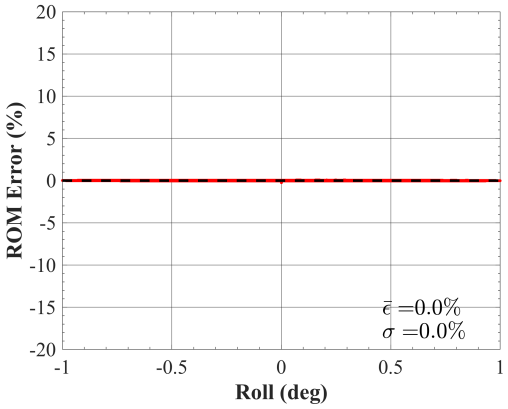

(b) ROM error ($k = 0.05$)

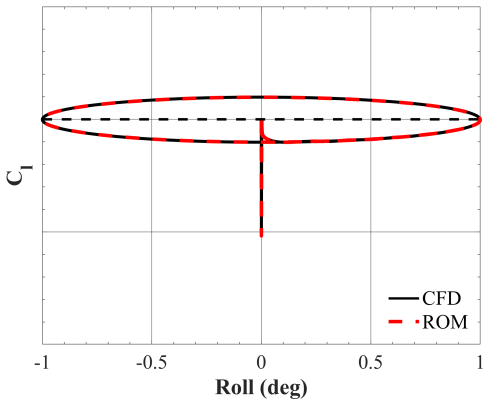

(c) Rolling moment coefficient ($k = 0.10$)

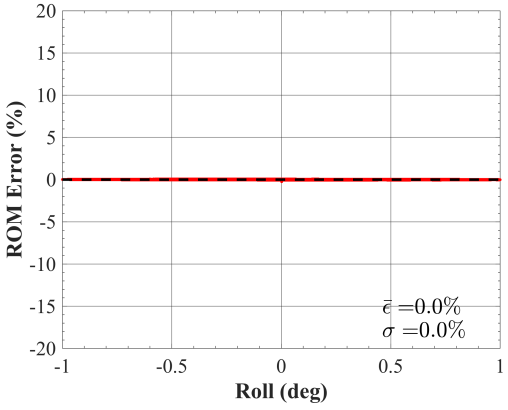

(d) ROM error ($k = 0.10$)

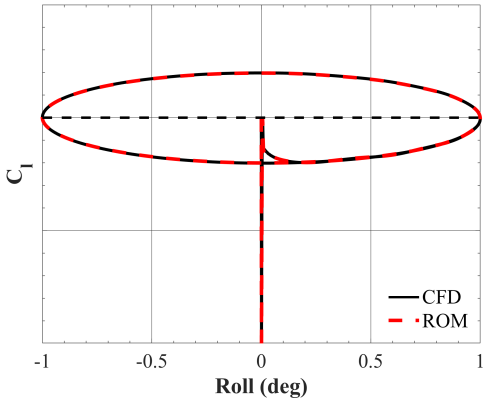

(e) Rolling moment coefficient ($k = 0.20$)

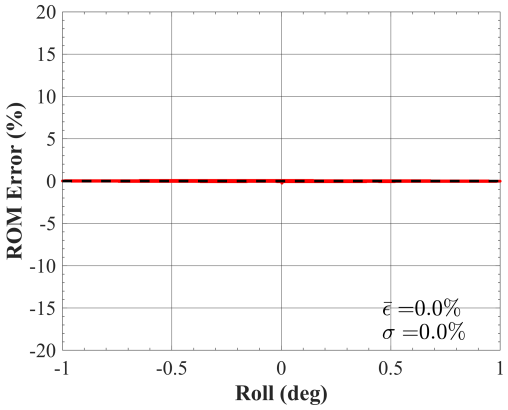

(f) ROM error ($k = 0.20$)

Figure 54: Flexible X-56A: ROM vs. CFD rolling moment coefficient results (left) and ROM error (right) for forced rolling oscillation with one degree amplitude for $k = 0.05$ (top), 0.10 (middle), and 0.20 (bottom) at $\alpha = 0°$, $\beta = 0°$, $M = 0.13$.

8.1.5 Forced Yawing Oscillations

8.1.5.1 CFD Simulations

Figure 55 depicts the motion history for the forced yawing oscillations at reduced frequencies of $k = 0.05, 0.10$, and 0.20. As observed in Fig. 55, the 'quasisteady' ($k = 0.05$) case is characterized by a slow-varying oscillation with an approximate period of 12 seconds. This period of motion is halved in each of the successive 'quasiunsteady' ($k = 0.10$) and 'unsteady' ($k = 0.20$) cases. The motion duration is equivalent between the forced rolling and yawing oscillations given that both types calculate the reduced frequency in terms of the semispan reference length. As done for the forced rolling oscillations, three cycles were simulated for both the rigid and flexible vehicle cases to allow for the initial transient response to decay and to explore potential differences in the convergence of the hysteresis loops when accounting for structural flexibility.

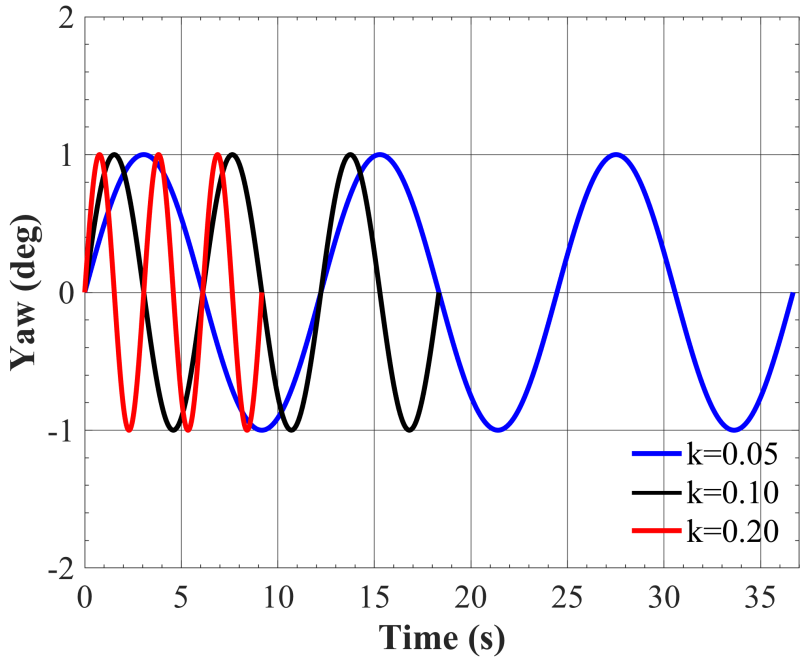

Figure 55: Motion history for forced yawing oscillations with one degree amplitude for $k = 0.05, 0.10$, and 0.20 at $\alpha = 0°$, $\beta = 0°$, $M = 0.13$.

The forced yawing oscillations were initialized using the same solutions as the forced rolling oscillation simulations since both motions have the same initial condition: $\alpha = 0°$, $\beta = 0°$, $M = 0.13$. Additionally, the dynamic strategy implemented was consistent between the two maneuver types, where a characteristic time step of $\Delta t^* \cong 0.002$ was use to advance the solution in time and 20 subiterations were used to converge the solution in pseudotime. Because the reference length ($L_{ref} = b_{ref}/2$) used for defining the motion frequency was consistent, the peak motion frequency between the maneuvers is identical. Thus, the time step resolution is again dictated by the highest frequency structural mode (11.95 Hz).

Table 11 summarizes the temporal parameters used in the forced yawing oscillation simulations. The total number of time steps was set based on resolving the 3 cycles of motion. The trajectory time history, defined by the aerodynamic angles (α and β), Mach number (M), and the Euler angles (ϕ, θ, and ψ), was converted to a motion input file using the trajectory postprocessing MATLAB code. For yawing oscillations, $\Delta\alpha = \Delta\beta = \Delta\phi = \Delta\theta = 0°$. and $\psi(t)$ is defined at each iteration.

Table 11: Temporal parameters for forced yawing oscillation simulations.

k	M	Δt (s)	Δt^*	N_{sub}	Total Time Steps
0.05	0.13	4.0E-04	0.002	20	91,705
0.10	0.13	4.0E-04	0.002	20	45,852
0.20	0.13	4.0E-04	0.002	20	22,926

The solution strategy proved to be robust in producing stable, well-converged dynamic simulations for both the rigid and flexible vehicle at every prescribed motion frequency. Examples of subiterative convergence for the $k = 0.20$ case are shown in Figures 56(a) and 56(b) for the rigid (top) and flexible (bottom) vehicle cases, respectively. The plots illustrate the order-of-magnitude convergence in the FUN3D time-accurate solution residual drop ($log(R/R_0)$) and the yawing moment coefficient (C_n) convergence versus fractional iterations. Iteration 1,911 is shown, which coincides with the positive peak yaw amplitude during the first oscillation cycle, where

each point signifies the convergence achieved at each of the 20 subiterations. The rigid simulation presents over 8-orders of convergence in residual drop with sufficient convergence in the yawing moment coefficient, based on a 0.0002% difference between the final two subiterations. Similar levels of convergence were achieved in the aeroelastic simulation. While not illustrated, the same convergence behavior was observed for the $k = 0.10$ and $k = 0.05$ motion cases with even greater orders of convergence in residual drop due to the increased number of time steps per oscillation cycle.

Figure 57 illustrates the FUN3D simulation results for the rigid vehicle undergoing forced yawing oscillations with one degree amplitude for $k = 0.05, 0.10$, and 0.20 at $\alpha = 0°$, $\beta = 0°$, $M = 0.13$. For brevity, only the side force coefficient (C_Y) and yawing moment coefficient (C_n) results are shown. The side force coefficient solution is characterized by an initial, negative peak due to the onset of grid motion followed by an abrupt transient decay leading to a counterclockwise hysteresis loop. A similar trend is observed with respect to the yawing moment coefficient. The impact of increasing reduced frequency is an aerodynamic damping effect, observed by a widening of the hysteresis loops for both coefficients. For each successive increase in reduced frequency, a proportional widening of the loops is observed. The minimum and maximum side force and yawing moment values are not affected by reduced frequency.

Figure 58 illustrates the FUN3D simulation results for the flexible vehicle undergoing forced yawing oscillations with one degree amplitude for $k = 0.05, 0.10$, and 0.20 at $\alpha = 0°$, $\beta = 0°$, $M = 0.13$. Overall, nearly identical results are observed between the rigid and flexible simulations. Minor differences in the initial static coefficient are found, though not distinguishable. As mentioned in the previous subsection, differences between the rigid and flexible cases are anticipated to be minimal given the agreement found when assessing indicial response sensitivities in Chapter 7.

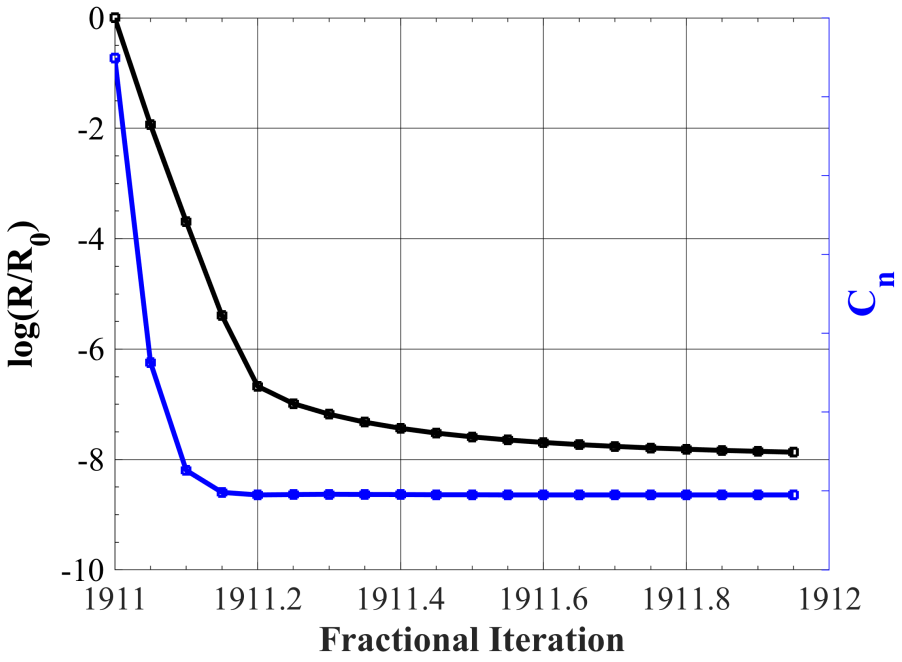

(a) Rigid

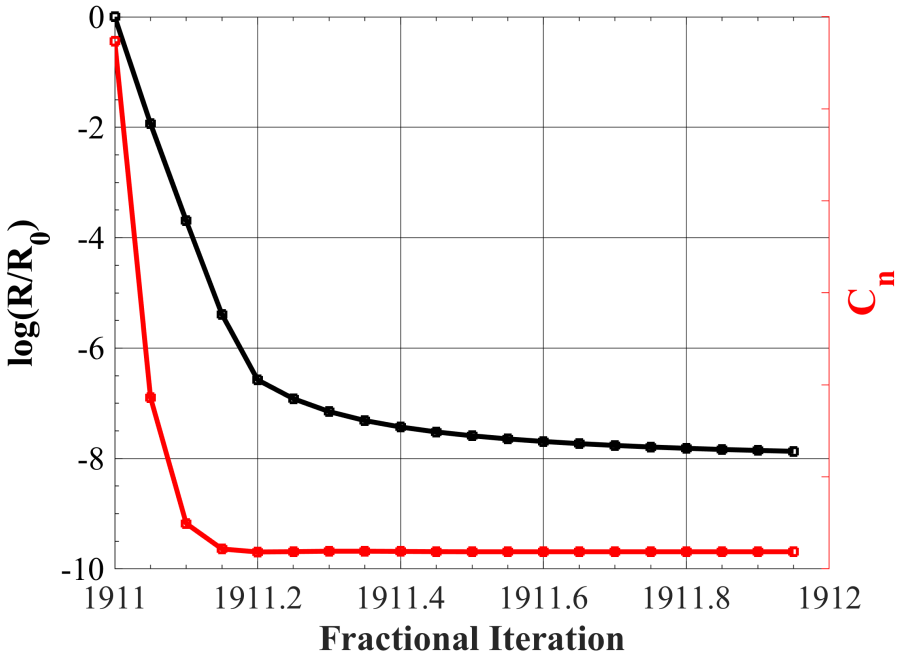

(b) Flexible

Figure 56: X-56A: FUN3D subiterative convergence for forced yawing oscillation with one degree amplitude, $k = 0.20$ at $\alpha = 0°$, $M = 0.13$ for the rigid (blue) and flexible (red) cases. Iteration 1,911 - peak yaw amplitude within first oscillation cycle.

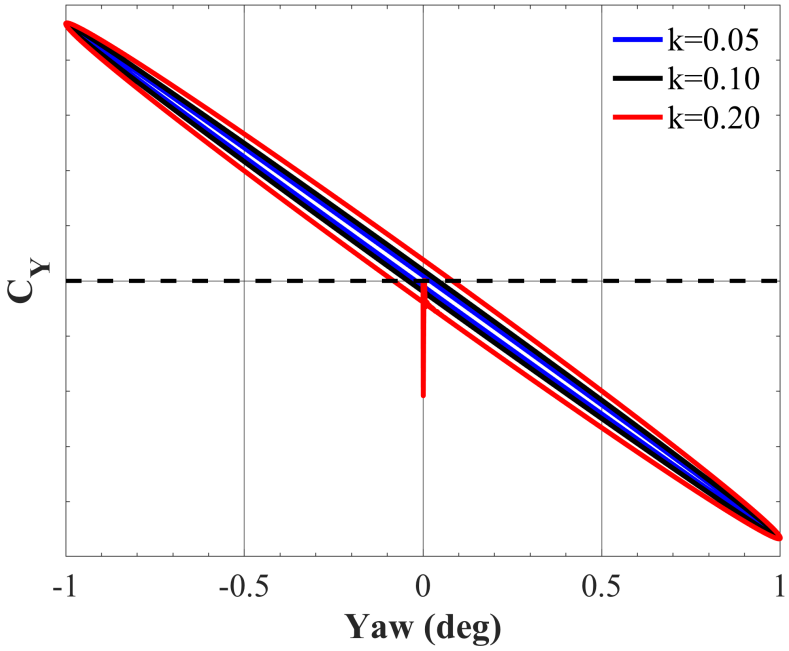

(a) Side force coefficient

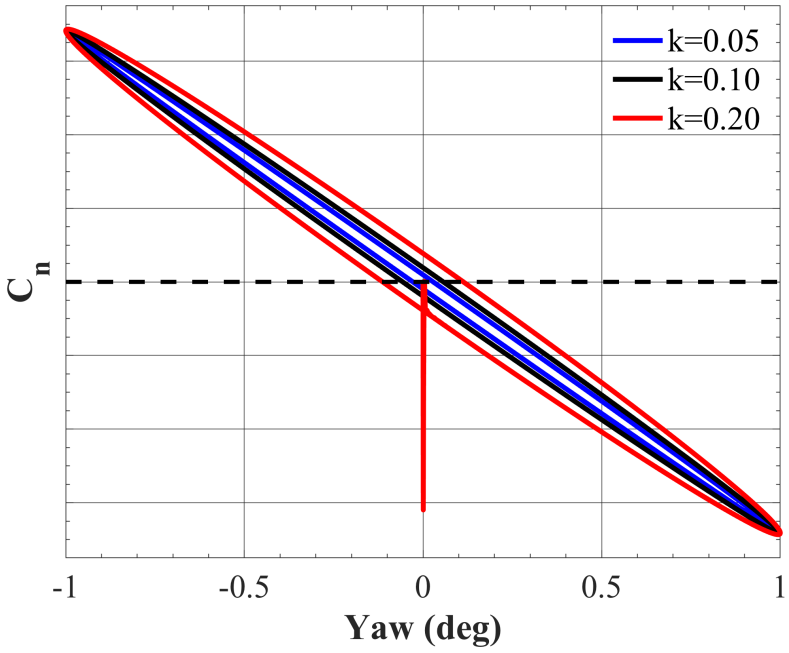

(b) Yawing moment coefficient

Figure 57: Rigid X-56A: FUN3D simulation results for forced yawing oscillations with one degree amplitude for $k = 0.05, 0.10$, and 0.20 at $\alpha = 0°$, $M = 0.13$.

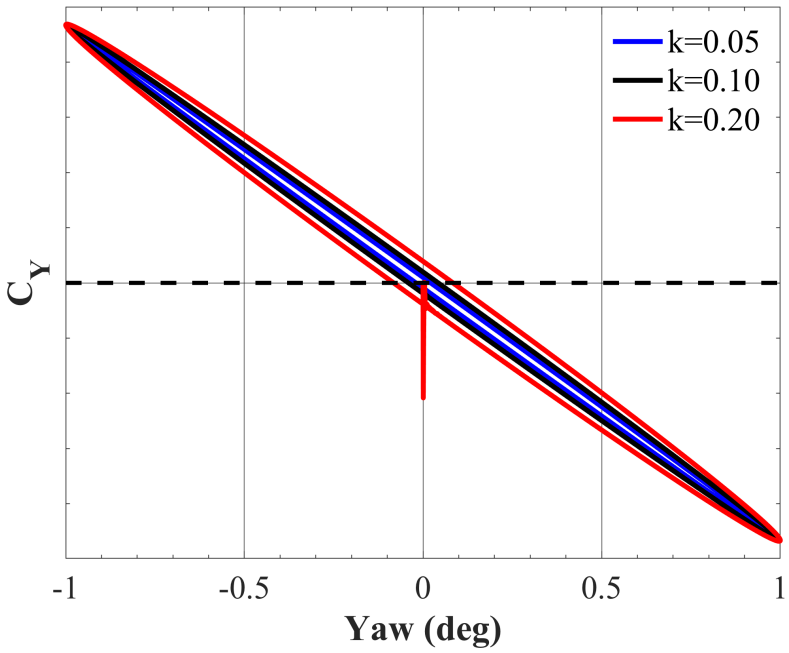

(a) Side force coefficient

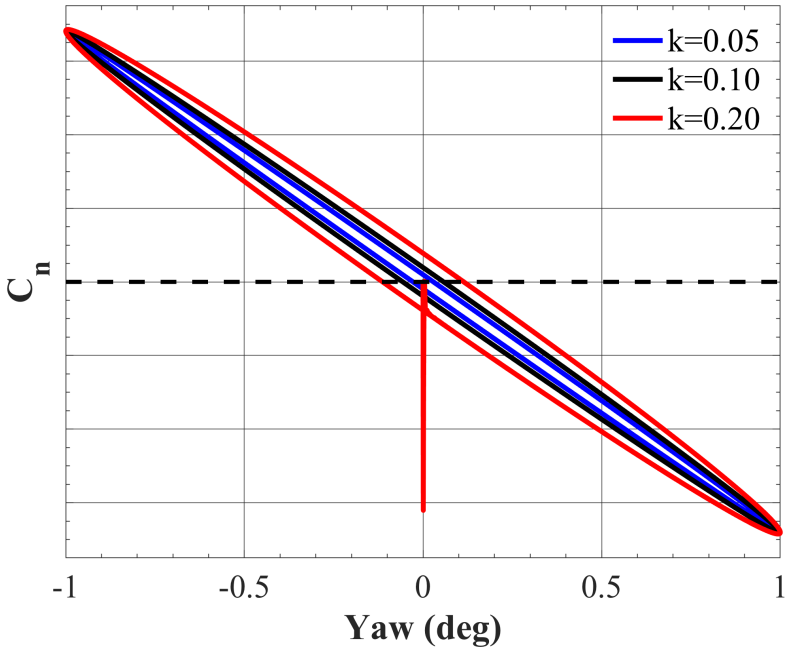

(b) Yawing moment coefficient

Figure 58: Flexible X-56A: FUN3D simulation results for forced yawing oscillations with one degree amplitude for $k = 0.05, 0.10$, and 0.20 at $\alpha = 0°$, $M = 0.13$.

8.1.5.2 ROM Predictions

Figure 59 illustrates a comparison between CFD and ROM results (left) and the ROM prediction error (right) for each of the forced yawing oscillation cases (top to bottom) with respect to side force coefficient for the rigid vehicle case. Overall, the ROM predictions show great qualitative agreement with CFD simulations, correctly resolving the initial transient response and the hysteresis loop widening with successive increases in reduced frequency. From a quantitative perspective, the trends in ROM error are consistent between each case with a mean error of and standard devation of zero for the quasisteady and quasiunsteady cases. For the unsteady case, a standard deviation of 0.1% is observed.

Figure 60 presents the CFD and ROM results (left) and the ROM prediction error (right) for each of the forced yawing oscillation cases (top to bottom) with respect to yawing moment coefficient for the rigid vehicle case. Similar to the previous force coefficient predictions, the ROM predictions are in great qualitative agreement with CFD simulation results for yawing moment coefficient, correctly resolving the initial transient response and the hysteresis loop widening with successive increases in reduced frequency. The mean error and standard deviation are both zero, representing an excellent quantitative match between CFD and ROM results.

Figures 61 and 62 present the CFD and ROM results (left) and the ROM prediction error (right) for each of the forced yawing oscillation cases (top to bottom) with respect to side force coefficient and yawing moment coefficient, respectively, for the flexible vehicle. Great qualitative agreement between CFD and ROM is found in each reduced frequency case. The ROM is able to resolve the initial peak transient, as well as the widening of the hysteresis loop. Overall, the mean ROM prediction error and standard deviation remains zero for each frequency. Thus, the ROM accurately predicts the unsteady lateral forces and moments encountered by the rigid and flexible X-56A aircraft performing forced yawing oscillations.

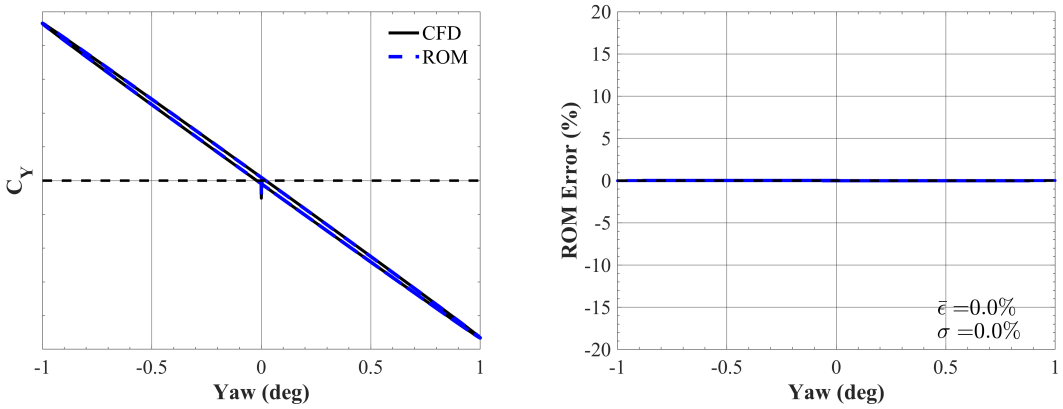

(a) Side force coefficient ($k = 0.05$)

(b) ROM error ($k = 0.05$)

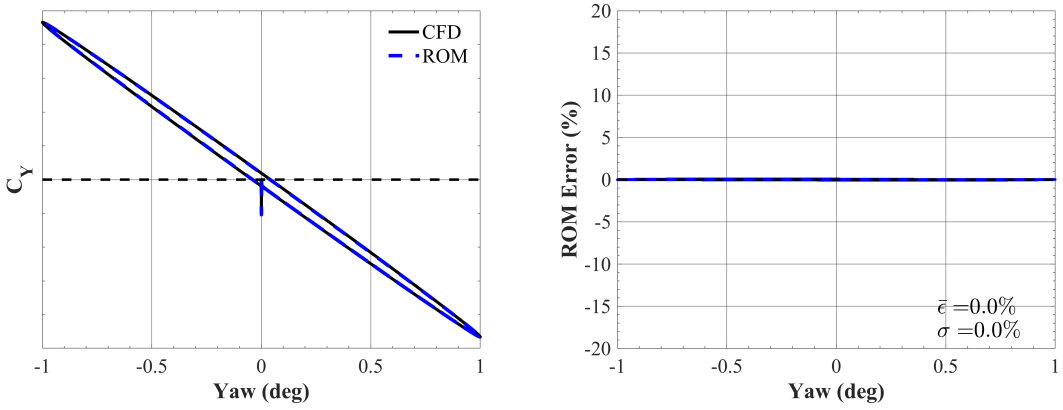

(c) Side force coefficient ($k = 0.10$)

(d) ROM error ($k = 0.10$)

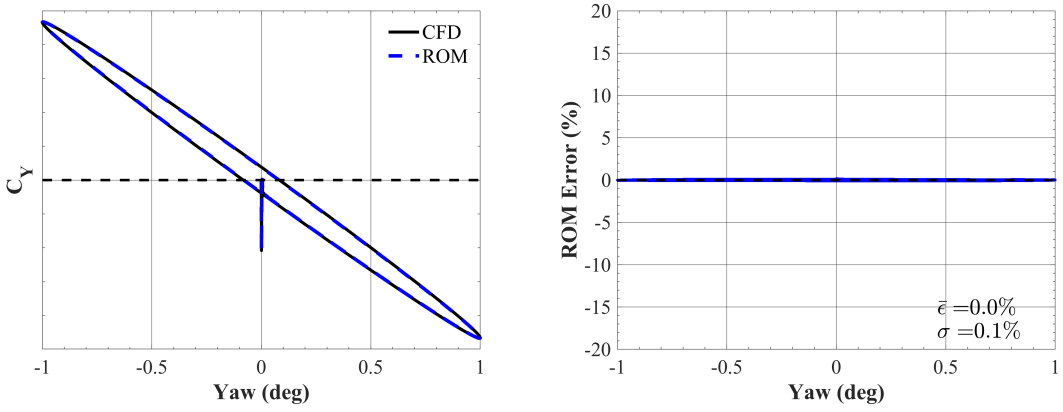

(e) Side force coefficient ($k = 0.20$)

(f) ROM error ($k = 0.20$)

Figure 59: Rigid X-56A: ROM vs. CFD side force coefficient results (left) and ROM error (right) for forced yawing oscillation with one degree amplitude for $k = 0.05$ (top), 0.10 (middle), and 0.20 (bottom) at $\alpha = 0°$, $\beta = 0°$, $M = 0.13$.

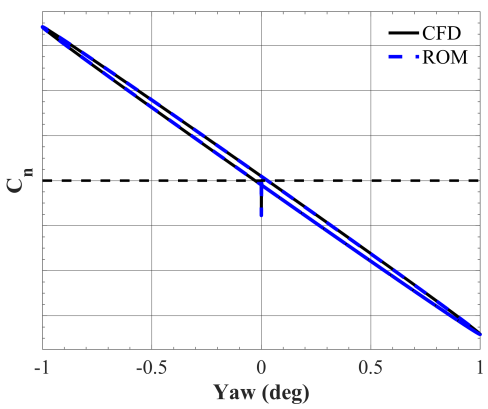

(a) Yawing moment coefficient ($k = 0.05$)

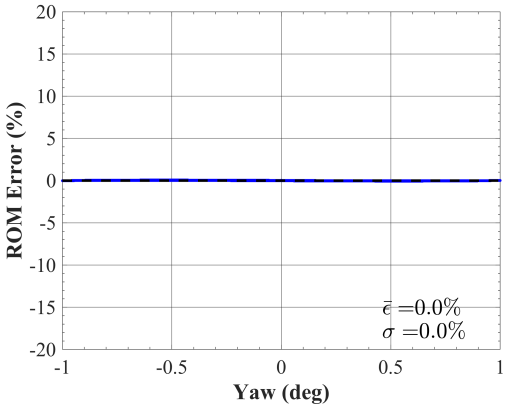

(b) ROM error ($k = 0.05$)

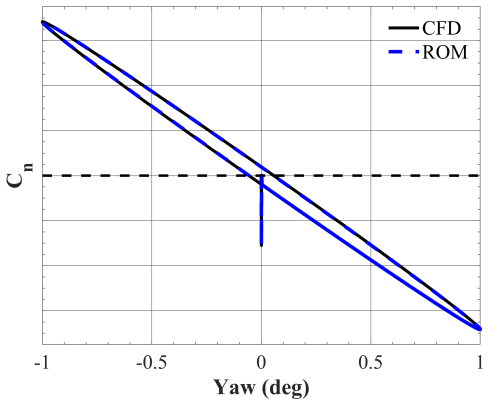

(c) Yawing moment coefficient ($k = 0.10$)

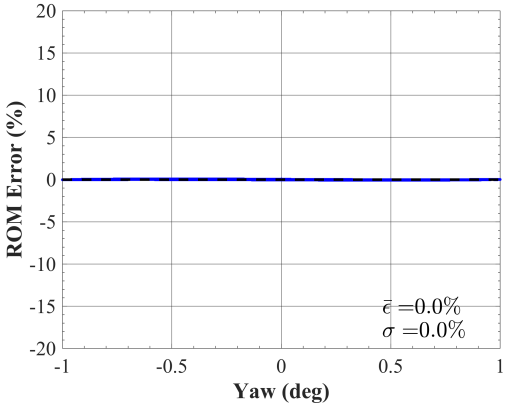

(d) ROM error ($k = 0.10$)

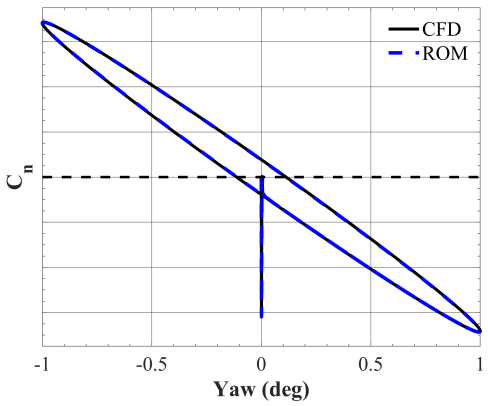

(e) Yawing moment coefficient ($k = 0.20$)

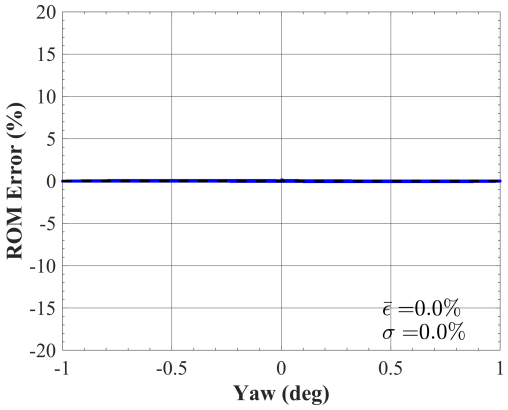

(f) ROM error ($k = 0.20$)

Figure 60: Rigid X-56A: ROM vs. CFD yawing moment coefficient results (left) and ROM error (right) for forced yawing oscillation with one degree amplitude for $k = 0.05$ (top), 0.10 (middle), and 0.20 (bottom) at $\alpha = 0°$, $\beta = 0°$, $M = 0.13$.

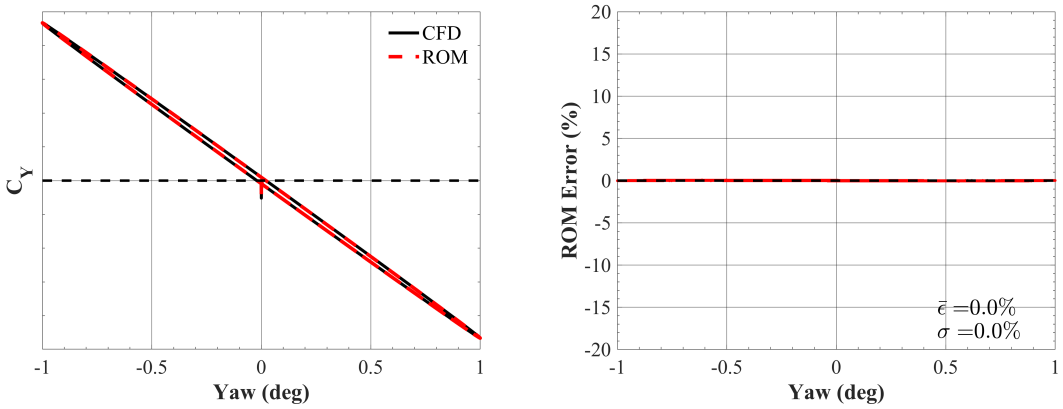

(a) Side force coefficient ($k = 0.05$)

(b) ROM error ($k = 0.05$)

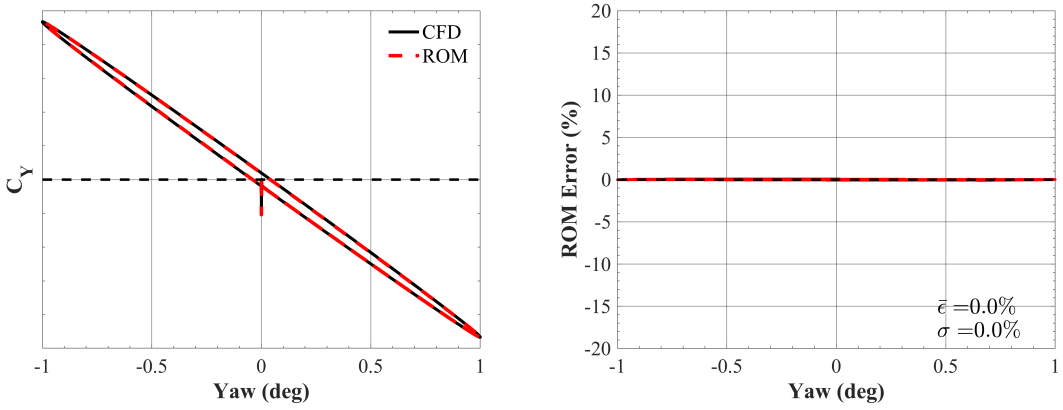

(c) Side force coefficient ($k = 0.10$)

(d) ROM error ($k = 0.10$)

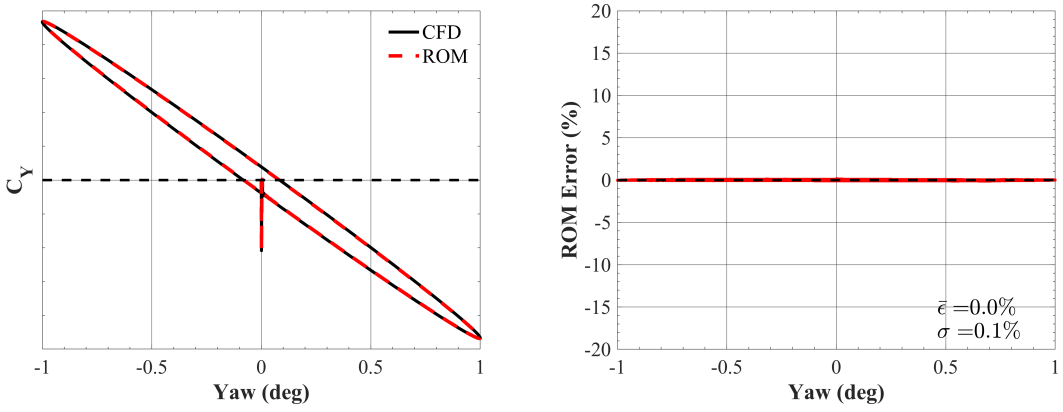

(e) Side force coefficient ($k = 0.20$)

(f) ROM error ($k = 0.20$)

Figure 61: Flexible X-56A: ROM vs. CFD side force coefficient results (left) and ROM error (right) for forced yawing oscillation with one degree amplitude for $k = 0.05$ (top), 0.10 (middle), and 0.20 (bottom) at $\alpha = 0°$, $\beta = 0°$, $M = 0.13$.

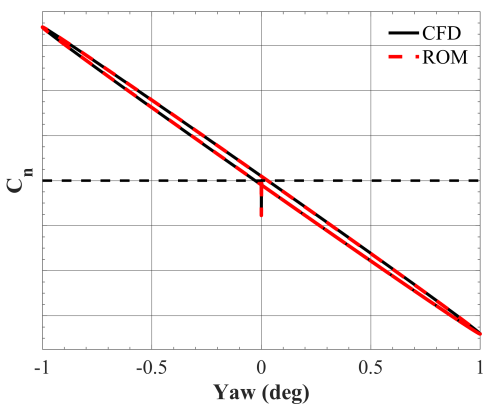

(a) Yawing moment coefficient ($k = 0.05$)

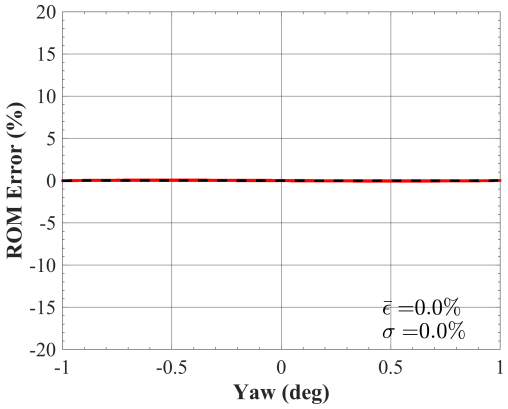

(b) ROM error ($k = 0.05$)

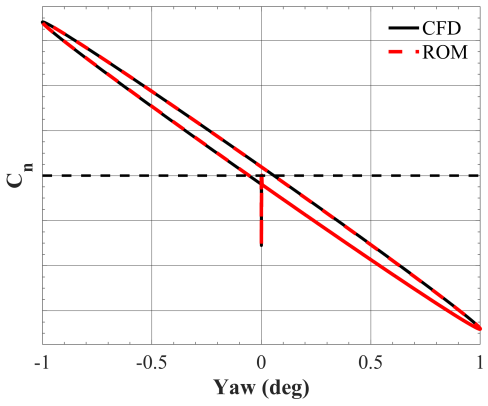

(c) Yawing moment coefficient ($k = 0.10$)

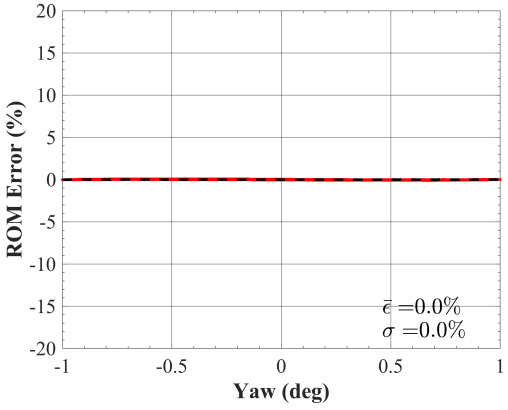

(d) ROM error ($k = 0.10$)

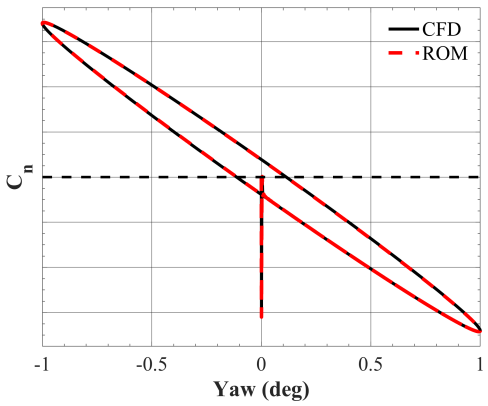

(e) Yawing moment coefficient ($k = 0.20$)

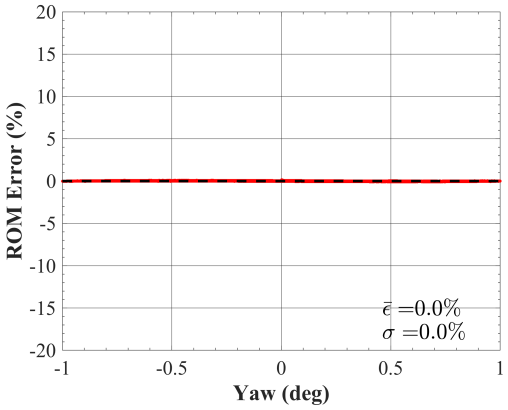

(f) ROM error ($k = 0.20$)

Figure 62: Flexible X-56A: ROM vs. CFD yawing moment coefficient results (left) and ROM error (right) for forced yawing oscillation with one degree amplitude for $k = 0.05$ (top), 0.10 (middle), and 0.20 (bottom) at $\alpha = 0°$, $\beta = 0°$, $M = 0.13$.

8.1.6 Forced Pitching Oscillations

8.1.6.1 CFD Simulations

Forced pitching oscillations were prescribed starting from an initial angle of attack $\alpha_0 = 0°$ with a pitch amplitude of $\Delta\theta = 1°$ at $\beta = 0°$, $M = 0.13$. The amplitude was limited to 1 degree to ensure a locally linear aerodynamic response with respect to angle of attack. Figure 63 depicts the motion history for the forced pitching oscillations at reduced frequencies of $k = 0.05, 0.10$, and 0.20. The 'quasisteady' ($k = 0.05$) case is characterized by a slower-varying oscillation with an approximate period of 0.9 seconds. This period of motion is halved in each of the successive 'quasiunsteady' ($k = 0.10$) and 'unsteady' ($k = 0.20$) cases. Three cycles were simulated for both the rigid and flexible vehicle cases to allow for the initial transient response to decay and to explore potential differences in the convergence of the hysteresis loops when accounting for structural flexibility.

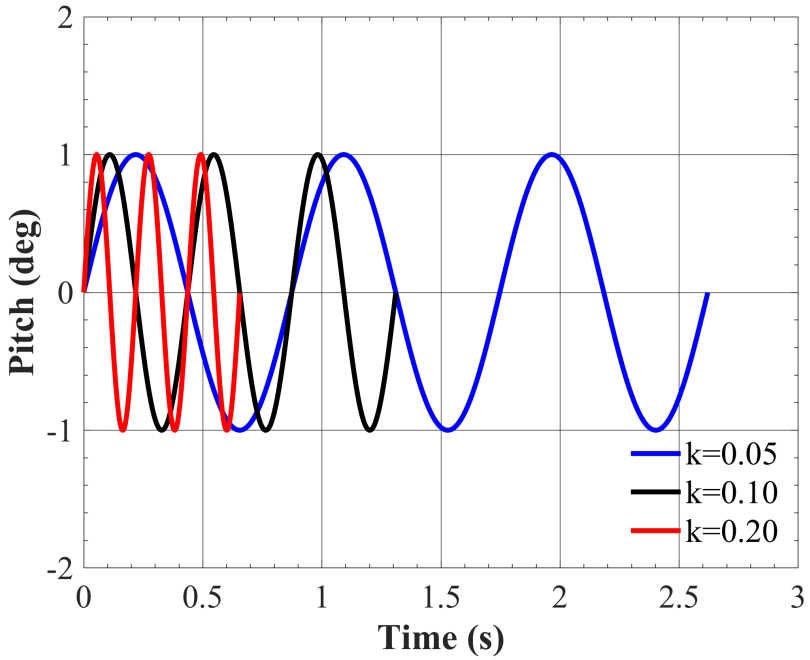

Figure 63: Motion history for forced pitching oscillations with one degree amplitude for $k = 0.05, 0.10$, and 0.20 at $\alpha = 0°$, $\beta = 0°$, $M = 0.13$.

The forced pitching oscillations were initialized from a well-converged, static time-accurate solution at $\alpha = 0°$, $\beta = 0°$, $M = 0.13$. Using a semichord reference length ($L_{ref} = c_{ref}/2$), the highest reduced frequency ($k = 0.20$) translates to a peak motion frequency of 4.58 Hz. Because the highest frequency structural mode (11.95 Hz) has a greater frequency than the most dynamic motion to be simulated, the time step was chosen based on the more strict requirements for resolving fluid-structure interactions. The characteristic time step chosen is based on resolving the highest structural mode frequency using a sampling factor of $N = 200$. A resulting characteristic time step of $s \approxeq 0.002$ was used to advance the solution in time and 20 subiterations were used to converge the solution in pseudotime.

Table 12 summarizes the temporal parameters used in the forced pitching oscillation simulations. The total number of time steps was set based on resolving the three cycles of motion. The trajectory time history, defined by the aerodynamic angles (α and β), Mach number (M), and the Euler angles (ϕ, θ, and ψ), was converted to a motion input file using the trajectory post-processing MATLAB code. For pitching oscillations, $\Delta\alpha = \Delta\beta = \Delta\phi = \Delta\psi = 0°$ while $\theta(t)$ is defined at each iteration. For forced oscillations, the body and inertial reference frame are equivalent and angle of attack is implicitly defined by $\alpha(t) = \alpha_0 + \theta(t)$.

Table 12: Temporal parameters for forced pitching oscillation simulations.

k	M	Δt (s)	Δt^*	N_{sub}	Total Time Steps
0.05	0.13	4.0E-04	0.002	20	6,551
0.10	0.13	4.0E-04	0.002	20	3,276
0.20	0.13	4.0E-04	0.002	20	1,638

The solution strategy proved to be robust in producing stable, well-converged dynamic simulations for both the rigid and flexible vehicle at every prescribed motion frequency. Examples of subiterative convergence for the $k = 0.20$ case are shown in Figures 64(a) and 64(b) for the rigid (top) and flexible (bottom) vehicle cases, respectively. The plots illustrate the order-of-magnitude convergence in the FUN3D

time-accurate solution residual drop ($log(R/R_0)$) and the pitching moment coefficient (C_m) convergence versus fractional iterations. Iteration 136 is shown, which coincides with the positive peak pitch amplitude during the first oscillation cycle, where each point signifies the convergence achieved at each of the 20 subiterations. The rigid simulation presents over 9-orders of convergence in residual drop with sufficient convergence in the pitching moment coefficient, based on a 0.0002% difference between the final two subiterations. Similar levels of convergence were achieved in the aeroelastic simulation with 8-orders of convergence in residual drop. While not illustrated here, similar convergence behavior was observed for the $k = 0.10$ and $k = 0.05$ cases.

Figure 65 illustrates the FUN3D lift and pitching moment coefficient results for the rigid vehicle undergoing forced pitching oscillations with 1 degree amplitude for $k = 0.05, 0.10$, and 0.20 at $\alpha_0 = 0°$, $\beta = 0°$, $M = 0.13$. The lift coefficient is characterized by an initial, positive peak due to the onset of grid motion followed by a transient decay that persists for the first quarter of the first cycle before converging to a clockwise hysteresis loop. The pitching moment coefficient encounters a strong negative peak, extending into the negative coefficient value range, followed by a more rapidly decaying transient response before transitioning to a counterclockwise hysteresis loop within the first eighth of the first cycle.

The impact of increasing reduced frequency is an aerodynamic damping effect, observed by a widening of the hysteresis loops for both coefficients. Additionally, the minimum and maximum lift coeffficient increase and decrease, respectively, as illustrated by a clockwise rotation of the hysteresis loop. By increasing the oscillation rate, the flow is unable to converge to a steady-state and the influence of previous motion states act to dampen the range of lift coefficient values encountered during oscillatory motions. The opposite trend is observed for the pitching moment coefficient with a counterclockwise rotation of the hysteresis loop.

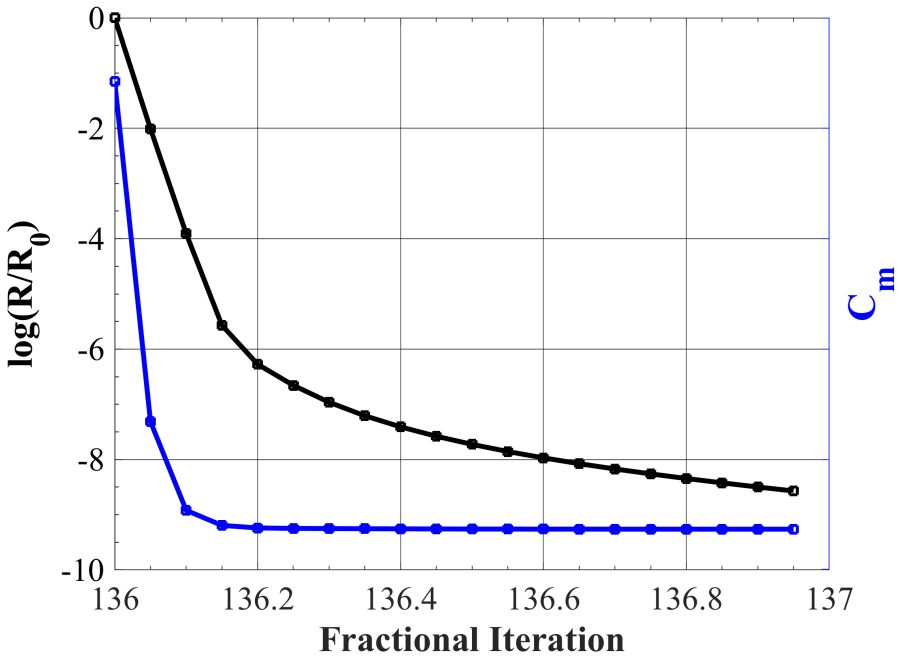

(a) Rigid

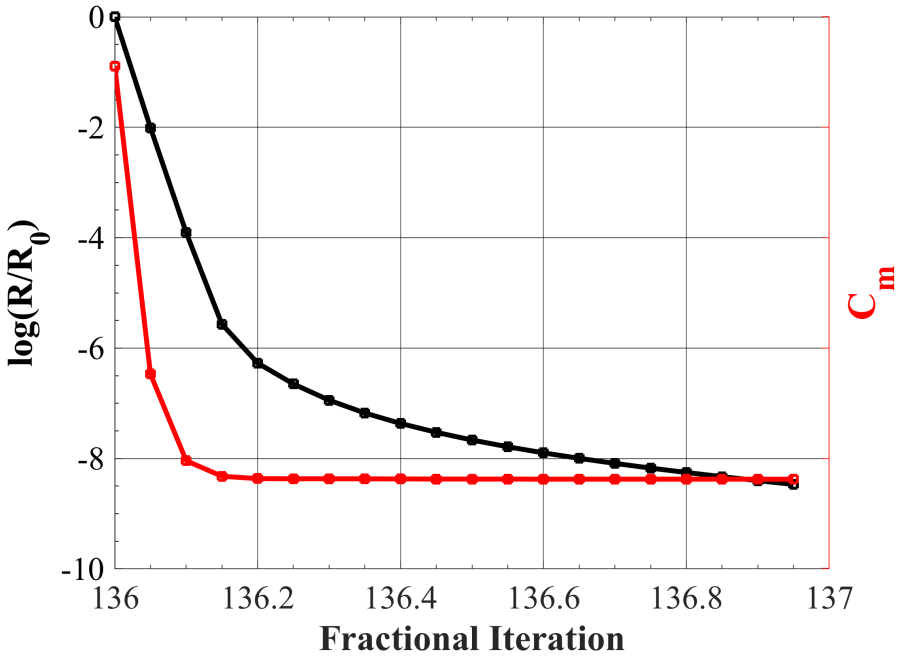

(b) Flexible

Figure 64: X-56A: FUN3D subiterative convergence for forced pitching oscillation with one degree amplitude, $k = 0.20$ at $\alpha = 0°$, $M = 0.13$ for the rigid (blue) and flexible (red) cases. Iteration 136 - peak pitch amplitude within first oscillation cycle.

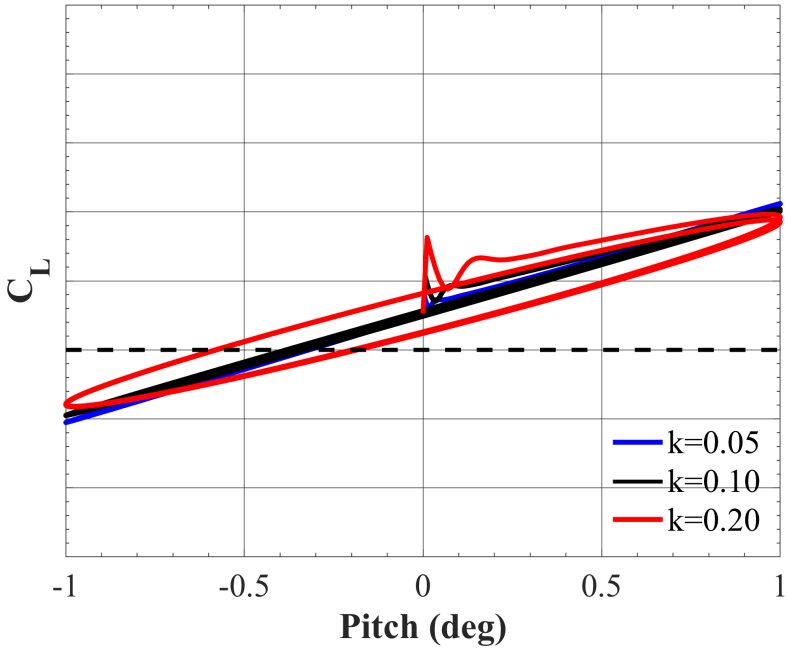

(a) Lift coefficient

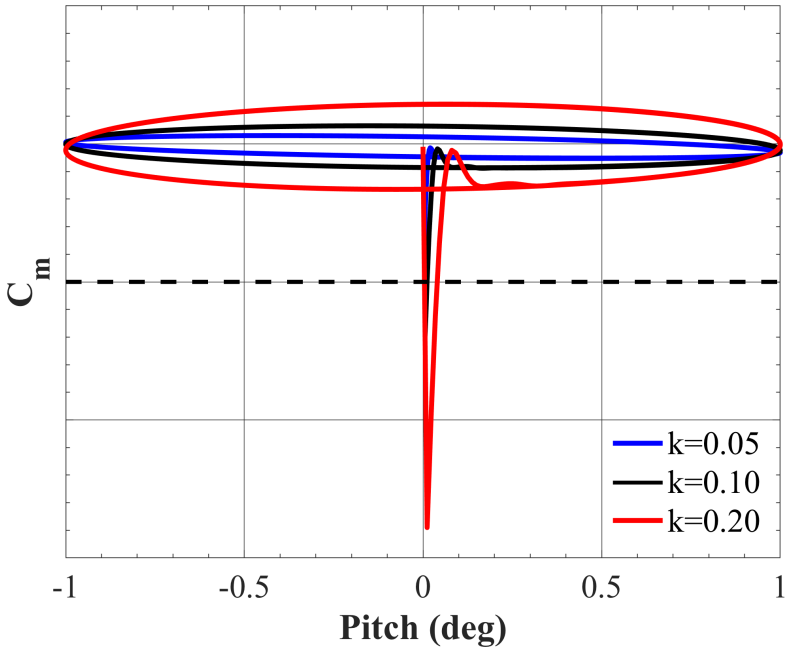

(b) Pitching moment coefficient

Figure 65: Rigid X-56A: FUN3D simulation results for forced pitching oscillations with one degree amplitude for $k = 0.05, 0.10$, and 0.20 at $\alpha_0 = 0°$, $M = 0.13$.

Figure 66 illustrates the FUN3D results for the flexible vehicle undergoing forced pitching oscillations with 1 degree amplitude for $k = 0.05, 0.10$, and 0.20 at $\alpha_0 = 0°$, $\beta = 0°$, $M = 0.13$. For comparisons to be made relative to the rigid simulation results, the range and scale of the plotted lift and pitching moment coefficient is identical between the rigid and aeroelastic simulations. The impact of fluid-structure interactions on the unsteady aerodynamic lift and pitching moment coefficient responses is significant. For each reduced frequency, the aerodynamic damping changes between successive cycles of motion with notable variations in hysteresis loop width, as well as the minimum and maximum coefficient values.

Relative to the rigid simulations, the aerodynamic damping in the lift coefficient response is more significant for the $k = 0.05$ and $k = 0.10$ cases, as evidenced by wider hysteresis loops. Furthermore, the hysteresis loops are rotated counterclockwise, translating to a wider range of lift coefficient values. In the $k = 0.20$ case, the average aerodynamic damping is similar in magnitude compared to the rigid simulations, where the primary difference is the cycle-to-cycle variation due to fluid-structure interactions. It is interesting to note that increasing the reduced frequency no longer corresponds to a straight-forward clockwise rotation of the hysteresis loops, as the $k = 0.10$ case produces the largest variation in lift coefficient values.

Similar, but less pronounced trends are found with respect to the pitching moment coefficient results. Relative to the rigid simulations, the variation in aerodynamic damping is less significant, likely due to the pitching moment coefficient being smaller in magnitude. At the lower reduced frequencies, response nonlinearity is observed despite the limited motion amplitude. Such nonlinearities result from the influence of fluid-structure interactions, when the structural deformation is capable of converging toward static aeroelastic states for slowly-varying motions.

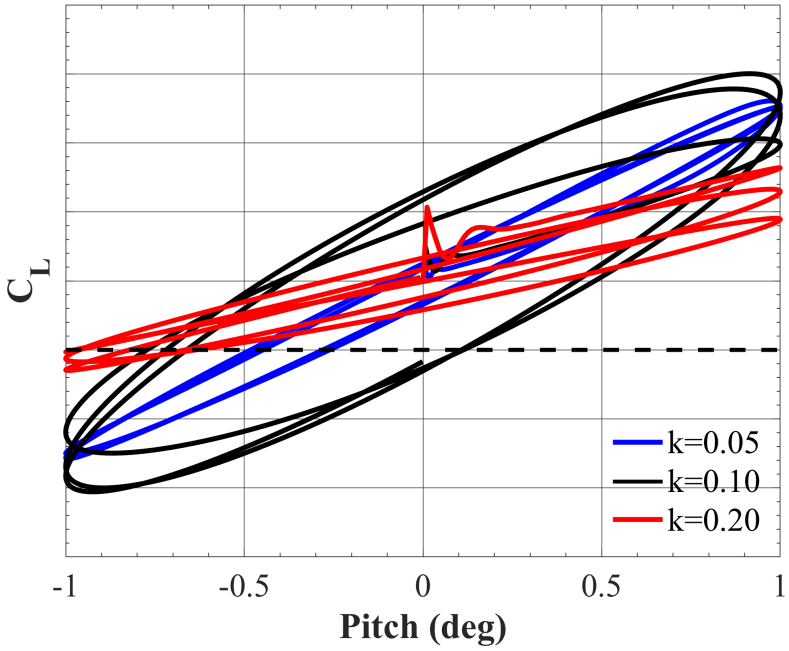

(a) Lift coefficient

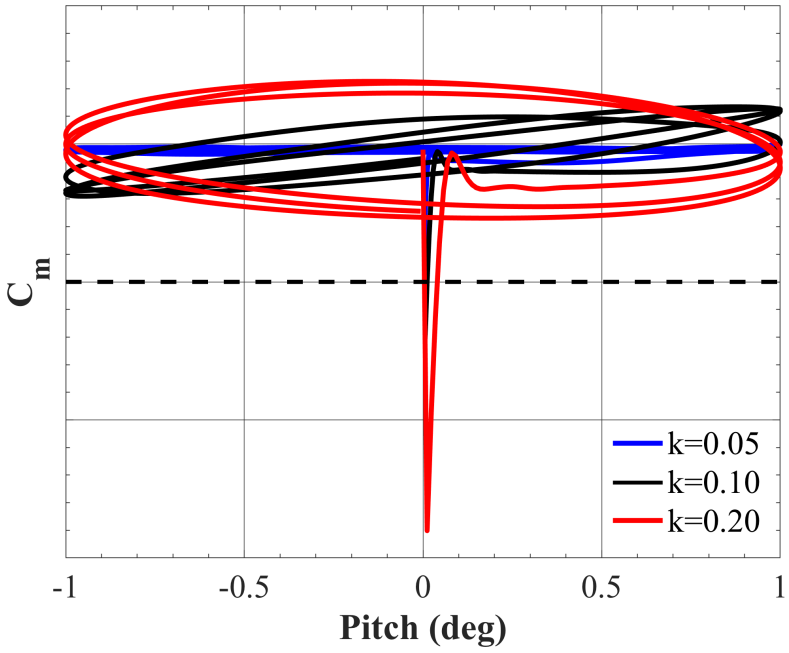

(b) Pitching moment coefficient

Figure 66: Flexible X-56A: FUN3D simulation results for forced pitching oscillations with one degree amplitude for $k = 0.05, 0.10$, and 0.20 at $\alpha_0 = 5°$, $M = 0.13$.

8.1.6.2 ROM Predictions

Figure 67 illustrates an updated comparison between CFD and ROM results (left) and the ROM prediction error (right) for each of the forced pitching oscillation cases (top to bottom) with respect to lift coefficient for the rigid vehicle case. Overall, the ROM predictions show great qualitative agreement with CFD simulation results, correctly resolving the initial transient response and the hysteresis loop widening with successive increases in reduced frequency. The standard deviation in ROM error is observed to increase with reduced frequency as the aerodynamic response becomes more reliant on previous motion states. Nevertheless, the ROM error is characterized by a mean error and standard deviation of $< 1\%$ across all simulated reduced frequencies.

Figure 68 presents the same plots with respect to pitching moment coefficient for the rigid vehicle. The ROM predictions are in great qualitative agreement with CFD simulations, correctly resolving the initial transient response and the hysteresis loop widening/rotation with increases in reduced frequency. The mean error and standard deviation remain $< 1\%$ for each frequency case. However, as reduced frequency decreases discrepancies between the ROM and CFD are observed at the minimum pitch angle, where the ROM tends to overpredict the pitching moment coefficient. This result can be explained by reviewing the static characterization study (Fig. 24(b)) of Section 7.1. The static pitching moment curve shows differences in slope, i.e., derivative value, in the increment between $\alpha = [-1^\circ \text{ to } 0^\circ]$ and $\alpha = [0^\circ \text{ to } 1^\circ]$. Because the traditional ROM typically assumes a symmetric step response about the initial angle of attack, i.e., $-C_{m_\alpha}|_0^1 = C_{m_\alpha}|_0^{-1}$, and because $C_{m_\alpha}|_0^1 < C_{m_\alpha}|_0^{-1}$, the ROM tends to overpredict at negative angles of attack. Inclusion of negative step responses may improve modeling accuracy for the linear pitching moment model of the X-56A. Overall, the ROM predicts the unsteady lift and pitching moment coefficients with comparable accuracy to full-order simulations for the rigid vehicle.

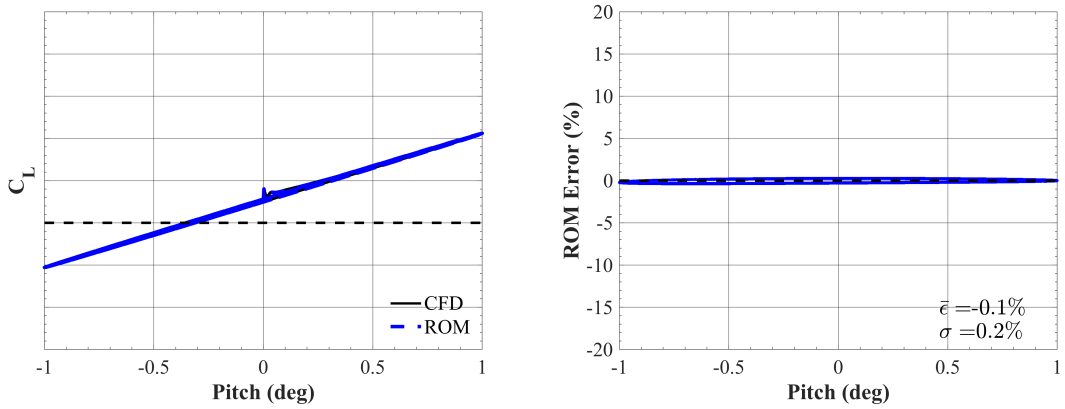

(a) Lift coefficient ($k = 0.05$) (b) ROM error ($k = 0.05$)

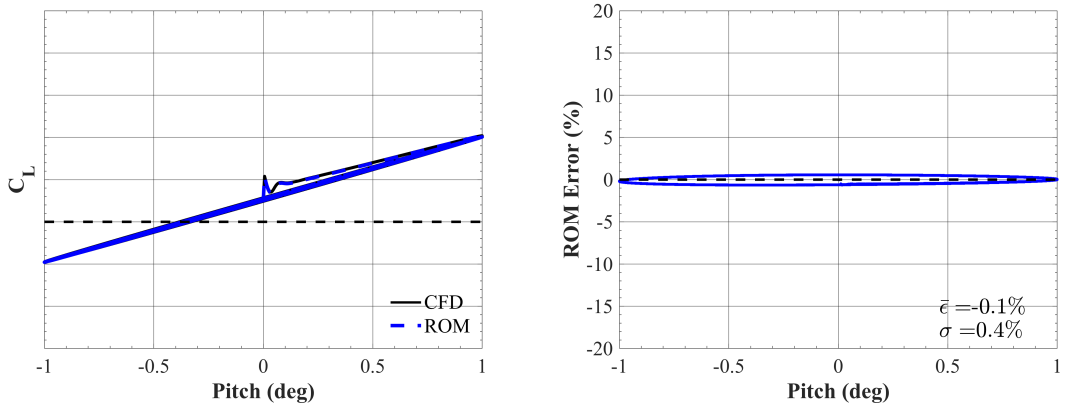

(c) Lift coefficient ($k = 0.10$) (d) ROM error ($k = 0.10$)

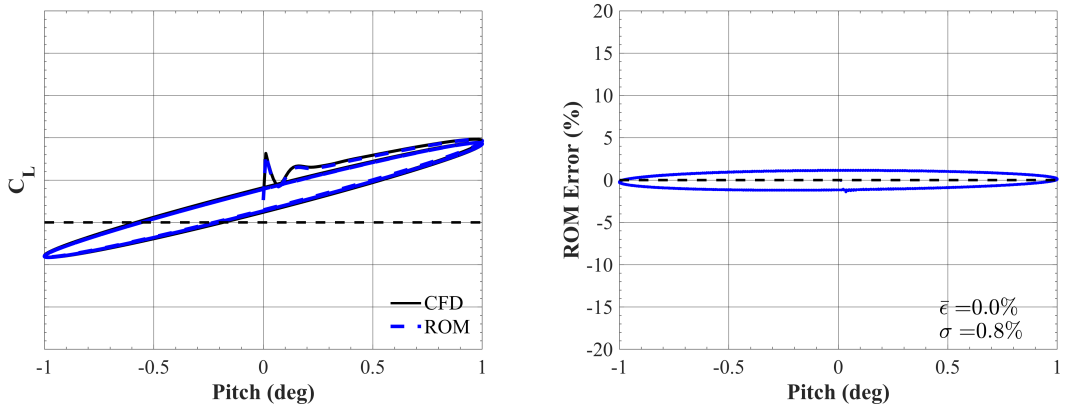

(e) Lift coefficient ($k = 0.20$) (f) ROM error ($k = 0.20$)

Figure 67: Rigid X-56A: ROM vs. CFD lift coefficient results (left) and ROM error (right) for forced pitching oscillation with 1 degree amplitude for $k = 0.05$ (top), 0.10 (middle), and 0.20 (bottom) at $\alpha_0 = 5°$, $\beta = 0°$, $M = 0.13$.

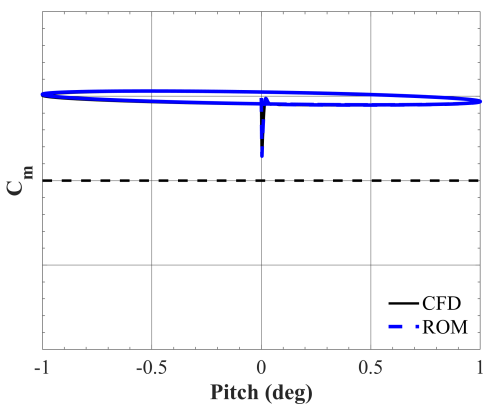

(a) Pitching moment coefficient ($k = 0.05$)

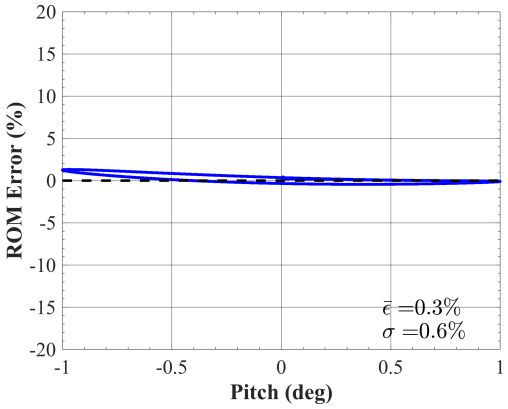

(b) ROM error ($k = 0.05$)

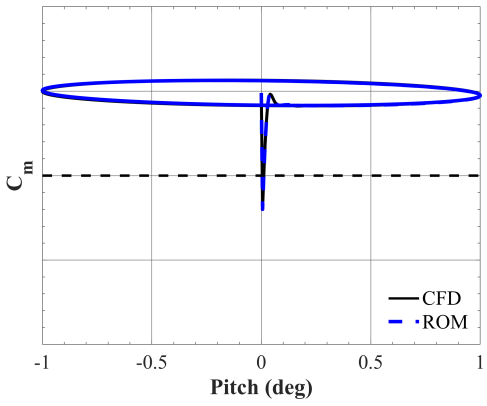

(c) Pitching moment coefficient ($k = 0.10$)

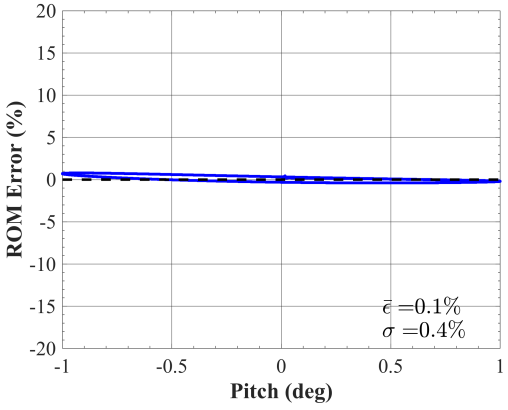

(d) ROM error ($k = 0.10$)

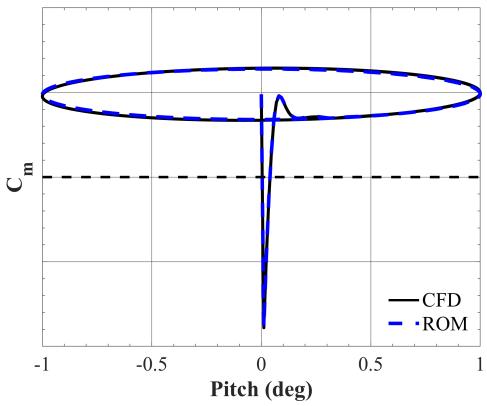

(e) Pitching moment coefficient ($k = 0.20$)

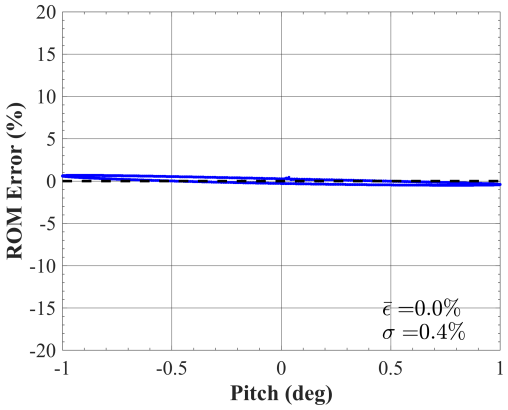

(f) ROM error ($k = 0.20$)

Figure 68: Rigid X-56A: ROM vs. CFD pitching moment coefficient results (left) and ROM error (right) for pitching pitching oscillation with 1 degree amplitude for $k = 0.05$ (top), 0.10 (middle), and 0.20 (bottom) at $\alpha_0 = 5°$, $\beta = 0°$, $M = 0.13$.

Figure 69 presents the CFD and ROM results (left) and the ROM prediction error (right) for each of the forced pitching oscillation cases (top to bottom) with respect to lift coefficient for the flexible vehicle. In the $k = 0.05$ case, the ROM accurately resolves the initial transient response, as well as cycle-to-cycle variations in the hysteresis loop due to fluid-structure interactions. A mean error and standard deviation of $< 1\%$ is obtained. As the reduced frequency is increased to $k = 0.10$ and $k = 0.20$, the ROM shows great qualitative agreement with aeroelastic CFD simulations for the duration of the three-cycle oscillation, while the mean error and standard deviation remain $< 1\%$ in each case. It is important to note that while the standard deviation remains close to zero, an increase is observed as reduced frequency is increased.

Figure 70 presents the same plots with respect to pitching moment coefficient for the flexible vehicle. In the $k = 0.05$ case, the hysteresis loops present low aerodynamic damping relative to the higher frequency cases, but a strong nonlinearity despite limiting the pitch amplitude to 1 degree. This nonlinearity results from convergence of the fluid-structure interactions, where the structure is allowed to deform closer toward static aeroelastic conditions for slower varying motions. Because the aeroelastic indicial responses capture these interactions across the motion frequency spectrum, the ROM is able to match CFD simulations with a mean error and standard deviation $< 1.5\%$. As reduced frequency increases to $k = 0.10$ and $k = 0.20$, the nonlinearity of the hysteresis loops decreases, approaching a more elliptical distribution for the most dynamic case. At each frequency, the ROM continues to capture the initial transient response, as well as cycle-to-cycle variations in the hysteresis loop width and orientation. The mean error and standard deviation remains below $< 1\%$ for both frequencies. The same overprediction of pitching moment at negative angles of attack is observed for the flexible vehicle, reinforcing the need to include negative step responses for maximum modeling accuracy.

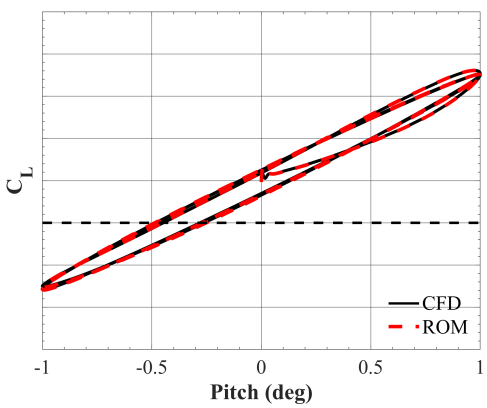

(a) Lift coefficient ($k = 0.05$)

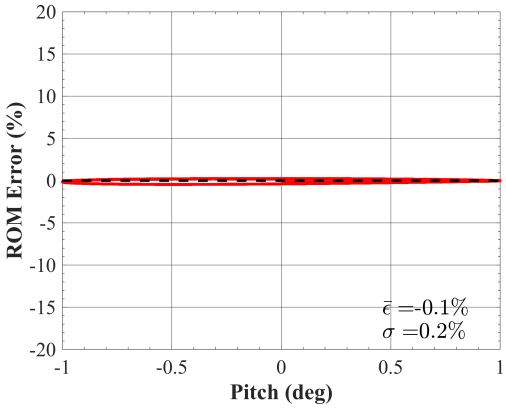

(b) ROM error ($k = 0.05$)

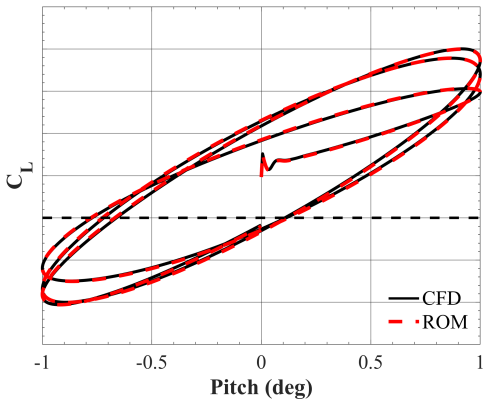

(c) Lift coefficient ($k = 0.10$)

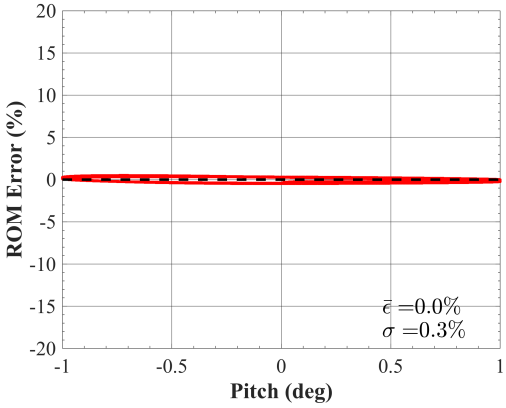

(d) ROM error ($k = 0.10$)

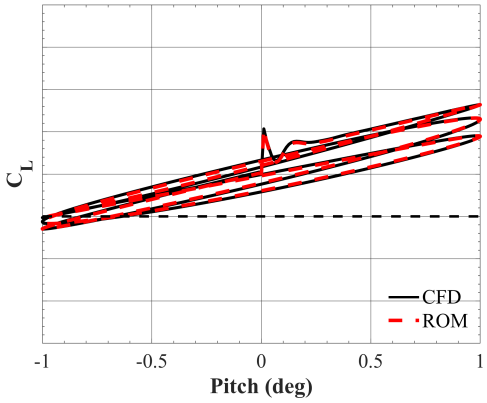

(e) Lift coefficient ($k = 0.20$)

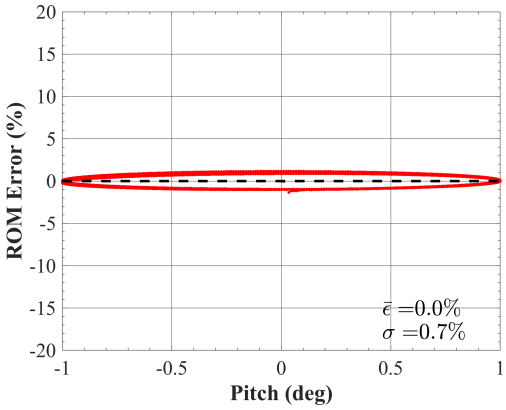

(f) ROM error ($k = 0.20$)

Figure 69: Flexible X-56A: ROM vs. CFD lift coefficient results (left) and ROM error (right) for forced pitching oscillation with 1 degree amplitude for $k = 0.05$ (top), 0.10 (middle), and 0.20 (bottom) at $\alpha_0 = 5°$, $\beta = 0°$, $M = 0.13$.

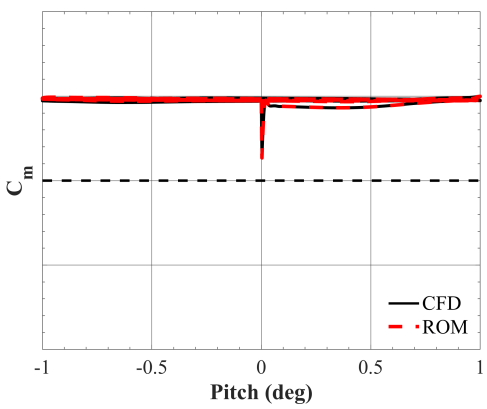

(a) Pitching moment coefficient ($k = 0.05$)

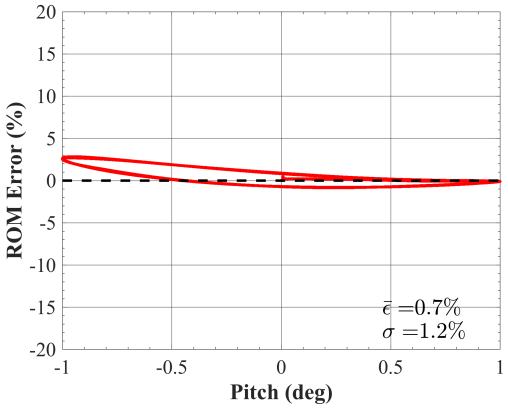

(b) ROM error ($k = 0.05$)

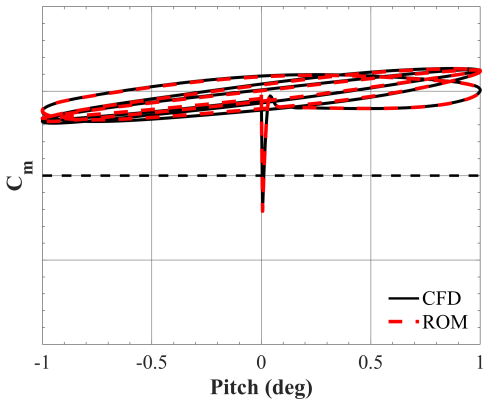

(c) Pitching moment coefficient ($k = 0.10$)

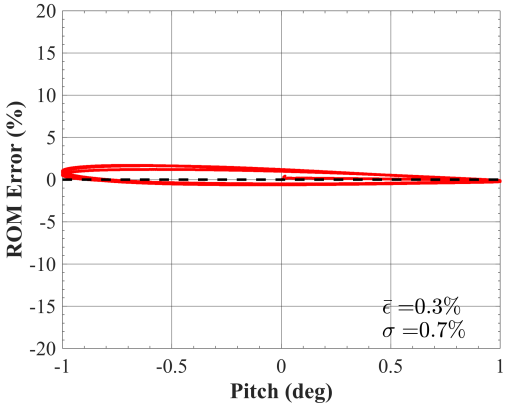

(d) ROM error ($k = 0.10$)

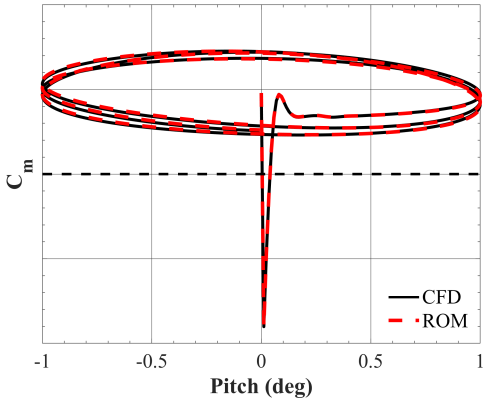

(e) Pitching moment coefficient ($k = 0.20$)

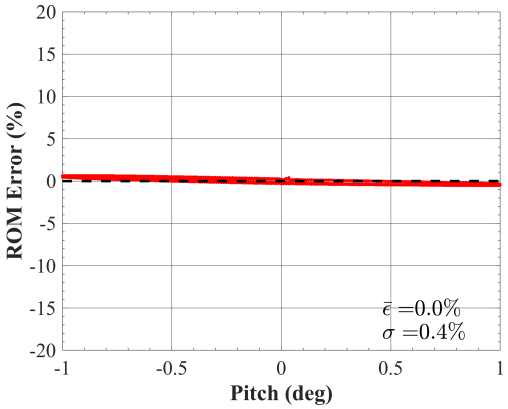

(f) ROM error ($k = 0.20$)

Figure 70: Flexible X-56A: ROM vs. CFD pitching moment coefficient results (left) and ROM error (right) for forced pitching oscillation with 1 degree amplitude for $k = 0.05$ (top), 0.10 (middle), and 0.20 (bottom) at $\alpha_0 = 5°$, $\beta = 0°$, $M = 0.13$.

8.1.6.3 ROM Predictions using Negative Step Responses

The results of the previous section illustrate a discrepancy between CFD simulations and ROM predictions at negative angles of attack for both the rigid and flexible vehicles. The static characterization plots of Section 7.1 provided insight into this discrepancy. The lift and pitching moment curve slopes were observed to be asymmetric about the mean angle of attack, $\alpha = 0°$. In Section 7.6, the sensitivity to negative step responses was assessed at the baseline flight condition. The step responses were shown to be asymmetric, primarily for pitching moment, for both the rigid and flexible flight vehicles. These differences may be attributed to static aerodynamic characterisitics, and in the case of the flexible vehicle, fluid-structure interactions due to structural deformation under asymmetric loading conditions. The current subsection presents updated ROM predictions using negative step responses for the linear pitch oscillations at various reduced frequencies.

In addition to the responses shown in Table 8, negative step changes in angle of attack and pitch rate using the trajectory inputs listed in Table 13. These longitudinal indicial responses were simulated using the same temporal parameters listed previously in Table 9. The *CFD2ROM* MATLAB code uses the indicial reponse due to a negative step in angle of attack for all trajectory points where $\alpha < 0°$ and uses the indicial responses due to a negative step in pitch rate for all trajectories points where both $\alpha < 0°$ and $q < 0°$.

Table 13: Motion file inputs for creating negative step indicial trajectories ($t > 0$).

Indicial	α (deg)	β (deg)	ϕ (deg)	θ (deg)	ψ (deg)	M_0
α-step	-1	0	0	0	0	0.13
q-step	0	0	0	$-\Delta q \cdot t$	0	0.13

Figures 71 illustrates a comparison between CFD and ROM results (left) and the ROM prediction error (right) for each of the forced pitching oscillation cases

(top to bottom) with respect to lift coefficient for the rigid vehicle. Relative to the previous results in Fig. 67, the mean error changes from -0.1% to 0.0%, -0.1% to 0.0%, and 0.0% to 0.1% for the $k = 0.05$, $k = 0.10$, and $k = 0.20$ cases, respectively. The standard deviation remained constant in each case when including negative step responses. Overall, a slight decrease in mean error is found for the quasisteady and unsteady reduced frequencies.

Figures 72 illustrates a comparison between CFD and ROM results (left) and the ROM prediction error (right) for each of the forced pitching oscillation cases (top to bottom) with respect to the pitching moment coefficient for the rigid vehicle. Relative to the previous results in Fig. 68, the mean error changes from 0.3% to -0.1%, 0.1% to -0.1%, and 0.0% to 0.1% for the $k = 0.05$, $k = 0.10$, and $k = 0.20$ cases, respectively. The standard deviation changes from 0.6% to 0.2%, 0.4% to 0.2%, and 0.4% to 0.3% for the $k = 0.05$, $k = 0.10$, and $k = 0.20$ cases, respectively. Overall, negligible differences in the mean error are observed, but reductions in standard deviation for each pitching moment coefficient prediction when including negative step responses. Additionally, the ROM error plots no longer show an overprediction at the negative angles of attack.

Figures 73 illustrates a comparison between CFD and ROM results (left) and the ROM prediction error (right) for each of the forced pitching oscillation cases (top to bottom) with respect to lift coefficient for the flexible vehicle. Relative to the previous results in Fig. 69, the mean error changes from 0.1% to 0.0%, 0.0 to 0.1%, and 0.0% to 0.1% for the $k = 0.05$, $k = 0.10$, and $k = 0.20$ cases, respectively. The standard deviation changes from 0.2% to 0.1%, 0.3% to 0.2%, and 0.7% to 0.7% for the $k = 0.05$, $k = 0.10$, and $k = 0.20$ cases, respectively. Overall, negligible performance improvements are generated when including negative step responses for lift coefficient predictions of the flexible vehicle.

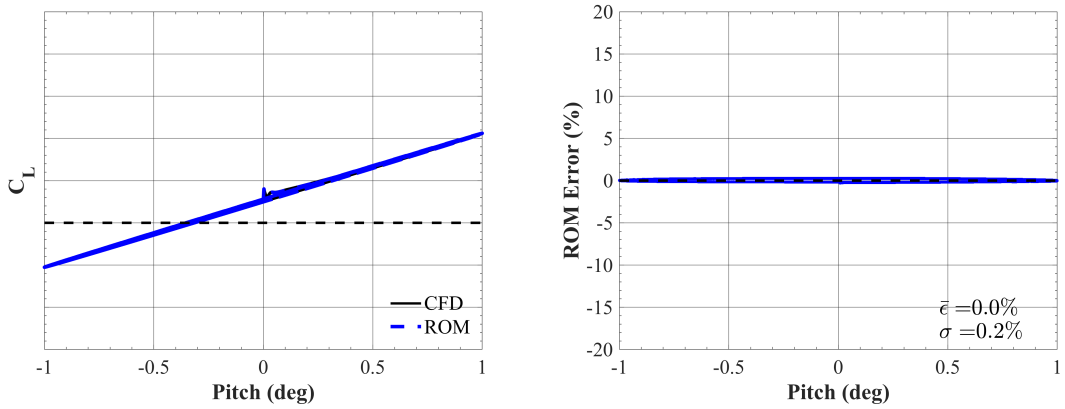

(a) Lift coefficient ($k = 0.05$) (b) ROM error ($k = 0.05$)

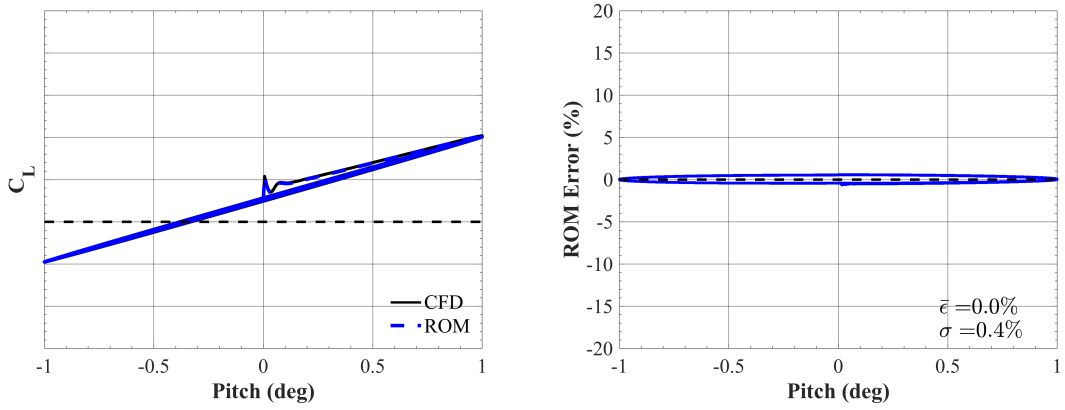

(c) Lift coefficient ($k = 0.10$) (d) ROM error ($k = 0.10$)

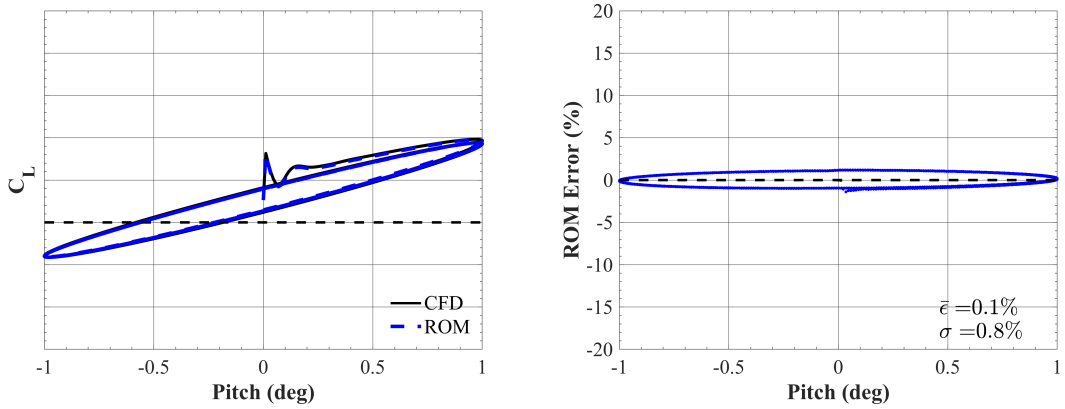

(e) Lift coefficient ($k = 0.20$) (f) ROM error ($k = 0.20$)

Figure 71: Rigid X-56A: ROM (w/ negative steps) vs. CFD lift coefficient results (left) and ROM error (right) for forced pitching oscillation with 1 degree amplitude for $k = 0.05$ (top), 0.10 (middle), and 0.20 (bottom) at $\alpha_0 = 5°$, $\beta = 0°$, $M = 0.13$.

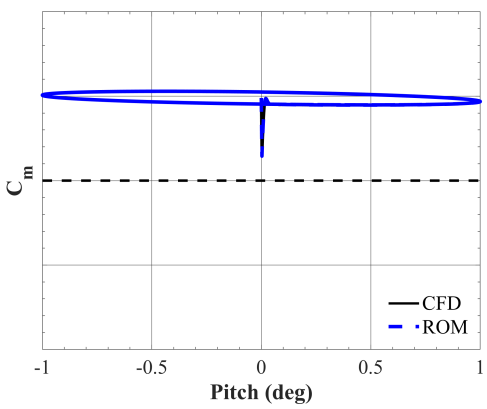

(a) Pitching moment coefficient ($k = 0.05$)

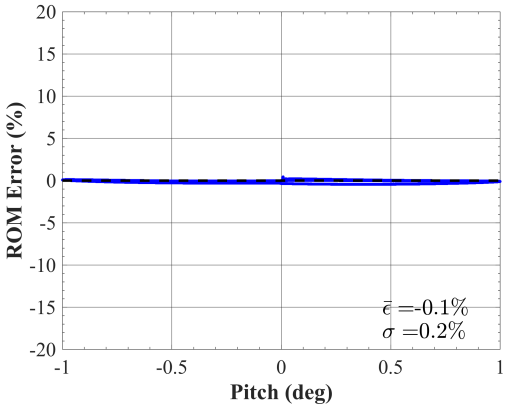

(b) ROM error ($k = 0.05$)

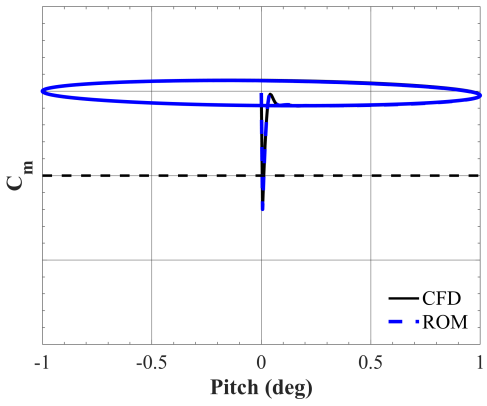

(c) Pitching moment coefficient ($k = 0.10$)

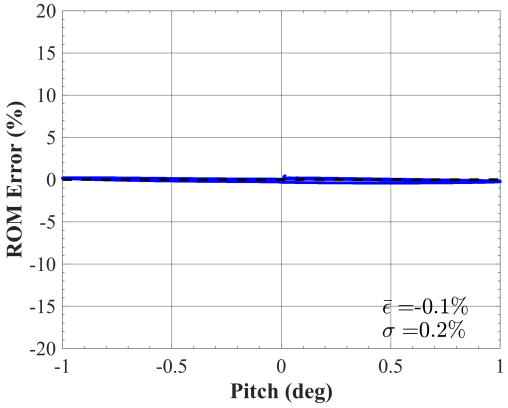

(d) ROM error ($k = 0.10$)

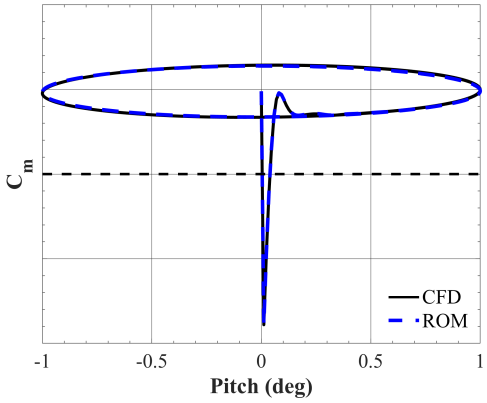

(e) Pitching moment coefficient ($k = 0.20$)

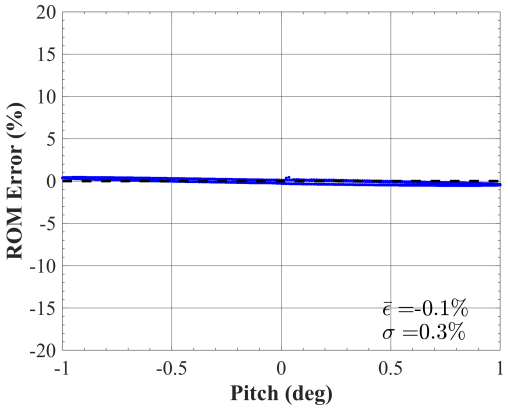

(f) ROM error ($k = 0.20$)

Figure 72: Rigid X-56A: ROM (w/ negative steps) vs. CFD pitching moment coefficient results (left) and ROM error (right) for pitching pitching oscillation with 1 degree amplitude for $k = 0.05$ (top), 0.10 (middle), and 0.20 (bottom) at $\alpha_0 = 5°$, $\beta = 0°$, $M = 0.13$.

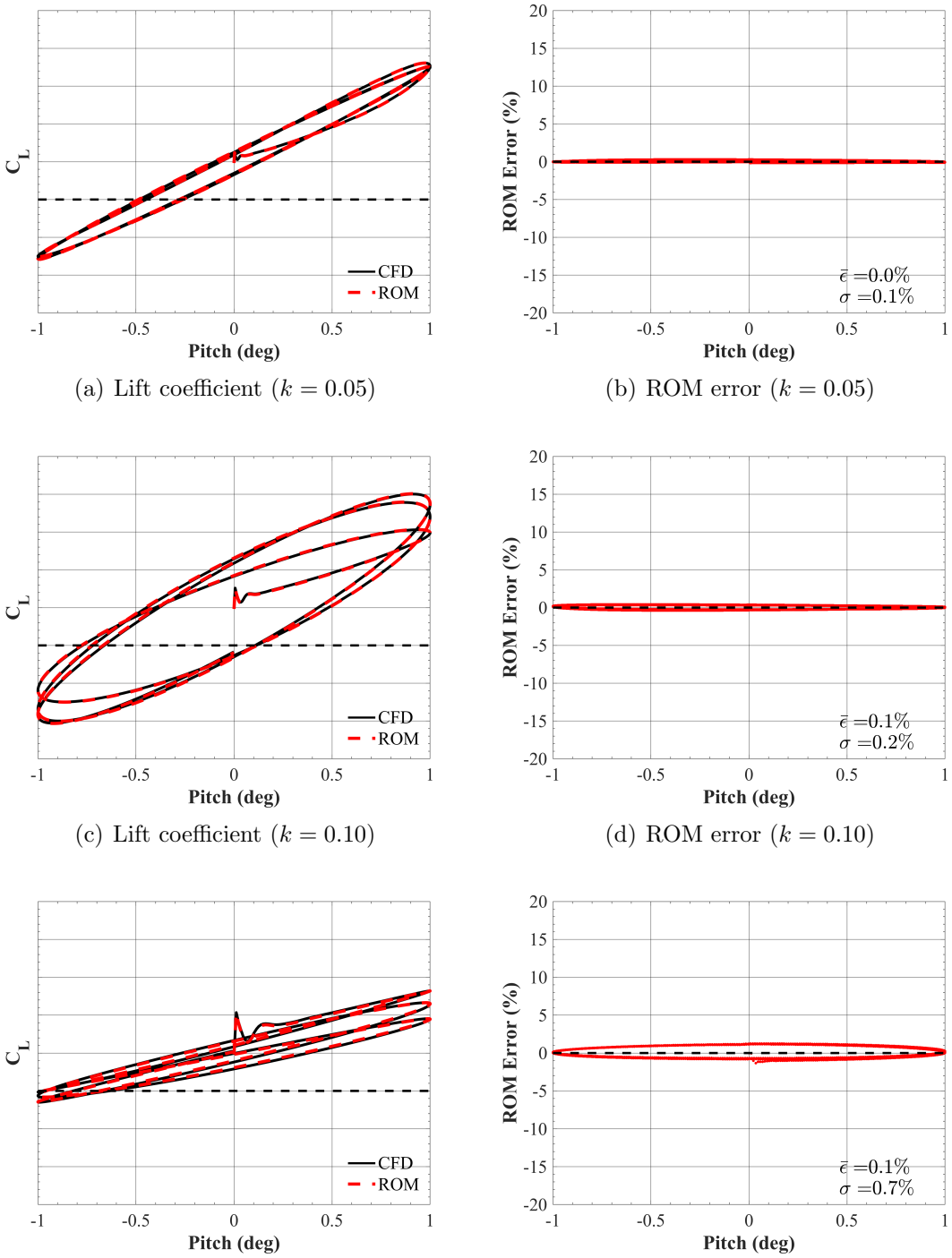

(a) Lift coefficient ($k = 0.05$)

(b) ROM error ($k = 0.05$)

(c) Lift coefficient ($k = 0.10$)

(d) ROM error ($k = 0.10$)

(e) Lift coefficient ($k = 0.20$)

(f) ROM error ($k = 0.20$)

Figure 73: Flexible X-56A: ROM (w/ negative steps) vs. CFD lift coefficient results (left) and ROM error (right) for forced pitching oscillation with 1 degree amplitude for $k = 0.05$ (top), 0.10 (middle), and 0.20 (bottom) at $\alpha_0 = 5°$, $\beta = 0°$, $M = 0.13$.

Figures 74 illustrates a comparison between CFD and ROM results (left) and the ROM prediction error (right) for each of the forced pitching oscillation cases (top to bottom) with respect to pitching moment coefficient for the flexible vehicle. Relative to the previous results in Fig. 70, the mean error changes from 0.7% to -0.3%, 0.3% to -0.1%, and 0.0% to -0.2% for the $k = 0.05$, $k = 0.10$, and $k = 0.20$ cases, respectively. The standard deviation changes from 1.2% to 0.4%, 0.7% to 0.3%, and 0.4% to 0.3% for the $k = 0.05$, $k = 0.10$, and $k = 0.20$ cases, respectively. Finally, it is observed that including negative step responses improves the ROM pitching moment coefficient predictions for the flexible vehicle as shown by a noticeable decrease in standard deviation. Additionally, the ROM error plots no longer show a strong overprediction at the negative angles of attack.

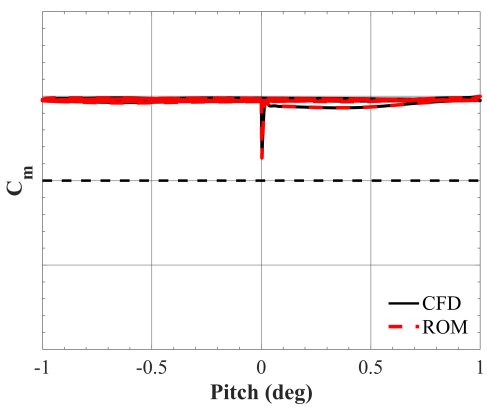

(a) Pitching moment coefficient ($k = 0.05$)

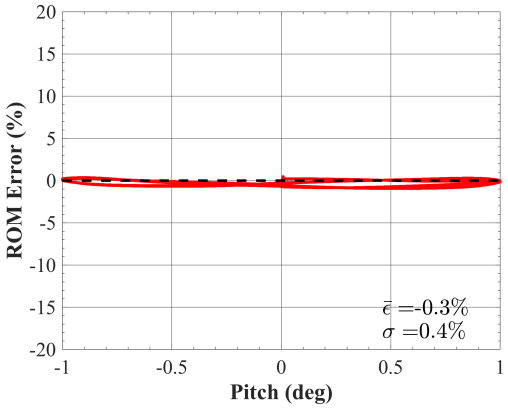

(b) ROM error ($k = 0.05$)

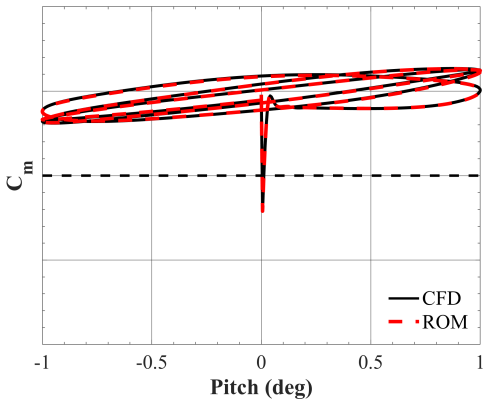

(c) Pitching moment coefficient ($k = 0.10$)

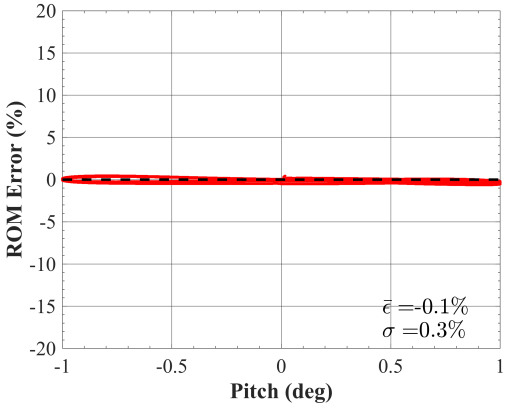

(d) ROM error ($k = 0.10$)

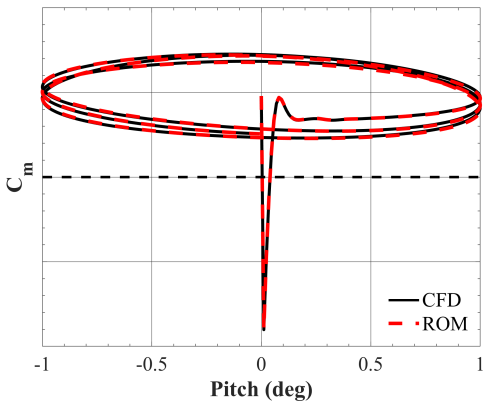

(e) Pitching moment coefficient ($k = 0.20$)

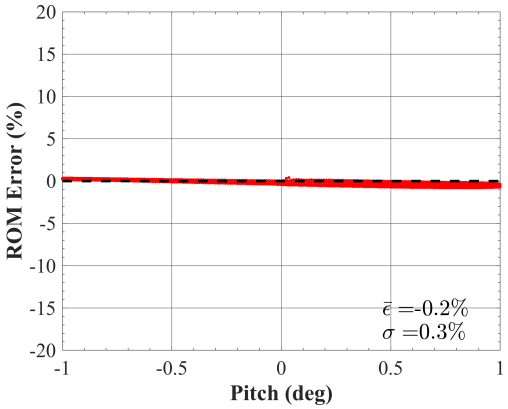

(f) ROM error ($k = 0.20$)

Figure 74: Flexible X-56A: ROM (w/ negative steps) vs. CFD pitching moment coefficient results (left) and ROM error (right) for forced pitching oscillation with 1 degree amplitude for $k = 0.05$ (top), 0.10 (middle), and 0.20 (bottom) at $\alpha_0 = 5°$, $\beta = 0°$, $M = 0.13$.

8.1.7 Summary

The present experiment sought to evaluate the unsteady aerodynamic prediction capabilities of the indicial response ROM method for flexible, maneuvering flight vehicles. This method leverages aeroelastic indicial responses due to step changes in longitudinal and lateral vehicle-state parameters to predict the response to arbitrary vehicle trajectories. These aeroelastic indicial responses were simulated using a coupled Euler-modal structural solver analysis. Such responses require more time steps compared to rigid simulations in order to allow for fluid-structure interactions to dampen in reaching a static aeroelastic state. Small-amplitude forced rolling, yawing, and pitching oscillations were selected as the test maneuvers in accordance with the use of a linear ROM.

This experiment demonstrated the prediction power of aeroelastic indicial response ROMs for single-plane motions at various reduced frequencies. While the differences between the rigid and aeroelastic forced oscillation simulations in the lateral planes (roll and yaw) were minimal, significant variations were shown in the forced pitching oscillation results. The aeroelastic hysteresis loops were characterized by cycle-to-cycle differences in aerodynamic damping and minimum and maximum coefficient values, which persisted for several cycles. This is attributed to the high degree of flexibility of the X-56A configuration in the longitudinal body-axis direction. For the unsteady case, the hysteresis loop maintained an elliptical shape. For slower motions, the vehicle structure has more time to deform toward a static aeroelastic state leading to more nonlinear and nonelliptical responses, even for small-amplitude motions. Using a single set of converged aeroelastic indicial responses at the initial condition, the ROM was capable of capturing the complex fluid-structure interactions present in CFD simulations at any frequency of interest with ROM prediction mean error and standard deviation consistently $< 1\%$. Marginal improvements were found when including negative step responses for ROM pitching moment predictions.

8.2 Experiment 2.2 - Nonlinear ROM (α) Evaluation

Experiment 2.2 addresses Research Question 2.2 and tests Hypothesis 2.2, both of which are restated below:

Research Question 2.2:
What are the unsteady aerodynamic ROM prediction capabilities for flexible flight vehicles maneuvering in nonlinear flight regimes?

Hypothesis 2.2: *With sufficient sampling of the flight space, a nonlinear aeroelastic indicial response ROM can resolve flow nonlinearities encountered up to stall angles of attack, where feasible response identification limits may be encountered.*

Experiment 2.1 demonstrated the ability of aeroelastic indicial responses to capture the frequency spectrum of fluid-structure interactions experienced with changes in the vehicle-state trajectory inputs. The aeroelastic indicial response ROM accurately predicts CFD-simulated unsteady aerodynamic forces and moments encountered by a flexible vehicle performing longitudinal and lateral forced oscillation motions at reduced frequencies ranging from quasisteady to unsteady levels. However, these oscillations were limited to small amplitudes to ensure a locally linear response with respect to the vehicle-state inputs.

Experiment 2.2 seeks to evaluate the prediction capabilities of a nonlinear aeroelastic indicial response ROM formulated to model the unsteady aerodynamic forces and moments of a flexible vehicle maneuvering across a wide range of angles of attack. Aeroelastic indicial responses are sampled at various angles of attack and simulated to form a database of time-accurate responses. For an arbitrary trajectory, defined in terms of $\alpha(t)$ and $q(t)$, this database of indicial responses is linearly interpolated to model the responses at each point in the trajectory. These interpolated responses are then convolved in the indicial response ROM to predict the unsteady aerodynamic

response for any maneuver defined within the limits of sampled angles of attack, at any frequency of interest.

Nonlinear indicial response ROMs have been shown in previous works [36, 38, 42] to provide accurate predictions compared to CFD simulations for rigid flight vehicles performing flight maneuvers across a wide range of angles of attack and Mach numbers. Ghoreyshi et al. [36] notes the primary limitation of the indicial response ROM methodology is in the evaluation of high incidence motions. Two problems are specified related to these motions: (1) the number of indicial responses required increases with aerodynamic nonlinearity and (2) the stability of CFD-calculated responses at large angles of attack.

The first problem relates more so to the ROM value over CFD simulations, as opposed to modeling capability. While the sampling requirements may increase for nonlinear portions of the flight envelope, these responses still encompass the frequency spectrum of the aerodynamic response and as such, could provide an increasing value relative to CFD simulations for an increase in the number of flight maneuvers to be evaluated. The second notion implies that responses that fail to reach converged steady-state values are incapable of being used in a convolution-based ROM. The results from Expt. 2.1 demonstrate that aeroelastic indicial responses are recovering complex, unsteady fluid-structure interactions that persist well-beyond the time required for convergence of rigid vehicle responses. Nonetheless, the corresponding aeroelastic indicial response ROM demonstrates an ability to resolve the complex fluid-structure interactions in full-order CFD maneuver simulations. Thus, it is expected that indicial responses at higher angles of attack are not necessarily 'unstable', but instead, capture physical flow unsteadiness for which a converged steady-state value is not expected. The problem then refocuses on the cost in sampling high angle-of-attack responses as dictated by the minimum simulation length required to model the motion state influence at a given angle of attack. Thus, it is expected

that aeroelastic indicial responses may be sampled at every angle of attack and successively used in the indicial response ROM for unsteady aerodynamic predictions across a wide range of angles of attack.

The primary limitation in this work relates to the ability of the CFD solver to properly deform the mesh without encountering negative volume errors, which would prevent response simulation at a given flight condition. Such problems may arise at large angles of attack or Mach numbers when the structural deformation may become significant. Regardless, the modal structural solver used in the present work is arbitrarily limited to small to moderate deflections. Coupling of the CFD flow solver to an FEM model may allow for identification of indicial responses for a greater portion of the expected flight envelope.

8.2.1 Purpose of Experiment

The following are identified as the main objectives of this numerical experiment:

1. Demonstrate the ability of aeroelastic nonlinear indicial response ROMs to accurately predict the unsteady aerodynamic response to longitudinal motions at any desired motion frequency across a sampled angle-of-attack range

2. Identify the predictive limitations of the original modeling formulation and provide extensions to modeling assumptions and/or sampling requirements, if necessary, for accurately predicting the unsteady aerodynamic responses for flexible flight vehicles.

8.2.2 Experiment Setup

The simulation framework outlined in Chapter 4 was used to generate full-order rigid and aeroelastic CFD solutions for the large-amplitude forced pitching oscillations as described in Section 6.4. Rigid and aeroelastic indicial responses were simulated with respect to the longitudinal vehicle-state parameters at the initial motion state using the best practices established in the Chapter 7. Motion files were generated for the forced oscillation and indicial response trajectories using the trajectory post-processing MATLAB code. Nonlinear ROM predictions were generated using the *CFD2ROM* MATLAB code.

Table 14 lists three forced pitch oscillation tests to be used in evaluating the nonlinear aeroelastic ROM's ability to capture the frequency spectrum within a nonlinear angle-of-attack range. For this evaluation, the flight space $\alpha = [0^\circ - 10^\circ]$ is to be sampled uniformly in 1 degree increments at the baseline flight condition. Indicial responses, one for each vehicle-state parameter, are simulated at each angle of attack to guarantee a rich sampling in evaluating the complete predictive capabilities of the nonlinear ROM.

Table 14: Nonlinear Model Tests: Forced Pitch Oscillation.

Case	α_0 (deg)	α_A	Reduced Frequency (k)
FOP-4	5	4	0.02
FOP-5	5	4	0.10
FOP-6	5	4	0.20

The surrogate modeling approach reviewed in Section 5.4 is used to interpolate among the sampled indicial responses, and the modeled indicial responses are then convolved with the motion history to make lift and pitching moment ROM predictions (Eq. 76) for oscillations of increasing motion rates. As was done with the linear model, the reduced frequencies range from quasisteady to unsteady values, which allows for

performance comparisons relative to the traditional stability derivative method. The mean angle of attack and pitch angle amplitude were chosen to be 5 degrees to ensure that each FO cover the entire prestall flight envelope.

8.2.3 Nonlinear ROM Generation

Experiment 2.2 seeks to evaluate the predictive capability of the aeroelastic nonlinear indicial response ROM at various reduced frequencies for longitudinal motions covering a wide range of angle of attack. Equation 16 represents the nonlinear reduced-order modeling formulation for longitudinal (C_j) unsteady aerodynamic predictions. The lift (C_L) and pitching moment (C_m) coefficients are a result of the steady-state contribution at the initial flight condition (C_{j_0}) and unsteady contributions due to changes in angle of attack (α) and pitch rate (q). In the nonlinear formulation, the indicial responses with respect to angle of attack (C_{j_α}) are now dependent on angle of attack. These responses are simulated as step changes in angle of attack at various initial angles of attack, α_i, such that $\alpha(t) = \alpha_i + 1$. A linear interpolation as a function of angle of attack is used to model the time-accurate responses at each point in the trajectory. These modeled responses are then used to generate traditional indicial response ROM unsteady aerodynamic predictions for nonlinear pitch oscillations using Eq. 76.

$$C_j(t) = C_{j_0} + \frac{d}{dt}\left[\int_0^t C_{j_\alpha}(t-\tau,\alpha)\alpha(\tau)d\tau\right] + \frac{d}{dt}\left[\int_0^t C_{j_q}(t-\tau)q(\tau)d\tau\right] \tag{76}$$

Table 15 defines the indicial responses simulated for the nonlinear ROM generation. Indicial responses due to step changes in angle of attack are simulated in one degree increments along the angle-of-attack range covered by the forced pitching oscillations using the traditional assumption of response symmetry about the mean angle of attack. Since pitch rate indicial responses are assumed to be linear, only a single indicial response is sampled at the initial flight condition, where $\alpha_0 = 5°$.

Table 15: Motion file inputs for creating indicial trajectories for nonlinear FO predictions ($t > 0$).

Indicial	α (deg)	β (deg)	ϕ (deg)	θ (deg)	ψ (deg)	M_0
α-step	6	0	0	0	0	0.13
α-step	7	0	0	0	0	0.13
α-step	8	0	0	0	0	0.13
α-step	9	0	0	0	0	0.13
α-step	10	0	0	0	0	0.13
q-step	5	0	0	$\Delta q \cdot t$	0	0.13

8.2.4 CFD Simulations

Forced pitching oscillations were prescribed starting from an initial angle of attack $\alpha_0 = 5^\circ$ with a pitch amplitude of $\Delta\theta = 4^\circ$ at $\beta = 0^\circ$, $M = 0.13$. Relative to Expt. 2.1, the amplitude was increased to four degrees to cover a wider angle-of-attack range for which static aerodynamics were previously characterized as nonlinear (Fig. 7.1). Figure 75 depicts the motion history for the forced pitching oscillations at reduced frequencies of $k = 0.05, 0.10$, and 0.20. Because the initial condition and simulated reduced frequencies are consistent between the forced pitching oscillations in Expts. 2.1 and 2.2, the same initialization solution and dynamic solution strategy was used in the present experiment. A characteristic time step of $s \approxeq 0.002$ was used to advance the solution in time and 20 subiterations were used to converge the solution in pseudotime. A summary of the temporal solution parameters can be found in Table 12 of Section 8.1.6.

The solution strategy proved to be robust in producing stable, well-converged dynamic simulations for both the rigid and flexible vehicle at every prescribed motion frequency. Examples of subiterative convergence for the $k = 0.20$ case are shown in Figures 76(a) and 76(b) for the rigid (top) and flexible (bottom) vehicle cases, respectively. The plots illustrate the order-of-magnitude convergence in the FUN3D time-accurate solution residual drop ($log(R/R_0)$) and the pitching moment coefficient (C_m) convergence versus fractional iterations. Iteration 136 is shown, which

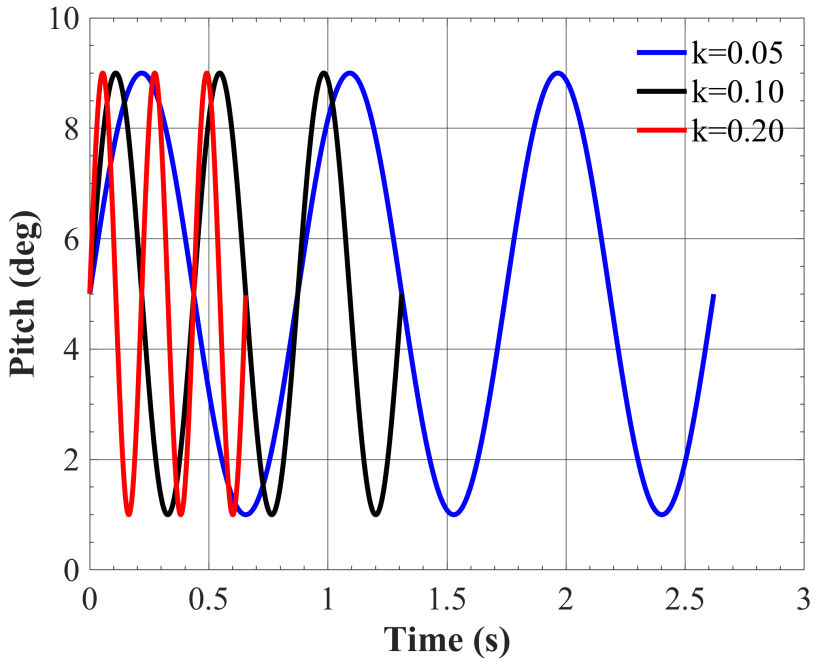

Figure 75: Motion history for forced pitching oscillations with 4 degree amplitude for $k = 0.05, 0.10$, and 0.20 at $\alpha_0 = 5°$, $\beta = 0°$, $M = 0.13$.

coincides with the positive peak pitch amplitude during the first oscillation cycle, where each point signifies the convergence achieved at each of the 20 subiterations. The rigid simulation presents over 8-orders of convergence in residual drop with sufficient convergence in the pitching moment coefficient, based on a 0.0002% difference between the final two subiterations. Similar levels of convergence were achieved in the aeroelastic simulation. While not illustrated here, similar convergence behavior was observed for the $k = 0.10$ and $k = 0.05$ cases.

Figure 77 illustrates the FUN3D simulation lift and pitching moment coefficient results for the rigid vehicle undergoing forced pitching oscillations with 4 degree amplitude for $k = 0.05, 0.10$, and 0.20 at $\alpha_0 = 5°$, $\beta = 0°$, $M = 0.13$. The lift and pitching moment coefficient trends are similar to those observed for the 1 degree amplitude oscillation (Fig. 65) from the previous experiment, but with a slight increase in aerodynamic damping as illustrated by a relative widening of the hysteresis loops.

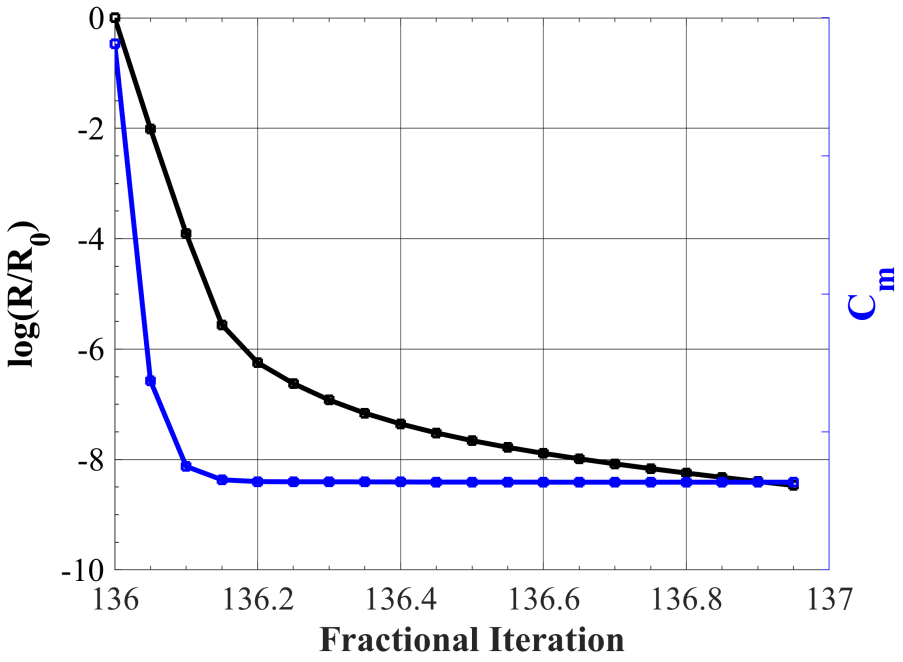

(a) Rigid

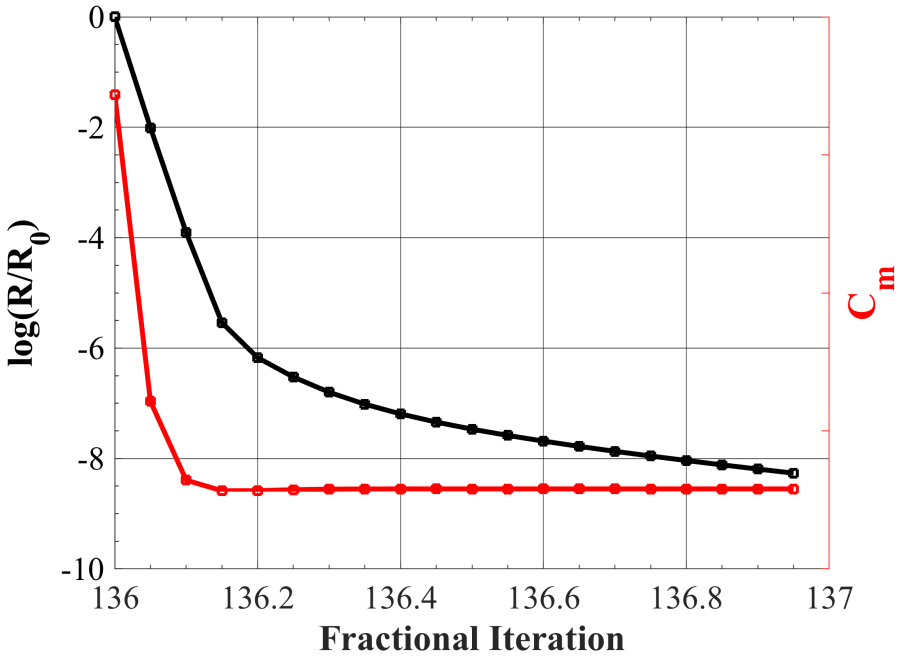

(b) Flexible

Figure 76: X-56A: FUN3D subiterative convergence for forced pitching oscillation with 4 degree amplitude, $k = 0.20$ at $\alpha_0 = 5°$, $M = 0.13$ for the rigid (blue) and flexible (red) cases. Iteration 136 - peak pitch amplitude within first oscillation cycle.

For each reduced frequency, fairly elliptical hysteresis loops are observed despite oscillating over a wider angle-of-attack range, indicating a fairly linear relationship between the aerodynamic response and angle of attack. This result is supported by the static characterization plots shown in Fig. 24 of Section 7.1. In these plots, the static lift and pitching moment curves depict a mostly linear aerodynamic response for $\alpha = [0^\circ$ to $10^\circ]$. In contrast, the lift and pitching moment curves for the flexible vehicle illustrate a nonlinearity over the same range.

Figure 78 illustrates the FUN3D results for the flexible vehicle undergoing forced pitching oscillations with a four degree amplitude for $k = 0.05, 0.10$, and 0.20 at the same initial condition. The range of plotted lift and pitching moment coefficient values was defined consistently between the rigid and flexible cases to allow for better comparisons. As initially shown in Expt 2.1, the aeroelastic lift and pitching moment hysteresis loops vary from cycle-to-cycle in terms of aerodynamic damping (width) and minimum and maximum coefficient values (rotation).

The lift responses appear to be qualitatively similar to the flexible results obtained for the one degree oscillations presented in Expt 2.1 (Fig. 66). The primary difference with the larger amplitude motion is an overall increase in aerodynamic damping as shown by a relative widening of the hysteresis loops, as well as a nonlinear distortion of the loop at minimum and maximum pitch angles. These nonliearities are observed for the smaller reduced frequencies as well. In the $k = 0.05$ case, the aerodynamic damping changes drastically between the upper and lower angle-of-attack ranges. For the slower-varying motions, the aeroelastic response has more time to converge toward steady-state where structural deformation is a maximum.

A comparison of the pitching moment responses for the one and four degree amplitude pitching motions shows a similar trend. At the higher reduced frequency ($k = 0.20$), the same initial transient response and cycle-to-cycle variations are observed, but over a wider range of coefficient values due to the increase in pitching

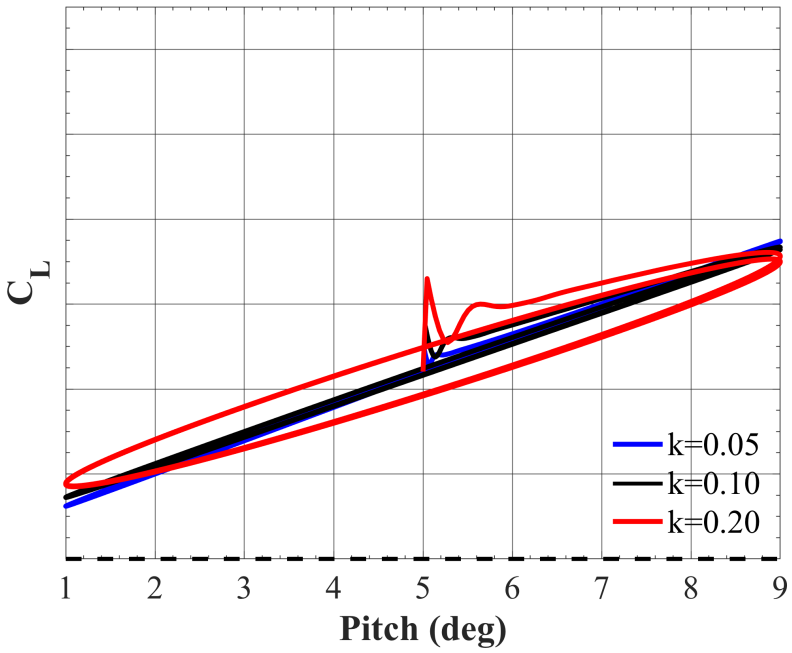

(a) Lift coefficient

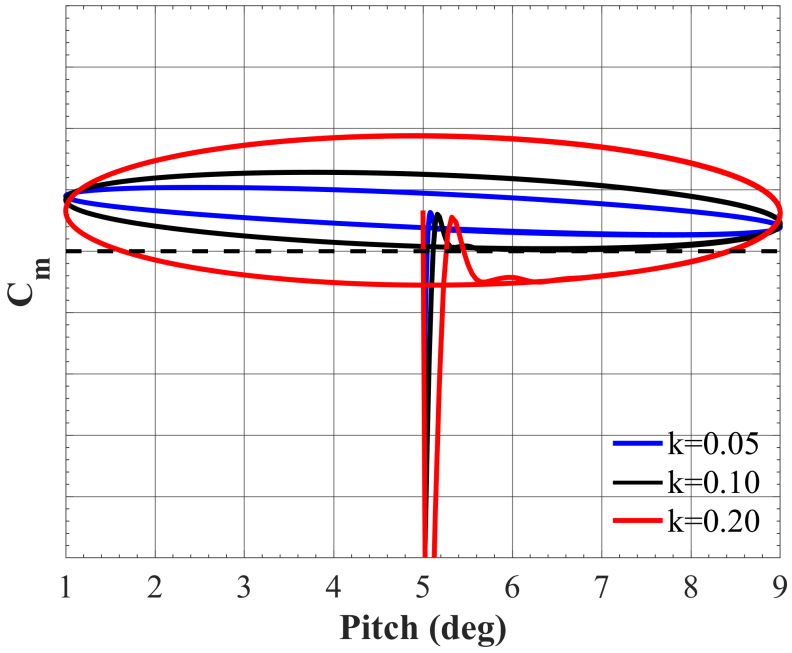

(b) Pitching moment coefficient

Figure 77: Rigid X-56A: FUN3D simulation results for forced pitching oscillations with 4 degree amplitude for $k = 0.05, 0.10$, and 0.20 at $\alpha_0 = 5°$, $M = 0.13$.

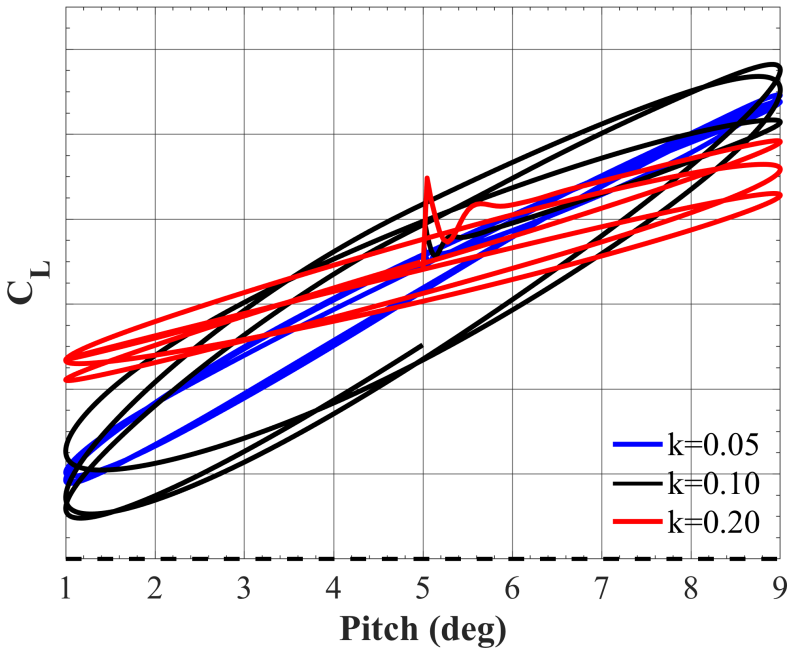

(a) Lift coefficient

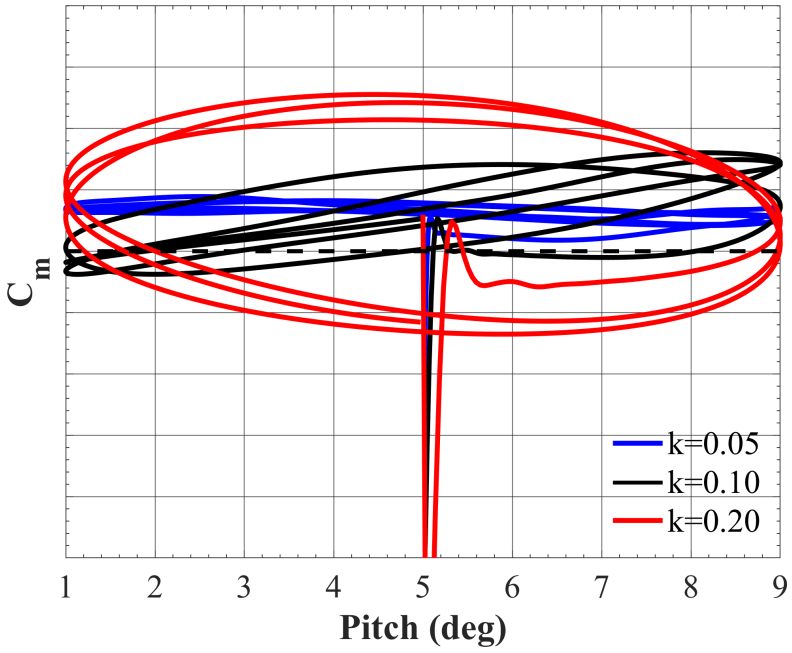

(b) Pitching moment coefficient

Figure 78: Flexible X-56A: FUN3D simulation results for forced pitching oscillations with 4 degree amplitude for $k = 0.05, 0.10$, and 0.20 at $\alpha_0 = 5°$, $M = 0.13$.

amplitude and a widening of the hysteresis loops. Even in the lower frequency case, the same nonlinear behavior resulting from the complex fluid-structure interactions is observed with an additional decrease in the aerodynamic damping during the upswing motion of the forced oscillation. Furthermore, the hysteresis loops are now characterized by a slightly nonlinear mean variation over the transversed pitch range. Overall, distinct differences are observed in the aerodynamic responses for larger amplitude forced oscillations, which require nonlinear modeling.

8.2.5 ROM Predictions

8.2.5.1 Linear ROM

Figure 79 illustrates a comparison between CFD and linear ROM results (left) and the ROM prediction error (right) for each of the forced pitching oscillation cases (top to bottom) with respect to lift coefficient for the rigid vehicle. The ROM predictions show great qualitative agreement with CFD simulation results, correctly resolving the initial transient response and the hysteresis loop widening with successive increases in reduced frequency. Quantitatively, the ROM error is characterized by a mean error and standard deviation of $< 1\%$ across all simulated reduced frequencies. These results reinforce the applicability of the linear ROM for unsteady lift predictions of the rigid vehicle oscillating from $\alpha = [0^\circ \text{ to } 10^\circ]$.

Figure 80 presents the same plots with respect to pitching moment coefficient for the rigid vehicle. The ROM predictions are in great qualitative agreement with CFD simulations, correctly resolving the initial transient response and the hysteresis loop widening/rotation with increases in reduced frequency. Again, the mean error and its standard deviation remain $< 1\%$ for each frequency. Overall, the linear ROM predicts the unsteady lift and pitching moment coefficients with comparable accuracy to full-order simulations of the large-amplitude forced oscilations.

Figure 81 presents the CFD and linear ROM results (left) and the ROM prediction error (right) for each of the forced pitching oscillation cases (top to bottom) with

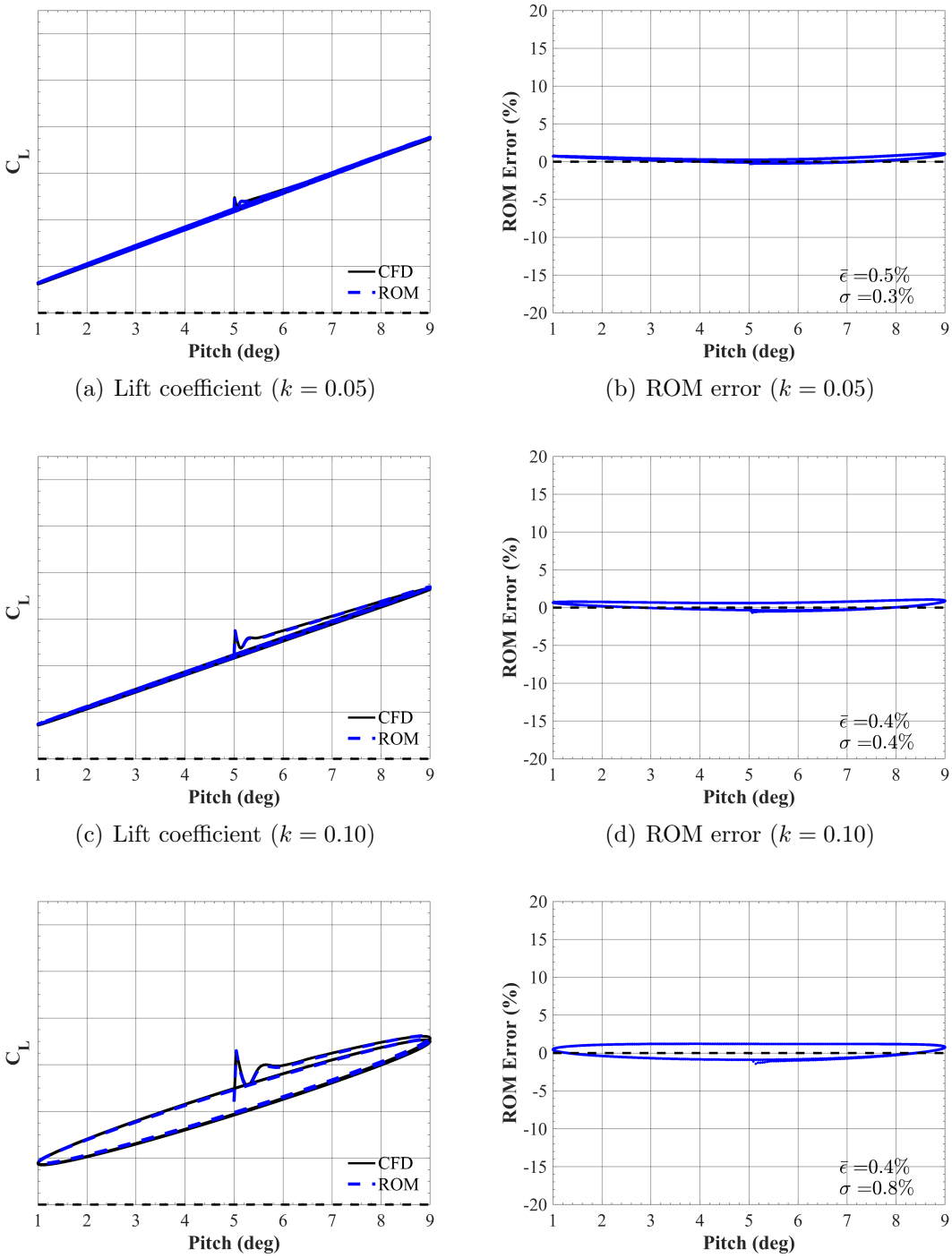

(a) Lift coefficient ($k = 0.05$)

(b) ROM error ($k = 0.05$)

(c) Lift coefficient ($k = 0.10$)

(d) ROM error ($k = 0.10$)

(e) Lift coefficient ($k = 0.20$)

(f) ROM error ($k = 0.20$)

Figure 79: Rigid X-56A: Linear ROM vs. CFD lift coefficient results (left) and ROM error (right) for forced pitching oscillation with 4 degree amplitude for $k = 0.05$ (top), 0.10 (middle), and 0.20 (bottom) at $\alpha_0 = 5°$, $\beta = 0°$, $M = 0.13$.

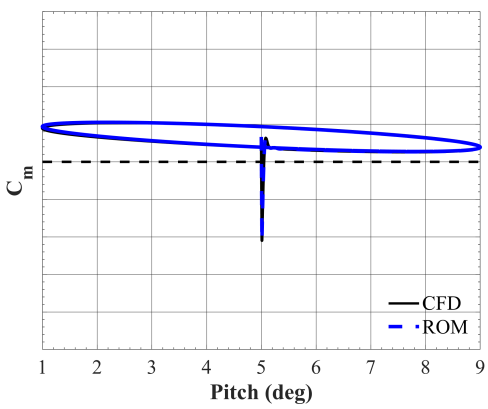

(a) Pitching moment coefficient ($k = 0.05$)

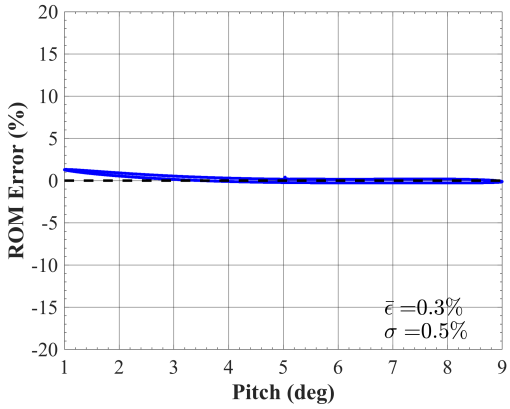

(b) ROM error ($k = 0.05$)

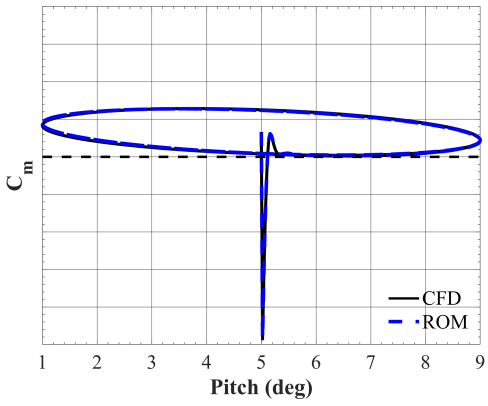

(c) Pitching moment coefficient ($k = 0.10$)

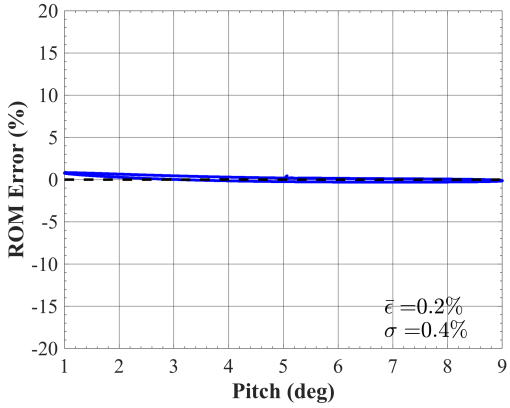

(d) ROM error ($k = 0.10$)

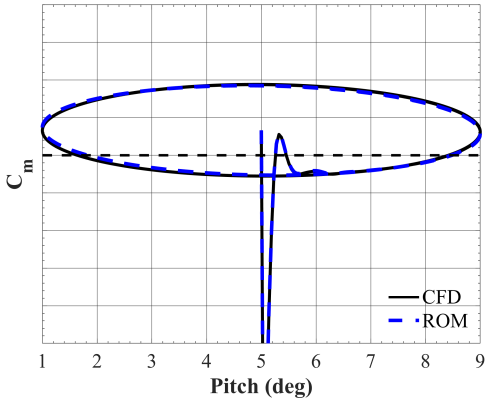

(e) Pitching moment coefficient ($k = 0.20$)

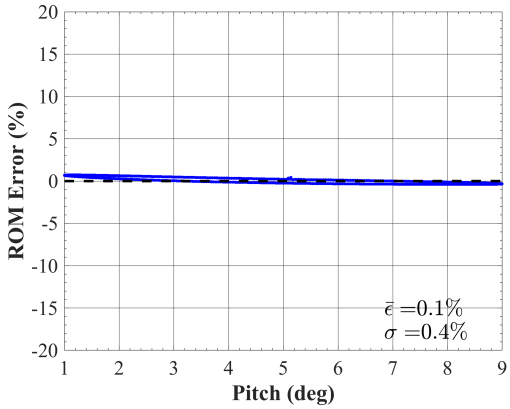

(f) ROM error ($k = 0.20$)

Figure 80: Rigid X-56A: Linear ROM vs. CFD pitching moment coefficient results (left) and ROM error (right) for forced pitching oscillation with 4 degree amplitude for $k = 0.05$ (top), 0.10 (middle), and 0.20 (bottom) at $\alpha_0 = 5°$, $\beta = 0°$, $M = 0.13$.

respect to lift coefficient for the flexible vehicle. In the $k = 0.05$ case, the ROM fails to capture the observed nonlinear variations with slight overpredictions across all pitch angles, resulting in a mean error of 1.4% and standard deviation of 1.0%. As the reduced frequency is increased to $k = 0.10$, the linear ROM does capture the qualitative shape of the hysteresis loop, but continues to overpredict, especially at higher angles of attack. In this case, the mean error and standard deviation remains are 3.1% and 1.7%, respectively. At $k = 0.20$, the linear ROM noticeably overpredicts at the lower and higher angles of attack, with a mean error of 3.0% and standard deviation of 2.6%. As expected, the nonlinear features of the lift coefficient time history for the large-amplitude pitching oscillations are not adequately predicted with the linear ROM.

Figure 82 presents the CFD and linear ROM results (left) and the ROM prediction error (right) for each of the forced pitching oscillation cases (top to bottom) with respect to pitching moment coefficient for the flexible vehicle. In the $k = 0.20$ case, the linear ROM matches the CFD simulations fairly well with $< 1\%$ mean error and standard deviation. In the $k = 0.10$ case, the linear ROM continues to show general agreement with CFD simulations. Only slight underprediction is observed at the higher angles of attack with the mean error and standard deviation remaining $< 1\%$. At the quasisteady frequency, the accuracy of the linear ROM predictions begins to deteriorate with a mean error of -1.4% and a standard deviation of 2.2%. The ROM generally underpredicts the pitching moment coefficient across the entire angle-of-attack range with the maximum error at the minimum and maximum angles of attack.

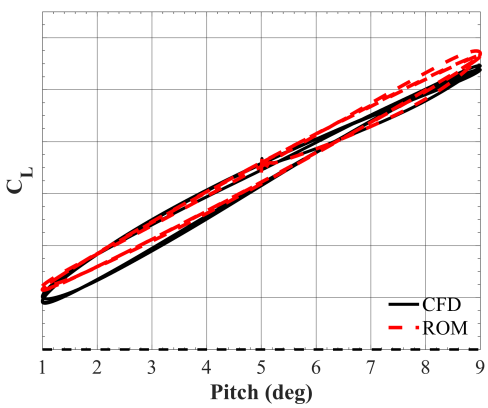

(a) Lift coefficient ($k = 0.05$)

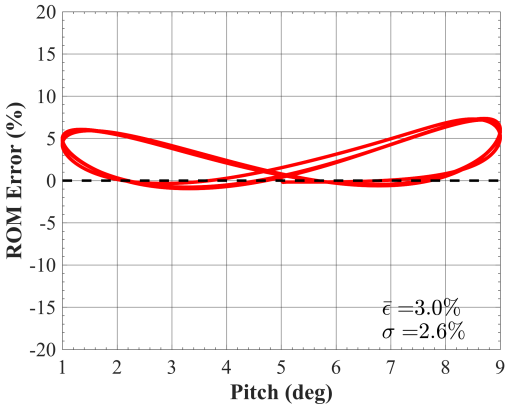

(b) ROM error ($k = 0.05$)

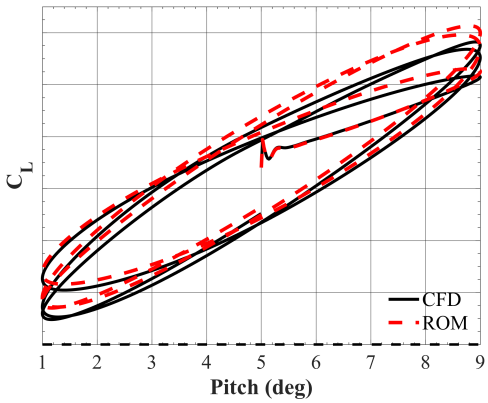

(c) Lift coefficient ($k = 0.10$)

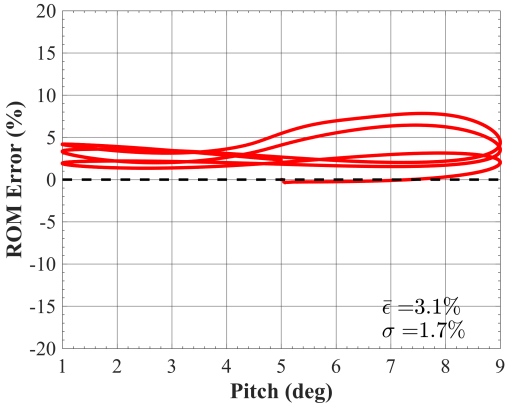

(d) ROM error ($k = 0.10$)

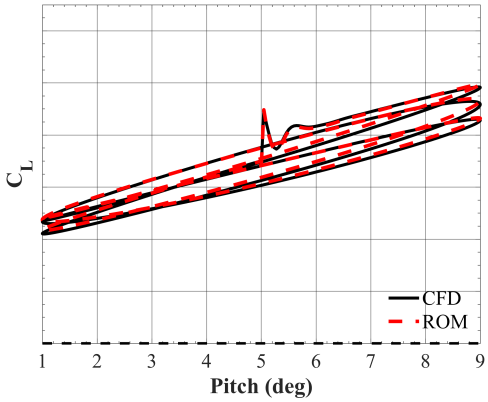

(e) Lift coefficient ($k = 0.20$)

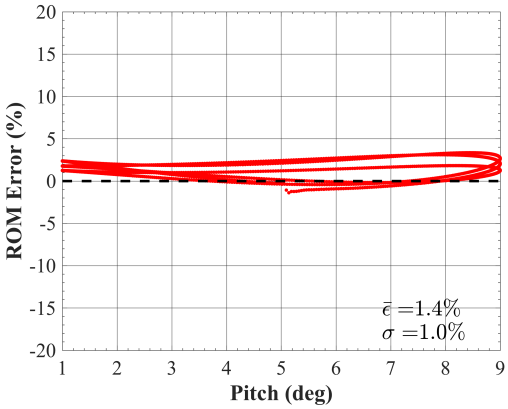

(f) ROM error ($k = 0.20$)

Figure 81: Flexible X-56A: Linear ROM vs. CFD lift coefficient results (left) and ROM error (right) for forced pitching oscillation with 4 degree amplitude for $k = 0.05$ (top), 0.10 (middle), and 0.20 (bottom) at $\alpha_0 = 5°$, $\beta = 0°$, $M = 0.13$.

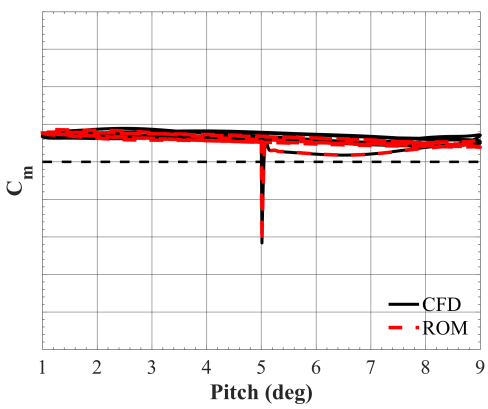

(a) Pitching moment coefficient ($k = 0.05$)

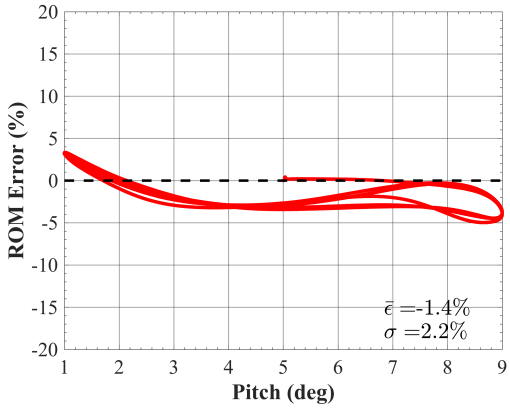

(b) ROM error ($k = 0.05$)

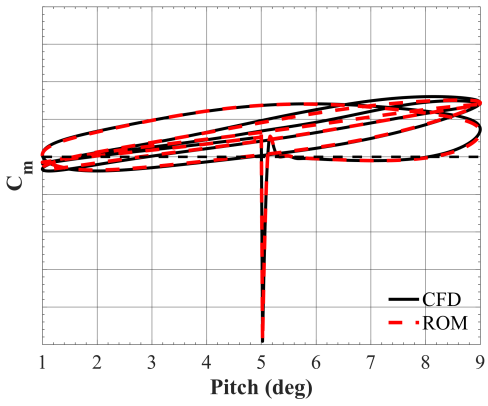

(c) Pitching moment coefficient ($k = 0.10$)

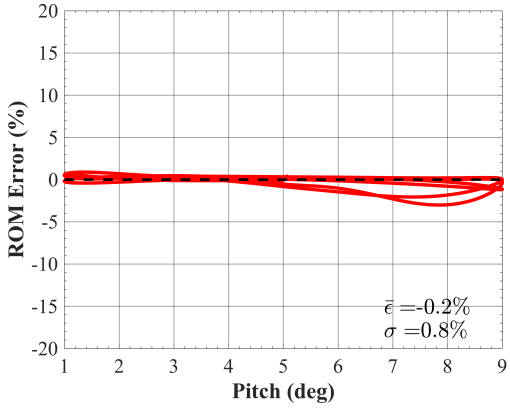

(d) ROM error ($k = 0.10$)

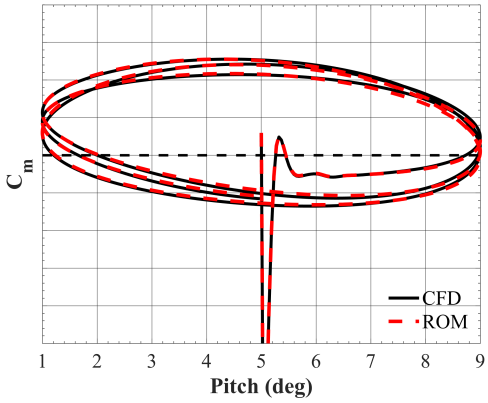

(e) Pitching moment coefficient ($k = 0.20$)

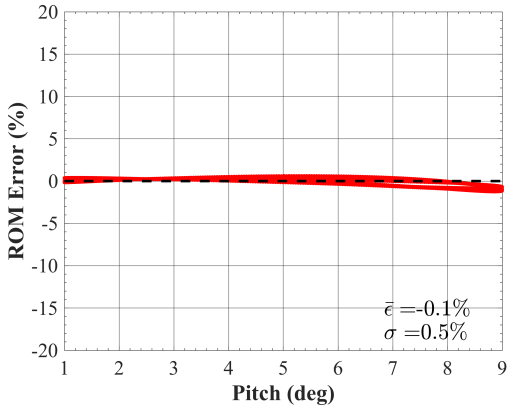

(f) ROM error ($k = 0.20$)

Figure 82: Flexible X-56A: Linear ROM vs. CFD pitching moment coefficient results (left) and ROM error (right) for forced pitching oscillation with 4 degree amplitude for $k = 0.05$ (top), 0.10 (middle), and 0.20 (bottom) at $\alpha_0 = 5°$, $\beta = 0°$, $M = 0.13$.

8.2.5.2 Nonlinear ROM (α) - Positive Steps

The current subsection evaluates the nonlinear ROM generated using the indicial responses sampled from $\alpha = [5^\circ$ to $9^\circ]$, as defined by Table 15. While negligible improvements are expected for the rigid vehicle, nonlinear ROM results are included to quantify the modeling accuracy gained and observe the ROM error trends when including a nonlinear sampling of the angle-of-attack space.

Figure 83 illustrates the CFD and nonlinear ROM results (left) and the ROM prediction error (right) for each of the forced pitching oscillation cases (top to bottom) with respect to lift coefficient for the rigid vehicle. In the $k = 0.05$ case, the mean error remains constant relative to the linear results (Fig. 79) while the standard deviation increases from 0.3% to 0.7%. This increase in standard deviation can be attributed to a greater overprediction at $\alpha = 1^\circ$. Because the symmetry of indicial responses is assumed, the slight nonlinearities encountered near $\alpha = 9^\circ$ are propagated in the model to the lower angle-of-attack range. By including these nonlinearities, a reduction in modeling error is observed for $\alpha(t) > \alpha_0$. These trends are found for each reduced frequency. Similar findings are shown for the nonlinear ROM pitching moment predictions in Fig. 84.

Figure 85 illustrates the CFD and nonlinear ROM results (left) and the ROM prediction error (right) for each of the forced pitching oscillation cases (top to bottom) with respect to lift coefficient for the flexible vehicle. In the $k = 0.20$ case, the same decrease in modeling error are observed for $\alpha(t) > \alpha_0$ while an increase in ROM error is found for $\alpha(t) < \alpha_0$. This change in ROM error behavior is also attributed to the assumption of symmetric indicial responses about the mean angle of attack. As a result the mean error reduces from 1.4% to 1.0%, whereas the standard deviation increases from 1.0% to 1.3%. As reduced frequency is decreased to $k = 0.10$, the ROM error at the lower angle-of-attack range shows a significant increase from $< 5\%$ to approximately 10%. This overprediction at negative angles of attack tends to

bias the modeling error at positive angles of attack as the ROM error begins to recover. The ROM shows an improvement in modeling accuracy during the first half of the first oscillation cycle when $\alpha(t) > \alpha_0$. Overall, the mean error remains relatively constant, and the standard deviation increases from 1.7% to 3.7%. At the quasisteady frequency, the 'infinity' pattern shown in the linear ROM error plot (Fig. 81) is reduced such that an overprediction is primarily confined to $\alpha(t) < \alpha_0$. The nonlinear ROM generally captures the variation in aerodynamic damping and hysteresis loop slope in the positive angle-of-attack range. Regardless, the mean error remains constant between the linear and nonlinear ROM while the standard deviation, biased by the negative angles of attack, increases from 2.6% to 4.3%.

Figure 86 illustrates the CFD and nonlinear ROM results (left) and the ROM prediction error (right) for each of the forced pitching oscillation cases (top to bottom) with respect to lift coefficient for the flexible vehicle. In the $k = 0.20$ case, the elliptical hysteresis loops were generally captured by the linear ROM (Fig. 82) and continue to be reasonably modeled by the nonlinear ROM with a mean error and standard deviation remaining $< 1\%$. In the $k = 0.10$ case, the nonlinear ROM shows good agreement with the CFD results, decreasing the -0.2% mean error obtained with the linear ROM to zero. The propagation of nonlinearity at positive angles of attack to the lower angle-of-attack range acts to increase the ROM error, which leads to a slight increase in standard deviation from 0.8% to 1.1%. Finally, the nonlinear ROM pitching moment predictions for the quasisteady case show negligible differences with respect to the mean error and standard deviation. However, the ROM error plot shows an ability of the ROM to better capture the response for $\alpha(t) > \alpha_0$. At lower angles of attack, the symmetry of step response assumptions serves to cause an underprediction of the pitching moment coefficient. These results, along with those shown for the rigid vehicle, illustrate the importance of including negative step responses for prediction ranges where nonlinearity in the static aerodynamic coefficients is observed.

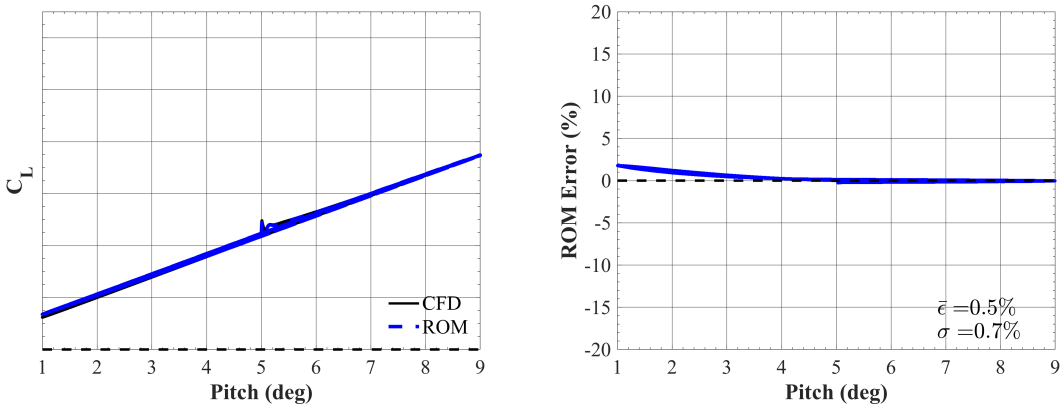

(a) Lift coefficient ($k = 0.05$) (b) ROM error ($k = 0.05$)

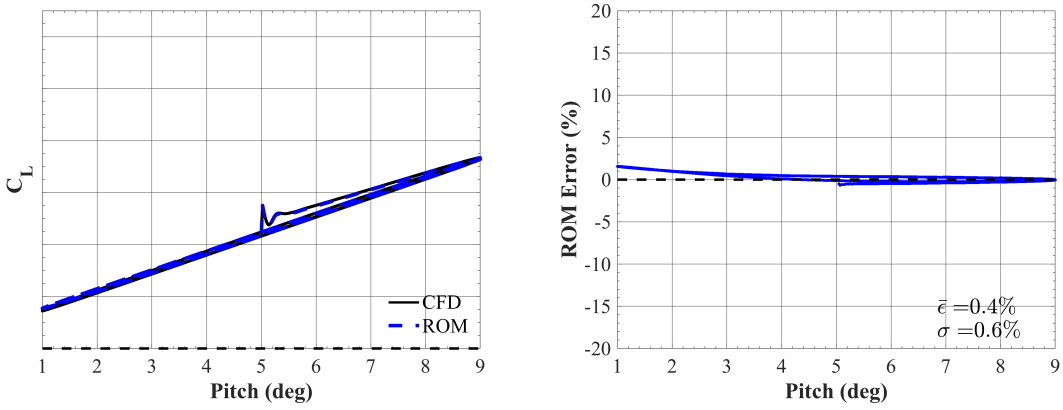

(c) Lift coefficient ($k = 0.10$) (d) ROM error ($k = 0.10$)

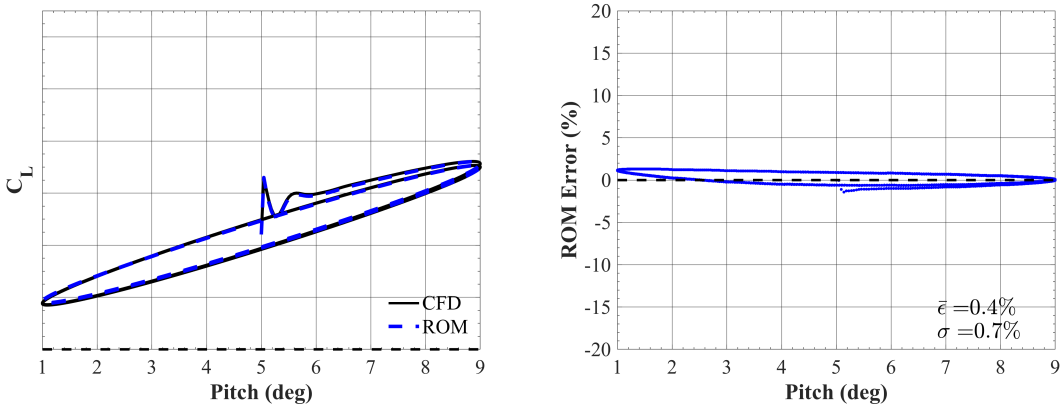

(e) Lift coefficient ($k = 0.20$) (f) ROM error ($k = 0.20$)

Figure 83: Rigid X-56A: Nonlinear ROM vs. CFD lift coefficient results (left) and ROM error (right) for forced pitching oscillation with 4 degree amplitude for $k = 0.05$ (top), 0.10 (middle), and 0.20 (bottom) at $\alpha_0 = 5°$, $\beta = 0°$, $M = 0.13$.

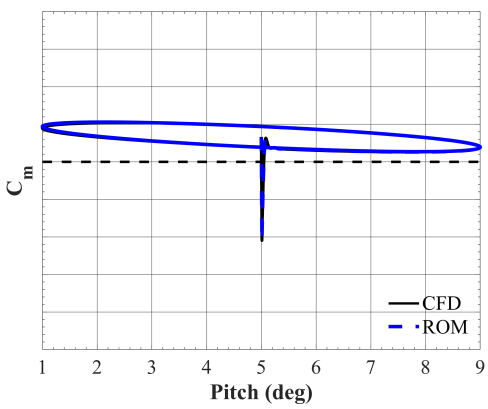

(a) Pitching moment coefficient ($k = 0.05$)

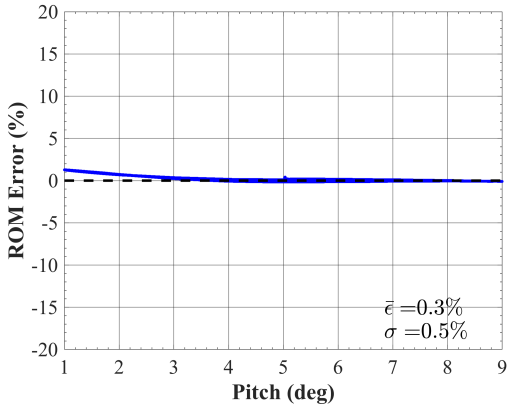

(b) ROM error ($k = 0.05$)

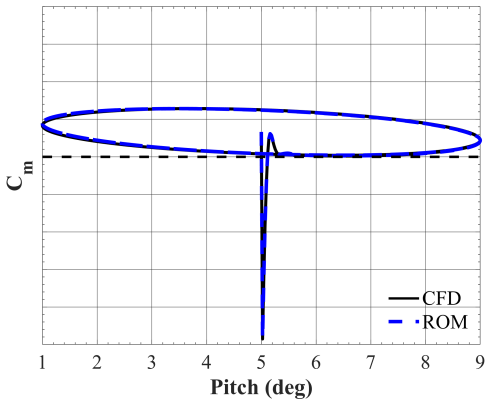

(c) Pitching moment coefficient ($k = 0.10$)

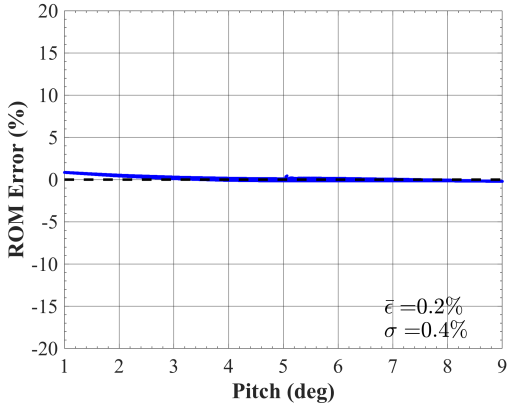

(d) ROM error ($k = 0.10$)

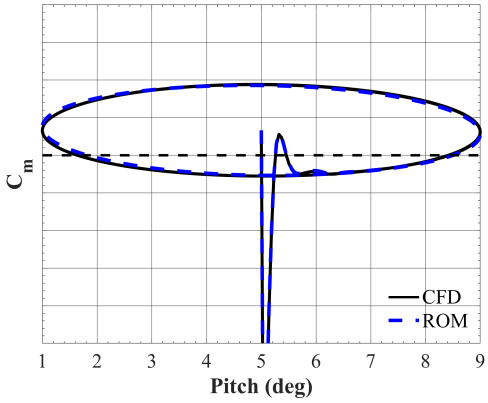

(e) Pitching moment coefficient ($k = 0.20$)

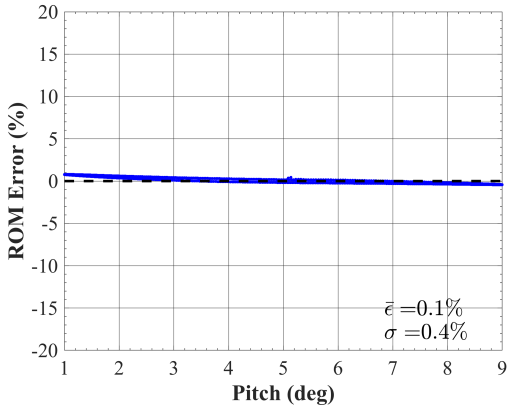

(f) ROM error ($k = 0.20$)

Figure 84: Rigid X-56A: Nonlinear ROM vs. CFD pitching moment coefficient results (left) and ROM error (right) for forced pitching oscillation with 4 degree amplitude for $k = 0.05$ (top), 0.10 (middle), and 0.20 (bottom) at $\alpha_0 = 5°$, $\beta = 0°$, $M = 0.13$.

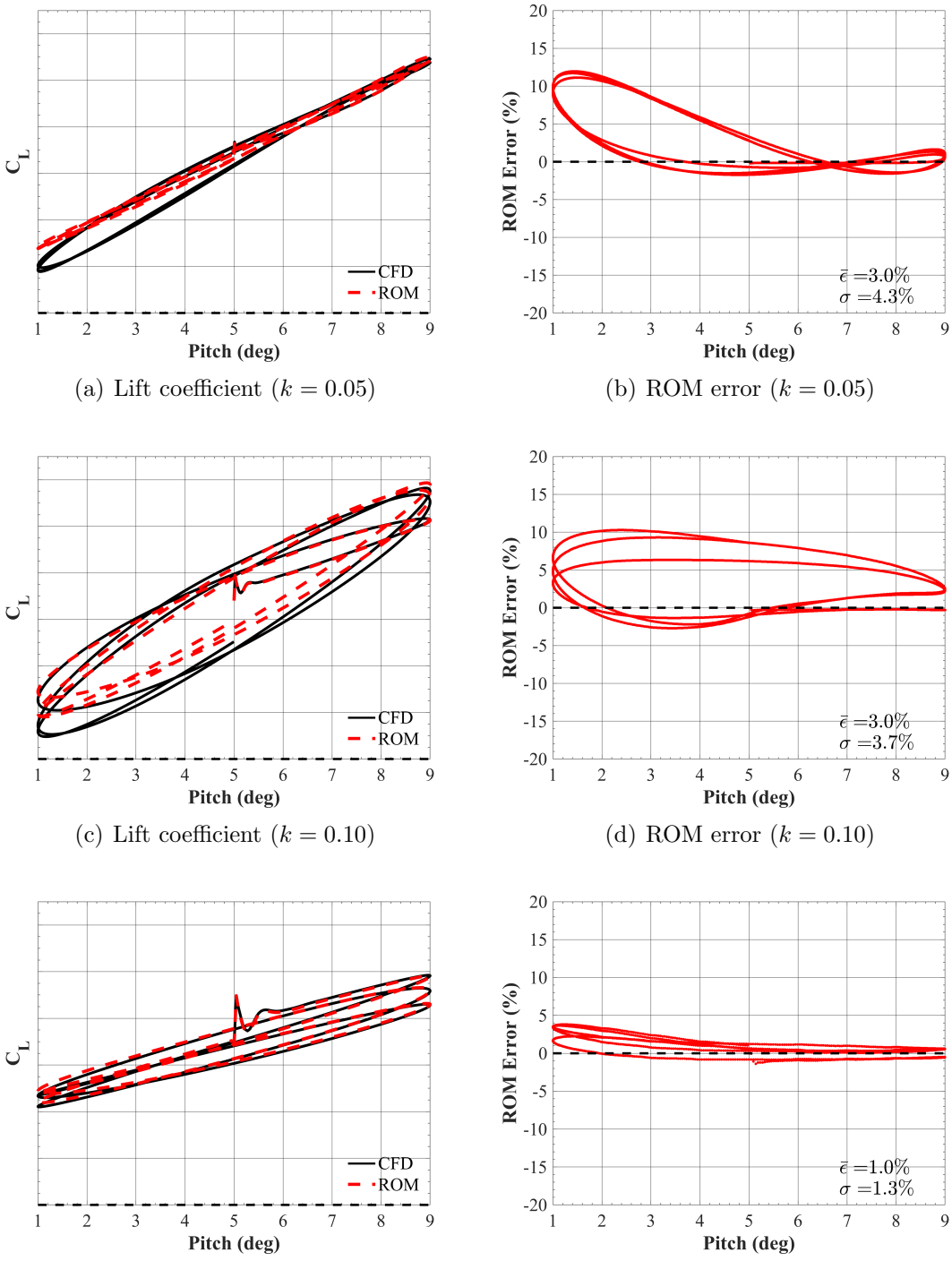

(a) Lift coefficient ($k = 0.05$)

(b) ROM error ($k = 0.05$)

(c) Lift coefficient ($k = 0.10$)

(d) ROM error ($k = 0.10$)

(e) Lift coefficient ($k = 0.20$)

(f) ROM error ($k = 0.20$)

Figure 85: Flexible X-56A: Nonlinear ROM vs. CFD lift coefficient results (left) and ROM error (right) for forced pitching oscillation with 4 degree amplitude for $k = 0.05$ (top), 0.10 (middle), and 0.20 (bottom) at $\alpha_0 = 5°$, $\beta = 0°$, $M = 0.13$.

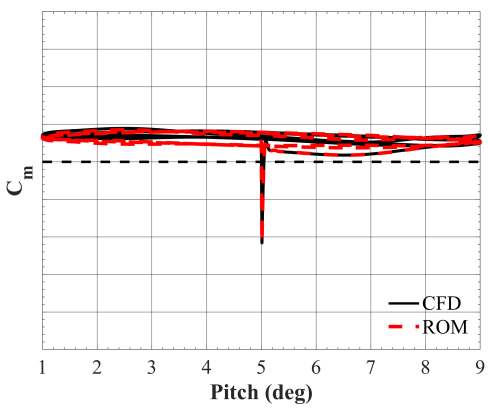

(a) Pitching moment coefficient ($k = 0.05$)

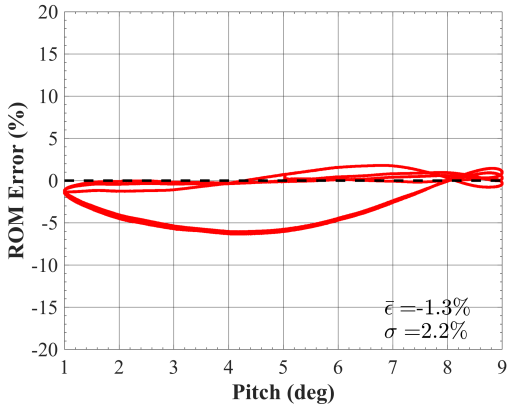

(b) ROM error ($k = 0.05$)

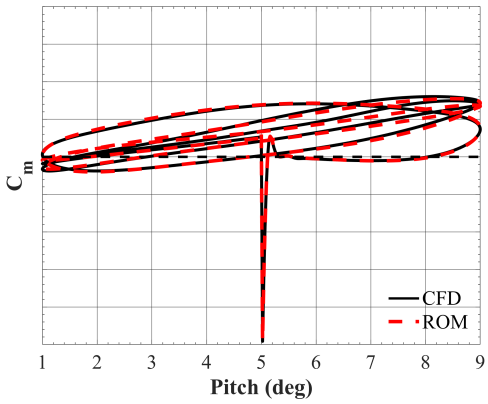

(c) Pitching moment coefficient ($k = 0.10$)

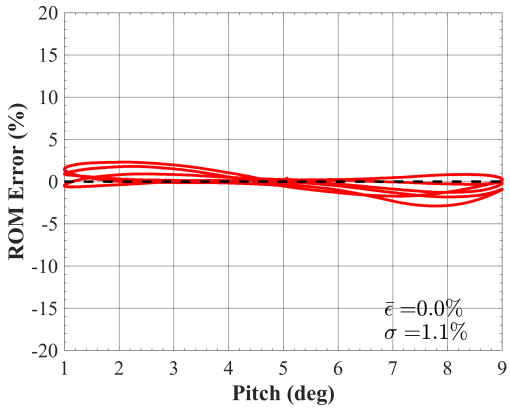

(d) ROM error ($k = 0.10$)

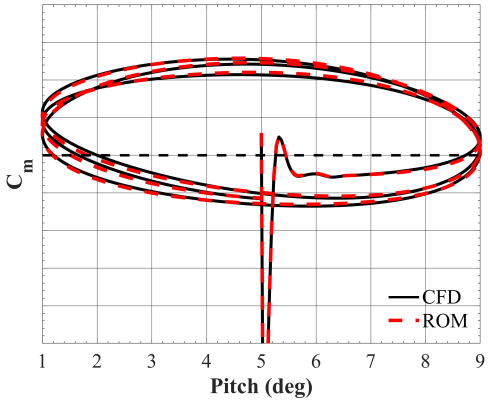

(e) Pitching moment coefficient ($k = 0.20$)

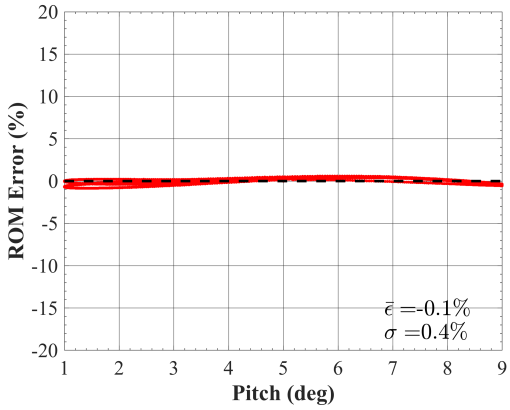

(f) ROM error ($k = 0.20$)

Figure 86: Flexible X-56A: Nonlinear ROM vs. CFD pitching moment coefficient results (left) and ROM error (right) for forced pitching oscillation with 4 degree amplitude for $k = 0.05$ (top), 0.10 (middle), and 0.20 (bottom) at $\alpha_0 = 5°$, $\beta = 0°$, $M = 0.13$.

8.2.5.3 Nonlinear ROM (α) - Adding Negative Steps

The current subsection evaluates the nonlinear ROM generated using the indicial responses sampled from $\alpha = [5^\circ$ to $9^\circ]$, as defined by Table 15, in addition to negative step responses for $\alpha < \alpha_0$, i.e., $\alpha = [1^\circ$ to $5^\circ]$. Table 16 defines the motion file inputs for creating negative angle-of-attack and pitch rate step functions. For the nonlinear ROM, negative angle-of-attack steps are sampled beginning from the initial angle of attack, $\alpha = 5^\circ$, down to the lowest angle of attack encountered during the large-amplitude forced pitching oscillation. Because pitch rate is traditionally assumed to be independent of angle of attack, a single negative pitch rate step is simulated at the initial/mean angle of attack. The nonlinear ROM then uses negative angle-of-attack step responses for $\alpha(t) < \alpha_0$ and positive angle-of-attack step responses for $\alpha(t) > \alpha_0$ to better capture the nonlinearities across the entire angle-of-attack range. The negative pitch rate step responses are utilized when $q(t) < 0$.

Table 16: Motion file inputs for creating negative step indicial trajectories for nonlinear FO predictions ($t > 0$).

Indicial	α (deg)	β (deg)	ϕ (deg)	θ (deg)	ψ (deg)	M_0
neg. α-step	1	0	0	0	0	0.13
neg. α-step	2	0	0	0	0	0.13
neg. α-step	3	0	0	0	0	0.13
neg. α-step	4	0	0	0	0	0.13
neg. q-step	5	0	0	$-\Delta q \cdot t$	0	0.13

Figure 87 shows the CFD and nonlinear ROM (including negative steps) results (left) and the ROM prediction error (right) for each of the forced pitching oscillation cases (top to bottom) with respect to lift coefficient for the rigid vehicle. Relative to the traditional nonlinear ROM (Figure 83), the ROM error for each reduced frequency is reduced in the negative angle-of-attack range, resulting in a low-magnitude symmetric error loop across the transversed angle-of-attack range. In each case, the mean error and standard deviation show improvements. The same general trends are observed for the pitchiing moment coefficient predictions illustrated in Fig. 88.

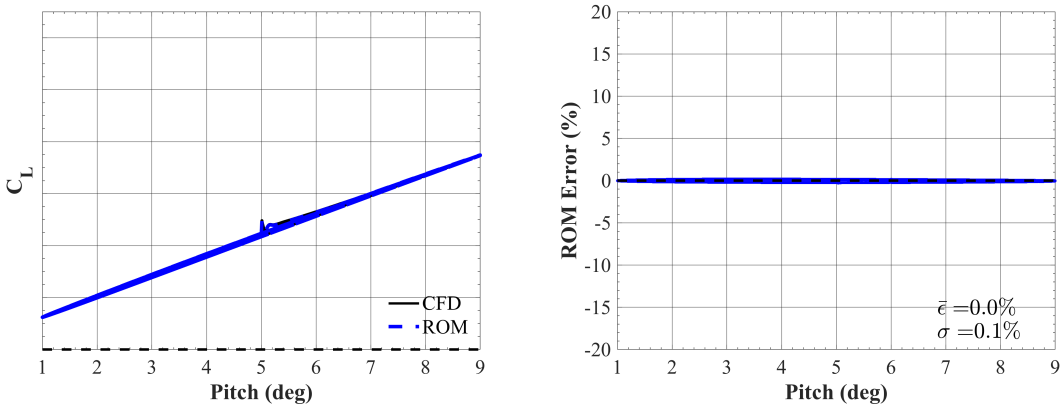

(a) Lift coefficient ($k = 0.05$)

(b) ROM error ($k = 0.05$)

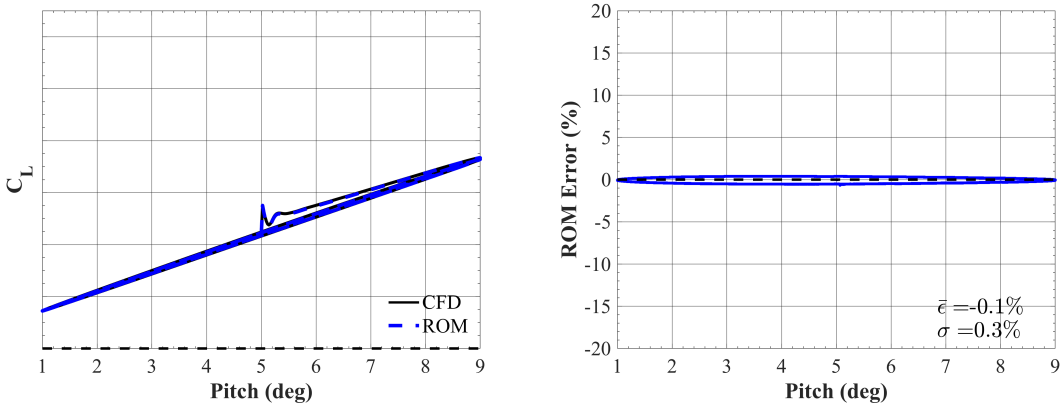

(c) Lift coefficient ($k = 0.10$)

(d) ROM error ($k = 0.10$)

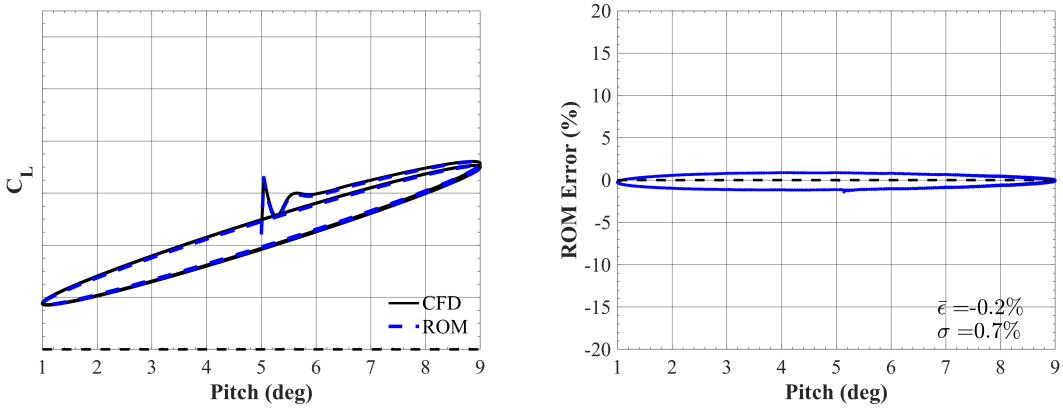

(e) Lift coefficient ($k = 0.20$)

(f) ROM error ($k = 0.20$)

Figure 87: Rigid X-56A: Nonlinear ROM with negative steps vs. CFD lift coefficient results (left) and ROM error (right) for forced pitching oscillation with 4 degree amplitude for $k = 0.05$ (top), 0.10 (middle), and 0.20 (bottom) at $\alpha_0 = 5°$, $\beta = 0°$, $M = 0.13$.

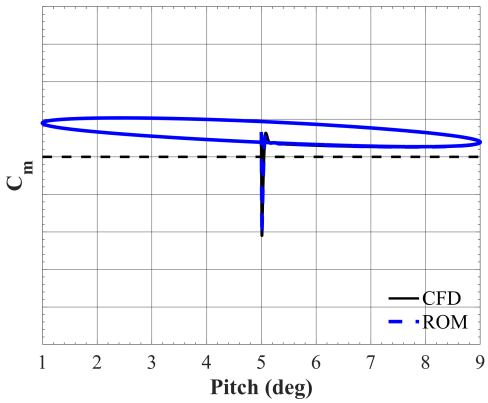

(a) Pitching moment coefficient ($k = 0.05$)

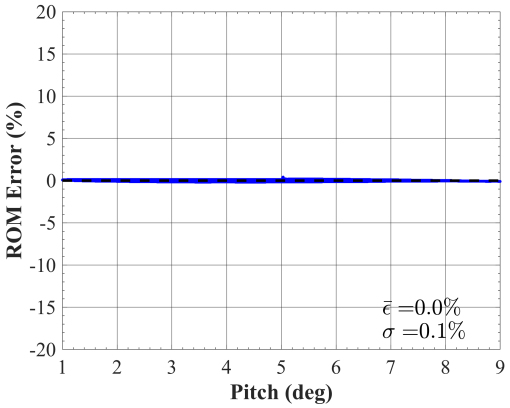

(b) ROM error ($k = 0.05$)

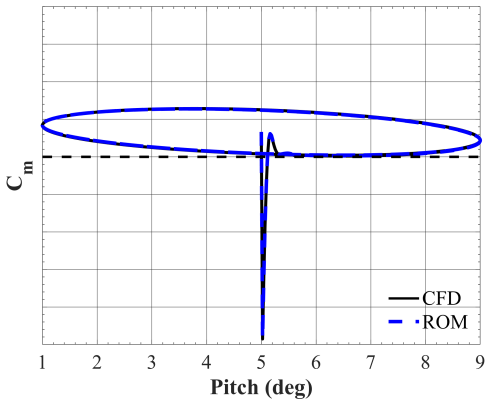

(c) Pitching moment coefficient ($k = 0.10$)

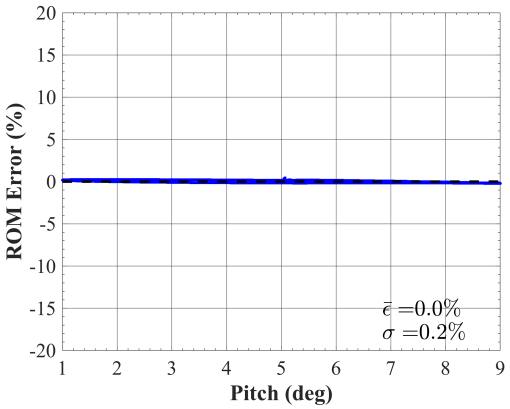

(d) ROM error ($k = 0.10$)

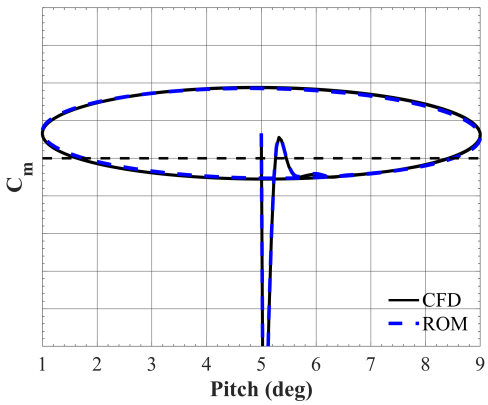

(e) Pitching moment coefficient ($k = 0.20$)

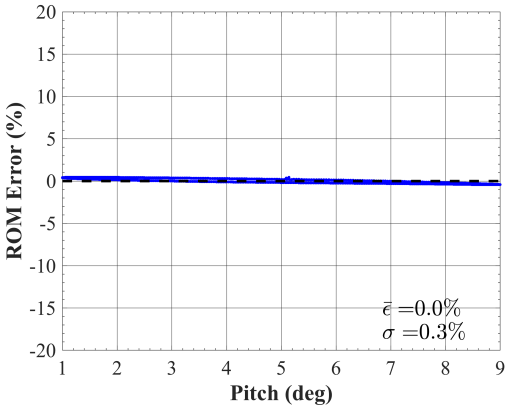

(f) ROM error ($k = 0.20$)

Figure 88: Rigid X-56A: Nonlinear ROM with negative steps vs. CFD pitching moment coefficient results (left) and ROM error (right) for forced pitching oscillation with 4 degree amplitude for $k = 0.05$ (top), 0.10 (middle), and 0.20 (bottom) at $\alpha_0 = 5°$, $\beta = 0°$, $M = 0.13$.

Figure 89 shows the CFD and nonlinear ROM (including negative steps) results (left) and the ROM prediction error (right) for each of the forced pitching oscillation cases (top to bottom) with respect to lift coefficient for the flexible vehicle. Relative to the nonlinear ROM using only positive steps (Fig. 85), the ROM predictions in the $k = 0.05$ and $k = 0.10$ cases show a drastic improvement in predicting the unsteady aerodynamic lift coefficient over three forced pitching oscillation cycles. The cycle-to-cycle differences in aerodynamic damping and minimum and maximum coefficient values are captured across the entire angle-of-attack range. For $k = 0.05$, the mean error and standard deviation decrease from 3.0% and 4.3% to 0.1% and 0.9%, respectively. Similar reductions are observed in the $k = 0.10$ case. For the unsteady $k = 0.20$ case, the nonlinear ROM predictions generally degrade when including negative step responses. Relative to CFD simulations, the ROM underpredicts the unsteady lift coefficient across the entire angle-of-attack range, shifting the mean error from 1.0% to -3.2%.

Figure 90 shows the CFD and nonlinear ROM (including negative steps) results (left) and the ROM prediction error (right) for each of the forced pitching oscillation cases (top to bottom) with respect to pitching moment coefficient for the flexible vehicle. Relative to the nonlinear ROM using only positive steps (Fig. 86), the ROM predictions in the $k = 0.05$ and $k = 0.10$ cases show a noticeable improvement in predicting the unsteady aerodynamic lift coefficient over three forced pitching oscillation cycles. The ROM error loops decrease in magnitude and show no strong bias toward positive or negative angles of attack. In the $k = 0.05$ case, the mean error decreases in magnitude from -1.3% to 0.2% while the standard deviation decreases from 2.2% to 0.9%. In the $k = 0.10$ case, the mean error does slightly increase from 0.0% to 0.5%, but the standard deviation decreases from 1.1% to 0.7%. Finally, the unsteady case shows negligible changes in modeling accuracy with a mean error change from -0.1% to 0.2% and a standard deviation increase from 0.4% to 0.6%.

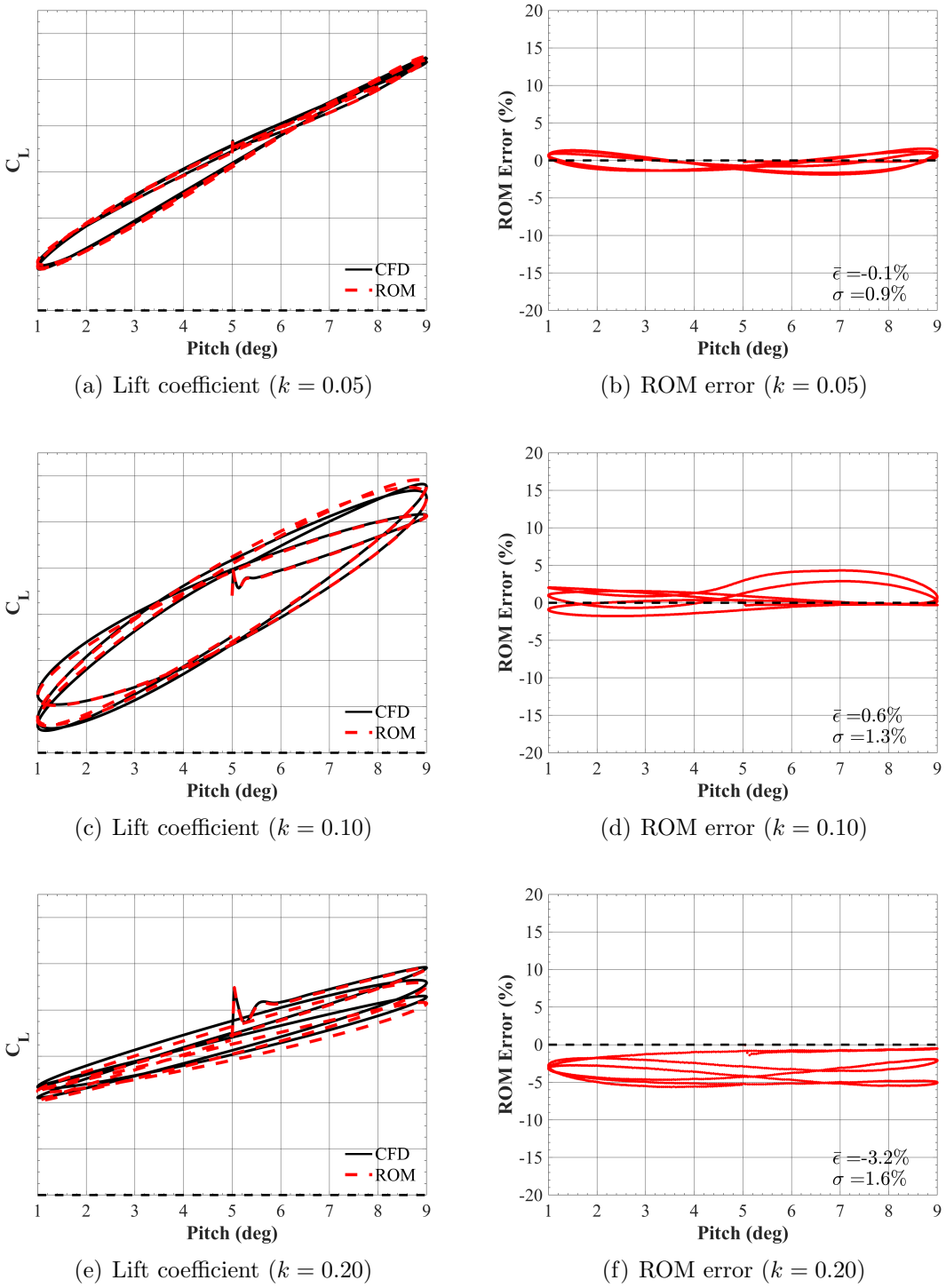

(a) Lift coefficient ($k = 0.05$)

(b) ROM error ($k = 0.05$)

(c) Lift coefficient ($k = 0.10$)

(d) ROM error ($k = 0.10$)

(e) Lift coefficient ($k = 0.20$)

(f) ROM error ($k = 0.20$)

Figure 89: Flexible X-56A: Nonlinear ROM with negative steps vs. CFD lift coefficient results (left) and ROM error (right) for forced pitching oscillation with 4 degree amplitude for $k = 0.05$ (top), 0.10 (middle), and 0.20 (bottom) at $\alpha_0 = 5°$, $\beta = 0°$, $M = 0.13$.

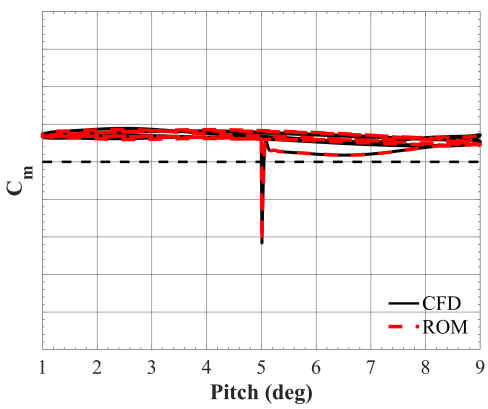

(a) Pitching moment coefficient ($k = 0.05$)

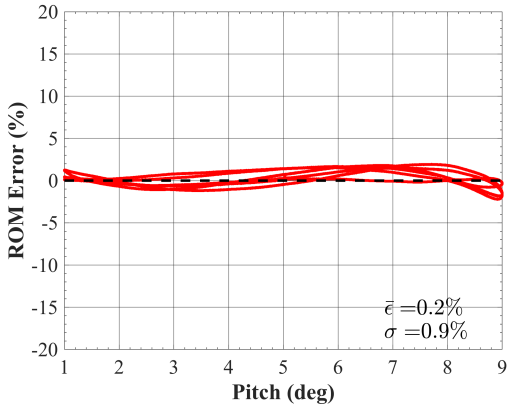

(b) ROM error ($k = 0.05$)

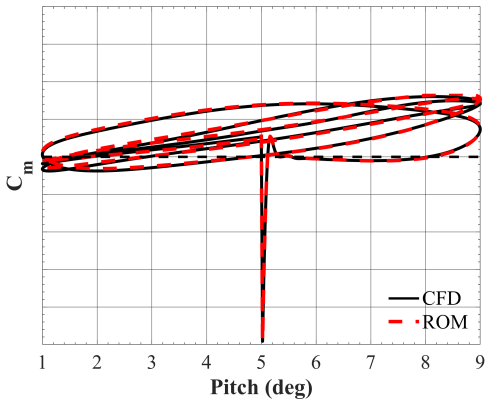

(c) Pitching moment coefficient ($k = 0.10$)

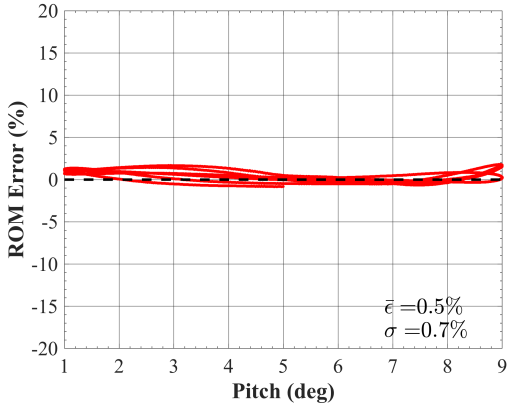

(d) ROM error ($k = 0.10$)

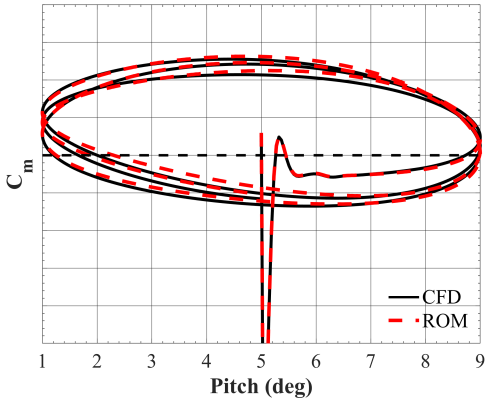

(e) Pitching moment coefficient ($k = 0.20$)

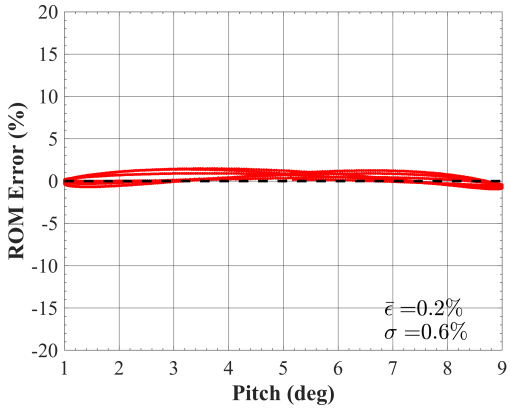

(f) ROM error ($k = 0.20$)

Figure 90: Flexible X-56A: Nonlinear ROM with negative steps vs. CFD pitching moment coefficient results (left) and ROM error (right) for forced pitching oscillation with 4 degree amplitude for $k = 0.05$ (top), 0.10 (middle), and 0.20 (bottom) at $\alpha_0 = 5°$, $\beta = 0°$, $M = 0.13$.

The aeroelastic ROM predictions depict an overall increase in modeling accuracy when including negative angle-of-attack and pitch rate indicial responses. For the quasisteady and quasiunsteady reduced frequencies, the lift and pitching moment coefficient responses are predicted with mean errors of $< 1\%$ and no remaining error bias in the lower angle-of-attack range. For the unsteady case, the ROM predictions generally degrade when including negative step responses, especially for the lift coefficient. The ROM lift coefficient prediction underpredicts across the entire angle-of-attack range relative to CFD simulations, and slightly overpredicts the pitching moment coefficient. Because modeling improvements were found at the lower reduced frequencies, these modeling discrepancies in the $k = 0.20$ case may be attributed to modeling inaccuracies relative to pitch rate, which is greatest in magnitude for the unsteady case.

8.2.5.4 Nonlinear ROM (α) - Including α Dependency for Pitch Rate

The present subsection investigates the nonlinear ROM accuracy when considering an angle-of-attack dependency for the pitch rate indicial responses. For the previous nonlinear ROM predictions, positive and negative angle-of-attack steps across the angle-of-attack range were utilized, in addition to a single positive and negative step response with respect to pitch rate at the mean angle of attack. Table 17 defines the motion file inputs for creating pitch rate step functions as a function of angle of attack. The updated nonlinear ROM then uses positive and negative angle-of-attack and pitch rate responses to better capture the nonlinearities across the entire angle-of-attack range.

Table 17: Motion file inputs for creating pitch rate indicial trajectories for nonlinear FO predictions ($t > 0$).

Indicial	α (deg)	β (deg)	ϕ (deg)	θ (deg)	ψ (deg)	M_0
q-step	1-4, 6-9	0	0	$\Delta q \cdot t$	0	0.13
neg. q-step	1-4, 6-9	0	0	$-\Delta q \cdot t$	0	0.13

Figure 91 illustrates the CFD and nonlinear ROM (included dependency for pitch rate responses) results (left) and the ROM prediction error (right) for each of the forced pitching oscillation cases (top to bottom) with respect to lift coefficient for the rigid vehicle. Relative to the previous nonlinear ROM (Fig. 87), which only included an angle-of-attack dependency for the angle-of-attack indicial responses, the lift coefficient predictions using the updated ROM show negligible changes in modeling accuracy for each of the reduced frequency cases. The mean error and standard deviation remains fairly constant. Similar results are found for the pitching moment predictions shown in Fig. 92.

Figure 93 illustrates the CFD and nonlinear ROM (included dependency for pitch rate responses) results (left) and the ROM prediction error (right) for each of the forced pitching oscillation cases (top to bottom) with respect to lift coefficient for the flexible vehicle. Relative to the previous nonlinear ROM (Fig. 89), the lift coefficient predictions using the updated ROM show small changes in modeling accuracy for each of the reduced frequency cases. In the $k = 0.05$ and $k = 0.20$ cases, the standard deviation decreases by a fraction of a percent. The mean error and standard deviation remains fairly constant for the $k = 0.10$ case. The pitching moment predictions for the updated nonlinear ROM are shown in Fig. 94. In the $k = 0.20$ case, the mean error increases by 0.1% whereas the standard deviation deccreases by 0.2%. In the remaining cases, the mean error and standard deviation generally increase by 0.1%.

Overall, use of a nonlinear ROM that includes an angle-of-attack dependency for the pitch rate indicial responses shows negligible changes in modeling accuracy for the unsteady lift and pitching moment predictions for both the rigid and flexible X-56A aircraft. For large-amplitude pitch oscillations, it is recommended that only the angle-of-attack indicial responses be dependent on angle of attack to reduce the computational costs associated with model identification.

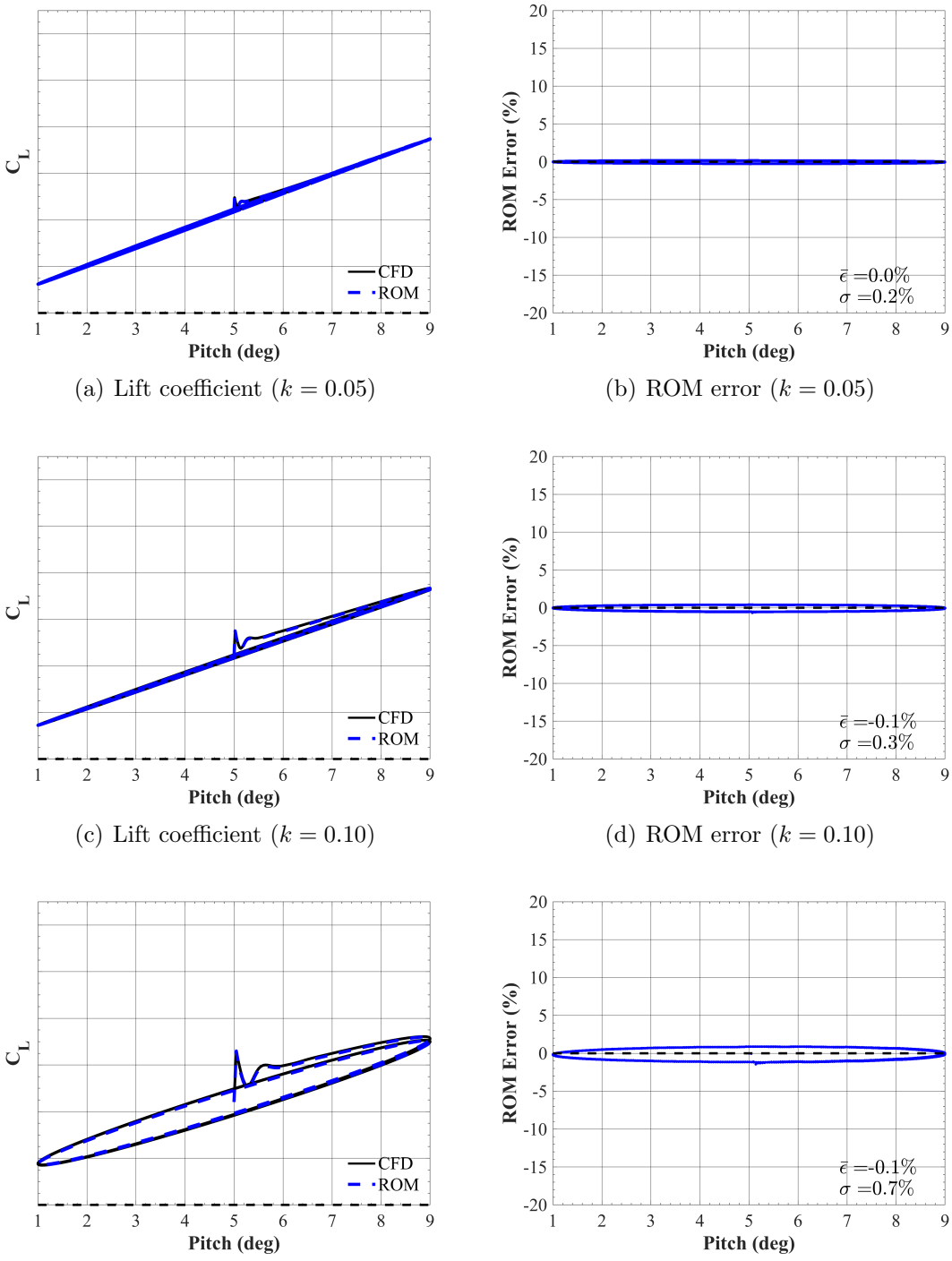

(a) Lift coefficient ($k = 0.05$)

(b) ROM error ($k = 0.05$)

(c) Lift coefficient ($k = 0.10$)

(d) ROM error ($k = 0.10$)

(e) Lift coefficient ($k = 0.20$)

(f) ROM error ($k = 0.20$)

Figure 91: Rigid X-56A: Nonlinear ROM (included for pitch rate responses) vs. CFD lift coefficient results (left) and ROM error (right) for forced pitching oscillation with 4 degree amplitude for $k = 0.05$ (top), 0.10 (middle), and 0.20 (bottom) at $\alpha_0 = 5°$, $\beta = 0°$, $M = 0.13$.

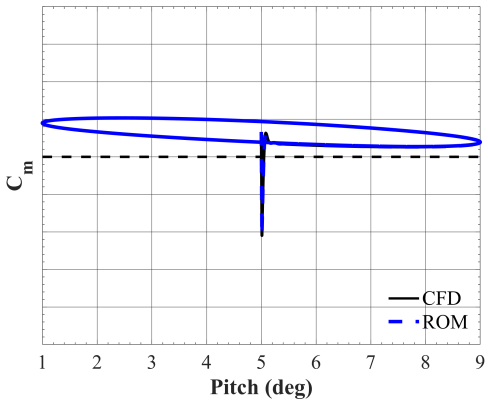

(a) Pitching moment coefficient ($k = 0.05$)

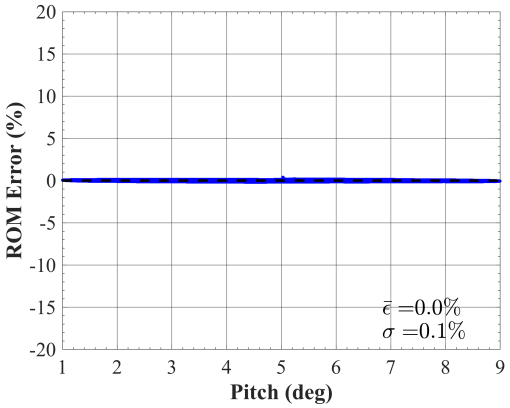

(b) ROM error ($k = 0.05$)

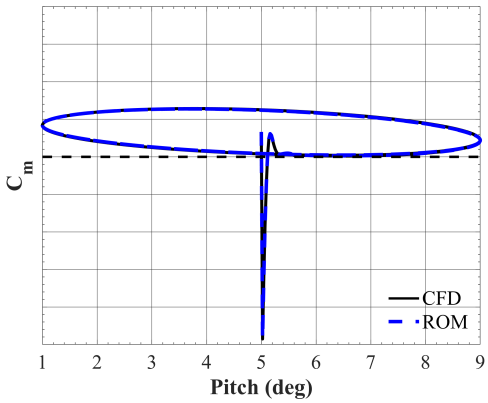

(c) Pitching moment coefficient ($k = 0.10$)

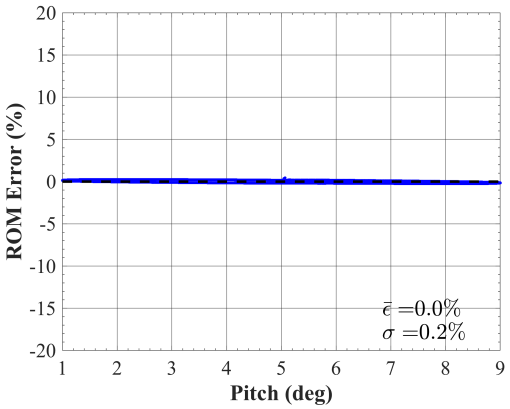

(d) ROM error ($k = 0.10$)

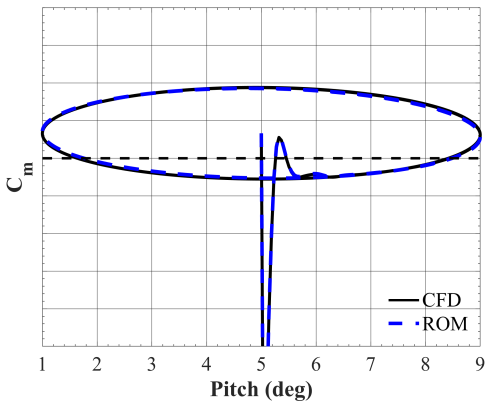

(e) Pitching moment coefficient ($k = 0.20$)

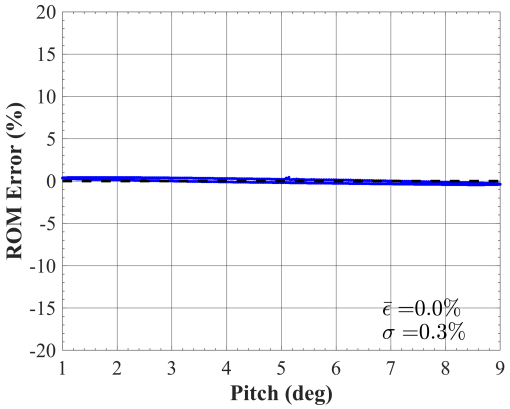

(f) ROM error ($k = 0.20$)

Figure 92: Rigid X-56A: Nonlinear ROM (included for pitch rate responses) vs. CFD pitching moment coefficient results (left) and ROM error (right) for forced pitching oscillation with 4 degree amplitude for $k = 0.05$ (top), 0.10 (middle), and 0.20 (bottom) at $\alpha_0 = 5°$, $\beta = 0°$, $M = 0.13$.

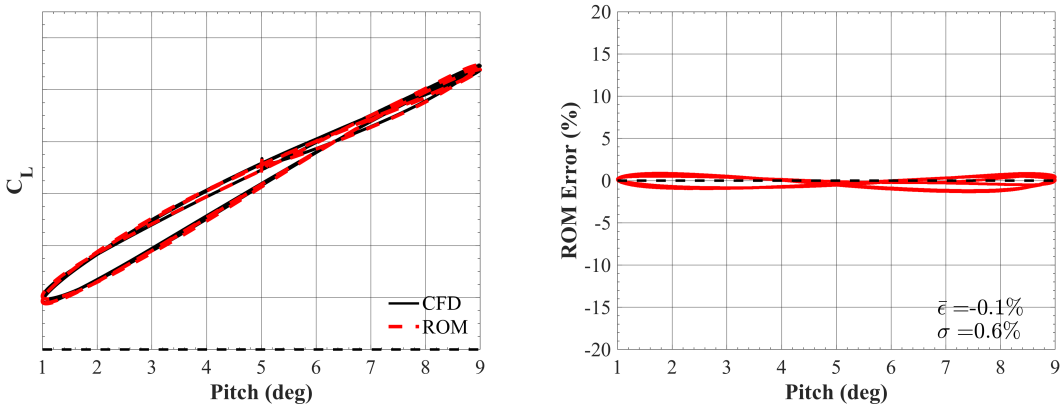

(a) Lift coefficient ($k = 0.05$)

(b) ROM error ($k = 0.05$)

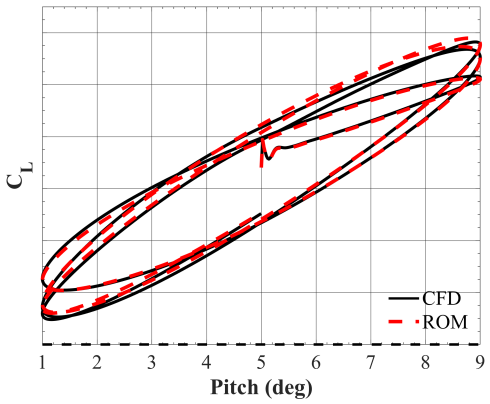

(c) Lift coefficient ($k = 0.10$)

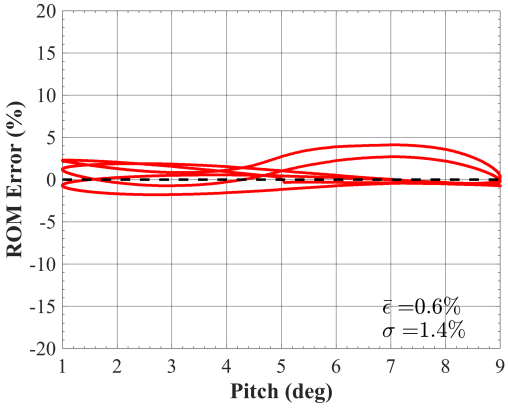

(d) ROM error ($k = 0.10$)

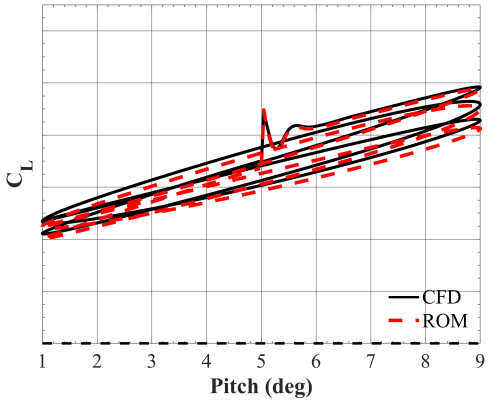

(e) Lift coefficient ($k = 0.20$)

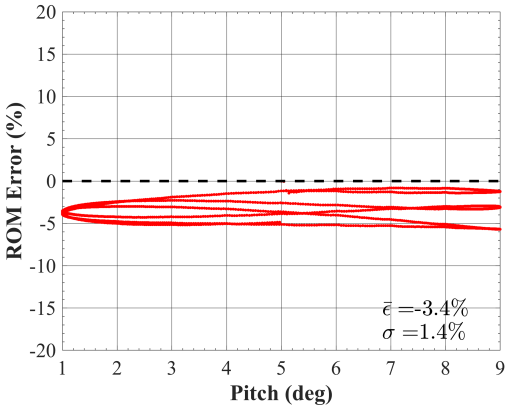

(f) ROM error ($k = 0.20$)

Figure 93: Flexible X-56A: Nonlinear ROM (included for pitch rate responses) vs. CFD lift coefficient results (left) and ROM error (right) for forced pitching oscillation with 4 degree amplitude for $k = 0.05$ (top), 0.10 (middle), and 0.20 (bottom) at $\alpha_0 = 5°$, $\beta = 0°$, $M = 0.13$.

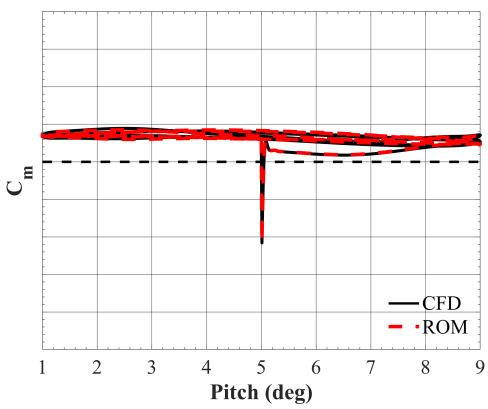

(a) Pitching moment coefficient ($k = 0.05$)

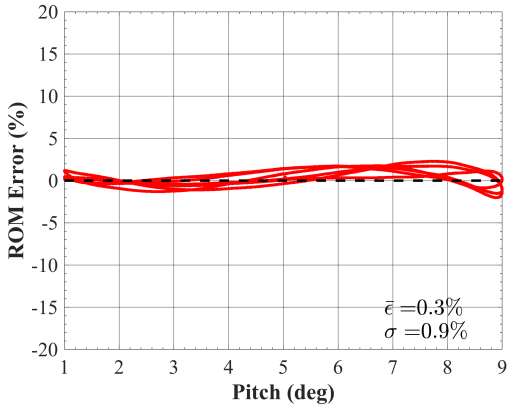

(b) ROM error ($k = 0.05$)

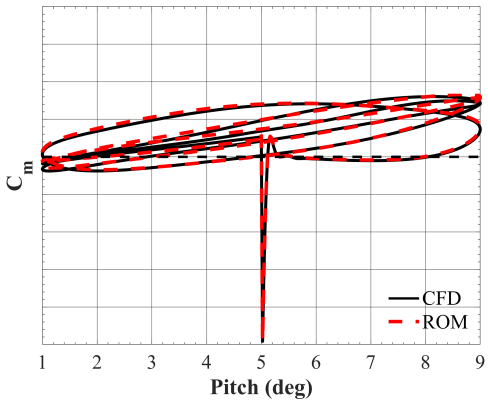

(c) Pitching moment coefficient ($k = 0.10$)

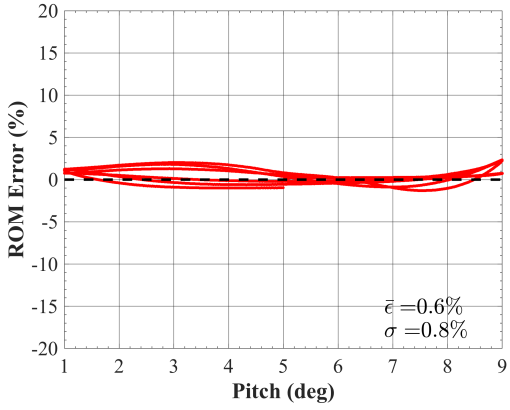

(d) ROM error ($k = 0.10$)

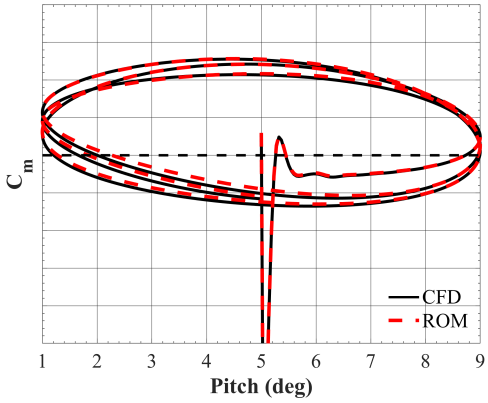

(e) Pitching moment coefficient ($k = 0.20$)

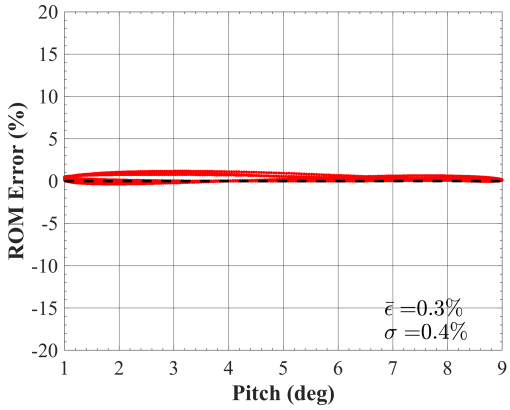

(f) ROM error ($k = 0.20$)

Figure 94: Flexible X-56A: Nonlinear ROM (included for pitch rate responses) vs. CFD pitching moment coefficient results (left) and ROM error (right) for forced pitching oscillation with 4 degree amplitude for $k = 0.05$ (top), 0.10 (middle), and 0.20 (bottom) at $\alpha_0 = 5°$, $\beta = 0°$, $M = 0.13$.

8.2.6 Summary

The present experiment sought to evaluate the unsteady aerodynamic prediction capabilities of a nonlinear indicial response ROM method, which accounted for indicial response sensitivity to angle of attack. Aeroelastic indicial responses were simulated at select points across the angle-of-attack flight envelope to capture the response sensitivity to initial angle of attack. A linear interpolation of this indicial response database was used to model the responses at each flight condition of a given trajectory.

Linear and nonlinear ROM predictions were compared to CFD simulation results for the unsteady lift and pitching moment coefficients of both a rigid and flexible X-56A performing large-amplitude forced pitching oscillations. With similar qualitative behavior as the small-amplitude forced pitching oscillations of Expt. 2.1, the rigid vehicle demonstrated mostly elliptical hysteresis loops with respect to the lift and pitching moment coefficients. These hysteresis loops generally converged within one quarter-cycle of simulation, and an increase in aerodynamic damping was observed for higher reduced frequencies. The aeroelastic responses for the flexible vehicle were characterized by complex fluid-structure interactions, which elicited cycle-to-cycle differences in aerodynamic damping and minimum/maximum coefficient values.

For the rigid vehicle, the linear ROM showed general agreement with the CFD results with less than 1% mean error and standard deviation observed for lift and pitching moment predictions. Minor improvements could be gained using a nonlinear ROM, where ROM modeling error decreased by accounting for angle-of-attack sensitivity and negative step responses for $\alpha(t) < \alpha_0$. For the flexible vehicle, the linear ROM proved incapable of capturing the nonlinearities suggested from the static characterization study in Chapter 7. Use of the nonlinear ROM with negative angle-of-attack step responses for $\alpha(t) < \alpha_0$, proved to effectively model the unsteady lift and pitching moment responses for the flexible vehicle across the range of simulated reduced frequencies.

8.3 Experiment 2.3 - Generalized ROM (α, M) Evaluation

In order to further evaluate the capabilities of the aeroelastic indicial response ROM, longitudinal and lateral unsteady aerodynamic predictions are generated and compared to CFD simulation results for a generalized 6DOF right turn maneuver. This variable-speed maneuver will enable testing of the Kriging surrogate modeling technique described in Section 5.4.

8.3.1 Purpose of Experiment

The following are identified as the main objectives of this numerical experiment:

1. Explore the differences in the unsteady aerodynamic responses between the rigid and flexible X-56A aircraft for a generalized flight test maneuver.

2. Demonstrate the generalized capability of a surrogate-based aeroelastic indicial response ROM to accurately predict the longitudinal and lateral unsteady aerodynamics during a variable-speed maneuver.

8.3.2 Experiment Setup

In order to demonstrate the generalized capability of the nonlinear aeroelastic ROM, a NASA Armstrong flight test maneuver for the X-56A is to be simulated and compared to ROM predictions. The vehicle-state time histories were acquired from GPS/accelerometer data and smoothed/interpolated for motion file generation. The X-56A performing a right turn (RT), illustrated in Figs. 95-96, enters and exits the maneuver from a straight and level condition. The angle of attack and sideslip angles are constrained within [-2° to 5°] and [-4° to 4°], respectively, and Mach numbers within [0.11 to 0.13]. The aircraft rolls right as the flight speed decreases and the yaw angle begins to increase up to 90 degrees. Finally, the aircraft begins to accelerate back to the initial flight speed while the yaw angle increases to a maximum of 180 degrees, i.e., a complete right turn.

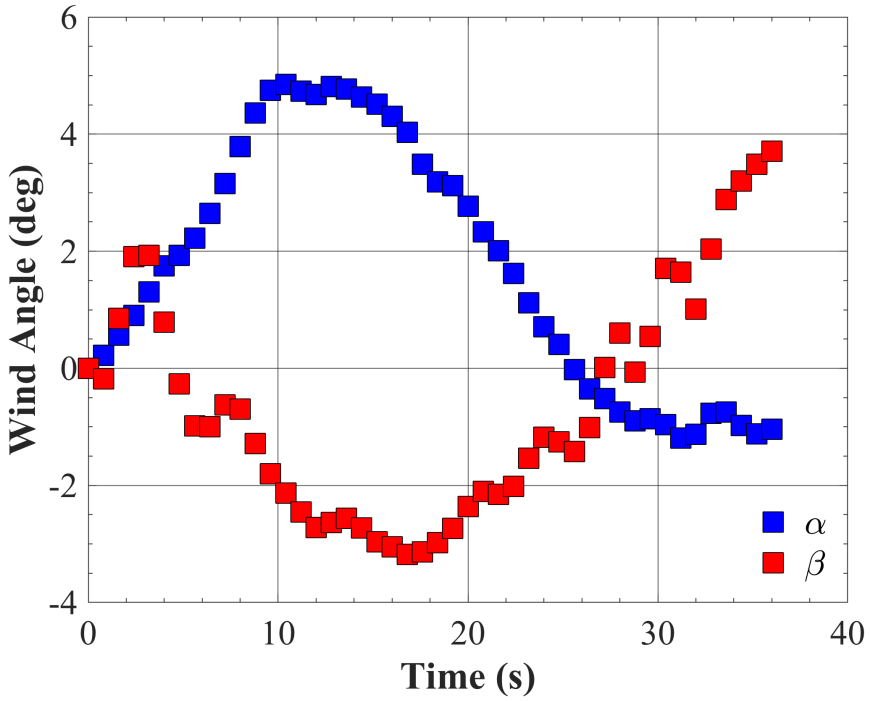

(a) Aerodynamic angles

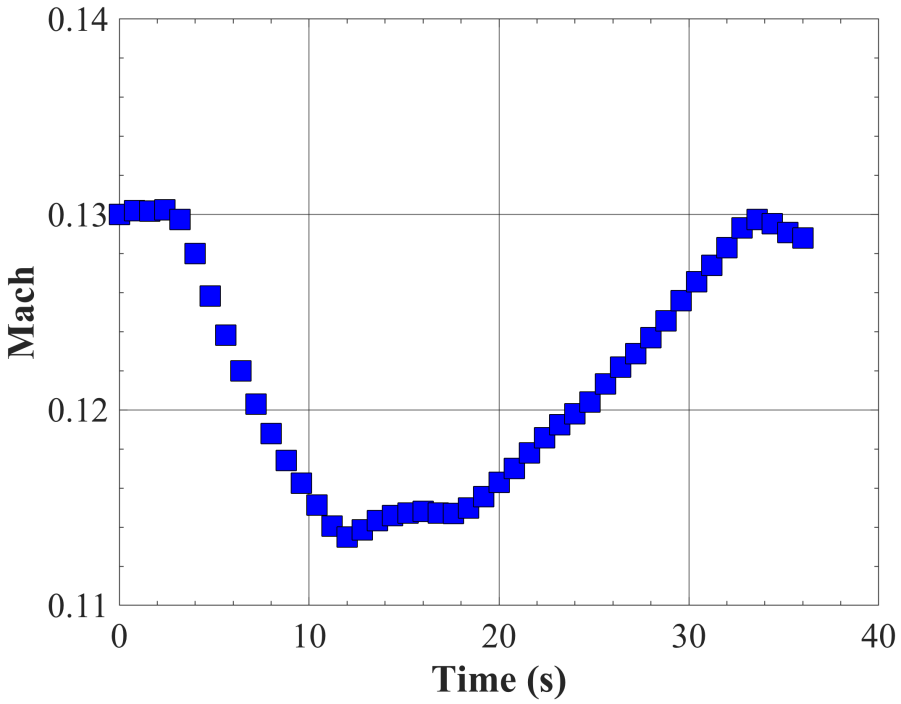

(b) Mach number

Figure 95: Right turn maneuver - (a) aerodynamic angles and (b) Mach number.

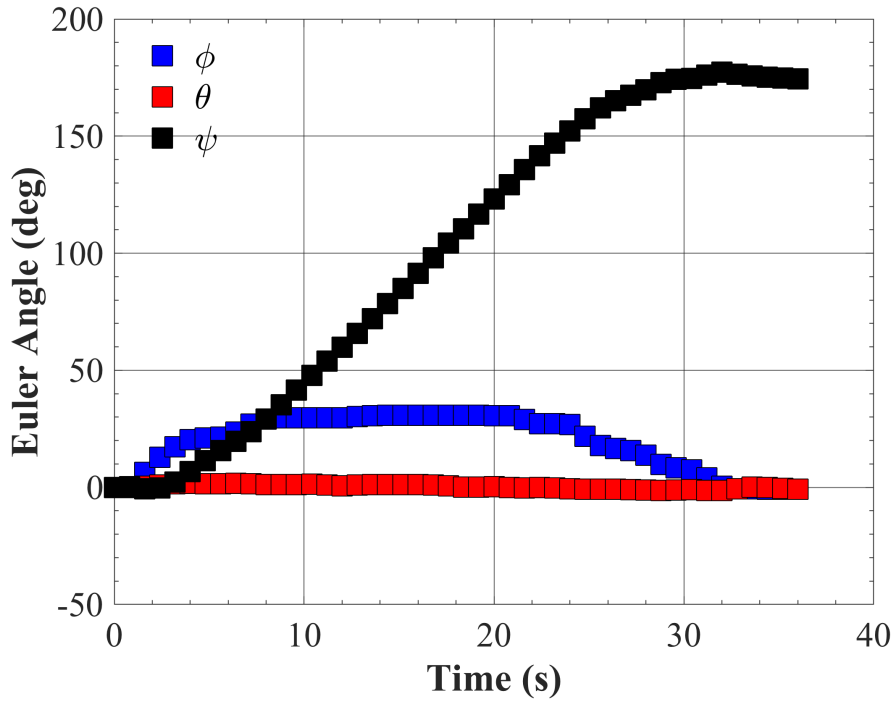

Figure 96: Right turn maneuver - Euler angles.

The simulation framework outlined in Chapter 4 was used to generate full-order rigid and aeroelastic CFD solutions. Rigid and aeroelastic indicial responses were simulated with respect to the longitudinal and lateral vehicle-state parameters at select angles of attack and Mach numbers using the best practices established in the Chapter 7. Motion files were generated for the trajectory and indicial response trajectories using the trajectory post-processing MATLAB code. Linear and nonlinear ROM predictions for the longitudinal and lateral unsteady aerodynamic responses were generated using the *CFD2ROM* MATLAB code.

8.3.3 Nonlinear ROM Generation

Experiment 2.3 seeks to evaluate the predictive capability of the aeroelastic nonlinear indicial response ROM over a range of angles of attack and Mach numbers. Equation 18 represents the traditional nonlinear reduced-order modeling formulation for longitudinal (C_j) unsteady aerodynamic predictions. The lift (C_L) and pitching

moment (C_m) coefficients are a result of the steady-state contribution at the initial flight condition (C_{j_0}) and unsteady contributions due to changes in angle of attack (α) and pitch rate (q). Equation 19 represents the nonlinear reduced-order modeling formulation for lateral (C_k) unsteady aerodynamic predictions. The side force (C_Y), rolling moment (C_l), and yawing moment (C_n) coefficients are calculated as a result of unsteady contributions due to changes in sideslip angle (β), roll rate (p), and yaw rate (r). The indicial responses due to step changes in the wind angles, α and β, are a function of angle of attack and Mach number, whereas the indicial responses due to step changes in the rotation rates are only a function of angle of attack.

$$C_j(t) = C_{j_0}(M) + \frac{d}{dt}\left[\int_0^t C_{j_\alpha}(t-\tau,\alpha,M)\alpha(\tau)d\tau\right] + \frac{d}{dt}\left[\int_0^t C_{j_q}(t-\tau,M)q(\tau)d\tau\right] \tag{18}$$

$$\begin{aligned} C_k(t) = \frac{d}{dt}\left[\int_0^t C_{k_\beta}(t-\tau,\alpha,M)\beta(\tau)d\tau\right] + \frac{d}{dt}\left[\int_0^t C_{k_p}(t-\tau,M)p(\tau)d\tau\right] \\ + \frac{d}{dt}\left[\int_0^t C_{k_r}(t-\tau,M)r(\tau)d\tau\right] \end{aligned} \tag{19}$$

Table 15 defines the indicial responses simulated for the nonlinear ROM generation. Indicial responses due to step changes in angle of attack and sideslip angle are simulated in one degree angle of attack and 0.02 Mach number increments along the angle-of-attack range covered during the right turn maneuver. Since rotation rate indicial responses are assumed to be dependent on Mach number, a single indicial response is sampled at $\alpha_0 = 0^\circ$ for each Mach number increment. Based on the results of Expt. 2.2, negative angle-of-attack step responses are also included. Table 19 lists the corresponding motion file inputs used to create the indicial trajectories for response identification.

Table 18: Matrix of indicial step cases for input to the kriging surrogate model.

α_0 (deg)	$M = 0.11$	$M = 0.13$
0	$\Delta\alpha, \Delta\beta, \Delta p, \Delta q, \Delta r$	$\Delta\alpha, \Delta\beta, \Delta p, \Delta q, \Delta r$
-2 to 0	$-\Delta\alpha$	$-\Delta\alpha$
1 to 5	$\Delta\alpha$	$\Delta\alpha$
-2 to 5	$\Delta\beta$	$\Delta\beta$

Table 19: Motion file inputs for creating indicial trajectories for nonlinear RT predictions ($t > 0$).

Indicial	α, deg	β, deg	ϕ, deg	θ, deg	ψ, deg	M_0
α- step	$\alpha_0 \pm 1$	0	0	0	0	0.11, 0.13
β- step	α_0	1	0	0	0	0.11, 0.13
p- step	0	0	$\Delta p \cdot t$	0	0	0.11, 0.13
q- step	0	0	0	$\Delta q \cdot t$	0	0.11, 0.13
r- step	0	0	0	0	$\Delta r \cdot t$	0.11, 0.13

Rigid and aeroelastic indicial step responses were computed with FUN3D using the temporal parameters presented in Table 20. Using the solution strategy developed in Experiment 1.1, the lateral responses were advanced using a time step of $\Delta t = 4E{-}04$ for a total of $4,000$ time steps, where convergence to steady state was achieved for both the rigid and aeroelastic simulations. For the longitudinal responses, 4,000 time steps were used to attain converged solutions for the rigid vehicle, whereas 6,550 time steps were used for the flexible vehicle.

Table 20: Temporal parameters for indicial responses simulations for RT maneuver predictions (rigid and flexible).

Indicial	Δt (s)	N_{sub}	Total Time Steps	Total Iterations	Structure
α-step	4.0E-04	20	4,000	80,000	Rigid
α-step	4.0E-04	20	6,550	131,000	Flexible
q-step	4.0E-04	20	4,000	80,000	Rigid
q-step	4.0E-04	20	6,550	131,000	Flexible
β-step	4.0E-04	20	4,000	80,000	Rigid/Flexible
p-step	4.0E-04	20	4,000	80,000	Rigid/Flexible
r-step	4.0E-04	20	4,000	80,000	Rigid/Flexible

8.3.4 CFD Simulations

The prescribed right turn maneuver is initialized from $\alpha_0 = 0°$, $\beta = 0°$, and $M = 0.13$. A characteristic time step of $\Delta t^* \cong 0.002$ was used to advance the solution in time and 20 subiterations were used to converge the solution in pseudotime. In order to simulate the complete 36 second maneuver, the vehicle-state parameters were defined for a total of 90,000 time steps.

The solution strategy proved to be robust in producing stable, well-converged dynamic simulations for both the rigid and flexible vehicle. Examples of subiterative convergence are shown in Figures 97(b) and 97(a) for the rigid (top) and flexible (bottom) vehicle cases, respectively. The plots illustrate the order-of-magnitude convergence in the FUN3D time-accurate solution residual drop ($log(R/R_0)$) and the pitching moment coefficient (C_n) convergence versus subiterations. The subiteration history shown corresponds to time step 25,000, which coincides with the peak angle of attack at 10 seconds into the maneuver. The rigid and aeroelastic simulations present over 8-orders of convergence in residual drop with convergence in the pitching moment coefficient based on a 0.0002% difference between the final two subiterations.

Figure 98 illustrates the FUN3D lift and pitching moment coefficient results for the rigid (blue) and flexible (red) vehicle undergoing the prescribed right turn maneuver. The lift coefficient results for the rigid and flexible vehicle generally correlate with the angle-of-attack time history, increasing and decreasing at identical instances in time. Additionally, the flexible vehicle shows a more significant response due to the aerodynamic loading at higher angles of attack with nearly a 50% increase in lift coefficient relative to the rigid vehicle. In contrast, the pitching moment coefficients results show an opposite correlation with angle of attack for both the rigid and flexible vehicles. Differences between the rigid and flexible pitching moment time histories are largely due to the initial offset with slight increases in deviation at peak angle of attack.

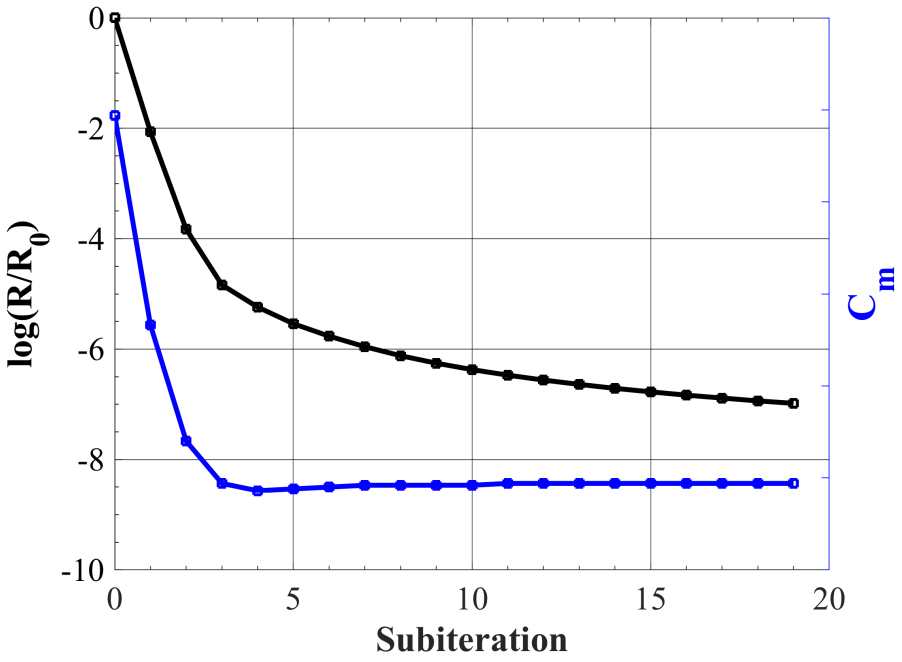

(a) Rigid

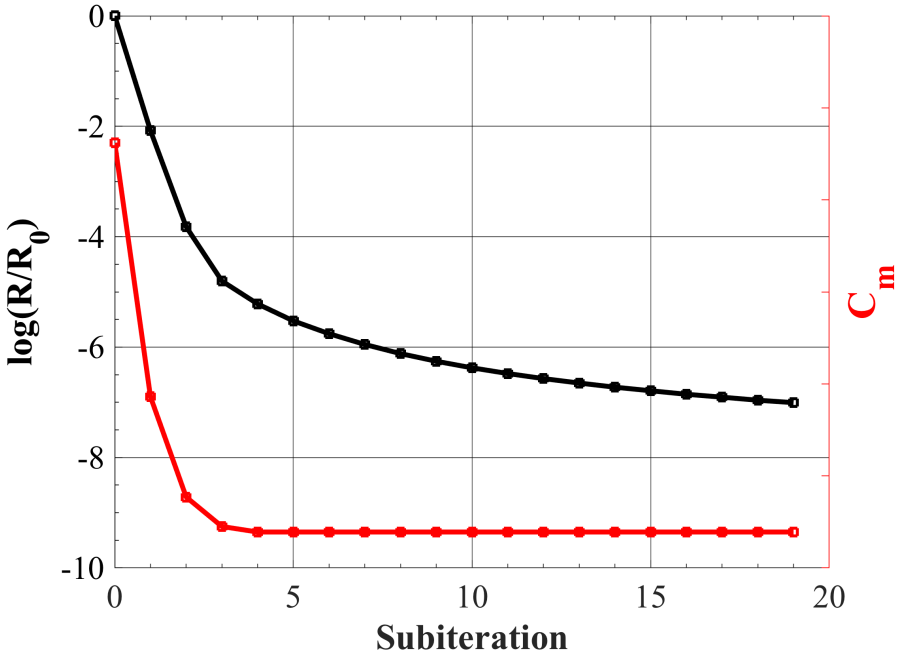

(b) Flexible

Figure 97: X-56A: FUN3D subiterative convergence during the right turn maneuver for the rigid (blue) and flexible (red) cases. Iteration 25,000 - near peak angle of attack at 10 seconds.

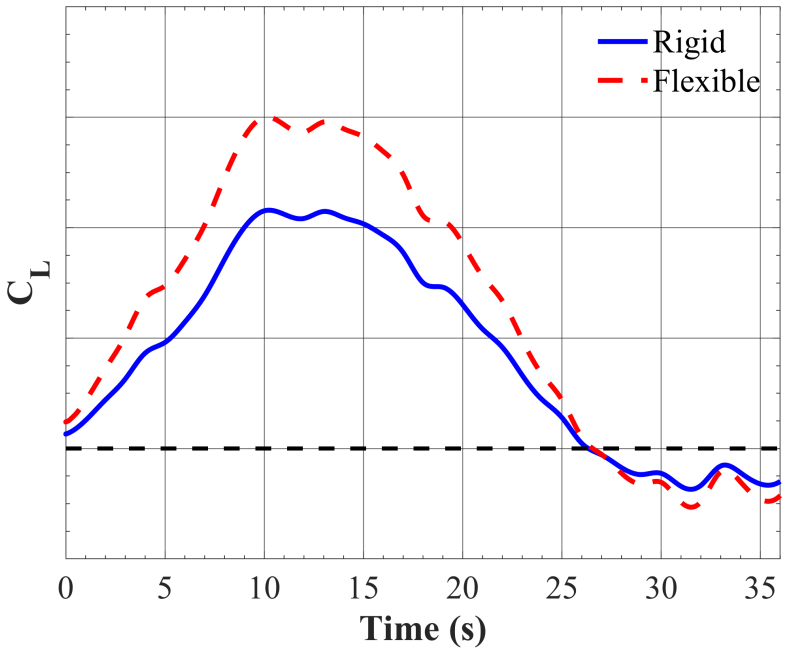

(a) Lift coefficient

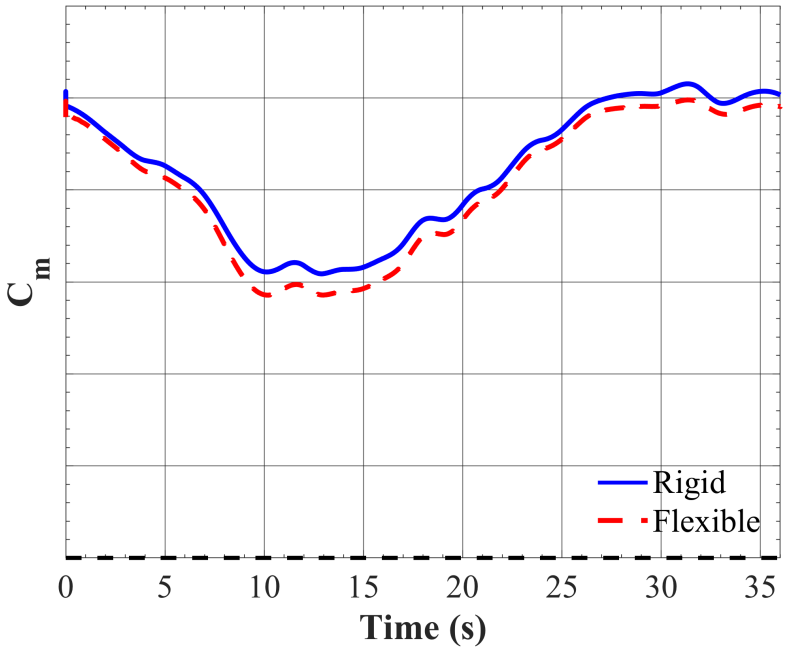

(b) Pitching moment coefficient

Figure 98: X-56A: FUN3D lift and pitching moment coefficient results for the rigid (blue) and flexible (red) vehicle undergoing a right turn maneuver.

Figure 99 illustrates the side force coefficient response for the rigid (blue) and flexible (red) vehicle. The side force coefficient shares the same general qualitative time-history as the sideslip angle with peak deviations between the rigid and flexible vehicles responses midway through the turn. Figure 100 illustrates the FUN3D rolling and yawing moment coefficient results for the rigid (blue) and flexible (red) vehicle undergoing the right turn maneuver. A complex nonlinear response is observed with a peak rolling moment coefficient attained approximately two seconds into the maneuver, when the speed begins to decrease and the X-56A begins to roll in initiating the turn. The rigid and flexible vehicle responses are in general agreement for most of the maneuver with the largest deviations observed from $t = [7.5 \text{ to } 20]$ seconds when the roll angle and angle of attack are at a maximum. The yawing moment coefficient is shown to be nearly identical between the rigid and flexible vehicles throughout the maneuver.

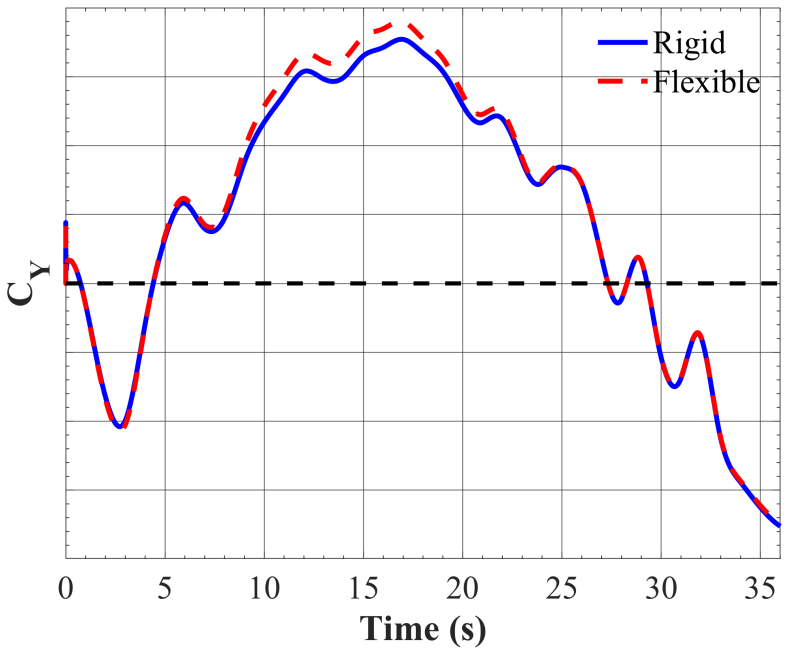

(a) Side force coefficient

Figure 99: X-56A: FUN3D side force coefficient results for the rigid (blue) and flexible (red) vehicle undergoing a right turn maneuver.

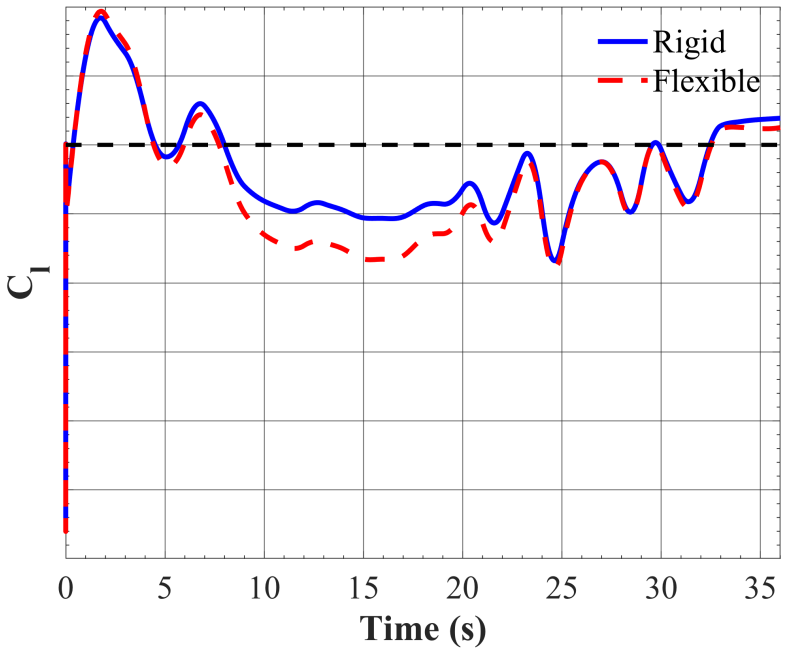

(a) Rolling moment coefficient

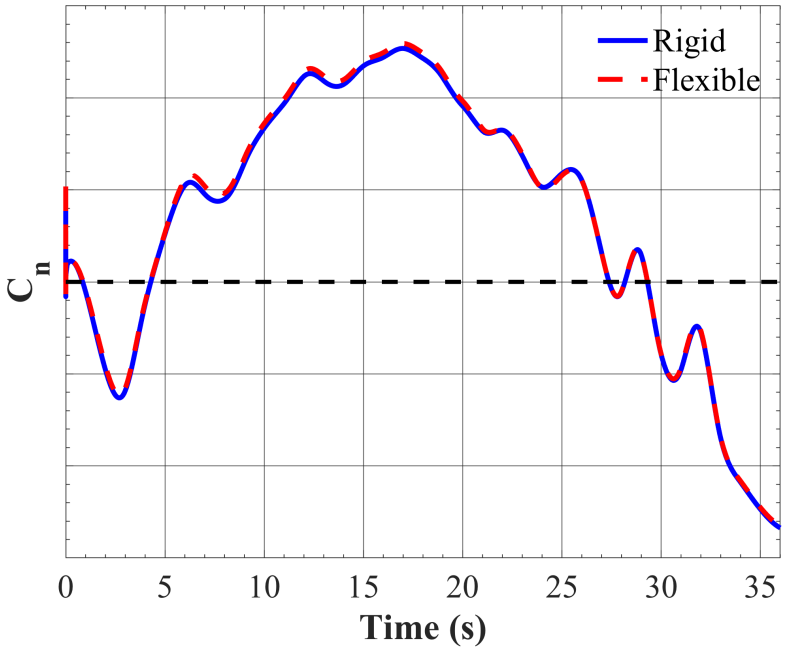

(b) Yawing moment coefficient

Figure 100: X-56A: FUN3D rolling and yawing moment coefficient results for the rigid (blue) and flexible (red) vehicle undergoing a right turn maneuver.

8.3.5 ROM Predictions

8.3.5.1 Linear ROM

Figure 101 illustrates a comparison between CFD and linear ROM results (left) and the ROM prediction error (right) for the lift and pitching moment responses of the rigid X-56A undergoing a right turn maneuver. The ROM prediction for lift coefficient are in great qualitative agreement with CFD results, where a mean percent error and standard deviation of 0.0% and 0.1% are observed. For pitching moment coefficient, the linear ROM is able to resolve the qualitative variation, but begins to deviate from the CFD results in the $t = [7.5 \text{ to } 22.5]$ second range when angle of attack is near peak magnitude (see Fig. 96). Because the linear ROM is unable to capture any nonlinear variations in pitching moment coefficient that may occur for $\alpha(t) >> \alpha_0$, the predictions degrade due to an apparent pitching moment nonlinearity near $\alpha = 5°$. A mean error of 6.4% and a standard deviation of 6.1% are found for the linear ROM's pitching moment prediction.

Figure 102 illustrates a comparison between CFD and linear ROM results (left) and the ROM prediction error (right) for the side force (top), rolling moment (middle), and yawing moment (bottom) coefficient responses. The ROM prediction for side force coefficient shows a general agreement with CFD results, but a mismatch is observed in the $t = [7.5 \text{ to } 22.5]$ second range, similar to the pitching moment coefficient predictions. In this case, the discrepancy is less severe with a mean error of -1.7% and a standard deviation of 1.8%. Similiar trends are observed with respect to the rolling moment coefficient, where a mean error and standard deviation of 2.8% and 2.9% are found, respectively. The yawing moment coefficient ROM predictions, while similar qualitatively to the side force coefficient, match fairly well with CFD. The largest error is found near $t = 7.5$ seconds, which coincides with a spike in sideslip angle. Regardless, the ROM does well in terms of quantified modeling accuracy with a mean error of -1.2% and a standard deviation of 1.9%.

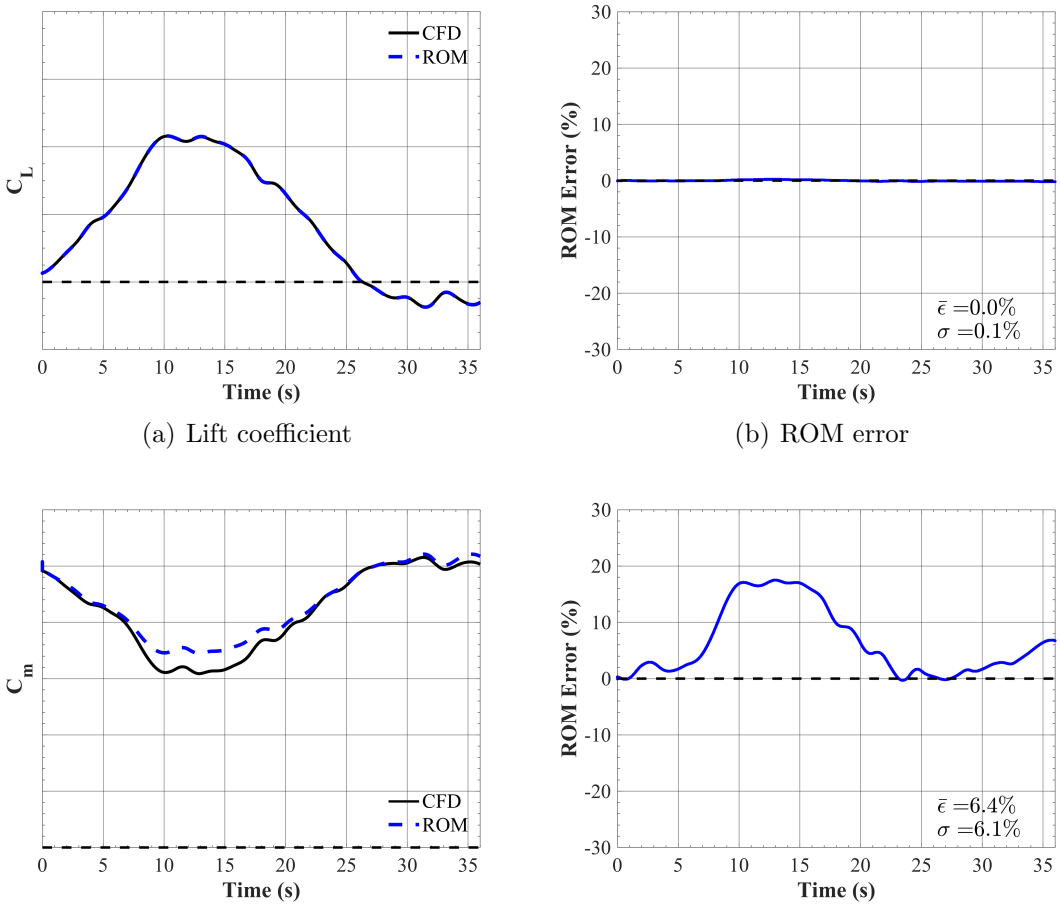

(a) Lift coefficient

(b) ROM error

(c) Pitching moment coefficient

(d) ROM error

Figure 101: Rigid X-56A: Linear ROM vs. CFD lift (top) and pitching moment (bottom) coefficient results (left) and ROM error (right) for the rigid vehicle undergoing a right turn maneuver.

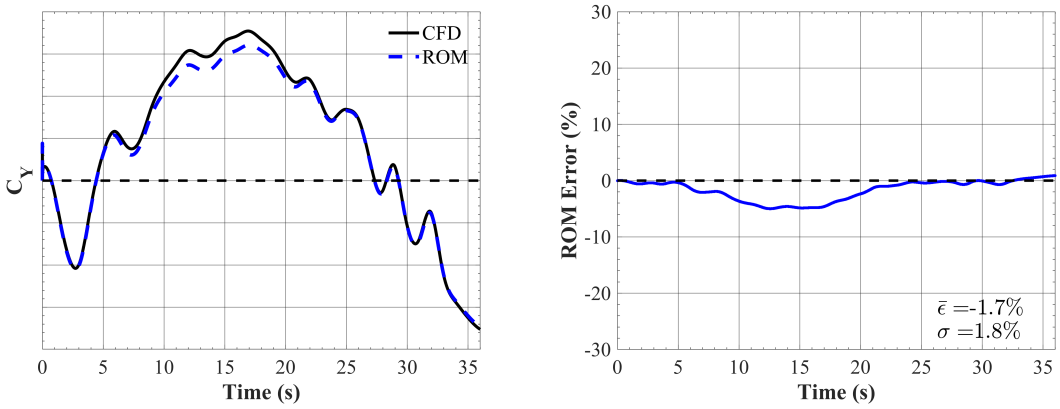

(a) Side force coefficient

(b) ROM error

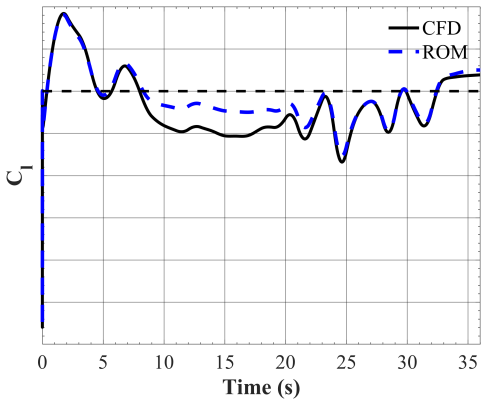

(c) Rolling moment coefficient

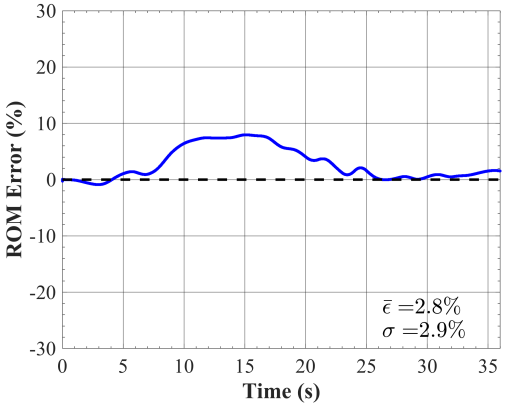

(d) ROM error

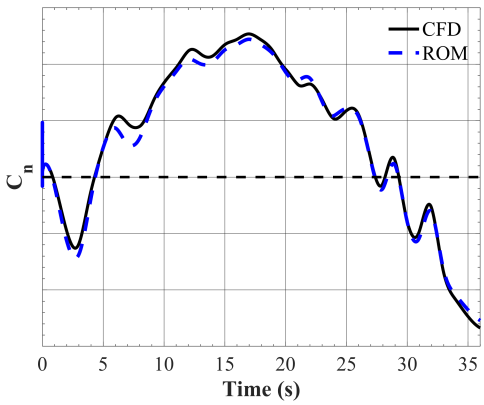

(e) Yawing moment coefficient

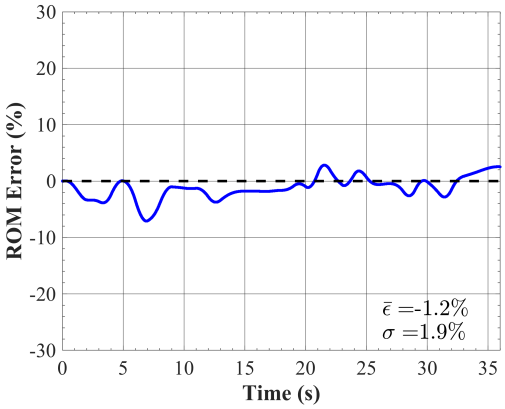

(f) ROM error

Figure 102: Rigid X-56A: Linear ROM vs. CFD side force (top), rolling moment (middle), and yawing moment (bottom) coefficient results (left) and ROM error (right) for the rigid vehicle undergoing a right turn maneuver.

Figure 103 illustrates a comparison between CFD and linear ROM results (left) and the ROM prediction error (right) for the lift and pitching moment responses of the flexible X-56A performing the right turn maneuver. In contrast to the rigid vehicle, the linear ROM presents noticeable modeling error for the lift coefficient in the $t = [5$ to 20] second range. In this time frame, the angle of attack is at a maximum, and the Mach number is at a minimum. A mean error of 4.2% and standard deviation of 4.8% are found with a maximum error near 15% at $t = 12.5$ seconds. The pitching moment prediction presents a similar trend as the rigid vehicle. The mean error and standard deviation is larger relative to the rigid vehicle prediction with values of 8.0% and 7.7% for the mean error and standard deviation, respectively.

Figure 104 illustrates a comparison between CFD and linear ROM results (left) and the ROM prediction error (right) for the side force (top), rolling moment (middle), and yawing moment (bottom) coefficient responses for the flexible vehicle. Again, the ROM error for the side force coefficient prediction varies similarly to those for the rigid vehicle with the largest deviation observed near $t = 15$ seconds. This ROM error is also observed for the rolling moment predictions, where the ROM tends to overpredict the coefficient value during the peak roll angle with a local error near 15%. The modeling accuracy for the yawing moment coefficient is fairly similar with mean error and standard deviation magnitude values near 2%.

Overall, the linear ROM is capable of qualitatively resolving the aerodynamic responses for the rigid vehicle undergoing the right turn maneuver. The lift coefficient showed the greatest agreement with CFD results, showing near zero values for mean error and standard deviation. Pitching and rolling moment coefficient predictions showed the greatest discrepancy with noticeable differences in the $t = [5$ to 20] second range. Similar trends were observed with respect to the flexible vehicle with the exception of overpredicting the lift coefficient, when the maximum angle of attack and minimum Mach number coincide.

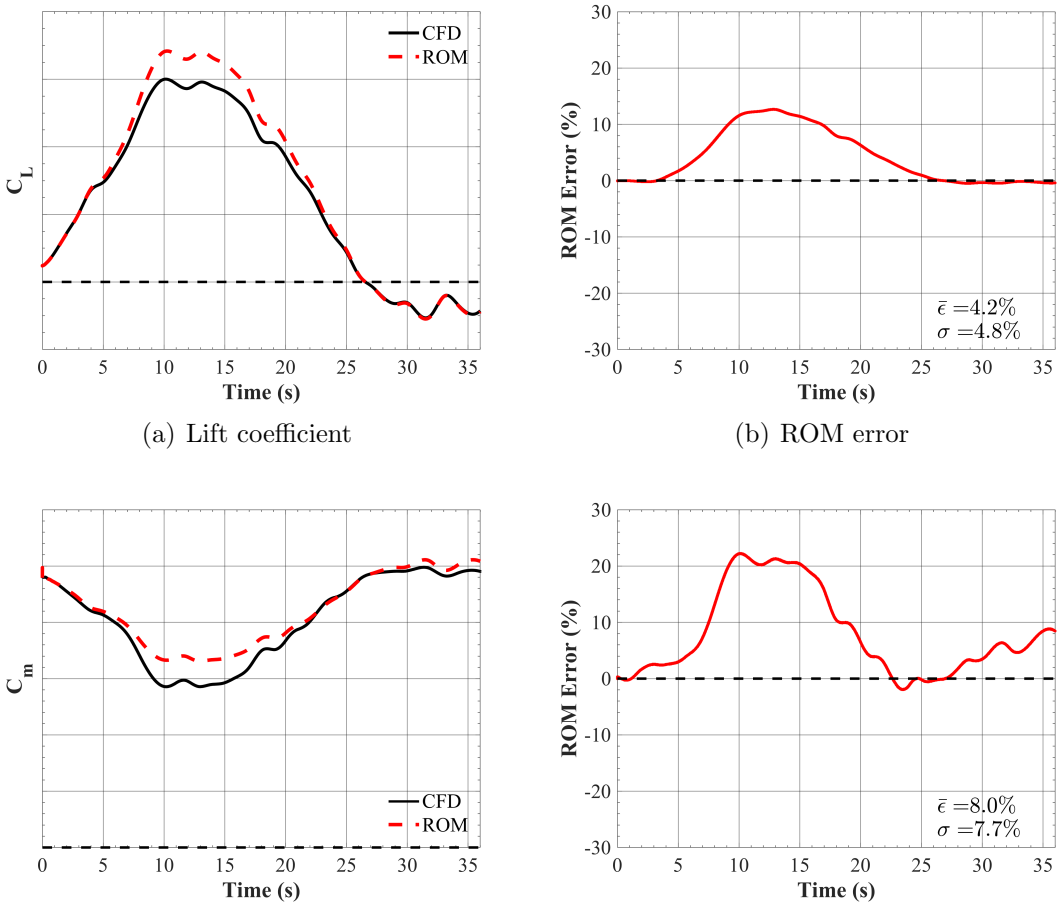

(a) Lift coefficient

(b) ROM error

(c) Pitching moment coefficient

(d) ROM error

Figure 103: Flexible X-56A: Linear ROM vs. CFD lift (top) and pitching moment (bottom) coefficient results (left) and ROM error (right) for the flexible vehicle undergoing a right turn maneuver.

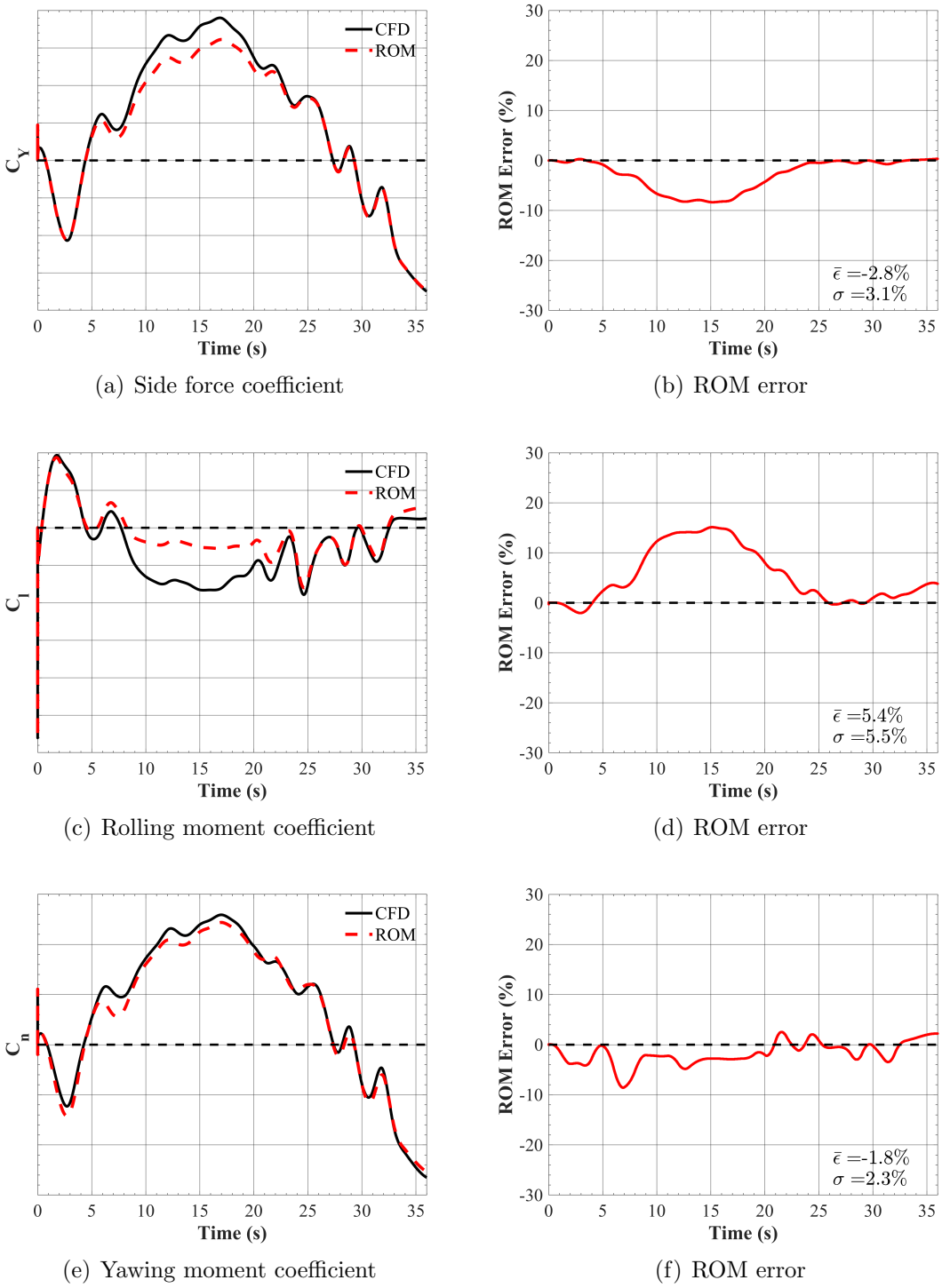

(a) Side force coefficient

(b) ROM error

(c) Rolling moment coefficient

(d) ROM error

(e) Yawing moment coefficient

(f) ROM error

Figure 104: Flexible X-56A: Linear ROM vs. CFD side force (top), rolling moment (middle), and yawing moment (bottom) coefficient results (left) and ROM error (right) for the flexible vehicle undergoing a right turn maneuver.

8.3.5.2 Nonlinear ROM (α)

Figure 105 illustrates a comparison between CFD and nonlinear ROM (α) results (left) and the ROM prediction error (right) for the lift and pitching moment responses of the rigid X-56A undergoing a right turn maneuver. Inclusion of the indicial response sensitivity to angle of attack shows virtually no improvement for the lift coefficient as it was already predicted fairly accurately with a mean error of 0.0% and standard deviation of 0.1%. In contrast, the pitching moment coefficient prediction shows noticeable improvement. The ROM now captures the minimum pitching moment coefficient in the $t = [5 \text{ to } 20]$ second range where the angle of attack reaches maximum value. Modeling of this pitching moment nonlinearity leads to a reduction in mean error from 6.4% to 1.0% with a similar decrease for standard deviation. Slight improvements are also observed with respect to the side force and rolling moment coefficients, as shown in Fig. 106. In each case, the coefficient values are better resolved near peak angles of attack with mean error and standard deviation values $< 1\%$ in magnitude. For the yawing moment coefficient, negligible changes are observed when including the angle-of-attack dependency.

Figure 107 illustrates a comparison between CFD and nonlinear ROM (α) results (left) and the ROM prediction error (right) for the lift and pitching moment responses of the flexible X-56A undergoing a right turn maneuver. The lift coefficient prediction shows minimal improvement relative to the linear ROM prediction with 0.4% and 0.7% decreases in mean error and standard deviation, respectively. Inclusion of the indicial response sensitivity to angle of attack only slightly reduced the overprediction of lift coefficient near $t = 12.5$ seconds. As shown in Chapter 7, the flexible vehicle's longitudinal responses are more sensitive to Mach number than the rigid vehicle. The discrepancy between ROM predictions and CFD results is attributed to not accounting for the indicial response sensitivity to Mach number, as the ROM error is greatest when the local Mach number is furthest from the initialized Mach number.

The pitching moment prediction does show great improvement when accounting for the angle-of-attack sensitivity alone with a mean error decrease from 8.0% to -1.3% and a 5.9% reduction in standard deviation.

Figure 108 illustrates a comparison between CFD and nonlinear ROM (α) results (left) and the ROM prediction error (right) for the side force (top), rolling moment (middle), and yawing moment (bottom) coefficient responses for the flexible vehicle. The side force coefficient prediction shows great qualitative agreement with CFD results for the duration of the right turn maneuver. Addition of the angle-of-attack sensitivity leads to a reduction in mean error magnitude from 2.8% to 0.2% with a similar decrease in standard deviation. Relative to the rigid vehicle, the nonlinear ROM better resolves the rolling moment coefficient with less than a 1.0% mean error and standard deviation. The yawing moment coefficient predictions show better agreement near peak angle of attack, but continue to be underpredicted during the spike in sideslip angle near $t = 7.5$ seconds.

In general, the nonlinear ROM accounting for angle-of-attack sensitivity showed significant improvement in modeling accuracy relative to the linear ROM when predicting the longitudinal and lateral force and moment coefficients for the rigid and flexible X-56A performing a right turn maneuver. The primary ROM modeling discrepancy remaining is an overprediction of the lift coefficient for the flexible vehicle. This overprediction occurs both at a maximum angle of attack and minimum Mach number. While indicial response sensitivity to angle of attack was modeled with the current ROM, only marginal improvements were found. This result suggests that the responses at $M = 0.13$ are not adequate for resolving the aerodynamic response at the minimum maneuver Mach number, $M = 0.11$. The next section investigates the utility of the surrogate-based ROM, described in Section 8.3.3, for resolving the indicial response sensitivity to angle of attack and Mach number.

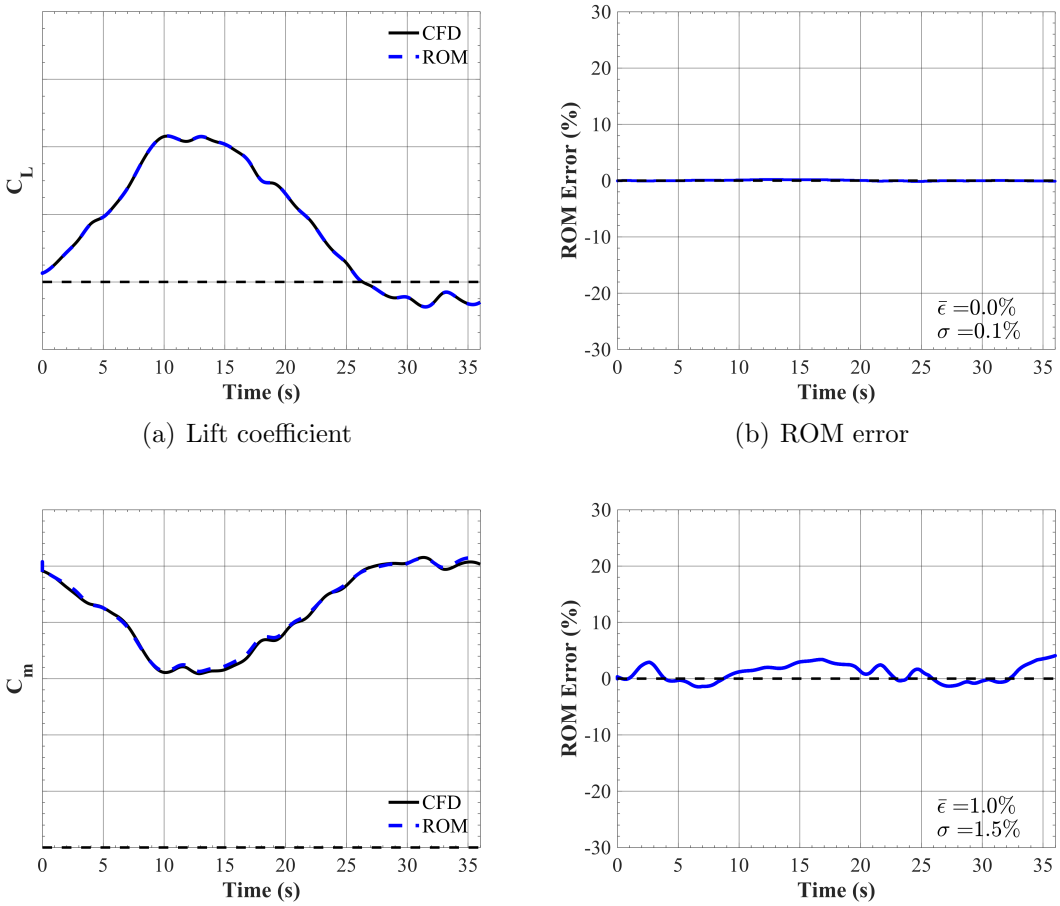

(a) Lift coefficient

(b) ROM error

(c) Pitching moment coefficient

(d) ROM error

Figure 105: Rigid X-56A: Nonlinear ROM (α) vs. CFD lift (top) and pitching moment (bottom) coefficient results (left) and ROM error (right) for the rigid vehicle undergoing a right turn maneuver.

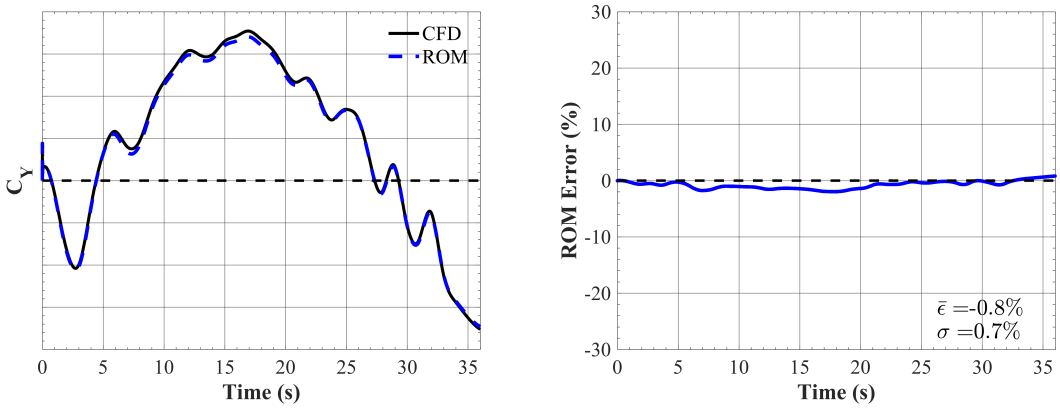

(a) Side force coefficient

(b) ROM error

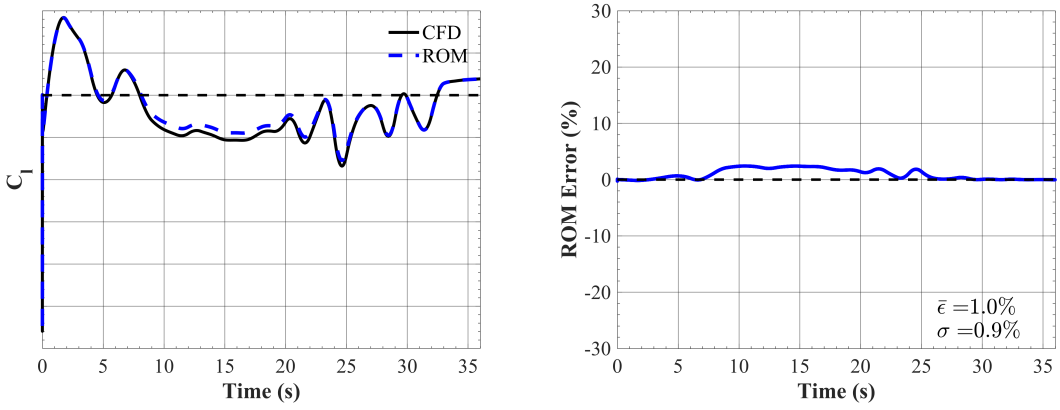

(c) Rolling moment coefficient

(d) ROM error

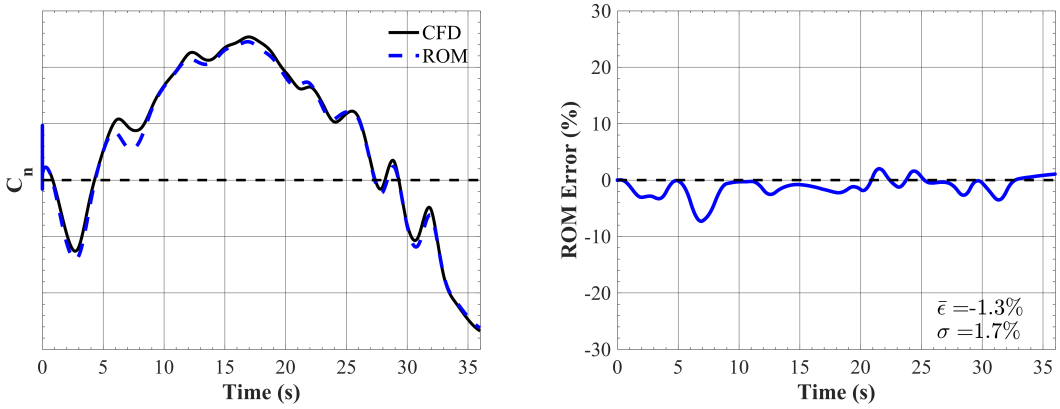

(e) Yawing moment coefficient

(f) ROM error

Figure 106: Rigid X-56A: Nonlinear ROM (α) vs. CFD side force (top), rolling moment (middle), and yawing moment (bottom) coefficient results (left) and ROM error (right) for the rigid vehicle undergoing a right turn maneuver.

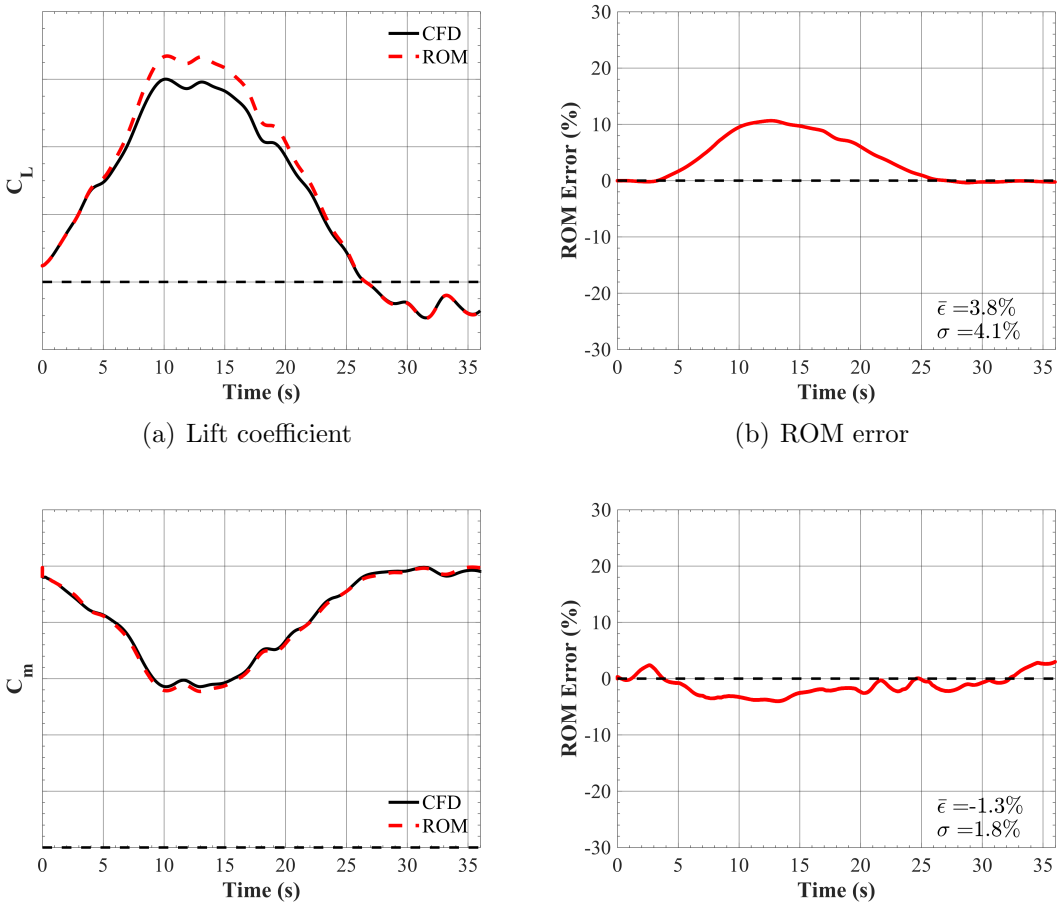

(a) Lift coefficient

(b) ROM error

(c) Pitching moment coefficient

(d) ROM error

Figure 107: Flexible X-56A: Nonlinear ROM (α) vs. CFD lift (top) and pitching moment (bottom) coefficient results (left) and ROM error (right) for the flexible vehicle undergoing a right turn maneuver.

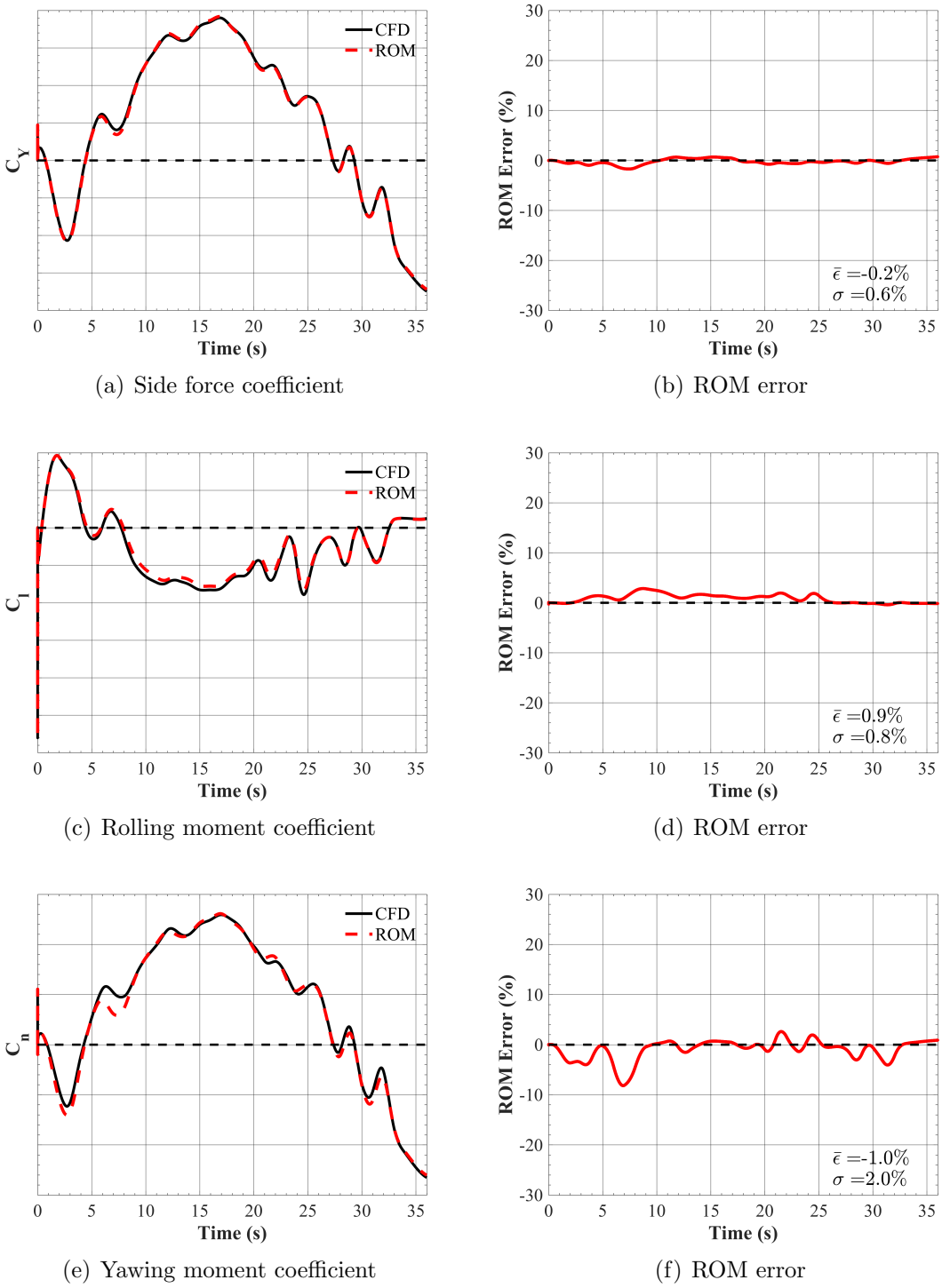

(a) Side force coefficient

(b) ROM error

(c) Rolling moment coefficient

(d) ROM error

(e) Yawing moment coefficient

(f) ROM error

Figure 108: Flexible X-56A: Nonlinear ROM (α) vs. CFD side force (top), rolling moment (middle), and yawing moment (bottom) coefficient results (left) and ROM error (right) for the flexible vehicle undergoing a right turn maneuver.

8.3.5.3 Nonlinear ROM (α, M)

Figure 109 illustrates a comparison between CFD and nonlinear ROM (α, M) results (left) and the ROM prediction error (right) for the lift and pitching moment responses of the rigid X-56A undergoing a right turn maneuver. The lift and pitching moment coefficient predictions obtained using the nonlinear ROM that accounted for the indicial response sensitivity to angle of attack (Fig. 105) were already accurately modeled with mean errors of 0.0% and 1.0%, respectively. The updated nonlinear ROM that models the indicial response sensitivity to both angle of attack and Mach number shows similar prediction quality with mean errors of -0.1% and 0.5%. A slight 'buzzing' is observed in the ROM error plots due to the Kriging modeling scheme used to model the indicial response at each point in the trajectory, though this behavior remains fairly limited and does not degrade overall solution quality. Figure 110 shows the side force, rolling moment, and yawing moment coefficient results. Overall, the mean error and standard deviation change by $< 1\%$ when including the Mach number sensitivity. This result is to be expected for the rigid vehicle, which showed a less significant sensitivity to Mach number over the range covered during the right turn maneuver (Section 7.4).

Figure 111 illustrates a comparison between CFD and nonlinear ROM (α, M) results (left) and the ROM prediction error (right) for the lift and pitching moment responses of the flexible X-56A. By including the indicial response sensitivity to Mach number, the lift coefficient predictions are now in great qualitative agreement with the CFD results. The peak lift coefficient, which coincides with the minimum Mach number experienced during the maneuver, is now predicted within 1% error. Over the 36 seconds of the maneuver, the mean error is 0.7% and the standard deviation is 0.8%. This is a considerable improvement over the nonlinear ROM from the previous subsection, which resulted in a mean error of 3.8% and 4.1% standard deviation. While less significant, the pitching moment coefficient predictions also show marginal

improvement with approximately a 0.5% reduction in mean error magnitude. Figure 110 illustrates a comparison between CFD and nonlinear ROM (α, M) results (left) and the ROM prediction error (right) for the side force (top), rolling moment (middle), and yawing moment (bottom) coefficients. In contrast to the rigid vehicle, a slight degradation is observed for the lateral force and moment coefficient predictions. While minimal, the side force coefficient becomes underpredicted and the rolling moment coefficient becomes overpredicted in the t = [10 to 20] second range. The yawing moment coefficient prediction remains relatively the same between the two modeling variants.

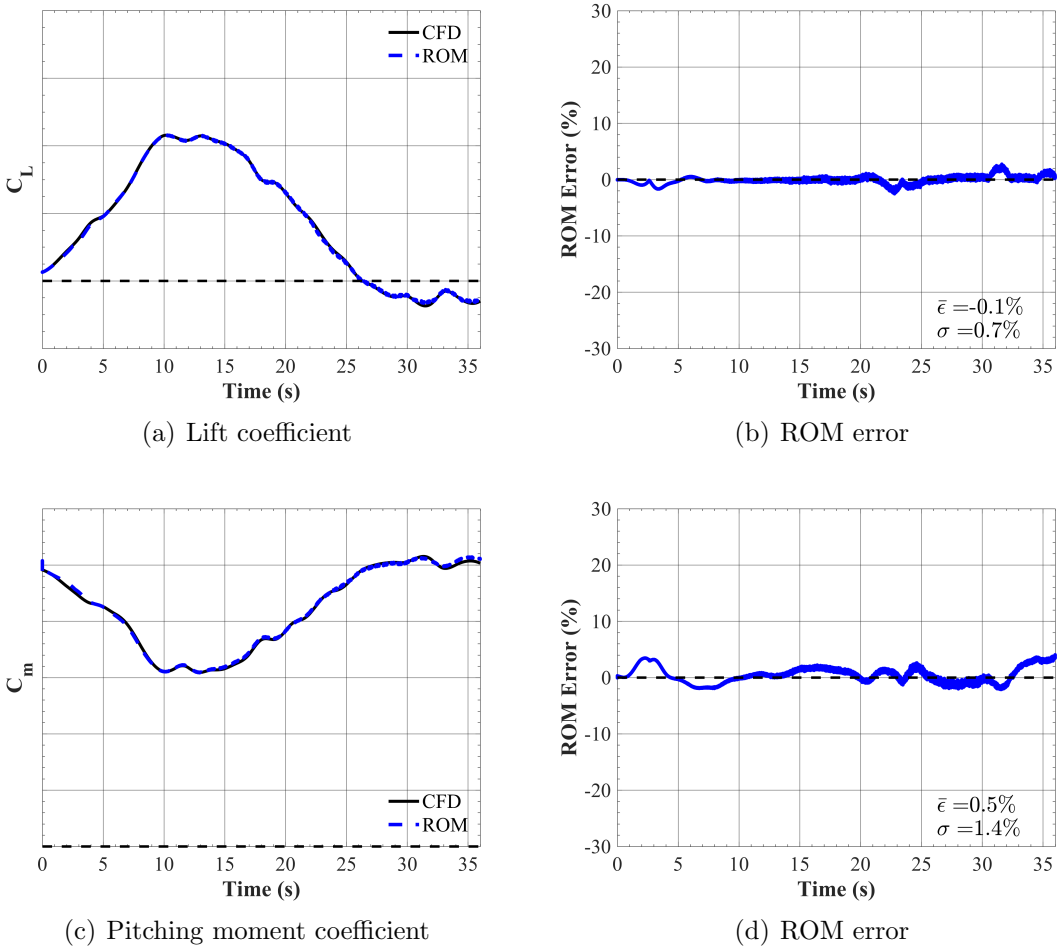

(a) Lift coefficient

(b) ROM error

(c) Pitching moment coefficient

(d) ROM error

Figure 109: Rigid X-56A: Nonlinear ROM (α, M) vs. CFD lift (top) and pitching moment (bottom) coefficient results (left) and ROM error (right) for the rigid vehicle undergoing a right turn maneuver.

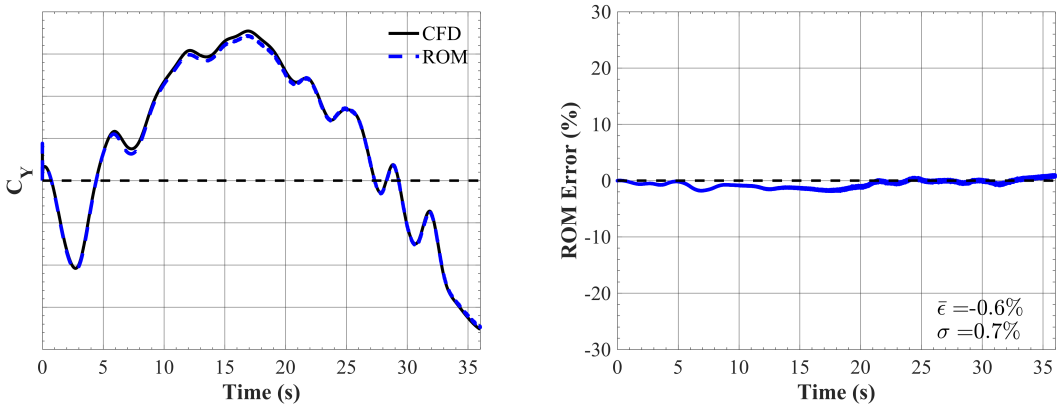

(a) Side force coefficient

(b) ROM error

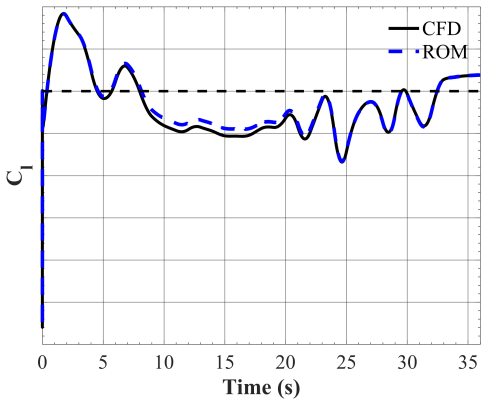

(c) Rolling moment coefficient

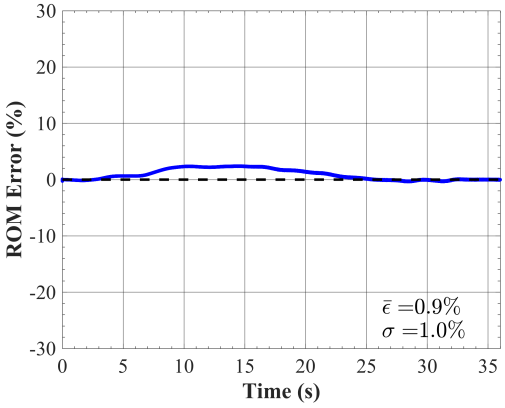

(d) ROM error

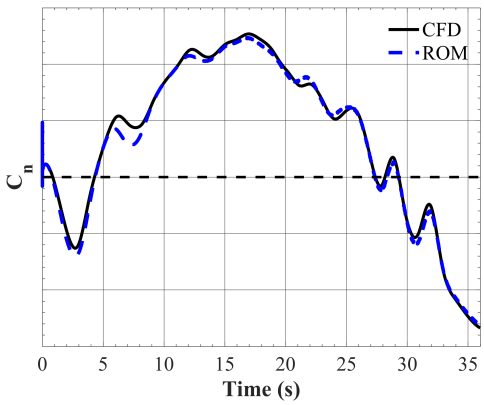

(e) Yawing moment coefficient

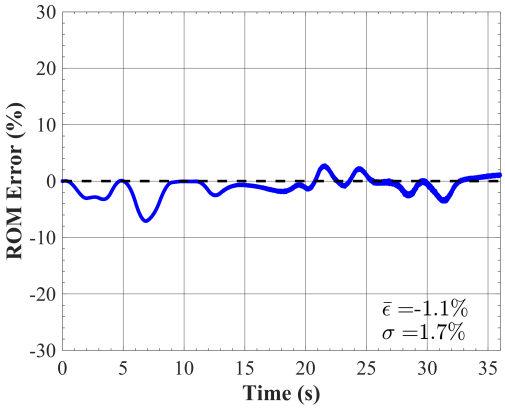

(f) ROM error

Figure 110: Rigid X-56A: Nonlinear ROM (α, M) vs. CFD side force (top), rolling moment (middle), and yawing moment (bottom) coefficient results (left) and ROM error (right) for the rigid vehicle undergoing a right turn maneuver.

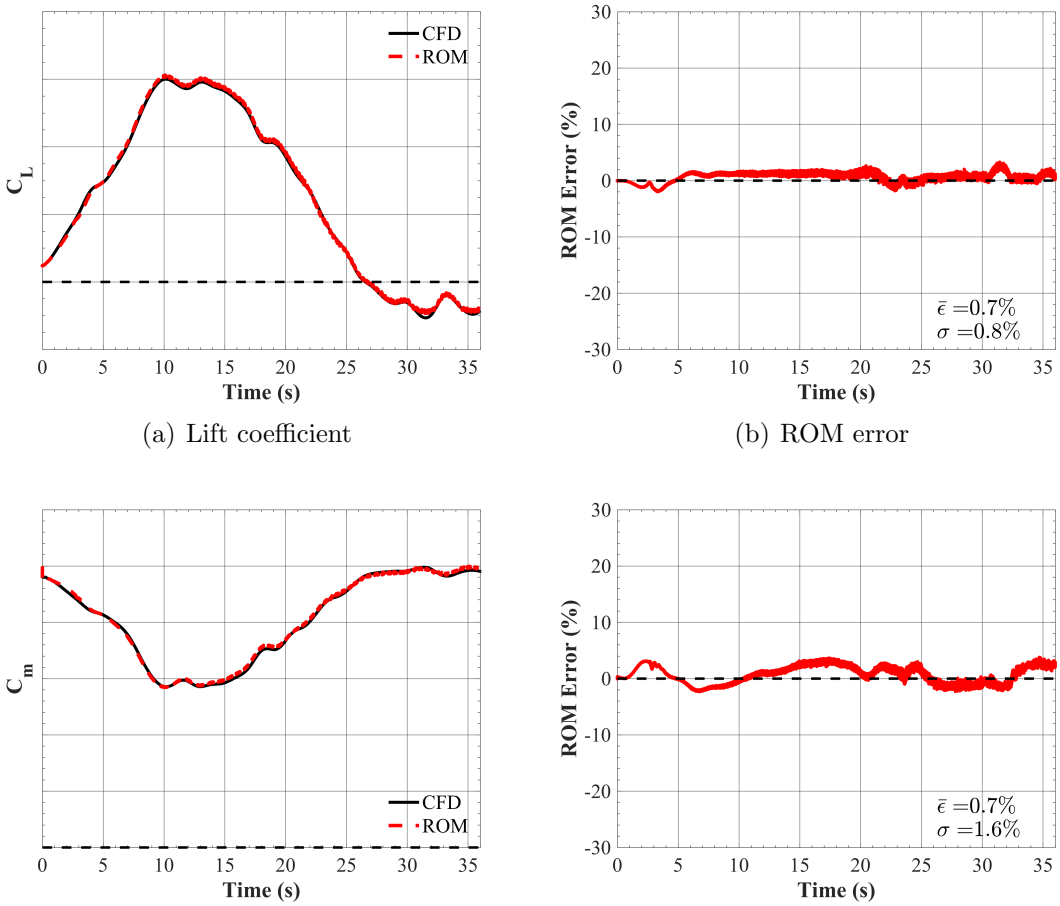

(a) Lift coefficient

(b) ROM error

(c) Pitching moment coefficient

(d) ROM error

Figure 111: Flexible X-56A: Nonlinear ROM (α, M) vs. CFD lift (top) and pitching moment (bottom) coefficient results (left) and ROM error (right) for the flexible vehicle undergoing a right turn maneuver.

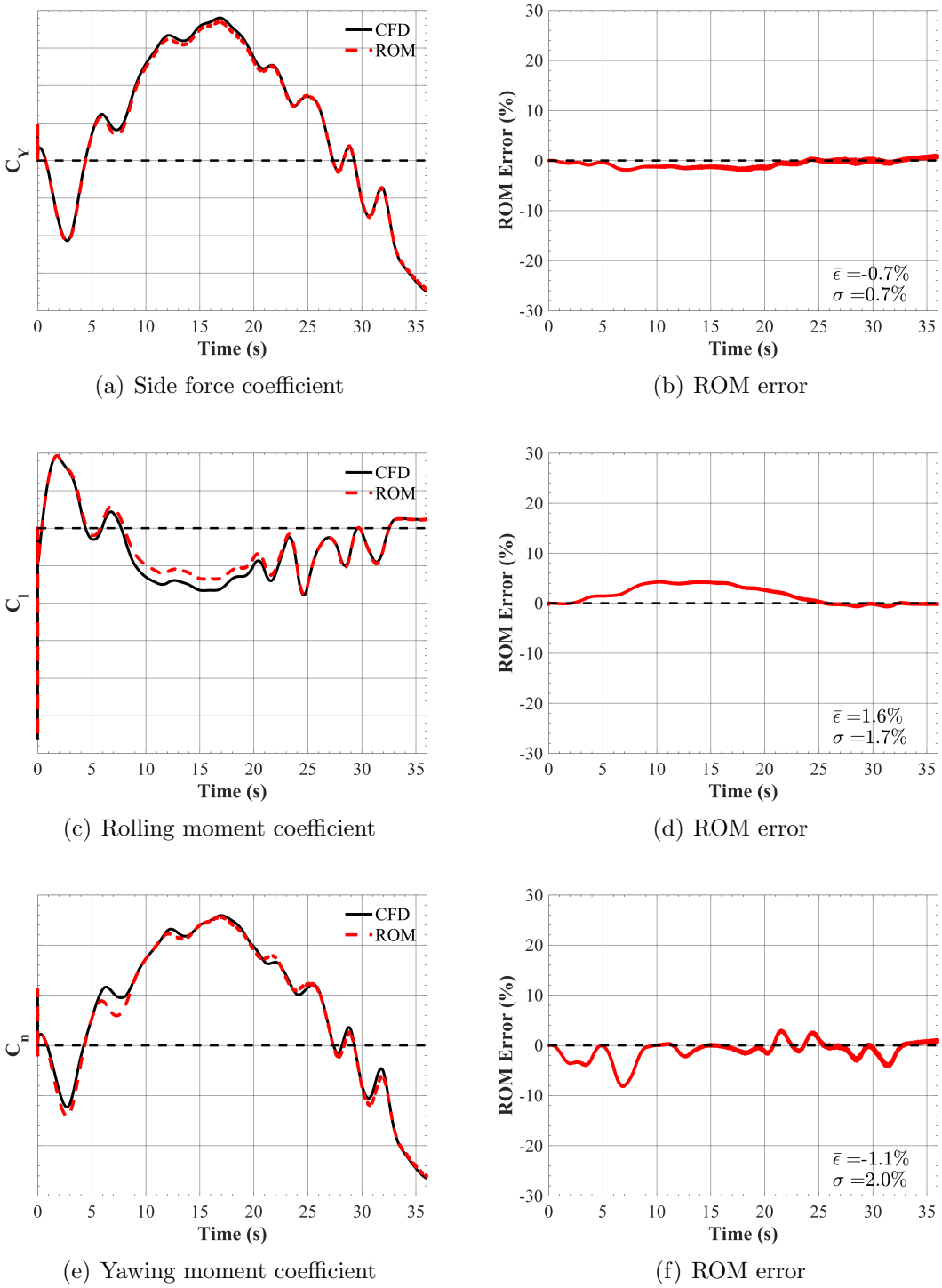

(a) Side force coefficient

(b) ROM error

(c) Rolling moment coefficient

(d) ROM error

(e) Yawing moment coefficient

(f) ROM error

Figure 112: Flexible X-56A: Nonlinear ROM (α, M) vs. CFD side force (top), rolling moment (middle), and yawing moment (bottom) coefficient results (left) and ROM error (right) for the flexible vehicle undergoing a right turn maneuver.

8.3.6 Summary

The present experiment sought to evaluate the unsteady aerodynamic prediction capabilities of a generalized nonlinear indicial response ROM method, which accounted for indicial response sensitivity to angle of attack and Mach number, for the evaluation of arbitrary flight test maneuvers. Aeroelastic indicial responses were simulated at select points across the X-56A flight envelope to capture the response sensitivity to initial angle of attack and Mach number. A kriging surrogate modeling method was implemented using the DACE MATLAB toolbox to model an aeroelastic indicial response database at each flight condition of a given trajectory.

An X-56A right turn flight test maneuver was acquired from the NASA Armstrong Flight Research Center and subsequently tested using the generalized nonlinear ROM formulation. This maneuver was characterized by angle of attack and sideslip angles constrained within $[-2^\circ$ to $5^\circ]$ and $[-4^\circ$ to $4^\circ]$, respectively, and Mach numbers within [0.11 to 0.13]. While limited in Mach number range, the flexible X-56A shows a non-negligible aerodynamic sensitivity for small Mach number increments as previously shown in Chapter 7.

The full-order CFD simulations showed a pronounced difference between the aerodynamic forces and moments experienced by the rigid and flexible vehicle. The lift coefficient had the most significant variation with peak coefficient values nearly 40% greater for the flexible vehicle relative to the rigid vehicle. The pitching moment coefficient showed a qualitatively similar trend between the two vehicles with the most pronounced difference being the shift in static pitching moment coefficient. The side force coefficients were in great agreement for a majority of the maneuver with a slight discrepancy observed during the turn when the angle of attack was at a maximum and the Mach number was at a minimum. The rolling moment coefficients showed a similar behavior with the flexible vehicle encountering a peak coefficient value nearly 50% greater in magnitude relative to the rigid vehicle. The yawing moment coefficients

were in agreement between the two vehicles for the duration of the maneuver.

Rigid and aeroelastic indicial responses were sampled and simulated in one degree angle-of-attack increments at $M = 0.11$ and $M = 0.13$ to adequately cover the maneuver flight space. Predictions for the longitudinal and lateral force and moment coefficients were generated for the rigid and flexible X-56A vehicle using a linear ROM, as well as nonlinear ROMs that included angle-of-attack and Mach number dependencies. The linear ROM showed a general capability to model the qualitative trend of the time-accurate forces and moments for both the rigid and flexible vehicle, but produced significant error as the angles of attack and Mach numbers during the trajectory deviated from the initial flight condition. Generation of a nonlinear ROM that accounted for the indicial response sensitivity to angle of attack showed a significant improvement in each aerodynamic coefficient for the rigid vehicle, and all but the lift coefficient for the flexible vehicle. The generalized nonlinear ROM, which included indicial response sensitivity to both angle of attack and Mach number, was able to capture the peak lift coefficient value that was overpredicted in the nonlinear ROM that didn't account for Mach number variations. Overall, the aeroelastic indicial response ROM was able to predict the longitudinal and lateral aerodynamic coefficients for the rigid and flexible X-56A vehicle undergoing a right turn maneuver with a mean ROM error and standard deviation of $< 2\%$.

CHAPTER IX

MODEL PERFORMANCE (RESEARCH QUESTION 3)

The experiments presented in Chapters 7-8 led to the establishment of a solution strategy for aeroelastic indicial response simulations, the investigation of indicial response sensitivities to flight conditions, and the evaluation of the technical approach for creating quantitatively accurate ROMs for flexible flight vehicles performing generalized trajectories in both linear and nonlinear flight regimes at various motion rates. The present chapter seeks to establish the computational efficiency of the aeroelastic indicial response ROM to determine its merits toward enabling viable VFS studies. This is aimed at answering Research Question 3, which is restated below:

Research Question 3:

What are the performance benefits of the aeroelastic indicial response ROM?

In order to address this research question, it is divided into two important components: the performance of aeroelastic indicial response ROMs relative to (1) high-fidelity CFD simulations and (2) quasisteady stability derivative predictions. In Section 9.1, the static and dynamic simulation computational costs are defined for both the full-order simulations and the indicial response simulations. Total costs for the linear and nonlinear ROMs generated are specified, in addition to their modeling accuracies, using the maneuver results obtained in Chapter 8. In Section 9.2, stability derivative predictions are generated for select maneuvers presented in Chapter 8 and compared, in terms of cost and accuracy, to the previously generated indicial response ROM predictions. These comparisons aid in understanding the benefits and limitations of the proposed ROM relative to the traditional flight dynamics method.

9.1 Experiment 3.1 - Reduced-Order Model vs. Full-Order Simulation

Experiment 3.1 addresses Research Question 3.1 and tests Hypothesis 3.1, both of which are restated below:

Research Question 3.1:
What are the performance benefits relative to full-order aeroelastic simulations?

Hypothesis 3.1: *The linear ROM provides a performance benefit relative to full-order simulations for single maneuver evaluations, whereas the nonlinear ROM becomes beneficial only for multiple maneuver evaluations.*

Indicial response models developed for maneuvering flight vehicle predictions require a large upfront cost associated with simulating indicial responses. Generalized 6DOF maneuvers incur additional costs associated with the identification of responses with respect to lateral vehicle-state motion parameters. For prescribed trajectories extending into nonlinear flight regimes, nonlinear indicial response ROMs require the interpolation of a database of sampled indicial responses as a function of angle of attack and Mach number. Once the model is identified, it may be reused to provide predictions for the unsteady aerodynamics encountered during any arbitrary trajectory (within the sampled flight envelope) at any motion rate in a matter of seconds. Because the ROM is created only once for a given vehicle's flight envelope, the computational benefits of the ROM grow with the number of maneuvers to be evaluated.

9.1.1 Purpose of Experiment

The following are identified as the main objectives of this numerical experiment:

1. Quantify the computational costs and modeling accuracy associated with linear and nonlinear aeroelastic indicial response ROMs for unsteady aerodynamic predictions relative to full-order dynamic aeroelastic simulations

2. Calculate the costs associated with generating a nonlinear ROM for the X-56A flight envelope and determine the number of maneuver evaluations needed for ROM benefits

3. Compare the relative performance of rigid vs. aeroelastic unsteady aerodynamic ROMs

9.1.2 Experiment Setup

Performance comparisons between the linear, nonlinear (α), and nonlinear (α, M) ROM variants to full-order simulations will be made using the small-amplitude forced oscillations in Section 8.1, the large-amplitude forced pitching oscillations in Section 8.2, and the right turn flight test maneuver in Section 9.1. Performance is quantified by computational cost, ROM mean error, and ROM standard deviation of error.

Computational costs, C, are defined using Eq. 77, where N_{proc} is the number of CPU processors and t_{wall} is the expended wall time for simulation execution. The rigid and aeroelastic indicial solutions were computed on the NASA Langley K4-cluster, consisting of Intel Gold 6148 Skylake processors. Full-order rigid and aeroelastic maneuver solutions were computed on the NASA Advanced Supercomputing (NAS) facility's Electra supercomputer Skylake nodes, consisting of Intel Xeon Gold 6148 Skylake processors. Identical processor types were used to ensure consistent performance comparisons. The total computational cost, C_{sim}, for maneuver predictions is defined by Eq. 78, where C_{stat} and C_{dyn} represent the computational costs for the static initialization and dynamic maneuver simulations, respectively.

$$C = N_{proc} * t_{wall} \tag{77}$$

$$C_{sim} = C_{stat} + C_{dyn} \tag{78}$$

Unsteady aeroelastic predictions for full-order maneuvers were generated using a *CFD2ROM* MATLAB code for indicial response modeling. The linear and nonlinear ROM predictions were computed in a matter of seconds for full-order maneuvers on a 2 GHz Intel Core i7 MacBook Pro personal laptop. Due to the negligible online computation times, ROM computational costs are isolated to the costs incurred for indicial response identification. Equation 79 expresses the ROM cost, C_{ROM}, as a function of the cost of static initialization solutions, C_{stat}, at each flight condition of interest, m, the cost of the longitudinal indicial response solutions, $C_{dyn}^{IR-long}$, the number of angle-of-attack indicial responses identified, n_α, the number of pitch rate indicial responses identified, n_q, the cost of the lateral indicial response solutions, C_{dyn}^{IR-lat}, the number of sideslip angle indicial responses identified, n_β, the number of roll rate indicial responses identified, n_p, and the number of yaw rate indicial responses identified, n_r.

$$C_{ROM} = C_{stat} * m + C_{dyn}^{IR-long} * [n_\alpha + n_q] + C_{dyn}^{IR-lat} * [n_\beta + n_p + n_r] \tag{79}$$

The ROM predictions presented in Chapter 8 were compared to CFD simulations results for each aerodynamic coefficient based on a modeling accuracy quantified using a time-dependent percent error, ϵ_i, for which the mean error, $\overline{\epsilon}$, and standard deviation, σ, were calculated over the duration of the trajectory. For the present comparisons, average ROM error, ϵ_{ROM}, and standard deviation, σ_{ROM}, are calculated for each maneuver using Eqs. 80-81, where n_{coeff} is the number of aerodynamic coefficients predicted.

$$\epsilon_{ROM} = \frac{\sum_{i=1}^{n_{coeff}} \overline{\epsilon}_i}{n_{coeff}} \tag{80}$$

$$\sigma_{ROM} = \frac{\sum_{i=1}^{n_{coeff}} \sigma_i}{n_{coeff}} \tag{81}$$

9.1.3 Indicial Response Simulation Costs

Table 21 lists the computational costs, measured in CPU hours, for simulating rigid and aeroelastic indicial responses. The indicial responses shown are those due to step changes in angle of attack (α-step), pitch rate (q-step), sideslip angle (β-step), roll rate (p-step), and yaw rate (r-step). For each simulation, the static initialiation solution cost, indicial trajectory simulation cost, and total cost is listed.

Table 21: CPU hours required to create a single indicial response solution.

	Rigid			**Aeroelastic**		
Case	Static	Dynamic	Total	Static	Dynamic	Total
α-step	6	65	71	6	280	286
q-step	6	65	71	6	280	286
β-step	6	65	71	6	70	76
p-step	6	65	71	6	70	76
r-step	6	65	71	6	70	76

For both the rigid and aeroelastic indicial responses, the time step resolves the highest frequency structural mode using a sampling of $N = 200$, resulting in a time step of $\Delta t = 4E - 04$ sec. The static rigid and aeroelastic solutions were generated using 75 time steps resulting in a cost of 6 CPU hours. The longitudinal and lateral indicial responses for the rigid vehicle were simulated for 1,000 time steps, which ensured steady-state convergence at the updated vehicle-state. For the flexible vehicle, weak fluid-structure interactions were observed in the indicial responses due to step changes in sideslip angle, roll rate, and yaw rate. As a result, similar convergence levels were reached when using 1,000 time steps as found for the rigid vehicle. The cost for 1,000 time steps was 65 and 70 CPU hours for the rigid and aeroelastic simulations, respectively. The longitudinal indicial responses for the flexible vehicle required approximately four times the number of time steps to achieve a sufficiently converged solution due the prescence of strong fluid-structure interactions. These 4,000 time steps correspond to approximately 5 periods of the lowest frequency structural mode.

9.1.4 Small-Amplitude Forced Oscillations

Table 22 summarizes the modeling accuracy metrics for the linear ROM in predicting the unsteady aerodynamic forces and moments for the small-amplitude forced rolling, yawing, and pitching oscillations presented in Section 8.1 of Chapter 8. Because the oscillation amplitude was limited to one degree, the linear ROM is correctly applied to a locally linear range, and the ability to capture the frequency spectrum may be investigated. For both the rigid and flexible vehicle, the indicial response ROM is able to accurately resolve the aerodynamic coefficients with mean error and standard deviation values of $< 0.5\%$ at reduced frequencies ranging from quasisteady to unsteady using a single indicial response for each vehicle-state parameter.

Table 22: Linear ROM prediction accuracy in terms of mean error and standard deviation.

		Rigid		**Aeroelastic**	
Case	k	ϵ (%)	σ (%)	ϵ (%)	σ (%)
FO-Roll	0.05	0.0	0.1	0.0	0.2
($\Delta\phi = 1°$)	0.10	0.0	0.1	0.0	0.1
	0.20	0.0	0.1	0.0	0.1
FO-Yaw	0.05	0.0	0.0	0.0	0.0
($\Delta\psi = 1°$)	0.10	0.0	0.0	0.0	0.0
	0.20	0.0	0.1	0.0	0.1
FO-Pitch	0.05	0.1	0.2	0.2	0.3
($\Delta\alpha = 1°$)	0.10	0.1	0.3	0.1	0.3
	0.20	0.1	0.4	0.2	0.5

The computational costs, measured in CPU hours, required for the full-order rigid and aeroelastic simulations of the small-amplitude forced oscillations are listed in Table 23. For consistent temporal resolution, the forced oscillations were simulated using the same time step used for indicial response identification ($\Delta t = 4E-04$ sec.). Each of the forced oscillation cases were simulated for a total of three cycles to allow for damping of numerical transients due to grid motion start and to observe cycle-to-cycle differences that arose during flexible vehicle simulations. In each case, the number of time steps required to simulate one cycle was dependent on the motion

frequency/period, calculated as a function of reduced frequency and reference length using Eq. 72. For the forced rolling and yawing oscillations, the reference length was based on the semispan, whereas a semichord reference length was used for forced pitching oscillations. As a result, the lateral oscillations were characterized by a greater motion frequency for equivalent levels of flow unsteadiness, and thus, required more time steps per cycle of motion.

Table 23: CPU hours required to create small-amplitude forced oscillation CFD solutions.

		Rigid			**Aeroelastic**		
Case	k	Static	Dynamic	Total	Static	Dynamic	Total
FO-Roll	0.05	6	5,726	5,732	6	6,240	6,246
($\Delta\psi = 1°$)	0.10	0	2,880	2,880	0	2,990	2,990
	0.20	0	1,440	1,440	0	1,550	1,550
FO-Yaw	0.05	0	5,803	5,803	0	6,167	6,167
($\Delta\phi = 1°$)	0.10	0	2,887	2,887	0	2,990	2,990
	0.20	0	1,453	1,453	0	1,550	1,550
FO-Pitch	0.05	0	423	423	0	453	453
($\Delta\alpha = 1°$)	0.10	0	213	213	0	237	237
	0.20	0	103	103	0	116	116
	Total	6	20,928	20,934	6	22,293	22,299

Since the small-amplitude forced oscillations were initialized from an identical flight condition, the static simulation costs are accounted for only once. Due to the efficiency of FUN3D's internal linear modal structural analysis, the total costs for the aeroelastic simulations were $< 10\%$ greater than those for the rigid simulations. The total cost for simulating the nine small-amplitude forced oscillations was 20,934 and 22,299 CPU hours for the rigid and aeroelastic simulations, respectively.

Table 24 lists the corresponding computational costs required in generating the linear ROM for the small-amplitude forced oscillations, initialized at $\alpha_0 = 0°$ and $M = 0.13$. For predicting the longitudinal coefficients, two indicial responses were required, one with respect to angle of attack and one for pitch rate. For the lateral coefficient predictions, one indicial response each was required with respect to sideslip

angle, roll rate, and yaw rate. The total computational costs for the linear ROM were 331 and 776 hours for the rigid and flexible vehicle, respectively. Once generated, the linear ROM is capable of generating online predictions in a matter of seconds for maneuvers at any motion rate of interest near the initial condition. For the rigid vehicle, the total ROM generation cost was approximately 63 times cheaper relative to full-order simulations. For the flexible vehicle, the relative cost savings were reduced, but still remained approximately 28 times cheaper than full-order dynamic aeroelastic simulations. This reduction in savings is primarily attributed to the increase number of iterations required for the simulation of the longitudinal indicial responses.

Table 24: CPU hours required to create linear ROM for forced oscillations initialized from $\alpha = 0°$, $M = 0.13$.

	Rigid			**Aeroelastic**		
Coeff.	Static	Dynamic	Total	Static	Dynamic	Total
Longitudinal	6	130	136	6	560	566
Lateral	0	195	195	0	210	210
Complete	6	325	331	6	770	776

9.1.5 Large-Amplitude Forced Pitching Oscillations

Table 25 summarizes the modeling accuracy metrics for the linear and nonlinear ROM in predicting the unsteady aerodynamic forces and moments for the large-amplitude forced oscillations presented in Section 8.2 of Chapter 8. These oscillations were initialized from $\alpha_0 = 5°$ and simulated using a 5° pitching amplitude resulting in an angle-of-attack range of $\alpha = [1° \text{ to } 9°]$. A wide angle-of-attack envelope helped to explore the limitations of the linear ROM and highlight the benefits of accounting of an indicial response sensitivity to angle of attack in a nonlinear ROM.

The linear ROM showed fairly good prediction accuracy for the rigid forced oscillations at each frequency with mean error and standard deviation $< 1\%$. The static characterization study presented in Section 7.1 support these findings with a relatively linear variation in lift and pitching moment for the given angle-of-attack

range. As a result, adding a nonlinear dependency on angle of attack served to only slightly reduce the mean error and standard deviation by a fraction of a percent. Relative to the rigid predictions, the linear ROM predictions were less accurate for the flexible vehicle with a mean error and standard deviation over five times worse. The static lift and pitching moment curves of Section 7.1 support this observation, as the flexible vehicle's curves present a stronger nonlinearity over the given angle-of-attack range. Due to this nonlinearity, the nonlinear ROM was able to better predict the quasisteady and quasiunsteady forced oscillation cases with mean error and standard deviation values $< 1\%$.

In the unsteady case, the modeling accuracy slightly degraded due to discrepancies at lower angles of attack (Fig. 89). It is important to note that this discrepancy arose when including negative step responses in the nonlinear model. When only using positive step responses, the nonlinear ROM was able to generate predictions with a mean error of 0.6% and standard deviation of 0.8%. Overall, the nonlinear ROM produces great qualitative agreement for both the rigid and flexible vehicle. In particular, cycle-to-cycle differences in the aerodynamic damping and minimum/maximum coefficients due to complex fluid-structure interactions were well-resolved for the flexible X-56A at each reduced frequency of interest.

Table 25: Linear and Nonlinear (α) ROM prediction accuracy in terms of mean error and standard deviation.

		Rigid		**Aeroelastic**	
Model	k	ϵ (%)	σ (%)	ϵ (%)	σ (%)
Linear	0.05	0.4	0.4	2.2	2.4
	0.10	0.3	0.4	1.7	1.3
	0.20	0.3	0.6	0.8	0.8
Nonlinear (α)	0.05	0.0	0.1	0.2	0.9
	0.10	0.1	0.3	0.6	1.0
	0.20	0.1	0.5	1.7	1.1

The computational costs, measured in CPU hours, required for the full-order rigid and aeroelastic simulations of the large-amplitude forced oscillations are listed in Table 26. Similar to the previous full-order simulations, a time step of $\Delta t = 4E-04$ sec. was used for each simulated frequency. Since each forced oscillation was initialized from the same flight condition, the static cost was accounted for once. The total simulation costs were 753 and 798 CPU hours for the rigid and flexible vehicle, respectively.

Table 26: CPU hours required to create large-amplitude forced oscillation CFD solutions.

	Rigid			**Aeroelastic**		
k	Static	Dynamic	Total	Static	Dynamic	Total
0.05	6	433	439	6	446	452
0.10	0	207	207	0	233	233
0.20	0	107	107	0	113	113
Total	6	747	753	6	792	798

Table 27 specifies the computational costs for linear and nonlinear ROM generation in support of large-amplitude pitch oscillation predictions. Because only the longitudinal plane of motion is considered, only angle-of-attack and pitch rate indicial responses were required for identification. For the linear ROM, a single response for each step type was simulated at the initial flight condition. For the nonlinear ROM, angle-of-attack indicial responses were simulated from eight different angles of attack to cover the motion range of interest, and a single pitch rate response was required at the initial flight condition since it was not assumed to depend on angle of attack. As a result, the total computational costs for the rigid and aeroelastic linear ROMs were 136 and 566, respectively. For the nonlinear ROM, the rigid simulation cost was 627 and the aeroelastic simulation cost was 2,562.

The linear ROMs for both the rigid and flexible vehicle incurred computational cost less than those required for the full-order simulations. In the case of the rigid

vehicle, the nonlinear ROM was also shown to be cheaper than the full-order simulation costs. However, for the flexible vehicle, the nonlinear ROM cost was nearly three times greater compared to full-order simulations. This reinforces the relative inefficiency of the multidisciplinary ROM relative to the rigid ROM for the number of test maneuvers evaluated. However, it is important to note that the total duration simulated for the three forced oscillations was approximately five seconds. Practically speaking, the nonlinear model is capable of evaluating any arbitrary longitudinal maneuver within the range of $\alpha = [1^\circ \text{ to } 9^\circ]$ at $M = 0.13$ at any frequency of interest. The performance benefits of the nonlinear aeroelastic ROM relative to full-order simulations would then be realized for approximately 15 seconds of simulated maneuver time. This duration is likely to be exceeded in characterizing the aerodynamics of an unconventional vehicle performing maneuvers in its planned flight envelope.

Table 27: CPU hours required to create linear ROM and nonlinear ROM (α) for large-amplitude pitch oscillation predictions.

	Rigid			**Aeroelastic**		
Model	Static	Dynamic	Total	Static	Dynamic	Total
Linear	6	130	136	6	560	566
Nonlinear (α)	42	585	627	42	2,520	2,562

9.1.6 Right Turn Flight Test Maneuver

Table 28 summarizes the modeling accuracy metrics for the linear, nonlinear (α), and nonlinear (α, M) ROM variants in predicting the longitudinal and lateral aerodynamic forces and moments encountered by a rigid and flexible X-56A performing a right turn flight test maneuver, as presented in Section 8.3. This maneuver was characterized by angle of attack and sideslip angles constrained within $[-2^\circ \text{ to } 5^\circ]$ and $[-4^\circ \text{ to } 4^\circ]$, respectively, and Mach numbers within [0.11 to 0.13]. The linear ROM uses a single set of indicial responses with respect to each vehicle-state parameter, simulated at the initial condition. The nonlinear (α) ROM leverages additional

indicial responses with respect to step changes in angle of attack and sideslip angle sampled in 1° increments across the maneuver angle-of-attack range. The nonlinear (α, M) ROM samples the angle-of-attack and sideslip angle indicial responses at each previous angle of attack at both $M = 0.11$ and 0.13. The indicial responses with respect to the rotation rates are now a function of Mach number and are sampled at the minimum and maximum flight maneuver Mach numbers (see Tables 18-19).

Table 28: Each ROM variant's prediction accuracy in terms of mean error and standard deviation.

	Rigid		**Aeroelastic**	
Model	ϵ (%)	σ (%)	ϵ (%)	σ (%)
Linear	1.2	2.6	4.4	4.7
Nonlinear (α)	0.8	1.0	1.4	1.9
Nonlinear (α, M)	0.6	1.1	1.0	1.4

The linear ROM predicts the aerodynamic coefficient's of the rigid vehicle with a mean error of 1.2% and a standard deviation of 2.6%. The addition of the indicial response sensitivity to angle of attack led to reductions in both metrics with a mean error of 0.8% and 1.0%. Including the modeling dependency on Mach number provided negligible performance improvements with a 0.2% decrease in mean error, but a 0.1% increase in standard deviation. This result is attributed to the rigid vehicle's limited sensitivity to Mach number for the given range of the right turn maneuver, where a slight increase in standard deviation may be attributed to kriging surrogate modeling error of the indicial responses at each point in the trajectory.

Relative to the rigid vehicle, the linear ROM was more inaccurate for the flexible vehicle predictions with a mean error of 4.4% and standard deviation of 4.7%. These results suggest a stronger nonlinear variation in angle of attack and/or Mach number for the given maneuver range compared to the rigid vehicle. The nonlinear (α) ROM showed considerable improvement relative to the linear ROM with an approximate decrease of 3% in both mean error and standard deviation. Finally, the addition of

the Mach number provided further decreases in mean error and standard deviation by nearly 0.5%.

Table 29 lists the computational costs for the rigid and aeroelastic simulations of the 36 second right turn maneuver. The total rigid simulation cost was 5,752, and the total aeroelastic simulation cost was 6,086. In comparison, the computational costs incurred in the generation of each ROM variant are included in Table 30. For the rigid vehicle, the linear ROM costed 331 hours, presenting nearly a 16 times savings over the full-order dynamic simulation with reasonable levels of accuracy. The nonlinear (α) ROM, which generated predictions within 1% of CFD results, required only a quarter of the full-order simulation costs. The generalized nonlinear ROM costed only half of the simulation costs. For the flexible vehicle, the linear ROM presented approximately an 8 times greater savings. The nonlinear (α) ROM variant costed about half the full-order simulation costs. Finally, the generalized nonlinear (α) and (α, M) ROM variants costed nearly the same as the full-order simulation. While the rigid ROM presents a cost benefit earlier than the aeroelastic ROM, these results show the utility of the method in either case for multiple maneuver evaluations.

Table 29: CPU hours required to create right turn maneuver CFD solutions.

Rigid			**Aeroelastic**		
Static	Dynamic	Total	Static	Dynamic	Total
6	5,746	5,752	6	6,080	6,086

Table 30: CPU hours required to create each ROM variant for right turn maneuver predictions.

		Rigid			**Aeroelastic**		
Model	Coeff.	Static	Dynamic	Total	Static	Dynamic	Total
Linear	Longitudinal	6	130	136	6	560	566
	Lateral	0	195	195	0	210	210
	Complete	6	325	331	0	770	776
Nonlinear (α)	Longitudinal	48	520	568	48	2,240	2,288
	Lateral	0	650	650	0	700	700
	Complete	48	1,170	1,218	48	2,940	2,988
Nonlinear (α, M)	Longitudinal	96	1,040	1,136	96	4,480	4,576
	Lateral	0	1,300	1,300	0	1,400	1,400
	Complete	96	2,340	2,436	96	5,880	5,976

9.1.7 Viable VFS for X-56A Flight Envelope

The previous section summarized the associated computational costs required for generating linear, nonlinear (α), and nonlinear (α, M) ROMs for each class of maneuvers in isolation, mostly for the purpose of characterizing the ROM prediction accuracy improvements for successive inclusions of nonlinear modeling dependencies. These ROMs often relied on the simulation of redundant indicial responses relative to the other variants. The present section outlines the cost benefits of a single generalized nonlinear ROM (α, M) applicable to all of the flight maneuvers considered in this work. Table 31 lists the static, dynamic and total simulation costs for each of the tested maneuvers in Sections 8.1-8.3 for both the rigid and flexible X-56A. The total rigid and aeroelastic simulation costs amounted to 27,433 and 29,177 CPU hours, respectively.

Table 31: CPU hours required to create all maneuver CFD solutions.

		Rigid			**Aeroelastic**		
Case	k	Static	Dynamic	Total	Static	Dynamic	Total
FO-Roll	0.05	6	5,726	5,732	6	6,240	6,246
($\Delta\phi = 1°$)	0.10	0	2,880	2,880	0	2,990	2,990
	0.20	0	1,440	1,440	0	1,550	1,550
FO-Yaw	0.05	0	5,803	5,803	0	6,167	6,167
($\Delta\psi = 1°$)	0.10	0	2,887	2,887	0	2,990	2,990
	0.20	0	1,453	1,453	0	1,550	1,550
FO-Pitch	0.05	0	423	423	0	453	453
($\Delta\alpha = 1°$)	0.10	0	213	213	0	237	237
	0.20	0	103	103	0	116	116
FO-Pitch	0.05	6	433	439	6	446	452
($\Delta\alpha = 4°$)	0.10	0	207	207	0	233	233
	0.20	0	107	107	0	113	113
Right Turn		0	5,746	5,746	0	6,080	6,080
	Total	12	27,421	27,433	12	29,165	29,177

The angle-of-attack range covered by the test maneuvers is $\alpha = [-2° \text{ to } 9°]$, and the Mach number varied from $M = [0.11 \text{ to } 0.13]$. Table 32 lists the indicial response samples required for generating a generalized nonlinear (α, M) ROM capable of evaluating all previously noted test maneuvers with a modeling accuracy quantified by a mean error and standard deviation of $< 2\%$. The indicial responses due to step changes in rotation rates are assumed to vary only with Mach number and can be simulated at $\alpha = 0°$ at the minimum and maximum Mach number covered by the right turn maneuver. The angle-of-attack and sideslip angle indicial responses are a function of angle of attack and must be sampled at each angle of attack transversed in 1° increments.

Table 32: Matrix of indicial step cases for input to the kriging surrogate model for all test maneuvers of interest.

α_0 (deg)	$M = 0.11$	$M = 0.13$
0	$\Delta p, \Delta q, \Delta r$	$\Delta p, \Delta q, \Delta r$
-2 to 9	$\Delta\alpha, \Delta\beta$	$\Delta\alpha, \Delta\beta$

The corresponding computational costs for the generalized ROM are listed in Table

33. The total rigid and aeroelastic indicial response simulation costs are 3,830 and 9,130 CPU hours, respectively. Compared to the 16 full-order maneuver simulations, the indicial response ROM is approximately seven times cheaper for the rigid vehicle predictions and approximately three times cheaper for the flexible vehicle. Once the ROM is generated, it may be used repeatedly to generate maneuver predictions in a matter of seconds/minutes depending on the maneuver length.

Table 33: CPU hours required to create generalized ROM (α, M) for all maneuver predictions.

	Rigid			**Aeroelastic**		
Model	Static	Dynamic	Total	Static	Dynamic	Total
Longitudinal	450	1,560	2,010	450	6,720	7,170
Lateral	0	1,820	1,820	0	1,960	1,960
Total	450	3,380	3,830	450	8,680	9,130

The generalized ROM for the maneuver predictions considered in this work is limited by the small Mach number range considered. The given range was largely attributed to only considering a select number of maneuvers for minimum viable method evaluations, but also to the limited Mach numbers of the X-56A flight envelope. The X-56A is generally confined to Mach numbers below $M = 0.20$ [101]. As such, the utility of a generalized nonlinear ROM is not fully exercised. Table 34 lists a matrix of indicial response cases required to generate a generalized nonlinear ROM (α, M) for the X-56A flight envelope, $\alpha = [-5^\circ$ to $10^\circ]$, $M = [0.10$ to $0.20]$, using a one degree sampling and Mach increment of 0.02, i.e., 96 sampled flight conditions. The corresponding computational costs for the rigid and aeroelastic ROM simulations would be 14,226 and 36,696 CPU hours, respectively.

Using the right turn maneuver costs as a baseline, the cost per second of simulated trajectory can be assumed to be 160 and 169 CPU hours for rigid and aeroelastic simulations, respectively. Figure 113 lists the computational costs in simulating a given maneuver flight time for a rigid (blue) and flexible (red) vehicle by the nonlinear ROM

Table 34: Matrix of indicial step cases for input to the kriging surrogate model for the X-56A flight envelope.

α_0 (deg)	$M = 0.10$	$M = 0.12$	$M = 0.14$	$M = 0.16$	$M = 0.18$	$M = 0.20$
0	$\Delta p, \Delta q, \Delta r$	$\Delta p, \Delta q, \Delta r$	$\Delta p, \Delta q, \Delta r$	$\Delta p, \Delta q, \Delta r$	$\Delta p, \Delta q, \Delta r$	$\Delta p, \Delta q, \Delta r$
-5 to 10	$\Delta\alpha, \Delta\beta$	$\Delta\alpha, \Delta\beta$	$\Delta\alpha, \Delta\beta$	$\Delta\alpha, \Delta\beta$	$\Delta\alpha, \Delta\beta$	$\Delta\alpha, \Delta\beta$

Table 35: CPU hours required to create generalized ROM (α, M) for X-56A flight envelope, $\alpha = [-5^\circ$ to $10^\circ]$, $M = [0.10$ to $0.20]$.

	Rigid			**Aeroelastic**		
Model	Static	Dynamic	Total	Static	Dynamic	Total
Longitudinal	576	6,630	7,206	576	28,560	29,136
Lateral	0	7,020	7,020	0	7,560	7,560
Total	576	13,650	14,226	576	36,120	36,696

(dashed) and full-order CFD simulations (solid). The rigid ROM is shown to outperform full-order CFD simulations for physical maneuver flight times exceeding a total of 90 seconds. In contrast, the aeroelastic ROM outperforms the full-order aeroelastic CFD simulations for maneuver flight times exceeding a total of 220 seconds. The required flight times prior to computational savings are likely to be a result of multiple maneuver evaluations about the baseline cruise condition. For modern flight vehicle programs, total maneuver flight times evaluated are likely to greatly surpass the four minutes of simulated flight time required for ROM benefits. While specific to the flight envelope of the X-56A, similar costs would be required in sampling 96 initial flight conditions of any vehicle's flight envelope. The nonlinearities present for the X-56A flight envelope were strong enough to warrant a fine sampling, $\Delta M = 0.02$, with respect to Mach number. For other vehicles, similar modeling accuracies might be achieved over a wider range of Mach numbers, where a coarse sampling of the Mach number space may be used for an equivalent nonlinear variation. Furthermore, the implementation of sampling strategies other than uniform sampling, such as latin hypercube or adaptive sampling, may serve to reduce the computational costs required for indicial response simulations.

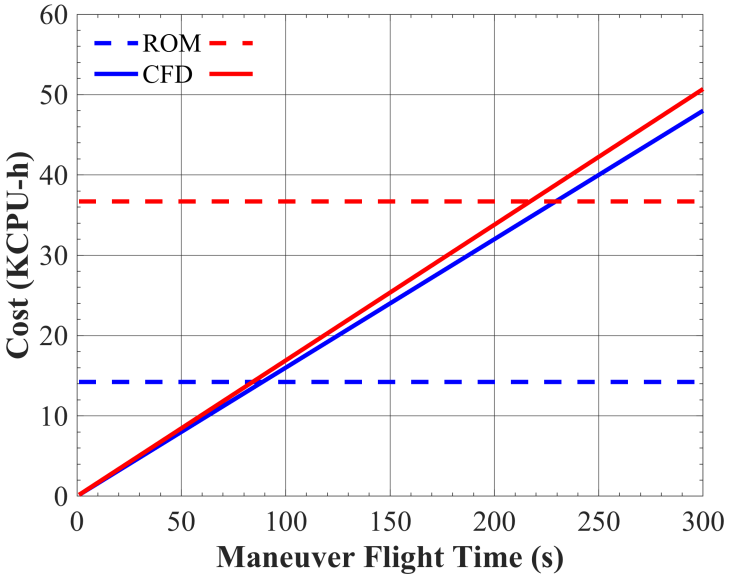

Figure 113: Maneuver flight time versus computational costs (in thousands of CPU-hours) for the rigid (blue) and aeroelastic (red) ROM predictions and full-order CFD simulations.

9.1.8 Summary

The present experiment sought to quantify the modeling accuracy and computational costs of the linear and nonlinear ROM variants used in evaluating the test maneuvers of Chapter 8. The linear ROM was tested using locally linear forced rolling, yawing, and pitching oscillations. The predictions for the unsteady longitudinal and lateral force and moment coefficients were found to be in great agreement with full-order rigid and aeroelastic simulations, characterized by an overall mean error and standard deviation of $< 0.5\%$, from quasisteady to unsteady reduced frequencies. The rigid and aeroelastic linear indicial response ROMs were approximately 63 and 28 times cheaper than the full-order simulations, respectively.

The nonlinear ROM (α) was tested using a large-amplitude forced oscillations that spanned $\alpha = [1^\circ \text{ to } 9^\circ]$ at a constant $M = 0.13$. Based on a uniform sampling of one degree in angle of attack for the angle-of-attack indicial responses and a single sample of the pitch rate indicial response at the initial flight condition, the nonlinear ROM

was able to produce accurate predictions for the unsteady lift and pitching moment coeficients with a mean error and standard deviation of $< 2\%$. The computational costs required for the rigid nonlinear ROM was comparable to the total costs for simulating the three motion frequency cases. The aeroelastic nonlinear ROM was approximately three times more expensive than the full-order simulations. It is important to note that the total trajectory time simulated was on the order of 5 seconds. For a single 15 sec. maneuver within the angle-of-attack range, the aeroelastic ROM would begin to show computational benefits relative to full-order simulations.

The modeling accuracy and computational costs were evaluated for the nonlinear ROM (α, M) in generating predictions for a flight space corresponding to $\alpha = [-2^\circ$ to $5^\circ]$ and $M = [0.11$ to $0.13]$, which were the bounds of a right turn flight test maneuver acquired from the NASA Armstrong Flight Research Center. The ROM was able to accurately model the longitudinal and lateral force and moment coefficients with a mean error and standard deviation of $< 1.5\%$. The total computational costs for the rigid and aeroelastic nonlinear ROM generation were 2,436 and 5,976 CPU hours, respectively. Relative to full-order simulations, the rigid ROM was approximately two times less, and the aeroelastic ROM cost was comparable in computational cost.

Finally, the computational costs were estimated for generating a generalized nonlinear ROM (α, M) applicable for the X-56A flight envelope, $\alpha = [-5^\circ$ to $10^\circ]$, $M = [0.10$ to $0.20]$, using a one degree sampling and Mach increment of 0.02, i.e., 96 sampled flight conditions. It was shown that the rigid ROM presents an increased cost savings relative to the aeroelastic ROM. However, the utility of the method was shown to increase with the number of maneuver evaluations required in characterizing the flight envelope of an unconventional vehicle.

9.2 Experiment 3.2 - Reduced-Order Model vs. Stability Derivative Model

Experiment 3.2 addresses Research Question 3.2 and tests Hypothesis 3.2, both of which are restated below:

Research Question 3.2:
What are the performance benefits relative to traditional stability derivative models?

Hypothesis 3.2: *Aeroelastic indicial response ROMs provide more accurate unsteady aerodynamic predictions compared to stability derivative models for maneuvers at high motion rates. For slowly-varying maneuvers, the stability derivative method remains the most efficient aerodynamic model.*

The stability derivative method introduced in Section 1.2.1 has been the traditional method for modeling aerodynamic loads for flight dynamics predictions since the early 1900s [12, 13]. The model, given by Eqs. 5-6, represents the longitudinal and lateral aerodynamic loads as linearly dependent functions of the steady-state aerodynamic coefficient at trim, C_{i_0}, perturbations in the vehicle-state and command variables, $\Delta\alpha$, $\Delta\beta$, Δq, Δp, Δr, and $\Delta\delta$, and the S&C derivatives, C_{j_α}, C_{j_q}, C_{k_β}, C_{k_p}, C_{k_r} and C_{j/k_δ}.

The static and dynamic derivatives of Eqs. 5 and 6 have been historically identified via wind tunnel testing through steady-state and forced-oscillation tests [48], respectively. For identifying dynamic derivatives, test rigs are used to force longitudinal or lateral sinusoidal oscillations about an aircraft's center of gravity to observe the dynamic aerodynamic response, often as a function of oscillation frequency and amplitude. Once initial transients decay, the derivatives may be determined by measuring the in-phase and out-of-phase aerodynamic response to the forced motion [58].

Numerical techniques, such as frequency domain or regression analyses, are then used to post-process experimental data to form estimates of the dynamic derivative values. Implementation of this procedure using CFD simulations has been extensively investigated by NATO-AVT 161 [19]. These single-valued derivatives may be identified as a function of angle of attack, Mach number, and frequency to generate a stability derivative database that may be interpolated to form nonlinear aerodynamic predictions. Because the flow is assumed to reach a steady-state instantaneously, the stability derivative model is quasisteady. This assumption inherently ignores any influence of previous motion states. Regardless, Bryan's approach has found widespread success in modeling the aerodynamics of conventional aircraft configurations maneuvering at slow motion rates.

The indicial response ROMs are essentially time-accurate extensions of the stability derivative method, where the dynamic responses represent the memory of the system and may be convolved with arbitrary trajectories to predict the unsteady aerodynamic response of maneuvering vehicles. For maneuvers characterized by complex fluid-structure interactions, the indicial response ROM was shown to accurately resolve the unsteady longitudinal and lateral force and moment coefficients for a range of motion rates in the previous section. Because the indicial response leverages dynamic responses identified using time-accurate simulations, the computational costs incurred limit the utility of this method for multiple maneuver evaluations. Furthermore, this method would only be beneficial to maneuvers characterized as unsteady.

The present section seeks to demonstrate how cost efficient stability derivative models may be extracted from indicial responses without the need for forced oscillation and regression analysis techniques. Then the performance of the extracted stability derivative models will be compared to indicial response ROM predictions to understand the benefits of leveraging both models to characterize quasisteady and unsteady maneuvers across a flight envelope of interest.

9.2.1 Purpose of Experiment

The following are identified as the main objectives of this numerical experiment:

1. Demonstrate a computationally efficient method for the calculation of traditional dynamic stability derivatives for flexible flight vehicles

2. Compare the performance benefits of the aeroelastic indicial response ROM relative to an extracted quasisteady stability derivative model for maneuvers spanning linear and nonlinear flight regimes at various motion rates

9.2.2 Experiment Setup

Figure 114 illustrates an approach for calculating traditional, quasisteady stability derivatives using both static data and indicial response functions for a nominal flight space. Calculation of the angle-of-attack stability derivative data is rather straight forward by use of a series of static rigid or static aeroelastic simulations at each sampled combination of angle of attack and Mach number. The quasisteady angle-of-attack derivative, $C_{j_\alpha}(\infty)$, is then calculated locally as the difference in static longitudinal aerodynamic coefficient divided by the step taken in angle of attack between the points. For the sideslip angle stability derivative, $C_{k_\beta}(\infty)$, static simulations are conducted at the flight condition of interest, e.g., $\alpha = 1^\circ$, $M = 0.11$, using sideslip values of $\beta = 0^\circ$ and 1°. The difference between these static solutions yields the stability derivative.

The quasisteady stability derivatives for the pitch, $C_{j_q}(\infty)$, roll, $C_{k_p}(\infty)$, and yaw rates, $C_{k_r}(\infty)$, may be extracted from indicial responses simulated at the flight condition of interest. As shown on the right of Fig. 114 using an example for pitch rate, indicial response functions due to step changes in each rotation rate may be simulated, where the final converged value represents the quasisteady dynamic derivative with respect to each rotation rate. The benefit of this approach is that the rotation

rates are decoupled from the wind angles, α and β, allowing for their influences to be isolated and identified using a single simulation. This process may be used to calculate the stability derivatives for either rigid or flexible vehicles.

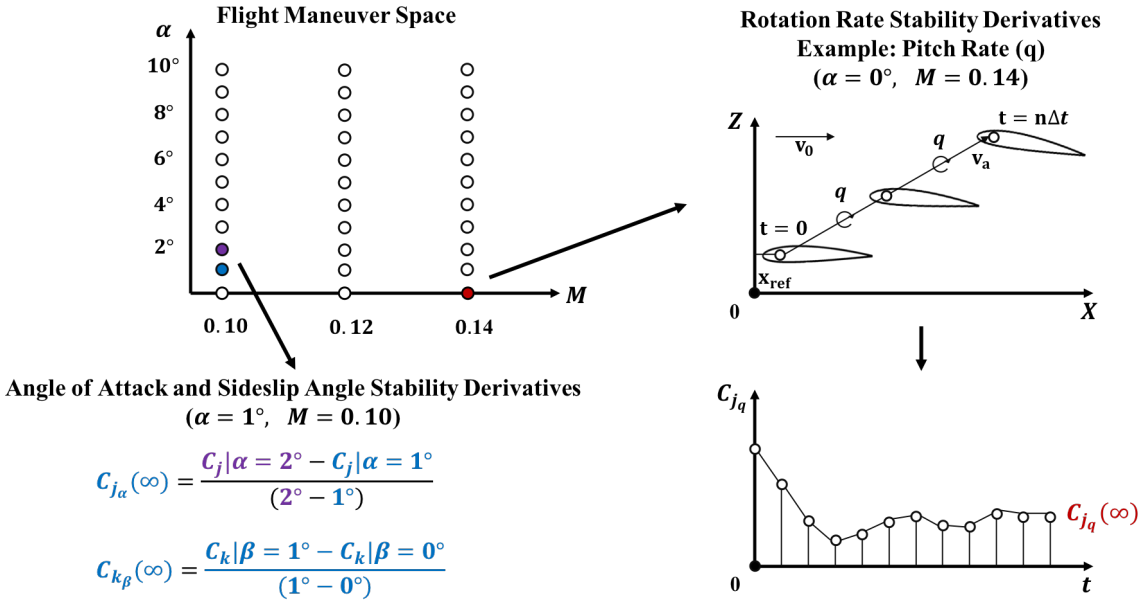

Figure 114: Calculation of CFD-based stability derivatives using static data and indicial response functions.

Once these derivatives have been calculated/simulated at each flight condition of interest, a nonlinear stability derivative model may be created to predict the longitudinal and lateral force and moment coefficients for aircraft performing slowly-varying maneuvering using the formulation shown in Eqs. 82-83. The modeling costs associated with this stability derivative approach are less relative to the indicial response ROM as static data may be used to identify the derivatives with respect to angle of attack and sideslip angle.

$$C_j = C_{j_0} + C_{j_\alpha}(\infty, \alpha, M)\Delta\alpha + C_{j_q}(\infty, M)\Delta q \tag{82}$$

$$C_k = C_{k_0} + C_{k_\beta}(\infty, \alpha, M)\Delta\beta + C_{k_p}(\infty, M)\Delta p + C_{k_r}(\infty, M)\Delta r \tag{83}$$

9.2.3 Linear ROM Comparison

Figure 115 illustrates a comparison between ROM and stability derivative (SD) predictions relative to CFD side force coefficient results for the rigid X-56A performing a small-amplitude forced rolling oscillation presented in Section 8.1. The SD method is relatively accurate compared to CFD simulations, correctly resolving the thickening of the hysteresis loops for increases in reduced frequency. Because motion history is unaccounted for, the SD predictions are unable to predict the aerodynamic transient due to the step change in roll rate at the beginning of the simulation. Additionally, in the $k = 0.02$ case, the SD method slightly overpredicts the side force coefficient for negative roll angles and underpredicts the value for positive roll angles. The same general behavior is observed with respect to the rolling moment coefficient in Fig. 116. While less noticeable, the SD method slightly underpredicts the rolling moment coefficient for negative roll angles and overpredicts the value for positive roll angles.

Figure 117 illustrates a comparison between ROM and stability derivative (SD) predictions relative to CFD side force coefficient results for the flexible X-56A performing the same rolling oscillation. The comparison for the rolling moment coefficient predictions are shown in Fig. 118. Due to the similarity between rigid and flexible vehicle lateral aerodynamic responses, the same qualitative trends are observed with respect to each coefficient for the flexible vehicle.

Table 36 lists the linear ROM and SD prediction accuracy in terms of overall mean error and standard deviation. Relative to the ROM, the stability derivative does a reasonable job of matching the predictions with the exception of a slight discrepancy observed in the unsteady aeroelastic case. A noticeable increase in standard deviation is observed for both the rigid and aeroelastic predictions. This increase is attributed to the inability of the SD method to predict the initial transients due to onset of grid motion. Because the aerodynamic transients are relatively fast, the SD method does a great job of capturing the hysteresis loop behavior for each frequency.

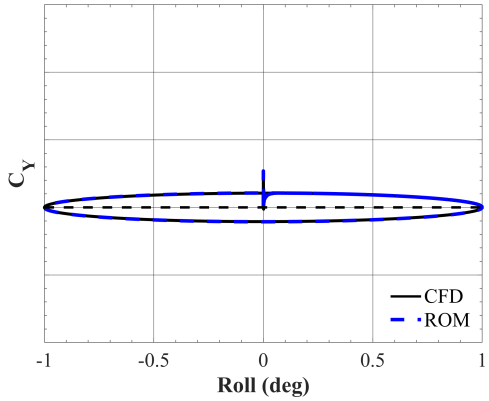

(a) Side force coefficient - ROM ($k = 0.05$)

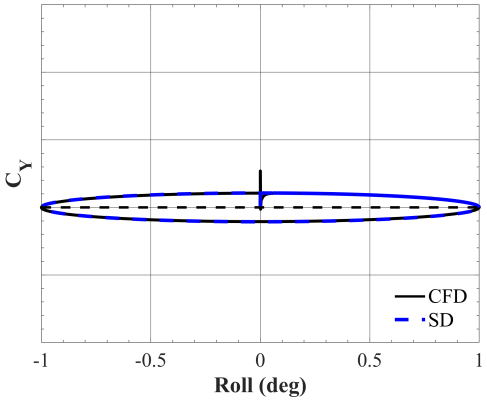

(b) Side force coefficient - SD ($k = 0.05$)

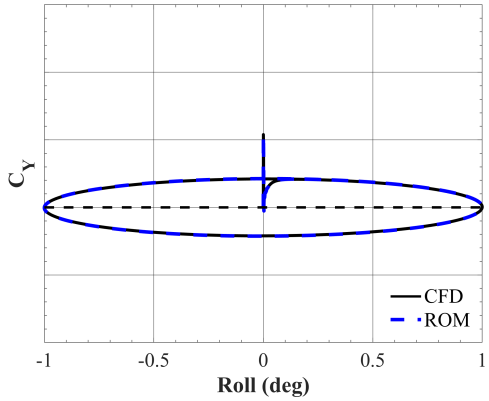

(c) Side force coefficient - ROM ($k = 0.10$)

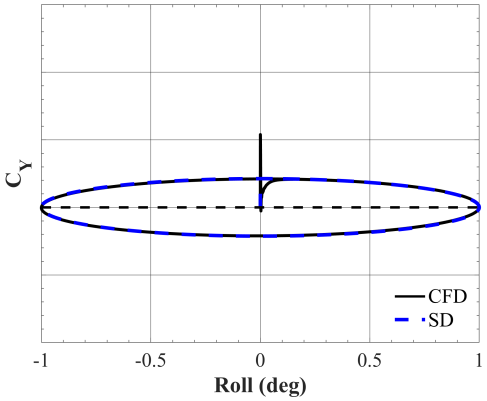

(d) Side force coefficient - SD ($k = 0.10$)

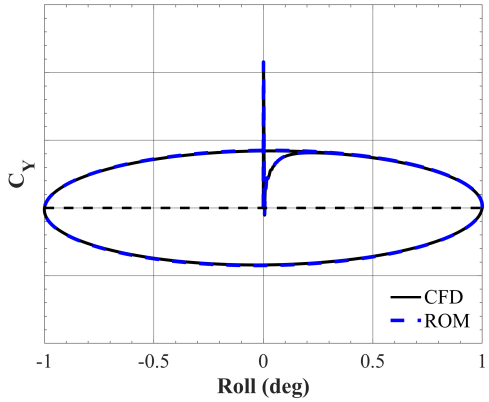

(e) Side force coefficient - ROM ($k = 0.20$)

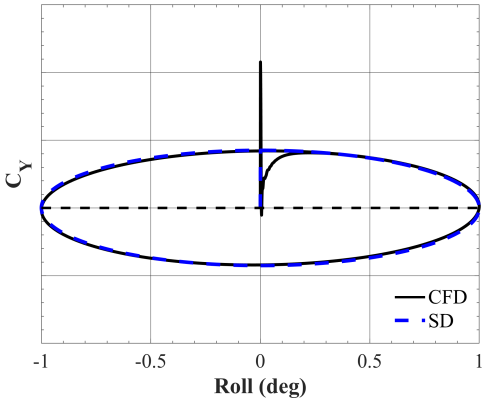

(f) Side force coefficient - SD ($k = 0.20$)

Figure 115: Rigid X-56A: ROM (left) and SD method (right) vs. CFD side force coefficient results for forced rolling oscillation with one degree amplitude for $k = 0.05$ (top), 0.10 (middle), and 0.20 (bottom) at $\alpha = 0°$, $\beta = 0°$, $M = 0.13$.

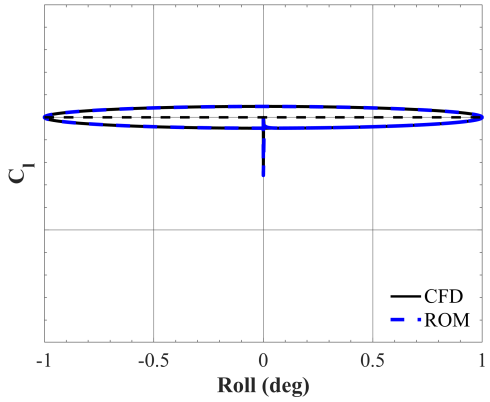

(a) Rolling moment coefficient - ROM ($k = 0.05$)

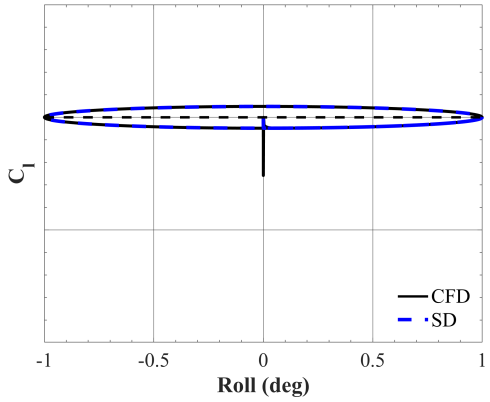

(b) Rolling moment coefficient - SD ($k = 0.05$)

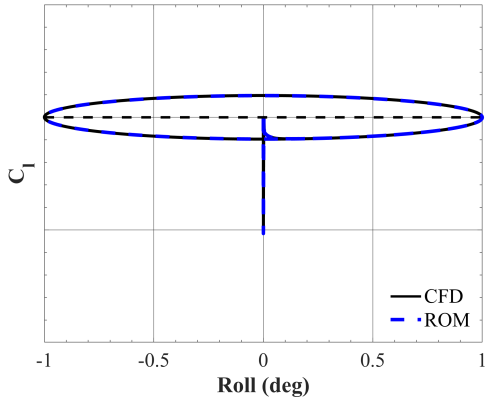

(c) Rolling moment coefficient - ROM ($k = 0.10$)

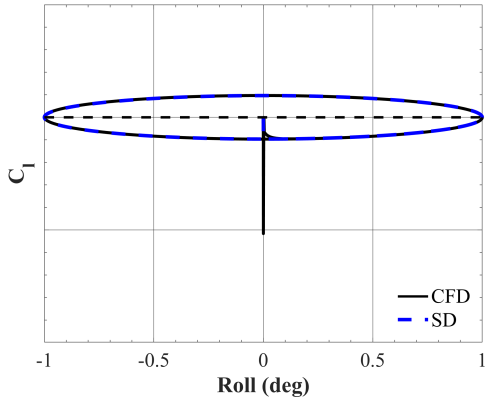

(d) Rolling moment coefficient - SD ($k = 0.10$)

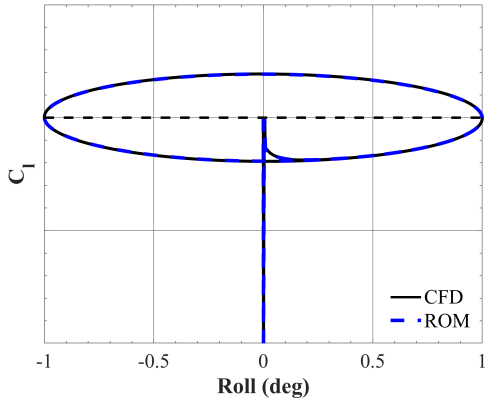

(e) Rolling moment coefficient - ROM ($k = 0.20$)

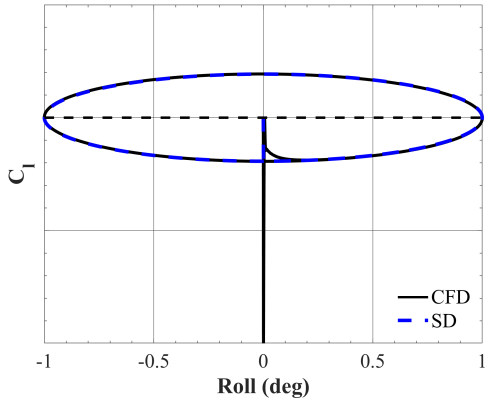

(f) Rolling moment coefficient - SD ($k = 0.20$)

Figure 116: Rigid X-56A: ROM (left) and SD method (right) vs. CFD rolling moment coefficient results for forced rolling oscillation with one degree amplitude for $k = 0.05$ (top), 0.10 (middle), and 0.20 (bottom) at $\alpha = 0°$, $\beta = 0°$, $M = 0.13$.

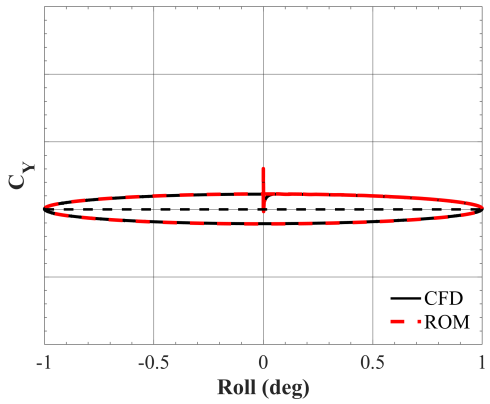

(a) Side force coefficient - ROM ($k = 0.05$)

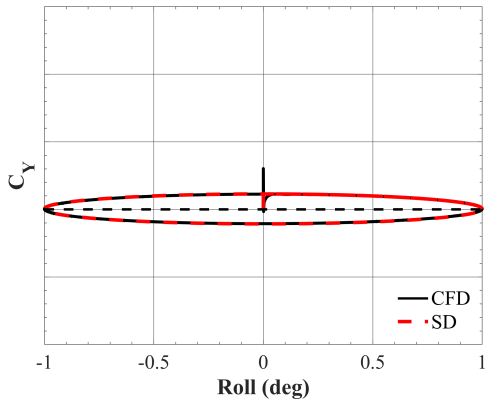

(b) Side force coefficient - SD ($k = 0.05$)

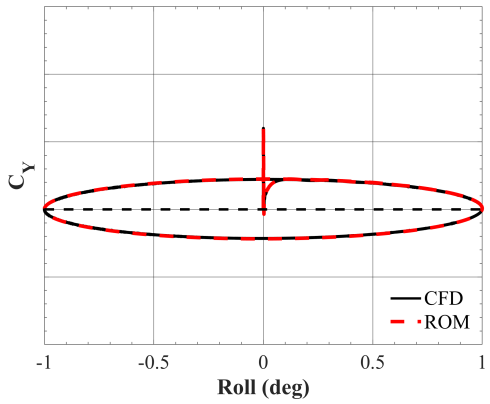

(c) Side force coefficient - ROM ($k = 0.10$)

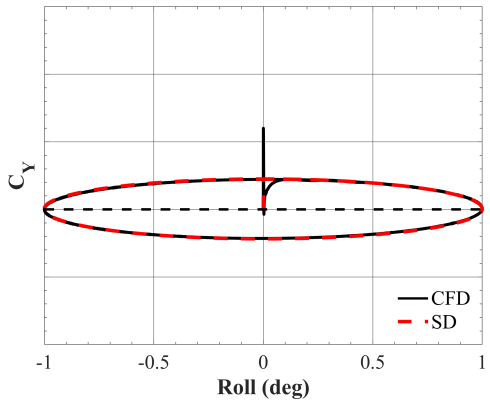

(d) Side force coefficient - SD ($k = 0.10$)

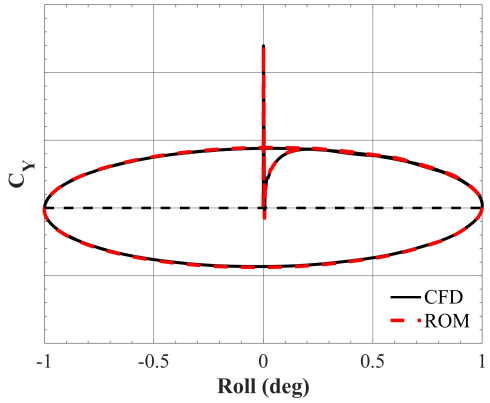

(e) Side force coefficient - ROM ($k = 0.20$)

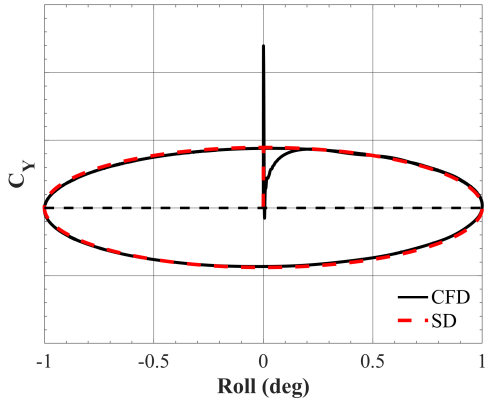

(f) Side force coefficient - SD ($k = 0.20$)

Figure 117: Flexible X-56A: ROM (left) and SD method (right) vs. CFD side force coefficient results for forced rolling oscillation with one degree amplitude for $k = 0.05$ (top), 0.10 (middle), and 0.20 (bottom) at $\alpha = 0°$, $\beta = 0°$, $M = 0.13$.

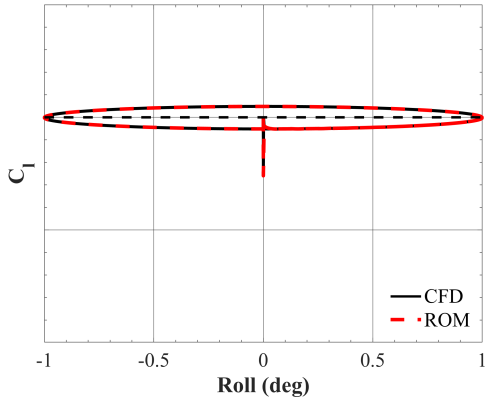

(a) Rolling moment coefficient - ROM ($k = 0.05$)

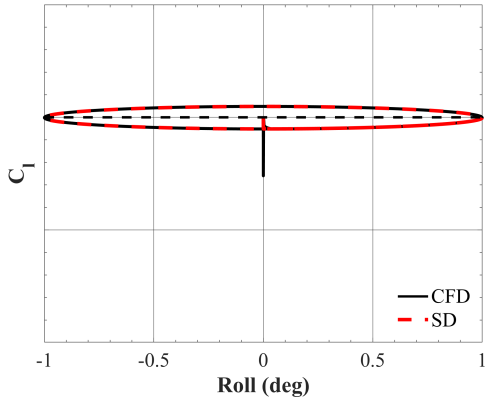

(b) Rolling moment coefficient - SD ($k = 0.05$)

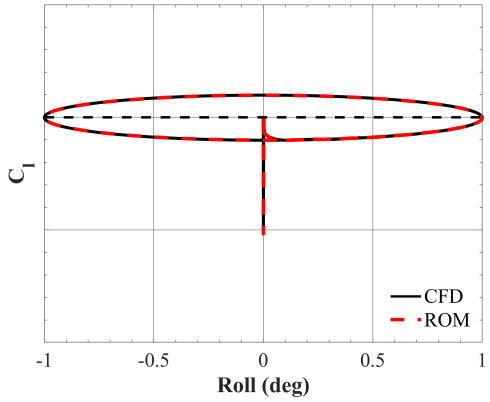

(c) Rolling moment coefficient - ROM ($k = 0.10$)

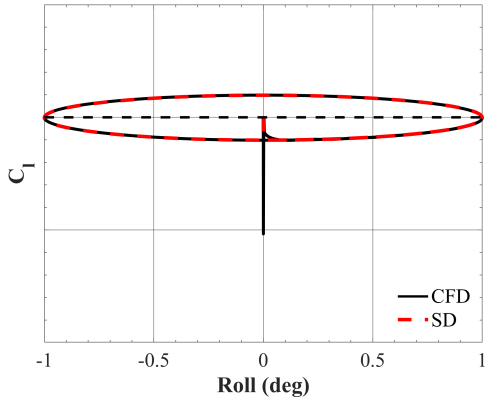

(d) Rolling moment coefficient - SD ($k = 0.10$)

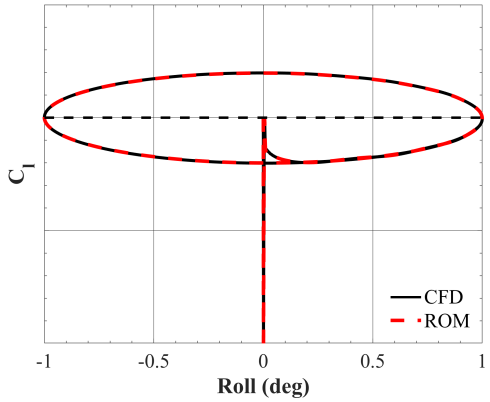

(e) Rolling moment coefficient - ROM ($k = 0.20$)

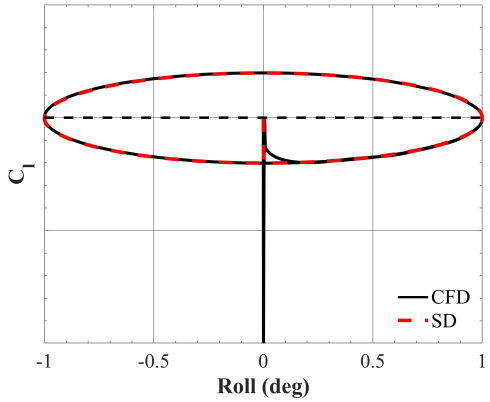

(f) Rolling moment coefficient - SD ($k = 0.20$)

Figure 118: Flexible X-56A: ROM (left) and SD method (right) vs. CFD rolling moment coefficient results for forced rolling oscillation with one degree amplitude for $k = 0.05$ (top), 0.10 (middle), and 0.20 (bottom) at $\alpha = 0°$, $\beta = 0°$, $M = 0.13$.

Table 36: Linear ROM and SD prediction accuracy in terms of mean error and standard deviation.

		Rigid		**Aeroelastic**	
Case	k	ϵ (%)	σ (%)	ϵ (%)	σ (%)
ROM	0.05	0.0	0.1	0.0	0.2
	0.10	0.0	0.1	0.0	0.1
	0.20	0.0	0.1	0.0	0.1
SD	0.05	0.0	0.6	0.0	0.6
	0.10	0.0	0.9	0.0	0.9
	0.20	0.0	1.3	0.1	0.8

In the small-amplitude forced rolling oscillation predictions at $\alpha = 0°$, the only nonzero vehicle-state parameter is the roll rate. For this reason, the only stability derivative used is the one extracted from the indicial response due to a step change in roll rate. Thus, the computational costs between the ROM and SD for this specific case are equivalent.

9.2.4 Nonlinear ROM (α) Comparison

Figure 119 illustrates a comparison between ROM and SD predictions relative to CFD lift coefficient results for the rigid X-56A performing large-amplitude forced pitching oscillations, as presented in Section 8.2. In contrast to the small-amplitude forced oscillations, the SD predictions show noticeable disagreement for the large-amplitude forced pitching oscillations. It is important to note that the angle-of-attack SD values were sampled as a function of angle of attack in the same manner as the angle-of-attack indicial responses. Thus, interpolation of the SD values at each angle of attack should account for the static nonlinear variation, but not the influence of previous motion states. While the SD model predicts a thickening of the hysteresis loops for increases in reduced frequency, the degree of thickening is overpredicted. Additionally, the model generally underpredicts the lift coefficient for $\alpha(t) < \alpha_0$ and overpredicts the coefficient for $\alpha(t) > \alpha_0$. These discrepancies appear to reduce as the reduced frequency is decreased to quasisteady levels.

Figure 120 shows the ROM and SD predictions relative to to CFD pitching moment coefficient results for the rigid X-56A. Relative to the lift coefficient predictions, the SD predictions for pitching moment are in better agreement with CFD results. In the quasisteady case, the hysteresis loop width and the minimum and maximum coefficient values are reasonably predicted. As reduced frequency is increased, the SD method tends to overpredict and underpredict the pitching moment coefficient at lower and upper angles of attack, respectively. These prediction inaccuracies further increase in the unsteady case.

Figure 121 illustrates a comparison between ROM and SD predictions relative to CFD lift coefficient results for the flexible X-56A performing large-amplitude forced pitching oscillations. In each frequency case, the SD method is only capable of predicting a single hysteresis loop due to the use of quasisteady derivatives, which include no influence of previous motion states. In the quasisteady case, the SD prediction captures the qualitative mean variation of the hysteresis loops, but fail to accurately resolve the aerodynamic damping over the oscillation cycles. As reduced frequency is increased, the inability of the SD method to capture cycle-to-cycle differences in minimum/maximum coefficient values, as well as aerodynamic damping, becomes more obvious.

Figure 122 illustrates a comparison between ROM and SD predictions relative to CFD pitching moment coefficient results for the flexible X-56A. Similar to the lift coefficient results, the SD predictions are only able to resolve a single hysteresis loop due to its quasisteady assumption. In the $k = 0.05$ case, the SD prediction generally encompasses the minimum and maximum coefficient values, but is unable to account for the nonlinear unsteadiness resulting from fluid-structure interactions. In the $k = 0.20$ case, the SD prediction generally captures the first quarter-cycle but begins to show large discrepancies afterward with a strong overprediction of pitching moment coefficient for $\alpha(t) < \alpha_0$ and no resolution of cycle-to-cycle differences in

aerodynamic damping. In the unsteady case, the structure has less time to deform, and the aerodynamic response is largely dominated by the bulk aerodynamic response to vehicle motion. As a result, cycle-to-cycle differences are observed, but an elliptical hysteresis loop behavior is retained. Thus, the SD predictions do a reasonable job of resolving the mean hysteresis loop rotation and minimum/maximum coefficient values. However, cycle-to-cycle differences are not accurately modeled. A summary of the modeling accuracy metrics for the nonlinear (α) ROM and SD predictions is listed in Table 37.

Table 37: Nonlinear (α) ROM and SD prediction accuracy in terms of mean error and standard deviation.

		Rigid		**Aeroelastic**	
Case	k	ϵ (%)	σ (%)	ϵ (%)	σ (%)
ROM (α)	0.05	0.0	0.1	0.2	0.9
	0.10	0.1	0.3	0.6	1.0
	0.20	0.1	0.5	1.7	1.1
SD (α)	0.05	0.1	2.9	0.3	6.6
	0.10	0.3	4.3	1.0	13.6
	0.20	0.5	6.2	3.1	17.9

Table 38 lists the computational costs, measured in CPU hours, required to create the nonlinear ROM and SD models for the large-amplitude pitch oscillation predictions. While the SD showed poor modeling accuracy relative to the ROM, it did have required significantly less costs. The rigid SD model was approximately six times cheaper to generate than the rigid ROM. The aeroelastic SD model was approximately eight times cheaper than the aeroelastic ROM.

Table 38: CPU hours required to create nonlinear (α) ROM and SD model for large-amplitude pitch oscillation predictions.

	Rigid			**Aeroelastic**		
Model	Static	Dynamic	Total	Static	Dynamic	Total
ROM (α)	42	585	627	42	2,520	2,562
SD (α)	42	65	107	42	280	322

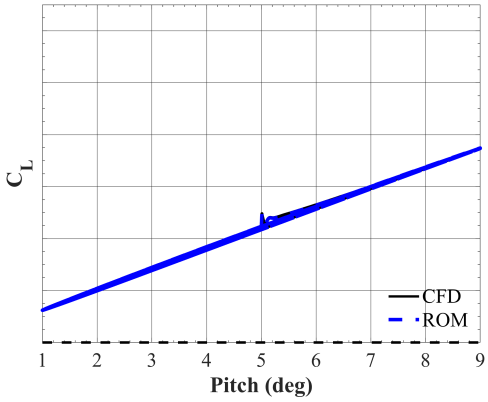

(a) Lift coefficient - ROM ($k = 0.05$)

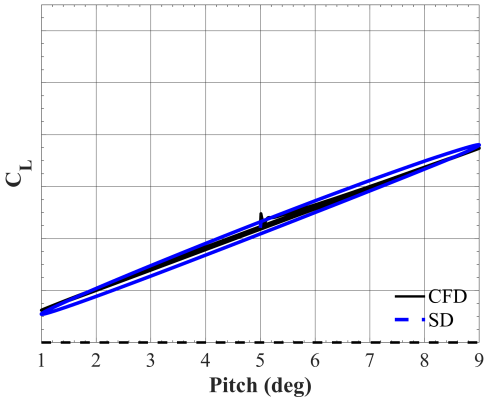

(b) Lift coefficient - SD ($k = 0.05$)

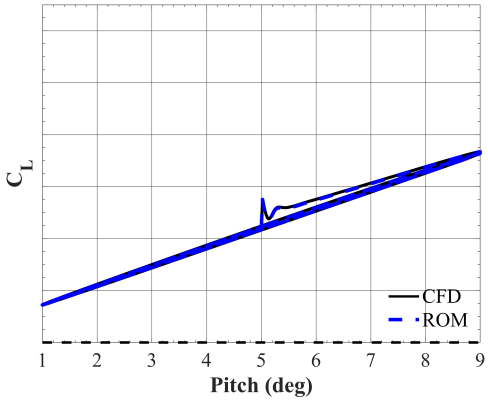

(c) Lift coefficient - ROM ($k = 0.10$)

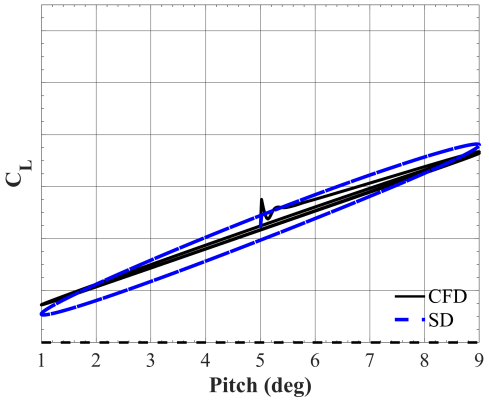

(d) Lift coefficient - SD ($k = 0.10$)

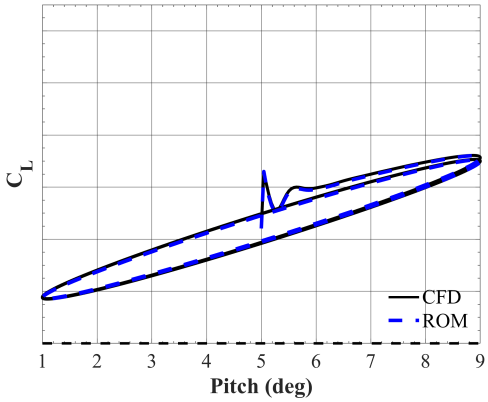

(e) Lift coefficient - ROM ($k = 0.20$)

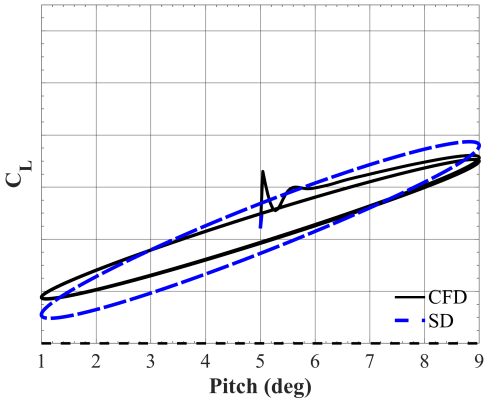

(f) Lift coefficient - SD ($k = 0.20$)

Figure 119: Rigid X-56A: Nonlinear ROM (left) and SD method (right) vs. CFD lift coefficient results for forced pitching oscillation with 4 degree amplitude for $k = 0.05$ (top), 0.10 (middle), and 0.20 (bottom) at $\alpha_0 = 5°$, $\beta = 0°$, $M = 0.13$.

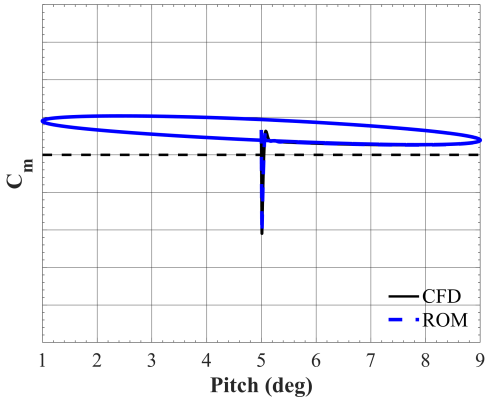

(a) Pitching moment coeff. - ROM ($k = 0.05$)

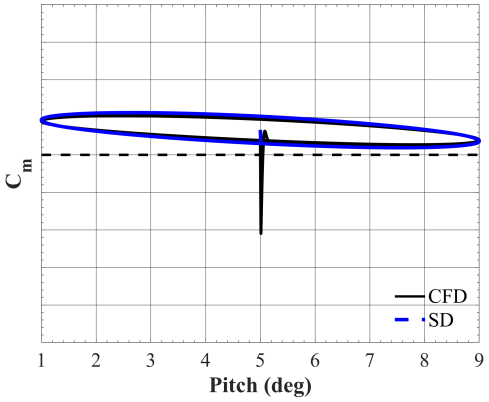

(b) Pitching moment coeff. - SD ($k = 0.05$)

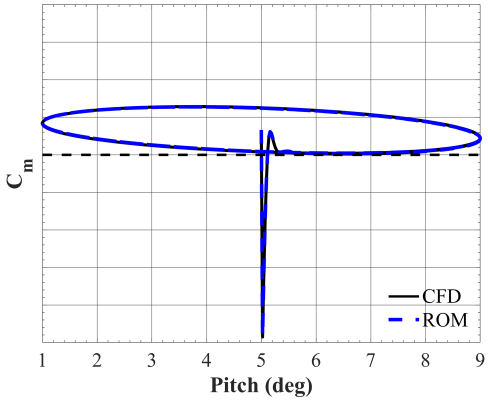

(c) Pitching moment coeff. - ROM ($k = 0.10$)

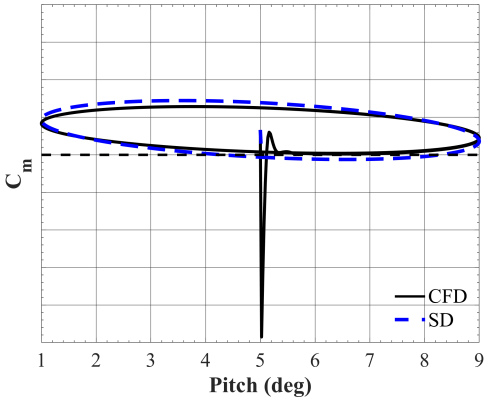

(d) Pitching moment coeff. - SD ($k = 0.10$)

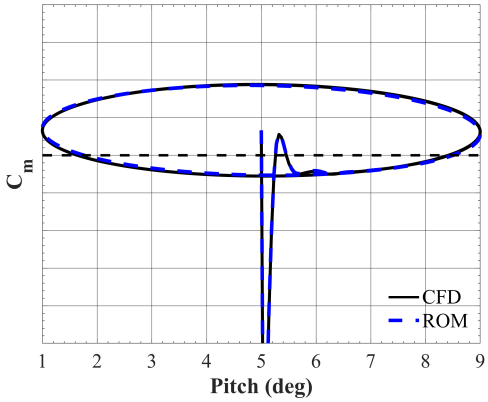

(e) Pitching moment coeff. - ROM ($k = 0.20$)

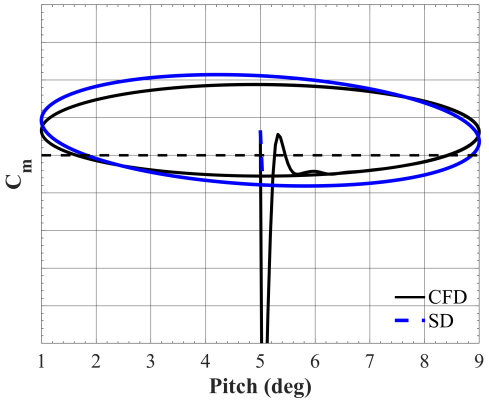

(f) Pitching moment coeff. - SD ($k = 0.20$)

Figure 120: Rigid X-56A: Nonlinear ROM (left) and SD method (right) vs. CFD pitching moment coefficient results for forced pitching oscillation with 4 degree amplitude for $k = 0.05$ (top), 0.10 (middle), and 0.20 (bottom) at $\alpha_0 = 5°$, $\beta = 0°$, $M = 0.13$.

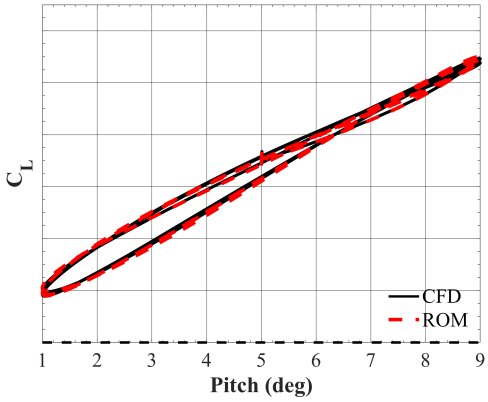

(a) Lift coefficient - ROM ($k = 0.05$)

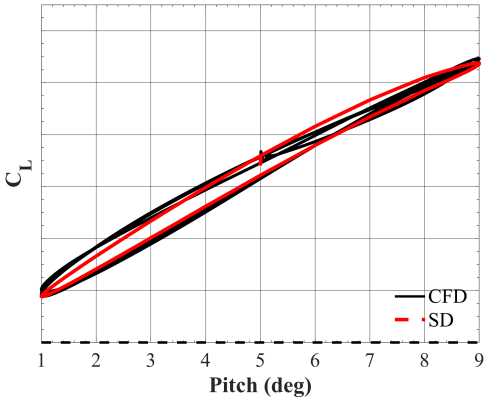

(b) Lift coefficient - SD ($k = 0.05$)

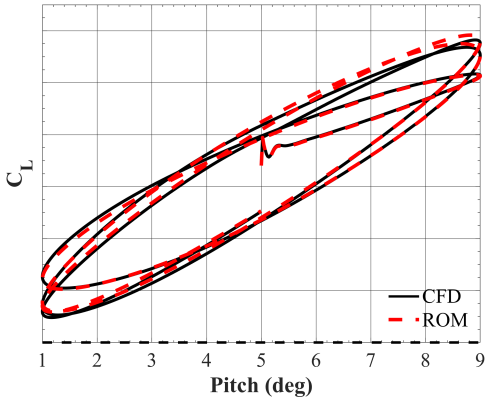

(c) Lift coefficient - ROM ($k = 0.10$)

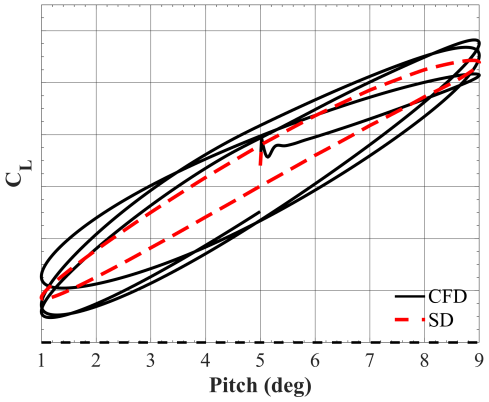

(d) Lift coefficient - SD ($k = 0.10$)

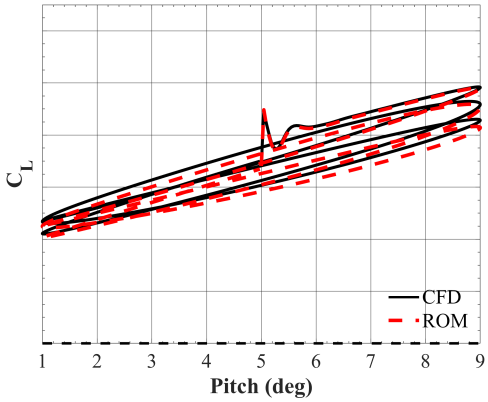

(e) Lift coefficient - ROM ($k = 0.20$)

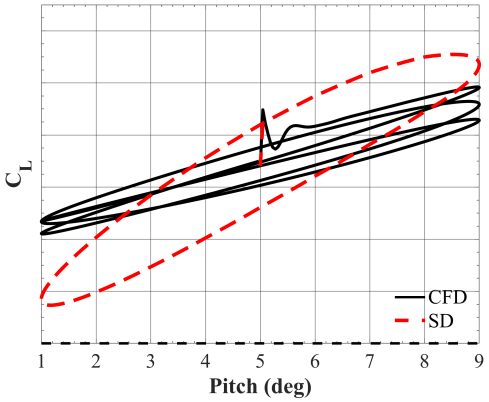

(f) Lift coefficient - SD ($k = 0.20$)

Figure 121: Flexible X-56A: Nonlinear ROM (left) and SD method (right) vs. CFD lift coefficient results for forced pitching oscillation with 4 degree amplitude for $k = 0.05$ (top), 0.10 (middle), and 0.20 (bottom) at $\alpha_0 = 5°$, $\beta = 0°$, $M = 0.13$.

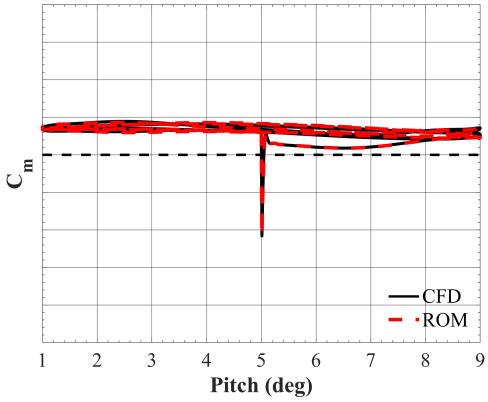

(a) Pitching moment coeff. - ROM ($k = 0.05$)

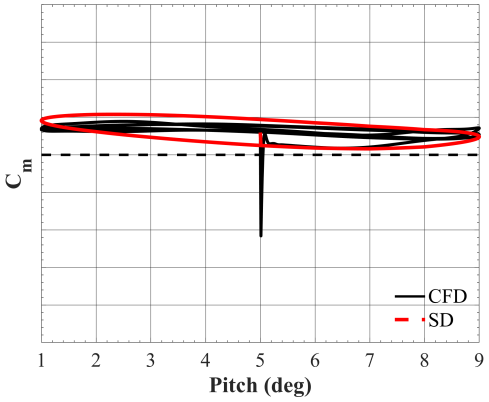

(b) Pitching moment coeff. - SD ($k = 0.05$)

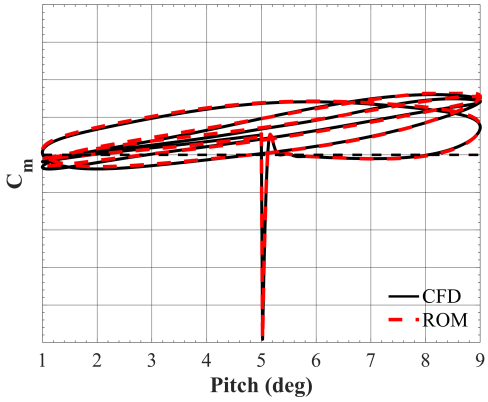

(c) Pitching moment coeff. - ROM ($k = 0.10$)

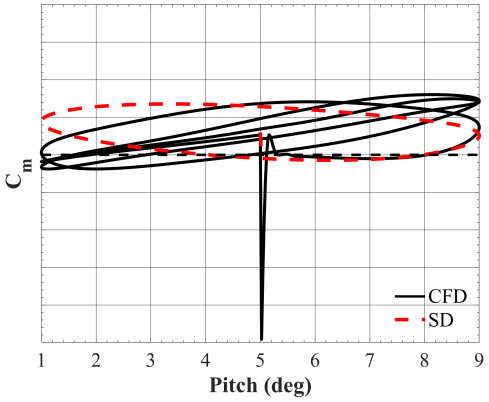

(d) Pitching moment coeff. - SD ($k = 0.10$)

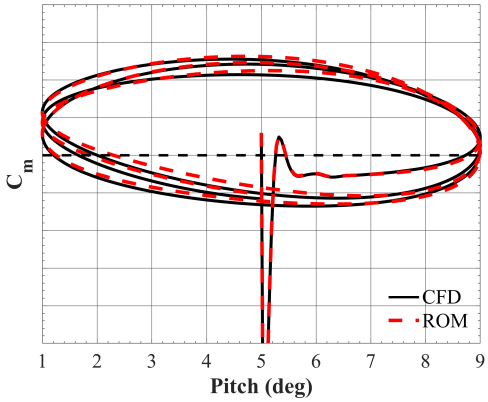

(e) Pitching moment coeff. - ROM ($k = 0.20$)

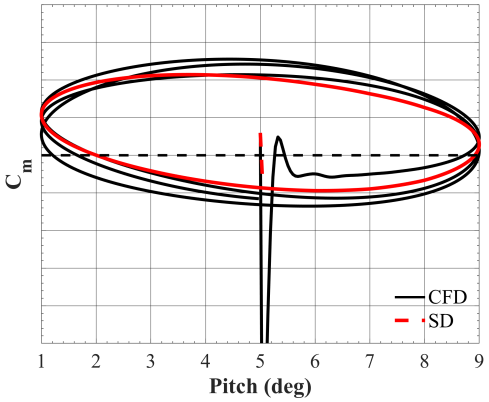

(f) Pitching moment coeff. - SD ($k = 0.20$)

Figure 122: Flexible X-56A: Nonlinear ROM (left) and SD method (right) vs. CFD pitching moment coefficient results for forced pitching oscillation with 4 degree amplitude for $k = 0.05$ (top), 0.10 (middle), and 0.20 (bottom) at $\alpha_0 = 5°$, $\beta = 0°$, $M = 0.13$.

9.2.5 Nonlinear ROM (α, M) Comparison

Figure 123 illustrates a comparison between ROM and SD predictions relative to CFD lift (top) and pitching moment coefficient (bottom) results for the rigid X-56A performing the right turn flight test maneuver, as presented in Section 8.3. Figure 124 shows the ROM and SD predictions relative to CFD side force (top), rolling moment (middle), and yawing moment coefficient (bottom) results. In general, the ROM and SD models are in great qualitative agreement with only minor discrepancies for the lift and pitching moment coefficient. Relative to the SD model, the ROM shows a minor solution 'buzzing' as a result of the propogation of kriging indicial response models through the convolution calculation. Otherwise, the models are expected to compare similarly given that the right turn maneuver occurs over a 36 second duration, and as such, can be classified as a slowly-varying or quasisteady maneuver. The same trends are observed for the flexible vehicle predictions, as shown in Figs. 125-126.

Table 39 lists the mean error and standard deviation for the ROM and SD method in predicting the longitudinal and lateral aerodynamics during the right turn maneuver. As expected, no appreciable difference is observed for either the rigid or aeroelastic predictions between the ROM and SD method. Table 40 lists the computational costs required in generating the nonlinear (α, M) ROM and SD models. While the SD method incurs a greater static simulation cost due to the identification of angle-of-attack and sideslip angle stability derivatives, the overall costs are reduced due to the decreased number of indicial responses sampled. For the rigid vehicle predictions, the SD method is nearly five times cheaper to generate relative to the ROM. Likewise, the SD method is approximately six times cheaper relative to the ROM for aeroelastic predictions. Given the comparable accuracy between the SD and ROM predictions and the cost benefits of the SD method, it is apparent why the stability-derivative method has been routinely used over the past century. For slowly-varying maneuvers, the method can provide fairly accurate predictions relative to full-order simulations.

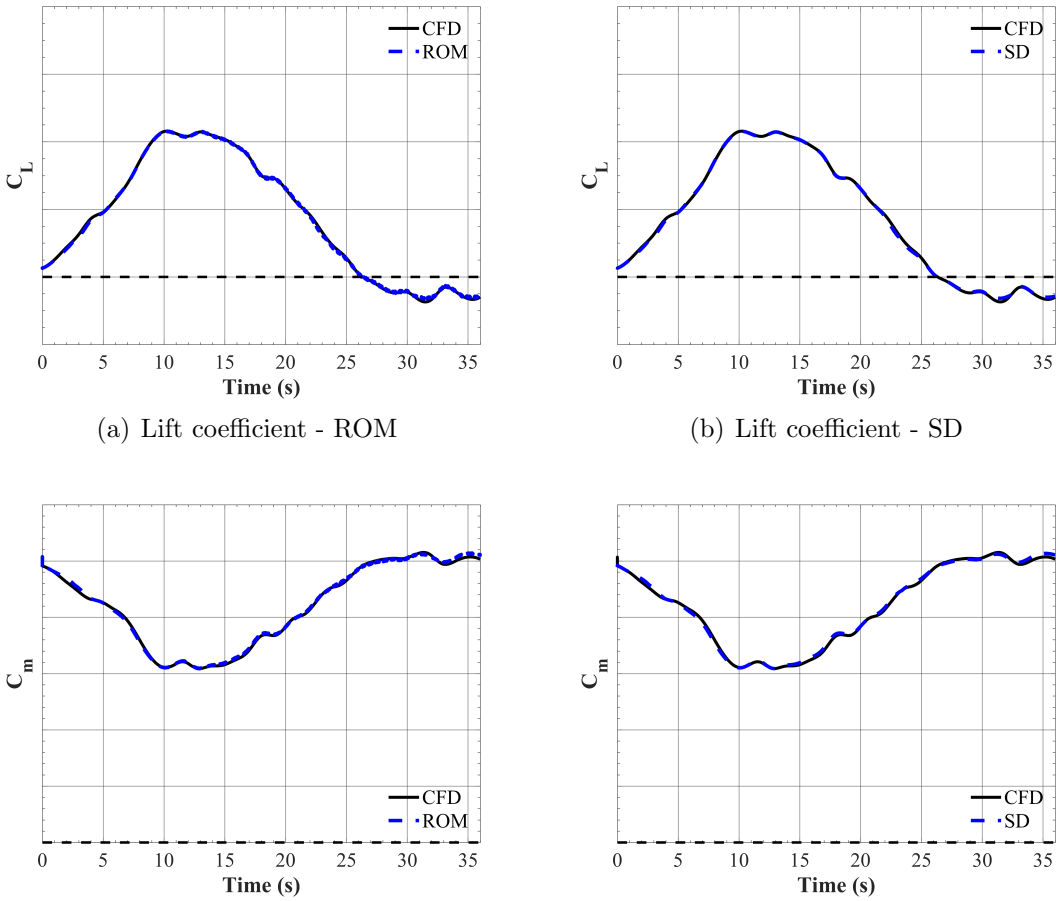

(a) Lift coefficient - ROM

(b) Lift coefficient - SD

(c) Pitching moment coefficient - ROM

(d) Pitching moment coefficient - SD

Figure 123: Rigid X-56A: Nonlinear ROM (α, M) (left) and SD method (right) vs. CFD lift (top) and pitching moment (bottom) coefficient results for the rigid vehicle undergoing a right turn maneuver.

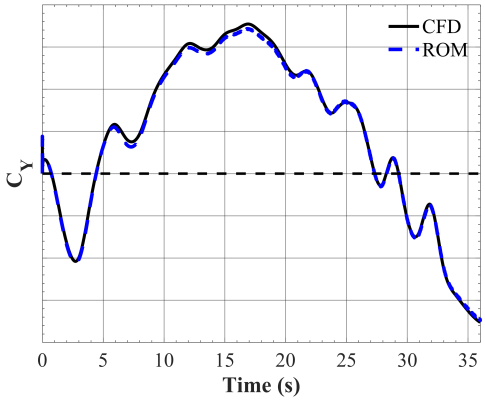

(a) Side force coefficient - ROM

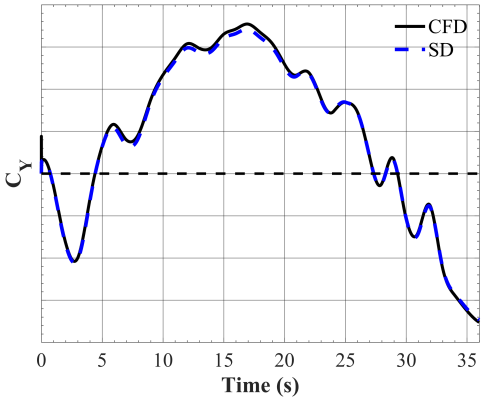

(b) Side force coefficient - SD

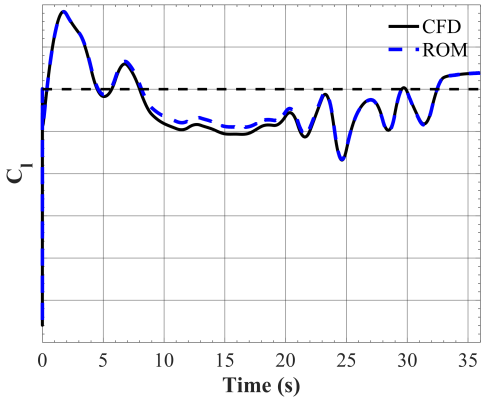

(c) Rolling moment coefficient - ROM

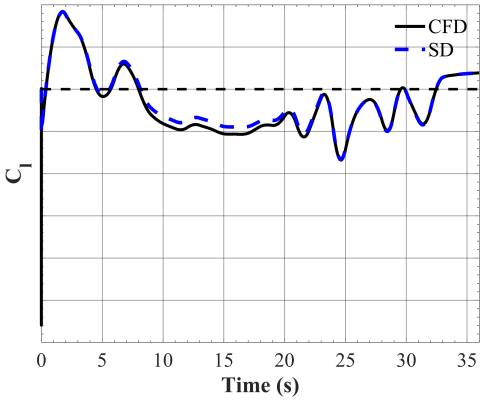

(d) Rolling moment coefficient - SD

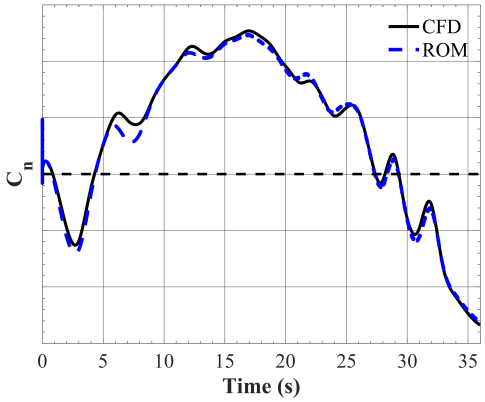

(e) Yawing moment coefficient - ROM

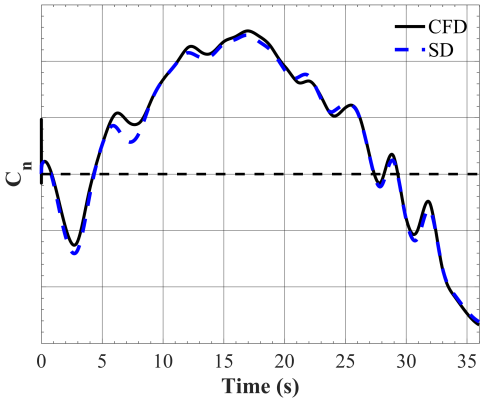

(f) Yawing moment coefficient - SD

Figure 124: Rigid X-56A: Nonlinear ROM (α, M) (left) and SD method (right) vs. CFD side force (top), rolling moment (middle), and yawing moment (bottom) coefficient results for the rigid vehicle undergoing a right turn maneuver.

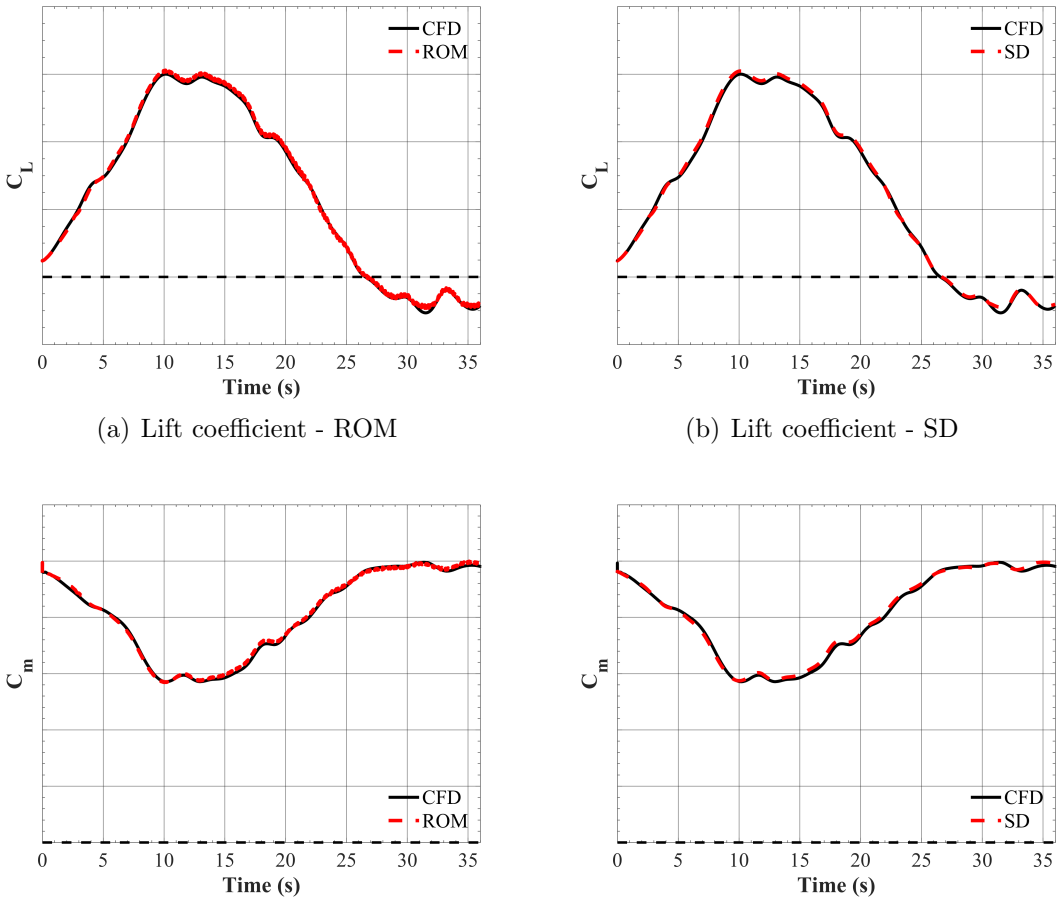

(a) Lift coefficient - ROM

(b) Lift coefficient - SD

(c) Pitching moment coefficient - ROM

(d) Pitching moment coefficient - SD

Figure 125: Flexible X-56A: Nonlinear ROM (α, M) (left) and SD method (right) vs. CFD lift (top) and pitching moment (bottom) coefficient results for the flexible vehicle undergoing a right turn maneuver.

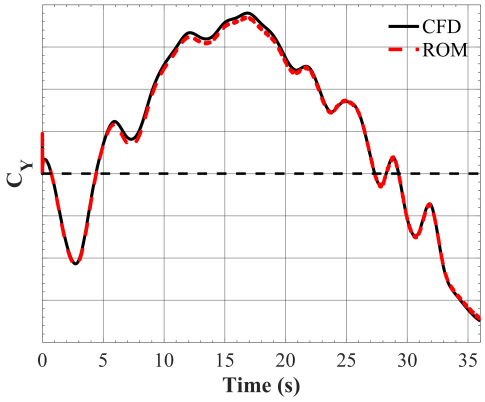

(a) Side force coefficient - ROM

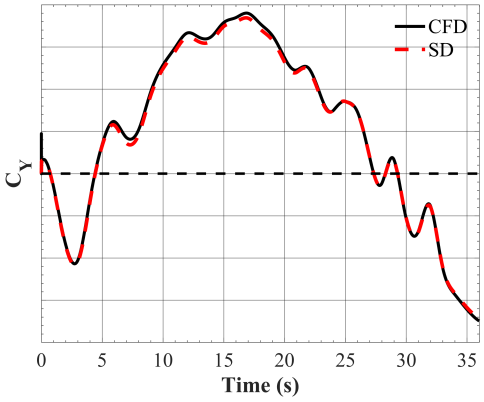

(b) Side force coefficient - SD

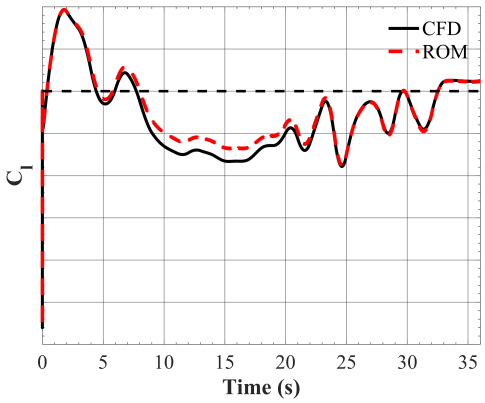

(c) Rolling moment coefficient - ROM

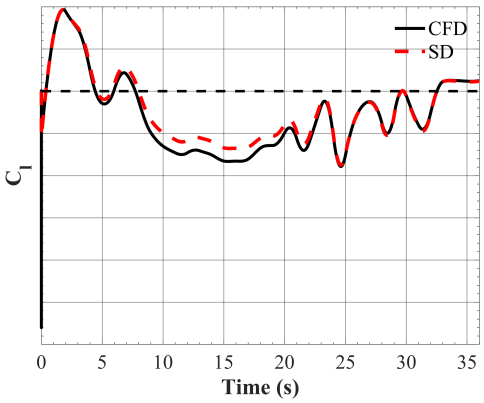

(d) Rolling moment coefficient - SD

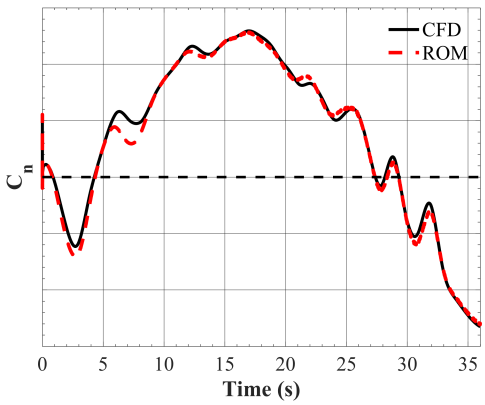

(e) Yawing moment coefficient - ROM

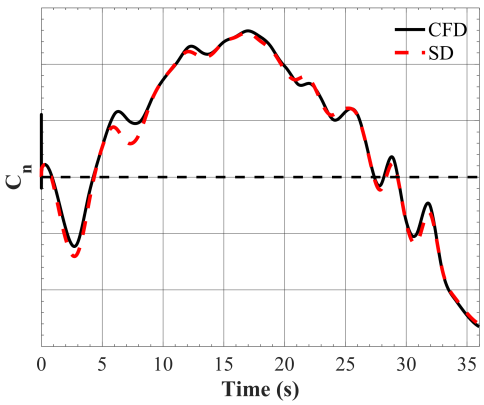

(f) Yawing moment coefficient - SD

Figure 126: Flexible X-56A: Nonlinear ROM (α, M) (left) and SD method (right) vs. CFD side force (top), rolling moment (middle), and yawing moment (bottom) coefficient results for the flexible vehicle undergoing a right turn maneuver.

Table 39: Nonlinear (α, M) ROM and SD prediction accuracy for the right turn maneuver in terms of mean error and standard deviation.

	Rigid		**Aeroelastic**	
Model	ϵ (%)	σ (%)	ϵ (%)	σ (%)
ROM (α, M)	0.6	1.1	1.0	1.4
SD (α, M)	0.6	1.1	1.0	1.4

Table 40: CPU hours required to create the nonlinear (α, M) ROM and SD models for right turn maneuver predictions.

		Rigid			**Aeroelastic**		
Model	Coeff.	Static	Dynamic	Total	Static	Dynamic	Total
ROM (α, M)	Longitudinal	96	1,040	1,136	96	4,480	4,576
	Lateral	0	1,300	1,300	0	1,400	1,400
	Complete	96	2,340	2,436	96	5,880	5,976
SD (α, M)	Longitudinal	192	130	322	192	560	752
	Lateral	0	260	260	0	280	280
	Complete	192	390	582	192	840	1,032

9.2.6 Summary

The present section sought to demonstrate a computationally efficient method for calculating traditional dynamic stability derivatives for both rigid and flexible flight vehicles through a combination of static and indicial response simulations, and following, compare the performance benefits of the indicial response ROM relative to the stability derivative method for maneuvering spanning linear and nonlinear flight regimes at various rates of motion. Angle-of-attack and sideslip angle stability derivatives were calculated using a series of static simulations, as is tradionally done, and the stability derivatives with respect to the rotation rates were extracted from converged indicial response simulations.

For slowly-varying maneuvers, such as the right turn flight test maneuver, the stability derivative model was able to predict the longitudinal and lateral aerodynamic responses with comparable accuracy to the ROM, but with nearly five times the cost savings. This highlights the utility of such a method for commercial aircraft,

or similar vehicles, which maneuver at low equivalent reduced frequencies, such that previous motion rates have negligible impact on the aerodynamics. For high rates of motion, the stability derivative method was unable to accurately resolve the unsteady aerodynamic forces and moment coefficients for quasisteady to unsteady forced pitching oscillations. In particular, the flexible vehicle was characterized by cycle-to-cyle differences in aerodynamic damping and minimum and maximum coefficient values due to complex fluid-structure interactions. While more expensive, the indicial response method is more appropriate for rapid maneuvers and/or those dominated by complex time-varying vehicle deformations.

CHAPTER X

CONCLUSION

This chapter concludes the dissertation with a summary of conclusions from the experiments performed, a summary of the primary contributions, and a discussion of potential avenues for future work that can leverage and extend the method presented in this dissertation. In the development of the aeroelastic indicial response reduced-order method, a series of experiments was performed to identify, evaluate, and quantify the performance capabilities of the method. These experiments provided a means of answering the research questions posed and showcasing the benefits of the method for efficient unsteady aerodynamic predictions of flexible, maneuvering flight vehicles. The experiments and pertinent conclusions made are summarized here.

In Chapter 7, the first experiment sought to establish guidelines for the static and dynamic solution strategy implemented in the identification of aeroelastic indicial responses for flexible vehicles. It was determined that the most efficient means of attaining the initial static aeroelastic solution was to perform a time-accurate static aeroelastic simulation using a coarse time step, based on resolving a single period of the highest frequency structural mode, and using an artifically high structural damping ratio to quickly reach the deformed static aeroelastic state. Use of a static rigid solution to restart the static aeroelastic simulation did not serve to accelerate convergence or reduce the associated static computational costs. This result is attributed to the disparate fluid state achieved due to the large wing and centerbody structural deformations of the X-56A. For less flexible vehicles or for vehicles encountering numerically unstable flow conditions, use of a rigid restart solution may aid in solution convergence.

For dynamic indicial response simulations, a fine time step was chosen based on resolving the highest frequency structural mode by a factor of $N = 200$. For the flexible vehicle, the number of time steps required for indicial response identification was different between longitudinal and lateral vehicle-state parameters. For step changes in sideslip angle, roll rate, and yaw rate, minimal differences were observed between the responses for the rigid and flexible vehicle. To achieve steady-state convergence, the number of time steps chosen was based on resolving a single period of the lowest frequency structural mode. For step changes in angle of attack and pitch rate, the fluid-structure interactions were significant, leading to complex, periodic oscillations, which dampened out over an extended period of time relative to the lateral responses. The number of time steps required for longitudinal responses was determined to coincide with approximately five periods of the lowest frequency structural mode.

Experiment 1.2 aimed to explore how indicial response sensitivity varied with respect to changes in the flight space variables between the rigid and flexible vehicle. Indicial responses due to step changes in each vehicle-state parameter were sampled at various angles of attack, Mach numbers, and sideslip angles. Traditionally, only the angle-of-attack and sideslip angle indicial responses are assumed to be dependent on angle of attack. The results of this experiment showed the validity of this dependency for the rotation rates as well, for both the rigid and flexible vehicle. Additionally, the angle-of-attack sensitivity was shown to be much stronger for the flexible vehicle, which poses a requirement for a finer sampling of the angle-of-attack flight space relative to the rigid vehicle. However, it is important to note that the flight envelope is likely to be limited when accounting for vehicle flexibility. In regard to Mach number sensitivity, it is traditionally assumed that each indicial response is dependent on Mach number. Toward evaluating this assumption, rigid and aeroelastic indicial responses were simulated across a Mach number range of $M = [0.10 \text{ to } 0.20]$. While negligible differences were observed for the rigid responses, the aeroelastic responses

showed a signficiant difference in transient and converged responses despite the limited Mach number range. In regard to sideslip angle, negligible indicial response sensitivity was observed for the rigid and flexible vehicle. Overall, the experiment led to the conclusion that traditional modeling dependencies with respect to angle of attack and Mach number remain valid for the aeroelastic indicial response ROM but require a finer sampling for a given flight envelope.

The dynamic solution strategy guidlines established in Chapter 7 were used in Chapter 8 to conduct a series of experiments in evaluating the aerodynamic prediction capabilities of indicial response ROMs applied to maneuvering, flexible flight vehicles. In Expt. 2.1, the linear aeroelastic indicial response ROM was shown to capture the fluid-structure interactions present in high-fidelity dynamic aeroelastic simulations of the X-56A undergoing small-amplitude rolling, yawing, and pitching oscillations. Unsteady longitudinal and lateral aerodynamic force and moment coefficient predictions were generated for quasisteady, quasiunsteady, and unsteady reduced frequencies with a mean error and standard deviation of $< 0.5\%$. These results demonstrate the ability of indicial responses to capture the frequency spectrum of the vehicle response at a given flight condition.

In Expt 2.2, a nonlinear ROM was generated, which included indicial response sensitivity to angle of attack. ROM predictions were generated for a large-amplitude forced pitching oscillation at various reduced frequencies. Angle-of-attack indicial responses were sampled in one degree increments throughout the angle-of-attack oscillation range. A linear interpolation was used to model these indicial responses as a function of the time-varying angle of attack for the tested forced oscillation. The nonlinear ROM was shown to outperform the linear ROM, better resolving the cycle-to-cyle differences in the hysteresis loops as a result of fluid-structure interactions, as well as nonlinear variations in minimum/maximum coefficient values and aerodynamic damping. Overall, the nonlinear ROM was able to predict the unsteady lift

and pitching moment coefficients over a range of reduced frequencies with $< 2\%$ mean error and standard deviation.

In Expt. 2.3, a generalized nonlinear ROM was generated to account for flight maneuver variations in angle of attack and Mach number. The angle-of-attack and sideslip angle indicial responses were sampled as a function of angle of attack and Mach number, whereas the rotation rate indicial responses were sampled only as a function of Mach number. This database of time-dependent indicial responses was interpolated using a kriging surrogate modeling toolbox to predict an indicial response for each point in a candidate test trajectory. Predictions were generated for a right turn flight test maneuver acquired from the NASA Armstrong Flight Research Center. The generalized ROM was shown to predict the longitudinal and lateral aerodynamic force and moment coefficients over the duration of the 36 second maneuver with a mean error and standard deviation below 1.4%.

Based on the maneuver predictions shown in Chapter 8, quantified assessments of computational cost and modeling accuracy were made for the aeroelastic indicial response ROM. In Expt. 3.1, the performance benefits of the ROM were compared to the full-order dynamic aeroelastic simulations. For the small-amplitude maneuver evaluations, the rigid and aeroelastic indicial response ROMs proved to be approximately 63 and 28 times cheaper than the full-order simulations. For the nonlinear ROM that included an angle-of-attack dependency, the computational cost for the rigid ROM was comparable to the full-order simulation costs, whereas the aeroelastic ROM was approximately three times more expensive. It is important to note that the total trajectory time simulated was on the order of five seconds. For a single 15 second maneuver within the sampled angle-of-attack range, the aeroelastic ROM would provide more efficient predictions relative to full-order simulations. Finally, the computational costs were estimated for generating a generalized nonlinear ROM applicable to the X-56A flight envelope, spanning 15 degrees in angle of attack over

the Mach envelope limits, resulting in 96 sampled flight conditions. The utility of the method was shown to increase with the number of maneuver evaluations to be made. These results highlight the efficiency of the unsteady aerodynamic ROM relative to full-order simulations, enabling aircraft designers to assess the performance of future flexible aircraft to a greater extent, potentially allowing for the discovering of unwanted performance issues prior to flight testing.

The final experiment sought to assess the performance of the proposed aeroelastic indicial response ROM compared to the traditional stability derivative method. In the process, a computationally efficient method was demonstrated for calculating traditional dynamic stability derivatives for flexible flight vehicles. The quasisteady stability derivative method was shown to predict the longitudinal and lateral force and moment coefficients for the slowly-varying right turn maneuver with comparable accuracy to the aeroelastic ROM but with six times less computational costs. These results support the historical use of the stability derivative method for aircraft maneuvering at low equivalent reduced frequencies. As for rapid maneuvers, the stability derivative method and ROM predictions were compared for a large-amplitude pitch oscillations at quasisteady, quasiunsteady, and unsteady reduced frequencies. Here, the ROM was shown to model the unsteady lift and pitching moment hysteresis loops with significantly more accuracy compared to the stability derivative method. These forced oscillations were characterized by cycle-to-cycle differences in aerodynamic damping and minimum and maximum coefficient values as a result of fluid-structure interactions. The aeroelastic indicial response ROM was able to accurately resolve these intricate variations in each cycle with mean error and standard deviation of $< 1.5\%$. These results highlight the ability of the unsteady aerodynamic ROM to outperform the traditional stability derivative method for flexible flight vehicles maneuvering at high rates of motion, a domain for which stability derivative models are especially unsuitable when accounting for vehicle flexibility.

In summary, these experiments revealed that the aeroelastic indicial response reduced-order model was capable of modeling the unsteady longitudinal and lateral force and moment coefficients encountered by a flexible vehicle maneuvering at various rates of motion, and thus partially or completely supported all hypotheses associated with the primary research questions posed in this dissertation.

10.1 Contributions

The central research objective of this work was to develop a reduced-order modeling approach capable of providing quantitatively accurate, yet computationally efficient predictions of the nonlinear, unsteady aerodynamics encountered by maneuvering, flexible flight vehicles. Linear and nonlinear formulations for the aeroelastic ROM were developed and demonstrated through experimental testing of the highly flexible X-56A Multi-Utility Technology Testbed aircraft. The contributions from the various components of this work are listed below:

- Development of a reduced-order modeling method for predicting the nonlinear, unsteady aerodynamics of flexible maneuvering flight vehicles.
- Identification of an efficient numerical solution strategy for dynamic modal aeroelastic simulations of flexible maneuvering flight vehicles.
- Improved understanding of the nonlinear, unsteady aerodynamic behavior of the flexible X-56A aircraft.
- Quantification of the performance benefits of multidisciplinary ROMs in comparison to traditional unsteady aerodynamics ROMs.
- Demonstration of a computationally efficient method for the calculation of traditional dynamic stability derivatives for flexible flight vehicles.

- Provide the first practical demonstration of FUN3D's multiple motion driver capability for rigid, deforming mesh simulations of fixed-wing aircraft.

10.2 Opportunities for Future Research

The indicial response reduced-order modeling approach has been successfully demonstrated as an enabler for viable virtual flight simulation predictions. The method was shown to outperform the traditional stability derivative method for a flexible flight vehicle maneuvering at quasisteady to unsteady forced oscillation motions, whereas the stability derivative predictions proved to be more efficient for a slowly-varying, 36 second right turn flight test maneuver. It is evident that both methods can provide utility within modern flight dynamic prediction frameworks. Integration of ROMs into current practice will require development of a methodology for mapping candidate flight test maneuvers to equivalent reduced frequencies, downselecting the appropriate prediction method (stability derivative of unsteady ROM), and assessing the flight space model sampling based on vehicle flexibility.

Furthermore, for future flight vehicle assessments, mesh-independent solutions should be identified and a mode sensitivity study should be conducted relative to coupled CFD-FEM predictions prior to model identification to ensure computational benefits are attained using an accurate system representation. However, it is important to note that the methodology is independent of the structural model used, and a coupled CFD-FEM full-order analysis may be used for ROM identification. Validation of FUN3D's multiple-motion driver for maneuvering, flexible fixed-wing simulations may provide insight to the limits of applying the linear modal structural solver.

For future applications, the aeroelastic indicial response ROM presented in this dissertation lays the foundation for efficient structural loads analysis and/or control law evaluation when combined with spatial reduced-order models. While vehicle-level

aerodynamic quantities were recorded due to step changes in the vehicle-state parameters defining a trajectory, microlevel aerodynamic quantities such as the primitive variables may also be recorded and predicted over time. As a means of reducing the computational costs and data storage requirements, spatial reduced-order models, such as Proper Orthogonal Decomposition, may be leveraged to consolidate the field variable distributions to a set of primitive 'modes' that can be recorded, predicted using indicial response theory, and recombined to estimate the load distributions of a vehicle over the course of a maneuver. Additionally, peak wing/body deflections may serve as outputs to characterize the structural performance of flexible vehicles.

Furthermore, the indicial response ROM method might be used to support efficient system identification. The traditional approach for characterizing the flight dynamics of a vehicle consists of simulating or experimental testing forced oscillations and using system identification (SysID) methods for estimating dynamic derivatives. In the case of numerical simulation, this approach can yield reasonable results, but the required computational resources can render it impractical for populating large databases. As shown in this dissertation, indicial response ROMs may be capable of providing dynamic derivatives directly, or in support of traditional approaches, may be used to generate efficient specialty input maneuvers for which system identification methods can be applied.

Additionally, it was previously believed that indicial response ROMs required asymptotic steady state convergence for application. As such, initial efforts toward generating indicial response predictions at unsteady prestall and stall flight conditions were quickly disregarded. The results in this dissertation show that the complex, periodic oscillations are physical representations of the system response due to flow unsteadiness. Because these indicial responses represent the memory of the system, such nonconverged responses are to be expected in unsteady flight regimes as a result of flow separation and vorticity effects. The primary research questions then

pertain to the computational costs required for unsteady response identification and the required length of motion history to be included for accurate predictions for stall recovery maneuvers.

Finally, because indicial response theory is generally applicable to all discrete-time, time-invariant systems, it may be used for any models governed by equations that fulfill these characteristics. In general, the majority of numerical simulations may be characterized as such systems. Using the nonlinear extension presented by kriging surrogate models, indicial response ROMs may be generated for predicting linear and weakly nonlinear systems. Using modern numerical simulation tools, any aerodynamic system or vehicle that is parameterized by grid motion may be investigated using indicial response theory as an efficient means of generating CFD simulation predictions. One example is the application to rotorcraft simulations. By parameterizing the blade speed, inclination, and/or position, the aerodynamic response may be isolated due to step changes in any of these step inputs. These responses may then be convolved to predict the unsteady aerodynamic loads during rotorcraft flight. With the increasing use of CFD simulations in engineering design and analysis, the benefits of indicial response theory should be leveraged for improving the efficiency of dynamic CFD simulations.

APPENDIX A

INDICIAL RESPONSE SAMPLING

A.1 Linear Forced Oscillations

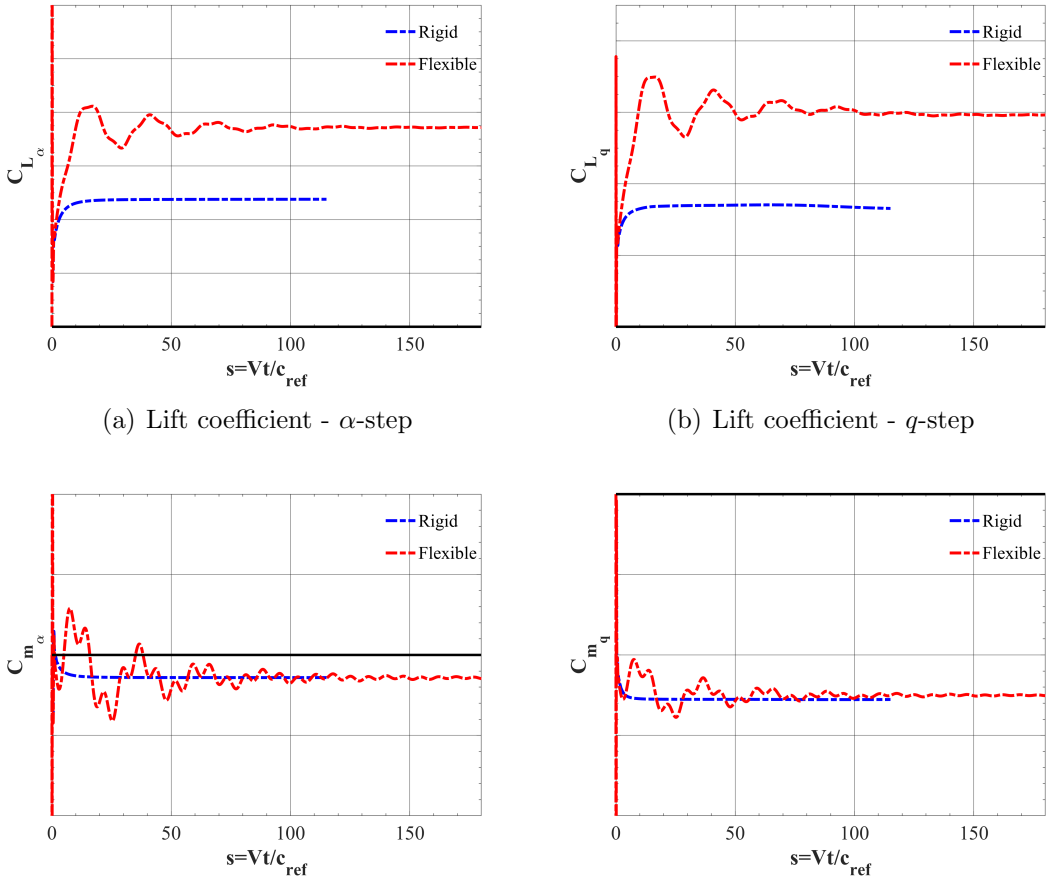

(a) Lift coefficient - α-step

(b) Lift coefficient - q-step

(c) Pitching moment coefficient - α-step

(d) Pitching moment coefficient - q-step

Figure 127: Lift (top) and pitching moment (bottom) coefficient indicial responses with respect to unit steps in angle of attack (left) and pitch rate (right) for the flexible (red) and rigid (blue) vehicles at $\alpha = 0°, \beta = 0°, M = 0.13$.

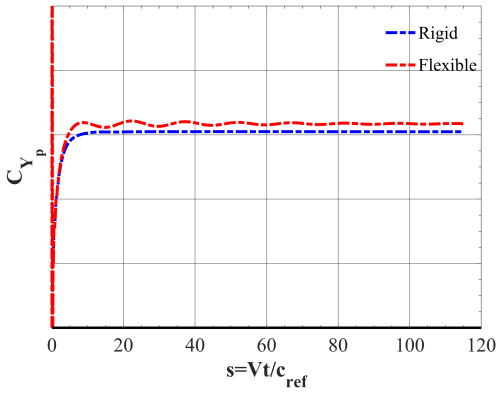

(a) Side force coefficient - p-step

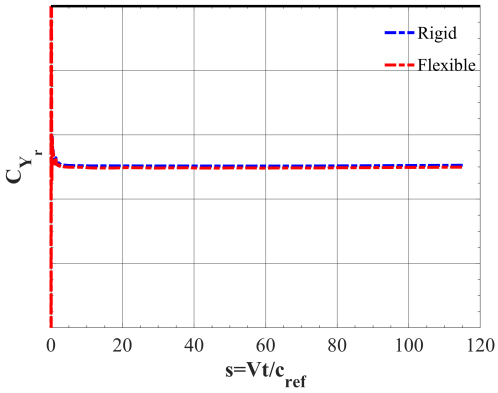

(b) Side force coefficient - r-step

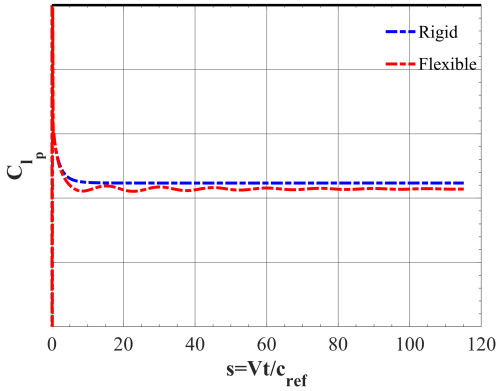

(c) Rolling moment coefficient - p-step

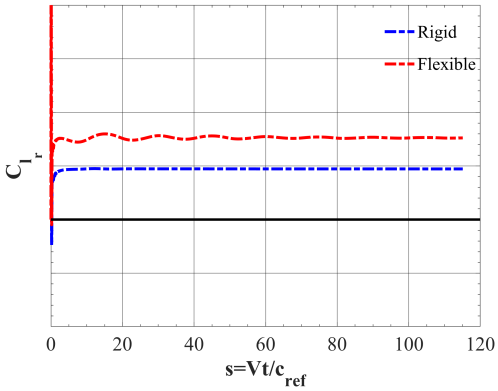

(d) Rolling moment coefficient - r-step

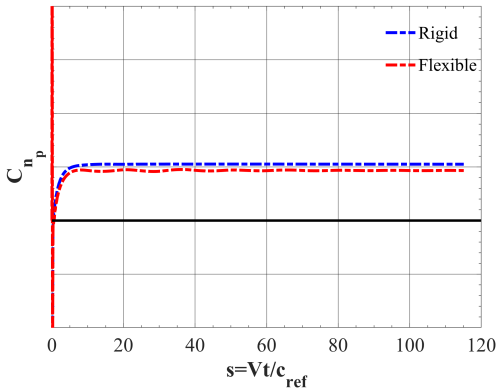

(e) Yawing moment coefficient - p-step

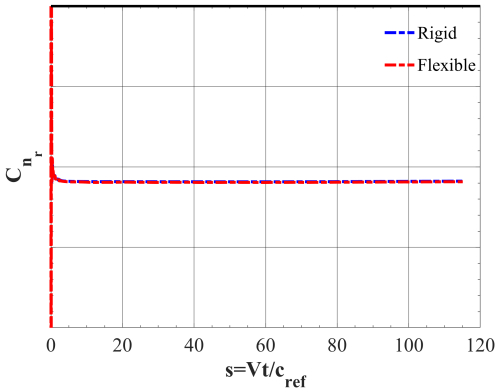

(f) Yawing moment coefficient - r-step

Figure 128: Side force (top), rolling moment (middle), and yawing moment (bottom) coefficient indicial responses with respect to unit steps in roll rate (left) and yaw rate (right) for the flexible (red) and rigid (blue) vehicle at $\alpha = 0°, \beta = 0°, M = 0.13$.

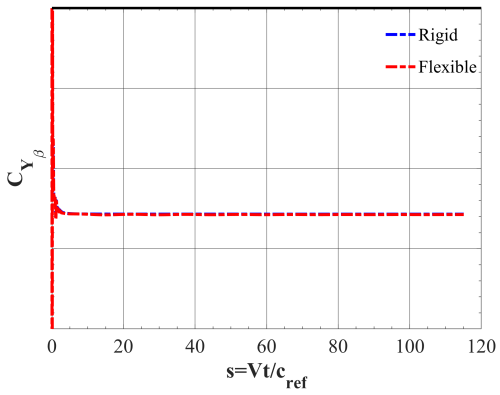

(a) Side force coefficient - β-step

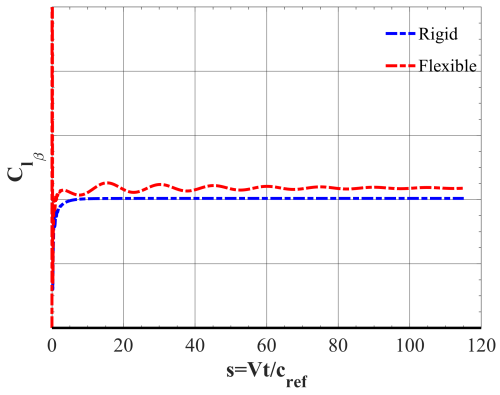

(b) Rolling moment coefficient - β-step

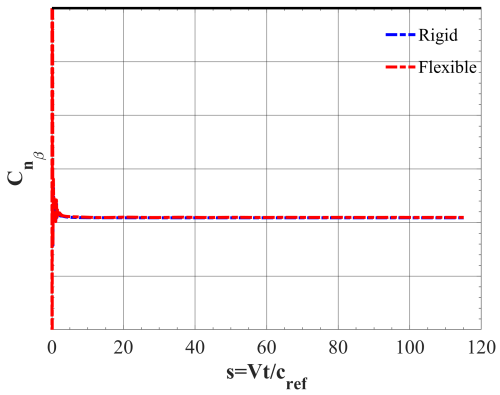

(c) Yawing moment coefficient - β-step

Figure 129: Side force (top), rolling moment (middle), and yawing moment (bottom) coefficient indicial responses with respect to a unit step in sideslip angle for the flexible (red) and rigid (blue) vehicle at $\alpha = 0°, \beta = 0°, M = 0.13$.

A.2 Nonlinear Forced Pitching Oscillation

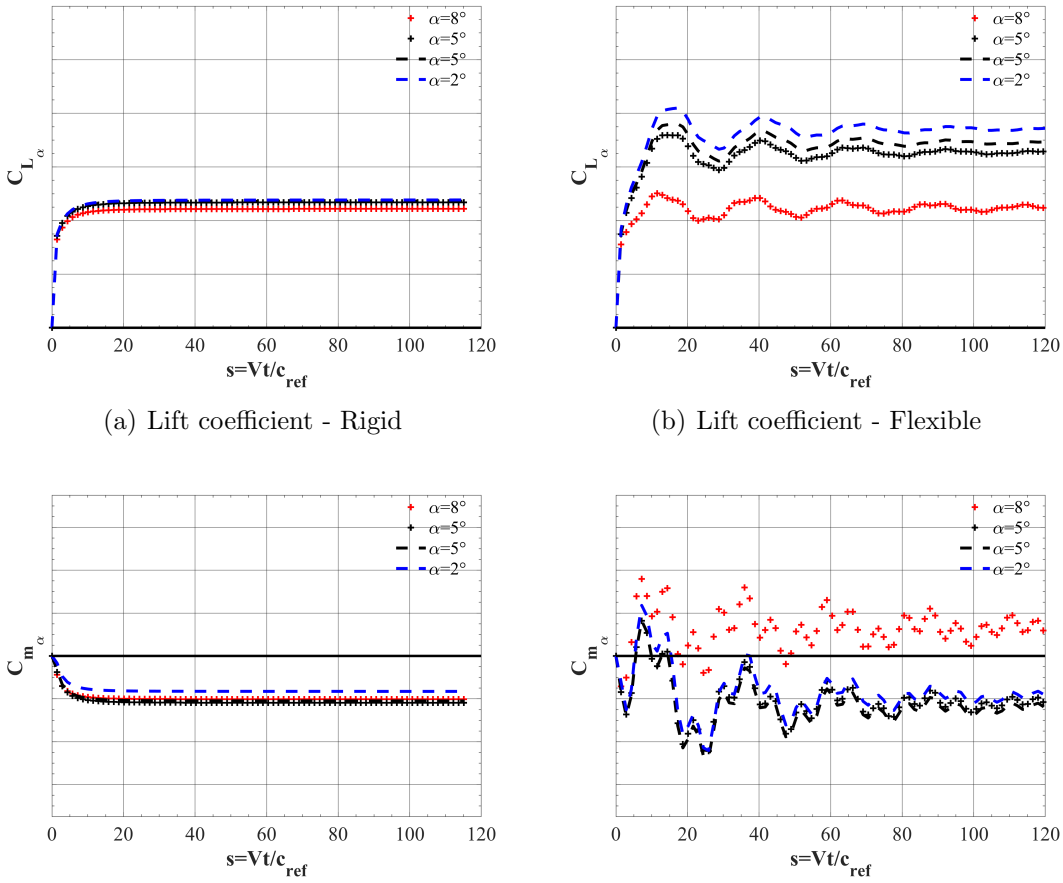

(a) Lift coefficient - Rigid

(b) Lift coefficient - Flexible

(c) Pitching moment coefficient - Rigid

(d) Pitching moment coefficient - Flexible

Figure 130: Lift (top) and pitching moment (bottom) coefficient indicial responses with respect to positive (+) and negative (dashed) steps in angle of attack for the rigid (left) and flexible (right) vehicle at $\alpha = 2°$, $5°$, and $8°$.

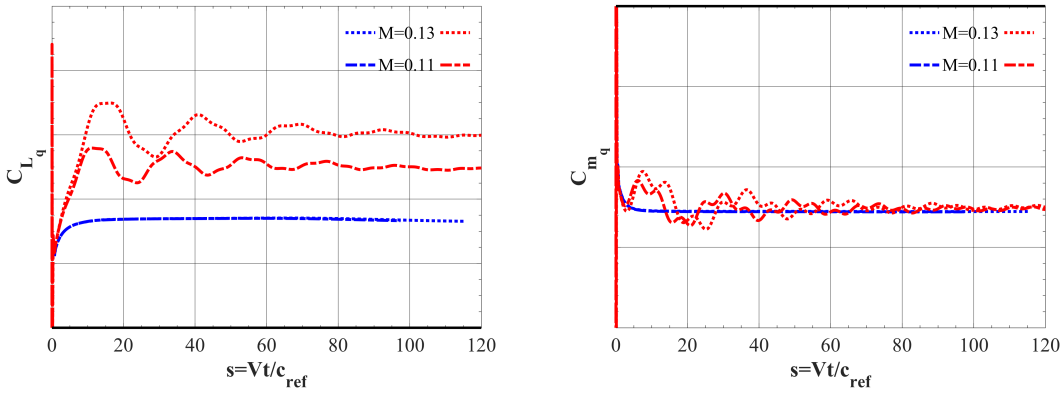

(a) Lift coefficient - q-step

(b) Pitching moment coefficient - q-step

Figure 131: Lift (left) and pitching moment (right) coefficient indicial responses with respect to unit step in pitch rate for the flexible (red) and rigid (blue) vehicles at $\alpha = 5°, \beta = 0°, M = 0.13$.

A.3 Right Turn Maneuver

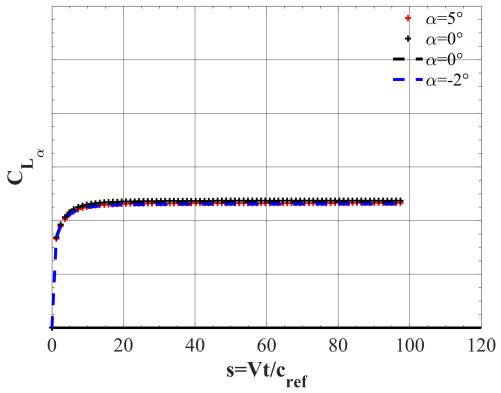

(a) Lift coefficient - $M = 0.11$

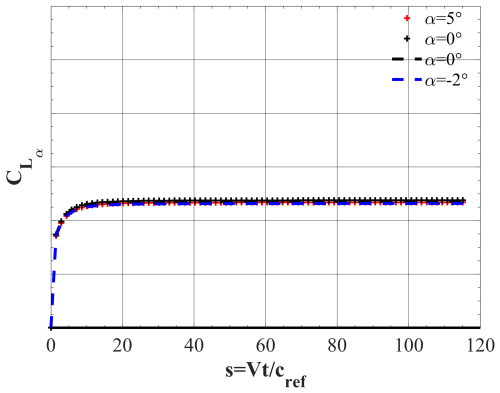

(b) Lift coefficient - $M = 0.13$

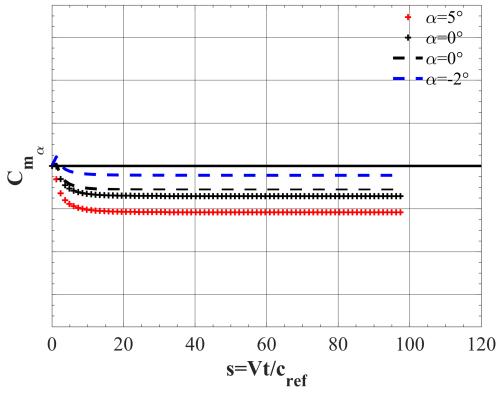

(c) Pitching moment coefficient - $M = 0.11$

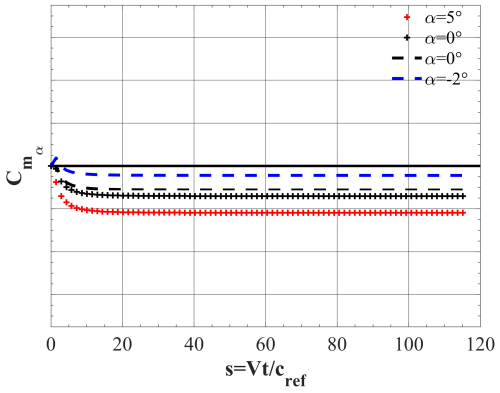

(d) Pitching moment coefficient - $M = 0.13$

Figure 132: Lift (top) and pitching moment (bottom) coefficient indicial responses with respect to positive (+) and negative (dashed) steps in angle of attack for the rigid vehicle at $\alpha = -2°$, $0°$, and $5°$, $M = 0.11$ (left) and 0.13 (right).

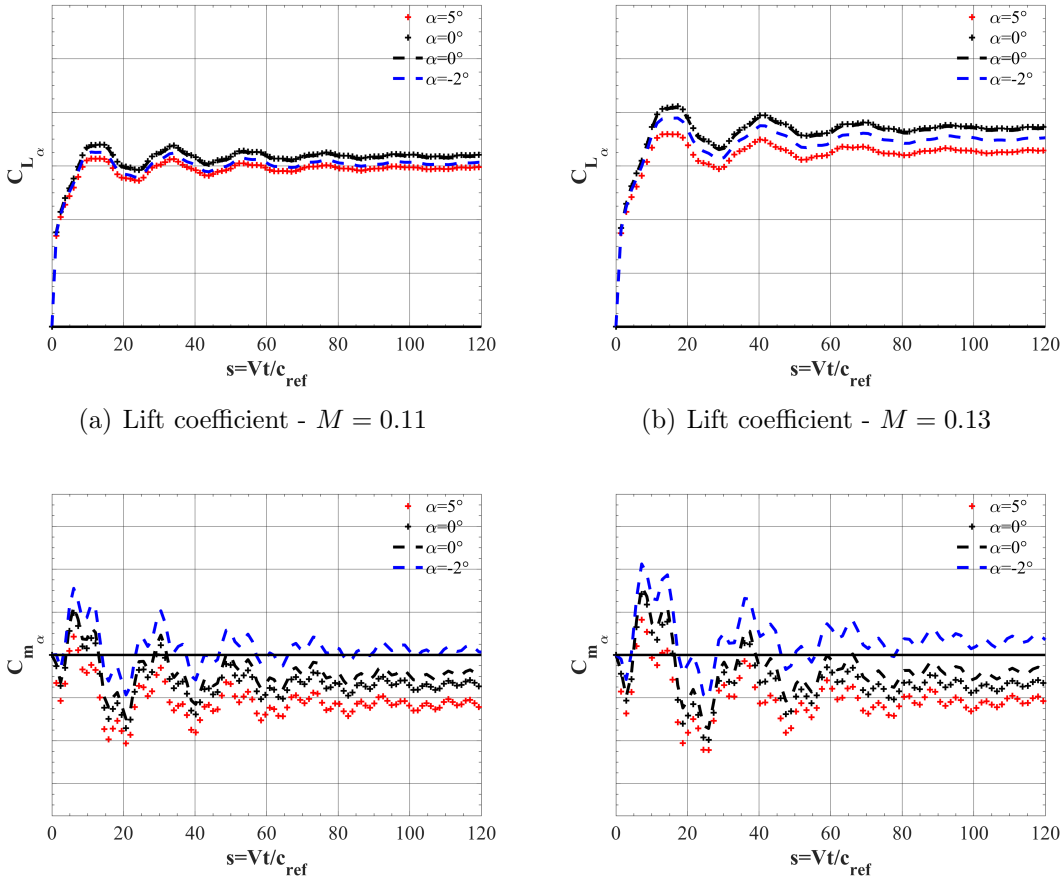

(a) Lift coefficient - $M = 0.11$

(b) Lift coefficient - $M = 0.13$

(c) Pitching moment coefficient - $M = 0.11$

(d) Pitching moment coefficient - $M = 0.13$

Figure 133: Lift (top) and pitching moment (bottom) coefficient indicial responses with respect to positive (+) and negative (dashed) steps in angle of attack for the flexible vehicle at $\alpha = -2°$, $0°$, and $5°$, $M = 0.11$ (left) and 0.13 (right).

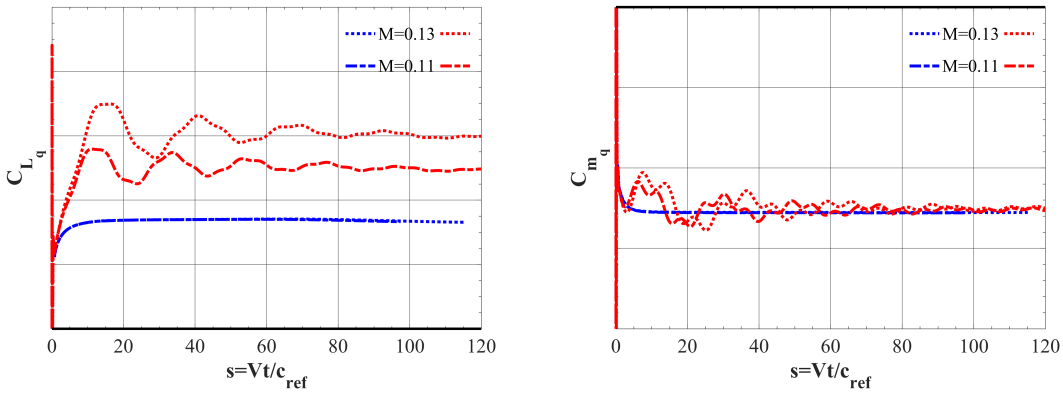

(a) Lift coefficient - q-step

(b) Pitching moment coefficient - q-step

Figure 134: Lift (left) and pitching moment (right) coefficient indicial responses with respect to unit step in pitch rate for the flexible (red) and rigid (blue) vehicles at $\alpha = 0°, \beta = 0°, M = 0.11$ and 0.13.

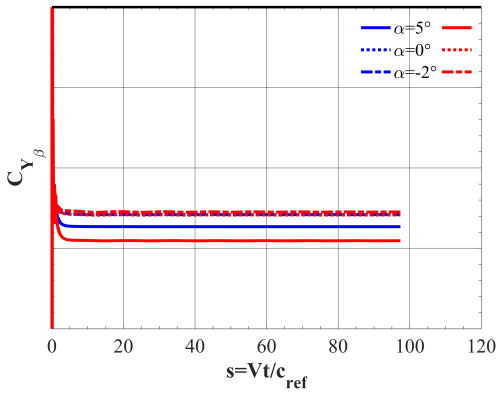

(a) Side force coefficient - $M = 0.11$

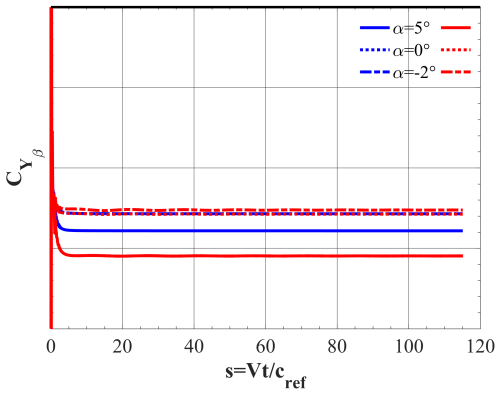

(b) Side force coefficient - $M = 0.13$

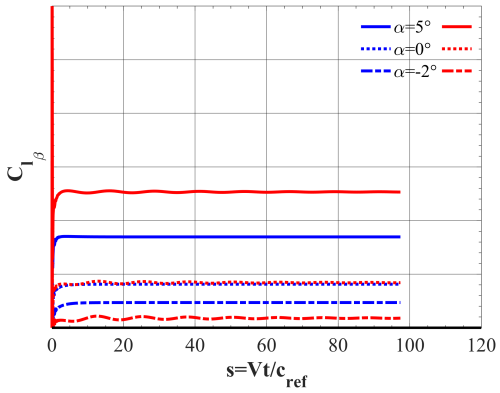

(c) Rolling moment coefficient - $M = 0.11$

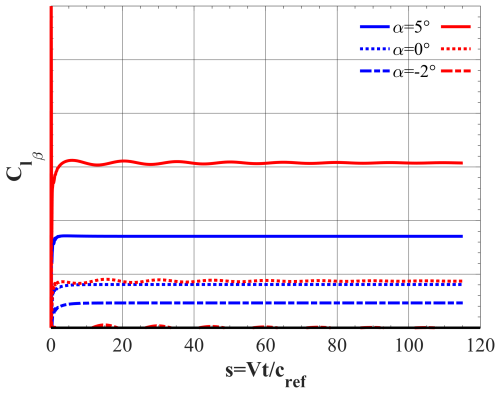

(d) Rolling moment coefficient - $M = 0.13$

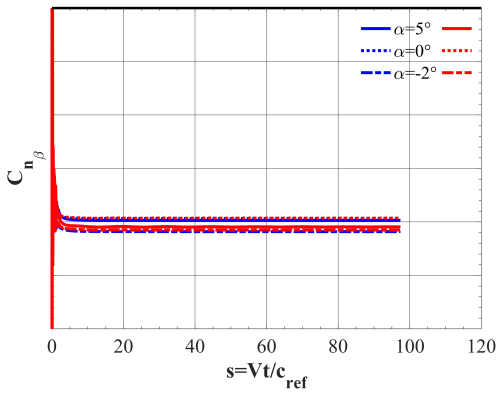

(e) Yawing moment coefficient - $M = 0.11$

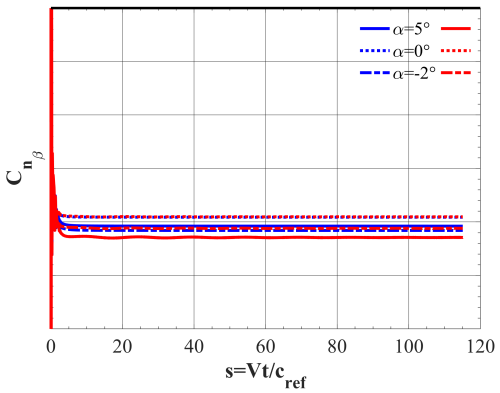

(f) Yawing moment coefficient - $M = 0.13$

Figure 135: Side force (top), rolling moment (middle), and yawing moment (bottom) coefficient indicial responses with respect to unit step in sideslip angle for the flexible (red) and rigid (blue) vehicles at $\alpha = 0°, \beta = 0°, M = 0.11$ (left) and 0.13 (right).

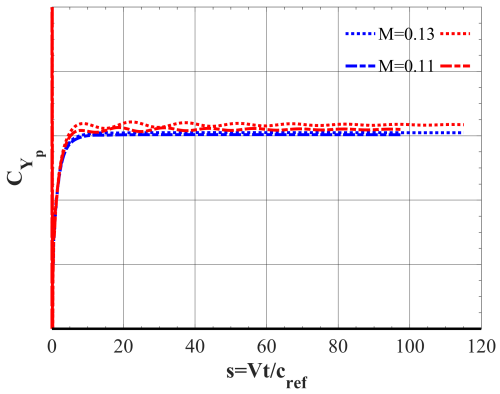

(a) Side force coefficient - p-step

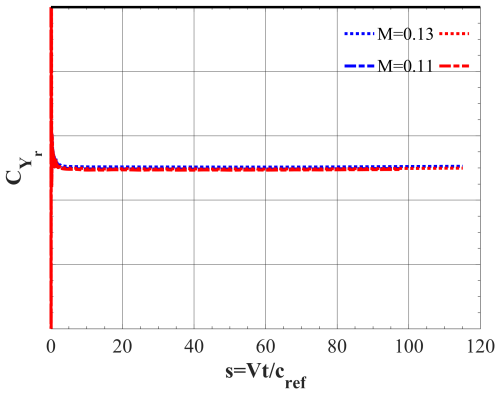

(b) Side force coefficient - r-step

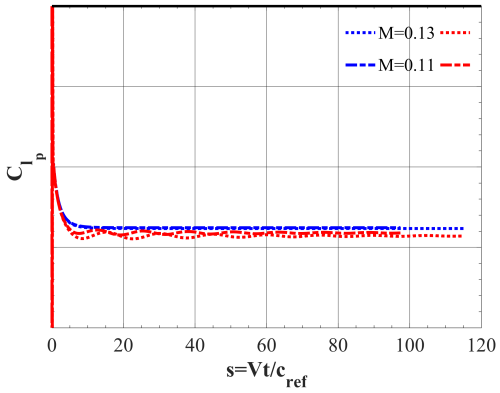

(c) Rolling moment coefficient - p-step

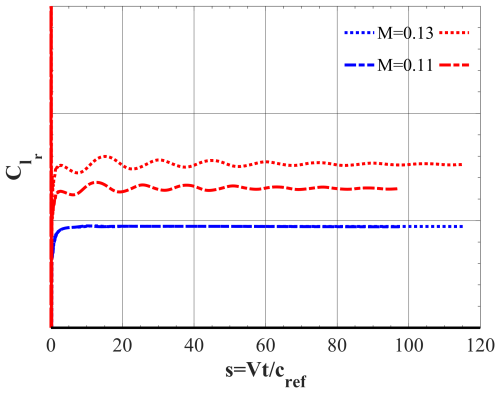

(d) Rolling moment coefficient - r-step

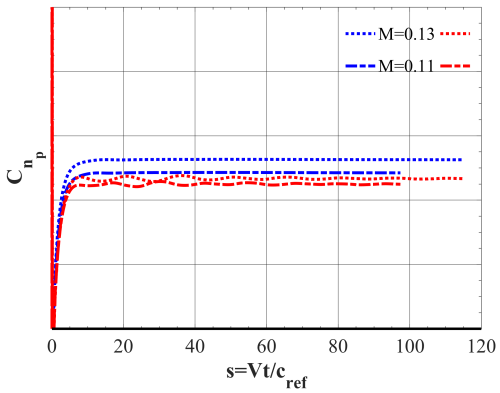

(e) Yawing moment coefficient - p-step

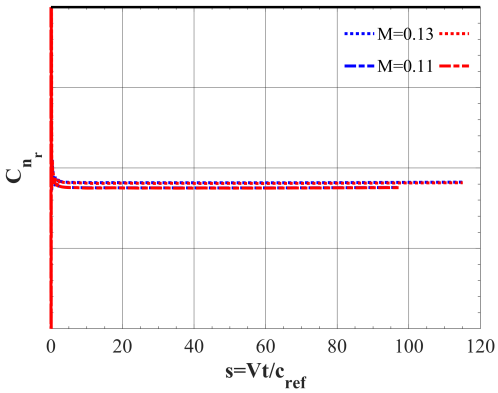

(f) Yawing moment coefficient - r-step

Figure 136: Side force (top), rolling moment (middle), and yawing moment (bottom) coefficient indicial responses with respect to unit step in roll (left) and yaw (right) rate for the flexible (red) and rigid (blue) vehicles at $\alpha = 0°, \beta = 0°, M = 0.11$ and 0.13.

REFERENCES

[1] Anderson, W. K. and Bonhaus, D. L., "An implicit upwind algorithm for computing turbulent flows on unstructured grids," *Computers & Fluids*, vol. 23, no. 1, pp. 1–21, 1994.

[2] Arevalo, S., Atwood, C., Bell, P., Blacker, T., Dey, S., Fisher, D., Fisher, D., Genalis, P., Gorski, J., Harris, A., and others, "A new dod initiative: The computational research and engineering acquisition tools and environments (create) program," in *Journal of Physics: Conference Series*, vol. 125, p. 012090, IOP Publishing, 2008.

[3] Babcock, D. A. and Arena, A., "Estimating aircraft stability derivatives through finite element analysis," *AIAA Paper*, vol. 5174, p. 2004, 2004.

[4] Balajewicz, M. and Dowell, E., "Reduced-order modeling of flutter and limit-cycle oscillations using the sparse volterra series," *Journal of Aircraft*, vol. 49, no. 6, pp. 1803–1812, 2012.

[5] Balajewicz, M., Nitzsche, F., and Feszty, D., "Application of multi-input volterra theory to nonlinear multidegree-of-freedom aerodynamic systems," *AIAA journal*, vol. 48, no. 1, p. 56, 2010.

[6] Ballhaus, W. and Goorjian, P., "Computation of unsteady transonic flows by the indicial method," *AIAA journal*, vol. 16, no. 2, pp. 117–124, 1978.

[7] Beranek, J., Nicolai, L., Buonanno, M., Burnett, E., Atkinson, C., Holm-Hansen, B., and Flick, P., "Conceptual design of a multi-utility aeroelastic demonstrator," *AIAA Paper 2010-9350*, pp. 1–15, 2010.

[8] Biedron, R. and Thomas, J., "Recent enhancements to the fun3d flow solver for moving-mesh applications," in *47th AIAA Aerospace Sciences Meeting including The New Horizons Forum and Aerospace Exposition*, p. 1360, 2009.

[9] Biedron, R., Vatsa, V., and Atkins, H., "Simulation of unsteady flows using an unstructured navier-stokes solver on moving and stationary grids," in *23rd AIAA Applied Aerodynamics Conference*, p. 5093, 2005.

[10] Biedron, R. T., Carlson, J.-R., Derlaga, J. M., Gnoffo, P. A., Hammond, D. P., Jones, W. T., Kleb, B., Lee-Rausch, E. M., Nielsen, E. J., Park, M. A., and others, "Fun3d manual: 13.3," 2018.

[11] Biedron, R. T., Carlson, J.-R., Derlaga, J. M., Gnoffo, P. A., Hammond, D. P., Jones, W. T., Kleb, W. L., Lee-Rausch, E. M., Nielsen, E. J., Park, M. A., and others, "Fun3d manual: 13.2," 2017.

[12] Bryan, G. H., *Stability in aviation: an introduction to dynamical stability as applied to the motions of aeroplanes*. Macmillan and Co., limited, 1911.

[13] Bryan, G. and Williams, W., "The longitudinal stability of aerial gliders," *Proceedings of the Royal Society of London*, vol. 73, pp. 100–116, 1904.

[14] Chambers, J. R. and Hall, R. M., "Historical review of uncommanded lateral-directional motions at transonic conditions," *Journal of Aircraft*, vol. 41, no. 3, pp. 436–447, 2004.

[15] Charlton, E. F., "Numerical stability and control analysis towards falling-leaf prediction capabilities of splitflow for two generic high-performance aircraft models," 1998.

[16] Chwalowski, P. and Heeg, J., "Fun3d analyses in support of the first aeroelastic prediction workshop," in *51st AIAA Aerospace Sciences Meeting including the New Horizons Forum and Aerospace Exposition*, p. 785, 2013.

[17] Cummings, R. M., Jirásek, A., Petterson, K., and Schmidt, S., "Saccon static and dynamic motion flow physics simulation using cobalt," *AIAA Paper*, vol. 4691, p. 2010, 2010.

[18] Cummings, R. M., Morton, S. A., and McDaniel, D. R., "Experiences in accurately predicting time-dependent flows," *Progress in Aerospace Sciences*, vol. 44, no. 4, pp. 241–257, 2008.

[19] Cummings, R. M. and Schutte, A., "An integrated computational/experimental approach to ucav stability & control estimation: overview of nato rto avt-161," *AIAA paper*, vol. 4392, p. 2010, 2010.

[20] Cummings, R. M. and Schütte, A., "The nato sto task group avt-201 on extended assessment of stability and control prediction methods for nato air vehicles," in *32nd AIAA Applied Aerodynamics Conference*, pp. 2014–2000, 2014.

[21] Da Ronch, A., Badcock, K., Wang, Y., Wynn, A., and Palacios, R., "Nonlinear model reduction for flexible aircraft control design," in *AIAA Atmospheric Flight Mechanics Conference*, p. 4404, 2012.

[22] Da Ronch, A., Vallespin, D., Ghoreyshi, M., and Badcock, K., "Computation of dynamic derivatives using cfd," in *28th Applied Aerodynamics Conference, AIAA-2010-4817, Chicago, Illinois*, 2010.

[23] Da Ronch, A., Vallespin, D., Ghoreyshi, M., and Badcock, K., "Evaluation of dynamic derivatives using computational fluid dynamics," *AIAA journal*, vol. 50, no. 2, pp. 470–484, 2012.

[24] Da Ronch, A., McCracken, A., Badcock, K., Ghoreyshi, M., and Cummings, R., "Modeling of unsteady aerodynamic loads," in *AIAA Atmospheric Flight Mechanics Conference*, p. 6524, 2011.

[25] Da Ronch, A., McCracken, A. J., Badcock, K. J., Widhalm, M., and Campobasso, M., "Linear frequency domain and harmonic balance predictions of dynamic derivatives," *Journal of Aircraft*, 2013.

[26] Da Ronch, A., Tantaroudas, N. D., Timme, S., and Badcock, K. J., "Model reduction for linear and nonlinear gust loads analysis," 2013.

[27] Dean, J. P., Clifton, J. D., Bodkin, D. J., and Ratcliff, J., "High resolution cfd simulations of maneuvering aircraft using the create-av/kestrel solver," *AIAA Paper 2011*, vol. 1109, 2011.

[28] Dowell, E. H., "A simple method for converting frequency domain aerodynamics to the time domain," 1980.

[29] Faller, W. E. and Schreck, S. J., "Neural networks: applications and opportunities in aeronautics," *Progress in Aerospace Sciences*, vol. 32, no. 5, pp. 433–456, 1996.

[30] Forsythe, J. R., Lynch, C. E., Polsky, S., and Spalart, P., "Coupled flight simulator and cfd calculations of ship airwake using hpcmp create-av kestrel," in *53th AIAA Aerospace Sciences Meeting, SciTech*, pp. 1–18, 2015.

[31] Frink, N. T., "Strategy for dynamic cfd simulations on saccon configuration," *AIAA paper*, vol. 4559, p. 2010, 2010.

[32] Frink, N. T., Hiller, B. R., Murphy, P. C., Cunningham, K., and Shah, G. H., "Investigation of reduced-order modeling for aircraft stability and control prediction," in *AIAA Scitech 2019 Forum*, p. 0980, 2019.

[33] Garrick, I., "On some reciprocal relations in the theory of nonstationary flows," 1938.

[34] Ghoreyshi, M., Badcock, K., Da Ronch, A., Marques, S., Swift, A., and Ames, N., "Framework for establishing the limits of tabular aerodynamic models for flight dynamics analysis," *Journal of Aircraft*, vol. 48, no. 1, pp. 42–55, 2011.

[35] Ghoreyshi, M. and Cummings, R. M., "Aerodynamics modeling of a maneuvering aircraft using indicial functions," in *50th AIAA Aerospace Sciences Meeting*, pp. 2012–689, 2012.

[36] Ghoreyshi, M. and Cummings, R. M., "Challenges in the aerodynamics modeling of an oscillating and translating airfoil at large incidence angles," *Aerospace Science and Technology*, vol. 28, no. 1, pp. 176–190, 2013.

[37] Ghoreyshi, M. and Cummings, R. M., "Unsteady aerodynamic modeling of aircraft control surfaces by indicial response methods," *AIAA journal*, 2014.

[38] Ghoreyshi, M. and Cummings, R. M., "Unsteady aerodynamics modeling for aircraft maneuvers: A new approach using time-dependent surrogate modeling," *Aerospace Science and Technology*, vol. 39, pp. 222–242, 2014.

[39] Ghoreyshi, M., Frink, N. T., van Rooij, M., Lofthouse, A. J., Cummings, R. M., and Nayani, S., "Collaborative evaluation of cfd-to-rom dynamic modeling," in *at AIAA Science and Technology Forum and Exposition (SciTech 2016), San Diego, California*, 2016.

[40] Ghoreyshi, M., Jirásek, A., and Cummings, R. M., "Computational investigation into the use of response functions for aerodynamic-load modeling," *AIAA journal*, vol. 50, no. 6, pp. 1314–1327, 2012.

[41] Ghoreyshi, M., Jirásek, A., and Cummings, R. M., "Computational approximation of nonlinear unsteady aerodynamics using an aerodynamic model hierarchy," *Aerospace Science and Technology*, vol. 28, no. 1, pp. 133–144, 2013.

[42] Ghoreyshi, M., Jirásek, A., and Cummings, R. M., "Reduced order unsteady aerodynamic modeling for stability and control analysis using computational fluid dynamics," *Progress in Aerospace Sciences*, vol. 71, pp. 167–217, 2014.

[43] Ghoreyshi, M., Post, M. L., and Cummings, R. M., "Cfd calculation of aerodynamic indicial functions for a generic fighter configuration," *Journal of Aircraft*, vol. 30, no. 5, pp. 660–668, 2012.

[44] Ghoreyshi, M., Post, M. L., Cummings, R. M., Da Ronch, A., and Badcock, K. J., "Transonic aerodynamic loads modeling of x-31 aircraft," 2012.

[45] Ghoreyshi, M., Vallespin, D., Da Ronch, A., Badcock, K., Vos, J., and Hitzel, S., "Simulation of aircraft manoeuvres based on computational fluid dynamics," *AIAA paper*, vol. 8239, 2010.

[46] Godfrey, A. G. and Cliff, E. M., "Direct calculation of aerodynamic force derivatives-a sensitivity-equation approach," *AIAA Paper*, vol. 393, p. 1998, 1998.

[47] Greenberg, H., "Determination of stability derivatives from flight data," *Journal of the Aeronautical Sciences*, vol. 16, no. 1, 1949.

[48] Greenberg, H., "A survey of methods for determining stability parameters of an airplane from dynamic flight measurements," 1951.

[49] Greenwell, D. I., "A review of unsteady aerodynamic modelling for flight dynamics of manoeuvrable aircraft," *AIAA paper*, vol. 5276, p. 2004, 2004.

[50] Hall, R. M., Biedron, R. T., Ball, D. N., Bogue, D. R., Chung, J., Green, B. E., and Chambers, J., "Computational methods for stability and control (comsac): the time has come," *AIAA paper*, vol. 6121, 2005.

[51] Jameson, A., "Computational aerodynamics for aircraft design.," *Science(Washington)*, vol. 245, no. 4916, pp. 361–371, 1989.

[52] Jones, R. T., "Operational treatment of the nonuniform-lift theory in airplane dynamics," 1938.

[53] Juang, J.-N., "Applied system identification," 1994.

[54] Juang, J.-N. and Pappa, R. S., "An eigensystem realization algorithm for modal parameter identification and model reduction," *Journal of Guidance*, vol. 8, no. 5, pp. 620–627, 1985.

[55] Juang, J.-N., Phan, M., Horta, L. G., and Longman, R. W., "Identification of observer/kalman filter markov parameters: theory and experiments," *Journal of Guidance, Control, and Dynamics*, vol. 16, no. 2, pp. 320–329, 1993.

[56] Kim, T., "Efficient reduced-order system identification for linear systems with multiple inputs," *AIAA journal*, vol. 43, no. 7, p. 1455, 2005.

[57] Kim, T., Hong, M., Bhatia, K. G., and SenGupta, G., "Aeroelastic model reduction for affordable computational fluid dynamics-based flutter analysis," *AIAA journal*, vol. 43, no. 12, p. 2487, 2005.

[58] Klein, V., Murphy, P. C., Curry, T. J., and Brandon, J. M., "Analysis of wind tunnel longitudinal static and oscillatory data of the f-16xl aircraft," 1997.

[59] Kroll, N., Abu-Zurayk, M., Dimitrov, D., Franz, T., Führer, T., Gerhold, T., Görtz, S., Heinrich, R., Ilic, C., Jepsen, J., and others, "Dlr project digital-x: towards virtual aircraft design and flight testing based on high-fidelity methods," *CEAS Aeronautical Journal*, vol. 7, no. 1, pp. 3–27, 2016.

[60] Kurdila, A. J., Prazenica, R. J., Rediniotis, O., and Strganac, T., "Multiresolution methods for reduced-order models for dynamical systems," *Journal of Guidance, Control, and Dynamics*, vol. 24, no. 2, pp. 193–200, 2001.

[61] Küssner, H. G., "Zusammenfassender bericht über den instationären auftrieb von flügeln," *Luftfahrtforschung*, vol. 13, no. 12, pp. 410–424, 1936.

[62] Le Roy, J. F. and Morgand, S., "Saccon cfd static and dynamic derivatives using elsa," in *28th AIAA Applied Aerodynamics Conference*, p. 4562, 2010.

[63] Leishman, J., "Indicial lift approximations for two-dimensional subsonic flow as obtained from oscillatory measurements," *Journal of Aircraft*, vol. 30, no. 3, pp. 340–351, 1993.

[64] Li, W. W. and Pak, C.-G., "Aeroelastic optimization study based on the x-56a model," *AIAA Paper 2014-2052*, pp. 1–21, 2014.

[65] Li, W. W. and Pak, C.-G., "Mass balancing optimization study to reduce flutter speeds of the x-56a aircraft," *Journal of Aircraft*, pp. 1–21, 2014.

[66] Limache, A. and Cliff, E., "Aerodynamic sensitivity theory for rotary stability derivatives," *Journal of aircraft*, vol. 37, no. 4, pp. 676–683, 2000.

[67] Lophaven, S. N., Nielsen, H. B., and Søndergaard, J., *DACE: a Matlab kriging toolbox*, vol. 2. Citeseer, 2002.

[68] Lucia, D. J. and Beran, P. S., "Reduced-order model development using proper orthogonal decomposition and volterra theory," *AIAA journal*, vol. 42, no. 6, 2004.

[69] Mader, C. A. and Martins, J. R., "Computation of aircraft stability derivatives using an automatic differentiation adjoint approach," *AIAA journal*, vol. 49, no. 12, pp. 2737–2750, 2011.

[70] Mader, C. A., *Stability-Constrained Aerodynamic Shape Optimization with Applications to Flying Wings*. PhD thesis, University of Toronto (Canada), 2012.

[71] Magnus, R., "Calculations of some unsteady transonic flows about the naca 64a006 and 64a010 airfoils," tech. rep., GENERAL DYNAMICS SAN DIEGO CA CONVAIR DIV, 1977.

[72] Mangalam, S. M. and Brenner, M. J., "Fly-by-feel sensing and control: Aeroservoelasticity," *AIAA Paper 2014-2189*, pp. 1–8, 2014.

[73] Mavris, D. N., DeLaurentis, D. A., Bandte, O., and Hale, M. A., "A stochastic approach to multi-disciplinary aircraft analysis and design," in *36th Aerospace Sciences Meeting & Exhibit, Reno, NV*, 1998.

[74] Mazelsky, B., "Determination of indicial lift and moment of a two-dimensional pitching airfoil at subsonic mach numbers from oscillatory coefficients with numerical calculations for a mach number of 0.7," tech. rep., NATIONAL AERONAUTICS AND SPACE ADMINISTRATION WASHINGTON DC, 1952.

[75] Mazelsky, B. and Drischler, J. A., "Numerical determination of indicial lift and moment functions for a two-dimensional sinking and pitching airfoil at mach numbers 0.5 and 0.6," tech. rep., NATIONAL AERONAUTICS AND SPACE ADMINISTRATION WASHINGTON DC, 1952.

[76] McCracken, A., Akram, U., Da Ronch, A., and Badcock, K., "Requirements for computer generated aerodynamic models for aircraft stability and control analysis," 2012.

[77] McCracken, A. J., Kennett, D. J., Badcock, K. J., and Da Ronch, A., "Assessment of tabular models using cfd," in *AIAA Atmospheric Flight Mechanics (AFM) Conference*, p. 4978, 2013.

[78] McDaniel, D., Tuckey, T., and Morton, S. A., "Multiple bodies, motion, and mash-ups: Handling complex use-cases with kestrel," *AIAA paper*, vol. 415, pp. 13–17, 2014.

[79] McDaniel, D. R., Sears, D. R., Tuckey, T. R., Tillman, B., and Morton, S. A., "Aerodynamic control surface implementation in kestrel v2. 0," *AIAA Paper*, vol. 1175, pp. 4–7, 2011.

[80] Meakin, R., Atwood, C., and Hariharan, N., "Development, deployment, and support of a set of multi-disciplinary, physics-based simulation software products aiaa paper 2011-1104," in *49th AIAA Aerospace Sciences Meeting, january*, vol. 15, 2011.

[81] Mialon, B., Khrabov, A., Da Ronch, A., Cavagna, L., Zhang, M., and Ricci, S., "Benchmarking the prediction of dynamic derivatives: Wind tunnel tests, validation, acceleration methods," in *28th AIAA Applied Aerodynamics Conf., Chicago, AIAA Paper*, vol. 8244, p. 2010, 2010.

[82] Mialon, B., Khrabrov, A., Khelil, S. B., Huebner, A., Da Ronch, A., Badcock, K., Cavagna, L., Eliasson, P., Zhang, M., Ricci, S., and others, "Validation of numerical prediction of dynamic derivatives: The dlr-f12 and the transcruiser test cases," *Progress in Aerospace Sciences*, vol. 47, no. 8, pp. 674–694, 2011.

[83] Morton, S., Eymann, T., McDaniel, D., Sears, D., Tillman, B., and Tuckey, T., "Rigid and maneuvering results with control surface and 6dof motion for kestrel v2," in *49th AIAA Aerospace Sciences Meeting including the New Horizons Forum and Aerospace Exposition*, p. 1106, 2011.

[84] Morton, S. A., Eymann, T. A., Lamberson, S., McDaniel, D. R., Sears, D. R., Utrilla, J., and Tuckey, T. R., "Relative motion simulations using an overset multimesh paradigm with kestrel v3," *AIAA paper*, vol. 712, pp. 9–12, 2012.

[85] Morton, S. A., Lamberson, S. E., and McDaniel, D. R., "Static and dynamic aeroelastic simulations using kestrel-a create aircraft simulation tool," *AIAA Paper 2012-1800*, 2012.

[86] Morton, S. A., McDaniel, D. R., Sears, D., Tillman, B., and Tuckey, T., "Rigid, maneuvering, and aeroelastic results for kestrel-a create simulation tool," *AIAA Paper 2010*, vol. 1233, 2010.

[87] Morton, S. A., McDaniel, D. R., Sears, D. R., Tillman, B., and Tuckey, T. R., "Kestrel v2. 0–6dof and control surface additions to a create simulation tool," *AIAA Paper 2010*, vol. 511, 2010.

[88] Morton, S. A., Tillman, B., McDaniel, D. R., Sears, D. R., and Tuckey, T. R., "Kestrel–a fixed wing virtual aircraft product of the create program," in *DoD High Performance Computing Modernization Program Users Group Conference (HPCMP-UGC), 2009*, pp. 148–152, IEEE, 2009.

[89] Nicolai, L., Hunten, K., Zink, S., and Flick, P., "System benefits of active flutter suppression for a sensorcraft-type vehicle," *AIAA Paper 2010-9349*, pp. 1–12, 2010.

[90] Pagliuca, G. and Timme, S., "Model reduction for flight dynamics simulations using computational fluid dynamics," *Aerospace Science and Technology*, vol. 69, pp. 15–26, 2017.

[91] Pak, C.-G. and Truong, S., "Creating a test validated finite-element model of the x-56a aircraft structure," *Journal of Aircraft*, pp. 1–24, 2014.

[92] Pak, C.-G. and Truong, S., "Creating a test validated structural dynamic finite element model of the x-56a aircraft," *AIAA Paper 2014-3157*, pp. 1–39, 2014.

[93] Park, M. A. and Green, L. L., "Steady-state computation of constant rotational rate dynamic stability derivatives," *AIAA paper*, vol. 4321, p. 2000, 2000.

[94] Park, M. A., Green, L. L., Montgomery, R. C., and Raney, D. L., "Determination of stability and control derivatives using computational fluid dynamics and automatic differentiation," 1999.

[95] Phillips, W. H., "Flying qualities from early airplanes to the space shuttle," *Journal of Aircraft*, vol. 12, no. 4, 1989.

[96] Prazenica, R., Kurdila, A., and Silva, W., "Multiresolution methods for representation of volterra series and dynamical systems," in *41st Structures, Structural Dynamics, and Materials Conference and Exhibit*, p. 1754, 2000.

[97] Raveh, D. E., "Reduced-order models for nonlinear unsteady aerodynamics," *AIAA journal*, vol. 39, no. 8, pp. 1417–1429, 2001.

[98] Raveh, D. E., "Identification of computational-fluid-dynamics based unsteady aerodynamic models for aeroelastic analysis," *Journal of Aircraft*, vol. 41, no. 3, pp. 620–632, 2004.

[99] Raveh, D. E., Levy, Y., and Karpel, M., "Aircraft aeroelastic analysis and design using cfd-based unsteady loads," *AIAA Paper*, vol. 1325, p. 2000, 2000.

[100] Raveh, D. E., Levy, Y., and Karpel, M., "Efficient aeroelastic analysis using computational unsteady aerodynamics," *Journal of Aircraft*, vol. 38, no. 3, pp. 547–556, 2001.

[101] Reasor, D. A., Bhamidipati, K. K., and Chin, A. W., "X-56a aeroelastic flight test predictions," in *54th AIAA Aerospace Sciences Meeting*, p. 1053, 2016.

[102] Reisenthel, P. H., "Development of a nonlinear indicial model using response functions generated by a neural network (in order to predict dynamics of maneuvering aircraft and missiles)," 1997.

[103] Reisenthel, P. H., "Prediction of unsteady aerodynamic forces via nonlinear kernel identification," in *International forum on aeroelasticity and structural dynamics*, 1999.

[104] Reisenthel, P. H. and Bettencourt, M. T., "Data-based aerodynamic modeling using nonlinear indicial theory," *AIAA paper*, pp. 99–0763, 1999.

[105] Ripepi, M., Verveld, M., Karcher, N., Franz, T., Abu-Zurayk, M., Görtz, S., and Kier, T., "Reduced-order models for aerodynamic applications, loads and mdo," *CEAS Aeronautical Journal*, pp. 1–23, 2018.

[106] Roth, G. L., Livingston, J. W., Blair, M., and Kolonay, R., "Create-av davinci: Computationally based engineering for conceptual design," *AIAA 2010*, vol. 1232, 2010.

[107] Salas, M., "Digital flight: The last cfd aeronautical grand challenge," *Journal of Scientific Computing*, vol. 28, no. 2, pp. 479–505, 2006.

[108] Samareh, J., "Discrete data transfer technique for fluid-structure interaction," in *18th AIAA Computational Fluid Dynamics Conference*, p. 4309, 2007.

[109] Sankaran, V., Sitaraman, J., Wissink, A., Datta, A., Jayaraman, B., Potsdam, M., Mavriplis, D., Yang, Z., O'Brien, D., Saberi, H., and others, "Application of the helios computational platform to rotorcraft flowfields," *AIAA paper*, vol. 1230, p. 2010, 2010.

[110] Sears, W. R., "Some aspects of non-stationary airfoil theory and its practical application," *Journal of the Aeronautical Sciences*, vol. 8, no. 3, pp. 104–108, 1941.

[111] Shelton, A. B., Martin, C., and Silva, W. A., "Computing aerodynamic damping of a generic missile with cfd," in *2018 AIAA Aerospace Sciences Meeting*, p. 0535, 2018.

[112] Silva, W., "Identification of nonlinear aeroelastic systems based on the volterra theory: progress and opportunities," *Nonlinear Dynamics*, vol. 39, no. 1, pp. 25–62, 2005.

[113] Silva, W. A., "Application of nonlinear systems theory to transonic unsteady aerodynamic responses," *Journal of Aircraft*, vol. 30, no. 5, pp. 660–668, 1993.

[114] Silva, W. A., "Extension of a nonlinear systems theory to general-frequency unsteady transonic aerodynamic responses," 1993.

[115] Silva, W. A., *Identification of linear and nonlinear aerodynamic impulse responses using digital filter techniques*. National Aeronautics and Space Administration, Langley Research Center, 1997.

[116] Silva, W. A., "Reduced-order models based on linear and nonlinear aerodynamic impulse responses," in *NASA CONFERENCE PUBLICATION*, pp. 369–380, NASA, 1999.

[117] Silva, W. A., "Recent enhancements to the development of cfd-based aeroelastic reduced-order models," in *Proceedings of the 48th AIAA/ASME/ASCE/AHS/ASC Structures, Structural Dynamics, and Materials Conference, April*, 2007.

[118] Silva, W. A., "Simultaneous excitation of multiple-input/multiple-output cfd-based unsteady aerodynamic systems," *Journal of Aircraft*, vol. 45, no. 4, pp. 1267–1274, 2008.

[119] Silva, W. A. and Bartels, R. E., "Development of reduced-order models for aeroelastic analysis and flutter prediction using the cfl3dv6. 0 code," *Journal of Fluids and Structures*, vol. 19, no. 6, pp. 729–745, 2004.

[120] Silva, W. A., Haji, M. R., and Prazenica, R. J., "Recent applications of the volterra theory to aeroelastic phenomena," 2005.

[121] Silva, W. A., *Discrete-time linear and nonlinear aerodynamic impulse responses for efficient CFD analyses*. The College of William and Mary, 1997.

[122] Singh, R. and Baeder, J. D., "Direct calculation of three-dimensional indicial lift response using computational fluid dynamics," *Journal of Aircraft*, vol. 34, no. 4, pp. 465–471, 1997.

[123] Skujins, T. and Cesnik, C. E., "Reduced-order modeling of unsteady aerodynamics across multiple mach regimes," *Journal of Aircraft*, vol. 51, no. 6, pp. 1681–1704, 2014.

[124] Suh, P. M., Chin, A. W., and Mavris, D. N., "Virtual deformation control of the x-56a model with simulated fiber optic sensors," *AIAA Paper 2013-4844*, pp. 1–32, 2013.

[125] Suh, P. M., Chin, A. W., and Mavris, D. N., "Robust modal filtering and control fo the x-56a model with simulated fiber optic sensor failures," *AIAA Paper 2014-2053*, pp. 1–27, 2014.

[126] Suh, P. M. and Mavris, D. N., "Modal filtering for control of flexible aircraft," *AIAA Paper 2013-1741*, pp. 1–38, 2013.

[127] Tantaroudas, N. D. and Da Ronch, A., "Nonlinear reduced-order aeroservoelastic analysis of very flexible aircraft," *Advanced UAV Aerodynamics, Flight Stability and Control: Novel Concepts, Theory and Applications*, p. 143, 2017.

[128] Theodorsen, T. and Mutchler, W., "General theory of aerodynamic instability and the mechanism of flutter," 1935.

[129] Thompson, J. R., Frink, N. T., and Murphy, P. C., "Guidelines for computing longitudinal dynamic stability characteristics of a subsonic transport," *AIAA paper*, vol. 4819, p. 2010, 2010.

[130] Tobak, M. and Chapman, G. T., "Nonlinear problems in flight dynamics involving aerodynamic bifurcations," 1985.

[131] Tobak, M., Chapman, G. T., and Schiff, L. B., "Mathematical modeling of the aerodynamic characteristics in flight dynamics," in *Proceedings of the Berkeley-Ames Conference on Nonlinear Problems in Control and Fluid Dynamics*, vol. 2, p. 435, Math Science Pr, 1984.

[132] Tormalm, M. and Schmidt, S., "Computational study of static and dynamic vortical flow over the delta wing saccon configuration using the foi flow solver edge," *AIAA paper*, vol. 4561, p. 2010, 2010.

[133] Volterra, V., "Theory of functionals and of integral and integro-differential equations," 1930.

[134] Wagner, H., "Über die entstehung des dynamischen auftriebes von tragflügeln," *ZAMM-Journal of Applied Mathematics and Mechanics/Zeitschrift für Angewandte Mathematik und Mechanik*, vol. 5, no. 1, pp. 17–35, 1925.